Multiphysics Modeling and Simulation of the Behavior of Cemented Tailings Backfill

submitted by

Liang Cui

under the supervision of

Dr. Mamadou Fall

Thesis submitted to the
Faculty of Graduate and Postdoctoral Studies
In partial fulfillment of the requirements
for the Doctorate in Philosophy degree in Civil Engineering

Department of Civil Engineering
Faculty of Engineering
University of Ottawa

May 2017

ABSTRACT

One of the most novel technologies developed in the past few decades is to convert mine wastes into cemented construction materials, otherwise known as cemented tailings backfill (CTB). CTB is an engineered mixture of tailings (waste aggregates), water and hydraulic binders. It is extensively used worldwide to stabilize underground cavities created by mining operations and maximize the recovery of ore from pillars. Moreover, the application of CTB is also an environmentally friendly means of disposing potential acid generating tailings underground. During and after its placement into underground mine excavations or stopes, complex multiphysics processes (including thermal, **T**, hydraulic, **H**, mechanical, **M**, and chemical, **C,** processes) take place in the CTB mass and thus control its behavior and performance. With the interaction of the multiphysics processes, the field variables (temperature, pore water pressure, stress and strain) and geotechnical properties of CTB undergo substantial changes. Therefore, the prediction of the field performance of CTB structures during their life time, which has great practical importance, must incorporate these THMC processes. Moreover, the self-weight effect, water drainage through barricades, thermal expansion and chemical shrinkage can contribute to the volumetric deformation of CTB. Consequently, CTB exhibits unique consolidation behavior compared to conventional geomaterials (e.g., soil). Furthermore, the consolidation processes can result in relative displacement between the rock mass and CTB. The resultant rock mass/CTB interface resistance can reduce the effects of the overburden pressure or the vertical stress (i.e., arching effect). Hence, a full understanding, through multiphysics modeling and simulation of CTB behaviors, is crucial to reliably assess and predict the performance of CTB structures. Yet, there are currently no models or tools to predict the fully coupled multiphysics behavior of CTB. In this Ph.D. study, a series of mathematical models which include an evolutive elastoplastic model, a fully coupled THMC model, a multiphysics model of consolidation behavior and a multiphysics model of the interaction between the rock mass/CTB interface are developed and validated. There is excellent agreement between the modeled results and experimental and/or in-situ monitored data, which proves the accuracy and predictive ability of the developed models. Furthermore, the validated multiphysics models are applied to a series of engineering issues, which are relevant for the field design of CTB structures, to investigate the self-desiccation process, consolidation behavior of CTB structures as well as to assess the pressure on barricades and the strength development in CTB structures. The obtained results show that CTB has different behaviors and performances under different backfilling conditions and design strategies, and the developed multiphysics models

can accurately model CTB field behavior. Therefore, the research conducted in this Ph.D. study provides useful tools and technical information for the optimal design of CTB structures.

ACKNOWLEDGEMENT

First and foremost, I would like to express my immense and heartfelt appreciation and respect to my supervisor, Dr. Mamadou Fall, for his enduring support, guidance and encouragement that have helped me to overcome countless difficulties in both my academic and personal lives.

I would like to sincerely acknowledge Dr. Erman Evgin, Dr. Bahram Daneshfar, and Dr. Sai Vanapalli at the University of Ottawa, Dr. Paul Simms at the University of Carleton, and Dr. Amit Kumar Verma at the Indian Institute of Technology Dhanbad for their invaluable feedback and advice towards my research. I am truly grateful to all of you.

I also thank Mr. Jean Claude Célestin, for his advice, technical support and assistance throughout this research study. I would like to express my gratitude to my colleagues for all of their continuous support and encouragement.

Lastly, I want to thank my family, for their unconditional love, frequent reassurance, and tremendous patience with me during all these years.

Table of Contents

List of Figures

List of Tables

List of Symbols and Abbreviations

A =material constant used to predict I_{b2};
A_{const1}, A_{const2}, A_{const3} =hydration model parameters;
A_E = material constant of elastic modulus model;
A_{p1}, A_{p2}, A_{p3} =constants used for prediction of CTE of cement paste;
a_1, a_2, a_3 =model parameters of MSDPu yield function;
a_{TC}, b_{TC}, c_{TC} =material constants of TC model;
$a_{\psi 1}$, $a_{\psi 2}$ =fitting parameters of CTB dilation angle;
B_1, B_2 =fitting parameters of cement paste CTE;
B_C =stop width;
$B_{\upsilon 1}$, $B_{\upsilon 2}$, $B_{\upsilon 3}$, $B_{\upsilon 4}$, $B_{\upsilon 5}$ =fitting parameters of Poisson's ratio model;
b =ratio of the locus size of MSDPu model;
b_i =fitting constant (i =1 to 10) of hardening/softening parameter;
$b_{\psi 1}$, $b_{\psi 2}$, $b_{\psi 3}$ =fitting parameters of CTB dilation angle;
C =specific heat capacity;
C_b =apparent binder density;
C_c =compressibility;
C_i =specific heat capacity (i refers to air, water and solid);
C_{intf} =material parameters of D-P criterion;
C_m =binder content;
C_K, D_K =material constants of saturated hydraulic conductivity model;
C_{K1}, C_{K2} =material constants used to predict K_{sat};
C_{Pw} =isothermal compression modulus of water;
C_V =coefficient of consolidation;
C_v =specific heat of CTB;
C_Y =parameter of yield function;
c =cohesion;
c_0 =reference temperature for gas;
c_B =cohesion of CTB;
c_{B1}, c_{B2} =fitting parameters of CTB cohesion model;
c_i =cohesion of CTB (Pa) in i direction;
c_{intf} =interface adhesion;
c_{n1}, c_{n2} =fitting parameters of interface normal stiffness;
c_{s1}, c_{s2}, c_{s3} =fitting parameters of interface shear stiffness;
D =material parameter used to predict I_{b1};
D_1, D_2, D_3, D_4 =material parameters used to predict α_{D-P};
$\boldsymbol{D}^e$ =tangent elastic modulus;

$D_{\alpha 1}$, $D_{\alpha 2}$, $D_{\alpha 3}$, $D_{\alpha 4}$ =parameters of α_{D-P} in D-P model;
d = maturity constant;
d_1 , d_2 , d_3 , d_4 =fitting parameters used to predict D ;
d_{w1} , d_{w2} , d_{w3} , d_{w4} and d_{w5} =fitting parameters of water retention curve;
$d_{\alpha i}$ =fitting parameters of (i =1 to 10);
E =elastic modulus;
E_a =apparent activation energy;
E_p , $E_{tailings}$ =elastic modulus of cement paste and tailings;
E_{u_p} =ultimate stiffness of dense cement paste;
E_∞ =ultimate elastic modulus;
e =void ratio;
e_0 =initial void ratio;
F_{intf} =yield function of CTB/rock interface;
F_{scc} =yield function of SCC model;
F_δ , F_c =fitting parameters of interface friction angle and adhesion;
f_{m1} , f_{m2} , f_{m3} =fitting constants used to predict m_{WRC} ;
$f_{\alpha 1}$, $f_{\alpha 2}$ =fitting constants used to predict α_{WRC} ;
$f_{28\_20^\circ C}$ =compressive strength after curing for 28 days at 20°C;
f_{B1} , f_{B2} , f_{B3} , f_{B4} =fitting parameters of CTB stiffness;
f_{E0} , f_{E1} , f_{E2} , f_{E3} , f_{E4} =fitting parameters of CTB elastic modulus model;
f_c =compressive strength;
$f_{tailings}$, f_{uc} , f_{hp} , f_{uma} , f_{cap-w} , f_{cap-a} =volumetric ratio of tailings, unhydrated cement, hydration products, unhydrated mineral admixture, capillary water, capillary air with respect to total volume of CTB;
$\boldsymbol{g}$ =gravitational acceleration;
H_C =stope height;
H_c =total heat released by cement hydration;
H_{cem} =total heat available for cement;
H_m =total height of filled stope;
H_T =total heat available for binder hydration;
$h_{filling}$ =height of filled stope;
I_1 =first stress invariant;
I_a = I_1 at the intersecting point of the elliptical cap and I_1 axis;
I_b = I_1 at the intersecting point of the elliptical cap and I_1 axis;
I_{b1} = I_b related to plastic volumetric strain;
I_{b2} = I_b related to binder hydration;
I_c =intersecting point of two yield loci of MSDPu model;
J_2 =second deviatoric stress invariant;
K_b , K_s =bulk modulus of the porous media and solid phase (grain);
K^e =interface stiffness matrix;

K_s^e, K_n^e and K_t^e =shear, normal and tensile interface stiffness;
K_{earth} =coefficient of earth pressure;
K_i =coefficient of earth pressure in i direction;
K_{sat} =saturated hydraulic conductivity of CTB;
K_{s-i} =initial bulk modulus of CTB;
ΔK_{s-f} =the increase of bulk modulus of CTB;
K_T =saturated hydraulic conductivity of tailings;
K_w =bulk modulus of the capillary water;
K_ψ =material parameter of interface dilation angle;
$K_{\psi 1}(\xi)$, $K_{\psi 2}(\xi)$ =material parameters of CTB dilation angle;
k =intrinsic permeability;
k_a, k_w, $k_{tailings}$ =thermal conductivity of tailings, water and air, respectively;
k_{const1}, k_{const2}, $k_{fc\_50°C}$ =parameter of TMC model;
k_{eff} =effective thermal conductivity;
k_{dry}, k_{sat} =thermal conductivity of dry porous media saturated porous media;
k_r =relative permeability;
k_{ri} =relative permeability $i = w, a$;
k_T =thermal conductivity of CTB;
L_1, L_2 =fitting parameters of elastic modulus of cement paste;
L_B =stope length;
M_{s1}, M_{s2}, M_{s3}, M_{c1}, M_{c2} =fitting parameters of c_B;
M_a =molecular mass of air;
M' =constrained modulus;
M^* =slope index of yield surface of SCC model;
m_{ab-w} =mass of the absorbed water;
m_{hc} =mass of the chemically combined water;
m_{hc0} =initial cement mass;
$m_{hc-initial}$ =initial cement mass;
$\dot{m}_{hydr}$ =water sink term in the water balance equation;
m_{n-w} =mass of the chemically combined water;
m_{WRC} =material parameter of water retention model;
N_0, N_1, N_2, N_3 =fitting parameters of internal friction angle ϕ_B;
$N_{\upsilon i}$ =fitting parameters of Poisson's ratio model;
n =porosity;
n_0 =initial porosity;
n_1, n_2 =fitting parameters of interface friction angle;
n_3, n_4 =fitting parameters of interface adhesion;
P_c =capillary pressure;
P_i =fluid pressure $i = w, a$;

P_{wr} =reference pore water pressure;
$\bar{P}$ =average pore pressure;
p' =effective mean stress;
p_n , p_r =normal load stress that acts on the CPB sample, and the reference stress;
p'_s =size of the yield surface of SCC model;
Q_{ad} , Q_{cd} =amount of heat transfer induced by advection and conduction;
Q_{CPB} =plastic potential function of CPB;
Q_{CTB} =plastic potential function of CTB;
Q_{hydr} =heat source term;
Q_{intf} =interface plastic potential function;
Q_m =sink term induced by drainage;
Q_T =source term induced by cement hydration;
$\mathbf{q}$ =conductive heat flux;
q =deviatoric stress;
$q_{\max,20}$ =maximum rate of released heat at a temperature of 20°C;
R =universal gas constant;
R_{r1} , R_{r2} =fitting constants used to predict θ_r ;
R_L =roughness index of the rock wall;
R_{intf1} , R_{intf2} , R_{intf3} , R_{intf4} =material constants of hardening/softening parameter;
$R_{n-w/hc}$ =mass ratio of chemically combined water and hydrated cement;
$R_{\alpha i}$ =fitting constant of strain hardening/softening parameter model;
S =saturation degree;
S_e =effective saturation degree;
S_{ij} =stress deviator;
S_T =sulphide mass content with respect to total mass of dry tailings;
S_w =sulphate content in mixing water;
T =absolute temperature;
T_0 =reference temperature for gas;
T_a =temperature of pore air;
T_r =reference temperature;
T_s =temperature of solid phase;
T_w =temperature of pore water;
t =elapsed time;
t_1 , k_ξ =hydration parameters;
t_e =hydration equivalent age;
t_{eqi} =equivalent time of hydration model;
t_0 =initial setting time;
u =pore-water pressure;
V_a =volume of the pore air;

V_{ab-w} , V_{ch-w} , $V_{ab/n}$ = physically adsorbed water volume, chemically combined water volume, and the total volume of the physically and chemically combined water in the capillary state;
V_{ch-s} =volume of solid phase related to hydration products;
V_{ch-w} =volume of pore water related to binder hydration;
V_F =velocity of the pore fluid;
$V_{filling}$ =filling rate of CTB;
V_m =volume of solid skeleton related to effective stress;
V_{pw} =volume of pore water related to the PWP;
V_{sp} =volume of pore water related to water seepage;
V_T =total volume of the CTB and water;
V_{Ts} =volume of solid skeleton related to thermal expansion;
V_{Tw} =volume of pore water related to thermal expansion;
v_1 , v_2 =volume fraction of tailings and ultimate cement paste with respect to the total volume of solid phase;
v_{ab-w} , v_{ch-w} =specific volume of physically absorbed water and chemically combined water;
v_c =specific volume of cement;
$v_{filling}$ =filling rate;
$v_{tailings}$ =specific volume of tailings;
$\mathbf{v}^{ri}$ =Darcy's velocity of fluid $i = w, a$;
$\mathbf{v}_s$ =phase velocity with respect to the fixed spatial axes;
v_w =specific volume of the capillary water;
W =material constant used predict I_{b2} ;
W_c =mass of unhydrated cement;
w_1 , w_2 =fitting constants of interface dilation angle;
w/c =water to cement ratio;
w_ψ =inverse of one GPa;
X =material constant used predict I_{b2} ;
X_{cem} , X_{FA} , X_{slag} =weight fraction of cement, fly ash and slag to total binder weight;
X_{FA-CaO} =weight ratio of CaO to fly ash;
$\mathbf{x}\left(x_1, x_2, x_3\right)$ =Eulerian coordinate system;
x_i =mass fraction of clinker composition $i = C_3S$, C_2S , C_3A , C_4AF , SO_3 , CaO , MgO ;
Z =material constant used predict I_{b2} ;
z =vertical distance from the stope floor;
Δ =total relative displacement;
Δ_e , Δ_p =elastic and plastic part of relative displacement;
Δ_κ =cumulative plastic displacement;
α =parameter of MSDPu model;
α_{Biot} =Biot's effective stress coefficient;
α_{D-P} , C_{D-P} =material parameters of the D-P criterion;

α_i =fill state angles in i direction;
α_{intf} =material parameters of D-P criterion;
α_p , $\alpha_{tailings}$ =CTE of cement paste and tailings;
α_T =CTE of CTB;
α_{Ts} =CTE of the CPB solid phase;
α_{Tw} =CTE of capillary water;
α_{uc} , α_{hp} , α_{uma} =CTE of the unhydrated cement, hydration products and unhydrated mineral admixture;
α_{WRC} =material parameter of water retention model;
α_Y =parameter of yield function;
β =hydration shape parameter;
β_{ch} =coefficient of the chemical shrinkage;
β_{Pw} =isothermal compression modulus of water;
β_{TMC} =parameter of TMC model;
χ =integration variable of Gibson's solution;
δ_i =internal friction angle in i direction;
δ_{ij} =Kronecker's delta;
δ_{intf} =interface friction angle;
ε =total strain;
ε_c =strain induced by chemical shrinkage;
ε_e =elastic strain;
ε_F =fraction of pore space occupied by fluid with respect to the pore space;
$\varepsilon_{\max}$ =maximum plastic volumetric strain;
ε_p =plastic strain;
ε_T =strain induced by thermal expansion;
ε_v =volumetric strain;
ε_v^p =plastic volumetric strain;
ϕ =porosity;
ϕ_B =internal friction angle of CTB;
ϕ_{hydr} =variation of porosity by binder hydration;
ϕ_r =internal friction angle of rock;
φ =internal friction angle;
φ_F =pore fluid pressure gradient;
γ_B =unit weight of CTB;
γ_m =unit weight of wet backfill;
γ_{sub} =submerged unit weight of backfill;
γ_w =unit weight of water;
κ =cumulative plastic strain;
κ_1 , κ_2 =strain hardening/softening parameters;
κ_i =parameter of 3D model developed by Li et al., 2005;
κ_s =value of cumulative plastic strain when $\alpha_{D-P}\left(\xi,\kappa\right)$ reaches its peak point;

λ, μ =Lame's parameters;
λ_p =plastic multiplier;
λ_i =parameter of 3D model developed by Li et al., 2005;
μ_0 =reference dynamic gas viscosity when temperature is 273K;
μ_F =dynamic viscosity;
μ_i =dynamic viscosity $i = w, a$;
ν =poison's ratio;
θ =volumetric water content;
θ_r =residual water contents;
θ_s =saturated water content;
ρ_{CTB} =backfilling density;
ρ_F =fluid density;
ρ_i =density (i refers to air, water and solid);
ρ_r =reference water density;
$\boldsymbol{\sigma}$ =total stress;
$\boldsymbol{\sigma}'$ =effective stress;
$\boldsymbol{\sigma}'_m$ =mean effective stress;
$\boldsymbol{\sigma}'_n$ =effective normal stress acting on the interface;
σ_h =horizontal stress;
σ_{hi} =horizontal stress in i direction;
σ'_{hi} =effective horizontal stresses;
$\boldsymbol{\sigma}_{p\_axial}$ =measured peak stress value from UCS tests;
$\boldsymbol{\sigma}_s$ =true strength of CTB;
σ_v =vertical stress;
σ'_v =effective vertical stress;
σ_x =longitudinal stress in CTB;
σ_y =transverse stress in CTB;
σ_z =vertical stress in CTB;
τ =hydration time parameter;
τ_T =hydration time parameter;
υ =Poisson's ratio;
ξ =binder hydration degree;
ξ_0 =reference degree of hydration;
ξ_u =ultimate degree of hydration;
ψ_B =dilation angle of CTB;
ψ_{intf} =interface dilation angle.

CPB=cemented paste backfill;
CTB=cemented tailings backfill;
CTE=coefficient of thermal expansion;
DST=direct shear test.

CHAPTER 1

General Introduction

1.1. Introduction

Underground mining operations mainly consist of blasting, crushing, milling ore rock and metal extraction. A large volume of mine waste including both crushed rocks and tailings are generally stored on the ground surface. A study on mine waste disposal by Blight (2009) indicated that over one billion tons of mine waste can be produced in a single mine during an operation period of 50 years. Due to various dangerous substances (i.e., heavy/toxic metals, radioactive elements, etc.), the resultant mine wastes can cause serious problems for both human health and the environment (e.g., acid mine drainage) (Lottermoser, 2010).

Mine waste management techniques comprise surface and underground disposal methods. The former can be further classified as storage as tailing dams, with densified tailings methods (e.g. thickened tailings disposal, surface paste tailings) and through co-disposal techniques (mixing of tailings and waste rock) (Mark, 2006). However, all of the surface disposal methods have the potential to cause their own geotechnical (e.g. tailings dam failure and thickened tailings liquefaction induced by earthquakes) and geoenvironmental (i.e., acid mine drainage) issues (Landriault et al., 1997; Akcil and Koldas, 2006; Coussy et al., 2012). Compared with surface tailings storage methods, the underground recycling of mine waste is a more effective alternative means of tailings disposal for the mining industries. Specifically, mine waste can be used to fill underground mined-out voids (called stopes) generated during ore extraction processes. The differences in the types of materials used mean that underground backfill can be hydraulic fill, rockfill or cemented paste backfill or cemented tailings backfill (CTB) (Potvin and Thomas, 2005). Among all of these different types of backfills, CTB, as a relatively new technology, has been extensively used in several mines around the world, especially in Canada (Fall and Benzaazoua, 2005).

CTB is an engineered mixture of binder (i.e., cement, fly ash or blast furnace slag), milled tailings with a solid percentage between 75% and 85%, and water. The adopted binder content ranges from 3 wt% to 7 wt%. Water (fresh or mine processed) is added to the mix to allow its transportability. The adopted binder content and relative high solid content can ensure that the designed backfill is able to provide the required mechanical strength for underground mining operations (Fall and Benzaazoua, 2005; Kesimal et al., 2005; Fall et al., 2008; Nasir, 2008). With the aid of CTB technology, the amount of surface stored mine waste (tailings) and the associated geoenvironmental hazards can be substantially reduced. Moreover, the backfill mass can act as ground support for the adjacent pillars to assure the stability and safety of the underground excavation, and maximize mining cycles and productivity. Also, CTB serves as a mucking (trafficked) floor to support the weight of loading equipment (Benzaazoua et al., 2004; Rankine and Sivakugan, 2007; Simms and Grabinsky, 2009).

1.2. Problem statement

During and after placement into stopes, the CTB structure is subjected to strongly coupled multiphysics (thermal, hydraulic, mechanical and chemical) processes. Due to the interaction between these multiphysics processes, the temperature, suction, stress and material properties will substantially change with time. Moreover, the development of volumetric deformation (i.e., the consolidation process) induced by the coupled THMC processes can result in relative displacement along the rock mass/CTB interface. Correspondingly, the interface resistance (i.e., the adhesion and friction force) will be mobilized and reduce the influence of the self-weight stress on the CTB structure (i.e., arching effect). Therefore, in order to reliably assess the performance of CTB in stopes, the coupled THMC processes, consolidation behavior due to multiphysics processes and multiphysics interaction between the rock mass/CTB interface must be fully considered and explained with mathematical models. However, due to the complexity of these multiphysics processes, current research on the aforementioned issues is very limited. Before this Ph.D. study, there are no studies that address these issues.

1.3. Objectives of the research

The main objectives of this research are to develop novel multiphysics models and conduct multiphysics numerical simulations to reliably assess the behavior or performance of CTB structures. These will contribute to significantly improving the understanding of CTB behaviors and allow backfill engineers to optimally design CTB structures. The specific objectives of this research work are summarized as follows:

1. To provide background information on CTB performance properties, coupled THMC processes, methods that describe multiphysics modeling, and existing mathematical modeling methods of CTB materials;
2. To develop multiphysics models for the assessment and prediction of CTB behavior. This objective includes:

   2.1 the development of an evolutive elastoplastic model to study the mechanical behavior of CTB;

   2.2 the development of a fully coupled THMC model to assess and predict the multiphysics processes and their influence on CTB behavior;

2.3 the development of a multiphysics model of the consolidation behavior of CTB to study and predict the consolidation behavior of the structure; and

2.4 the development of an integrated multiphysics model to assess and predict the arching effects of CTB structures.

3. To numerically study the field behavior of CTB structures by using the developed multiphysics model. This objective includes the following sub-objectives that addresses issues which are relevant for the field design of CTB structures:

3.1 to study the self-desiccation behavior of CTB structures;

3.2 to study the consolidation behavior of CTB structures under different backfilling conditions;

3.3 to study the pressure on barricades;

3.4 to study the strength development and distribution in CTB structures.

4. To provide technical information and tools that contribute to a better understanding of the behavior of CTB structures and better design of CTB structures

1.4. Research approach and methods

The research approach and methods adopted in this study are schematically shown in Figure 1.1.

In this Ph.D. study, a series of mathematical models including (1) an evolutive elastoplastic model, (2) a fully coupled THMC model, (3) a multiphysics model of consolidation behavior and (4) a multiphysics model that analyzes the arching effect are developed to provide the theoretical basis and fundamental tools for the assessment of CTB behavior and performance. These models and tools are applied to a series of engineering issues to understand the field behavior of CTB structures and thus gain valuable information on their optimal design (Figure 1.1).

To explain the mechanical behavior, a new evolutive elastoplastic model has been developed to address the vital role of binder hydration in the changes in the mechanical behavior and properties of CTB. Double hardening/softening parameters, which include effective incremental plastic strain and degree of binder hydration, are adopted. A non-associated plastic potential function based on the dilation angle is employed to formulate the plastic deformation and dilation of CTB. Mechanical parameters, such as cohesion, internal friction and dilation angle, stiffness, and Poisson’s ratio are expressed as functions of the degree of binder hydration. Then, the developed model is implemented in a finite element code, COMSOL Multiphysics, and then validated against experimental data obtained from laboratory tests performed in this study and by other researchers.

To explain the coupled THMC processes, a new multiphysics model is developped in this study. The governing equations of the model result from a combination of a set of conservation and constitutive equations. Four balance equations (water and air mass, momentum (mechanical equilibrium) and energy conservation equations) are taken into consideration. The model considers the full coupling among the thermal, hydraulic, and chemical (binder hydration) processes and CTB deformation as well as changes in CTB properties resultant of the coupling, such as stress-strain relationship, thermal conductivity, permeability, porosity, and strength. The model coefficients are identified in terms of measurable parameters. The predictive ability of the developed model is then tested against laboratory and field tests conducted on CTB.

To explain for the volumetric deformation in CTB, a 3D coupled multiphysics model of the consolidation behavior of CTB has been developed based on the principles of the continuity of pore space. Pore space continuity requires that the pore space changes related to the solid skeleton of CTB and the solid phase must equal the total volume change of the pore water and pore air. Since the volume change (i.e., consolidation process) in CTB is dominated by multiphysics processes, the principles of conservation of mass, energy and momentum are incorporated into the consolidation model. The predictive ability of the proposed model is validated against experimental data. Furthermore, some of the important features of the developed model are highlighted by a comparison between the simulated results and Gibson's solution.

To explain for the arching effects of CTB, a multiphysics model of the interaction in the interface has been developed, and then coupled with the THMC and multiphysics model of the consolidation behavior to evaluate the stress distribution in CTB. The model coefficients are determined in terms of measurable parameters. The predictive ability of the developed model is verified through a series of field studies under distinct backfilling conditions. The verified model is then applied to a series of engineering issues to investigate the influence of the stope geometry, rock temperature, rock wall roughness, binder content, initial backfill temperature, water drainage, backfilling rate and strategy on the interaction between rock mass/backfill interface and resultant stress distribution in CTB.

To apply multiphysics modeling in CTB, the developed models are used to assess the self-desiccation and consolidation behaviors of CTB structures, the changes of the pressure on barricades and the strength development and distribution in CTB structures. All of these engineering issues focus on the practical problems that backfilling operators and design engineers face in practice. Therefore, the obtained results can provide valuable insight into CTB performance under different backfilling conditions. Moreover, recommendations for an optimal CTB design will be provided.

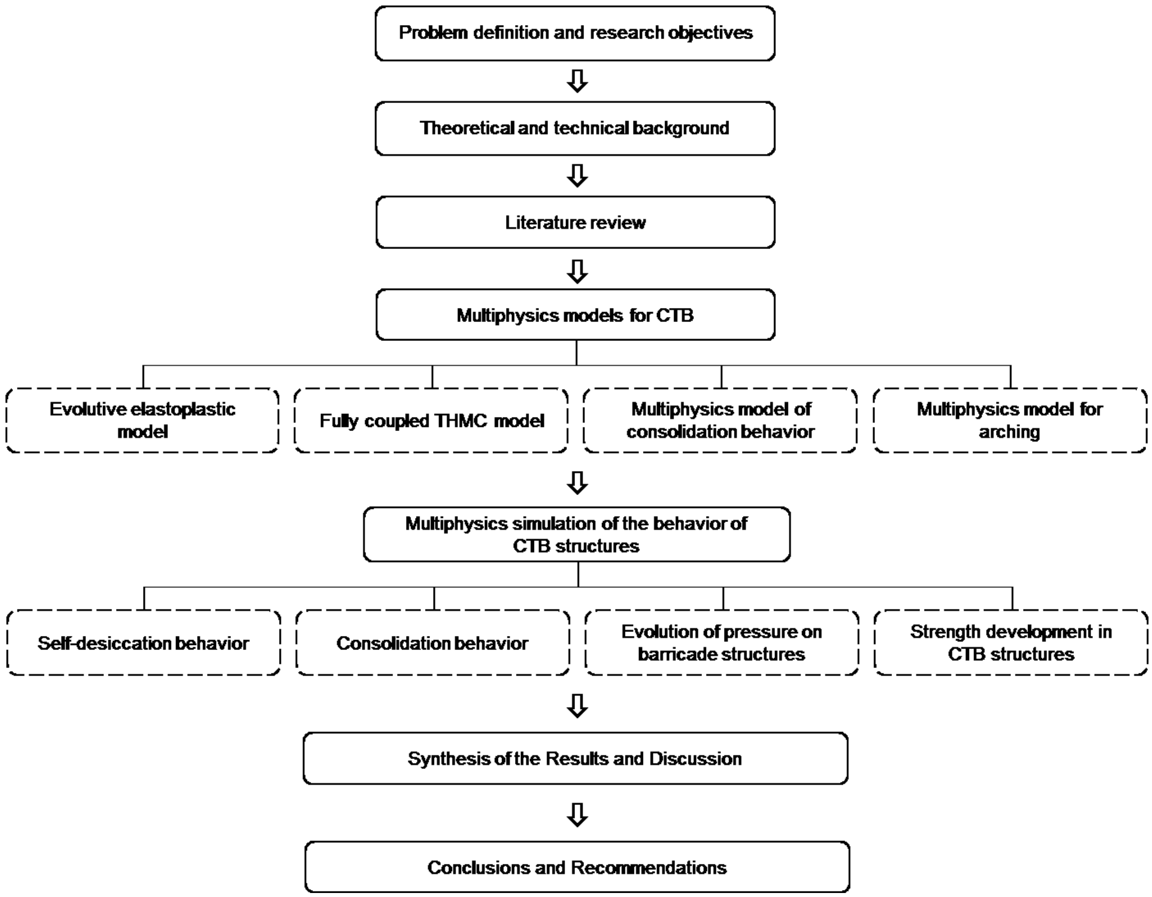

Figure 1.1. Research and study approach

1.5. Tasks and organization of thesis

This thesis is organized into seven chapters which contain the discussion of the different tasks and objectives of the current Ph.D. study. Figure 1.2 presents the structure of the main tasks that have been carried out.

Chapter One is a general introduction, which comprises problem statements, objectives, and research methods employed in this research.

Chapter Two is structured to provide a comprehensive literature review and/or background information on CTB technique and performance, fully coupled THMC processes, and methods that describe the multiphysics processes in CTB.

Chapter Three presents a literature review on previous modeling studies on CTB with focus on analytical and mechanical constitutive models, as well as coupled modeling studies on CTB.

Chapters Four and Five are structured into a paper-based thesis format, which comprises eight technical papers. It should be noted that because the main results of the chapters are presented as technical papers, some information is repeated in these papers. This is because each paper is independently written (i.e. without taking into account the content of the other papers or the rest of the document) and in accordance with the manuscript preparation instructions of the corresponding publication medium.

Chapter Four focuses on the development of fundamental multiphysics models for CTB, which consist of four technical papers. First, a new evolutive elastoplastic model is provided in **Section 4.2** to explain for the mechanical behavior of CTB. Then, a fully coupled THMC model is proposed in **Section 4.3** to characterize the coupled multiphysics processes. Moreover, a multiphysics model of the consolidation behavior is derived in **Section 4.4** to explain for the volume changes in CTB. In addition, a new multiphysics model for the arching effect is developed in **Section 4.5** to assess the stress distribution in CTB.

Chapter Five mainly focuses on the multiphysics simulation of the geotechnical behavior of CTB structures (issues which are relevant for the field design of CTB structures are addressed). This chapter is made of 4 technical papers which include the simulation of the self-desiccation of CTB structures (**Section 5.2**), consolidation behavior of CTB structures (**Section 5.3**), development of pressure on barricades (**Section 5.4**) and strength development in CTB structures (**Section 5.5**).

In **Chapter Six,** the obtained results are synthesized and discussed to provide valuable insight into the multiphysics modeled CTB behaviors under different backfilling conditions and design strategies, which can help backfilling engineers to create optimal CTB designs.

Chapter Seven presents the summary, conclusions and directions for future research.

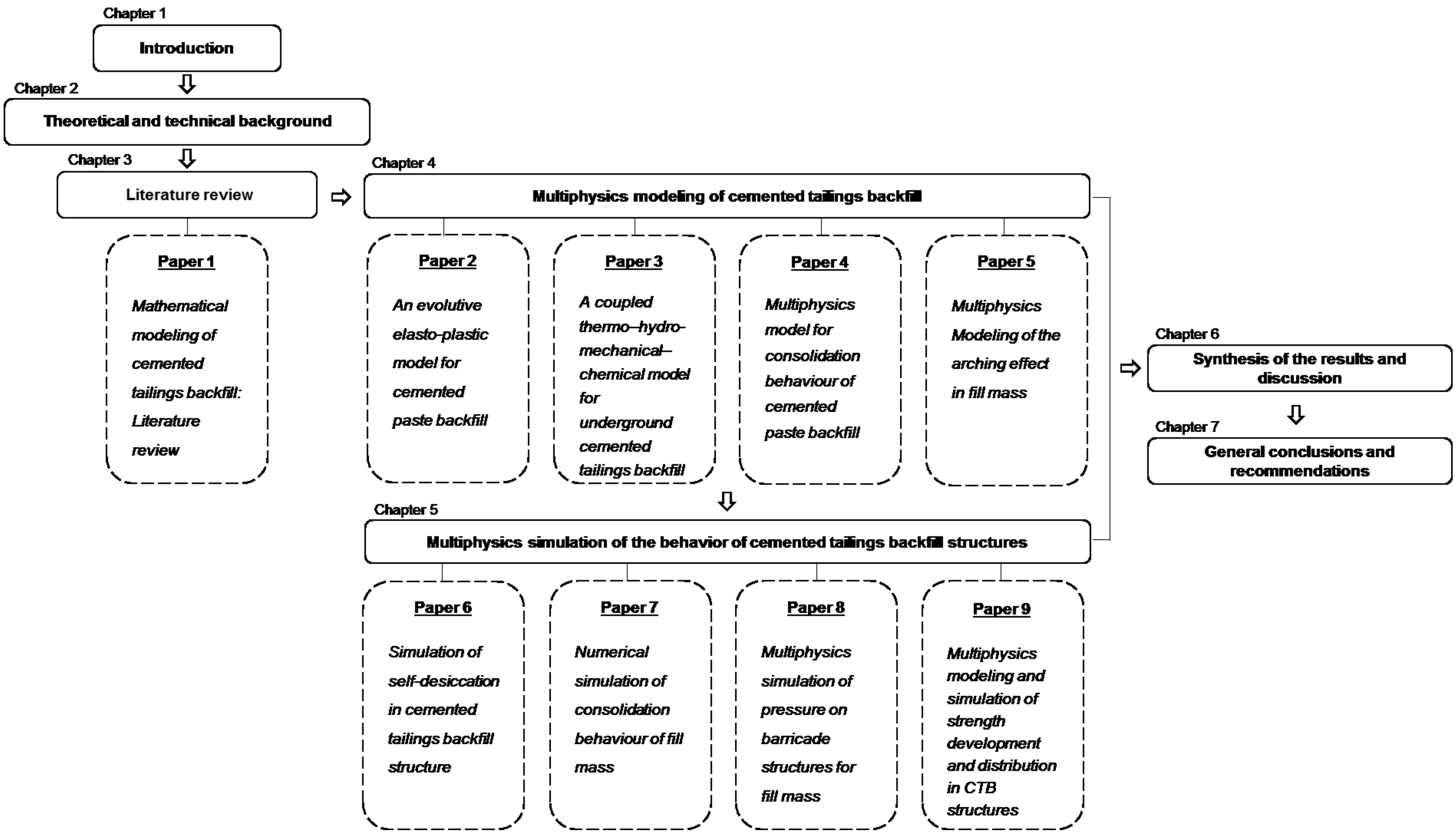

Figure 1.2. Tasks and organization of the thesis

1.6. References

Akcil, A., Koldas, S., 2006. Acid mine drainage (AMD): causes, treatment and case studies. Journal of Cleaner Production 14, 1139-1145.

Benzaazoua, M., Fall, M., Belem, T., 2004. A contribution to understanding the hardening process of cemented pastefill. Miner Eng 17, 141-152.

Blight, G., 2009. Geotechnical engineering for mine waste storage facilities. CRC Press.

Coussy, S., Benzaazoua, M., Blanc, D., Moszkowicz, P., Bussière, B., 2012. Assessment of arsenic immobilization in synthetically prepared cemented paste backfill specimens. J Environ Manage 93, 10-21.

Fall, M., Benzaazoua, M., 2005. Modeling the effect of sulphate on strength development of paste backfill and binder mixture optimization. Cem Concr Res 35, 301-314.

Fall, M., Benzaazoua, M., Saa, E., 2008. Mix proportioning of underground cemented tailings backfill. Tunn Undergr Sp Tech 23, 80-90.

Kesimal, A., Yilmaz, E., Ercikdi, B., Alp, I., Deveci, H., 2005. Effect of properties of tailings and binder on the short-and long-term strength and stability of cemented paste backfill. Mater Lett 59, 3703-3709.

Landriault, D., Verburg, R., Cincilla, W., Welch, D., 1997. Paste technology for underground backfill and surface tailings disposal applications. Proceedings of Short Course Notes, Canadian Institute of Mining and Metallurgy, Technical Workshop; p. 1997.

Lottermoser, B., 2010. Mine wastes: characterization, treatment and environmental impacts. Springer Science & Business Media.

Mark, R., 2006. Closure of tailings facilities: Current practice review and guidelines for success.

Nasir, O., 2008. Modeling of coupled processes in hydrating cemented paste backfill structures and application to the analysis of their performance. University of Ottawa, Canada.

Potvin, Y., Thomas, E., 2005. Handbook on mine fill. Australian Centre for Geomechanics.

Rankine, R.M., Sivakugan, N., 2007. Geotechnical properties of cemented paste backfill from Cannington Mine, Australia. Geotech Geol Eng 25, 383-393.

Simms, P., Grabinsky, M., 2009. Direct measurement of matric suction in triaxial tests on early-age cemented paste backfill. Can Geotech J 46, 93-101.

CHAPTER 2

Theoretical and Technical Background

2.1. Introduction

In order to provide a better understanding of the multiphysics processes in CTB, a review of the fundamental theoretical and technical background information on CTB is provided in this chapter. Specifically, background information on CTB technology is provided in Section 2.2, which includes the preparation, delivery methods, backfilling strategies, CTB properties and general rules of CTB design. In Section 2.3, current knowledge on binder hydration and some of the factors that affect binder hydration are reviewed and discussed. After that, a general review of the thermo-hydro-mechano-chemical (THMC) coupled processes in CTB is provided in Section 2.3 along with research methods used to examine these processes.

2.2. Background information - cemented tailings backfill

Underground mining activities can result in large amounts of mine waste on the ground surface. The disadvantages of surface waste disposal methods are obvious including the high cost of waste disposal at the surface (e.g., tailings ponds) and the associated environmental issues (e.g., acid mine drainage). Alternatively, as one of the most novel technologies in past decades, CTB can turn these mine wastes into cemented construction materials, which has been extensively used worldwide and become a standard operation for underground mines. The application of CTB technology in mining operations can have substantial economic and environmental benefits (Rankine and Sivakugan, 2007; Cihangir et al., 2012; Li, 2014) due to the fact that a large amount of tailings are used in the preparation of CTB and then delivered to the stopes. CTB technology has proven to be an effective tailings management approach which can minimize the associated geoenvironmental issues (e.g., failure of surface impoundment dams, and acid mine drainage) (Yilmaz et al., 2004; Yin et al., 2012). Moreover, the use of CTB is an effective means for ground support (critical for underground mine work safety) as well as for the reduction of the mining cycle and speeding up of production (increases mine productivity) (Nasir and Fall, 2010; Pokharel and Fall, 2010; Yin et al., 2012; Li, 2014).

2.2.1. Mixture designs and preparation

Due to the fact that the cost of backfilling operations can account for about 20% of total mine operation costs and cement consumption can make up 80% of the backfill costs (Grice, 1998), the optimal design of CTB mixtures is crucial for the reduction of cement consumption and achievement of the target strength. To reduce the cement consumption for the preparation of CTB, blast furnace slag, pozzolans and non-ferrous slag and fly ash (FA) are commonly used as alternative binding agents in the mining industry.

Apart from the cost management and strength control, the transportability of fresh CTB in pipelines is another important factor for CTB design. Studies on CTB preparation (for e.g., Benzaazoua et al., 2004; Fall et al., 2008) have indicated that the cement content, tailings fineness, water to cement (w/c) ratio, and tailings density are the most important factors that can affect CTB transportability (slump).

To prepare CTB, the mine tailings used should have more than 75% solid, which can be achieved through dewatering. Specifically, densified tailings can be obtained by using different types of equipment, such as disk filters, high-capacity thickeners, and gravity settling tanks. Then, the resulting filter cakes are sent to a spiral (or screw) mixer together with binder and water to produce CTB with a specific consistency.

2.2.2. Transportation and delivery methods

After being mixed with water in the backfill plant on the mine surface, fresh CTB paste is transported (by gravity or through pumping) into the stope through an underground distribution system (Landriault et al., 1997). As a non-Newtonian fluid, the rheological properties of fresh CTB paste govern its transportation in pipelines. To commence and maintain the flow through a pipeline system, the pumping pressure is required to be larger than the yield stress of the CTB paste which is a crucial indicator of the magnitude of the force between solid particles (Haiqiang et al., 2016). To analyze the flowability of fresh CTB, the yield stress and viscosity are both required. In practice, the most common analysis methods for CTB flowability include: rheological (yield stress, viscosity) measurements, slump flow test and vane shear test. The slump test is a simple way which is commonly practiced in the mining industry to determine CTB consistency (Belem and Benzaazoua, 2008). The vane shear test can be used to measure the yield stress. A study on the rheological properties of CTB by Wu et al. (2013) found that the cement content, binder type, temperature and elapsed time after preparation have significant influences on CTB flowability. Moreover, to optimize the delivery systems, there needs to be a balance among the velocity, relative density and pipe diameter (Landriault et al., 1997).

2.2.3. Backfilling strategy and rate

In order to avoid the situation where the pressure exerted by fresh CTB paste exceeds the barricade strength, multiple filling sequences are commonly adopted during backfilling operations (Abdul-Hussain and Fall, 2012). Specifically, the stope is first partially filled with a CTB plug (typically with a high binder content) which is allowed to cure with sufficient time. Then, subsequent backfilling sequences typically with a low binder content are carried out.

Aside from filling sequences, the backfilling rate is another important factor of CTB designs, which refers to the rate at which the stope is backfilled by CTB materials, and can be expressed by the volume (m^3/h), or height of the stope (m/h). Due to the different mining operation sequences, the filling rate can differ from one mine to another or one stope to another (Nasir and Fall, 2010). Rapid filling can contribute to increases of mining cycles which in turn, enhances mining production. However, similar to the adopted backfilling sequences, the pressure that acts on the barricade and the potential barricade failure are major influential factors for the backfilling rates. Moreover, the CTB mixture recipe, backfill setting time and arching effect need to be considered when deciding on the rate of backfilling.

2.2.4. Properties of CTB and factors that affect them

To describe the behavior and performance of CTB, it is important to discuss the properties (including physical, thermal, hydraulic, mechanical and chemical properties) of CTB.

In terms of the physical properties, the porosity (or void ratio), unit weight, water content and degree of saturation are used to analyze the THMC processes in CTB. Extensive laboratory and in-situ studies have been conducted that investigate the physical properties of CTB. Based on the obtained results from experimental investigations (Fall et al. 2007; Belem and Benzaazoua, 2008; Yilmaz et al., 2009; Yilmaz et al., 2014) and in-situ measurements (Rankine and Sivakugan, 2007), it has been found that the physical properties are affected by the mixture recipe, extent of consolidation, and backfilling and curing conditions (e.g., temperature, backfilling strategy and rate, and drainage conditions). Moreover, experimental studies carried out on the THMC processes (Ghirian and Fall, 2013; Fall and Ghirian, 2014; Ghirian and Fall, 2015) have confirmed that they have significant impacts on the physical properties of CTB.

With respect to the thermal properties, the heat transfer induced by thermal conduction is directly related to thermal conductivity. Previously obtained results (Abbasy, 2009; Célestin and Fall, 2009; Ghirian and Fall, 2013, 2015) have found that (1) the thermal conductivity of CTB is mainly dependent on that of the tailings (especially the quartz content), (2) increasing fineness of tailings can enhance thermal conductivity due to increased density of fine tailings, (3) the thermal conductivity shows a trend of increase with curing time, and (4) compared to tailings, the influence of the w/c ratio, cement type and content, curing time and sulphate content is minimal.

Hydraulic conductivity is considered to be a key parameter for the characterization of the pore water flow in CTB in terms of the hydraulic properties. Due to the fact the saturation conditions can transfer from a saturated to an unsaturated state due to drainage and water consumption through cement hydration, extensive experimental studies (Godbout et al., 2007; Fahey et al., 2010; Abdul-Hussain and Fall, 2012; Ghirian and Fall, 2013; Pokharel and Fall, 2013; Ghirian and Fall, 2015) have been carried out to investigate the changes in hydraulic conductivity in CTB. Their results confirm that the mix components, curing conditions (temperature and time) and consolidation behavior (i.e., void ratio) have significant influences on the hydraulic conductivity. Apart from the hydraulic conductivity, the water retention parameters control the changes in negative pore water pressure in CTB. Experimental studies on the water retention behavior of CTB (Abdul-Hussain and Fall, 2012; Suazo et al., 2016) found that cement hydration has a significant influence on the water retention capacity of CTB.

As the stability of CTB structures is important, the mechanical properties have been the subject of interest of backfill engineers and researchers. Extensive experimental tests, including uniaxial compressive strength (UCS) (e.g. Belem et al., 2002; Fall et al., 2007; Fall and Pokharel, 2011), direct shear (e.g. Fall and Nasir, 2010), triaxial compression (e.g. Fall et al., 2007; Rankine and Sivakugan, 2007; Veenstra, 2013), and consolidation (e.g. Yilmaz et al., 2009; Yilmaz et al., 2011; Ghirian and Fall, 2015) tests have been conducted to investigate the characteristics of strength, elastic modulus, Poisson's ratio, chemical and strain hardening, post-peak strain softening, volumetric changes, cohesion and internal friction angle as well as the related changes. It has been found that (1) the mechanical properties can be significantly improved with curing time due to the THMC processes in the CTB, and (2) the mixture recipe and curing conditions have significant influences.

The chemical properties of CTB depend on the chemical and mineralogical characteristics of its constituents, including the mixing water and tailings chemistry and mineralogy, and binder chemical compositions. These can significantly influence the cement hydration and CTB behavior (Benzaazoua et al., 2002). Therefore, when determining the progression of cement hydration quantitatively, the effects of the chemical properties must be incorporated, which means that the hydration model should be related to the mixture recipe rather than just a simple function of curing time.

2.2.5. Geotechnical design of CTB

After placement into underground stopes, CTB structures should provide a stable platform for mine workers and ground support for the surrounding rocks (Belem and Benzaazoua, 2004). Hence, strength acquisition and stability have great practical importance in CTB design. A study on CTB by Gala et al. (2011) indicated that the development of strength is affected by cement hydration, self-desiccation (suction) and consolidation processes. Moreover, due to the development of consolidation in CTB, a relative displacement along the rock mass/backfill interface gradually occurs, which results in the generation of interface shear stress (i.e., an interface resistance with respect to the self-weight stress). Correspondingly, part of the stress inside the backfill is transferred to the adjacent rock walls, which is known as the arching effect (as shown in Figure 2.1). As a result, the vertical stress is less than the overburden pressure of the backfill (Li et al., 2003). To fulfill their intended functions, CTB structures should satisfy certain static and dynamic design requirements (Rankine and Sivakugan, 2007). For the former, the CTB should (1) have a UCS equal to the overburden stress at the base of the stope in accordance with traditional design criteria (Belem and Benzaazoua, 2004), In general, the required UCS in a typical mine stope is commonly less than 5 MPa, or a range of 0.2 to 4 MPa (e.g., Grice, 1998; Revell, 2000); (2) have enough strength to support equipment loading as the mucking floor; (3) prevent surrounding rock movement and sloughing; (4) maintain stability during undercut mining and flow openings; and (6) form early-age mechanical strength. Moreover, CTB structures are required to be stable even in the event of blasting and/or seismic loadings (Grice and Bloss, 2001).

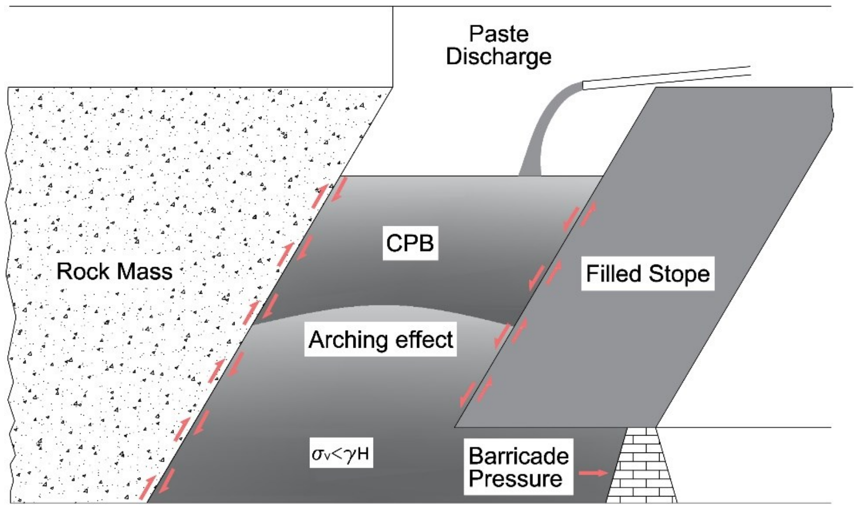

Figure 2.1. Schematic diagram of backfilled stope and stress distribution in stope

2.3. Background information - binder hydration and some influential factors

The most common binder used in the preparation of CTB is ordinary Portland cement (OPC) (normally Type I). Moreover, to improve the CTB strength and/or control the binder cost, pozzolanic materials (e.g., FA and blast furnace slag) are frequently u blended with OPC (Belem and Benzaazoua, 2004; Kesimal et al., 2005). After mixing with water, a series of complex hydration reactions occur in CTB and gradually bond the tailings particles. The key features of the OPC, binder hydration and associated influential factors are discussed in the following subsections.

2.3.1. Definition and composition of cement

Cement is usually a powder substance which can bond with other materials after being mixed with water. Cement can be further classified into non-hydraulic and hydraulic based on the setting characteristics; namely, that the former will not set under wet conditions while the latter will set and produce hydration products. The most common hydraulic cement is Portland cement. According to ASTM C150, Portland cement can be further classified into Types I, II, III, IV, V and VI. Type I is used in common or general-purpose applications. In terms of the composition, the main constituents of anhydrous cement clinkers include silicates (26%-53% C_3S, and 16%-54% C_2S), and aluminates (3%-15% C_3A and 8%-12% C_4AF) (Hansen et al., 1973).

2.3.2. Portland cement hydration

When mixed with water, cement hydration reactions occur and gradually produce three main types of cement hydration products including calcium silicate hydrate (C-S-H), calcium hydroxide ($Ca(OH)_2$ or CH), and calcium sulphoaluminate known as ettringite ($3CaO.Al_2O_3.3CaSO_4.31H_2O$). C-S-H is formed by the hydration of C_3S and C_2S at different rates. It occupies approximately 60% (by volume) of the total cement hydration products in hardened cement. Its structure ranges from poorly crystalline to amorphous (Mehta and Monteiro, 1993). The nanostructure of C-S-H was elucidated by Beaudoin et al. (2011) and Alizadeh (2009). CH is a by-product of the hydration of calcium silicate and takes up to 20% of the cement hydration products. CH has crystals that are thin to large hexagonal prisms in shape (Double et al., 1983). Ettringite is the product of the hydration of the aluminate phases and gypsum. It has a needle-like morphology (Double et al., 1983).

2.3.3. Setting, hardening and heat of cement hydration

There are five distinct stages in cement hydration, including initial, induction, acceleration (or setting), deceleration (or hardening) and densification (as shown in Figure 2.2) (Bullard et al., 2011). Based on previous studies on cement hydration (Neville, 1995; Swaddiwudhipong et al., 2002; Soroka, 2003; Bullard et al., 2011; Winter, 2012), the characteristics of the different stages are presented as follows:

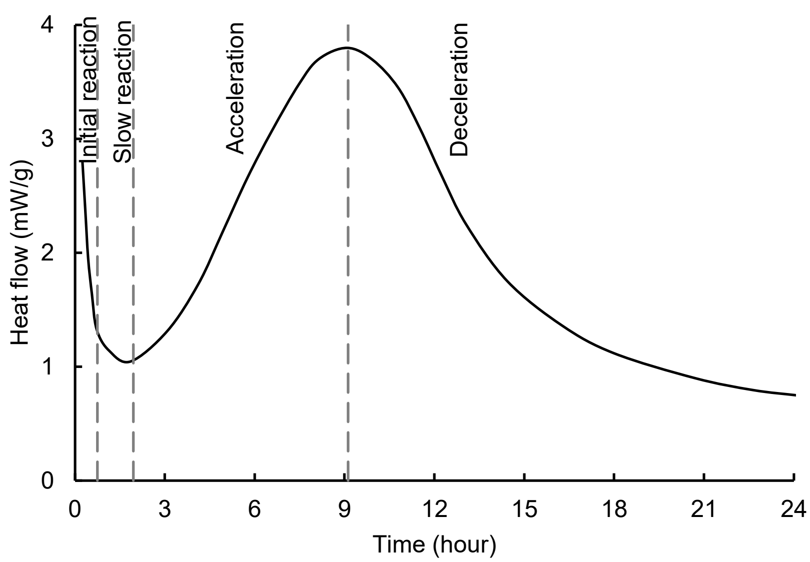

Figure 2.2. Rate of hydration with curing time (Bullard et al., 2011)

(1) Pre-induction: After exposed to mixing water, the initial reaction occurs immediately. During the period of preinduction, the aluminates and gypsum dissolve rapidly and release a significant amount of heat.

(2) Induction: With the formation of C-S-H and ettringite around the calcium silicates (C_3S and C_2S), the hydration rate is gradually retarded. During this stage, the cement paste is plastic without heat release.

(3) Acceleration: After the induction period, the hydration rate increases and a large amount of heat is generated. As a result, the pore space is further refined and bond strength is enhanced.

(4) Deceleration: Due to the continuous formation of C-S-H and CH around the particles, the hydration rate slows down.

(5) Densification: Hydration occurs at a very slow rate which is controlled by the species diffusion through the pore network.

2.3.4. Main factors that affect cement hydration

Lin and Meyer (2009) carried out a study on cement hydration and indicated that the factors that affect cement hydration include w/c ratio, fineness of the cement, and curing temperature and pressure (see Figure 2.3).

As shown in Figure 2.3a, a high curing pressure can lead to an increase in the hydration rate, this is because the accessibility of cement grains to water required for hydration is increased with curing pressure, which in turn, increases the degree of hydration (Zhou and Beaudoin, 2003). Furthermore, the amount of curing pressure can also result in the densification of the material matrix (i.e., decrease in the porosity), which can contribute to the development of compressive strength (Roy et al., 1972).

Moreover, from Figure 2.3b, it has been found that the cement hydration rate is highly dependent on the curing temperature. High curing temperatures could increase the rate of cement hydration reactions. Consequently, the cement hydration products have higher density and short-term compressive strength. However, it should be pointed out that high curing temperatures (e.g., above 85°C) can reduce the mechanical strength at the advanced ages due to the higher porosity, less uniform microstructure and coarser pore structure (Kjellsen et al., 1990; Maltais and Marchand, 1997; Elkhadiri et al., 2009)

The dependence of the hydration rate on the w/c ratio becomes obvious with a reduction in the w/c ratio, as shown in Figure 2.3c. Namely, a lower w/c ratio could increase the rate of hydration. In their studies on cement hydration, Goto and Roy (1981) and Bentz et al. (2009) indicated that a reduction in the w/c ratio could reduce the porosity (decrease the hydraulic conductivity) and improve the mechanical strength.

In terms of the cement fineness, finer cement particles with a larger surface area can contribute to a higher contact area with water. Correspondingly, the hydration rate will be affected. Furthermore, finer cement particles also mean that the consistency of the cement hydration products will be less thick, which in turn, means that water diffusion into the region without hydrated cement will be easier. Hence, finer cement particles reduce the setting time, accelerate the hardening process and enhance the mechanical strength (Ginebra et al., 2004; Bentz et al., 2008; Lin and Meyer, 2009) (Figure 2.3d).

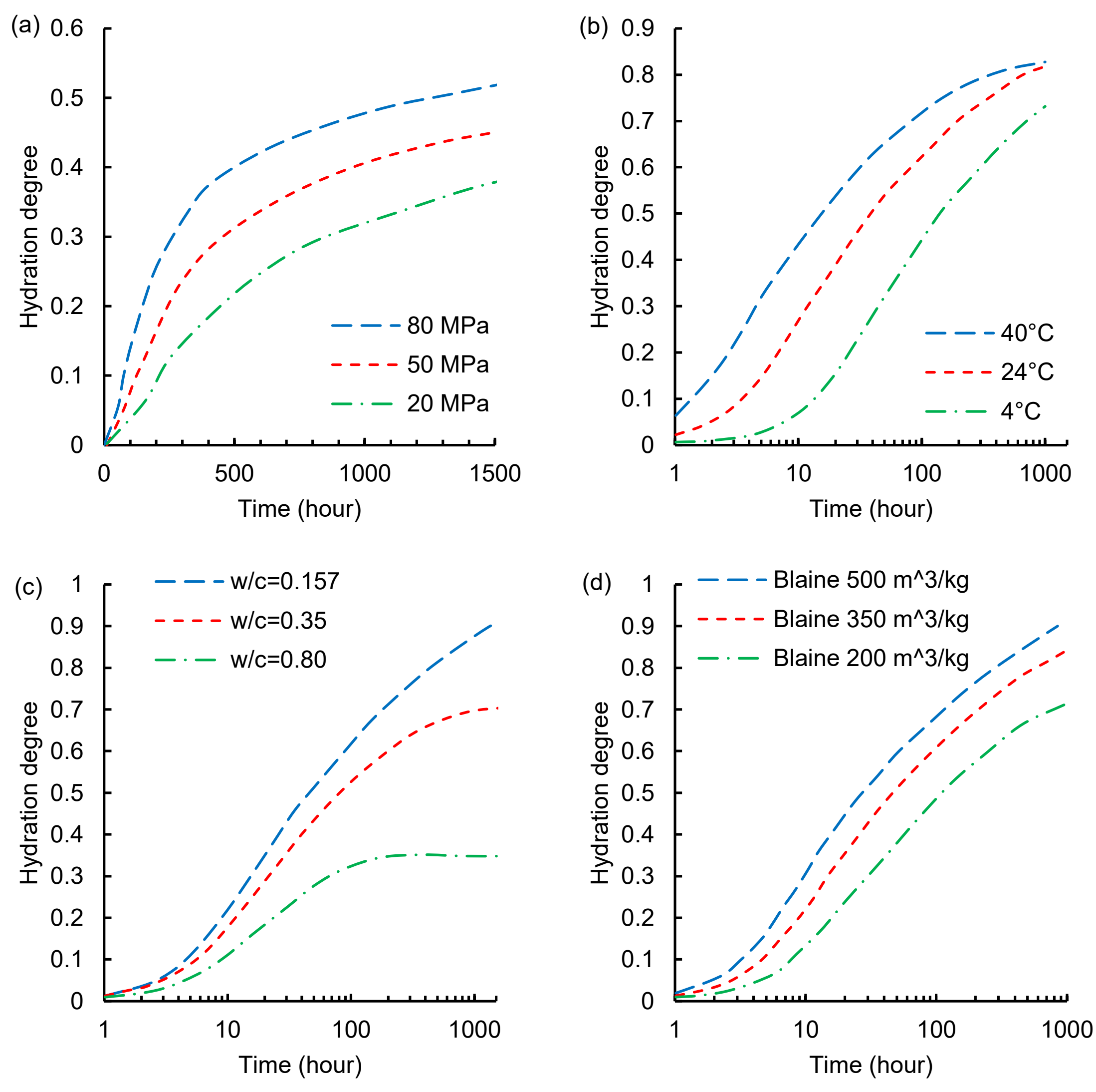

Figure 2.3. Evolution of cement hydration under different (a) curing stress, (b) curing temperature, (c) w/c ratio, and (d) cement fineness (source: Lin and Meyer, 2009)

2.4. Thermo-hydro-mechanical-chemical coupled processes in CTB

THMC processes are one of the most important phenomena in geotechnical and environmental engineering. The main objective of this section is to provide a concise explanation of the governing interactions for THMC processes in CTB. Moreover, the methods that describe the THMC processes in CTB are summarized in this Section.

2.4.1. Coupled THMC processes in CTB

Once prepared and placed, the CTB structure, which is part of a geotechnical system, is subjected to strong coupled thermal (T), hydraulic (H), mechanical (M) and chemical (C) (THMC) processes or factors (Ghirian and Fall, 2013, 2014) (Figure 2.4).

In terms of the thermal process, the heat released by cement hydration (Ghirian and Fall, 2015), heat transfer between the surrounding rock mass and CTB (Nasir and Fall, 2010) and the heat advection induced by the pore water flow in CTB (Wu et al., 2012) contribute to the variation of the temperature in CTB. The temperature changes have been confirmed through in-situ measurements (see for e.g.,Thompson et al., 2009).

In terms of the chemical process, cement hydration not only is exothermic, but also consumes pore water and converts the pore water into hydrate products (i.e., chemically combined water) (Powers, 1958). However, the volume of chemically combined water is less than that of the original capillary water (Powers, 1958). As a result, chemical shrinkage occurs which can contribute to volumetric changes (i.e., the consolidation process) in CTB (Ghirian and Fall, 2014).

In terms of the hydraulic process, the water consumption due to cement hydration (Wu et al., 2012; Ghirian and Fall, 2013, 2015), water drainage through the barricade (i.e., a retaining structure to keep fresh CTB in stopes) (Helinski, 2008) and the pore water downward flow under the gravity effect can cause pore water pressure changes in CTB.

In terms of the mechanical process, there are several contributors to the development of CTB deformation in stopes including the chemical shrinkage induced by cement hydration, gravity induced deformation, water drainage and thermal deformation in CTB. Moreover, it has been found in previous experimental studies on CTB that the material properties including mechanical properties (e.g., strength, cohesion, internal frictional angle and elastic modulus), hydraulic properties (e.g., hydraulic conductivity, water retention curves related parameters) and thermal properties (e.g., thermal conductivity) significantly change in CTB with curing time (Belem et al., 2002; Benzaazoua et al., 2004; Fall et al., 2007; Célestin and Fall, 2009; Simms and Grabinsky, 2009; Yilmaz et al., 2011; Ghirian and Fall, 2013; Pokharel and Fall, 2013).

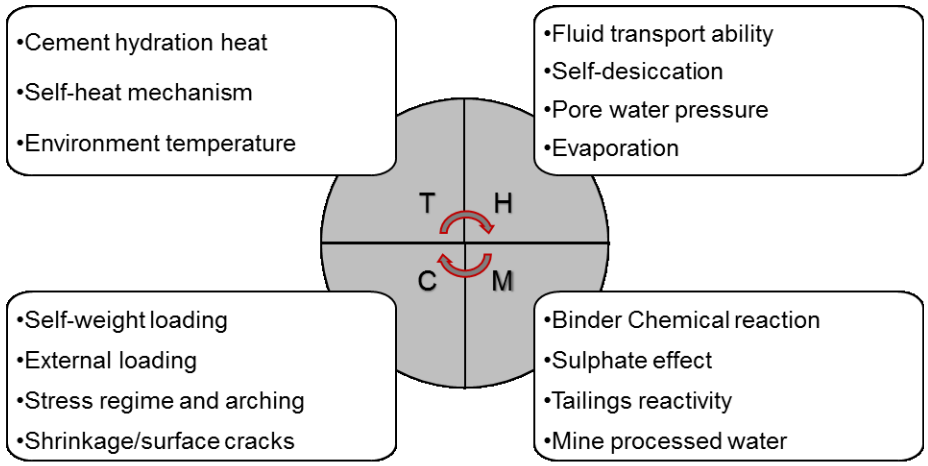

Figure 2.4. Coupled THMC processes in CTB (source: Ghirian and Fall, 2013)

2.4.2. Methods that describe multiphysics in CTB

The strong multiphysics interaction processes control CTB behavior and performance. Methods that describe the multiphysics in CTB can be classified into three categories.

(1) Physical modeling (i.e., experimental studies and in-situ measurements) has been extensively adopted by backfill designers and researchers (e.g., Grabinsky and Bawden, 2007; Helinski, 2008; Célestin and Fall, 2009; Ghirian and Fall, 2013, 2014, 2015). The obtained results provide insight into a better understanding of CTB behavior and changes in CTB properties. However, due to the limitations of experimental devices, measurements methods, mixture recipes, and the adopted curing and backfilling conditions, physical modeling is mainly used for the qualitative analysis of CTB behavior.

(2) Analytical methods (i.e., limit equilibrium theory) provide a simple closed-form solution to describe the CTB behavior (e.g., Li et al., 2003; Belem et al., 2004; Li, 2014). An analytical solution is derived through a series of assumptions, including that there is the uniform distribution of horizontal stress at any given elevation, the properties of the rock mass/backfill interface (friction angle and adhesion) are constant, and there is a constant earth pressure coefficient (i.e., the relation between horizontal and vertical stress). However, these assumptions create limitations, so that analytical methods are unable to reproduce the THMC processes in CTB. Therefore, the resulting analyses and

assessments from the use of analytical methods have limited contributions to the optimal design of CTB structures.

(3) Numerical modeling of multiphysics processes in CTB is conducted based on the developed coupled multiphysics models. Due to the complex controlling mechanisms (i.e., coupled multiphysics) of the behavior and performance of CTB, various partially coupled numerical models have been developed to predict its behavior. A thermo-chemo-mechanical (TCM) model was proposed by Fall and Nasir (2009) to simulate the response of CTB under thermal loading conditions. In order to explain the coupled thermal and hydraulic processes in CTB, a thermo-hydro-chemical (THC) model was then developed by Wu et al. (2014). A hydro-chemo-mechanical (HCM) model which couples cement hydration with conventional consolidation analysis was presented by Helinski et al. (2007). Although the developed partially coupled models provide a more accurate way to assess CTB, there is currently no tool to predict the fully coupled THMC behavior of CTB.

2.5. Conclusions

Theoretical and technical background information on CTB has been summarized in this chapter. The literature review identifies complex multiphysics behavior (i.e., THMC processes) as the controlling mechanism of CTB performance. In order to characterize its behavior, different analysis techniques have been provided. However, due to the complex multiphysics processes in CTB, there is currently no tool to predict the fully coupled multiphysics behavior and performance of CTB. Therefore, to reliably assess the behavior and performance of CTB, multiphysics modeling of CTB is conducted in this Ph.D. research.

2.6. References

Abbasy, F., 2009. Thermal conductivity of mine backfill. Concordia University, Montreal, Quebec, Canada.

Abdul-Hussain, N., Fall, M., 2012. Thermo-hydro-mechanical behavior of sodium silicate-cemented paste tailings in column experiments. Tunn Undergr Sp Tech 29, 85-93.

Alizadeh, R.A., 2009. Nanostructure and engineering properties of basic and modified calcium-silicate-hydrate systems. University of Ottawa, Canada.

Beaudoin, J.J., Patarachao, B., Raki, L., Alizadeh, R., 2011. Adsorption of methylene blue as a descriptor of C–S–H nanostructure. Cem Concr Compos 33, 246-250.

Belem, T., Benzaazoua, M., Bussière, B., Dagenais, A., 2002. Effects of settlement and drainage on strength development in mine paste backfill. Proceedings of 9th International Conference, Tailings and Mine Waste; p. 139-148.

Belem, T., Benzaazoua, M., 2004. An overview on the use of paste backfill technology as a ground support method in cut-and-fill mines. Proceedings of the 5th International Symposia on Ground support in Mining and Underground Construction. Perth, Australia; p. 28-30.

Belem, T., Harvey, A., Simon, R., Aubertin, M., 2004. Measurement and prediction of internal stresses in an underground opening during its filling with cemented fill. Proceedings of the 5th International Symposium on Ground Support in Mining and Underground Construction; p. 28-30.

Bentz, D.P., Sant, G., Weiss, J., 2008. Early-age properties of cement-based materials. I: Influence of cement fineness. J Mater Civil Eng 20, 502-508.

Bentz, D.P., Peltz, M.A., Winpigler, J., 2009. Early-age properties of cement-based materials. II: Influence of water-to-cement ratio. J Mater Civil Eng 21, 512-517.

Benzaazoua, M., Belem, T., Bussiere, B., 2002. Chemical factors that influence the performance of mine sulphidic paste backfill. Cem Concr Res 32, 1133-1144.

Benzaazoua, M., Fall, M., Belem, T., 2004. A contribution to understanding the hardening process of cemented pastefill. Miner Eng 17, 141-152.

Bullard, J.W., Jennings, H.M., Livingston, R.A., Nonat, A., Scherer, G.W., Schweitzer, J.S., Scrivener, K.L., Thomas, J.J., 2011. Mechanisms of cement hydration. Cem Concr Res 41, 1208-1223.

Célestin, J.C.H., Fall, M., 2009. Thermal conductivity of cemented paste backfill material and factors affecting it. Int J Min Reclam Environ 23, 274-290.

Cihangir, F., Ercikdi, B., Kesimal, A., Turan, A., Deveci, H., 2012. Utilisation of alkali-activated blast furnace slag in paste backfill of high-sulphide mill tailings: effect of binder type and dosage. Miner Eng 30, 33-43.

Double, D., Hewlett, P., Sing, K., Raffle, J., 1983. New developments in understanding the chemistry of cement hydration and discussion. Philosophical Transactions of the Royal Society of London A: Mathematical, Physical and Engineering Sciences 310, 53-66.

Elkhadiri, I., Palacios, M., Puertas, F., 2009. Effect of curing temperature on cement hydration. Ceram Silik 53, 65-75.

Fahey, M., Helinski, M., Fourie, A., 2010. Consolidation in accreting sediments: Gibson's solution applied to backfilling of mine stopes. Geotechnique 60, 877-882.

Fall, M., Belem, T., Samb, S., Benzaazoua, M., 2007. Experimental characterization of the stress-strain behavior of cemented paste backfill in compression. J Mater Sci 42, 3914-3922.

Fall, M., Benzaazoua, M., Saa, E., 2008. Mix proportioning of underground cemented tailings backfill. Tunn Undergr Sp Tech 23, 80-90.

Fall, M., Nasir, O., 2009. Numerical modeling of the coupled thermo-chemo-mechanical response of cemented paste backfill structures in deep mine temperature conditions. Proceedings of 3rd Canada-US Rock Mechanical Symposium and 20th Canadian Rock Mechanics Symposium Toronto, ON, Canada; p. 125-126.

Fall, M., Nasir, O., 2010. Mechanical behavior of the interface between cemented tailings backfill and retaining structures under shear loads. Geotech Geol Eng 28, 779-790.

Fall, M., Pokharel, M., 2011. Strength development and sorptivity of tailings shotcrete under various thermal and chemical loads. Can J Civil Eng 38, 772-784.

Fall, M., Ghirian, A., 2014. Coupled thermo-hydro-mechanical-chemical evolution of cemented paste backfill and implications for backfill design-experimental results. Proceedings of 11th International symposium on mining with backfill, MineFill 2014 Perth, Australia; p. 183-196.

Galaa, A.M., Thompson, B.D., Grabinsky, M.W., Bawden, W.F., 2011. Characterizing stiffness development in hydrating mine backfill using ultrasonic wave measurements. Can Geotech J 48, 1174-1187.
Ghirian, A., Fall, M., 2013. Coupled thermo-hydro-mechanical-chemical behavior of cemented paste backfill in column experiments. Part I: physical, hydraulic and thermal processes and characteristics. Eng Geol 164, 195-207.
Ghirian, A., Fall, M., 2014. Coupled thermo-hydro-mechanical-chemical behavior of cemented paste backfill in column experiments: Part II: Mechanical, chemical and microstructural processes and characteristics. Eng Geol 170, 11-23.
Ghirian, A., Fall, M., 2015. Coupled Behavior of Cemented Paste Backfill at Early Ages. Geotech Geol Eng 33, 1141-1166.
Ginebra, M., Driessens, F., Planell, J., 2004. Effect of the particle size on the micro and nanostructural features of a calcium phosphate cement: a kinetic analysis. Biomaterials 25, 3453-3462.
Godbout, J., Bussière, B., Belem, T., 2007. Evolution of cemented paste backfill saturated hydraulic conductivity at early curing time.
Goto, S., Roy, D.M., 1981. The effect of w/c ratio and curing temperature on the permeability of hardened cement paste. Cem Concr Res 11, 575-579.
Grabinsky, M., Bawden, W., 2007. In situ measurements for geomechanical design of cemented paste backfill systems. Proceedings of Proceedings of the 9th International Symposium in Mining with Backfill, Montréal, Que.
Grice, T., 1998. Underground mining with backfill. Proceedings of the 2nd Annual Summit-Mine Tailings Disposal Systems Australian; p. 234-239.
Grice, A., Bloss, M.L., 2001. Cannington Mine paste fill system manual, 1st ed. In: BHP billiton, Cannington internal report. Cannington Mine, North West Queensland, Australia, p. 107.
Haiqiang, J., Fall, M., Cui, L., 2016. Yield stress of cemented paste backfill in sub-zero environments: Experimental results. Miner Eng 92, 141-150.
Hansen, T.C., Radjy, F., Sellevold, E.J., 1973. Cement paste and concrete. Annu Rev Mater Sci 3, 233-268.
Helinski, M., Fahey, M., Fourie, A., 2007. Numerical modeling of cemented mine backfill deposition. J Geotech Geoenviron 133, 1308-1319.
Helinski, M., 2008. Mechanics of mine backfill. University of Western Australia, Australia.
Kesimal, A., Yilmaz, E., Ercikdi, B., Alp, I., Deveci, H., 2005. Effect of properties of tailings and binder on the short-and long-term strength and stability of cemented paste backfill. Mater Lett 59, 3703-3709.
Kjellsen, K.O., Detwiler, R.J., Gjørv, O.E., 1990. Pore structure of plain cement pastes hydrated at different temperatures. Cem Concr Res 20, 927-933.
Landriault, D., Verburg, R., Cincilla, W., Welch, D., 1997. Paste technology for underground backfill and surface tailings disposal applications. Proceedings of Short Course Notes, Canadian Institute of Mining and Metallurgy, Technical Workshop; p. 1997.
Li, L., 2014. Generalized solution for mining backfill design. Int J Geomech 14, 04014006.
Li, L., Aubertin, M., Simon, R., Bussière, B., Belem, T., 2003. Modeling arching effects of narrow backfilled stopes with FLAC. Proceedings of the 3rd International Symposium on FLAC & FLAC 3D Numerical Modeling in Geomechanics Ontario, Canada; p. 211-219.
Lin, F., Meyer, C., 2009. Hydration kinetics modeling of Portland cement considering the effects of curing temperature and applied pressure. Cem Concr Res 39, 255-265.

Maltais, Y., Marchand, J., 1997. Influence of curing temperature on cement hydration and mechanical strength development of fly ash mortars. Cem Concr Res 27, 1009-1020.
Mehta, P.K., Monteiro, P.J., 1993. Concrete structures, properties and materials. Prentice-Hall, New Jersey, USA, 447.
Nasir, O., Fall, M., 2010. Coupling binder hydration, temperature and compressive strength development of underground cemented paste backfill at early ages. Tunn Undergr Sp Tech 25, 9-20.
Neville, A.M., 1995. Properties of concrete.
Pokharel, M., Fall, M., 2010. Coupled thermochemical effects on the strength development of slag-paste backfill materials. J Mater Civil Eng 23, 511-525.
Pokharel, M., Fall, M., 2013. Combined influence of sulphate and temperature on the saturated hydraulic conductivity of hardened cemented paste backfill. Cem Concr Compos 38, 21-28.
Powers, T.C., 1958. Structure and physical properties of hardened Portland cement paste. J Am Ceram Soc 41, 1-6.
Rankine, R.M., Sivakugan, N., 2007. Geotechnical properties of cemented paste backfill from Cannington Mine, Australia. Geotech Geol Eng 25, 383-393.
Revell, M., 2000. Cannington backfill taking the pig out of paste. Proceedings of Paste Technology Seminar Perth, Australia; p. 1-12.
Roy, D.M., Gouda, G., Bobrowsky, A., 1972. Very high strength cement pastes prepared by hot pressing and other high pressure techniques. Cem Concr Res 2, 349-366.
Simms, P., Grabinsky, M., 2009. Direct measurement of matric suction in triaxial tests on early-age cemented paste backfill. Can Geotech J 46, 93-101.
Soroka, I., 2003. Concrete in hot environments. CRC Press.
Suazo, G., Fourie, A., Doherty, J., 2016. Experimental Study of the Evolution of the Soil Water Retention Curve for Granular Material Undergoing Cement Hydration. J Geotech Geoenviron, 04016022.
Swaddiwudhipong, S., Chen, D., Zhang, M., 2002. Simulation of the exothermic hydration process of Portland cement. Adv Cem Res 14, 61-69.
Thompson, B., Grabinsky, M., Bawden, W., Counter, D., 2009. In-situ measurements of cemented paste backfill in long-hole stopes. Proceedings of the 3rd CANUS Rock Mechanics Symposium Toronto; p. 197-198.
Veenstra, R.L., 2013. A design procedure for determining the in situ stresses of early age cemented paste backfill. University of Toronto, Canada.
Winter, N.B., 2012. Understanding cement: An introduction to cement production, cement hydration and deleterious processes in concrete. Microanalysis Consultants.
Wu, D., Fall, M., Cai, S.-j., 2012. Coupled modeling of temperature distribution and evolution in cemented tailings backfill structures that contain mineral admixtures. Geotech Geol Eng 30, 935-961.
Wu, D., Fall, M., Cai, S., 2013. Coupling temperature, cement hydration and rheological behavior of fresh cemented paste backfill. Miner Eng 42, 76-87.
Wu, D., Fall, M., Cai, S.-j., 2014. Numerical modeling of thermally and hydraulically coupled processes in hydrating cemented tailings backfill columns. Int J Min Reclam Environ 28, 173-199.
Yilmaz, E., Belem, T., Benzaazoua, M., 2014. Effects of curing and stress conditions on hydromechanical, geotechnical and geochemical properties of cemented paste backfill. Eng Geol 168, 23-37.
Yilmaz, E., Belem, T., Bussière, B., Benzaazoua, M., 2011. Relationships between microstructural properties and compressive strength of consolidated and unconsolidated cemented paste backfills. Cem Concr Compos 33, 702-715.

Yilmaz, E., Benzaazoua, M., Belem, T., Bussière, B., 2009. Effect of curing under pressure on compressive strength development of cemented paste backfill. Miner Eng 22, 772-785.
Yilmaz, E., Kesimal, A., Ercikdi, B., 2004. Strength development of paste backfill simples at Long term using different binders. Proceedings of the 8th Symposium MineFill Beijing, China; p. 281-285.
Yin, S., Wu, A., Hu, K., Wang, Y., Zhang, Y., 2012. The effect of solid components on the rheological and mechanical properties of cemented paste backfill. Miner Eng 35, 61-66.
Zhou, Q., Beaudoin, J.J., 2003. Effect of applied hydrostatic stress on the hydration of Portland cement and C3S. Adv Cem Res 15, 9-16.

CHAPTER 3

Mathematical Modeling of Cemented Tailings Backfill: Literature Review (Paper I)

3. Paper I: Mathematical Modeling of Cemented Tailings Backfill: Literature Review

Liang Cui, Mamadou Fall

Civil Engineering Department, University of Ottawa, Ottawa, ON, Canada (Submitted)

Abstract

The purpose of this literature review is to discuss the existing mathematical models, related advantages and limitations, and likely areas for further research for cemented tailings backfill (CTB). Such modeling is essential for the reliable assessment of CTB behavior and performance which are controlled by strongly coupled multiphysics (thermal, hydraulic, mechanical and chemical) processes. In this review paper, the existing mathematical models are classified into three categories which are analytical, mechanical constitutive and coupled multiphysics models. For each category, a critical discussion of each model is carried out to identify its applicability and potential further developments with a comparison of the corresponding controlling mechanism. Then, a comparison of the existing models is provided for each category of mathematical models. Consequently, this paper provides a comprehensive understanding and unique aspects of modeling CTB behavior and performance under complex multiphysics conditions.

Keywords: cemented tailings backfill; multiphysics; model; review

3.1. Introduction

Cemented tailings backfill (CTB) is one of the most novel materials in the past few decades in which mine wastes are made into cement structure materials (Helinski et al., 2007b; Ghirian and Fall, 2013, 2014; Haiqiang et al., 2016; Koupouli et al., 2016). CTB is prepared as a free-flowing mixture of mine tailings, hydraulic binder (Portland cement, blast furnace slag and/or fly ash) and water. Its use has become a standard practice in underground mines around the world (Yilmaz et al., 2004; Sivakugan et al., 2006; Fall et al., 2009). After preparation, fresh CTB is delivered into underground mined-out voids (called stopes) through pipeline systems through gravity flow and/or by pumping (le Roux et al., 2005; Yumlu, 2008). CTB structures can also provide ground support for the surrounding stopes, which can increase the recovery of ore bodies in underground mines (Mitchell et al., 1982; Ouellet et al., 2007; Benzaazoua et al., 2008; Nasir and Fall, 2010). Correspondingly, an accurate and reliable assessment of CTB behavior and performance has become one of the major tasks for backfill designers and engineers. Hence, the identification of the controlling mechanisms of behavior and performance of CTB structures is required. During and after placement, CTB structures are subjected to complex multiphysics (thermal, hydraulic, mechanical and chemical (THMC)) processes. The interaction of these multiphysics processes means that changes in cementation, temperature, pore water pressure, stress and strain take place in both experimental (e.g., Ghirian and Fall, 2013, 2014) and field studies on CTB (e.g., Belem et al., 2004b; Doherty et al., 2015). Therefore, complex multiphysics processes must be incorporated into the assessment of CTB performance in practice.

The current analysis techniques can be classified into two categories for backfill designs, which are physical and mathematical modeling. For the former, extensive experimental studies and in-situ monitoring programs have been conducted to investigate the controlling mechanisms of CTB behavior and associated influential factors. For instance, laboratory experiments have been carried out to analyze the changes in the (1) mechanical properties, such as the strength, elastic modulus, cohesion, and internal friction angle (see for e.g., Mitchell, 1989; Pierce, 1999; Fall et al., 2005; Fall et al., 2007; Koupouli et al., 2016), (2) hydraulic properties, such as the hydraulic conductivity and water retention (see for e.g., Belem et al., 2001; Godbout et al., 2007; Fall et al., 2009; Simms and Grabinsky, 2009; Ghirian and Fall, 2013; Pokharel and Fall, 2013), (3) thermal properties, such as the thermal conductivity (see for e.g., Celestin, 2009; Célestin and Fall, 2009), and (4) the coupled processes in CTB (see for e.g., Abdul-Hussain and Fall, 2012; Ghirian and Fall, 2013, 2014; Yilmaz et al., 2014).

Moreover, field investigations (e.g., Belem et al., 2004a; le Roux et al., 2005; Helinski et al., 2010; Thompson et al., 2012) have also provided substantial evidence that the complex CTB behavior is controlled by coupled multiphysics processes in CTB.

In comparison to physical experiments on CTB, mathematical modeling is more cost-effective and saves on time and material resources. Therefore, mathematical modeling can be used as an effective tool to investigate the effects of the various parameters (e.g., mixture recipe, curing and backfilling conditions) to achieve a better understanding of the performance of CTB. Consequently, mathematical modeling has attracted increasing attention in the literature, although the number of publications that address coupled multiphysics processes in CTB is still relatively limited. Mathematical models can be developed by using both specific assumptions and physical laws that govern the behavior of CTB (e.g., mass, momentum and energy conservation principles). Modeled solutions are determined through both analytical and numerical methods to predict CTB behavior. Therefore, an extensive literature review is conducted on the existing works on mathematical modeling including both analytical and numerical analyses on CTB in this paper to offer a comprehensive understanding of the fundamental and unique aspects of modeling CTB when subjected to coupled multiphysics processes. Moreover, as the mechanical stability of CTB structures is important, the mechanical constitutive models in the literature are separately provided. Therefore, the studies on mathematical modeling are classified into three categories, including analytical, mechanical constitutive, and coupled multiphysics models in this paper. For each category, the pertinent controlling mechanisms (i.e., coupled multiphysics processes) and unique characteristics of CTB behavior are first reviewed. Then, a critical discussion will be carried out on the models found in relevant studies against the identified controlling mechanisms, which will contribute to identifying their advantages, limitations and areas for further research.

3.2. Analytical models of CTB

As mentioned in Section 3.1, the complex multiphysics processes in CTB means that CTB demonstrates unique characteristics in comparison to common geomaterials such as soil, as follows: (1) with the progression of the hydration reaction, the capillary water in CTB is gradually consumed and converted into chemically combined water. As a result, since the hydrated volume is less than the volume of the unhydrated constituents (cement and water) (Helinski et al., 2007b), a reduction in positive pore-water pressure takes place, followed by the build-up of negative pore-water pressure, which is known as self-desiccation; (2) self-desiccation is accompanied by chemical shrinkage which contributes to the volumetric deformation of CTB (Helinski, 2008). Apart from chemical shrinkage, the volume changes of CTB are also related to the water drainage through the barricades, self-weight stress due to dynamic loads during backfill operations and thermal stress induced expansion or contraction (Ghirian and Fall, 2014, 2015). As a result, the volume change controlled by the multiphysics processes form the unique consolidation behavior of CTB; (3) with the progression of multiphysics consolidation processes in CTB, the rock mass/backfill interface resistance will be mobilized which will reduce the effects of the overburden pressure on the vertical stress (i.e., the arching effect) (Belem and Benzaazoua, 2008; Fall and Nasir, 2010). To study these phenomena (i.e., self-desiccation, consolidation and arching effect), analytical solution methods have been extensively applied due to the simplicity of the closed-form function. The analytical solution methods that have been applied for CTB are summarized and discussed in the following section.

3.2.1. Self-desiccation modeling

Helinski et al. (2007b) derived an analytical model to determine the variations in pore water pressure resultant of chemical shrinkage based on an experimental study on cement paste by Powers and Brownyard (1947). To derive the closed-form solution, the model assumes that (1) the volume differences between the deformed skeleton and unhydrated capillary water are compensated by the expansion (i.e., strain compatibility) of the capillary water, (2) CTB is in a fully saturated state at all stages of the process with time, and (3) pore water flow is not considered. Then, based on Terzaghi's effective stress principle (i.e., the effective stress changes are equal in magnitude and opposite in sign to the changes in pore-water pressure), an incremental closed-form analytical solution to self-desiccation is derived:

$$du = \frac{0.064 W_c K_w}{V_T \left\{ n + K_w \middle/ \left[K_{s-i} + \Delta K_{s-f} \exp\left(\frac{-d}{\sqrt{t - t_0}} \right) \right] \right\}} \tag{3.1}$$

where u is the pore-water pressure, W_c is the mass of the unhydrated cement, V_T is the total volume of the CTB and water (bulk volume), n is the porosity, K_w is the bulk stiffness of water, K_{s-i} and ΔK_{s-i} respectively represent the initial bulk modulus and the increase in bulk modulus at the completion of hydration, and the term $\exp\left(-d \middle/ \sqrt{t - t_0}\right)$

denotes the degree of hydration (i.e., progression of cement hydration) with d a maturity constant, t time and t_0 initial setting time.

As demonstrated in Eq. (3.1), the hydration reaction is quantitatively determined with a simple exponential function and coupled into the analysis of self-desiccation. Due to the assumption of a full saturation condition, the pore air pressure and negative pore water pressure in CTB are neglected. Moreover, the absence of pore water flow which results in the volume expansion of the pore water is the only driving force for the variation of the positive pore water pressure. Therefore, this analytical model is suitable for determining the changes in the pore water pressure and self-desiccation behavior of CTB at the early ages. Long-term behavior can be predicted by incorporating the negative pore water pressure and pore water flow into the analysis.

3.2.2. Consolidation modeling - Gibson's solution

Backfilling operations are a dynamic process which means that the total pressure that acts on the floor is not constant. Therefore, conventional analysis means of consolidation (i.e., Terzaghi consolidation theory) is not suitable for CTB. In order to study the consolidation behavior of CTB with increasing height, Gibson's solution (Gibson, 1958) derived from the pore-water mass balance equation for accretion layers of thick clay is applied (e.g., Helinski, 2008; Fahey et al., 2010; Shahsavari and Grabinsky, 2014):

$$\begin{aligned} u = & -\gamma_B z\left(1+\frac{V_{filling} z}{2C_v}\right)+\frac{\gamma_B V_{filling}}{2C_v}\left(\pi C_v t\right)^{-\frac{1}{2}}\cdot\exp\left(-\frac{z^2}{4C_v t}\right)\cdot \\ & \int_0^{\infty}\chi^2\coth\left(\frac{V_{filling}\chi}{2C_v}\right)\sinh\left(\frac{z\chi}{2C_v t}\right)\exp\left(-\frac{\chi^2}{4C_v t}\right)d\chi \end{aligned} \tag{3.2}$$

where γ_B is the unit weight of the CTB, z is the vertical distance from the stope floor, $V_{filling}$ is the filling rate, χ is an integration variable and C_v is the coefficient of consolidation (C_v = $M'K_{sat}/\gamma_w$ with M' as the constrained modulus, K_{sat} hydraulic conducitivity of CTB, and γ_w as the unit weight of water and).

As opposed to Terzaghi's consolidation theory, Gibson's solution provides the means to capture the consolidation behavior of materials with thickness of the accretion layers. However, the applicability of Gibson's solution is limited as it assumes that there are (1) constant material parameters (e.g., permeability coefficient and constrained modulus), (2) elastic deformation and (3) small strain conditions. Therefore, the influence of chemical processes on the material properties and volume changes, and finite strain are not taken into account.

3.2.3. Arching effect modeling - Limit equilibrium analysis

After placement into underground stopes, the consolidation process will result in the development of rock mass/backfill interface resistance which consists of interface frictional shear stress and adhesion. As a result, the vertical stress becomes less than overburden pressure (i.e., arching effect occurs). To analyze the stress distribution, several analytical models have been proposed based on the limit equilibrium analysis.

A commonly used analytical model for the arching effect is Marston's cohesionless model (Marston, 1930). The following assumptions are made when deriving Marston's model: (1) there is uniform distribution of horizontal stress at any given elevation in CTB, (2) the interface friction angle is equal to the internal friction angle of the CTB, (3) the interface adhesion is neglected, and (4) the variation in pore water pressure is not considered. Therefore, Marston's model is derived based on the force balance equation in the vertical direction, as follows:

$$\sigma_h = \frac{\gamma_B B_B}{2\tan\phi_B}\left[1-\exp\left(-\frac{2K_{earth}\tan\phi_B H_B}{B_B}\right)\right]$$
$$\sigma_v = \sigma_h / K_{earth} \tag{3.3}$$

where σ_h and σ_v respectively denote the horizontal and vertical stresses in the CTB, γ_{CTB} is the unit weight of the CTB, ϕ_B is the interface friction angle, B_C and H_C respectively denote the width and the total height of the filled stope, and K_{earth} is a coefficient of the earth pressure.

Since interface adhesion is not taken into consideration in Marston's model, a modified version (i.e., Terzaghi's cohesive model) was proposed by Terzaghi (1943):

$$\sigma_h = \frac{\gamma_B B_B - 2c_B}{2\tan\phi_B}\left[1-\exp\left(-\frac{2K_{earth}\tan\phi_B H_B}{B_B}\right)\right]$$
$$\sigma_v = \sigma_h / K_{earth} \tag{3.4}$$

where c_B is the interface adhesion and assumed to equal the cohesion of the backfill materials.

Experimental studies on the rock mass/backfill interface (Nasir and Fall, 2008; Fall and Nasir, 2010; Koupouli et al., 2016) have shown that the interface adhesion varies from 8 kPa to 33 kPa. Due to the low levels of adhesion generated along the interface, both Marston's and Terzaghi's cohesive models have been used to predict the arching effect of CTB (e.g., Aubertin et al., 2003; Li et al., 2003; Belem et al., 2004a).

To study the three-dimensional stress distribution in CTB, Belem et al. (2004b) proposed an analytical model based on Marston's model with monitored data taken from the Doyon Gold Mine:

$$\sigma_x = \frac{\gamma_B H_m (H_m - z)}{3(B_B + L_B)}\left\{1 - \exp\left[-\frac{2(h_{filling} - z)}{B}\right]\right\} \tag{3.5}$$
$$\sigma_z = \sigma_y = \sigma_x / 1.8$$

where σ_x, σ_y and σ_z respectively denote the longitudinal, transverse and vertical stresses in CTB, z is the elevation point of measurement with respect to the floor of the stope (i.e., z =0 at the floor), L_B is the stope length, and H_m and $h_{filling}$ represent the total height of the filled stope and filled height of the backfill, respectively.

In order to obtain a general 3D form (i.e., interface materials (friction angle and adhesion which differs for each rock wall, and the coefficient of the earth pressure which differs in each direction) of an analytical solution to the arching effect, Marston's model was extended into a 3D model by Li et al. (2005):

$$\sigma_v = \frac{\gamma_B - (\kappa_{13} B_B^{-1} + \kappa_{24} L_B^{-1})}{\lambda_{13} B_B^{-1} + \lambda_{24} L_B^{-1}}\left\{1 - \exp\left[-h(\lambda_{13} B_B^{-1} + \lambda_{24} L_B^{-1})\right]\right\} \tag{3.6}$$
$$\sigma_{hi} = K_i \sigma_v + 2c_B \tan\alpha_i$$

With

$$\lambda_{13} = K_1 \tan\delta_1 + K_3 \tan\delta_3$$
$$\lambda_{24} = K_2 \tan\delta_2 + K_4 \tan\delta_4$$
$$\kappa_{13} = c_1 + c_3 + 2c(\tan\alpha_1 \tan\delta_1 + \tan\alpha_3 \tan\delta_3)$$
$$\kappa_{24} = c_2 + c_4 + 2c(\tan\alpha_2 \tan\delta_2 + \tan\alpha_4 \tan\delta_4)$$

where σ_{hi} is the horizontal stress, K_i is the coefficient of the earth pressure in different directions, δ_i and α_i denote the interface friction and fill state angles, c_i is the interface adhesion, and λ_i and κ_i are the model coefficients. As indicated in Li et al. (2005), the general solution (i.e., Eq. (3.6)) is equivalent to the Marston's model under certain assumptions (i.e., uniform interface materials and coefficient of earth pressure).

It should be noted that these analytical models for the arching effect of CTB are used to explain for the development of total stress rather than effective stress, that is, the changes in pore water pressure are not considered. Therefore, to study the development of effective stress in CTB, Li and Aubertin (2009) incorporated hydrostatic pressure into the general analytical solution (i.e., Eq. (3.6)):

$$\begin{aligned} \sigma'_v = {} & \frac{\gamma_m - 2c_m(\lambda_{1m} B^{-1} + \lambda_{2m} L^{-1})}{M_m}\left[1 - \exp(-H_m M_m)\right]\exp\left[(H_m - h) M_{sat}\right] \\ & + \frac{\gamma_{sub} - 2c_{sat}(\lambda_{1sat} B^{-1} + \lambda_{2sat} L^{-1})}{M_{sat}}\left[1 - \exp\left[(H_m - h) M_{sat}\right]\right] \\ & + p_0 \exp\left[(H_m - h) M_{sat} - H_m M_m\right] \end{aligned} \tag{3.7}$$

$$\sigma'_{hi} = K_{isat} \sigma'_v + 2c_{sat} \tan\alpha_{isat} \tag{3.8}$$

With

$$\lambda_{1m} = 1 + 2\tan\alpha_{1m}\tan\delta_m$$

$$\lambda_{2m} = 1 + 2\tan\alpha_{2m}\tan\delta_m$$

$$\lambda_{1sat} = 1 + 2\tan\alpha_{1sat}\tan\delta_{sat}$$

$$\lambda_{2sat} = 1 + 2\tan\alpha_{2sat}\tan\delta_{sat}$$

$$M_m = 2\left(B^{-1}K_{1m} + L^{-1}K_{2m}\right)\tan\delta_m$$

$$M_{sat} = 2\left(B^{-1}K_{1sat} + L^{-1}K_{2sat}\right)\tan\delta_{sat}$$

where γ_{sub} represents the submerged unit weight of CTB, γ_m is the unit weight of wet backfill, σ'_v and σ'_{hi} respectively denote the effective vertical and horizontal stresses, K_i is to a coefficient of the earth pressure (m and sat refer to the moist and saturated states), δ_i and α_i are the interface friction and fill state angles, c_i is the interface adhesion, H_m is the wet (moist) backfill height, h is the backfill depth, λ and M are the model coefficients.

A literature review on the analytical models show that (1) the analytical methods provide a simple closed-form solution to assess CTB behavior and performance, (2) only partial coupling or a single physical process is taken into account during the derivation of the analytical models, and (3) the applicability of the analytical models is mainly limited by their assumptions. A detailed comparison of the analytical models is listed in Table 3.1.

Table 3.1. Summary and comparison of current analytical models of CTB

Analytical model	Considered multiphysics process	Remarks	Source
Self-desiccation model	Hydraulic Chemical Mechanical	1) able to predict the self-desiccation behavior in fully saturated state; 2) skeleton modulus changes with cement hydration; 3) hydration model is a function of time (mixture recipe and curing conditions are not considered); 4) no pore air pressure and no negative pore water pressure; 5) constant total pressure (dynamic backfilling is not considered).	Helinski et al. (2007b)
Consolidation model	Hydraulic Mechanical	1) able to predict consolidation with drained base and constant filling rate; 2) constant material properties (permeability, constrained modulus and coefficient of consolidation); 3) small strain and elastic deformation are assumed.	Fahey et al. (2010)

	Marston's model	Mechanical	1) interface resistance only consists of friction force; 2) increasing backfilling height is the main driving force for stress development; 3) does not consider filling rate and strategy; 4) no coupled multiphysics are considered.	Marston (1930)
	Terzaghi cohesive model	Mechanical	Similar to Marston's model but includes interface adhesion into interface shear resistance.	Terzaghi (1943)
Arching effect model	3D model in Belem et al.	Mechanical	Similar to Marston's model except the relationship of longitudinal, transverse and vertical stresses are obtained from data in Doyon Gold Mine.	Belem et al. (2004b)
	Model in Li et al.	Mechanical	Similar to Marston's model except the interface material parameters (friction angle and adhesion) differ for each rock wall, and coefficient of earth pressure differs in each direction.	Li et al. (2005)
	Model in Li and Aubertin	Mechanical hydraulic	1) similar to model in Li et al. except incorporates pore water pressure; 2) able to predict the development of effective stress with hydrostatic pressure (no excess pore water pressure and negative pore water pressure).	Li and Aubertin (2009)

3.3. Mechanical constitutive models of CTB

Mechanical stability is one of the most important design criteria of CTB structures. Therefore, the prediction of the mechanical behavior of CTB has practical importance for backfill designers and engineers (Fall et al., 2007). Based on the obtained experimental results, it has been found that (1) the mechanical properties (e.g., elastic modulus, cohesion, internal friction angle) change with time (e.g., Pierce, 1999; Belem et al., 2001; Benzaazoua et al., 2004; Yilmaz et al., 2004; Fall et al., 2007), which means that constant model coefficients assumed in common geomaterials (e.g., soil) are unsuitable for CTB materials, (2) the elastoplastic behavior dominates the response of CTB material parameters under different types of loading conditions such as unconfined compression tests, (e.g., Kesimal et al., 2005; Fall et al., 2007), triaxial compression tests (e.g., Belem et al., 2000; Fall et al., 2007; Rankine and Sivakugan, 2007; Simms and Grabinsky, 2009) and direct shear tests (e.g., Fall and Nasir, 2010; Koupouli et al., 2016), (3) strain hardening and softening behavior controls the plastic regime of CTB, especially for CTB samples that are cured for longer than 7 days (e.g., Fall et al., 2007; Ghirian and Fall, 2014), (4) hardening induced by cement hydration is the primary contributor to the rapid increase in CTB strength (e.g., Nasir and Fall, 2008; Abdul-

Hussain and Fall, 2012), which demonstrates that chemical hardening should be taken into consideration in the mechanical behavior of CTB. However, compared with the obtained experimental results, the corresponding studies on mechanical models are extremely limited due to the complex controlling mechanisms. The mechanical constitutive models of CTB materials reported in the literature are summarized in the following section.

3.3.1. Mises-Schleicher and Drucker-Prager unified (MSDPu) criterion

To characterize the behavior of hard rock and other brittle materials with low porosity, Aubertin and Simon (1996) proposed an inelastic Mises-Schleicher and Drucker-Prager unified ($MSDP_u$) criterion. As this criterion can reproduce the transitional states associated with particular types of mechanical responses, such as yielding, failure, and residual strength (Aubertin and Li, 2004), it was applied to describe the mechanical behavior of CTB (e.g., Aubertin et al., 2003; Li et al., 2010). The yield surface of $MSDP_u$ consists of a shear failure envelope and an elliptical cap (as shown in Figure 3.1a). The two parts of the yield loci are associated with each other by means of a MacCauley bracket operator (i.e., $\langle x \rangle = \left(x + |x|\right)/2$) that acts on the intersecting point (i.e., I_c).

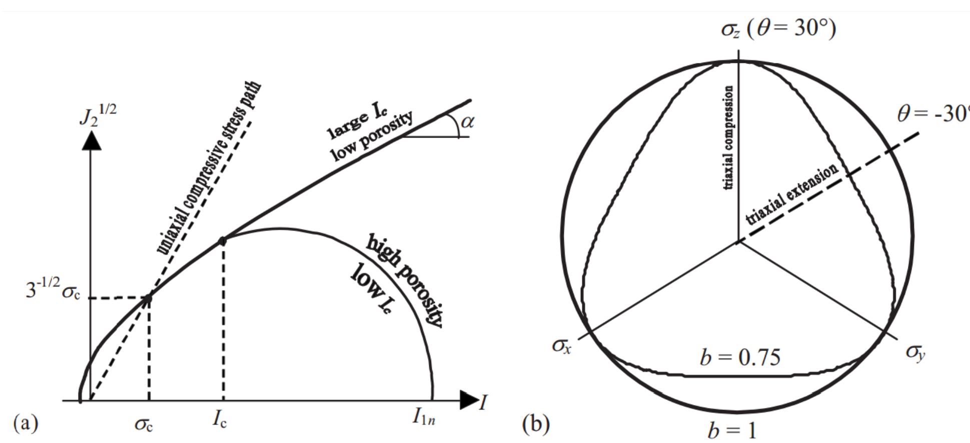

Figure 3.1. Yield surface of MSDPu criterion in (a) the I - J_2 plane and (b) the π plane (Li et al., 2010)

The $MSDP_u$ yield function can be expressed in terms of the first stress invariant I_1 and second invariant of the deviatoric stress J_2:

$$F_{MSDP_u} = J_2 - \frac{b^2\left\{\alpha^2\left(I_1^2 - 2a_1I_1\right) + a_2^2 - a_3\left\langle I_1 - I_c\right\rangle^2\right\}}{b^2 + \left(1 - b^2\right)\sin^2\left(45^\circ - 1.5\theta\right)} a_3 \tag{3.9}$$

where α , a_1 , a_2 and a_3 are the model parameters obtained from basic material properties, and b is the ratio of the locus size (see Figure 3.1b).

The $MSDP_u$ yield criterion can be used to describe the development of volumetric plastic deformation in CTB materials with the incorporation of an elliptical cap surface. However, the yield surface changes with the development of plastic strain (i.e., strain hardening and softening behavior) and a chemical reaction (i.e., chemical hardening) are not considered and constant model coefficients are still assumed in its application to CTB (Aubertin et al., 2003; Shirazi et al., 2006; Li et al., 2010). Moreover, the MSDPu criterion was originally proposed for rock materials. The corresponding model coefficients were thus determined through conventional tests (such as biaxial compression and tension tests) on rock materials. However, due to the relatively low strength of CTB (e g., the UCS can reach around 1 MPa after 28-days of curing) compared to rock materials, these laboratory tests are not commonly applied to CTB materials, especially early-age samples. Therefore, the extension of the MSDPu criterion so that the effects of chemical shrinkage and plastic strain are taken into account, and easier methods to identify the model coefficients, are required to accurately predict the plastic behavior of CTB.

3.3.2. Structured Cam Clay model

After placement into stopes, the volumetric plastic strain of fresh CTB will develop during consolidation, which is similar to the plastic behavior of natural soft soils, such as clay. Therefore, Helinski et al. (2007a) derived the Structured Cam Clay (SCC) model (structured means the changes in the void ratio and the resultant enhanced yield stress) proposed by Liu et al. (1998) to study the consolidation behavior of CTB. The yield locus of the SCC model is characterized through an elliptic function and the aspect ratio of the yield surface is identified by a conventional slope index M^* of the critical state line in p' - q stress space (p' refers to the effective mean stress and q is the deviatoric stress). The resulting elliptical yield surface passes through the origin of the stress coordinates.

Thus, the yield surface is identified by the yield function F_{scc} :

$$F_{scc} = \left(\frac{2q}{M^* p_s'} \right)^2 + \left(\frac{2p' - p_s'}{p_s'} \right)^2 - 1 = 0 \tag{3.10}$$

where p_s' denotes the size of the yield surface, namely the intersecting point of the ellipse with the p' axis. The corresponding yield surface is presented in Figure 3.2.

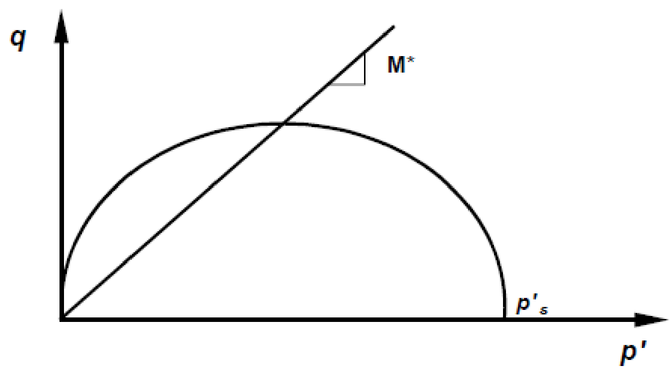

Figure 3.2. Yield surface of SCC model (Liu and Carter, 2002)

In order to incorporate the effects of cement hydration and damage induced by the development of plastic deformation, Helinski et al. (2007a) identified the chemical hardening and damage contributors to the yield stress. Consequently, the SCC model is able to explain (1) the development of volumetric plastic deformation, (2) the chemical hardening behavior induced by cement hydration and (3) the strain hardening behavior of CTB. However, the applicability of the SCC model to CTB materials is limited because (1) the adopted exponential hydration model only considers the influence of curing time, which cannot capture the impacts of the mixture recipe and (2) strain softening is not incorporated into the yield function, which means that the post-peak plastic behavior of CTB under compression loading conditions cannot be modeled.

Hence, after conducting a literature review on mechanical constitutive models, it was found that (1) the adopted mechanical models were originally used for common geomaterials (rock and soil), and therefore the corresponding models mainly capture conventional mechanical behaviors such as volumetric plastic strain and/or strain hardening behavior; (2) post-peak strain softening behavior is not taken into account; and (3) although cementation has been identified as a significant factor in the mechanical behavior of CTB, there is the need for an analytical description of the cement hydration by incorporating the influence of the mixture recipe and curing conditions . A detailed comparison of the mechanical constitutive models is provided in Table 3.2

Table 3.2. Summary and comparison of existing mechanical constitutive models of CTB

Mechanical model	Considered multiphysics processes	Remarks	Source
$MSDP_u$ model	Mechanical	1) able to predict the volumetric plastic strain; 2) does not consider strain hardening/softening or chemical hardening behavior.	Li et al. (2010)
SCC model	Chemical Mechanical	1) able to predict the volumetric plastic strain; 2) able to capture the strain and chemical hardening behavior; 3) does not consider strain softening behavior; 4) cannot model the influence of mixture recipe on cementation.	Helinski et al. (2007a)

3.4. Coupled multiphysics models of CTB

During and after pouring into underground stopes, CTB behavior is governed by fully coupled thermo-hydro-mechano-chemical (THMC) processes. Specifically, cement hydration occurs after mixing with water. Due to the exothermic characteristics of cement hydration (Bentz, 1997), the temperature in CTB will change with time, which can have a significant influence on the rate of the chemical reaction (Escalante-Garcıa and Sharp, 1998). Moreover, with the consumption of capillary water, the liquid pore water is gradually converted into solid hydrate products (i.e., chemically combined water) (Powers and Brownyard, 1947). Due to the fact that the volume of the hydrate products is less than that of the original capillary water and binder (i.e., self-desiccation effect) (Helinski et al., 2007a), changes to the saturation state and chemical shrinkage occur. The former can result in the variation of pore water pressure and consequently influence the effective stress in CTB. The latter can directly contribute to the deformation of CTB. Furthermore, with the development of volumetric deformation in CTB (i.e., consolidation process), relative displacement between the rock mass/backfill interface occurs and results in the formation of interface shear stress that acts on the CTB. As a result, the influence of the self-weight stress on the vertical stress within the stope can be reduced (i.e., arching effect) (Aubertin et al., 2003). Therefore, strongly coupled multiphysics

(THMC) processes govern the behavior and performance of CTB structures. To predict and assess the behavior and performance of CTB, several coupled models have been proposed in the literature, which are reviewed and summarized in the following section.

3.4.1. Thermo-chemical model

Nasir and Fall (2009) developed a coupled thermo-chemical (TC) model to predict the temperature changes in CTB. Heat conduction due to the thermal gradient and heat generation induced by cement hydration are taken into consideration. Since the hydraulic process is not considered, heat advection caused by pore fluid flow is neglected. The TC model is written as follows:

$$\rho C_v \frac{\partial T}{\partial t} - \nabla \cdot \left(k_T \nabla T\right) = q_{\max,20} c_{TC} \sin^{a_{TC}}\left(\xi \pi\right) \exp\left(-b_{TC} \xi\right) \exp\left[\frac{E_a}{R}\left(\frac{1}{293} - \frac{1}{T}\right)\right] \quad (3.11)$$

where C_v is the specific heat, ρ is the density, t is time, T is temperature, k_T the thermal conductivity, $q_{\max,20}$ denotes the maximum rate of released heat at a temperature of 20°C, a_{TC}, b_{TC} and c_{TC} are the material constants, ξ is the degree of binder hydration, E_a is the activation energy, and R is the universal gas constant.

As demonstrated in Eq. (3.11), Fourier's law is used to define the heat conduction in CTB. For heat generation (i.e., the source term on the right side of Eq. (3.11)), a model which incorporates the degree of cement hydration with temperature into the rate of heat release was proposed by Schindler et al. (2004):

$$\xi = \exp\left[-\ln\left(1 + \frac{t_{eqi}}{t_1}\right)^{-k_\xi}\right] \quad (3.12)$$

where t_{eqi} represents the equivalent time, and t_1 and k_ξ are the hydration parameters.

Moreover, to describe the effects of binder hydration and temperature on hydraulic conductivity, an empirical function for k_T was proposed based on experimental data reported in Célestin and Fall (2009). Therefore, the TC model explains the temperature changes due to heat conduction and release through cement hydration in CTB. However, only the coupled thermal and chemical processes are considered, and the temperature variations caused by the fluid flow (i.e., heat advection) cannot be predicted by this model.

3.4.2. Thermo-hydro-chemical model

Wu et al. (2014) proposed a thermo-hydro-chemical (THC) model to characterize the temperature and pore water pressure changes in CTB. For the thermal process, the heat advection induced by pore water flow was considered as the hydraulic process was incorporated into the model. Moreover, similar to the TC model developed by Nasir and Fall (2009), the heat generation by cement hydration was quantitatively determined by modeling the degree of hydration. The water loss due to drainage and the water retention behavior (i.e., description of negative pore water pressure) were considered for the hydraulic process. The modeling of the degree of hydration model captured the influence of the mixture recipe and curing temperature on the progression of the hydration reaction in terms of the chemical process. Thus, the THC model was developed based on energy and mass balance equations:

$$\rho C_v \frac{\partial T}{\partial t} + \rho C_v V_F \cdot \nabla T - \nabla \cdot \left(k_T \nabla T \right) = Q_T \tag{3.13}$$

$$\frac{\partial}{\partial t}\left(\rho_F \varepsilon_F \right) + \nabla \cdot \left(-\rho_F k \frac{k_r}{\mu_F} \varphi_F \right) = Q_m \tag{3.14}$$

where V_F is the velocity of the pore fluid (pore air and water), Q_T is the source term induced by cement hydration, ρ_F is the fluid density, ε_F is the fraction of pore space occupied by fluid with respect to the pore space, Q_m is the sink term induced by drainage, k is the intrinsic permeability, k_r is the relative permeability, μ_F is the dynamic viscosity, and φ_F the pore fluid pressure gradient.

To derive the constitutive relation, Fourier's law was used to describe the heat conduction, Darcy's law to characterize the pore fluid flow, and the water retention model developed by Van Genuchten (1980) were adopted in this THC model. Moreover, modeling of the degree of hydration was employed to derive the source term Q_T:

$$Q_T = H_T \left(\frac{\tau}{t} \right)^{\beta} \left(\frac{\beta \tau}{t} \right) \alpha\left(t\right) \exp\left[\frac{E}{R} \left(\frac{1}{293} - \frac{1}{T} \right) \right] \tag{3.15}$$

where H_T denotes the total ultimate heat released by binder hydration; β and τ are the hydration parameters; and $\alpha\left(t\right)$ is the binder hydration index at curing time t.

The model coefficients are determined by incorporating the influence of binder hydration into the permeability coefficient and water retention model parameters. Thus, the influence of the chemical process is demonstrated in terms of both the source term Q_T in the energy equation and model coefficients. However, the water sink term Q_m in Eq. (3.14) is assumed to be only related to water drainage, which means that the water consumption by cement hydration is not taken into consideration. Moreover, due to the absence of mechanical processes, this THC model cannot capture the variation of porosity (deformation) dependent material properties (e.g., the permeability and thermal conductivity).

3.4.3. Thermo-mechano-chemical model

Since strength is a key parameter for the designing of CTB structure, Nasir and Fall (2010) established a 2D numerical model to predict the development and distribution of undrained unconfined compressive strength (UCS) in CTB. The proposed model was coupled with the TC model developed by Nasir and Fall (2009) (see Section 3.4.1) to take into account the coupled effect of temperature and cement hydration. In the model, cement hydration is considered as the only factor that improves the strength of CTB. The derived prediction model for UCS is written in the following form:

$$\frac{\xi}{1-\xi}=\frac{f_c\left[k_{fc\_50^{\circ}C}-\beta_{TMC}\left(50^{\circ}C-T\right)\right]}{f_{28\_20^{\circ}C}\left[1-k_{const2}\left(T-20^{\circ}C\right)\right]-f_c}+k_{const1} \tag{3.16}$$

where f_c denotes the compressive strength, $f_{28\_20^{\circ}C}$ is the compressive strength after curing for 28 days at 20°C, ξ denotes the degree of hydration, and β_{TMC}, k_{const1}, k_{const2} and $k_{fc\_50^{\circ}C}$ are model constants.

The modified Bentz model (Bentz, 2006) which takes into consideration the effect of temperature on the reaction rate is used to describe the progression of the hydration reaction:

$$\frac{\partial\xi}{\partial t}=A_{const1}\frac{\left(A_{const2}-\xi\right)^2\left(1-\xi\right)}{A_{const3}-\xi}\exp\left[\frac{E}{R}\left(\frac{1}{293}-\frac{1}{273+T}\right)\right] \tag{3.17}$$

where A_{const1}, A_{const2} and A_{const3} are the hydration model parameters which are related to mixture recipe.

As demonstrated in the UCS prediction model (Eq. (3.16)), the temperature T and degree of hydration ξ govern the development of strength in CTB. The former can be obtained by using the TC model (Eq. (3.13)). The latter is explained by using Eq. (3.17). Then, the TMC processes interact with each other. However, it should be noted that the Mechanical component of this TMC model can only simulate the strength development in CTB, namely, the development of deformation and stress cannot be obtained from this TMC model. Hence, this TMC model is a hybrid numerical/analytical model for CTB. Moreover, because the TC model is directly incorporated into the strength prediction model, the TMC model automatically inherits the features of the TC model (e.g., without taking into consideration heat advection).

Therefore, compared with the identified controlling mechanisms (i.e., coupled thermo-hydro-mechano-chemical processes), the literature review on coupled multiphysics models demonstrates that (1) since only partially coupled physical processes are considered, the existing multiphysics models can only be used to predict very limited changes in field quantities (e.g., temperature or pore water pressure), (2) the proposed multiphysics models are valid only for very specific cases due to their assumptions, which reduce the accuracy and predictive ability of the developed models, and (3) for the accurate prediction of the variation of field quantities and material properties, a fully coupled multiphysics (THMC) model is required. A detailed comparison of the coupled multiphysics models is provided in Table 3.3.

Table 3.3. Summary and comparison of existing coupled multiphysics models of CTB

Coupled model	Balance equation	Constitutive relation	Remarks	Source
TC model	Energy	Fourier's Law	1) Heat conduction and generation by cement hydration are considered; 2) Heat advection induced by pore water flow is ignored; 3) inconsistent thermal conductivity based on experimental data in literature.	Nasir and Fall (2009)
THC model	Energy Mass	Fourier's Law Darcy's Law van Genuchten model	1) heat conduction, advection and generation are considered; 2) able to explain the pore water pressure changes under drainage conditions; 3) water loss by cement hydration is ignored; 4) model coefficients are related to cement hydration; 5) unable to reproduce the variation of porosity dependent material properties due to the absence of mechanical process.	Wu et al. (2014)
TMC model	Energy	Fourier's Law	1) inherits the features of TC model; 2) able to predict the development and distribution of UCS in CTB under dynamic thermal load conditions; 3) a hybrid numerical/analytical model.	Nasir and Fall (2010)

3.5. Conclusions

The behavior and performance of CTB are governed by strongly coupled thermo-hydro-mechano-chemical processes, which means that the assessment and prediction of CTB must incorporate coupled multiphysics processes. The following conclusions are drawn based on the findings obtained from the literature review in this chapter.

1) Analytical models provide simple closed-form solutions to explain specific features (i.e., self-desiccation, consolidation and arching effect) of CTB. Constant material properties are usually adopted. Therefore, the simplicity of analytical solutions means that they are extensively applied to predict the behavior of CTB. Analytical

solutions are derived based on assumptions (e.g., no negative pore water pressure in self-desiccation, elastic deformation in Gibson's solution, and uniform distribution of horizontal stress at any given elevation in arching effect) which, in turn, to a large extent, limit the predictive ability of analytical models.

2) The existing mechanical constitutive models of CTB reproduce conventional elastoplastic behavior (e.g., volumetric plastic strain and strain hardening behaviors) of geomaterials. However, they were originally developed for conventional geomaterials (such as rock and soil) and they are not coupled with a chemical model that describes the evolution of the cement hydration in a CTB system, which means they cannot fully capture CTB behaviors (e.g., chemical hardening, post-peak strain softening and enhanced material properties with curing time).
3) Existing multiphysics models only consider partially coupled physical processes, which significantly reduces their predictive ability.
4) Therefore, reliable and accurate assessment of CTB behavior and performance can only be realized with a fully coupled multiphysics model. Consequently, one of the key tasks is to develop multiphysics models specific to CTB materials and simulate the behavior of field CTB structures.

3.6. References

Abdul-Hussain, N., Fall, M., 2012. Thermo-hydro-mechanical behavior of sodium silicate-cemented paste tailings in column experiments. Tunn Undergr Sp Tech 29, 85-93.

Aubertin, M., Li, L., 2004. A porosity-dependent inelastic criterion for engineering materials. Int J Plasticity 20, 2179-2208.

Aubertin, M., Li, L., Arnoldi, S., Belem, T., Bussière, B., Benzaazoua, M., Simon, R., 2003. Interaction between backfill and rock mass in narrow stopes. Soil and Rock America 1, 1157-1164.

Aubertin, M., Simon, R., 1996. A multiaxial failure criterion that combines two quadric surfaces. Proceedings of 2nd North American Rock Mechanics Symposium.

Belem, T., Benzaazoua, M., 2008. Design and application of underground mine paste backfill technology. Geotech Geol Eng 26, 147-174.

Belem, T., Benzaazoua, M., Bussière, B., 2000. Mechanical behavior of cemented paste backfill. Proceedings of 53rd Canadian Geotechnical Conference Montreal; p. 373-380.

Belem, T., Bussière, B., Benzaazoua, M., 2001. The effect of microstructural evolution on the physical properties of paste backfill. Proceedings of Tailings and Mine Waste Fort Collins, Colorado; p. 365-374.

Belem, T., Harvey, A., Simon, R., Aubertin, M., 2004a. Measurement and prediction of internal stresses in an underground opening during its filling with cemented fill. Proceedings of the 5th International Symposium on Ground Support in Mining and Underground Construction; p. 28-30.

Belem, T., Harvey, A., Simon, R., Aubertin, M., 2004b. Measurement of internal pressures of a gold mine pastefill during and after the stope backfilling. Proceedings of 5th International Symposium on Ground Support in Mining and Underground Construction; p. 619-630.

Bentz, D.P., 1997. Three‐dimensional computer simulation of Portland cement hydration and microstructure Development. J Am Ceram Soc 80, 3-21.

Bentz, D.P., 2006. Influence of water-to-cement ratio on hydration kinetics: simple models based on spatial considerations. Cem Concr Res 36, 238-244.

Benzaazoua, M., Bussière, B., Demers, I., Aubertin, M., Fried, É., Blier, A., 2008. Integrated mine tailings management by combining environmental desulphurization and cemented paste backfill: application to mine Doyon, Quebec, Canada. Miner Eng 21, 330-340.

Benzaazoua, M., Fall, M., Belem, T., 2004. A contribution to understanding the hardening process of cemented pastefill. Miner Eng 17, 141-152.

Celestin, H.J.C., 2009. Geotechnical properties of cemented paste backfill and tailings liners: effect of mix components and temperature. University of Ottawa, Canada.

Célestin, J.C.H., Fall, M., 2009. Thermal conductivity of cemented paste backfill material and factors affecting it. Int J Min Reclam Environ 23, 274-290.

Doherty, J.P., Hasan, A., Suazo, G.H., Fourie, A., 2015. Investigation of some controllable factors that impact the stress state in cemented paste backfill. Can Geotech J 52, 1901-1912.

Escalante-Garcıa, J., Sharp, J., 1998. Effect of temperature on the hydration of the main clinker phases in Portland cements: Part II, blended cements. Cem Concr Res 28, 1259-1274.

Fahey, M., Helinski, M., Fourie, A., 2010. Consolidation in accreting sediments: Gibson's solution applied to backfilling of mine stopes. Geotechnique 60, 877-882.

Fall, M., Adrien, D., Celestin, J., Pokharel, M., Toure, M., 2009. Saturated hydraulic conductivity of cemented paste backfill. Miner Eng 22, 1307-1317.

Fall, M., Belem, T., Samb, S., Benzaazoua, M., 2007. Experimental characterization of the stress-strain behavior of cemented paste backfill in compression. J Mater Sci 42, 3914-3922.

Fall, M., Benzaazoua, M., Ouellet, S., 2005. Experimental characterization of the influence of tailings fineness and density on the quality of cemented paste backfill. Miner Eng 18, 41-44.

Fall, M., Nasir, O., 2010. Mechanical behavior of the interface between cemented tailings backfill and retaining structures under shear loads. Geotech Geol Eng 28, 779-790.

Ghirian, A., Fall, M., 2013. Coupled thermo-hydro-mechanical-chemical behavior of cemented paste backfill in column experiments. Part I: physical, hydraulic and thermal processes and characteristics. Eng Geol 164, 195-207.

Ghirian, A., Fall, M., 2014. Coupled thermo-hydro-mechanical-chemical behavior of cemented paste backfill in column experiments: Part II: Mechanical, chemical and microstructural processes and characteristics. Eng Geol 170, 11-23.

Ghirian, A., Fall, M., 2015. Coupled Behavior of Cemented Paste Backfill at Early Ages. Geotech Geol Eng 33, 1141-1166.

Gibson, R., 1958. The progression of consolidation in a clay layer increasing in thickness with time. Geotechnique 8, 171-182.

Godbout, J., Bussière, B., Belem, T., 2007. Evolution of cemented paste backfill saturated hydraulic conductivity at early curing time.

Haiqiang, J., Fall, M., Cui, L., 2016. Yield stress of cemented paste backfill in sub-zero environments: Experimental results. Miner Eng 92, 141-150.

Helinski, M., 2008. Mechanics of mine backfill. University of Western Australia, Australia.
Helinski, M., Fahey, M., Fourie, A., 2007a. Numerical modeling of cemented mine backfill deposition. J Geotech Geoenviron 133, 1308-1319.
Helinski, M., Fahey, M., Fourie, A., 2010. Behavior of cemented paste backfill in two mine stopes: measurements and modeling. J Geotech Geoenviron 137, 171-182.
Helinski, M., Fourie, A., Fahey, M., Ismail, M., 2007b. Assessment of the self-desiccation process in cemented mine backfills. Can Geotech J 44, 1148-1156.
Kesimal, A., Yilmaz, E., Ercikdi, B., Alp, I., Deveci, H., 2005. Effect of properties of tailings and binder on the short-and long-term strength and stability of cemented paste backfill. Mater Lett 59, 3703-3709.
Koupouli, N.J., Belem, T., Rivard, P., Effenguet, H., 2016. Direct shear tests on cemented paste backfill-rock wall and cemented paste backfill-backfill interfaces. Journal of Rock Mechanics and Geotechnical Engineering (In press).
le Roux, K., Bawden, W.F., Grabinsky, M.F., 2005. Field properties of cemented paste backfill at the Golden Giant mine. Mining Technology 114, 65-80.
Li, L., Aubertin, M., 2009. A three-dimensional analysis of the total and effective stresses in submerged backfilled stopes. Geotech Geol Eng 27, 559-569.
Li, L., Aubertin, M., Belem, T., 2005. Formulation of a three dimensional analytical solution to evaluate stresses in backfilled vertical narrow openings. Can Geotech J 42, 1705-1717.
Li, L., Aubertin, M., Shirazi, A., 2010. Implementation and application of a new elastoplastic model based on a multiaxial criterion to assess the stress state near underground openings. Int J Geomech 10, 13-21.
Li, L., Aubertin, M., Simon, R., Bussière, B., Belem, T., 2003. Modeling arching effects of narrow backfilled stopes with FLAC. Proceedings of the 3rd International Symposium on FLAC & FLAC 3D Numerical Modeling in Geomechanics Ontario, Canada; p. 211-219.
Liu, M., Carter, J., 2002. A structured Cam Clay model. Can Geotech J 39, 1313-1332.
Liu, M., Carter, J., Desai, C., Xu, K., 1998. Analysis of the compression of structured soils using the disturbed state concept. University of Sydney, Department of Civil Engineering, Centre for Geotechnical Research.
Marston, A., 1930. The theory of external loads on closed conduits in the light of the latest experiments. Proceedings of Highway Research Board.
Mitchell, R., 1989. Stability of cemented tailings mine backfill. Proceedings of Computer and Physical Modeling in Geotechnical Engineering Balkema, Rotterdam; p. 501-507.
Mitchell, R.J., Olsen, R.S., Smith, J.D., 1982. Model studies on cemented tailings used in mine backfill. Can Geotech J 19, 14-28.
Nasir, O., Fall, M., 2008. Shear behavior of cemented pastefill-rock interfaces. Eng Geol 101, 146-153.
Nasir, O., Fall, M., 2009. Modeling the heat development in hydrating CPB structures. Comput Geotech 36, 1207-1218.
Nasir, O., Fall, M., 2010. Coupling binder hydration, temperature and compressive strength development of underground cemented paste backfill at early ages. Tunn Undergr Sp Tech 25, 9-20.
Ouellet, S., Bussière, B., Aubertin, M., Benzaazoua, M., 2007. Microstructural evolution of cemented paste backfill: mercury intrusion porosimetry test results. Cem Concr Res 37, 1654-1665.
Pierce, M.E., 1999. Laboratory and numerical analysis of the strength and deformation behavior of paste backfill. Queen's University, Kingston.

Pokharel, M., Fall, M., 2013. Combined influence of sulphate and temperature on the saturated hydraulic conductivity of hardened cemented paste backfill. Cem Concr Compos 38, 21-28.
Powers, T., Brownyard, T., 1947. Studies of the physical properties of hardened Portland cement paste. ACI J. Proc., 249-336.
Rankine, R.M., Sivakugan, N., 2007. Geotechnical properties of cemented paste backfill from Cannington Mine, Australia. Geotech Geol Eng 25, 383-393.
Schindler, A., Ruiz, J., Rasmussen, R., Chang, G., Wathne, L., 2004. Concrete pavement temperature prediction and case studies with the FHWA HIPERPAV models. Cem Concr Compos 26, 463-471.
Shahsavari, M., Grabinsky, M., 2014. Cemented paste backfill consolidation with deposition-dependent boundary conditions. Proceedings of the 67th Canadian Geotechnical Conference.
Shirazi, A., Li, L., Aubertin, M., 2006. Numerical Implementation of an Elasto-plastic Model Based on the MSDPu Multiaxial Criterion.
Simms, P., Grabinsky, M., 2009. Direct measurement of matric suction in triaxial tests on early-age cemented paste backfill. Can Geotech J 46, 93-101.
Sivakugan, N., Rankine, R., Rankine, K., Rankine, K., 2006. Geotechnical considerations in mine backfilling in Australia. Journal of Cleaner Production 14, 1168-1175.
Terzaghi, K., 1943. Theory of Consolidation. Wiley Online Library.
Thompson, B., Bawden, W., Grabinsky, M., 2012. In situ measurements of cemented paste backfill at the Cayeli Mine. Can Geotech J 49, 755-772.
Van Genuchten, M.T., 1980. A closed-form equation for predicting the hydraulic conductivity of unsaturated soils. Soil Sci Soc Am J 44, 892-898.
Wu, D., Fall, M., Cai, S.-j., 2014. Numerical modeling of thermally and hydraulically coupled processes in hydrating cemented tailings backfill columns. Int J Min Reclam Environ 28, 173-199.
Yilmaz, E., Belem, T., Benzaazoua, M., 2014. Effects of curing and stress conditions on hydromechanical, geotechnical and geochemical properties of cemented paste backfill. Eng Geol 168, 23-37.
Yilmaz, E., Kesimal, A., Ercikdi, B., 2004. Strength development of paste backfill simples at Long term using different binders. Proceedings of the 8th Symposium MineFill Beijing, China; p. 281-285.
Yumlu, M., 2008. Barricade pressure monitoring in paste backfill. Gospodarka Surowcami Mineralnymi 24, 233-244.

CHAPTER 4

Multiphysics Modeling of Cemented Tailings Backfill

4.1. Introduction

After placement into underground stopes, CTB behavior is governed by complex multiphysics (thermal, hydraulic, mechanical and chemical) processes. Consequently, the changes in field quantities (e.g., temperature, pore water pressure and stress) and material properties (e.g., elasticity, cohesion, permeability, thermal conductivity) take place in CTB structures. Moreover, the development of volumetric deformation in CTB (i.e., consolidation behavior) is closely related to these multiphysics processes. Specifically, water drainage through barricades, effects of self-weight stress, chemical shrinkage and thermal expansion (or contraction) can directly contribute to the consolidation process. Furthermore, with the progress of consolidation in CTB, the relative displacement along the rock mass/backfill interface may take place gradually, which can give rise to interface resistance (i.e., interface frictional stress and adhesion) that acts on the backfill mass. Consequently, the effect of self-weight stress on the vertical stress is reduced (i.e., the arching effect). Therefore, in order to obtain a reliable assessment of CTB behavior, a series of fundamental multiphysics models are required, which include a chemo-mechanical model (evolutive elastoplastic model), a fully coupled multiphysics (THMC) model, a multiphysics model of the consolidation behavior and multiphysics model for the arching effect.

However, based on a literature review of the mathematical modeling on CTB (Chapter 3), it is found that there is currently no tool to predict the CTB behaviors under fully coupled multiphysics processes. Moreover, the existing mechanical constitutive models were originally developed for conventional geomaterials (e.g., soil and rock) and do not include a chemical model that describes the progress of cement hydration, which means they cannot fully capture CTB behaviors. Therefore, the development of an evolutive elastoplastic model (chemo-mechanical model) specific to CTB materials is first presented in Section 4.2, which can be used to model CTB mechanical behaviors including chemical and strain hardening, post-peak softening, and enhanced material properties with curing time. Then, the development of a fully coupled thermo-hydro-mechano-chemical model is described in Section 4.3 to predict the changes in field parameters (temperature, pore water pressure and deformation) and material properties. For the characterization of the consolidation process, a multiphysics model of the consolidation behavior is outlined in Section 4.3 based on the principles of the continuity of pore space and conservation of mass, energy and momentum. The aforementioned contributors (i.e., water drainage through barricades, effects of self-weight stress, chemical shrinkage and thermal expansion (or contraction)) to the consolidation behavior of CTB are fully incorporated into the multiphysics model of the consolidation behavior. A multiphysics interface model is established in Section 4.5 to describe the arching effect of CTB. This interface model can be used to capture the elastoplastic behaviors (chemical hardening and strain hardening/softening) along the interface of the rock mass and CTB. Moreover, the adopted model coefficients are identified in terms of measurable parameters. Finally, the predictability of each developed model is validated by comparing the predicted results with the experimental data from laboratory and field studies on CTB.

4.2. Paper II: An evolutive elasto-plastic model for cemented paste backfill

Published in Computers and Geotechnics 71 (2016) 19-29

Liang Cui, Mamadou Fall

Abstract

An evolutive elasto-plastic model is developed in this research work to address the vital role of binder hydration in the evolution of the mechanical behavior and properties of cemented paste backfill (CPB). Double hardening/softening parameters, which include effective incremental plastic strain and degree of binder hydration, are adopted. A non-associated plastic potential function based on the dilation angle is employed to formulate the plastic deformation and dilation of CPB. Mechanical parameters, such as cohesion, internal friction and dilation angles, stiffness, and Poisson's ratio are expressed as functions of the degree of binder hydration. The developed model is implemented in a finite element code, COMSOL Multiphysics, and then validated against experimental data obtained from laboratory tests performed in this study and by other researchers. The validation results show good agreement between the predicted and experimental results, thus confirming the capabilities of the new constitutive model to well capture binder hydration induced evolution of the mechanical behavior and properties of CPB.

Keywords: Cemented paste backfill; Tailings; Binder hydration; Constitutive model; Elasto-plastic; Cement

4.2.1. Introduction

As a relatively new technology, cemented paste backfill (CPB, a mixture of dewatered tailings, water and binders) has been increasingly and intensively used for the backfilling of previously mined-out underground voids (which are called stopes) in many mines around the world over the past three decades (Kesimal et al., 2003; Klein and Simon, 2006; Fall et al., 2007; Rankine and Sivakugan, 2007; Fall et al., 2008; Célestin and Fall, 2009; Ghirian and Fall, 2014; Li, 2014). The application of CPB can produce substantial economic and environmental benefits (Yilmaz et al., 2004; Rankine and Sivakugan, 2007; Cihangir et al., 2012; Yin et al., 2012; Li, 2014) while reducing the risks associated with open stope mining methods, including rock bursts, in underground mines. Due to the fact that a large amount of tailings are used as the key component in the preparation of CPB and then returned to the stopes, the use of CPB has been proven as an effective tailings management approach compared with other surface tailings disposal methods. In other words, CPB technology may help in reducing the volume of surface tailings deposits and therefore minimizes the associated geoenvironmental problems (Yilmaz et al., 2003a; Simms et al., 2007; Yin et al., 2012; Ghirian and Fall, 2013). Moreover, the use of CPB is an effective method for ground support (critical for underground mine work safety) as well as for the reduction of the mining cycle and speeding up of production (increases mine productivity) (Helinski et al., 2007; Nasir and Fall, 2010; Pokharel and Fall, 2010; Yin et al., 2012; Li, 2014).

The most important design criterion of CPB is mechanical stability. As a major means of ground support CPB must satisfy the mechanical stability requirements to ensure safe underground working conditions for all mining personnel. This is essential because the failure of CPB not only has substantial financial ramifications, but can also result in severe injuries and/or fatalities (Nasir and Fall, 2009). Thus, the understanding and prediction of the mechanical behavior of CPB at any curing time are of great practical importance.

However, the assessing and predicting of the mechanical stability of CPB are complex and challenging tasks mainly due to the fact that its mechanical properties evolve with time because of the binder hydration process. It is well known that the mechanical behavior of any cementitious material is strongly affected by the evolution of the microstructure induced by the progression of cement hydration. Specifically, after mixing the binder and water, the chemical reactions (i.e. binder hydration) start immediately. As the curing time or binder hydration progresses, the hydration products, such as calcium silicate hydrate ($C\text{-}S\text{-}H$) and calcium hydroxide (CH), gradually form and precipitate into the porous structure of the CPB (Simon, 2005). Due to the bonding effect of the hydration products, the microstructure of the CPB will gradually form and change with time, which means that the mechanical properties of the CPB (e.g. strength, cohesion, and stiffness) start to develop and evolve with time until the binder hydration stops or significantly slows down (Tariq and Yanful, 2013; Ghirian and Fall, 2014).

Several experimental studies have been conducted in the past decade that investigate the mechanical behavior and properties of CPB (Benzaazoua et al., 2004; Kesimal et al., 2005; Simon, 2005; Klein and Simon, 2006; Fall et al., 2007; Ghirian and Fall, 2014). These studies have significantly contributed to understanding the mechanical behavior of CPB and its evolution with time at the experimental level. For example, it has been experimentally observed that the hardening/softening behavior dominates the mechanical response of CPB under static loading. Moreover, strain hardening/softening behaviors have been widely observed and well characterized in laboratory experiments, including through the use of unconfined compression strength (UCS) tests, (Kesimal et al., 2003; Yilmaz et al., 2003b; Fall et al., 2005; Kesimal et al., 2005; Simon, 2005; Yilmaz et al., 2011; Ghirian and Fall, 2014), as well as triaxial compression tests (Pierce, 1999; Belem et al., 2000; Fall et al., 2007; Simms and Grabinsky, 2009). As for the volumetric response, dilation has been documented after the peak stress state in triaxial tests performed on CPB and many other cementitious materials (e.g., concrete, mortar and cemented soils) (Najjar et al., 1990; Schnaid et al., 2001; Chen et al., 2010; Horpibulsuk et al., 2012).

Despite the tremendous contributions of the previous studies towards the understanding of the mechanical behavior of CPB and its evolution with time, most of these studies have only dealt with the experimental characterization of the mechanical behavior of CPB. However, in backfill engineering practices, success in assessing and predicting the mechanical stability of a CPB structure primarily depends on the choice and use of an appropriate mechanical constitutive model. However, a limited number of studies have been performed in the past years to develop a constitutive model which enables the description and prediction of the mechanical behavior of CPB. For example, Pierce (2001) used Mohr-Coulomb constitutive relation to analyze the stability of CPB mass. In this model, constant mechanical properties (e.g., elastic modulus, cohesion and internal friction angle) and perfectly plastic flow are assumed. Helinski et al. (2007) developed a structured cam clay model (i.e., cementation is taken into account) to analyze the consolidation behavior of CPB. In this model, the strain-hardening, cementation and possible damage are related to the evolution of yield surface, while the definition of the degree of maturity does not incorporate the mixing parameters (i.e., w/c, cement content) and curing condition (i.e., curing temperature). Furthermore, the validation of the proposed model in terms of hardening-softening and plastic volumetric expansion behavior are not performed. Hughes (2014) proposed a simple mechanical model (i.e., explicit model) to depict strain-softening behavior of CPB. A piece-wise function is adopted to control pre- and post-peak stress, which results in a sharp point shown in the stress-strain curve. Moreover, due to the fact that the constitutive relation is not derived from elastoplastic theory, there is no plastic strain in the model. In addition, the proposed model does not consider the evolution of the mechanical properties (e.g., cohesion, internal friction angle, elastic modulus) with the cement degree of hydration. The aforementioned disadvantages and limitations of the models developed in the previous works limit their applicability and ability to accurately predict the mechanical behavior of CPB. Hence, the main objective of this study is to develop and validate an evolutive elastoplastic model for CPB, which is able to describe and predict the mechanical response of CPB and its evolution with binder hydration.

4.2.2. Mathematical formulation of the constitutive model

In this study, it is assumed that there are small deformations with respect to the mechanical response. The continuum mechanics convention is used; namely, tensile stresses are positive, whereas compressive stresses are negative.

4.2.2.1. Binder hydration model

As mentioned in Section 4.2.1, the determining factor of the evolution of the mechanical properties of CPB is the binder hydration. Therefore, in order to quantitatively evaluate the impact of binder hydration on the mechanical properties and behaviors, it is more convenient to describe binder hydration by means of a normalized variable called the degree of binder hydration, ξ. The degree of binder hydration is defined as the cement fraction that has reacted (De Schutter, 1999). For cement-based materials, the development of the degree of binder hydration can be expressed by the following exponential function (Schindler and Folliard, 2003, 2005; Wu et al., 2014):

$$\xi(t) = \xi_u \cdot exp\left[-\left(\frac{\tau_T}{t}\right)^{\beta}\right] \tag{4.1}$$

where $\xi(t)$ is the degree of hydration, ξ_u is the ultimate degree of hydration, τ_T is the hydration time parameter at the temperature of the cement-based materials, t is the chronological age, and β represents the hydration shape parameters. The ultimate degree of hydration is determined by the water-cement ratio and mineral admixture (e.g., fly ash and blast furnace slag) weight ratio in terms of total binder content and can be described as a hyperbolic function (Kjellsen et al., 1991).

$$\xi_u = \frac{1.031 \cdot w/c}{0.194 + w/c} + 0.5 \cdot X_{FA} + 0.30 \cdot X_{slag} \tag{4.2}$$

where w/c represents the water-cement ratio, and X_{FA} and X_{slag} represent the weight fraction of fly ash and blast furnace slag with respect to the total weight of the binder, respectively. If the binder just consists of cement ($X_{FA} = X_{slag}$ =0), ξ_u is equal to 1 if the w/c is greater than 6.258 (Wu et al., 2014). In the model shown in Eq. (4.1), there are two unknown parameters, namely, the hydration time parameter, τ_T and the hydration shape parameter, β These two parameters will be determined based on the experimental data of the CPB in Section 4.2.3.

4.2.2.2. Stress-strain relation of CPB

When plastic strain is considered, the total strain, $\boldsymbol{\varepsilon}$, generated in the CPB is composed of two components: the recoverable (reversible) elastic strain, $\boldsymbol{\varepsilon_e}$, and the irreversible plastic strain, $\boldsymbol{\varepsilon_p}$, such that:

$$\boldsymbol{\varepsilon} = \boldsymbol{\varepsilon_e} + \boldsymbol{\varepsilon_p} \tag{4.3}$$

Due to the strain history dependence, the deformation model based on an elasto-plastic framework can be written in terms of infinitesimal increments:

$$\boldsymbol{d\sigma} = \boldsymbol{D^e d\varepsilon_e} = \boldsymbol{D^e} (d\varepsilon - d\boldsymbol{\varepsilon_p}) \tag{4.4}$$

where $\boldsymbol{\sigma}$ is the stress tensor, and $\boldsymbol{D^e}$ is the tangent elastic modulus matrix which is defined by:

$$\boldsymbol{D^e} = \begin{bmatrix} 2\mu+\lambda & \lambda & \lambda & 0 & 0 & 0 \\ & 2\mu+\lambda & \lambda & 0 & 0 & 0 \\ & & 2\mu+\lambda & 0 & 0 & 0 \\ & & & 2\mu & 0 & 0 \\ & sym. & & & 2\mu & 0 \\ & & & & & 2\mu \end{bmatrix} \tag{4.5}$$

with λ and μ as the Lame's parameters:

$$\lambda = \frac{E\upsilon}{(1+\upsilon)(1-2\upsilon)} \qquad \mu = \frac{E}{2(1+\upsilon)} \tag{4.6}$$

where E and υ are the elastic modulus and Poisson's ratio respectively, which depend on the evolution of the CPB microstructure induced by the progression of the binder hydration. Therefore, the elastic modulus and Poisson's ratio are no longer constant for CPB.

The precipitation and bonding effect caused by hydration products lead to stiffening (elastic aging) of CPB and cause variation in the elastic modulus, i.e., $E = E(\xi)$ at the macro-level. In order to facilitate the implementation of elastic modulus measurement in numerical analysis, the following analytical expression developed by De Schutter and Taerwe (1996) is adopted in this study:

$$\frac{E}{E_\infty} = \left(\frac{\xi - \xi_0}{\xi_u - \xi_0} \right)^{A_E} \tag{4.7}$$

where E_∞ and ξ_u are the ultimate elastic modulus and degree of hydration, ξ_0 refers to the reference degree of hydration, which means that below a threshold value, ξ_0, no elastic modulus development occurs. The value of ξ_0 is determined based on the experimental data provided by Wang and Fall (2014) who conducted a laboratory CPB study. A_E is a material constant which depends on the mix components of CPB. For the evaluation of the parameters A_E and E_∞, a regression analysis is performed based on experimental data from (Klein and Simon, 2006; Fall et al., 2007; Ghirian and Fall, 2014). ξ_u can be calculated by using Eq.(4.2). The calculation results adopted in this study are listed in Table 4.1. As can be seen in Figure 4.1, the calculated data fit well the measured data, and the coefficient of determination, R^2, equals to 0.95.

Table 4.1. Calculated parameters for prediction of elastic modulus

Parameter	ξ_0	ξ_u	E_∞	A_E
Value	0.09	1	1900 MPa	2.199

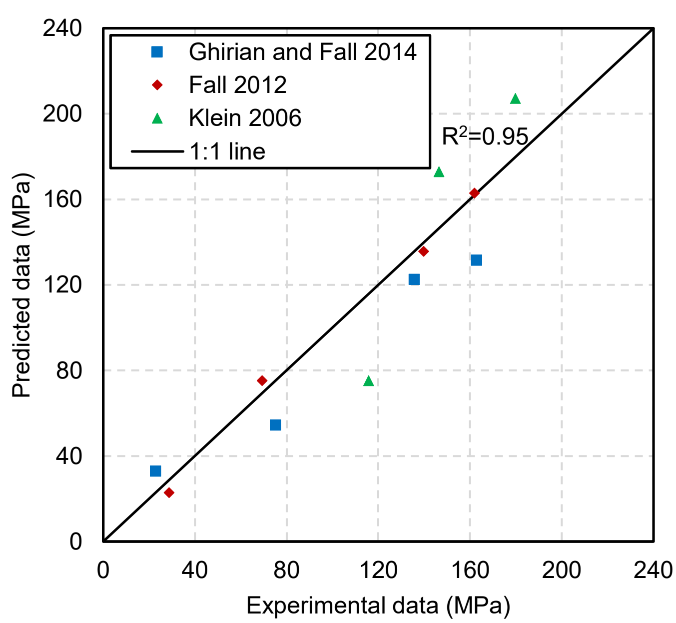

(a)

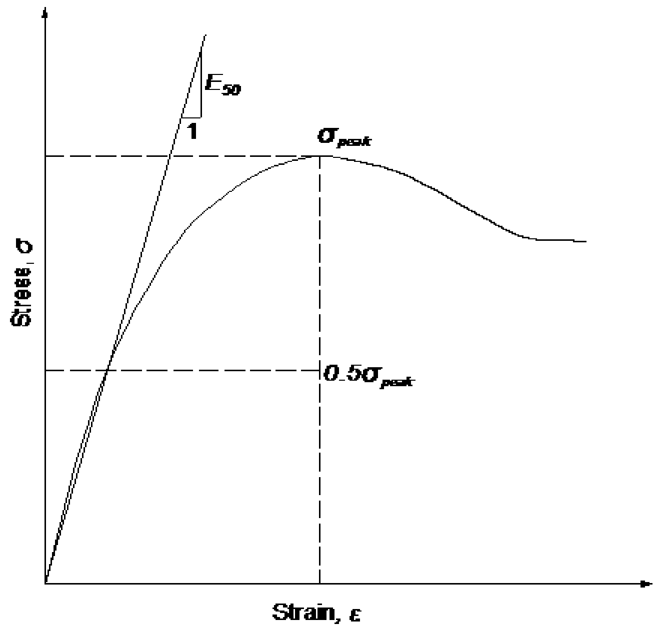

(b)

Figure 4.1. Evolution of elastic modulus and determination method: (a) Predicted values vs. measured data; (b) one typical stress-strain curve (secant modulus E_{50})

As mentioned in Section 4.2.1, the evolution of the mechanical properties, including the Poisson's ratio, is controlled by the progression of the binder hydration. Previous studies conducted on both CPB (Galaa et al., 2011) and cement paste (Sayers and Grenfell, 1993; Boumiz et al., 1996; Bittnar, 2006) have revealed that, as hydration progresses, the Poisson's ratio shows a descending trend, ranging from 0.5 (which corresponds to fresh paste) to the ultimate Poisson's ratio at the final degree of hydration. Therefore, the following equation is proposed to predict the evolution of the Poisson's ratio with the binder hydration.

$$\upsilon = 0.5\exp\left(B_{\upsilon 1}\xi\right) + B_{\upsilon 2}\xi^{B_{\upsilon 3}}\exp\left(B_{\upsilon 4}\xi^{B_{\upsilon 5}}\right) \tag{4.8}$$

where $B_{\upsilon 1}$, $B_{\upsilon 2}$, $B_{\upsilon 3}$, $B_{\upsilon 4}$ and $B_{\upsilon 5}$ are the fitting parameters which can be determined through UCS and triaxial compression tests. The measured data reported in Galaa et al., (2011) are adopted in this study to determine the five fitting parameters. Based on the results of the regression analysis, $B_{\upsilon 1}$=-0.2, $B_{\upsilon 2}$=-15000, $B_{\upsilon 3}$=7, $B_{\upsilon 4}$=-10.98 and $B_{\upsilon 5}$=0.7. As shown in Figure 4.2, the predicted values of the Poisson's ratio are in good agreement with the measured data, and the coefficient of determination, R^2, is equal to 0.97.

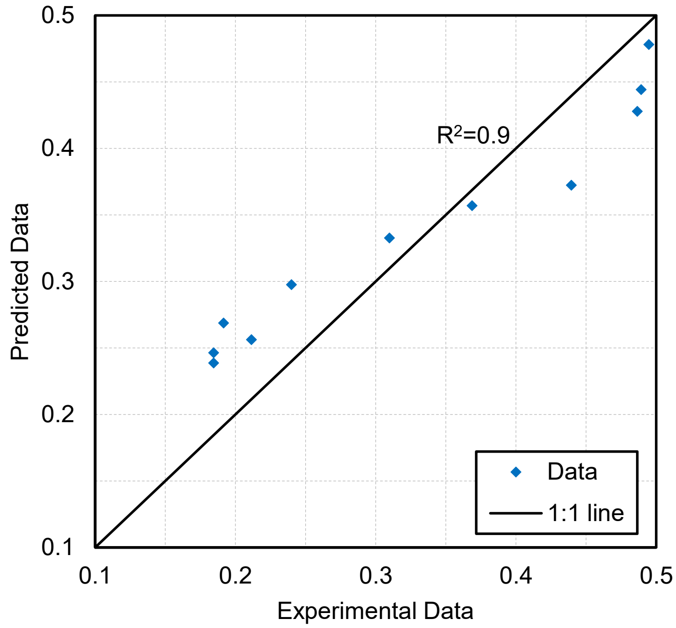

Figure 4.2. Comparison of experimental and predicted values of Poisson's ratio (experimental data on Poisson's ratio were obtained by measuring the longitudinal and radial strain of the CPB samples under static loading conditions (triaxial tests))

4.2.2.3. Plastic strain

In order to analyze the plastic deformation of CPB, the incremental theory of plasticity is needed. The following section deals with defining the yield surface (yield criterion) and plastic potential surface (e.g., defining the direction and magnitude of plastic increments).

4.2.2.3.1. Initial yield criterion

The Drucker-Prager (D-P) yield criterion is used, which is a pressure-sensitive model for determining whether the failure of the material has occurred (Yu et al., 2010). The D-P criterion, as a generalization of the von Mises criterion, has a number of advantages. Specifically, the influence of the hydrostatic stress on yield surface shape is defined by an additional term (i.e., first stress invariant I_1) in the von Mises expression (Doran et al., 1998). In addition, the material parameters of the D-P criterion not only can be directly determined by the test results, but may also be related to cohesion and the internal friction angle (Yuan, 2009). Moreover, compared with the Mohr-Coulomb yield criterion, the D-P criterion considers the effect of intermediate principal stress on the yield surface and represents a smooth yield surface, which makes it more mathematically convenient to use in three-dimensional applications (López Cela, 1998; Bigoni and Piccolroaz, 2004; Chen, 2007; Moresi et al., 2007). Due to the advantages, the D-P criterion is employed to characterize the yield behavior of CPB in this study. The D-P yield criterion can be expressed as:

$$f = \sqrt{J_2} + \alpha_{D-P}\left(I_1 - C_{D-P}\right) = 0 \tag{4.9}$$

where I_1 is the first stress invariant (i.e., $I_1 = \sigma_1 + \sigma_2 + \sigma_3$), $\sqrt{J_2}$ is the equivalent deviatoric stress defined by the stress deviator S_{ij} (i.e., $S_{ij} = \sigma_{ij} - I_1/3\delta_{ij}$, $J_2 = S_{ij}S_{ij}/2$), and α_{D-P} and C_{D-P} are the material parameters of the D-P criterion, which may be expressed by the internal friction angle, ϕ_B, and cohesion, c_B.

$$\alpha_{D-P} = \frac{2\sin\phi_B}{\sqrt{3}\left(3+\sin\phi_B\right)} \quad C_{D-P} = 3c_B\cot\phi_B \tag{4.10}$$

Due to progression of the binder hydration, hydration products will increase the cohesion between particles and significantly influence the microstructure of the CPB material. Consequently, the evolution of the mechanical parameters (i.e. cohesion and internal friction angle) in turn determines the variation of the yield surface. Therefore, it is necessary to establish the relationship between cohesion, $c_B = c_B\left(\xi\right)$, internal friction angle, $\phi_B = \phi_B\left(\xi\right)$ and binder hydration. The relationship between the two mechanical parameters and binder hydration can be developed based on direct shear test or triaxial test results. The details of the test procedures and results are shown in Section 4.2.3.

4.2.2.3.2. Subsequent yield criterion

Once the stress reaches the initial yield surface, plastic deformation ensues. Under continuous loading conditions, the microstructure of geo-materials will change with the development of plastic deformation, which results in the variation of the material properties, such as α_{D-P} and C_{D-P} in the D-P yield criterion (Jirásek and Bazant, 2002). Correspondingly, the evolution of the yield surface occurs. The increase of the yield stress which is needed in order to drive the plastic deformation is defined as strain hardening, whereas the decrease of the yield stress with plastic deformation after the peak stress is called strain softening (Derski et al., 2012). Compared with common geo-materials (e.g. rock and soil), the evolution of the yield surface of CPB material is not only determined by the plastic strain, but also controlled by the binder hydration which can influence the microstructure as well. Therefore, the hardening and softening behaviors of CPB are composed of two parts: chemical and strain hardening/softening behaviors:

$$\alpha_{D-P}\left(\xi,\kappa\right) = \alpha_{D-P}\left(\kappa\right) + \alpha_{D-P}\left(\xi\right) \tag{4.11}$$

where $\alpha_{D-P}\left(\kappa\right)$ is the plastic strain hardening/softening parameter and $\alpha_{D-P}\left(\xi\right)$ is the chemical hardening/softening parameter. Hence, $\alpha_{D-P}\left(\xi,\kappa\right)$ can characterize the chemo-plastic hardening/softening behavior of CPB. The chemical hardening/softening behavior can be demonstrated by the evolution of two key parameters of the D-P criterion as shown in Eq. (4.9), which can be rewritten as:

$$\alpha_{D-P}(\xi)=\frac{2\sin\phi_B(\xi)}{\sqrt{3}\left[3+\sin\phi_B(\xi)\right]}\qquad C_{D-P}(\xi)=3c_B(\xi)\cdot\cot\phi_B(\xi) \tag{4.12}$$

The plastic-strain hardening/softening process is attributed to the cumulative plastic strain, κ, (Jirásek and Bazant, 2002). The cumulative plastic strain can be expressed as follows:

$$\kappa=\int\sqrt{\frac{2}{3}d\varepsilon_p d\varepsilon_p} \tag{4.13}$$

In order to depict plastic strain hardening and softening, namely, the evolution of the yield function from inflation to deflation, a combined Weibull-normal distribution expression is used (Chen and Baladi, 1985):

$$\alpha_{D-P}(\kappa)=D_{\alpha1}\left\{\left[1-\exp(-D_{\alpha2}\kappa)\right]+\left[D_{\alpha3}\kappa\exp(-D_{\alpha4}\kappa)\right]\right\} \tag{4.14}$$

where $D_{\alpha1}$, $D_{\alpha2}$, $D_{\alpha3}$ and $D_{\alpha4}$ are the material constants which can be determined by using uniaxial or triaxial compression test data. Therefore, the hardening/softening parameter $\alpha_{D-P}(\xi,\kappa)$ can be expressed as:

$$\alpha_{D-P}(\xi,\kappa)=D_{\alpha1}\left\{\left[1-\exp(-D_{\alpha2}\kappa)\right]+\left[D_{\alpha3}\kappa\exp(-D_{\alpha4}\kappa)\right]\right\}+\frac{2\sin\phi_B(\xi)}{\sqrt{3}\left[3+\sin\phi_B(\xi)\right]} \tag{4.15}$$

In order to describe the hardening and softening behaviors of CPB materials, the isotropic hardening rule is adopted. Hence, the subsequent yield function can be expressed as follows:

$$F(I_1,\sqrt{J_2},\xi,\kappa)=\sqrt{J_2}+\alpha_{D-P}(\xi,\kappa)\left[I_1-C_{D-P}(\xi)\right]=0 \tag{4.16}$$

Therefore, for the loading function, the parameter $\alpha_{D-P}(\xi,\kappa)$ denotes the chemo-plastic strain hardening/softening parameter.

4.2.2.3.3. Plastic potential and plastic flow rule

When the stress increases beyond the yield point, the plastic strain increment is determined by the plastic potential and plastic flow rule. The former gives the direction of the plastic strain increment, while the latter gives its magnitude (Briaud, 2013). The plastic flow rule is defined by the plastic potential. Due to distinctive properties such as shear dilatancy and pressure-sensitive yielding, many geo-materials demonstrate non-associated behavior when deforming in the plastic regime (Vermeer and De Borst, 1984; Lade, 1988; Collins, 2002); namely, the direction of the plastic strain increment is not normal to the corresponding subsequent yield surface. Therefore, the non-associative flow rule has been commonly utilized for such materials, with the use of a plastic (flow) potential function that is different from the yield function.

$$d\boldsymbol{\varepsilon}_{\boldsymbol{p}} = d\lambda_p \frac{\partial Q_{CPB}}{\partial \boldsymbol{\sigma}} \tag{4.17}$$

where λ_p is a non-negative proportionality scalar called the plastic multiplier. The plastic multiplier can be determined using consistency conditions, such that the stress point must lie on the yield surface after the initial yield stress has been reached.

$$dF = \frac{\partial F}{\partial \boldsymbol{\sigma}} d\boldsymbol{\sigma} + \frac{\partial F}{\partial \kappa} d\kappa + \frac{\partial F}{\partial \xi} d\xi = 0 \tag{4.18}$$

By combining the flow rule $d\varepsilon_p = d\lambda_p \frac{\partial Q_{CPB}}{\partial \sigma}$ and elasto-plastic formula (4), the plastic multiplier can be rewritten as follows:

$$d\lambda_P = \frac{\left(\alpha_{D-P}\delta + \frac{s}{2\sqrt{J_2}}\right)\boldsymbol{D}^e d\boldsymbol{\varepsilon} + \frac{\partial F}{\partial \xi} d\xi}{\left(\alpha_{D-P}\delta + \frac{s}{2\sqrt{J_2}}\right)\boldsymbol{D}^e \frac{\partial Q_{CPB}}{\partial \boldsymbol{\sigma}} - \frac{\partial F}{\partial \kappa}\frac{\partial Q_{CPB}}{\partial \boldsymbol{\sigma}}} \tag{4.19}$$

For the definition of the plastic potential function, a number of researchers have suggested that it is suitable for the plastic function to be related to the dilation angle (Drucker, 1959; Vermeer and De Borst, 1984; Deb et al., 2013). Therefore, a simple plastic potential function, Q_{CPB}, for the D-P yield surface is considered, which is (Lubarda et al., 1996; Sumelka, 2014):

$$Q_{CPB} = \frac{2\sin\psi_B}{\sqrt{3}\left(3+\sin\psi_B\right)} I_1 + \sqrt{J_2} \tag{4.20}$$

where ψ_B denotes the dilation angle. Similarly, the dilation angle will be influenced by the binder hydration as well, namely, $\psi_B = \psi_B(\xi)$. In order to determine the dilation angle, a modified formula proposed by Houlsby (1991) is employed in this study to characterize the evolution of the dilation angle:

$$\sin(\psi_B) = K_{\psi 1}(\xi) \cdot \ln\left(\frac{p_n}{p_r}\right) + K_{\psi 2}(\xi) \tag{4.21}$$

where p_n and p_r respectively refer to the normal load stress that acts on the CPB sample, and the reference stress, namely the atmosphere pressure (101.325 kPa). $K_{\psi 1}(\xi)$ and $K_{\psi 2}(\xi)$ are the material parameters which evolve with binder hydration and will be determined from the direct shear test data in Section 4.2.3.

4.2.2.4. Constitutive relation

The incremental form of plastic strain can be expressed based on the plastic flow rule:

$$d\boldsymbol{\varepsilon}_p = \frac{\left(\alpha_{D-P}\delta + \frac{s}{2\sqrt{J_2}}\right)\boldsymbol{D}^e d\boldsymbol{\varepsilon} + \frac{\partial F}{\partial \xi} d\xi}{\left(\alpha_{D-P}\delta + \frac{s}{2\sqrt{J_2}}\right)\boldsymbol{D}^e - \frac{\partial F}{\partial \varepsilon_P}} \tag{4.22}$$

Then, the constitutive relation can be developed by substituting Eq.(4.22) into Eq. (4.4):

$$d\boldsymbol{\sigma} = \left\{\boldsymbol{D}^e - \frac{\boldsymbol{D}^e\left(\alpha_{D-P}\delta + \frac{s}{2\sqrt{J_2}}\right)\boldsymbol{D}^e}{\left(\alpha_{D-P}\delta + \frac{s}{2\sqrt{J_2}}\right)\boldsymbol{D}^e - \frac{\partial F}{\partial \varepsilon_P}}\right\} d\boldsymbol{\varepsilon} \tag{4.23}$$

Eq. (4.23) is the constitutive equation of CPB based on the D-P yield criterion.

4.2.3. Parameter determination, model verification and numerical simulation of experimental tests

In this section, the identification of the parameters of the proposed model is presented. Triaxial compression and direct shear tests were performed and the experimental data were utilized to determine the material parameters. Moreover, the capabilities of the developed model to predict the mechanical behavior of hydrating CPB are tested against well controlled laboratory experiments. These experiments were performed in the present study and other studies by other researchers. The procedures of the experimental mechanical tests performed are briefly described in the next subsection.

4.2.3.1. Experimental tests

Two mechanical tests, including undrained triaxial compression and direct shear tests, have been carried out in this study. In order to prepare the CPB samples, the adopted mixture recipe included 4.5% Portland cement type I (PCI) and a water to cement ratio (w/c) of 7.6. The tailings material, cement and water were mixed by using a concrete mixer, and homogenized for about 7 minutes. Then, the homogeneous CPB paste was poured into plastic cylinder molds. Subsequently, the molds were sealed and cured at room temperature. For the triaxial compression tests, the curing times were 7, 28 and 90 days, while the curing periods of the CPB samples for the direct shear tests were 1, 3, 7, 28, 60, 90 and 120 days.

The triaxial compression tests were conducted in accordance with ASTM D4767-02. The deviatoric stress and axial displacement were measured by using a load cell sensor and a linear variable displacement transformer (LVDT), respectively. The experimental data were then collected with a computer data acquisition system. The Tri-Flex 2 test system was utilized to measure the volume change of the CPB samples. A minimum of two samples were tested under each confining pressure.

In accordance with ASTM D5607-08, the direct shear tests were performed on CPB samples after different curing times. When the expected curing time was reached, the samples were removed from the molds and trimmed into cube specimens of the required size (60 mm×60 mm×25 mm). Two LVDTs were installed in the test system to measure the horizontal and vertical displacements, respectively, and the shear stress was measured through a load cell sensor. The test data were recorded by a computer data acquisition system throughout the testing. During the testing, shear force was applied at a rate of 1.0 mm/min. A minimum of three samples were tested under each vertical (normal) load force level.

4.2.3.2. Determination of parameters

In order to determine the degree of hydration that corresponded to the different curing times, the following values which were collected from (Schindler et al., 2004) are utilized in this study: w/c =7.6, τ_T =1.4 day, and β =0.394. The evolutive formulas of the mechanical properties could then be established. For the cohesion of CPB, the experimental results of the direct shear tests showed that there exists an approximate power relationship between cohesion and the degree of hydration. Therefore, the following empirical function is proposed in this study to describe the evolution of cohesion (kPa) with the degree of hydration:

$$c_B\left(\xi\right)=M_{c1}\xi^{M_{c2}} \tag{4.24}$$

where M_{c1} and M_{c2} are the fitting constants which can be determined through a regression analysis based on the experimental data of the direct shear tests. In this study, M_{c1} =478 kPa and M_{c2} =3.3. Figure 4.3 shows a comparison of the experimental and predicted data of the cohesion. Meanwhile, the predicted data are also compared with the experimental data reported in (Ghirian and Fall, 2014). It can be seen that the values of cohesion increase with curing time which contributes to the growth of bonds between tailings particles with the advance of binder hydration.

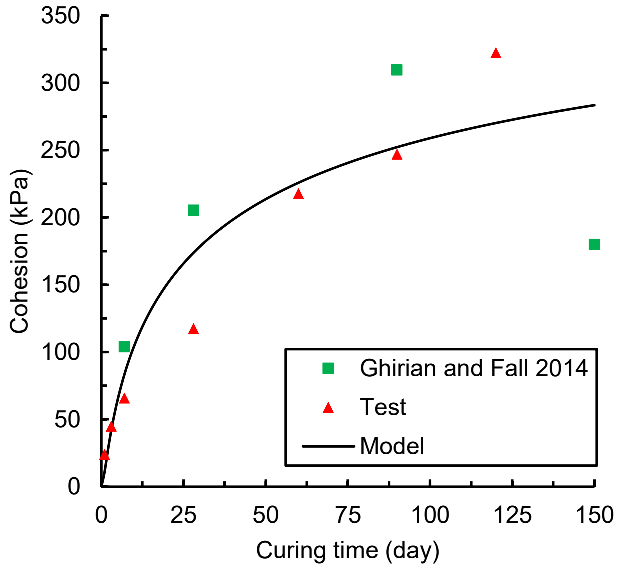

(a)

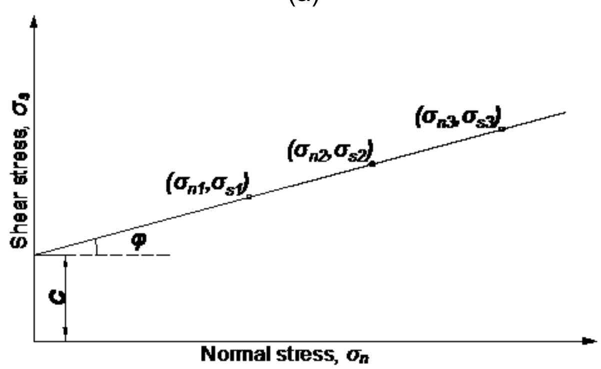

(b)

Figure 4.3. Evolution of Cohesion and determination method: (a) Predicted values vs. measured data; (b) one typical shear stress-normal stress

Similarly, the internal friction angle (in degrees) can be expressed as a function of the degree of hydration through the regression method and the resulting expression can be written as follows:

$$\phi_B(\xi) = N_1\xi^{N_2} + N_3\xi \tag{4.25}$$

where N_1, N_2 and N_3 are the fitting parameters which can be determined by the experimental data. Based on results of a regression analysis on the experimental data, N_1=-176.9°, N_2=2 and N_3=174.2°. The evolution of the internal friction angle with curing time is plotted in Figure 4.4. The experimental data reported in (Ghirian and Fall, 2014) are also collected and compared with the predicted values of the internal friction angle. As can be seen in Figure 4.4, there is an opposite variation trend in comparison to cohesion with curing time. Specifically, the total trend of the internal friction angle displays a decreasing trend with the progression of the binder hydration.

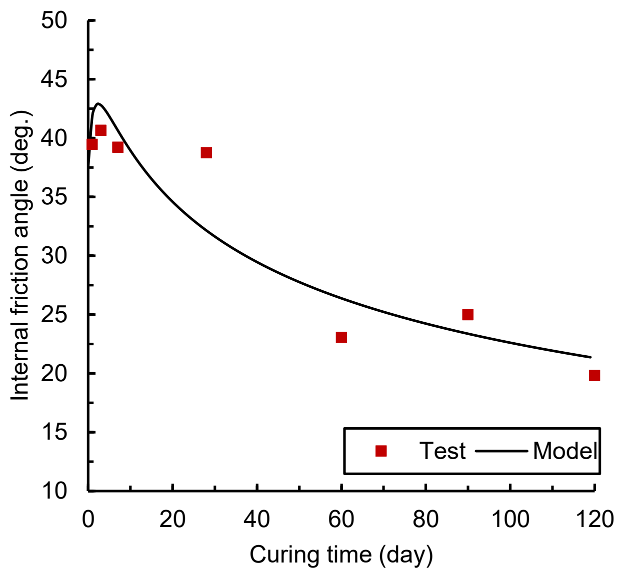

Figure 4.4. Comparison of test data and prediction of internal friction angle with curing time

The dilation angle is calculated by using the direct shear test data. Then, the material parameters $K_{\psi 1}(\xi)$ and $K_{\psi 2}(\xi)$ in the dilation angle expression (Eq. (4.21)) can be determined through a regression analysis. The following fitting functions are proposed to calculate $K_{\psi 1}(\xi)$ and $K_{\psi 2}(\xi)$:

$$K_{\psi 1}(\xi) = a_{\psi 1}\xi + a_{\psi 2} \tag{4.26}$$

$$K_{\psi 2}(\xi) = b_{\psi 1}\xi^2 + b_{\psi 2}\xi + b_{\psi 3} \tag{4.27}$$

where $a_{\psi 1}$, $a_{\psi 2}$, $b_{\psi 1}$, $b_{\psi 2}$ and $b_{\psi 3}$ are the fitting parameters. In this study, $a_{\psi 1}$=-0.2126, $a_{\psi 2}$=0.01257, $b_{\psi 1}$=1.239, $b_{\psi 2}$=-0.6461 and $b_{\psi 3}$=0.01115 based on the experimental data from the direct shear tests. The results plotted in Figure 4.5 are evidence of an upward trend with curing time and downward trend with normal stress levels. Overall, a good agreement between the test data and model prediction is reached.

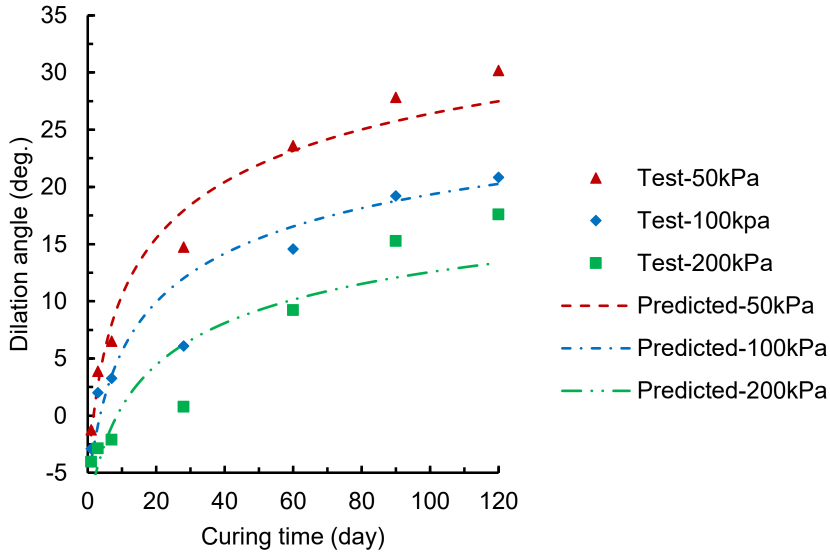

Figure 4.5. Comparison of test data and prediction of dilation angle with curing time

In order to simulate the hardening/softening behavior of CPB, four unknowns ($D_{\alpha 1}$, $D_{\alpha 2}$, $D_{\alpha 3}$ and $D_{\alpha 4}$) that exist in $\alpha_{D-P}(\kappa)$ are needed, which can be determined by the UCS or triaxial compression test data. In this study, the UCS test data reported in (Ghirian and Fall, 2014) are adopted. The following fitting equation is proposed to predict the evolution of the four unknowns with progression of the binder hydration:

$$D_{\alpha 1} = d_{\alpha 1} \exp\left(d_{\alpha 2} \xi\right) \tag{4.28}$$

$$D_{\alpha 2} = d_{\alpha 3} \xi^{d_{\alpha 4}} + d_{\alpha 5} \tag{4.29}$$

$$D_{\alpha 3} = d_{\alpha 6} \xi^{d_{\alpha 7}} + d_{\alpha 8} \tag{4.30}$$

$$D_{\alpha 4} = d_{\alpha 9} \exp\left(d_{\alpha 10} \xi\right) \tag{4.31}$$

where $d_{\alpha i}$ is the fitting parameters (i =1 to 10). Through a regression analysis of the reported experimental data in (Ghirian and Fall, 2014), $d_{\alpha 1}$ =3.895, $d_{\alpha 2}$ =-6.024, $d_{\alpha 3}$ =272.8, $d_{\alpha 4}$ =6.786, $d_{\alpha 5}$ =78.77, $d_{\alpha 6}$ =45930, $d_{\alpha 7}$ =22.25, $d_{\alpha 8}$ =143, $d_{\alpha 9}$ =15.87 and $d_{\alpha 10}$ =2.757 are adopted in this study. The fitting results are shown in Figure 4.6. It is found that the hardening/softening parameter, $\alpha_{D-P}(\kappa)$, evolves with curing time. Therefore, it can be concluded that the evolution of the hardening/softening parameter, $\alpha_{D-P}(\kappa)$, is consistent with the variation of the material properties (i.e. cohesion, internal friction and dilation angles, stiffness, and Poisson's ratio), which demonstrates the vital role that binder hydration has played in CPB, namely, the evolution of the material properties of CPB is influenced by the binder hydration.

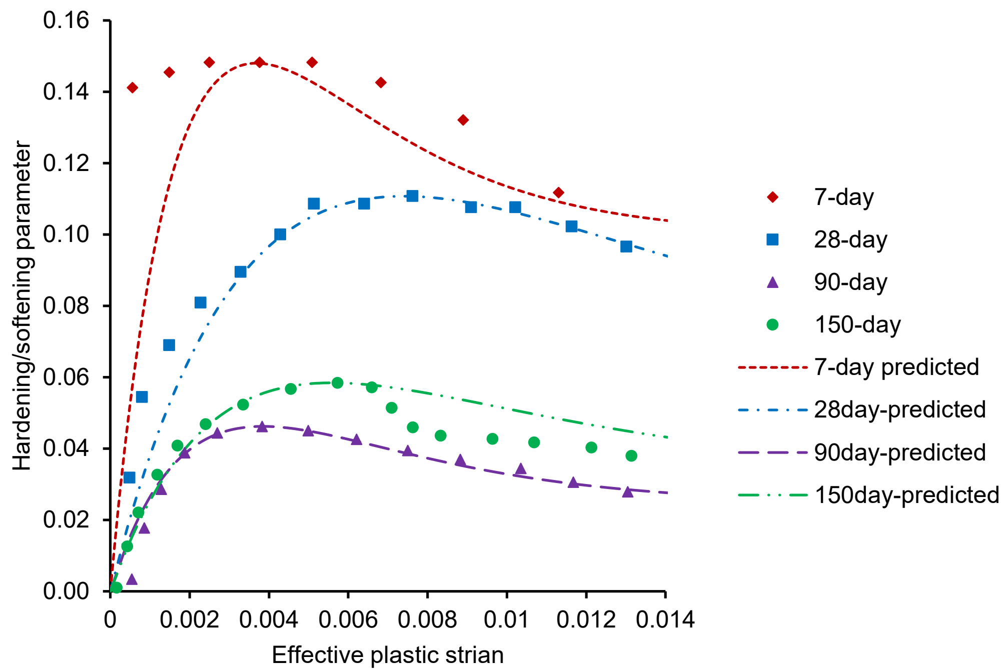

Figure 4.6. Comparison of test data and prediction model of hardening/softening parameters

4.2.4. Model verification and numerical simulation of experimental tests

The proposed evolutive elasto-plastic model is implemented in a FEM code, COMSOL Multiphysics® Version 4.4. This code can perform analysis of diverse categories, including: stationary and time-dependent, linear and nonlinear, eigenfrequency, modal and frequency response analyses by using FEM together with adaptive meshing and error control which employ a variety of numerical solvers (COMSOL, 2013). The capabilities of the developed elasto-plastic model to predict and capture the time-dependent (induced by the progression of binder hydration) evolution of the mechanical behavior of CPB are tested against several well controlled laboratory mechanical tests performed in this study and by other researchers (Pierce, 1999; Belem et al., 2000; Kesimal et al., 2003; Kesimal et al., 2005; Fall et al., 2007; Simms and Grabinsky, 2009; Ghirian and Fall, 2014) on CPB of various ages. This model verification will provide confidence in its validity and reliability for binder hydration induced evolution of the mechanical behavior of CPB.

4.2.4.1. Hardening/softening behavior simulation

As mentioned in Section 4.2.2, the hardening/softening behavior of CPB is controlled by both binder hydration and strain development. To verify the model, numerical simulation of the UCS and triaxial compression tests was performed and the simulation results were compared with numerous experimental data reported in the literature.

Figure 4.7 shows the comparison of the simulation results and reported experimental data of the UCS tests for both short-term cured (7 and 28 days) and long-term cured (more than 28 days) samples. Detailed information on the reported tests is shown in Table 4.2.

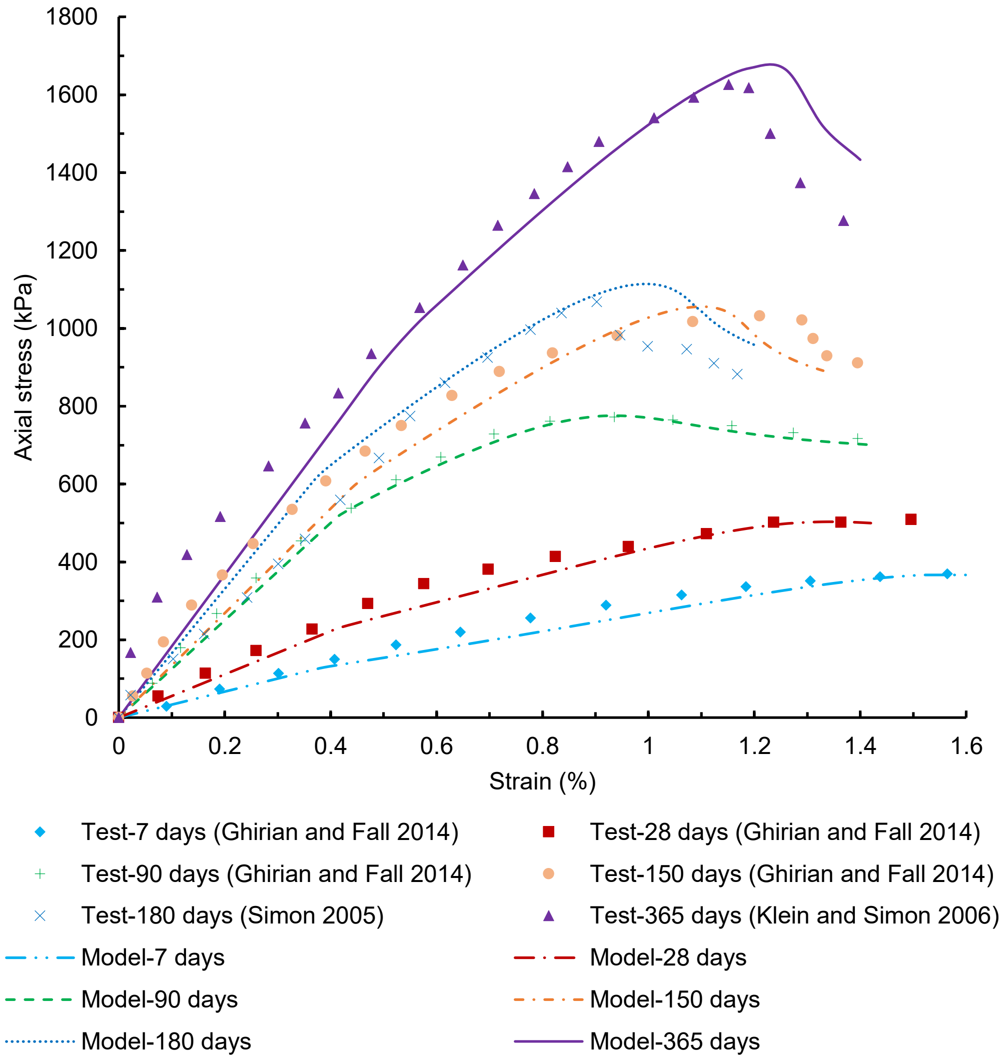

Figure 4.7. Comparison of numerical prediction and experimental data of UCS tests

Table 4.2. Information on reported tests

Source	Belem et al. 2000	Simon 2005	Kesimal et al. 2005	Klein and Simon 2006	Fall et al. 2007	Ghirian and Fall 2014
Binder content (%)	4.5	5	7	5	4.5	4.5
W/B ratio	6.36	7.8	4.6	7.8	7	7.6
Water	-	DW	TW	DW	TW	TW
Binder	PCI/Slag at (20/80)	PC10/FA at (50/50)	OPC	PC10/FA at (70/30)	PCI/ PCV at (50/50)	PCI
Tailings	Mill tailings	Mine tailings	Mine tailings	Mine tailings	Mine tailings	Silica
Test	UC/TC	UC	UC	UC	UC/TC	UC

* W/B-water to binder ratio; UC-uniaxial compression test; TC-triaxial compression test; PCI-Portland cement type I; OPC-ordinary Portland cement; PC10-Portland cement type 10 (=PCI);TW-tap water; DW- deionized water; FA-fly ash

As shown in Figure 4.7, the predicted axial stress-strain and UCS values are in good agreement with the experimental results. It is interesting to notice that the stress-strain curves of the short-term and long-term cured CPB samples illustrate different evolution trends in terms of strain hardening/softening behavior. For the short-term (7 and 28 days) cured samples, the strain hardening behavior is dominant during uniaxial compression testing, while for the long-term (90, 150, 180 and 365 days) cured samples, the strain hardening/softening behavior becomes obvious with increasing stiffness. Similar behaviors have also been observed in previous experimental studies (Annor, 1999; Fall et al., 2007; Sainsbury and Urie, 2007). In addition, both the laboratory and simulation results demonstrate that the stress level increases with curing time, which proves that chemical hardening does have a significant impact on the mechanical behavior of CPB.

The simulated UCS values are plotted against the experimental data collected from (Belem et al., 2000; Kesimal et al., 2005; Klein and Simon, 2006; Fall et al., 2007; Ghirian and Fall, 2014), see Figure 4.8. The simulation results show good agreement with the test data, and the coefficient of determination, R^2, is equal to 0.98.

In order to further verify the proposed model under confining pressure conditions, simulation of the triaxial compression tests was performed and compared with the experimental data reported in the literature (see Figure 4.8) (Pierce, 1999; Belem et al., 2000; Fall et al., 2007; Simms and Grabinsky, 2009). Table 4.3 Shows detailed information from the reported tests.

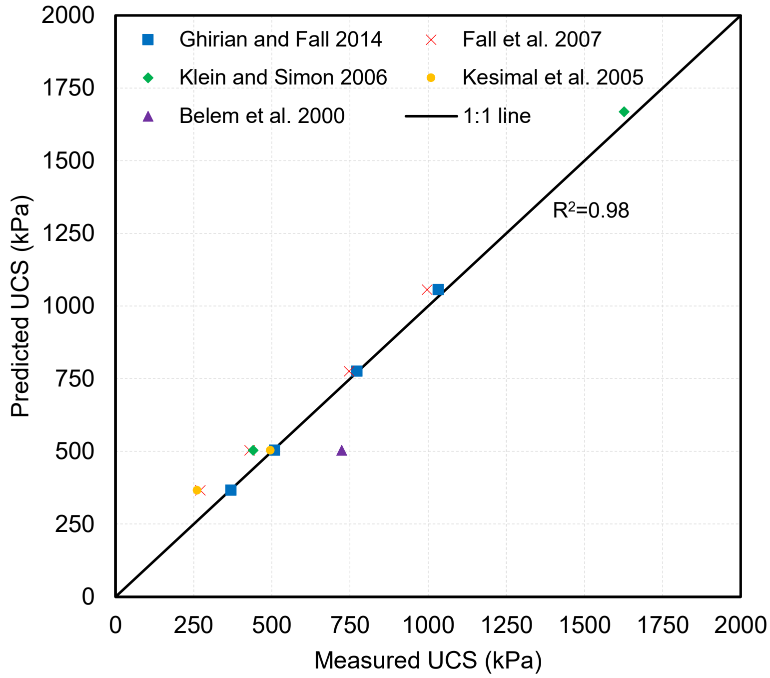

Figure 4.8. Predicted versus measured UCS for various CPB samples

Table 4.3. Information from reported tests

Source	Belem et al. 2000	Fall et al. 2007	Simms and Grabinsky 2009
Binder content (%)	4.5	4.5	5
W/B ratio	6.36	7	7.14
Water	-	TW	-
Binder	PCI/Slag at (20/80)	PCI/ PCV at (50/50)	PCI
Tailings	Mill tailings	Mine tailings	Golden Giant tailings
Test	UC/TC	UC/TC	TC

* W/B-water to binder ratio; UC-uniaxial compression test; TC-triaxial compression test; PC-Portland cement; TW-tap water; FA-fly ash

The simulation results which are plotted against the reported experimental data in (Pierce, 1999; Belem et al., 2000; Fall et al., 2007; Simms and Grabinsky, 2009) at different confining pressure levels that range from 20 to 800 kPa are presented in Figure 4.9.

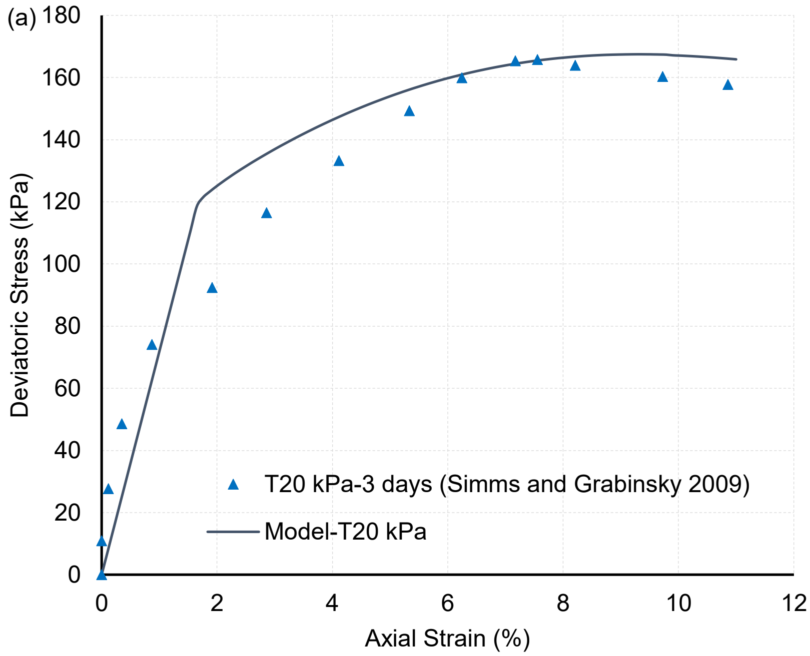

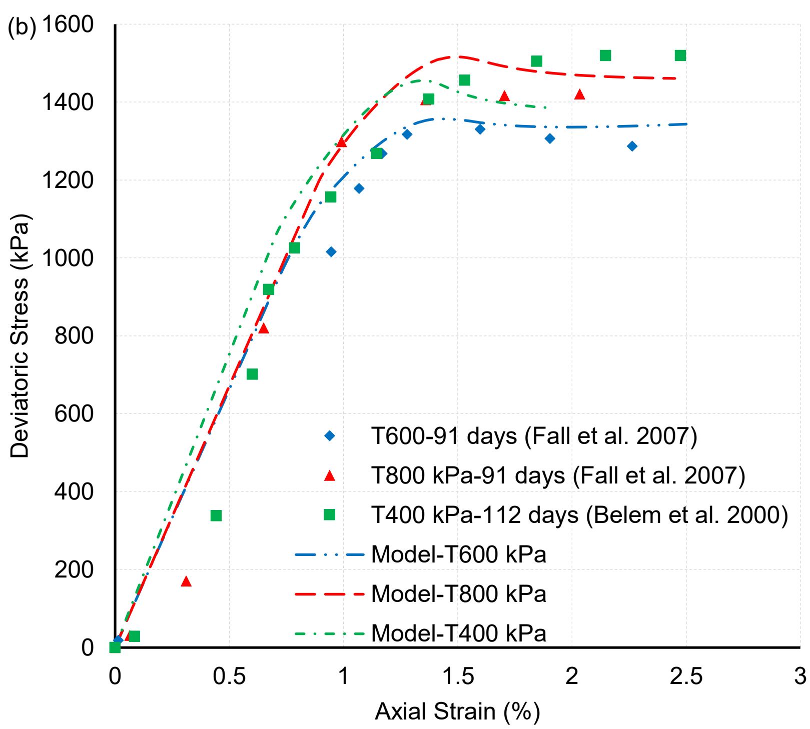

Figure 4.9. Comparison between numerical prediction and corresponding test data for triaxial testing on CPB samples: (a) short-term cured, and (b) long-term cured samples

As shown in Figure 4.9, it can be seen that the simulated deviatoric stress-axial strain curve is in good agreement with that of the experimental data. The deviatoric stress-axial strain curves exhibit a similar development trend to that of the UCS curves. For the short-term cured CPB samples, the stress-strain relation mainly demonstrates strain hardening behavior. As curing time increases, the strain hardening/softening behavior is evident. Similar to the UCS curves, the peak stress values show a clearly ascending trend with respect to curing time.

By comparing the numerical simulation results and experimental data (i.e., UCS and triaxial compression test data), it can be concluded that the proposed evolutive elasto-plastic model is capable of predicting the strain hardening/softening behavior of CPB and capturing the influence of binder hydration on the mechanical behaviors.

4.2.4.2. Volumetric response simulation

Besides the stress-strain relation, the volumetric behavior of CPB under loading conditions is also critical. In order to verify the ability of the model to predict the volumetric response, the numerical simulation results are compared with the experimental data from the triaxial compression tests.

Figures 4.10-4.12 show comparisons of the predicted results and the experimental data of the volumetric strain in the triaxial compression tests. The volumetric strain shows a two-stage evolution with deviatoric stress development. Firstly, it can be observed that the volumetric strain of CPB gradually reduces with deviatoric stress and the volume contraction is maintained in the elastic regime. Subsequently, around the peak stress, the volume expansion (also called volume dilation) is initiated and continues throughout the softening regime. Based on the experimental data, the volume expansion is reduced as the confining pressure is increased. From a microstructure point of view, different mechanisms dominate the two-stage changes of volumetric strain. Specifically, the volume contraction is attributed to the compression of pore space which is occupied by pore air. During the curing period, pore water is continuously consumed by binder hydration and the former water occupied pore space gradually becomes empty. Therefore, when a compression load is applied, the pore space will be compacted and the volume of the CPB sample will decrease (volume contraction), while volume expansion is induced by the onset, spread and intensification of microcracks after the yield point (Klimczak and Schultz, 2013). The corresponding lateral strain exhibits a similar evolution trend. The simulated lateral strain shows that, during the first stage of the triaxial compression testing, the lateral strain is relatively small, then the lateral strain shows a rapidly ascending trend with deviatoric stress.

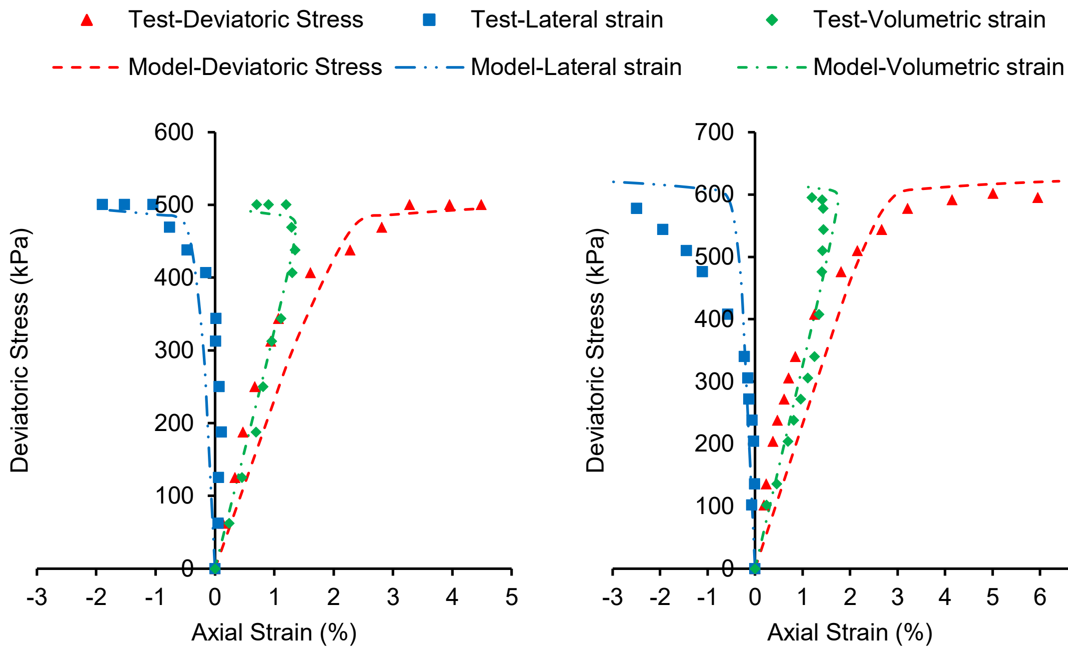

(a) (b)

Figure 4.10. Comparison of the simulation results and experimental data of triaxial testing on CPB samples after 7 days of curing: (a) confining pressure-200 kPa; (b) confining pressure-300 kPa.

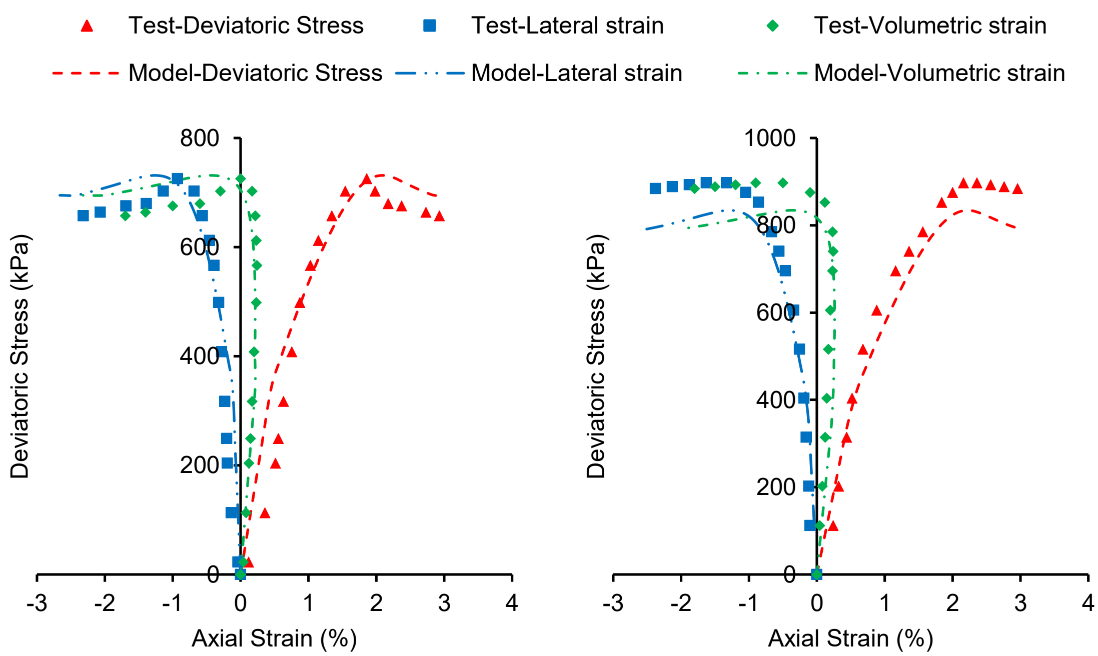

(a) (b)

Figure 4.11. Comparison of the simulation results and experimental data of triaxial testing on CPB samples after 28 days of curing: (a) confining pressure-200 kPa; (b) confining pressure-300 kPa

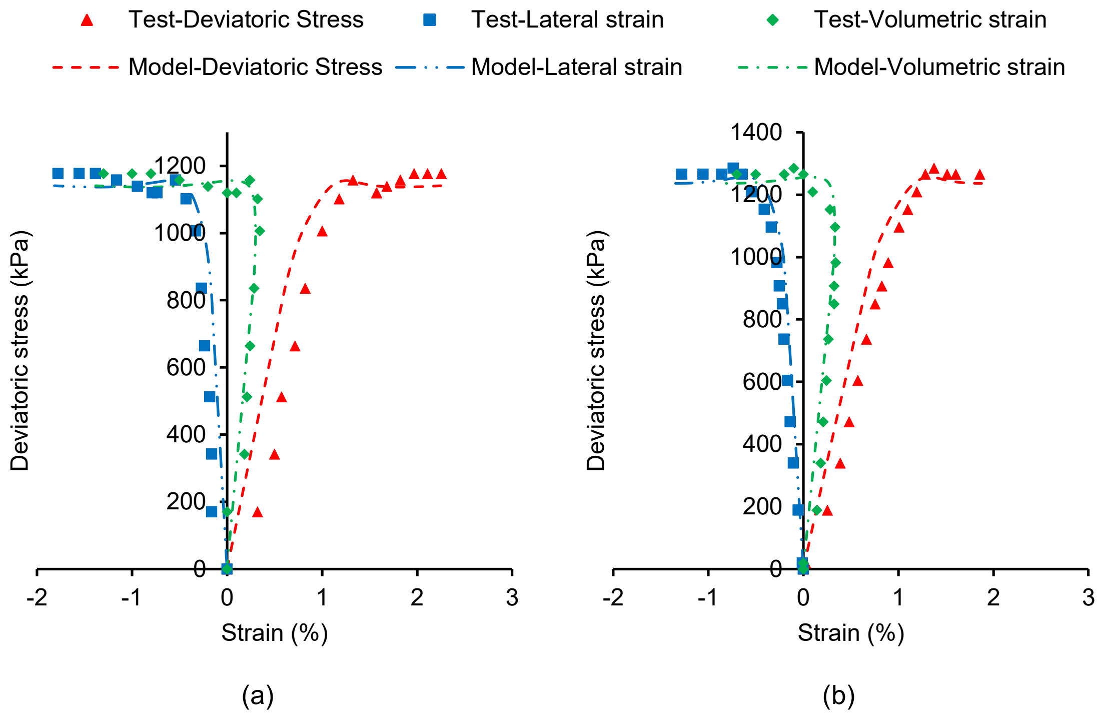

Figure 4.12. Comparison of the simulation results and experimental data of triaxial testing on CPB samples after 90 days of curing: (a) confining pressure-400 kPa; (b) confining pressure-500 kPa

According to the comparisons of the numerical simulation results and numerous experimental data, it can be concluded that the developed model is not only capable of predicting the stress-strain and hardening/softening behaviors, but also reproduces well the volumetric response of CPB.

4.2.5. Summary and Conclusion

Based on the results obtained in this study, the following conclusions can be established.

(i) An evolutive elasto-plastic model based on the D-P yield criterion has been developed to capture the mechanical behavior of hydrating CPB. The model takes into consideration the degree of binder hydration and its effect on the evolution of the mechanical properties (i.e. cohesion, internal friction and dilation angles, stiffness, and Poisson’s ratio) and mechanical behavior (i.e. stress-strain, hardening/softening and volumetric dilation). Due to the fact that the hardening/softening behavior of CPB is controlled by both binder hydration and plastic strain, the model adopts double parameters of hardening/softening, including degree of binder hydration and effective plastic strain. Moreover, non-associative plastic flow is employed to accurately model the plastic behavior.

(ii) The comparison results demonstrate good agreement between the model prediction and experimental data, which verifies the capability of the proposed model to reproduce the mechanical behavior of CPB including volumetric response and hardening/softening behavior. Furthermore, the comparison results also show that binder hydration plays a critical role in the evolution of the mechanical properties of CPB materials and dominates the corresponding mechanical behaviors, which proves the necessity of the development of an evolutive elasto-plastic mechanical model.

(iii) Due to the fact that the model fully considers the influence of binder hydration on the material properties and mechanical behavior, the developed evolutive elasto-plastic mechanical model is useful for the development of fully coupled multiphysics modeling of CPB. In the future, the developed model here can be incorporated into a fully coupled model to reveal the interaction of multiphysics processes in CPB, which could optimize CPB designs.

4.2.6. Acknowledgements

The authors would like to thank the Natural Sciences and Engineering Research Council of Canada (NSERC) and the University of Ottawa.

4.2.7. References

Annor, A.B., 1999. A study of the characteristics and behavior of composite backfill material. McGill University, Montreal, Canada.

Belem, T., Benzaazoua, M., Bussière, B., 2000. Mechanical behavior of cemented paste backfill. Proceedings of 53rd Canadian Geotechnical Conference Montreal; p. 373-380.

Benzaazoua, M., Fall, M., Belem, T., 2004. A contribution to understanding the hardening process of cemented pastefill. Miner Eng 17, 141-152.

Bigoni, D., Piccolroaz, A., 2004. Yield criteria for quasibrittle and frictional materials. Int J Solids Struct 41, 2855-2878.

Bittnar, Z., 2006. Microstructure-based micromechanical prediction of elastic properties in hydrating cement paste. Cem Concr Res 36, 1708-1718.

Boumiz, A., Vernet, C., Tenoudji, F.C., 1996. Mechanical properties of cement pastes and mortars at early ages: evolution with time and degree of hydration. Advanced Cement Based Materials 3, 94-106.

Briaud, J.L., 2013. Geotechnical engineering: unsaturated and saturated soils. John Wiley & Sons, New Jersey.

Célestin, J.C.H., Fall, M., 2009. Thermal conductivity of cemented paste backfill material and factors affecting it. Int J Min Reclam Environ 23, 274-290.

Chen, W.F., 2007. Plasticity in reinforced concrete. J. Ross Publishing, New York.
Chen, W.F., Baladi, G.Y., 1985. Soil plasticity: theory and implementation. Elsevier, New York.
Chen, X.T., Shao, J.F., Davy, C.A., Skoczylas, F., 2010. Experimental study and constitutive modeling of elasto-plastic damage in heat-treated mortar. Int J Numer Anal Met 34, 357-382.
Cihangir, F., Ercikdi, B., Kesimal, A., Turan, A., Deveci, H., 2012. Utilisation of alkali-activated blast furnace slag in paste backfill of high-sulphide mill tailings: effect of binder type and dosage. Miner Eng 30, 33-43.
Collins, I.F., 2002. Associated and non-associated aspects of the constitutive laws for coupled elastic/plastic materials. Int J Geomech 2, 259-267.
COMSOL, 2013. Introduction to COMSOL Multiphysics®, <http://www.comsol.com/shared/downloads/IntroductionToCOMSOLMultiphysics.pdf>.
De Schutter, G., 1999. Hydration and temperature development of concrete made with blast-furnace slag cement. Cem Concr Res 29, 143-149.
De Schutter, G., Taerwe, L., 1996. Degree of hydration-based description of mechanical properties of early age concrete. Mater Struct 29, 335-344.
Deb, D., Das, K.C., Raja Sekhar, G., 2013. Generalized symmetric formulation of tangential stiffness for nonassociative plasticity. Journal of Engineering Mechanics 139, 105-113.
Derski, W., Izbicki, R., Kisiel, I., Mróz, Z., 2012. Rock and soil mechanics. Elsevier, New York.
Doran, B., Köksal, H.O., Polat, Z., Karakoç, C., 1998. The use of Drucker-Prager criterion in the analysis of reinforced concrete members by finite elements. Turkish Chamber of Civil Engineers 9, 1616-1625.
Drucker, D.C., 1959. A definition of stable inelastic material. Journal of Applied Mechanics 26, 101-106.
Fall, M., Belem T, M., B., 2005. Tensile and compressive properties of underground paste backfill. Proceedings of 58th Canadian Geotechnical Conference; and 6th Joint IAH-CNC and CGS Groundwater Speciality Conferences Saskatchewan.
Fall, M., Belem, T., Samb, S., Benzaazoua, M., 2007. Experimental characterization of the stress-strain behavior of cemented paste backfill in compression. J Mater Sci 42, 3914-3922.
Fall, M., Benzaazoua, M., Saa, E., 2008. Mix proportioning of underground cemented tailings backfill. Tunn Undergr Sp Tech 23, 80-90.
Galaa, A.M., Thompson, B.D., Grabinsky, M.W., Bawden, W.F., 2011. Characterizing stiffness development in hydrating mine backfill using ultrasonic wave measurements. Can Geotech J 48, 1174-1187.
Ghirian, A., Fall, M., 2013. Coupled thermo-hydro-mechanical-chemical behavior of cemented paste backfill in column experiments. Part I: physical, hydraulic and thermal processes and characteristics. Eng Geol 164, 195-207.
Ghirian, A., Fall, M., 2014. Coupled thermo-hydro-mechanical-chemical behavior of cemented paste backfill in column experiments: Part II: Mechanical, chemical and microstructural processes and characteristics. Eng Geol 170, 11-23.
Helinski, M., Fourie, A., Fahey, M., Ismail, M., 2007. Assessment of the self-desiccation process in cemented mine backfills. Can Geotech J 44, 1148-1156.
Horpibulsuk, S., Rachan, R., Suddeepong, A., 2012. State of the art in strength development of soil-cement columns. Proceedings of the ICE-Ground improvement; p. 201-215.

Houlsby, G.T., 1991. How the dilatancy of soils affects their behavior. Proceedings of the 10th European Conference on Soil Mechanics and Foundation Engineering Florence; p. 1189-1202.
Hughes, P.B., 2014. Design guidelines: underhand cut and fill cemented paste backfill sill beams. University of British Columbia, Vancouver, Canada.
Jirásek, M., Bazant, Z.P., 2002. Inelastic analysis of structures. John Wiley & Sons, Chichester.
Kesimal, A., Ercikdi, B., Yilmaz, E., 2003. The effect of desliming by sedimentation on paste backfill performance. Miner Eng 16, 1009-1011.
Kesimal, A., Yilmaz, E., Ercikdi, B., Alp, I., Deveci, H., 2005. Effect of properties of tailings and binder on the short-and long-term strength and stability of cemented paste backfill. Mater Lett 59, 3703-3709.
Kjellsen, K.O., Detwiler, R.J., Gjørv, O.E., 1991. Development of microstructures in plain cement pastes hydrated at different temperatures. Cem Concr Res 21, 179-189.
Klein, K., Simon, D., 2006. Effect of specimen composition on the strength development in cemented paste backfill. Can Geotech J 43, 310-324.
Klimczak, C., Schultz, R.A., 2013. Shear-enhanced compaction in dilating granular materials. International Journal of Rock Mechanics and Mining Sciences 64, 139-147.
Lade, P.V., 1988. Effects of voids and volume changes on the behavior of frictional materials. Int J Numer Anal Met 12, 351-370.
Li, L., 2014. Generalized solution for mining backfill design. Int J Geomech 14, 04014006.
López Cela, J.J., 1998. Analysis of reinforced concrete structures subjected to dynamic loads with a viscoplastic Drucker-Prager model. Appl Math Model 22, 495-515.
Lubarda, V., Mastilovic, S., Knap, J., 1996. Some comments on plasticity postulates and non-associative flow rules. Int J Mech Sci 38, 247-258.
Moresi, L., Mühlhaus, H.B., Lemiale, V., May, D., 2007. Incompressible viscous formulations for deformation and yielding of the lithosphere. Geological Society 282, 457-472.
Najjar, Y., Zaman, M., Faruque, M., 1990. Elasto-plastic constitutive modeling of plain concrete and an optimization procedure for parameter evaluation. Comput Geotech 9, 185-208.
Nasir, O., Fall, M., 2009. Modeling the heat development in hydrating CPB structures. Comput Geotech 36, 1207-1218.
Nasir, O., Fall, M., 2010. Coupling binder hydration, temperature and compressive strength development of underground cemented paste backfill at early ages. Tunn Undergr Sp Tech 25, 9-20.
Pierce, M.E., 1999. Laboratory and numerical analysis of the strength and deformation behavior of paste backfill. Queen's University, Kingston.
Pierce, M.E., 2001. Stability analysis of paste backfill exposures at brunswick mine. Proceedings of 2nd International FLAC Symposium Lyon, France; p. 147-156.
Pokharel, M., Fall, M., 2010. Coupled thermochemical effects on the strength development of slag-paste backfill materials. J Mater Civil Eng 23, 511-525.
Rankine, R.M., Sivakugan, N., 2007. Geotechnical properties of cemented paste backfill from Cannington Mine, Australia. Geotech Geol Eng 25, 383-393.
Sainsbury, D.P., Urie, R., 2007. Stability analysis of horizontal and vertical paste fill exposures at the Raleigh Mine. Proceedings of Minefill 2007 Montreal, Quebec.
Sayers, C., Grenfell, R., 1993. Ultrasonic propagation through hydrating cements. Ultrasonics 31, 147-153.

Schindler, A., Ruiz, J., Rasmussen, R., Chang, G., Wathne, L., 2004. Concrete pavement temperature prediction and case studies with the FHWA HIPERPAV models. Cem Concr Compos 26, 463-471.
Schindler, A.K., Folliard, K.J., 2003. Influence of supplementary cementing materials on the heat of hydration of concrete. Proceedings of Advances in Cement and Concrete IX Conference Colorado; p. 17-26.
Schindler, A.K., Folliard, K.J., 2005. Heat of hydration models for cementitious materials. Aci Mater J 102, 24-33.
Schnaid, F., Prietto, P.D., Consoli, N.C., 2001. Characterization of cemented sand in triaxial compression. J Geotech Geoenviron 127, 857-868.
Simms, P., Grabinsky, M., 2009. Direct measurement of matric suction in triaxial tests on early-age cemented paste backfill. Can Geotech J 46, 93-101.
Simms, P., Grabinsky, M., Zhan, G., 2007. Modeling evaporation of paste tailings from the Bulyanhulu mine. Can Geotech J 44, 1417-1432.
Simon, D., 2005. Microscale analysis of cemented paste backfill. University of Toronto, Canada.
Sumelka, W., 2014. A note on non-associated Drucker-Prager plastic flow in terms of fractional calculus. Journal of Theoretical and Applied Mechanics 55, 571-574.
Tariq, A., Yanful, E.K., 2013. A review of binders used in cemented paste tailings for underground and surface disposal practices. J Environ Manage 131, 138-149.
Vermeer, P.A., De Borst, R., 1984. Non-associated plasticity for soils, concrete and rock. Heron 29, 1-64.
Wu, D., Fall, M., Cai, S.J., 2014. Numerical modeling of thermally and hydraulically coupled processes in hydrating cemented tailings backfill columns. Int J Min Reclam Environ 28, 173-199.
Yilmaz, E., Belem, T., Bussière, B., Benzaazoua, M., 2011. Relationships between microstructural properties and compressive strength of consolidated and unconsolidated cemented paste backfills. Cem Concr Compos 33, 702-715.
Yilmaz, E., Kesimal, A., Deveci, H., Ercikdi, B., 2003a. The factors affecting the performance of paste backfill; physical, chemical and mineralogical characterization. Proceedings of the 1st Engineering Sciences Congress for Young Researcher (MBGAK'03) Istanbul.
Yilmaz, E., Kesimal, A., Ercikdi, B., 2004. Strength development of paste backfill simples at Long term using different binders. Proceedings of the 8th Symposium MineFill Beijing, China; p. 281-285.
Yilmaz, E., Kesimal, A., Ercikdi, B., Alp, I., 2003b. Determination of the optimum cement content for paste backfill samples. Proceedings of 18th International Mining Congress & Exhibition of Turkey Antalya, Turkey.
Yin, S., Wu, A., Hu, K., Wang, Y., Zhang, Y., 2012. The effect of solid components on the rheological and mechanical properties of cemented paste backfill. Miner Eng 35, 61-66.
Yong Wang, M.F., 2014. Initial temperature-dependence of strength development and self-desiccation in cemented paste backfill that contains sodium silicate. Cement and Concrete Composites (submitted).
Yu, T., Teng, J.G., Wong, Y.L., Dong, S.L., 2010. Finite element modeling of confined concrete-I: Drucker-Prager type plasticity model. Eng Struct 32, 665-679.
Yuan, K.Y., 2009. Energy based coupled elastoplastic damage-healing formulations for earth moving processes. University of California, Los Angeles.

4.3. Paper III: A coupled thermo-hydro-mechanical-chemical model for underground cemented tailings backfill

Published in Tunnelling and Underground Space Technology 50 (2015) 396-414

Liang Cui, Mamadou Fall

Abstract

Cemented paste backfill (CPB), a mixture of tailings, water and binder, is extensively used in underground mines worldwide for ground support and tailings disposal. The prediction of the behavior of CPB structures from early to advanced ages is of great practical importance. Once placed underground, the behavior of CPB is controlled by complex multiphysics (thermal, hydraulic, chemical and mechanical) processes. Modeling of the coupled THMC processes that occur in CPB is crucial for reliably assessing and predicting the performance of CPB structures. Yet there is currently no tool to predict the thermo-hydro-mechanical-chemical (THMC) behavior of CPB, or the performance of CPB under coupled THMC loadings. Therefore, a new multiphysics model is presented in this paper to describe and predict the coupled THMC behavior of CPB and its evolution with time. The governing equations of the model result from a combination of a set of conservation and constitutive equations. Four balance equations (water and air mass, momentum (mechanical equilibrium) and energy conservation equations) are taken into consideration. The model considers full coupling between the thermal, hydraulic, chemical (binder hydration) processes and CPB deformation as well as changes in CPB properties resultant of these phenomena, such as stress-strain relationship, thermal conductivity, permeability, porosity, and strength. The model coefficients are identified in terms of measurable parameters. The predictive ability of the developed model is then tested against laboratory and field tests conducted on CPB. Good agreement between the modeling results and experimental data confirms the capability of the developed model to well capture the THMC behavior of CPB and its evolution.

Keywords: Cemented paste backfill; Tailings; THMC; Coupling processes; Multiphysics; Modeling

4.3.1. Introduction

With the rapid development of backfill technology in the mining sector, the application of cemented paste backfill (CPB) has become a standard practice around the world (Benzaazoua et al., 2002; Belem and Benzaazoua, 2004; Fall and Nasir, 2009; Ghirian and Fall, 2014). CPB is an engineered mixture of tailings from the processing operations of the mine, additives such as Portland cement, blast furnace slag and fly ash, and water. After preparation, the CPB is usually delivered into the mined-out stope by means of reticulated pipelines or gravity. Consequently, the backfilled stope not only provides support for the adjacent stopes, but also ensures a higher recovery of resources as less ore is left behind in the pillars. Compared to other types of mine backfill, such as hydraulic fill and rockfill, CPB is more versatile for mine designers. First, the water content of CPB is extremely reduced but it is still able to be transported through high-pressure positive displacement pumps (le Roux et al., 2005). Moreover, the tailings, as the major ingredient of CPB, are pumped into underground space, which can, to an extreme extent, eliminate the need for constructing large surface storage tailings dams (Sivakugan et al., 2006) and minimize the associated cost and environmental issues (Fall et al., 2004; Yilmaz et al., 2004; Ghirian and Fall, 2014). Furthermore, another benefit is the faster and higher mechanical strength acquisition of CPB as compared to rockfill and hydraulic fill (Yilmaz et al., 2003; Nasir and Fall, 2010; Veenstra, 2013), which, in turn, means that it is more economical. Therefore, CPB has started to replace both hydraulic fill and cemented rockfill in underground mining operations.

The critical design criteria of CPB structures consist of structural stability, durability, design cost and environmental performance (Belem and Benzaazoua, 2004; Fall and Nasir, 2009; Ghirian and Fall, 2013a). Once prepared and placed underground, the CPB structure is simultaneously subjected to mechanical (**M**, e.g., geomechanical conditions of the mine, filling rate and strategy, backfill self-weight), hydraulic (**H**, e.g., suction, pore water pressure (PWP) development, water drainage), chemical (**C**, e.g., cement hydration), and thermal (**T**) loads from early to advanced ages (Fall and Ghirian, 2014) as explained in Section 4.3.2. For instance, the temperature of the surrounding rocks naturally increases with depth due to the influence of the geothermal gradient. Moreover, binder hydration can generate significant amounts of heat (internal source of heat) inside the CPB structure (Fall et al., 2010). These external and internal sources of heat will directly affect the binder hydration rate, and thus influence the strength development of CPB as well as cause mechanical deformation through thermal expansion. In addition, as the binder hydration reaction proceeds, some of the pore water will be consumed by the binder hydration, which contributes to the dissipation of the excess pore water pressure in the CPB. Consequently, there will be a gradual transition from saturated to unsaturated conditions in the backfill medium, which can result in an increase of the effective stress in the CPB. Moreover, the CPB structure can also experience mechanical deformation under gravity (backfill self-weight), and shrinkage strain induced by binder hydration. Hence, the performance of the CPB structure is controlled by complex coupled multiphysics processes, including thermal (T), hydraulic (H), mechanical (M) and chemical (C) (THMC) processes. These complex and varying coupled THMC processes create their own special challenges for the design of stable and cost-effective CPB structures. Understanding and modeling of the coupled THMC processes that occur in CPB are crucial for reliably assessing and predicting the performance of CPB structures.

To address and understand the multiphysics processes that occur in CPB and their effects on CPB behavior, comprehensive research with experimental analysis, field measurement and numerical modeling is needed. Until now, however, despite the tremendous progress made in understanding the behavior of CPB, most of the previous studies have only investigated the isolated effects of one influencing factor (mechanical, chemical, hydraulic, or thermal) on the behavior of CPB. For example, due to the significance of mechanical stability, many research efforts (e.g., Mitchell, 1989; Lawrence, 1992; Belem et al., 2000; Benzaazoua and Belem, 2000; Fall et al., 2005; Simon, 2005; Fall et al., 2007; Nasir and Fall, 2008) have concentrated on investigating the mechanical properties (e.g., uniaxial compressive strength, shear strength, cohesion and internal friction angles), microstructural evolution and the corresponding influencing factors. Moreover, the evolution of the hydraulic process in CPB is also investigated via both laboratory experiments and in-situ measurements (Belem et al., 2001; Yumlu, 2008; Fall et al., 2009; Thompson et al., 2012). For the thermal process, it has been observed that thermal properties such as thermal conductivity evolve with binder hydration (De Souza, 2006; Célestin and Fall, 2009), and the temperature rise and distribution in CPB are largely controlled by both the heat released by the binder hydration and thermal load exerted by the surrounding rock (Williams et al., 2001; Fall and Samb, 2008; Orejarena and Fall, 2008; Yumlu, 2008; Fall et al., 2010).

In response to the limited knowledge on the coupled processes in CPB, studies have been gradually carried out on the multiphysics processes in CPB at the experimental (laboratory, field) and modeling levels. Some experimental studies have been carried out to better understand the HM (e.g., Yilmaz et al., 2014), THM (e.g., Abdul-Hussain and Fall, 2012) or THMC (e.g.,Ghirian and Fall, 2013a, 2014) behavior of CPB. As the understanding on the mechanisms of coupled processes in CPB is increasing, numerical modeling has also made progress in furthering the work in this area. Various partially coupled numerical models have been developed to predict the behavior of CPB. A thermo-chemo-mechanical (TCM) model (Fall and Nasir, 2009) was proposed to simulate the response of CPB under thermal loading conditions. In order to describe the coupled thermal and hydraulic processes in CPB, a thermo-hydro-chemical (THC) model was developed (Wu et al., 2014). A hydro-chemo-mechanical (HCM) model which couples cement hydration with conventional consolidation analysis was presented by (Helinski et al., 2007). However, to date, no studies have been conducted on the development of a fully coupled multiphysics model to predict the THMC behavior of CPB. A reliable and effective assessment and prediction of the behavior and performance of CPB are vital for the coupling of all of these THMC factors. In addition, the assessing of such CPB structures and comparing of several possible CPB designs prior to their construction require a robust and reliable multiphysics (THMC) model or computational tool which incorporates knowledge of these various coupled mechanisms at the material level. Unfortunately, there is currently no tool to predict the THMC behavior of CPB, or the performance of CPB under coupled THMC loadings. Therefore, the objective of this study is to develop a multiphysics model to analyze and predict the THMC behavior of CPB.

4.3.2. Coupled THMC processes considered

CPB can be treated as a multiphase porous medium which consists of liquid (capillary water and physically adsorbed water), gaseous (pore air) and solid (binder, tailings and hydration products) phases. Once placed into a stope, a series of strong interactions between the coupled THMC processes immediately take place in the CPB structure. Figure 4.13 depicts the main THMC processes that can affect the CPB behavior, which are taken into consideration in this study. The interaction between the coupling processes dominates the evolution of the material properties and behavior of the CPB structure.

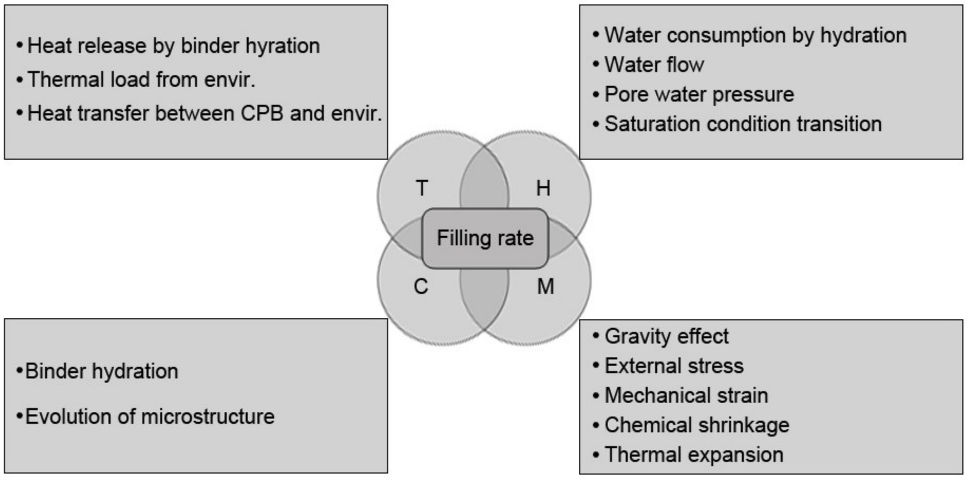

Figure 4.13. Schematic of interactions amongst multiphysics processes in CPB (envir.: environment)

Chemical process

Binder hydration commences right after the CPB is mixed and the progression of the chemical reaction influences the CPB properties and behavior in four key aspects: (i) as the chemical reaction proceeds, the resulting hydration products precipitate and refine the capillary pore space between the tailings particles. This pore refinement and connection between the solid particles significantly contribute to microstructural changes. The microstructural variation leads to the evolution of several material properties, such as thermal (e.g., thermal conductivity) (Abbasy, 2009), hydraulic (e.g., saturated hydraulic conductivity) (Fall et al., 2009) and mechanical (e.g., uniaxial compressive strength) (Yilmaz et al., 2015) properties; (ii) capillary pore water is gradually consumed during binder hydration, which not only contributes to the change in the degree of saturation, but also results in the evolution of the pore water pressure (Ghirian and Fall, 2013a); (iii) the heat released by exothermic binder hydration will influence the temperature distribution in the CPB structure and the binder hydration rate (Nasir and Fall, 2010). The evolution of the temperature can, to a certain extent, result in mechanical deformation via thermal expansion; and (iv) due to the fact that the volume of the hydration products is less than the combined volume of the reacted cement and water (Powers and Brownyard, 1947), binder hydration can directly cause mechanical deformation through chemical shrinkage.

Hydraulic process

The impacts of the hydraulic process result from the variation in water content in the CPB structure. There are several factors that contribute to the evolution of the water content, including self-desiccation, surface evaporation, water seepage from the surrounding rock, and pore water flow and drainage (Belem and Benzaazoua, 2004; Abdul-Hussain and Fall, 2011; Ghirian and Fall, 2013a). Self-desiccation is induced by water consumption in binder hydration. Although the surface evaporation occurs in underground mine cavities, the influence of water loss through evaporation is limited to the shallow part, close to the top surface of the CPB (Ghirian and Fall, 2013a). The evolution of the water content can have strong influences on several processes, such as: (i) the unhydrated binder is gradually covered by the precipitated hydration product, which inhibits pore water from diffusing inward to reach the unhydrated cement cores and gradually reduces the hydration rate (Nawy, 2008; Kumar et al., 2009); (ii) the change in water content can result in the reduction of the pore water pressure followed by development of matric suction in the porous medium, which, in turn, significantly influences the effective stress, strength and mechanical deformation in the CPB structure (Le Roux et al. 2005, Ghirian and Fall 2014); (iii) pore water flow, self-desiccation and drainage will contribute to the variation of the temperature distribution and heat transfer in CPB due to the different thermal properties (i.e., thermal conductivity and specific heat capacity) of the liquid, gas and solid phases of the CPB.

Thermal process

The evolution of the temperature distribution in a CPB structure can also result in the variation of three other processes: (i) sensitivity of the binder hydration to temperature, namely, the temperature can have impacts on the hydration rate (Poole et al., 2007). The temperature can further affect CPB properties in binder hydration, such as the strength (Fall et al., 2010), microstructure, saturated hydraulic conductivity (Fall et al., 2009) and self-desiccation intensity and rate (Wu et al., 2014); (ii) thermal gradients can lead to mechanical deformation through thermal expansion or contraction; and (iii) the temperature level is also a significant influencing factor in the surface evaporation rate (Ghirian and Fall, 2013a).

Mechanical process

Field CPB is subjected to various types of stresses (e.g., self-weight pressure, stresses induced by the surrounding rock mass, thermal stresses). As a geotechnical material, CPB is fully deformable and able to experience elasto-plastic behavior, thermal expansion and chemical shrinkage strains. The resulting volumetric deformation can give rise to variation in the porosity or void ratios. Consequently, the material properties controlled by porosity will evolve: (i) in the hydraulic process, as the saturated hydraulic conductivity is related to the porosity/void ratio. Hence, the volumetric deformation resultant of the mechanical process will influence the hydraulic properties; (ii) similar to the hydraulic process, the thermal conductivity shows an inverse relation with porosity

(Abbasy, 2009). Therefore, variation in thermal conductivity will occur with the development of volumetric deformation; (iii) the impacts of mechanical stress on binder hydration are relatively minimal due to the relative low stresses experienced in CPB structures.

Filling rate

The filling rate is the rate at which the CPB materials are pumped into the stope. This rate can greatly vary from one mine or stope to another (Nasir and Fall, 2010) and various filling strategies can be used in backfill practices (option of filling with or without an initial plug). In practice, backfilling strategies that require multiple stages and different filling rates are often used to balance safety concerns, cost, and productivity requirements. The backfilling rate and strategies not only can affect the stress variation in the CPB mass, but also influence the evolution of the pore water pressure on the barricade (Thompson et al., 2012). Hence, the backfilling rate and strategies should be considered and incorporated into the coupled multiphysics analysis of CPB.

4.3.3. Theoretical formulations of the coupled THMC model

4.3.3.1. Basis of the mathematical formulations and general assumptions

To develop a fully coupled THMC model for CPB, the following main assumptions are made.

(i) The CPB material is considered to be a multiphase (solid, liquid and gas) porous medium. The constituents (solid, water, dry air) are considered as three independent overlapping continua in the context of the theory of mixtures. Water is wet, whereas dry air is not, so dry air is considered to be the ideal gas. The solid grains and liquid water are incompressible, but the porous medium is deformable.

(ii) The voids in a soil skeleton may be filled with water and/or air. Due to the relatively low temperature in the CPB, it is assumed that water does not undergo a phase transition in CPB.

(iii) It is assumed that there are small deformations of the solid skeleton with respect to its mechanical response.

(iv) All of the components of the CPB material at any given time in the representative elementary volume (REV) maintain thermodynamic equilibrium, i.e. locally, the phases are at the same temperature.

(v) The compressive stress is taken to be negative.

4.3.3.2. Continuity equations

In order to describe the transport of conserved quantities, such as mass, energy and momentum in a CPB structure, the continuity equations need to be defined. Then, the fully coupled THMC model (governing equations) can be formulated when the constitutive equations (e.g., stress and strain relationships, Darcy's law, or Fourier's law) are substituted into the continuity equations viz. mass, energy and momentum (mechanical equilibrium) equations. In this study, four balance equations: (i) water mass, (ii) air mass, (iii) momentum (mechanical equilibrium), and (iv) energy conservation equations are considered. The solid phase mass conservation equation is used in the water and air balance equations.

4.3.3.2.1. Mass conservation equation

As binder hydration progresses, pore water is gradually consumed and converted into hydration products (solid phase). Hence, there exists a sink term in water mass balance equations, and a source term in solid phase mass balance equations. Therefore, based on the volume-averaging method, the mass balance equations can be respectively described in Lagrangian forms (i.e. the variation of state variables with respect to the moving coordinate system) in terms of a material derivative, viz., $D(\cdot)/Dt = \partial(\cdot)/\partial t + \mathbf{v}_s \cdot \nabla(\cdot)$ with respect to the velocity of the solid phase $\mathbf{v}_s$.

$$(1-\phi)\frac{D\rho_s}{Dt} - \rho_s \frac{D\phi}{Dt} + \rho_s (1-\phi)\nabla \cdot \mathbf{v}_s = \phi S \dot{r}_{hydr} \tag{4.32}$$

$$S\rho_w \frac{D\phi}{Dt} + \phi S \frac{D\rho_w}{Dt} + \phi\rho_w \frac{DS}{Dt} + \nabla \cdot \left(\phi S \rho_w \mathbf{v}^{rw}\right) + \phi S \rho_w \nabla \cdot \mathbf{v}_s = -\phi S \dot{r}_{hydr} \tag{4.33}$$

$$\phi(1-S)\frac{D\rho_a}{Dt} + (1-S)\rho_a \frac{D\phi}{Dt} - \phi\rho_a \frac{DS}{Dt} + \nabla \cdot \phi(1-S)\rho_a \mathbf{v}^{ra} + \phi(1-S)\rho_a \nabla \cdot \mathbf{v}_s = 0 \tag{4.34}$$

where ρ_i denotes the density and the subscript, i, refers to the three different phases (air, water and solid), ϕ is the porosity, and S is the degree of saturation in the liquid phase, $\dot{r}_{hydr}$ means the rate of water consumption per unit volume in the liquid phase due to binder hydration, $\mathbf{v}_s$ and $\mathbf{v}^{ri}$ denote the phase velocity with respect to the fixed spatial axes (Eulerian coordinates), and the corresponding relative apparent velocity of the fluids in the porous medium, respectively, which can be written as:

$$\mathbf{v}_i = \mathbf{v}_{ri} + \mathbf{v}_s \tag{4.35}$$

$$\mathbf{v}^{rw} = \phi S \mathbf{v}_{rw} \tag{4.36}$$

$$\mathbf{v}^{ra} = \phi(1-S)\mathbf{v}_{ra} \tag{4.37}$$

Assume that the solid phase displacement is $\mathbf{u}$ (a vector field). With respect to the Eulerian coordinate system $\mathbf{x}(x_1, x_2, x_3)$, the volumetric strain of the solid phase can be expressed as:

$$\varepsilon_v = \frac{\partial u_i}{\partial x_i} = \nabla \cdot \mathbf{u} \tag{4.38}$$

Based on the definition of the volumetric strain of the solid phase, the divergence of the solid phase velocity can be rewritten in terms of the soil skeleton volumetric strain ε_v (Bear and Buchlin, 1991):

$$\nabla \cdot \mathbf{v}_s = \nabla \cdot \dot{\ } \quad \frac{D\varepsilon}{Dt} \quad \frac{\partial \varepsilon_v}{\partial t} + \mathbf{v}_s \cdot \nabla \varepsilon_v \approx \frac{\partial \varepsilon_v}{\partial t} \ \left(\partial \varepsilon_v / \partial t >> \nabla \varepsilon_v \right) \tag{4.39}$$

Through a rearrangement of the mass balance equation of the solid phase, viz. Eq. (4.32), the time rate of the change of the porosity can be derived as:

$$\frac{D\phi}{Dt} = \frac{(1-\phi)}{\rho_s}\frac{D\rho_s}{Dt} + (1-\phi)\nabla \cdot \mathbf{v}_s - \frac{\phi S}{\rho_s}\dot{m}_{hydr} \tag{4.40}$$

Due to the assumption of a small strain of the porous media, the second term that exists in the material derivative of the fluid quantities, i.e. $\mathbf{v}_s \cdot \nabla(\cdot)$ is negligible. Therefore, by substituting Eqs. (4.39) and (4.40) into Eqs. (4.33) and (4.34), the fluid mass conservation equations that involve a solid phase mass balance equation can be rewritten as:

$$\phi S \frac{\partial \rho_w}{\partial t} + \phi \rho_w \frac{\partial S}{\partial t} + S\rho_w \left[\frac{\partial \varepsilon_v}{\partial t} + \frac{(1-\phi)}{\rho_s}\frac{\partial \rho_s}{\partial t} \right] - \phi S \dot{m}_{hydr} \left(\frac{\ }{\rho_s} \quad -1 \right) = -\nabla \cdot \left(\phi S \rho_w \mathbf{v}^{rw} \right) \tag{4.41}$$

$$\phi(1-S)\frac{\partial \rho_a}{\partial t} - \phi \rho_a \frac{\partial S}{\partial t} + (1-S)\rho_a \left[\frac{(1-\phi)}{\rho_s}\frac{\partial \rho_s}{\partial t} + \frac{\partial \varepsilon_v}{\partial t} - \frac{\phi S}{\rho_s}\dot{m}_{hydr} \right] \quad \nabla \cdot \phi(1-S)\rho_a \mathbf{v}^{ra} \tag{4.42}$$

4.3.3.2.2. Momentum conservation equation

In the CPB structure, inertial forces can be neglected due to the fact that the hydro-thermal phenomena are relatively slow. Therefore, the momentum conservation (i.e. mechanical equilibrium) equation can be written in a rate form (Gawin et al., 2006):

$$\nabla \cdot \left(\frac{\partial \boldsymbol{\sigma}}{\partial t} \right) + \frac{\partial \left[(1-\phi)\rho_s + \phi S \rho_w + \phi(1-S)\rho_a \right]}{\partial t}\mathbf{g} = 0 \tag{4.43}$$

where $\boldsymbol{\sigma}$ is the (macroscopic) total stress tensor, and $\mathbf{g}$ is the acceleration of gravity.

4.3.3.2.3. Energy conservation equation

The heat transfer in CPB consists of three aspects, including heat conduction, advection and generation, induced by an exothermic chemical reaction (binder hydration). In addition, our formulation assumes that all of the phases are in local thermal equilibrium, viz. $T_s = T_w = T_a = T$. Therefore, the following total energy balance equation is adopted in this study:

$$\left[(1-\phi)\rho_s C_s + \phi S \rho_w C_w + \phi(1-S)\rho_a C_a \right] \frac{\partial T}{\partial t} + Q_{ad} + Q_{cd} = Q_{hydr} \tag{4.44}$$

where C_i refers to the specific heat capacity (i refers to air, water and solid), Q_{ad} and Q_{cd} denote the amount of heat transfer induced by advection and conduction, respectively, and Q_{hydr} represents the heat production due to the exothermic reaction of binder hydration.

4.3.3.3. Binder hydration model

Binder hydration refers to the exothermic reaction between the binder and water in CPB. As mentioned in Section 4.3.2, binder hydration can cause microstructural variation and has significant impacts on CPB in terms of both its material properties and behaviors. The prerequisite for a quantitative evaluation of these influences on the evolution of CPB properties is to define the extent of the advancement of binder hydration, namely, the degree of binder hydration. An exponential function proposed by Schindler and Folliard (2003) has been successfully applied in other studies to predict the progression of binder hydration for CPB materials (Wu et al., 2012; Cui and Fall, 2016), and is adopted in this study.

$$\xi(t_e) = \xi_u \cdot \exp\left[-\left(\frac{\tau}{t_e}\right)^{\beta}\right] \tag{4.45}$$

$$\text{with } \begin{cases} \xi_u = \dfrac{1.031 \cdot w/c}{0.194 + w/c} + 0.5 \cdot X_{FA} + 0.30 \cdot X_{slag} \\ t_e = \sum_0^t \exp\left[-\dfrac{E_a}{R}\left(\dfrac{1}{T} - \dfrac{1}{T_r}\right)\right] \cdot \Delta t \end{cases}$$

where ξ is the degree of hydration, ξ_u is ultimate degree of hydration, τ is the hydration time parameter (hours), β represents the hydration shape parameters, t_e is the equivalent age at the reference temperature T_r, T is the temperature of the CPB, E_a is the activation energy (J/mol), R is the natural gas constant (8.314 J/mol/K), w/c is the water-cement ratio, and X_{FA} and X_{slag} respectively represent the weight fraction of fly ash and blast furnace slag with respect to the total weight of the binder. In order to determine the rate of heat generation, the apparent activation energy should be defined. In this study, the following equation is adopted to characterize the apparent activation energy (Hansen and Pedersen, 1977):

$$E_a(T) = \begin{cases} 33,500 + 1,470(20 - T)\, J/mol & T < 20^{\circ}C \\ 33,500 & T \geq 20^{\circ}C \end{cases} \tag{4.46}$$

4.3.3.4. Backfilling rate

The backfilling of the stope (i.e. underground mined-out space) is a dynamic process and in practice, backfilling in multiple stages is a commonly adopted strategy to avoid exceeding the strength of the barricade (Thompson et al., 2009). In order to simulate the effect of the backfilling rate, $v_{filling}$, the following equation proposed by Nasir and Fall (2010) is adopted:

$$v_{filling} = \Delta h / \Delta t \tag{4.47}$$

where h refers to the height of the backfill.

4.3.3.5. Constitutive relations

4.3.3.5.1. Mechanical model

The water consumption caused by binder hydration (self-desiccation) can lead to skeleton changes (i.e., chemical shrinkage). In addition, thermal expansion induced by the temperature gradient in the CPB is taken into consideration in this study as well. Therefore, the total strain, $\boldsymbol{\varepsilon}$, generated in the CPB structure consists of four components , viz. elastic, $\boldsymbol{\varepsilon}_e$, plastic, $\boldsymbol{\varepsilon}_p$, thermal, $\boldsymbol{\varepsilon}_T$, and chemical, $\boldsymbol{\varepsilon}_c$, strains, which obey the theory of superposition.

$$\boldsymbol{\varepsilon} = \boldsymbol{\varepsilon}_e + \boldsymbol{\varepsilon}_p + \boldsymbol{\varepsilon}_T + \boldsymbol{\varepsilon}_c \tag{4.48}$$

The elastic deformation of CPB can be completely expressed in terms of a single “effective” stress variable which simplifies the deformation modeling and reduces the model parameters. Hence, the deformation model based on a thermo-chemo-elasto-plastic framework can be written in the following general form:

$$\boldsymbol{\sigma}' = \mathbf{D}^e \boldsymbol{\varepsilon}_\mathbf{e} = \mathbf{D}^e \left(\boldsymbol{\varepsilon} - \boldsymbol{\varepsilon}_\mathbf{p} - \boldsymbol{\varepsilon}_\mathbf{T} - \boldsymbol{\varepsilon}_\mathbf{c} \right) \tag{4.49}$$

where $\boldsymbol{\sigma}'$ is the effective stress vector responsible for all backfill skeleton deformations, and $\mathbf{D}^e$ is the fourth-order tensor of material stiffness. In considering the effects of pore water and pore air pressures, the total stress vector $\boldsymbol{\sigma}$ is decomposed into effective stress $\boldsymbol{\sigma}'$ and average pore pressure $\bar{P}$.

$$\boldsymbol{\sigma} = \boldsymbol{\sigma}' - \alpha_{Biot} \bar{P} \boldsymbol{\delta}_\mathbf{ij} \tag{4.50}$$

where α_{Biot} is the Biot’s effective stress coefficient and $\boldsymbol{\delta}_{ij}$ is the Kronecker’s delta. The Biot’s coefficient can be defined as:

$$\alpha_{Biot} = 1 - K_b / K_s \tag{4.51}$$

where K_b and K_s represent the bulk modulus of the porous media and solid phase (grain), respectively. For CPB materials, the bulk modulus will evolve with binder hydration. The average pore pressure can be expressed as:

$$\bar{P} = S P_w + (1 - S) P_a \tag{4.52}$$

where P_w and P_a denote pore liquid (water) and pore (dry) air pressures, respectively, and S accounts for the degree of saturation.

4.3.3.5.1.1. Plastic strain

It has been documented that, under static loading, the mechanical response of CPB is dominated by hardening/softening behaviors (Fall et al., 2007; Simms and Grabinsky, 2009; Ghirian and Fall, 2014). Moreover, volumetric expansion is evident after the peak stress in triaxial tests on CPB (Cui and Fall, 2016). In order to characterize the mechanical behavior and the influence of binder hydration on the mechanical response, the evolutive elasto-plastic mechanical model developed by Cui and Fall (2016) is adopted in this study. A full description of the mechanical model can be found in (Cui and Fall, 2016); therefore, only a brief description will be provided here. By incorporating the influence of binder hydration and plastic strain on the mechanical behavior of CPB, an evolutive yield function based on the Drucker-Prager (D-P) yield criterion is used to define both the initial yield and the following loading functions:

$$F(I_1,\sqrt{J_2},\xi,\kappa)=\sqrt{J_2}+\alpha_{D-P}\left(\xi,\kappa\right)\left[I_1+C_{D-P}\left(\xi\right)\right]=0 \tag{4.53}$$

where I_1 is the first stress invariant, $\sqrt{J_2}$ is the equivalent deviatoric stress, $\alpha_{D-P}\left(\xi,\kappa\right)$ and $C_{D-P}\left(\xi\right)$ are the material parameters and control the chemo-plastic strain hardening/softening behavior. The two parameters can be expressed by the internal friction angle and cohesion which evolve with binder hydration, namely, $\phi_B=\phi_B\left(\xi\right)$ and $c_B=c_B\left(\xi\right)$.

$$\begin{gathered}C_{D-P}\left(\xi\right)=3c_B\left(\xi\right)\cdot\cot\phi_B\left(\xi\right)\\ \alpha_{D-P}\left(\xi,\kappa\right)=D_{\alpha1}\left\{\left[1-\exp(-D_{\alpha2}\kappa)\right]+\left[D_{\alpha3}\kappa\exp(-D_{\alpha4}\kappa)\right]\right\}+\frac{2\sin\phi_B\left(\xi\right)}{\sqrt{3}\left[3+\sin\phi_B\left(\xi\right)\right]}\end{gathered} \tag{4.54}$$

where $D_{\alpha1}$, $D_{\alpha2}$, $D_{\alpha3}$ and $D_{\alpha4}$ are the material constants, which can be determined with uniaxial or triaxial compressive test data, and κ is the cumulative plastic strain and can be defined as follows:

$$\kappa=\int\sqrt{\frac{2}{3}d\varepsilon_p d\varepsilon_p} \tag{4.55}$$

Moreover, the non-associative flow rule is utilized to determine the plastic strain increment. Correspondingly, the plastic potential function is defined based on the determination of the dilation angle, ψ_B, :

$$Q_{CTB}=\frac{2\sin\psi_B\left(\xi\right)}{\sqrt{3}\left[3+\sin\psi_B\left(\xi\right)\right]}I_1+\sqrt{J_2} \tag{4.56}$$

Detailed information about the determination of the mechanical properties, such as cohesion, internal friction angle, elastic modulus and dilation angle, are provided in (Cui and Fall, 2016).

4.3.3.5.1.2. Chemical shrinkage

With the consumption of water in the reactive porous media of the CPB, the meniscus of the liquid-gaseous interface will gradually form and result in a progressive increase in capillary pressure. Consequently, the skeleton of the CPB will suffer increasing compression and the volume of the solid skeleton will decrease (called chemical shrinkage). Based on a previous study on cement paste (Powers and Brownyard, 1947), two sources that contribute to chemical shrinkage are identified, viz. chemically combined water induced by hydration reactions, and physically absorbed water by cement gel. The volume of these two types of water is less than the volume of the capillary water with the same mass.

In terms of isotropic chemical shrinkage, the volumetric strain induced by binder hydration can be related to the degree of hydration, as follows (Gawin et al., 2008):

$$d\boldsymbol{\varepsilon}_c = \beta_{ch}\mathbf{I}d\xi \tag{4.57}$$

where β_{ch} is a coefficient of the chemical shrinkage and stands for the total chemical shrinkage strain at complete hydration. In this study, the model from (Powers and Brownyard, 1947) is adopted to derive the coefficient of chemical shrinkage. The model indicated that the mass ratio, $R_{n-w/hc}$, of chemically combined water, m_{n-w}, and hydrated cement, m_{hc} will keep constant during the hydration reaction for a given cement type.

$$R_{n-w/hc} = m_{n-w}/m_{hc} = 0.187x_{C_3S} + 0.158x_{C_2S} + 0.665x_{C_3A} + 0.2130x_{C_4AF} \tag{4.58}$$

where x denotes the mass fraction of the clinker composition. The hydrated cement can be related to the degree of cement hydration, ξ, and the initial cement mass, $m_{hc-initial}$,:

$$m_{hc} = \xi \cdot m_{hc-initial} \tag{4.59}$$

During the hydration reaction, a certain amount of water will be physically absorbed by the hydration products. In previous studies (Powers and Brownyard, 1947; Brouwers, 2004), it has been concluded that the mass of the absorbed water, m_{ab-w}, equals the mass of the chemically combined water, m_{n-w},.

$$m_{n-w} = m_{ab-w} \tag{4.60}$$

In order to quantitatively determine the variation in the volume that is induced by chemical shrinkage, the specific volume (inverse of density) of the chemically combined water, v_{ch-w}, and the absorbed water, v_{ab-w}, should be determined. It has been proven that the specific volumes of these two types of water do not vary for all types of cement (Brouwers, 2004):

$$\begin{aligned} v_{ch-w} &= 0.72\ \text{cm}^3/\text{g} \\ v_{ab-w} &= 0.90\ \text{cm}^3/\text{g} \end{aligned} \tag{4.61}$$

Due to the fact that chemical shrinkage is induced by the variation in the volume of physically and chemically combined water, the volume change, V_{ch}, caused by chemical shrinkage can be expressed as:

$$V_{ch} = V_{ab/n} - V_{ab-w} - V_{ch-w} \tag{4.62}$$

where V_{ab-w}, V_{ch-w} and $V_{ab/n}$ denote the physically adsorbed water volume, chemically combined water volume, and the total volume of the physically and chemically combined water in the capillary state, respectively.

Then, the variation of the shrinkage strain ε_c, solid phase density ρ_s and porosity ϕ_{hydr} induced by binder hydration can be derived as follows:

$$\varepsilon_c = \frac{V_{ch}}{V} = \frac{\left(m_{n-w} + m_{ab-w}\right)v_w - m_{n-w} \cdot v_{ch-w} - m_{ab-w} \cdot v_{ab-w}}{m_{w-initial}v_w + m_{\mathrm{hc}-initial}v_c + m_{tailings}v_{tailings}} \tag{4.63}$$

$$\rho_s = \frac{m_s}{V_s} = \frac{m_{hc-initial} + m_{tailings} + \left(m_{ab-w} + m_{n-w}\right)}{m_{hc-initial}v_c + m_{tailings}v_{tailings} + m_{ab-w}v_{ab-w} + m_{n-w}v_{ch-w}} \tag{4.64}$$

$$\phi_{hydr} = \frac{V_{cp}}{V} = \frac{m_{w-initial}v_w - m_{n-w}v_{ch-w} - m_{ab-w}v_{ab-w}}{m_{w-initial}v_w + m_{\mathrm{hc}-initial}v_c + m_{tailings}v_{tailings}} \tag{4.65}$$

where m denotes the mass and v is the specific volume.

For the convenience of practical application, commonly employed mix parameters (i.e. binder content, C_m, and water to cement ratio, w/c) are used to rewrite the derived formula of the chemical strain.

$$C_m = \frac{m_{hc-initial}}{m_{tailings} + m_{hc-initial}}$$
$$w/c = \frac{m_{w-initial}}{m_{hc-initial}} \tag{4.66}$$

Then, the substituting of Eqs. (4.58), (4.59) and (4.66) into Eqs.(4.63), (4.64) and (4.65) yields:

$$\varepsilon_c = \frac{\left(2v_w - v_{ch-w} - v_{ab-w}\right)R_{n-w/hc}}{\left(w/c\right)v_w + v_c + \left(1/C_m - 1\right)v_{tailings}}\xi \tag{4.67}$$

$$\rho_s = \frac{m_s}{V_s} = \frac{1 + \left(1/C_m - 1\right) + 2R_{n-w/hc}\xi}{v_c + \left(1/C_m - 1\right)v_{tailings} + \left(v_{ch-w} + v_{ab-w}\right)R_{n-w/hc}\xi} \tag{4.68}$$

$$\phi_{hydr} = \frac{\left(w/c\right)v_w - \left(v_{ch-w} + v_{ab-w}\right)R_{n-w/hc}\xi}{\left(w/c\right)v_w + v_c + \left(1/C_m - 1\right)v_{tailings}} \tag{4.69}$$

Then, the incremental shrinkage strain can be written as follows:

$$d\varepsilon_c = \left[\frac{\left(2v_w - v_{ch-w} - v_{ab-w}\right)R_{n-w/hc}}{\left(w/c\right)v_w + v_c + \left(1/C_m - 1\right)v_{tailings}}\right]d\xi \tag{4.70}$$

By using Eq. (4.57) as a comparison, the coefficient of the chemical shrinkage, β_{ch}, can be expressed as:

$$\beta_{ch} = \frac{\left(2v_w - v_{ch-w} - v_{ab-w}\right)R_{n-w/hc}}{\left(w/c\right)v_w + v_c + \left(1/C_m - 1\right)v_{tailings}} \tag{4.71}$$

4.3.3.5.1.3. Thermal expansion

Due to the exothermal binder hydration, temperature gradients occur inside the CPB structure, which, in turn, results in the development of thermal stress. The isotropic thermal strain, $\boldsymbol{\varepsilon}_T$, can be defined as:

$$d\boldsymbol{\varepsilon}_{\boldsymbol{T}} = \alpha_T dT\mathbf{I} \tag{4.72}$$

where α_T is a coefficient of the thermal expansion and $\mathbf{I}$ is the second-order volumetric unity tensor. Based on previous studies on cementitious materials (e.g., mortar, cemented soil and concrete) (e.g., Emanuel and Hulsey, 1977; Mindess et al., 2003; Sellevold and Bjøntegaard, 2006), the evolution of the coefficient of thermal expansion (CTE) is controlled by solid constituents (e.g., aggregate and cement), moisture content and degree of hydration. In order to quantitatively evaluate the CTE, a model (Neville and Brooks, 1987) is adopted to predict the evolution of the CTE of the CPB:

$$\alpha_T = \alpha_p - \frac{2f_{tailings}\left(\alpha_p - \alpha_{tailings}\right)}{1 + E_p/E_{tailings} + f_{tailings}\left(1 - E_p/E_{tailings}\right)} \tag{4.73}$$

where $f_{tailings}$ is the volumetric content of the tailings, $E_p/E_{tailings}$ is the ratio of the elastic modulus of the cement paste to the tailings, $\alpha_{tailings}$ is the CTE of the tailings, and for the CTE of the binder paste, α_p, the value will evolve with the contents of the components (i.e., unhydrated binder and hydration products) with regard to the total volume of the cement paste. The following model proposed by Choktaweekarn and Tangtermsirikul (2009) is utilized to predict the CTE of the binder paste:

$$\alpha_p = A_{p1}f_{uc}\alpha_{uc} + A_{p2}f_{hp}\alpha_{hp} + A_{p3}f_{uma}\alpha_{uma} \tag{4.74}$$

where α_{uc}, α_{hp} and α_{uma} are the CTE of the unhydrated cement, hydration products and unhydrated mineral admixture (e.g., fly ash and blast-furnace slag), respectively. Based on reported experimental data from a previous study (Choktaweekarn and Tangtermsirikul, 2009), A_{p1}, A_{p2}, and A_{p3} are the constants and equal to 0.284, 1.230 and 1.499, respectively. f_{uc}, f_{hp} and f_{uma} are the corresponding volumetric fractions with respect to the total volume of the CPB mixture. For CPB materials, the relation of the volumetric ratios of every constituent can be expressed as:

$$f_{uc} + f_{hp} + f_{uma} + f_{tailings} + f_{cap-w} + f_{cap-a} = 1 \tag{4.75}$$

where $f_{tailings}$, f_{cap-w}, and f_{cap-a} refer to the volumetric ratio of the tailings, capillary water and capillary air with respect to the total volume of the CPB mixture, respectively. If the binder just consists of cement (i.e., the f_{uma} equals zero), Eqs. (4.74) and (4.75) can be rewritten as follows:

$$\alpha_p = A_{p1} f_{uc} \alpha_{uc} + A_{p2} f_{hp} \alpha_{hp} \tag{4.76}$$

$$f_{uc} + f_{hp} + f_{tailings} + f_{cap-w} + f_{cap-a} = 1 \tag{4.77}$$

Due to the fact that the volumetric ratio of unhydrated cement and hydrated products evolve with the advancement of the binder hydration, the volumetric ratio of the hydration products can be obtained based on the derived results of the CTE of the CPB as follows:

$$f_{hp} = \frac{m_{hc} v_c + m_{ab-w} v_{ab-w} + m_n v_{ch-w}}{m_w v_w + m_{\text{hc}-initial} v_c + m_{tailins} v_{tailings}} = \frac{v_c + R_{n-w/hc}\left(v_{ch-w} + v_{ab-w}\right)}{(w/c) v_w + v_c + \left(1/C_m - 1\right) v_{tailings}} \xi \tag{4.78}$$

$$f_{uc} = \frac{(1-\xi) m_{hc-initial} v_c}{m_w v_w + m_{\text{hc}-initial} v_c + m_{tailins} v_{tailings}} = \frac{v_c}{(w/c) v_w + v_c + \left(1/C_m - 1\right) v_{tailings}} (1-\xi) \tag{4.79}$$

$$f_{tailings} = \frac{m_{tailings} v_{tailings}}{m_w v_w + m_{\text{hc}-initial} v_c + m_{tailins} v_{tailings}} = \frac{\left(1/C_m - 1\right) v_{tailings}}{(w/c) v_w + v_c + \left(1/C_m - 1\right) v_{tailings}} \tag{4.80}$$

The substituting of Eqs. (4.78) and (4.79) into Eq. (4.76) yields:

$$\alpha_p = \frac{A_{p1} \alpha_{uc} v_c (1-\xi) + A_{p2} \alpha_{hp} \left[v_c + R_{n-w/hc}\left(v_{ch-w} + v_{ab-w}\right)\right] \xi}{(w/c) v_w + v_c + \left(1/C_m - 1\right) v_{tailings}} \tag{4.81}$$

For cement paste, the following equation proposed by Kamali et al. (2004) is adopted in this study to describe the evolution of the elastic modulus (GPa) of the cement paste.

$$E_p = L_1 \cdot \left(1 - \phi_{hydr}\right)^{L_2} \tag{4.82}$$

where L_1 and L_2 are the fitting parameters. For Portland cement Type I, the two fitting parameters amount to 46.03 GPa and 3.16 (Kamali et al., 2004), respectively, ϕ_{hydr} refers to the capillary porosity.

By substituting Eqs. (4.69), (4.70), (4.81) and (4.82) into Eq. (4.73), the CTE of the CPB can be derived as follows:

$$\alpha_T = \alpha_p - \frac{2 v_{tailings} \left(1/C_m - 1\right)\left(\alpha_p - \alpha_{tailings}\right)}{\left[(w/c) v_w + v_c\right]\left\{1 + \left[L_1 \cdot \left(1 - \phi_{hydr}\right)^{L_2}\right] \big/ E_{tailings}\right\} + 2 v_{tailings}\left(1/C_m - 1\right)} \tag{4.83}$$

$$\text{with} \begin{cases} \alpha_p = \dfrac{A_{p1} \alpha_{uc} v_c (1-\xi) + A_{p2} \alpha_{hp} \left[v_c + R_{n-w/hc}\left(v_{ch-w} + v_{ab-w}\right)\right] \xi}{(w/c) v_w + v_c + \left(1/C_m - 1\right) v_{tailings}} \\ \phi_{hydr} = \dfrac{(w/c) v_w - \left(v_{ch-w} + v_{ab-w}\right) R_{n-w/hc} \xi}{(w/c) v_w + v_c + \left(1/C_m - 1\right) v_{tailings}} \end{cases}$$

4.3.3.5.2. Fluid flow model

As mentioned in Section 4.3.3.1, the fluid phase in CPB is assumed to consist of liquid water and dry air. By incorporating the gravity effect, Darcy's law is used to describe the fluid flow for liquid water and dry air:

$$\mathbf{v}^{ri} = -k\frac{k_{ri}}{\mu_i}\left(\nabla P_i - \rho_i g \nabla D_i\right) \tag{4.84}$$

where k is the intrinsic permeability of CPB, k_{ri} is the relative permeability with respect to each fluid, μ_i indicates the fluid dynamic viscosity, and P_i refers to the pore fluid pressure, D_i represents the elevation. The intrinsic permeability, k, can be derived from the relationship between the hydraulic conductivity, K_{sat}, and permeability, k.

$$k = K_{sat}\mu_i / \rho_i g \tag{4.85}$$

Hence, in order to determine the intrinsic permeability of CPB, the hydraulic conductivity should be defined. Based on the measured experimental data of the saturated hydraulic conductivity of CPB reported by Ghirian and Fall (2013a), the following exponential function is proposed to simulate the evolution of the hydraulic conductivity (i.e., coefficient of permeability) of the CPB with binder hydration:

$$K_{sat} = K_T \exp\left(C_{K1}\xi^{C_{K2}}\right) \tag{4.86}$$

where K_T is the saturated hydraulic conductivity of the tailings, and C_{K1} and C_{K2} are the fitting parameters. Based on the regression analysis on the measured data of K_{sat} reported by Ghirian and Fall (2013a), C_{K1} =-8.173 and C_{K2} =4.035.

For the relative permeability, its analytic expressions for liquid (e.g., pore water) and gas (e.g., pore air) have been derived by Van Genuchten (1980) and Luckner et al. (1989) based on the model in (Mualem, 1976), respectively.

$$k_{rw}\left(S_e\right) = \sqrt{S_e}\left[1-\left(1-S_e^{1/m_{WRC}}\right)^{m_{WRC}}\right]^2 \tag{4.87}$$

$$k_{ra}\left(S_e\right) = \sqrt{1-S_e}\left(1-S_e^{1/m_{WRC}}\right)^{2m_{WRC}} \tag{4.88}$$

where m_{WRC} is the material parameter, and the effective degree of saturation (i.e., normalized water content), S_e, can be defined as follows (Van Genuchten, 1980):

$$S_e = \left(\theta - \theta_r\right) / \left(\theta_s - \theta_r\right) \tag{4.89}$$

where θ, θ_s and θ_r are the volumetric, saturated and residual water contents, respectively. For the residual water content, θ_r, an empirical function has been proposed by Abdul-Hussain and Fall (2011) to characterize its evolution with binder hydration.

$$\theta_r = R_{r1} \cdot \exp(-R_{r2} \cdot \xi) \tag{4.90}$$

where R_{r1} and R_{r2} are the two adimensional fitting constants and equal to 1.314 and 7.538 respectively based on the experimental data reported by Abdul-Hussain and Fall (2011).

Moreover, the volumetric water content, θ, may be related to the capillary pressure (matric suction) based on the water retention curve (WRC) (Williams, 1982). Numerous empirical equations for the simulation of the WRC have been proposed and a detailed review of the empirical equations is found in Fredlund and Xing (1994). Among these proposed models, the van Genuchten model (Van Genuchten, 1980) has been successfully applied to simulate the WRC of CPB (Abdul-Hussain and Fall, 2011; Ghirian and Fall, 2013a). The model can be reduced to a two-parameter formula as follows:

$$\theta = \theta_r + \left(\theta_s - \theta_r\right) \Big/ \left[1 + \left(\alpha_{WRC} P_c\right)^{n_{WRC}}\right]^{m_{WRC}} \quad (4.91)$$

where α_{WRC}, m_{WRC} and n_{WRC} are the fitting parameters and $n_{WRC} = 1/\left(1 - m_{WRC}\right)$. By substituting the van Genuchten model into Eq. (4.89), this yields:

$$S_e = 1 \Big/ \left[1 + \left(\alpha_{WRC} P_c\right)^{\frac{1}{1-m_{WRC}}}\right]^{m_{WRC}} \quad (4.92)$$

In order to characterize the influence of binder hydration on the WRC, two parameters, viz. α_{WRC} and m_{WRC}, are needed. Based on the measured data of the WRC of the CPB reported by Abdul-Hussain and Fall (2011) and Ghirian and Fall (2013a), the following models are proposed:

$$m_{WRC} = f_{m1} \xi^{f_{m2}} + f_{m3} \quad (4.93)$$

$$\alpha_{WRC} = f_{\alpha 1} e^{f_{\alpha 2} \xi} \quad (4.94)$$

where f_{m1}, f_{m2}, f_{m3}, $f_{\alpha 1}$ and $f_{\alpha 2}$ are the fitting constants. Through a regression analysis of the measured data reported by Abdul-Hussain and Fall (2011) and Ghirian and Fall (2013a), f_{m1} =0.0415, f_{m2} =4.231, f_{m3} =0.4073, $f_{\alpha 1}$ =0.2103 kPa^{-1} and $f_{\alpha 2}$ =-6.921.

It has been recognized that the fluid (water and air) dynamic viscosity (i.e., μ_w and μ_a) is highly dependent on the temperature (Mason and Monchick, 1963). Based on the findings published by Thomas and Sansom (1995), the following model is utilized to describe the influence of temperature on the dynamic viscosity (Pa·s) of pore water:

$$\mu_w = 0.6612\left(T - 229\right)^{-1.562} \quad (4.95)$$

with T being the absolute temperature.

For the dynamic viscosity of gas, μ_a, it is well known that the Sutherland's viscosity law is a widely used expression to predict the temperature dependence of viscosity:

$$\mu_a = \mu_0 \cdot \left(T/T_0 \right)^{1.5} \cdot \left[\left(T_0 + c_0 \right) / \left(T + c_0 \right) \right] \tag{4.96}$$

For air, μ_0 =1.716×10^{-5} Pa·s, T_0 =273 K and c_0 =111 K.

In addition, the sink term, $\dot{m}_{hydr}$, in a water mass balance equation should be defined. As mentioned in the subsection on chemical shrinkage, the water consumption induced by binder hydration can be categorized into physically adsorbed water, m_{ab-w} , and chemically combined water, m_{n-w} , namely:

$$m_{hydr} = m_{ab-w} + m_{n-w} \tag{4.97}$$

The substituting of Eqs. (4.58), (4.59) and (4.60) into Eq. (4.97) yields:

$$m_{hydr} = 2m_{hc-initial} R_{n-w/hc} \xi \tag{4.98}$$

Then, the water sink term, $\dot{m}_{hydr}$, can be derived from the time derivative of Eq. (4.45).

$$\begin{aligned} \dot{m}_{hydr} = 2m_{hc-initial} & \left(0.187 x_{C_3S} + 0.158 x_{C_2S} + 0.665 x_{C_3A} + 0.2130 x_{C_4AF} \right) \\ & \times \left\{ \left(\frac{\tau}{t_e} \right)^{\beta} \left(\frac{\beta}{t_e} \right) \xi(t_e) \exp\left[\frac{E_a}{R} \left(\frac{1}{273 + T_r} - \frac{1}{273 + T} \right) \right] \right\} \end{aligned} \tag{4.99}$$

4.3.3.5.3. Heat transfer and generation

The evolution of heat in CPB can be attributed to two sources, viz. heat transfer and heat production. The former can be divided into heat advection due to the fluid motion, and heat conduction due to the temperature gradient. The latter is induced by exothermal binder hydration.

4.3.3.5.3.1. Heat advection

Heat advection may result from both liquid water and dry air flow. Therefore, the heat advection (apparent quantity), Q_{ad} be expressed in the following form:

$$Q_{ad} = \left(\rho_w C_{w-p} \mathbf{v}^{rw} + \rho_a C_{a-p} \mathbf{v}^{ra} \right) \cdot \nabla T \tag{4.100}$$

where $\mathbf{v}$ refers to the fluid Darcy velocity and C is the fluid specific heat capacity at a constant pressure. Similar to the dynamic viscosity of fluid, the fluid density is dependent on the temperature as well. In this study, air is considered to be the ideal gas. Accordingly, the density of air can be expressed as:

$$\rho_a = \frac{M_a}{R \cdot T} P_a \tag{4.101}$$

with M_a as the molar mass of air, R the universal gas constant of air, and P_a absolute pressure of pore air.

Compared with air density, the influence of pressure on water density is limited and often questionable (Alnajim, 2004). Therefore, the following formula given by Sercombe et al. (2001) is adopted in this study:

$$\rho_w = 314.4 + 685.6\left\{1-\left[\left(T-273.15\right)/374.14\right]^{1/0.55}\right\}^{0.55} \tag{4.102}$$

4.3.3.5.3.2. Heat conduction

In order to characterize the heat conduction in CPB, and between the CPB structure and surrounding rocks, Fourier's law is utilized to analyze the heat conduction process.

$$\mathbf{q} = -k_{eff}\nabla T \tag{4.103}$$

where $\mathbf{q}$ denotes the conductive heat flux, ∇T is the temperature gradient, k_{eff} is the effective thermal conductivity of the CPB, which can be expressed by the following formula given by Somerton et al. (1973):

$$k_{eff} = k_{dry} + \sqrt{S_{eff}}\left(k_{sat} - k_{dry}\right) \tag{4.104}$$

where k_{dry} and k_{sat} represent the thermal conductivity of the porous media in the saturated state and a completely dry condition. For the characterization of the saturated thermal conductivity, k_{sat}, the following formula proposed by Côté and Konrad (2005) has been successfully applied in the prediction of k_{sat} for CPB materials (Ghirian and Fall, 2013a).

$$k_{sat} = k_{tailings}^{1-\phi} k_w^{\phi} \tag{4.105}$$

where $k_{tailings}$ and k_w refer to the mean value of the tailings and the water thermal conductivities, respectively.

Compared with saturated conditions, the dry thermal conductivity, k_{dry}, corresponds to the completely opposite situation in that the water that has fully saturated the pore space is completely occupied by dry air. Therefore, a similar prediction model is used in this study to characterize dry thermal conductivity.

$$k_{dry} = k_{tailings}^{1-\phi} k_a^{\phi} \tag{4.106}$$

with k_a as the air thermal conductivity.

4.3.3.5.3.3. Heat generation

Binder hydration is a long-term process in CPB, which not only consumes pore water but also releases heat. Moreover, for large underground stopes, the backfilling process may take a long time. Based on a previous experimental study (Schindler and Folliard, 2003), the rate of heat generation (i.e. the volumetric heat-source intensity), Q_{hydr}, (W/m^3), of cementitious material can be expressed as follows:

$$Q_{hydr} = H_T\left(\frac{\tau}{t_e}\right)^{\beta}\cdot\left(\frac{\beta}{t_e}\right)\cdot\xi\left(t_e\right)\cdot\exp\left[\frac{E_a}{R}\left(\frac{1}{273+T_r}-\frac{1}{273+T}\right)\right] \tag{4.107}$$

$$\text{with} \begin{cases} H_T = \left(H_{cem} \cdot X_{cem} + 461 \cdot X_{slag} + 1800 \cdot x_{CaO/FA} \cdot X_{FA}\right) C_b \\ H_{cem} = 500x_{C_3S} + 260x_{C_2S} + 866x_{C_3A} + 420x_{C_4AF} + 624x_{SO_3} + 1186x_{FreeCaO} + 850x_{MgO} \end{cases}$$

where H_T is the total heat available for binder hydration, T_r is the reference temperature, and T is the temperature of the cement-based materials, H_{cem} is the total heat of the hydration of the cement, C_b is the apparent binder density with respect to the total volume of the CPB mixture, X_i is the weight ratio of the corresponding minerals in terms of the total binder content and x_i is the weight ratio of the corresponding compound in terms of the total cement content.

4.3.4. Model validation and simulation

The coupled THMC model presented above is implemented into a finite element method (FEM) code, COMSOL Multiphysics. With COMSOL, a wide range of analyses can be carried out, including stationary and time-dependent, linear and nonlinear, eigenfrequency and modal analyses by using FEM together with adaptive meshing and error control which use a variety of numerical solvers (COMSOL, 2014).

Five case studies were used to test the capabilities of the developed model to describe and predict the THMC behavior of CPB. The case studies cover both laboratory experiments and field measurements. Table 4.4 shows the input parameters, boundary conditions and initial values used for the numerical simulations of each case study.

Table 4.4. Input parameters, boundary conditions and initial values of simulated models

	Case Study 1	Case Study 2	Case Study 3	Case Study 4	Case Study 5
Cement content	4.5%	4.5%	5%	7.4%	7.6%
w/c ratio	7.6	7.6	6.6	4.5	4.5
Height of each fill layer (m)	0.5	0.2	0.56	1st : 5.96 2nd: 7.44 3rd : 6.70	0.1
Backfill layers	3	1	1	3	1
Insulation materials					
Category	Thermal insulating foam sealant	Thermal insulation glass wool blanket	N/A	N/A	Granite rock
Thermal conductivity (W/(m k))	0.024	0.035	N/A	N/A	2.9
Heat capacity (J/(kg k))	1400	840	N/A	N/A	850
Density (kg/m^3)	30	30	N/A	N/A	2600
Mechanical module					

Top surface	Free	Load	Free	Free	Boundary load
Lateral sides	Roller	Roller	Contact Pair	Contact Pair	Boundary load
Bottom side	Fixed	Fixed	Fixed	Fixed	Fixed
Volume force	Gravity	Gravity	Gravity	Gravity	N/A
Hydraulic module					N/A
Top surface	Mass flux	No flow	No flow	Mass flux	
Lateral sides	No flow	No flow	No flow	No flow	
Bottom side	No flow	No flow	No flow	No flow	
Volume force	Gravity	Gravity	Gravity	Gravity	
Initial value of each fill layer	Hydraulic head=0	Hydraulic head=0	Hydraulic head=0	Hydraulic head=0	
Thermal module					N/A
Top side(°C)	20.75	22	Recorded room temp.	21.7	
Lateral sides (°C)	20.75	22	Recorded room temp.	21.7	
Bottom side (°C)	20.75	22	Recorded room temp.	21.7	
Initial temperature of each fill layer (°C)	20.75	22	Recorded room temp.	21.7	

4.3.4.1. Case Study 1: High column experiments with CPB to understand THMC processes

In order to experimentally study the coupled THMC behavior of CPB, experiments on high columns with CPB were carried out in previous research (Ghirian and Fall, 2013a; 2014). In the studies, staged backfilling strategy is adopted and completed in 3 layers that were 50 cm each in height for 3 consecutive days. Each backfilling stage was completed in very short time (in 5 minutes). The high column tests were performed under insulated-undrained conditions. During the high column test, extensive laboratory testing and measurements were carried out, including the monitoring of the variation of the pore water pressure, temperature distribution and vertical settlement in the CPB columns. The monitored positions were located at three different heights, including 25 cm from the bottom, in the middle of the column, (75 cm from the bottom) and at the top of the column (125 cm from the bottom). In addition, the study also presented the evolution of CPB properties with time, such as the uniaxial compressive strength, and saturated hydraulic and thermal conductivities. Detailed explanations of the experimental programs conducted and the results obtained can be found in Ghirian and Fall (2013a, 2014)

This study on experiments carried out with high columns was selected and simulated to verify the validity and reliability of the developed model for predicting and simulating the THMC behavior of the CPB observed in these column experiments. Due to the geometric characteristic of the cylinder column, an axisymmetric geometry model is adopted in the simulation. The model characteristics, mesh and monitoring point are shown in Figure 4.14. The simulation was performed in three stages to depict the backfilling sequence. Due to the fact that the backfilling process of each layer is completed in a rather short period of time (in 5 minutes), the backfilling process can be considered as immediate complement compared with the time interval of backfilling (1 day). Therefore, the backfilling process is simulated in a layer-by-layer manner and each previously stored solution is set as initial values of dependent variable for next step of simulation.

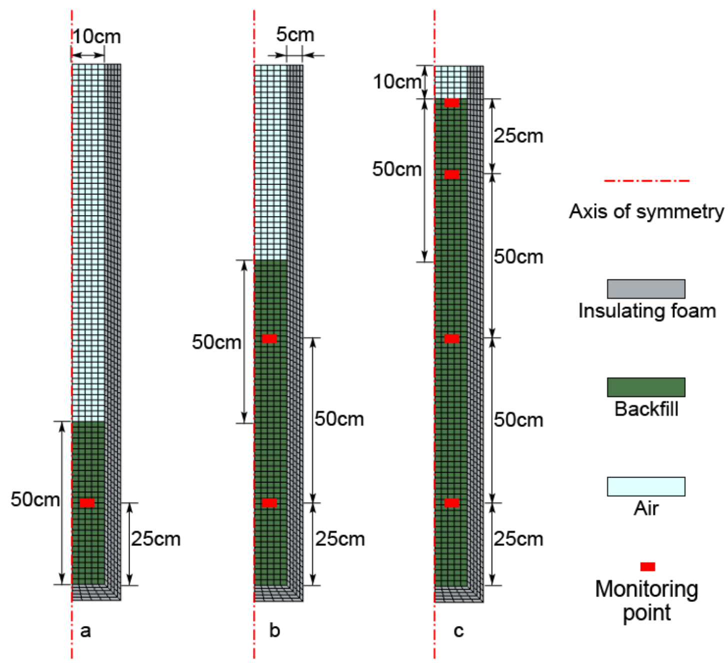

Figure 4.14. Geometry and mesh of the simulated model and monitoring point: a. 1st stage of backfilling; b. 2nd stage of backfilling; c 3rd stage of backfilling.

Thermal process

Figure 4.15 shows a comparison between the simulation results and measured data of the temperature in the CPB column for both short-term curing (a) and long-term curing (b). It can be seen that the simulated evolution of temperature is in good agreement with the experimental data in terms of both maximum values and evolution trend. The fluctuation of the experimental data for long-term curing is due to the varied room temperature during the test. Moreover, the simulated thermal conductivity values are plotted against the experimental data in Figure 4.16. The simulation results show good agreement with the test data and the coefficient of determination, R^2, equals 0.97.

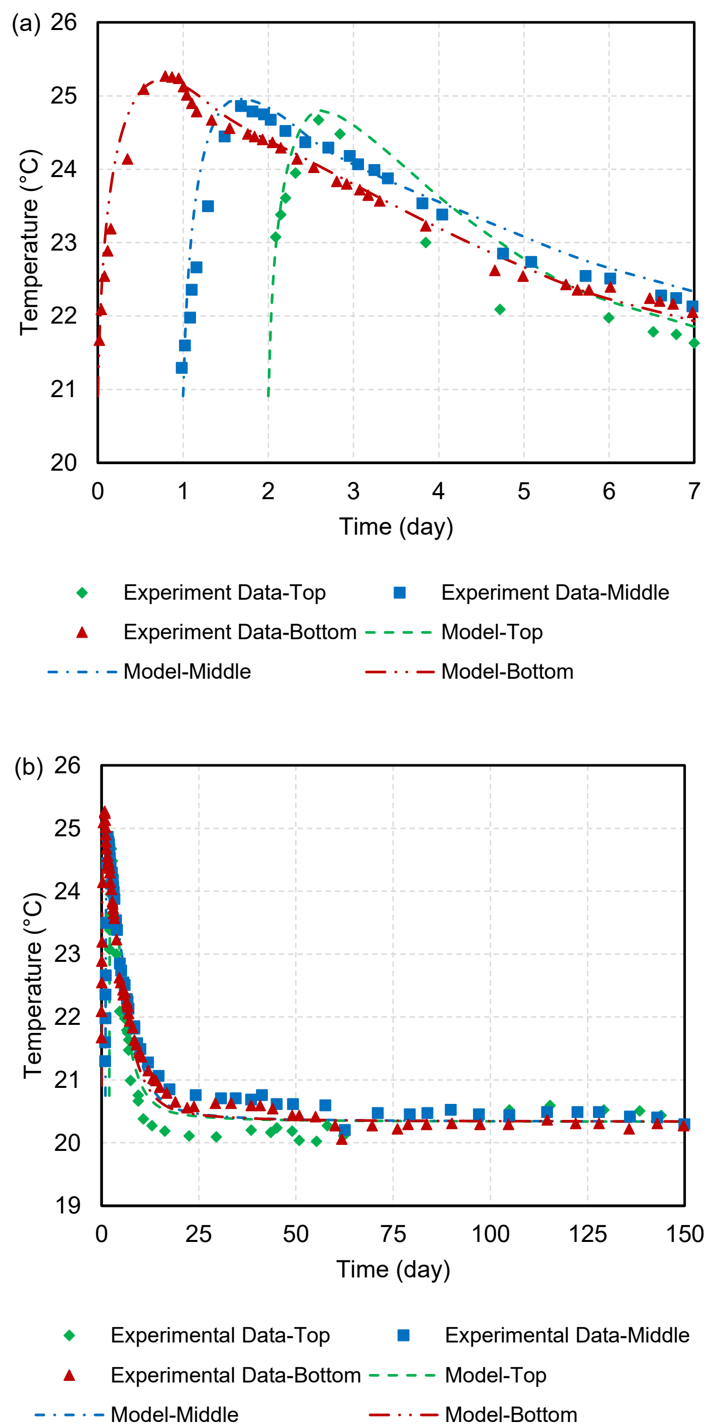

Figure 4.15. Comparison of numerical prediction and experimental data of temperature: (a) short-term curing; (b) long-term curing (Top: height of 125 cm from the bottom of the column; Middle: 75 cm from the bottom; Bottom: 25 cm from the bottom)

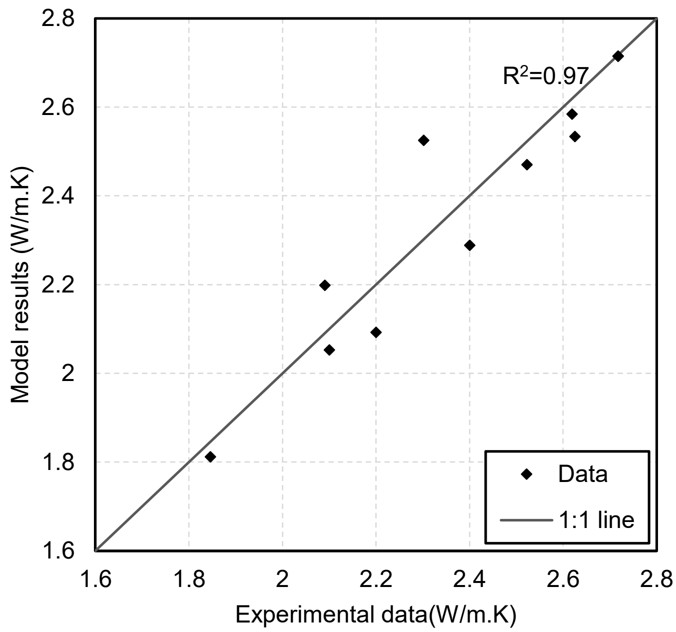

Figure 4.16. Comparison of thermal conductivity between predicted and experimental data

Hydraulic process

Figure 4.17 presents the evolution of pore water pressure (PWP) for early and advanced ages. As shown in the figure, there is good agreement between the predicted and experimental values. Both the simulation results and measured data demonstrate that the PWP immediately develops right after placement of the CPB layer, then gradually decreases with curing time. After 16 hours, a negative PWP develops rapidly inside the column. The early age evolution of the PWP is dominated by the advancement of the binder hydration. Specifically, the hydration reaction consumes pore water, which, in turn, contributes to the variation of the PWP. It is also interesting to note that immediately after the second backfill layer is placed into the column, the PWP of the bottom layer returns to a positive value, and the extent of the reduction of the PWP of this middle layer exceeds that of the bottom layer. These phenomena can be explained by the gravity water drainage through the middle layer. Subsequently, the PWP of both layers is progressively reduced and shows a similar trend to the evolution of the PWP after the first layer of backfill is placed into the column. A similar phenomenon took place followed by a different amount of PWP reduction after the third layer was poured into the column. After about 7 days, the negative PWP shows a steady trend of evolution and the PWP values of the three monitored points approach approximately -100 kPa for the bottom layer, -150 kPa for the middle layer, and -200 kPa for the top layer.

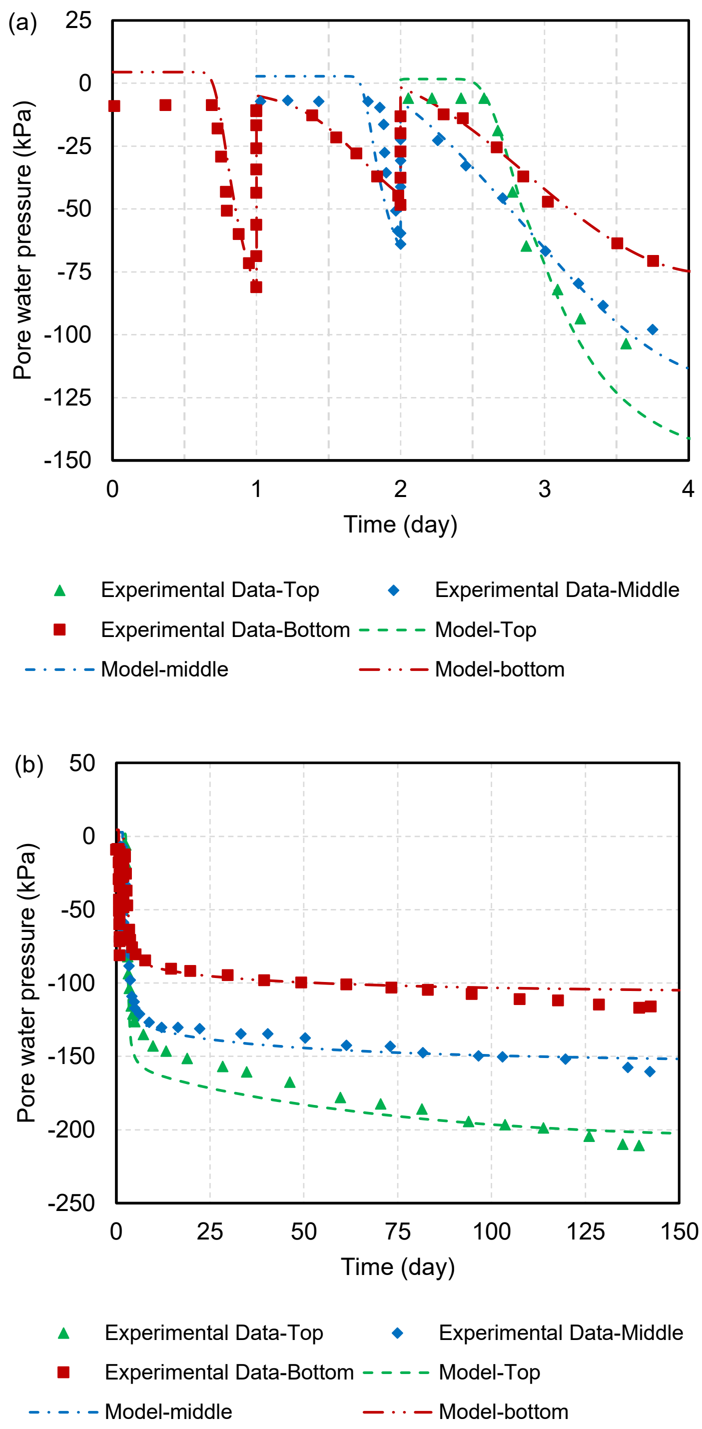

Figure 4.17. Comparison of prediction results and experimental data of pore water pressure: (a) short term curing (b) long term curing (Top: height of 125 cm from the bottom of the column; Middle: 125 cm from bottom; Bottom: 25 cm from bottom)

As the water content is reduced, the initially saturated CPB gradually changes into an unsaturated condition. A simulation of the degree of saturation was conducted and the modeling results are presented in Figure 4.18. It can be observed that the variation of the degree of saturation is well captured in the simulation. Besides, as shown in Figure 4.19, the saturated hydraulic conductivity is also accurately predicted by the developed model and the corresponding coefficient of determination, R^2, reaches 0.92.

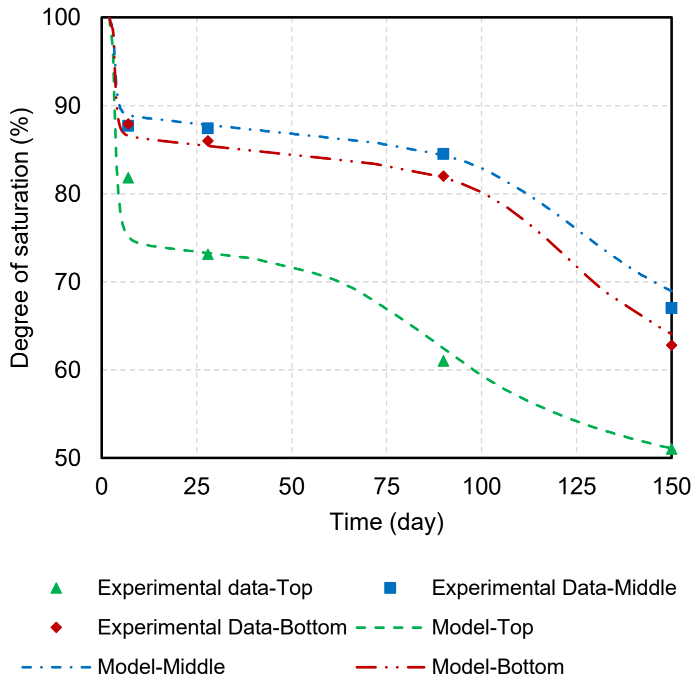

Figure 4.18. Computed evolution of degree of saturation against experimental data

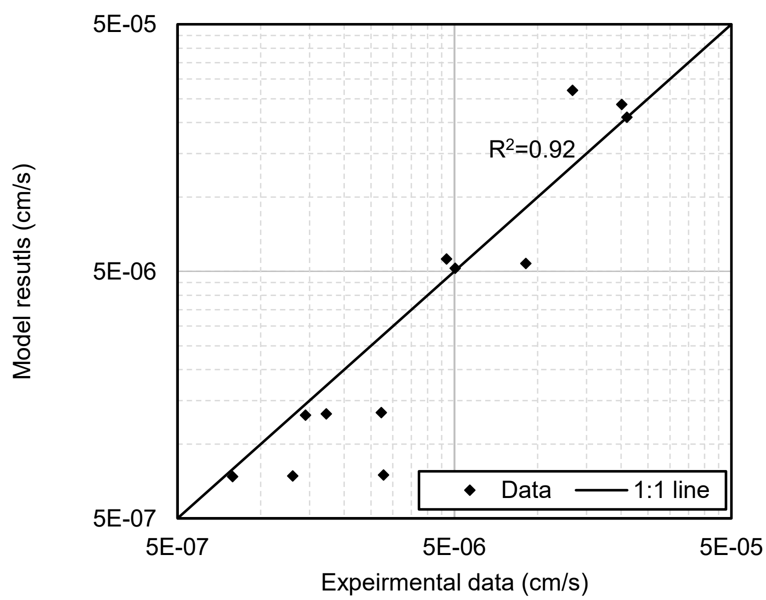

Figure 4.19. Computed evolution of hydraulic conductivity against experimental data

Mechanical process

The predictive ability of the CPB deformation model is verified against the experimental data of vertical settlement measured on the surface of the top layer in the CPB column. A comparison between the simulated and measured values is presented in Figure 4.20. From this figure, it can be noticed that the modeling results are in very good agreement with the measured data.

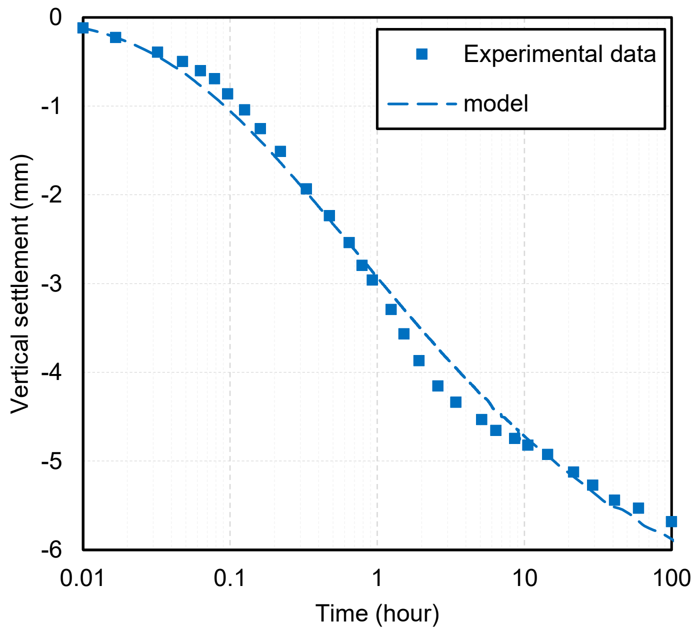

Figure 4.20. Predicted vertical settlement versus experimental data of vertical settlement

Apart from the measurement of vertical displacement of the high column, a series of UCS tests were performed at 7, 28, 90 and 150 days, which are collected and used to further validate the mechanical component of the developed model. As shown in Figure 4.21 the good agreement between predicted results and experimental data of stress-strain curve indicates the mechanical components of the developed model own the capability to mimic the characteristics of chemical and strain hardening-softening of CPB.

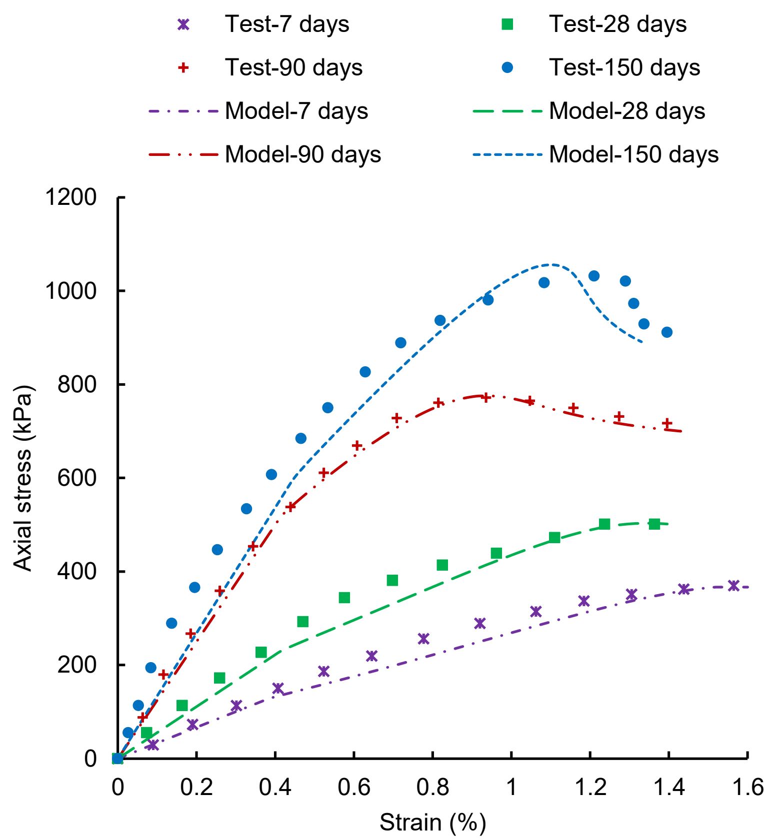

Figure 4.21. Comparison of numerical results and measured data of stress-strain relation

Hence, the comparison between predicted results and measured data in high column tests proves that the CPB behaviors including heat transfer and generation, pore water pressure evolution and deformation development can be well reproduced by the developed model.

4.3.4.2. Case Study 2: CPB cured under stress

It is well known that the in-situ properties and behavior of CPB differ from those measured in CPB cured in the laboratory under ordinary conditions, i.e. without application of the coupled processes during the curing of the CPB, to which the CPB will be subjected in the field (Le Roux et al., 2002; Fall and Ghirian, 2014; Yilmaz et al., 2014). In order to mimic the field curing conditions in the laboratory, several novel CPB curing systems have been designed to subject the CPB to various field conditions or coupled processes during curing, such as CPB cured under stress application (CUS) (Benzaazoua et al., 2006; Fahey et al., 2011; Ghirian and Fall, 2013b). In order to validate the developed model against the experimental data of CPB cured under gradually increased vertical pressure, the experimental tests performed by Ghirian and

Fall (2013a) were selected. In the tests, CPB is placed into a Perspex cylinder. The vertical pressure was applied onto the top surface of the CPB body through an axial piston driven by compressed air. In addition, the cell pressure apparatus was covered with a glass wool blanket as thermal insulation to reduce the heat transfer between the CPB and the surrounding environment. The experimental program, procedures and results obtained are detailed in (Ghirian and Fall, 2013b).

Since CPB was cured in a Perspex cylinder (Ghirian and Fall, 2013b), a 2D axisymmetric geometry model was adopted, and the geometry and mesh of the simulated model are presented in Figure 4.22. The application scheme of the vertical pressure is presented in Figure 4.23 (black line). During the simulation, the pressure application scheme used was expressed as a piecewise function and applied on the top surface of the CPB with a boundary load condition. According to the modeling results presented in Figure 4.23 the agreement between the predictive results and laboratory measured data of PWP is fairly good. During the initial stages, the evolution of PWP is dominated by the gravity of the fresh CPB due to the fluidic nature of the CPB at this stage of the curing. After this period, the PWP started to deviate, thus indicating that the CPB paste was gradually hardening. With curing time, a negative PWP developed after about 1 day of curing. From the comparison, the developed model is able to predict the evolution of the hydraulic process inside the CPB under stress curing conditions.

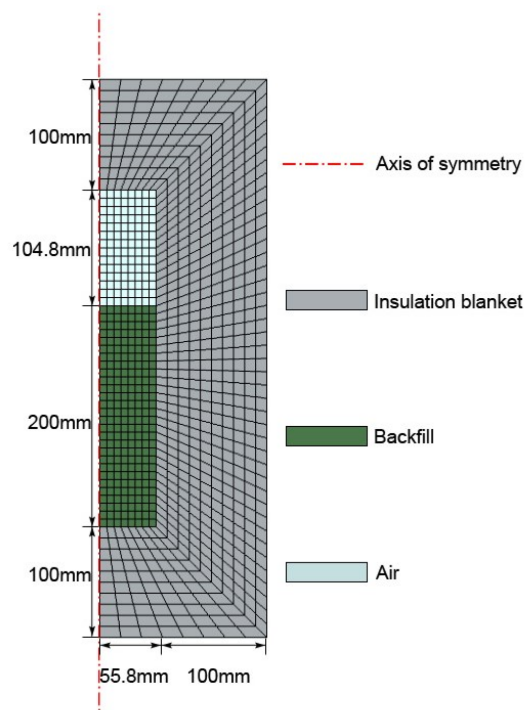

Figure 4.22 Geometry and mesh of simulated model in Case Study 2

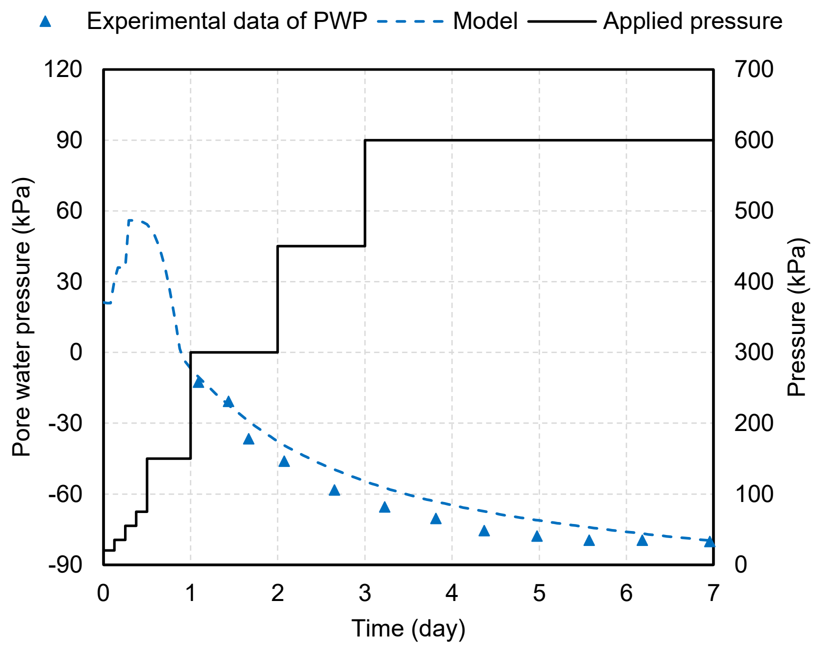

Figure 4.23. Comparison of prediction results and experimental data of pore water pressure

Figure 4.24 presents the predictive results and experimental data of the temperature in the CPB column under stress curing conditions. The simulation results of the temperature are in good agreement with the experimental results with respect to the peak value and variation trend.

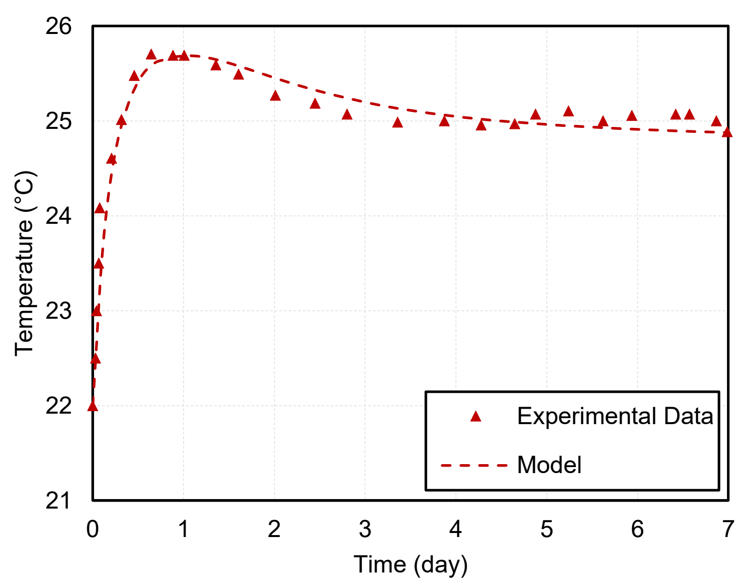

Figure 4.24. Comparison of numerical prediction and experimental data of temperature

Therefore, through the comparison of model predictions to experimental data of CUS tests, the predictability of CPB behavior under increased stress of the proposed model is validated.

4.3.4.3. Case Study 3: Experiment with scaled stope in laboratory

The heat emitted by CPB mass is able not only to exert significant influence on underground climate, but also to affect surround rock strength under certain circumstance (e.g., in the high Arctic due to the thawing of frozen rock). Therefore, in order to quantify the contribution of CPB to the heat load in mines, a physical model of scaled stope was established by De Souza and Hewitt (2005) to simulate and monitor the distribution and evolution of temperature in CPB and surrounding rocks. Compared with high column test (Case Study 1) and CUS test (Case Study 2), the scaled stope test can be considered as a more intuitive approach to increase the understanding the heat transfer and generation process in stope and surrounding wall. Therefore, the scaled stope test and related experimental data are chosen as another case study to further validate the developed model.

The scaled physical model of stope consisted of five granite blocks to simulate the stope roof, floor and walls. The wall blocks are 56 cm high*15 cm wide*27 cm deep. The base and roof blocks are 8 cm thick*50 cm wide*36 cm deep. The resulting dimension of backfill stope is 56 cm high*15 cm wide*27 cm deep. In order to monitor the temperature evolution in CPB, thermocouple probes were installed at 3 different level of CPB including top point (56cm from base), middle point (28 cm from base) and bottom point (base level) and the temperature was recorded over an 80-day period. In addition, the room temperature was collected during the test as well. Due to the relatively small geometry of the scaled stope, the measured data of temperature at the 3 locations are very close to each other. Hence, the experimental data of middle point is chosen to validate the predictability of the developed model for the heat release and transfer in CPB. The mesh and geometry of the simulated model and the monitoring point for Case Study 3 is presented in Figure 4.25. The related input parameters, initial values and boundary condition are listed in Table 4.4. It should be pointed out that the recorded room temperature is expressed as an interpolation function which is imposed on the stope walls as a Dirichlet boundary condition (i.e., temperature boundary condition).

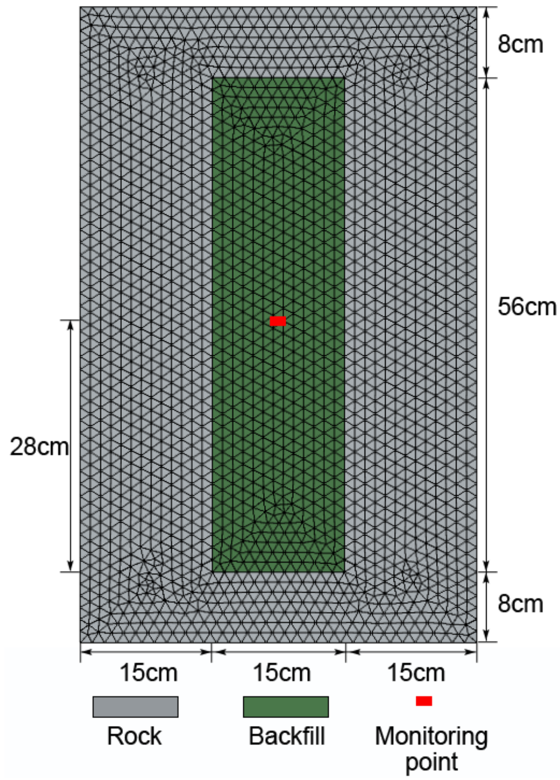

Figure 4.25. Geometry and mesh of simulated model and monitoring point in Case Study 3

A comparison between the predictive results and measured data of temperature evolution is presented in Figure 4.26. Both the simulation results and measured data show that the temperature rapidly increases during the early age. Simultaneously, the temperature difference between CPB and surrounding environment gradually becomes pronounced. Subsequently, the temperature in CPB decreases and evolves with ambient temperature. The simulation results of contour plot for different curing time (including 1, 7, 28 and 80 days) are presented in Figure 4.27. As shown in Figure 4.27, the temperature in CPB is higher than the temperature of stope wall for early ages (1 and 7 days). However, the temperature of CPB becomes close to granite rock's temperature and varies with the ambient temperature for a long-term curing time. Therefore, the evolution of temperature in CPB is controlled by two factors including heat release by binder hydration and the ambient room temperature. The good agreement between simulated results and experimental data indicates that the predictability of heat transfer and generation of the developed model is further validated.

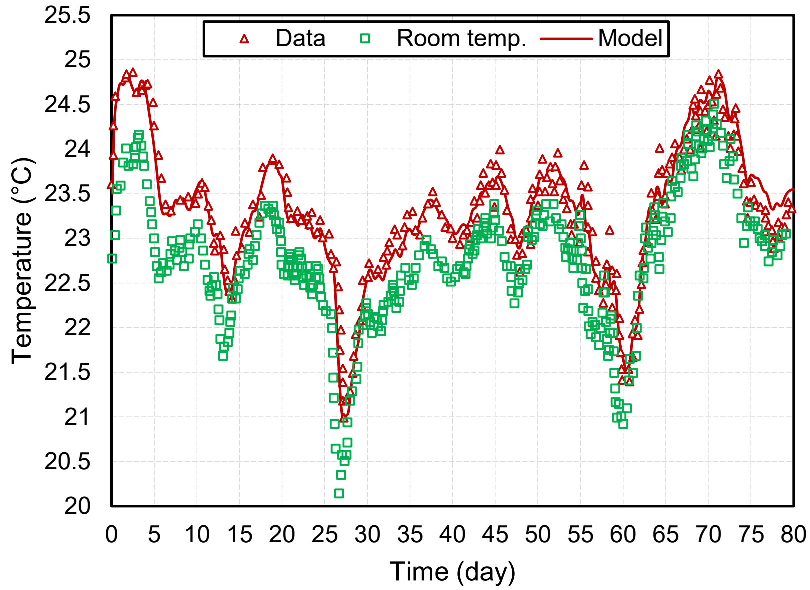

Figure 4.26. Comparison of numerical prediction and experimental data of temperature

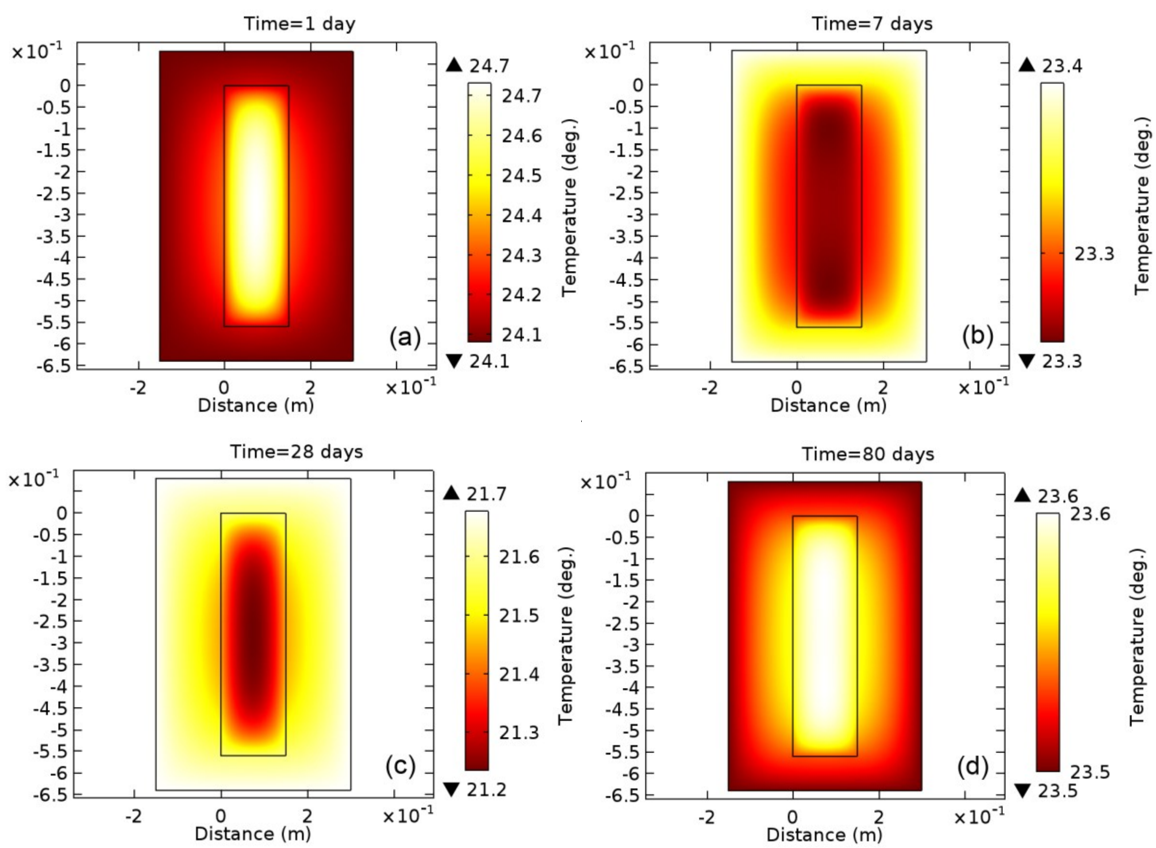

Figure 4.27. Simulated evolution of spatial distribution of temperature for different curing time: (a) 1 day; (b) 7 days; (c) 28 days; (d) 80 days

4.3.4.4. Case Study 4: Field study

In order to retain the fluid paste backfill in stope, the structural barricade (also called bulkhead) needs to be constructed. Correspondingly, the evolution of pore water pressure in CPB mass will exert a significant impact on the stability of barricade. In order to assess the loads (i.e., pore water press) that act on the barricade during and after backfilling, an in-situ monitoring program was conducted in the Cayeli mine (Yumlu, 2008). In the test, a Geokon Model 4500S standard piezometer was mounted on a rigid frame which was fixed in the center of the stope at 0.5 m from the floor of the stope. Piezometer used in the test had a built-in thermistor, the temperature in CPB was measured as well during the test. Detailed information about the test including the binder recipe and backfilling strategy, is presented in Table 4.4. The sensor location, mesh grid and geometry are presented in Figure 4.28.

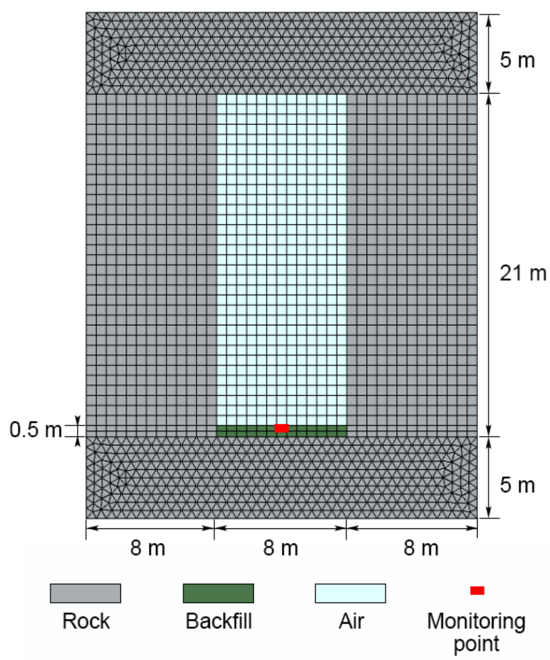

Figure 4.28. Mesh grid and geometry of simulated model and monitoring point in Case Study 4

The dynamic backfilling process in stope indicates the geometry of CPB mass will change with time, which can be considered as a deformation of the material frame (i.e., material coordinate system) with respect to the geometry frame (i.e., geometry coordinate system). In order to capture the evolution of CPB geometry, a deformed geometry interface (i.e., a built-in physics interface of COMSOL Multiphysics) was incorporated into the multiphysics analysis. The deformation geometry interface can be used to simulate the geometry evolution by removal or addition of material (e.g., the backfilling process). The backfilling rate adopted in Cayeli mine is 0.35 m/h which is set as the prescribed mesh velocity on the top surface of the deformed geometry (i.e., CPB mass). Moreover, in order to avoid low quality of the mesh induced by the deformed geometry, the automatic remeshing function in COMSOL Multiphysics was adopted as well.

As shown in Figure 4.29, the predictive results are in good agreement with the measured data of the PWP at the monitoring location. Specifically, both the simulated and measured results show that the PWP increases with time at the very beginning of the first backfilling stage. Afterward, the PWP shows a descending trend with time despite continued filling. In addition, it can be noticed that the PWP does not show an upward trend very much after the third backfill placement. Apart from the analysis of PWP at the monitoring point, it is of great interest to discuss the spatial distribution of PWP in CPB mass at different backfilling stages. As can be seen in Figure 4.30, the positive PWP gradually increases with CPB depth at curing age of 0.5 day (i.e., during the 1st filling stage). After the complement of 1st stage backfilling, CPB will be allowed to cure for 50 hours. During the curing time, the negative PWP pressure appears at the top domain of CPB as shown in Figure 4.30(b). The generation of negative PWP can be attributed to the water consumption by binder hydration and fluid migration under gravity effect in CPB. Afterward, although the 2nd stage backfilling is carried out, the majority of CPB domain is occupied by the negative PWP (e.g., at the age of 96 hours, Figure 4.30(c)). As expected, the positive PWP generated on the top domain of CPB at the 3rd stage of backfilling (Figure 4.30(d)) due to the placement of fresh paste into the stope.

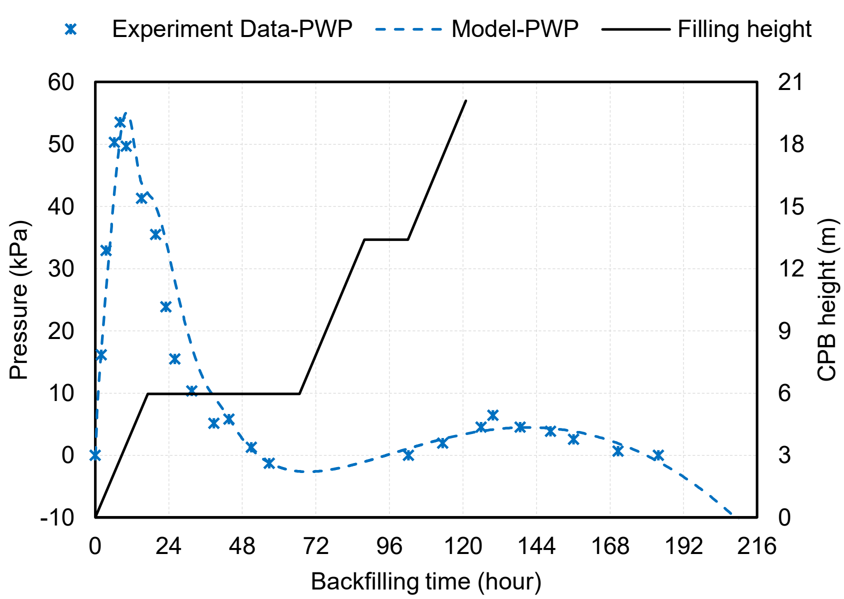

Figure 4.29. Comparison of numerical prediction and experimental data of PWP

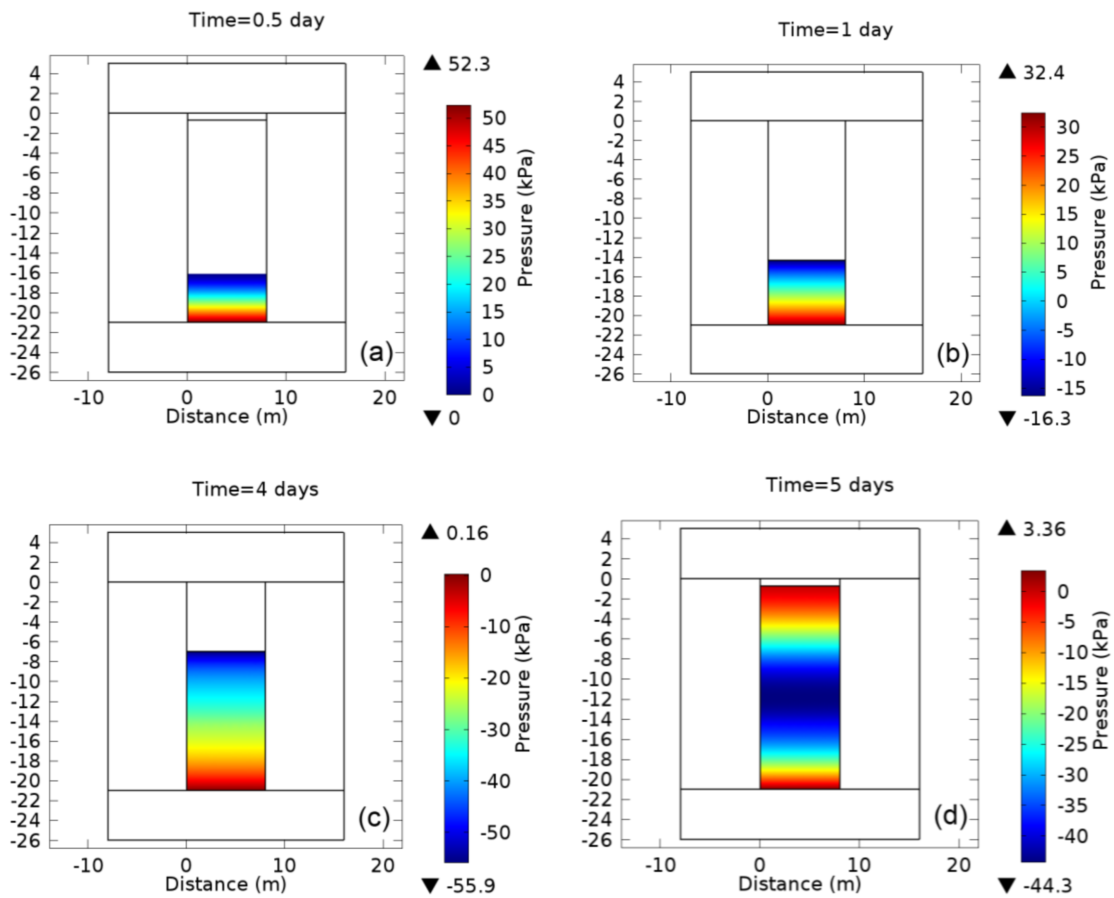

Figure 4.30. Simulated evolution of spatial distribution of pore water pressure for different curing time: (a) 0.5 day; (b) 1 days; (c) 4 days; (d) 5 days

With regard to the evolution of the temperature in the CPB structure at the monitoring point, the field data presented in Figure 4.31 are captured well by the simulated results. The spatial distribution of temperature on both CPB domain and the surrounding walls are presented in Figure 4.32. From Figure 4.32, it can be observed that the temperature evolves with backfilling process. Specifically, the heat released by binder hydration will lead to the increase in the temperature in CPB mass at very early age (as shown in Figure 4.32(a)). In addition, the heat transfer between CPB and surrounding rock also influences the distribution of temperature. Moreover, it can be seen that, due to the filling of fresh CPB, the temperature of the top surface of CPB mass is relatively low during backfilling process (Figure 4.32 (a) and (d)). The heat transfer between CPB and stope air plays a role in the temperature evolution of CPB as well.

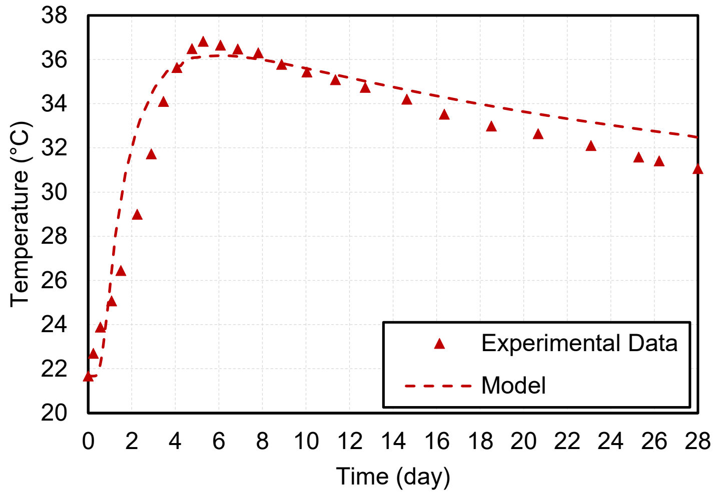

Figure 4.31. Comparison of numerical prediction and experimental data of temperature

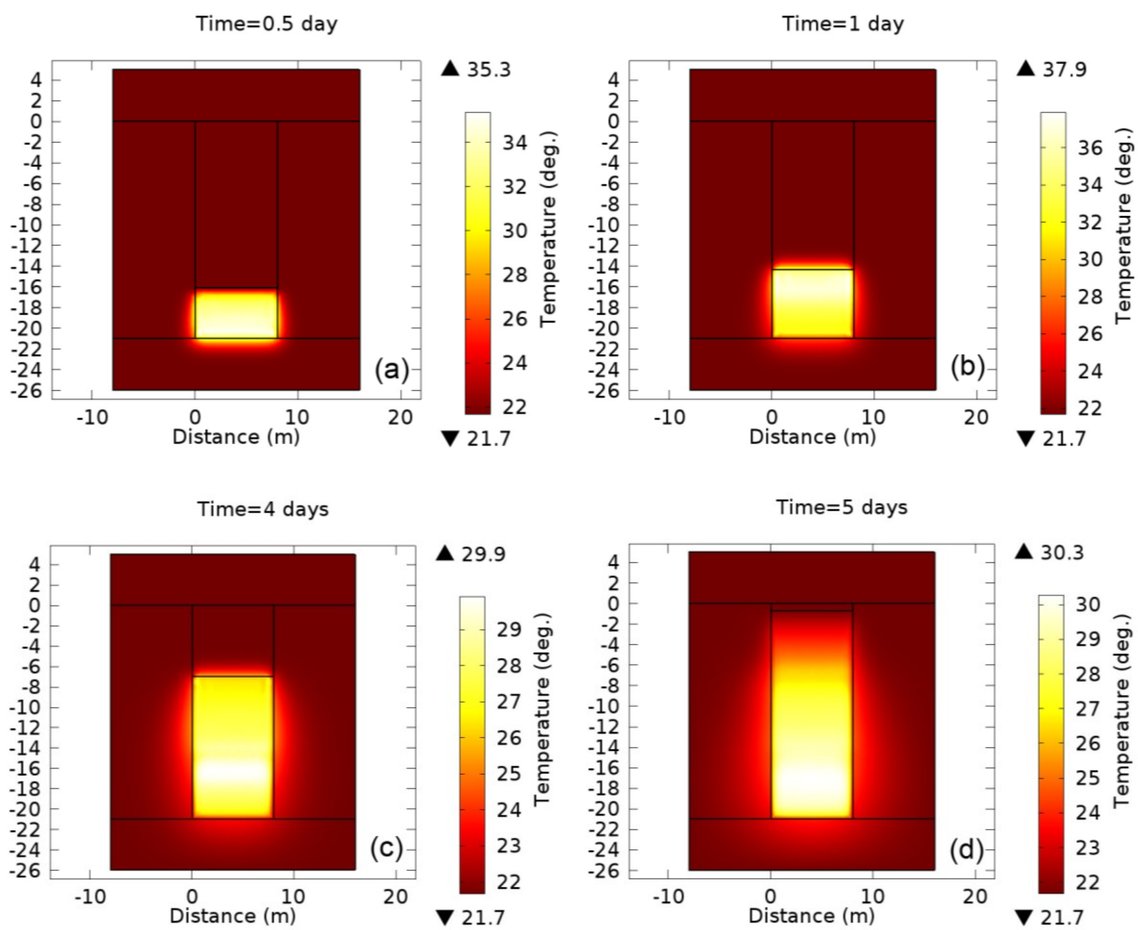

Figure 4.32. Simulated evolution of spatial distribution of temperature for different curing time: (a) 0.5 day; (b) 1 days; (c) 4 days; (d) 5 days

Based on the comparison between field data and predicted results, it can be concluded that (1) water consumption with the advancement of binder hydration, gravity water drainage and backfilling strategy play critical roles in the evolution of PWP and temperature in the CPB, (2) the influence of backfilling strategy (including backfilling rate) on the evolution of PWP and temperature can be well captured by the developed model and (3) the predictability of the developed model on the evolution of PWP and temperature is further validated.

4.3.4.5. Case Study 5: Time-dependent deformation behavior of CPB under triaxial compression stress

In order to validate the capability of the developed model to predict the deformation behavior under triaxial compression stress conditions, triaxial compression tests and corresponding simulation are performed in the study. For the preparation of CPB samples, the ground silica tailing, ordinary Portland cement type I (PCI) and tap water are employed in the study. 4.5% PCI and a water-cement ratio (w/c) of 7.6 is used as mix proportions. After mixing for 7 minutes, the CPB paste was poured into standard plastic cylinder molds ($2'' \times 4''$) which were sealed and cured at room temperature for 7 days and 28 days, respectively. Triaxial compression tests were conducted in accordance with ASTM D4767-02. A "S"-beam load cell with the capacity of 500lbs and rated output of 3.0785 mV/V is used to measure the deviatoric stress. For the measurement of axial displacement, a linear variable displacement transformer (LVDT) is utilized. The measurement range of LVDT is 50 mm and the linearity error is <± 0.25 mm. The volume change is recorded by Tri-Flex 2 test system. Under 200 kPa confining pressure, a minimum of 3 samples were tested for each curing time. The experimental data were then collected through a computer data acquisition system.

For the simulation, the axisymmetric geometry model is adopted. The mesh and geometry are presented in Figure 4.33. The adopted boundary conditions are listed in Table 4.4. As shown in Figure 4.34, a good agreement between predicted results and experimental data is obtained in terms of axial strain and volumetric strain. Both simulation results and measured data demonstrate that the volumetric strain first decreases with deviator stress (i.e., volumetric contraction), then, the volumetric expansion appears. This phenomenon is due to the fact that, with deviatoric stress increases, the elastic volumetric strain develops in CPB samples. However, when the stress reaches the yield point, stress will stay on the shear failure surface under loading condition. As a result, the direction of plastic volumetric strain is opposite to the mean stress, namely, volumetric expansion occurs. Therefore, mechanical component of the developed model is able to accurately simulate the development of volumetric strain of CPB under triaxial compression stress.

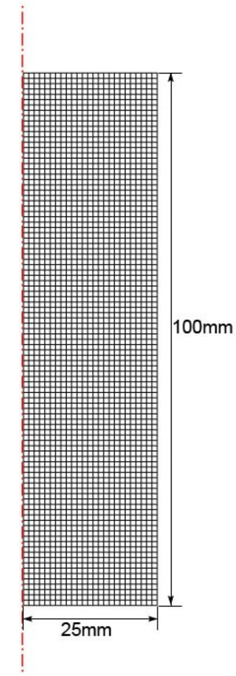

Figure 4.33. Mesh and geometry of triaxial compression test

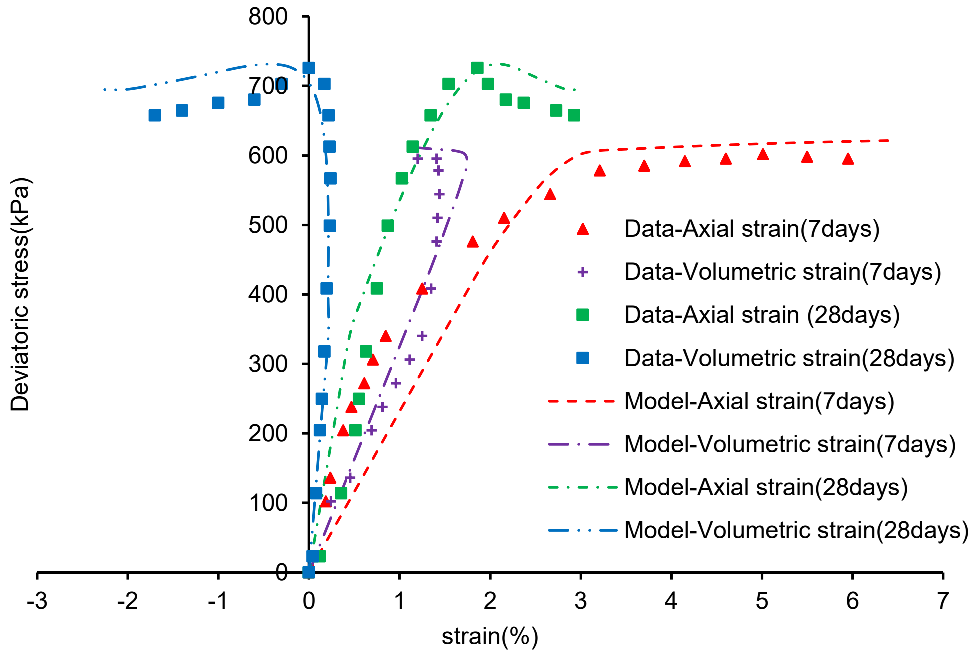

Figure 4.34. Comparison of simulated results and experimental data of triaxial compression tests

4.3.4.6. The validity of individual components of the coupled multiphysics model

Through five case studies, it has been proved that the developed multiphysics model is able to accurately predict the CPB behaviors (i.e., the evolution of temperature, pore water pressure and deformation). In order to more explicitly demonstrate the validity of the individual model component of the develop model, the relevant analysis based on the five case studies is provided as follows.

For the mechanical component, the predictability of total deformation (i.e., vertical settlement) has been validated through Case Study 1 as shown in Figure 4.20. Moreover, the prediction of pure elastoplastic strain is validated through the simulation of stress-strain relation of UCS tests in Case Study 1 (Figure 4.21) and triaxial compression tests in case study 5 (Figure 4.34). Therefore, it can be concluded that the combined effects of chemical shrinkage and thermal expansion can be correctly captured by the developed model. In addition, for Case Study 1, the relatively small temperature variation in CPB (i.e., temperature just increases by about 5 degrees as shown in Figure 4.15) will result in very small thermal expansion compared with chemical shrinkage, in other words, the thermal expansion can be ignored for Case Study 1. Consequently, the chemical shrinkage is accurately captured by the developed model. Although the contribution of thermal expansion to the total strain is limited in some specific cases (i.e., relatively low temperature gradient), the component fully demonstrates the interaction between thermal and mechanical processes. Therefore, it can be concluded that the mechanical components of the developed model possess the capability to accurately simulate the deformation development in CPB. Correspondingly, the evolution of porosity can be well captured by the mechanical model.

For the hydraulic component, the evolution of porosity is able to cause the variation of hydraulic conductivity (i.e., coefficient of permeability) and degree of saturation. In Case Study 1, the evolution of both degree of saturation (as shown in Figure 4.18) and hydraulic conductivity (as shown in Figure 4.19) are accurately predicted by the hydraulic model. The evolution of hydraulic conductivity and degree of saturation can directly change the pore water pressure in CPB porous media. Via Case Study 1 (Figure 4.17), 2 (Figure 4.23) and 4 (Figure 4.29), the predictability of the hydraulic model is fully validated.

For the thermal process, as discussed in Section 4.3.2, the evolution of temperature is controlled by heat advection, heat conduction and heat generation by binder hydration. Due to the fact that hydraulic components of the developed model can correctly simulate the hydraulic process in CPB, the correspondingly heat advection driven by the motion of pore fluid can be correctly predicted by the proposed model. For the heat conduction, the related thermal properties refer to the thermal conductivity which has been accurately simulated in Case Study 1 (as shown in Figure 4.16). For the heat generation, the heat released by binder hydration may become the unique heat source in some specific cases such as Case Study 1, 2 and 4 in which the initial and boundary temperature of CPB and surrounding rocks equal each other. The good agreement between predicted values and measured data of temperature as shown in Figure 4.15, Figure 4.24, and Figure 4.31 not only proves that the developed model is able to well capture the evolution of temperature, but also confirms that the heat generation by binder hydration can be accurately predicted by the thermal components of the proposed model. In addition, for the non-constant temperature boundary condition (e.g. Case Study 3), heat generation induced by binder hydration can be considered to be completed for long term curing time. For the case, it can be assumed that the temperature in CPB only evolves with the variation of boundary temperature. As shown in Figure 4.26, the accordance of predicted temperature with the measured data in CPB indicates the heat transfer between CPB and surrounding rock can be well predicted by the thermal components of the proposed model.

For the chemical component, the model of degree of binder hydration used in the paper can be considered as an empirical equation derived from extensive experimental data (Schindler and Folliard, 2003; Riding et al., 2012). The validation of predictability of the chemical model is conducted through the binder hydration associated heat release and water consumption. Specifically, the evolution of temperature and degree of saturation at the early age are dominated by the progression of binder hydration. As aforementioned, the developed model has the capability to predict the evolution of temperature and degree of saturation, namely, the heat source term in energy balance equation and water sink term in pore water mass balance equation are correctly derived from the binder hydration model. Hence, the predictability of chemical component of the developed model is validated.

Moreover, the backfilling rate is incorporated to simulate the backfilling sequence in Case study 4. Based on the comparison of simulated results and predicted values of PWP (Figure 4.29) and temperature (Figure 4.31), the influence of the dynamic backfilling can be well captured by the developed model.

In conclusion, based on the detailed analysis of validation processes through Case Study 1-5, each component of the coupled multiphysics model owns the ability to accurately predict the corresponding physical process in CPB, and CPB behavior under the coupled THMC processes can be well simulated by the coupled multiphysics model.

4.3.5. Discussion on the determination of model parameters

The fully coupled THMC model consists of four conservation equations including (i) water mass, (ii) air mass, (iii) momentum (mechanical equilibrium), and (iv) energy conservation equations. The corresponding governing equations are formulated through substitution of constitutive equations (e.g., stress and strain relationships, Darcy's law, or Fourier's law) into balance equations. Therefore, there exist a number of material properties and parameters in the developed model. For the purpose of practical application of the proposed model, the determination of model parameters needs to be discussed.

*Thermal process (**T**):* The parameter to evaluate the heat transfer processes is the effective thermal conductivity, k_{eff}, which is related to the thermal conductivity of CPB ingredients and the evolution of porosity. For the former part, laboratory measurement of thermal conductivity of CPB mixture needs to be conducted, while the evolutive porosity of CPB can be automatically updated by the deformation development in CPB during simulation.

*Hydraulic process (**H**):* The two constitutive relations including Darcy's Law and water retention relation (WRC) govern the hydraulic process. Therefore, standard saturated hydraulic conductivity test and the measurement of WRC should be performed for different curing time (e.g., 7 days, 28 days, 90 days and 120 days). Then, based on the measured data, the evolution Eqs. (4.86), (4.87), (4.88), (4.90) and (4.92) of hydraulic conductivity K_{sat}, relative permeability k_{rw} and k_{ra}, residual water content θ_r, and WRC can be determined through regression analysis. Correspondingly, in this paper, the values for fitting parameters (C_{k1} and C_{k2} in Eq. (4.86), R_{r1} and R_{r2} in Eq. (4.90), α_{WRC} and m_{WRC} in Eq.(4.92) are back calculated based on the reported experimental data in literature (Abdul-Hussain and Fall, 2011; Ghirian and Fall, 2013a), which can be used as reference values for the application of the developed model.

*Mechanical process (**M**):* In order to describe the strain development in CPB mass, an evolutive elastoplastic mechanical model is used. Moreover, the strain induced by thermal gradient and chemical shrinkage are considered as well. For the basic mechanical properties (i.e., elasticity, cohesion and internal frictional angle), the standard UCS tests and direct shear tests should be performed on CPB samples. Then the corresponding evolution equations with the progression of binder hydration can be obtained through regression analysis, which have been described in (Cui and Fall, 2016). For the plastic flow, the hardening/softening behavior is induced by the advance of binder hydration and plastic strain development, namely, the evolution of yield function is dominated by the material properties $C_{D-P}(\xi)$ and $\alpha_{D-P}(\xi,\kappa)$. Correspondingly, the fitting parameters (i.e. $D_{\alpha1}$, $D_{\alpha2}$, $D_{\alpha3}$ and $D_{\alpha4}$) of Eq. (4.54) can be determined with uniaxial or triaxial compressive test data. For the chemical shrinkage, the relevant model parameters are referred to the mass fraction of the clinker composition which are constants and dependent on the selection of binder type. For the thermal expansion, apart from the aforementioned mass fraction of clinker composition, the evolution equations of CTE and elasticity of cement paste can be obtained through standard CTE test and UCS test for different curing time.

*Chemical process(**C**):* The model parameters in binder hydration model refers to the CPB mixing parameters (i.e., water-cement ratio, and weight fraction of fly ash and blast furnace slag with respect to the total weight of the binder) which are constants for a certain CPB mix recipe. Consequently, the associated water sink term, Q_{hydr}, in mass balance equation and heat source term, $r^{\cdot}_{hydr}$, in energy equation can be evaluated.

4.3.6. Summary and conclusions

Based on the obtained results in this study, the following conclusions can be made.

i. The CPB materials can be treated as a complex and nonlinear multiphysics interaction system.

ii. A fully coupled THMC model has been developed to accurately characterize the coupled processes and the resulting influences on the CPB properties and behaviors. For the chemical process, the model fully considers the influence of binder hydration on the CPB properties and behavior. A series of evolutive prediction models of CPB material properties are established in this paper. For the mechanical process, combined with chemical shrinkage and thermal expansion, an evolutive elastoplastic model is incorporated into a strain analysis of CPB. For the hydraulic process, an effective degree of saturation is utilized to define the hydraulic properties and capillary pressure. For the thermal process, the heat released by binder hydration is characterized as a heat source term in an energy balance equation.

iii. Good agreement between the modeling results and measured data in terms of both laboratory experiments and in-situ measurements demonstrates the capability of the developed THMC model to well capture the evolution of CPB properties and behaviors.

iv. The accurate predictive ability of the proposed model means that it can be used as a helpful tool to conduct analysis of the interaction between the CPB body and surrounding rocks (e.g. arching effect) and volumetric strain development (e.g., consolidation) after CPB placement in stopes as well as to assess the performance of the CPB structure from the early to advanced ages. Therefore, the developed model is able to be utilized as an effective tool for the optimal design of CPB structures.

4.3.7. References

Abbasy, F., 2009. Thermal conductivity of mine backfill. Concordia University, Montreal, Quebec, Canada.

Abdul-Hussain, N., Fall, M., 2011. Unsaturated hydraulic properties of cemented tailings backfill that contains sodium silicate. Eng Geol 123, 288-301.

Abdul-Hussain, N., Fall, M., 2012. Thermo-hydro-mechanical behavior of sodium silicate-cemented paste tailings in column experiments. Tunn Undergr Sp Tech 29, 85-93.

Alnajim, A., 2004. Modelisation et simulation du comportement du beton sous hautes temperatures par une approche thermo-hygro-mecanique couplee. Application a des situations accidentelles. Universite de Merne la Vallee, Marne-la-Vallee, France.

Bear, J., Buchlin, J.M., 1991. Modeling and applications of transport phenomena in porous media. Kluwer Academic Publishers, Dordrecht, The Netherlands.

Belem, T., Benzaazoua, M., 2004. An overview on the use of paste backfill technology as a ground support method in cut-and-fill mines. Proceedings of the 5th International Symposia on Ground support in Mining and Underground Construction. Perth, Australia; p. 28-30.

Belem, T., Benzaazoua, M., Bussière, B., 2000. Mechanical behavior of cemented paste backfill. Proceedings of 53rd Canadian Geotechnical Conference Montreal; p. 373-380.

Belem, T., Bussière, B., Benzaazoua, M., 2001. The effect of microstructural evolution on the physical properties of paste backfill. Proceedings of Tailings and Mine Waste Fort Collins, Colorado; p. 365-374.

Benzaazoua, M., Belem, T., 2000. Optimization of sulfide-rich paste backfill mixtures for increasing long-term strength and stability. Proceedings of the 5th Conference on Clean Technology for Mining Industry Santiago, University of Concepción; p. 343-352.

Benzaazoua, M., Belem, T., Bussiere, B., 2002. Chemical factors that influence the performance of mine sulphidic paste backfill. Cem Concr Res 32, 1133-1144.

Benzaazoua, M., Belem, T., Yilmaz, E., 2006. Novel lab tool for paste backfill. Can Min J 127, 31-31.

Brouwers, H.J.H., 2004. The work of Powers and Brownyard revisited: Part 1. Cem Concr Res 34, 1697-1716.

Célestin, J.C.H., Fall, M., 2009. Thermal conductivity of cemented paste backfill material and factors affecting it. Int J Min Reclam Environ 23, 274-290.

Choktaweekarn, P., Tangtermsirikul, S., 2009. A model for predicting coefficient of thermal expansion of cementitious Paste. Science Asia 35, 57-63.

COMSOL, 2014. COMSOL Multiphysics 5.0 (Availabe online at: http://www.comsol.com).

Côté, J., Konrad, J.M., 2005. A generalized thermal conductivity model for soils and construction materials. Can Geotech J 42, 443-458.

Cui, L., Fall, M., 2016. An evolutive elasto-plastic model for cemented paste backfill. Comput Geotech 71, 19-29.
De Souza, E., 2006. Controlling heat loads from cemented mine backfill. Proceedings of 11th US/North American Mine Ventilation Symposium 2006 Pennsylvania, USA; p. 243-249.
De Souza, E., Hewitt, A., 2005. The contribution of cemented backfill to heat loads. Proceedings of 8th International Mine Ventilation Congress Brisbane, Australia; p. 87-93.
Emanuel, J.H., Hulsey, J.L., 1977. Prediction of the thermal coefficient of expansion of concrete. ACI Journal 74, 149-155.
Fahey, M., Helinski, M., Fourie, A., 2011. Development of specimen curing procedures that account for the influence of effective stress during curing on the strength of cemented mine backfill. Geotech Geol Eng 29, 709-723.
Fall, M., Adrien, D., Celestin, J., Pokharel, M., Toure, M., 2009. Saturated hydraulic conductivity of cemented paste backfill. Miner Eng 22, 1307-1317.
Fall, M., Belem T, M., B., 2005. Tensile and compressive properties of underground paste backfill. Proceedings of 58th Canadian Geotechnical Conference; and 6th Joint IAH-CNC and CGS Groundwater Speciality Conferences Saskatchewan.
Fall, M., Belem, T., Samb, S., Benzaazoua, M., 2007. Experimental characterization of the stress-strain behavior of cemented paste backfill in compression. J Mater Sci 42, 3914-3922.
Fall, M., Benzaazoua, M., Ouellet, S., 2004. Effect of tailings properties on paste backfill performance. Proceedings of the 8th International Symposium on Mining with Backfill Beijing, China; p. 193-202.
Fall, M., Célestin, J., Pokharel, M., Touré, M., 2010. A contribution to understanding the effects of curing temperature on the mechanical properties of mine cemented tailings backfill. Eng Geol 114, 397-413.
Fall, M., Ghirian, A., 2014. Coupled thermo-hydro-mechanical-chemical evolution of cemented paste backfill and implications for backfill design-experimental results. Proceedings of 11th International symposium on mining with backfill, MineFill 2014 Perth, Australia; p. 183-196.
Fall, M., Nasir, O., 2009. Numerical modeling of the coupled thermo-chemo-mechanical response of cemented paste backfill structures in deep mine temperature conditions. Proceedings of 3rd Canada-US Rock Mechanical Symposium and 20th Canadian Rock Mechanics Symposium Toronto, ON, Canada; p. 125-126.
Fall, M., Samb, S.S., 2008. Pore structure of cemented tailings materials under natural or accidental thermal loads. Materials and Characterization 59, 598-605.
Fredlund, D.G., Xing, A., 1994. Equations for the soil-water characteristic curve. Can Geotech J 31, 521-532.
Gawin, D., Pesavento, F., Schrefler, B.A., 2006. Hygro-thermo-chemo-mechanical modeling of concrete at early ages and beyond. Part II: shrinkage and creep of concrete. Int J Numer Meth Eng 67, 332-363.
Gawin, D., Pesavento, F., Schrefler, B.A., 2008. Modeling of cementitious materials exposed to isothermal calcium leaching, considering process kinetics and advective water flow. Part 1: theoretical model. Int J Solids Struct 45, 6221-6240.
Ghirian, A., Fall, M., 2013a. Coupled thermo-hydro-mechanical-chemical behavior of cemented paste backfill in column experiments. Part I: physical, hydraulic and thermal processes and characteristics. Eng Geol 164, 195-207.
Ghirian, A., Fall, M., 2013b. Experimental investigations of the thermo-hydro-mechanical-chemical behavior of cemented paste backfill. Proceedings of 23rd World Mining Congress Montreal, Canada; p. 21:21-11.

Ghirian, A., Fall, M., 2014. Coupled thermo-hydro-mechanical-chemical behavior of cemented paste backfill in column experiments: Part II: Mechanical, chemical and microstructural processes and characteristics. Eng Geol 170, 11-23.

Hansen, P.F., Pedersen, E.J., 1977. Maturity computer for controlled curing and hardening of concrete. Nordisk Betong 1, 21-25.

Helinski, M., Fahey, M., Fourie, A., 2007. Numerical modeling of cemented mine backfill deposition. J Geotech Geoenviron 133, 1308-1319.

Kamali, S., Moranville, M., Garboczi, E., Prené, S., Gérard, B., 2004. Hydrate dissolution influence on the Young's modulus of cement pastes. Proceedings of Proceedings Fracture Mechanics of Concrete Structures (FraMCoS-V) Routledge, Vail, Colorado; p. 631-638.

Kumar, M., Singh, N., Singh, N., 2009. Effect of water proofing admixture on the hydration of Portland cement. Indian J Chem Techn 16, 499.

Lawrence, C.D., 1992. The influence of binder type on sulfate resistance. Cem Concr Res 22, 1047-1058.

Le Roux, K., Bawden, W.F., Grabinsky, M., F. , 2002. Comparison of the material properties of in situ and laboratory prepared cemented paste backfill. Proceedings of The 104th CIM Annual Conference BC, Canada; p. 201-209.

le Roux, K., Bawden, W.F., Grabinsky, M.F., 2005. Field properties of cemented paste backfill at the Golden Giant mine. Mining Technology 114, 65-80.

Luckner, L., Van Genuchten, M.T., Nielsen, D., 1989. A consistent set of parametric models for the two - phase flow of immiscible fluids in the subsurface. Water Resources Research 25, 2187-2193.

Mason, E.A., Monchick, L., 1963. Survey of the equation of state and transport properties of moist gases. Proceedings of the 1963 International Symposium on Humidity and Moisture: Fundamentals and Standards; p. 257-272.

Mindess, S., Young, J.F., Darwin, D., 2003. Concrete, 2nd ed. Prentice Hall, Pearson Education, Inc., Upper Saddle River, New Jersey.

Mitchell, R., 1989. Stability of cemented tailings mine backfill. Proceedings of Computer and Physical Modeling in Geotechnical Engineering Balkema, Rotterdam; p. 501-507.

Mualem, Y., 1976. A new model for predicting the hydraulic conductivity of unsaturated porous media. Water Resour Res 12, 513-522.

Nasir, O., Fall, M., 2008. Shear behavior of cemented pastefill-rock interfaces. Eng Geol 101, 146-153.

Nasir, O., Fall, M., 2010. Coupling binder hydration, temperature and compressive strength development of underground cemented paste backfill at early ages. Tunn Undergr Sp Tech 25, 9-20.

Nawy, E.G., 2008. Concrete construction engineering handbook, 2nd ed. CRC press, Boca Raton, FL, USA.

Neville, A.M., Brooks, J.J., 1987. Concrete technology. Longman Scientific & Technical Harlow, New York.

Orejarena, L., Fall, M., 2008. Mechanical response of a mine composite material to extreme heat. Bulletin of Engineering Geology and the Environmnet 67, 387-396.

Poole, J.L., Riding, K.A., Folliard, K.J., Juenger, M.C., Schindler, A.K., 2007. Methods for calculating activation energy for Portland cement. Aci Mater J 104, 303-311.

Powers, T.C., Brownyard, T.L., 1947. Studies of the physical properties of hardened Portland cement paste. Proceedings of ACI Journal; p. 249-336.

Riding, K.A., Poole, J.L., Folliard, K.J., Juenger, M.C., Schindler, A.K., 2012. Modeling hydration of cementitious systems. Aci Mater J 109.

Schindler, A.K., Folliard, K.J., 2003. Influence of supplementary cementing materials on the heat of hydration of concrete. Proceedings of Advances in Cement and Concrete IX Conference Colorado; p. 17-26.
Sellevold, E.J., Bjøntegaard, Ø., 2006. Coefficient of thermal expansion of cement paste and concrete: mechanisms of moisture interaction. Mater Struct 39, 809-815.
Sercombe, J., Galle, C., Ranc, G., 2001. Modélisation du comportement du béton à haute température: Transferts des fluides et de chaleur et déformations pendant les transitoires thermiques, Note Technique SCCME.
Simms, P., Grabinsky, M., 2009. Direct measurement of matric suction in triaxial tests on early-age cemented paste backfill. Can Geotech J 46, 93-101.
Simon, D., 2005. Microscale analysis of cemented paste backfill. University of Toronto, Canada.
Sivakugan, N., Rankine, R., Rankine, K., Rankine, K., 2006. Geotechnical considerations in mine backfilling in Australia. Journal of Cleaner Production 14, 1168-1175.
Somerton, W.H., Keese, J.A., Chu, S.L., 1973. Thermal behavior of unconsolidated oil sands. Proceedings of the 48th Annual Fall Meeting of the Society of Petroleum Engineers Las Vegas, USA; p. paper SPE-4506.
Thomas, H.R., Sansom, M.R., 1995. Fully coupled analysis of heat, moisture, and air transfer in unsaturated soil. Journal of Engineering Mechanics 121, 392-405.
Thompson, B., Bawden, W., Grabinsky, M., 2012. In situ measurements of cemented paste backfill at the Cayeli Mine. Can Geotech J 49, 755-772.
Thompson, B., Grabinsky, M., Bawden, W., Counter, D., 2009. In-situ measurements of cemented paste backfill in long-hole stopes. Proceedings of the 3rd CANUS Rock Mechanics Symposium Toronto; p. 197-198.
Van Genuchten, M.T., 1980. A closed-form equation for predicting the hydraulic conductivity of unsaturated soils. Soil Sci Soc Am J 44, 892-898.
Veenstra, R.L., 2013. A design procedure for determining the in situ stresses of early age cemented paste backfill. University of Toronto, Canada.
Williams, P.J., 1982. The surface of the earth: an introduction to geotechnical science. Longman Inc., New York.
Williams, T.J., Denton, D.K., Larson, M.K., Rains, R.L., Seymour, J.B., Tesarik, D.R., 2001. Geomechanics of reinforced cemented backfill in an underground stope at the Lucky Friday Mine, Report of Investigations. Nitional Institute for Occupational Safety and Health, Pittsburgh, PA, pp. 1-24.
Wu, D., Fall, M., Cai, S.J., 2012. Coupled modeling of temperature distribution and evolution in cemented tailings backfill structures that contain mineral admixtures. Geotech Geol Eng 30, 935-961.
Wu, D., Fall, M., Cai, S.J., 2014. Numerical modeling of thermally and hydraulically coupled processes in hydrating cemented tailings backfill columns. Int J Min Reclam Environ 28, 173-199.
Yilmaz, E., Belem, T., Benzaazoua, M., 2014. Effects of curing and stress conditions on hydromechanical, geotechnical and geochemical properties of cemented paste backfill. Eng Geol 168, 23-37.
Yilmaz, E., Belem, T., Bussière, B., Mbonimpa, M., Benzaazoua, M., 2015. Curing time effect on consolidation behavior of cemented paste backfill containing different cement types and contents. Constr Build Mater 75, 99-111.
Yilmaz, E., Kesimal, A., Ercikdi, B., 2004. Strength development of paste backfill simples at Long term using different binders. Proceedings of the 8th Symposium MineFill Beijing, China; p. 281-285.

Yilmaz, E., Kesimal, A., Ercikdi, B., Alp, I., 2003. Determination of the optimum cement content for paste backfill samples. Proceedings of 18th International Mining Congress & Exhibition of Turkey Antalya, Turkey.

Yumlu, M., 2008. Barricade pressure monitoring in paste backfill. Gospodarka Surowcami Mineralnymi 24, 233-244.

4.4. Paper IV: Multiphysics model for consolidation behavior of cemented paste backfill

Published in ASCE International Journal of Geomachanics (2016) 04016077, 2-23
Liang Cui, Mamadou Fall

Abstract

In underground mining practices, cemented paste backfill, a mixture of tailings, cement and water, is widely adopted to fill extracted stopes. During and after the filling of the underground mine excavations or stopes with CPB, complex multiphysics processes (including thermal, hydraulic, mechanical and chemical) take place in the CPB mass. These multiphysics processes and their coupling govern the consolidation characteristics and behavior of CPB. As a result, conventional soil mechanics consolidation theories and models are not appropriate for the evaluation and prediction of the consolidation behavior of CPB. Therefore, based on the principles of the continuity of pore space and conservation of mass, energy and momentum, a 3D coupled multiphysics model of the consolidation behavior for CPB is developed in this study. The predictive ability of the proposed model is validated against experimental data. Good agreement between the predicted values and experimental data is obtained. Furthermore, some of the important features of the developed model are highlighted by a comparison between the simulated results and Gibson's solution.

Author keywords: Cemented paste backfill; tailings; multiphysics model; consolidation, mine.

4.4.1. Introduction

To stabilize rock mass, reduce rock wall closures and maximize ore recovery, cemented paste backfill (CPB) technology has been widely used in many mines worldwide (Fall and Samb, 2009; Yilmaz et al., 2009; Fall and Nasir, 2010; Helinski et al., 2010b; Pokharel and Fall, 2010; Ghirian and Fall, 2013a; Li, 2013; Pokharel and Fall, 2013; Ghirian and Fall, 2014; Cui and Fall, 2015b). As a major ground support tool for workers and pillar recovery in underground mines (Hustrulid and Hustrulid, 2001; Orejarena and Fall, 2010), the mechanical performance or behavior of CPB is considered as one of the most important design criteria in engineering practices. The consolidation behavior of CPB is of key interest in the design and safety assessment of CPB structures due to its significant influence on the development and distribution of effective stress in the CPB mass, the stress applied onto barricades and their stability, and liquefaction resistance of CPB (Helinski 2008; Fahey et al. 2010; Ghirian and Fall, 2014).

After placement of CTB into mined-out underground spaces known as stopes, there are strong multiphysics interaction processes, including thermal (T), hydraulic (H), mechanical (M) and chemical (C) physics (THMC) processes, in the CPB mass. These processes and their interactions or coupling govern the evolution of the mechanical properties and behaviors of CPB (Ghirian and Fall, 2013a, 2014; Cui and Fall, 2015b, a). For example, due to the addition of a binder agent into the CPB mixture, a chemical reaction that is called binder hydration starts immediately after mixing takes place. As the binder hydration proceeds, the capillary water is gradually consumed and converted into components of hydration products. Due to the influence of self-desiccation, viz. the volume of physically absorbed and chemically combined water is less than the capillary water with the same mass, chemical shrinkage occurs in the CPB mass. It should be noted that the net water loss in CPB gives rise to a reduction in the pore water pressure (PWP). The dissipation of the PWP will directly affect the effective stress that is acting on the solid skeleton of the CPB. Moreover, exothermic binder hydration causes the evolution of temperature inside the CPB, and correspondingly, the temperature gradient can result in thermal deformation (i.e., thermal expansion or contraction). Apart from chemical shrinkage and thermal deformation, the effect of self-weight pressure induced by the dynamic backfilling process also influences CPB deformation behavior and performance. Therefore, the consolidation behavior of CPB is closely tied to the coupled thermo-hydro-mechanical-chemical (THMC) processes.

To assess and better understand the consolidation behavior of CPB, extensive laboratory experiments have been conducted in past years. For example, conventional standard oedometer (e.g., Saebimoghaddam, 2010; Jamali, 2013), Rowe cell (e.g., Helinski, 2008; Helinski et al., 2010a), and saturated hydraulic conductivity (e.g., Belem et al., 2002; Helinski et al., 2007; Fall et al., 2009; Ghirian and Fall, 2013a; Pokharel and Fall, 2013) tests have been performed on CPB samples, and CPB has been cured under applied stress tests (e.g., Benzaazoua et al., 2006; Yilmaz et al., 2009; Yilmaz, 2010; Fall and Ghirian, 2014; Yilmaz et al., 2014; Yilmaz et al., 2015). From the previous experimental observations or studies, it can be concluded that nonlinear and substantial variations in the consolidation that is related to the material properties, such as coefficient of permeability and compressibility, are found in CPB. These studies have enabled a better understanding of the consolidation behavior and characteristics of CPB and highlighted the relevance of the aforementioned multiphysics processes in the consolidation behavior of CPB. They have also shown that due to the evolutive nature of CPB and the multiphysics processes that govern its mechanical behavior, the consolidation behavior of CPB cannot be properly described or captured by using a consolidation model based on conventional soil mechanics consolidation theories, such as Terzaghi’s one-dimensional consolidation theory (Terzaghi, 1943) and its extensions (e.g., Greenberg 1973; Mitchell et al. 1973; Barbour and Fredlund, 1973, Kaczmarek and Hueckel 1998; Kaczmarek 2001) or Biot’s general theory of three-dimensional consolidation (Biot 1941) and its extensions (e.g, Desai et al. 1979; Coussy 1989; Charlez 1991; Smith and Booker 1993; Sherwood 1994; Bai and Abousleiman 1997). For example, due to the limitations of the Terzaghi’s theory, viz. its assumptions including those on the constant total stress, saturated condition, constant material properties (e.g. coefficient permeability and compressibility) and small strain on which the theory is developed, the Terzaghi’s consolidation model is not considered to be valid for evaluating the consolidation behavior of CPB materials. However, at the time of writing, only a few studies on modeling (e.g., Helinski et al., 2007; Wood and Doherty, 2014) have been conducted to develop mathematical and/or numerical models that can capture and describe the consolidation behavior of CPB. For instance, based on the assumption that the saturated condition does not change in the CPB mass (i.e., degree of saturation equals 1; this is an oversimplification since the CPB is in an unsaturated state most of the time), Wood and Doherty (2014) developed a 1D hydro-mechanical-chemical (HMC) model based on a simple diffusion equation with a time-dependent source term. Based on the large-strain consolidation model proposed by Seneviratne et al. (1996) which was applied to uncemented tailings, Helinski et al. (2007) proposed a

1D hydro-mechanical-chemical (HMC) model to predict the consolidation behavior of CPB. Then, Helinski et al. (2010b) extended this 1D model to a 2D HMC model with plane strain or axisymmetric conditions to analyze the consolidation process. Despite the tremendous progress made by these studies in modeling the consolidation behavior of CPB, there is currently no consolidation model for CPB which incorporates the main multiphysics processes (THMC) and their couplings to which the CPB is subjected in mine stopes. Assessing of consolidation behavior of such CPB structures and comparing several possible CPB designs prior to their construction require a robust and reliable multiphysics model of the consolidation behavior or computational tool which incorporates knowledge of these various coupled processes at the material level. This has inspired the authors of the present paper to conduct the current research to develop a 3D multiphysics model that would describe and predict the consolidation behavior of CPB.

4.4.2. Modeling approach

The basic idea of developing a mathematical model of physical phenomena or processes is to utilize appropriate axioms or laws based on various assumptions that govern how these physical processes work (Reddy, 2006). In order to establish a multiphysics model to characterize the consolidation behavior of CPB, the following assumptions are adopted in this study:

i. The tailings particles are assumed to be incompressible, while the porous material is deformable;
ii. Compressive stress and strain are considered to be negative;
iii. Seepage into and out of the CPB element are driven by Darcy’s law; and
iv. Multiphase of CPB materials at a given time obey local thermodynamic equilibrium, i.e. locally, the phases are at the same temperature.

To characterize the consolidation behavior of CPB, a pore space continuity equation is utilized in this study. Pore space continuity requires the pore space changes related to the solid skeleton of CPB and solid phase must equal the total volume change of the pore water and pore air. As mentioned in the introduction, the volume change (i.e., consolidation process) in CPB is dominated by multiphysics processes, i.e. THMC processes (as shown in Figure 4.35), which means that the principles of conservation of mass, energy and momentum need to be applied.

Moreover, constitutive relations are needed to formulate the governing equations. For the thermal process (T), the heat transfer consists of conduction, advection and binder hydration induced heat generation. Thus, Fourier's law, fluid Darcy's velocity and a heat source term derived from the time rate of the change in heat released by binder hydration need to be applied. Darcy's law and water retention curve (WRC) relation are required for the hydraulic process (H). A stress-strain relationship should be derived for the mechanical process (M). It is important to point out that, as mentioned in the introduction, binder hydration induced volume changes (i.e., chemical shrinkage) and thermal expansion or contraction caused by the thermal gradient in the CPB mass should be incorporated into the strain analysis. Moreover, for CPB at very early ages, the stiffness of the CPB structure is relatively small and contractive plastic volumetric strain will occur during the dynamic backfilling process. Therefore, a portion of the cap yield surface is required to be combined with the shear-failure surface, which is able to ensure the occurrence of contractive plastic volumetric strain at the early ages. Moreover, double yield surfaces should possess chemical and strain induced softening/hardening behavior in the stress space, namely, the hardening parameters should be defined. For the chemical process (C), the rate of the binder hydration should be quantified. In order to solve the constitutive relation, the material properties that are in the corresponding constitutive relation should be determined in terms of measurable parameters.

Based on the aforementioned model development approach, the formulation of the multiphysics model is presented in the following section.

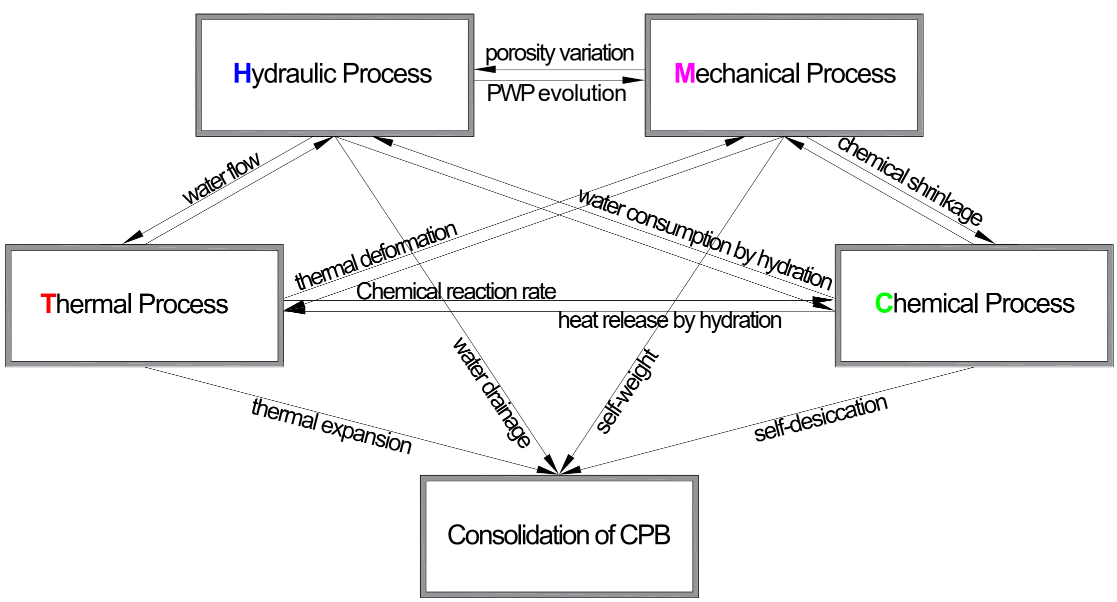

Figure 4.35. Schematic diagram of the multiphysics processes and their coupling considered in the consolidation behavior of CPB (PWP: pore water pressure)

4.4.3. Formulation of the multiphysics model

4.4.3.1. Continuity of pore space

CPB materials can be treated as a multiphase (i.e., solid, liquid and gas phase) porous medium. As mentioned in the section on the modeling approach, the consolidation process is dominated by strong multiphysics (THMC) interaction processes in the CPB mass. In order to quantitatively assess the volume changes of the CPB, the continuity of pore space is adopted in this study, viz. pore space changes related to the solid skeleton of the CPB and solid phase must equal the total volume change of the capillary water and pore air:

$$\underbrace{\left(-dV_{ch-s}+dV_{m}+dV_{Ts}\right)}_{A_1}=\underbrace{\left(-dV_{ch-w}+dV_{Tw}+dV_{sp}+dV_{pw}\right)}_{A_2}+\underbrace{dV_a}_{A_3} \tag{4.108}$$

where the three terms (i.e., A_1, A_2 and A_3) denote the volume changes of the skeleton of the CPB and solid phase, pore water and pore air, respectively. For the term A_1, V_{ch-s}, V_m and V_{Ts} respectively denote the volume changes induced by the refinement of the hydration products, variation of effective stress and thermal expansion, and the negative sign before V_{ch-s} denotes that the solid phase volume increase is equivalent to the decrease in pore space. It is important to emphasize that the term A_1 not only shows the variation of the volume of the solid skeleton of CPB (i.e., $dV_m + dV_{Ts}$), but also considers the solid phase volume changes induced by binder hydration (i.e., dV_{ch-s}). Therefore, the term A_1 fully represents the pore space changes induced by the evolution of the solid skeleton and solid phase. For the volume changes of the pore water (i.e., term A_2), dV_{ch-w}, V_{Tw}, V_{sp} and V_{pw} represent the volume changes of the pore water caused by the water consumption of the binder hydration, thermal expansion of the pore water, water seepage and evolution of PWP induced compression, respectively; for pore air (i.e., term A_3), V_a denotes the volume changes of the pore air which can be evaluated through a state equation of the ideal gas as well as a pore-air mass balance equation.

4.4.3.2. Chemical process: volume changes induced by binder hydration

As mentioned earlier, binder hydration plays a central role in interactive multiphysics processes. Thus, it is necessary to quantitatively determine the extent of the advancement of binder hydration, viz. by defining the degree of binder hydration, ξ. Based on previous studies on CPB (Wu et al., 2012; Cui and Fall, 2015a, 2016), an exponential function proposed by Schindler and Folliard (2003) has been successfully applied to predict the progression of the binder hydration for CPB materials:

$$\xi\left(t_e\right)=\xi_u\cdot\exp\left[-\left(\frac{\tau}{t_e}\right)^{\beta}\right] \tag{4.109}$$

$$\text{with}\begin{cases}\xi_u=\dfrac{1.031\cdot w/c}{0.194+w/c}+0.5\cdot X_{FA}+0.30\cdot X_{slag}\\ t_e=\int_0^t\exp\left[\dfrac{E_a}{R}\left(\dfrac{1}{T_r}-\dfrac{1}{T}\right)\right]dt\end{cases}$$

where ξ_u is the ultimate degree of hydration, τ and t_e represent the hydration time parameter (hours) and the equivalent age (hours), respectively, β denotes the dimensionless hydration shape parameter. Based on previous studies on cement (Schindler, 2004) and CPB (Cui and Fall, 2015a, b, 2016), the following values are employed in this study: τ =33.6 hours and β =0.394. T_r is the reference temperature, R equals to the universal gas constant (8.314 J/mol/K). For the binder components, Portland cement (ASTM Type I) is often used as the basic binding agent. In order to reduce the cement cost and upgrade product performance, pozzolanic materials such as fly ash and blast furnace slag can be utilized as alternative reagent binders. Correspondingly, w/c is the water-cement ratio, X_{FA} and X_{slag} respectively represent the weight fraction of the fly ash and blast furnace slag with respect to the total binder weight, E_a is the apparent activation energy (J/mol) and can be characterized by the following equation (Hansen and Pedersen, 1977):

$$E_a\left(T\right)=\begin{cases}33{,}500+1{,}470\times\left(293.15-T\right) & T<293.15K\\ 33{,}500 & T\geq 293.15K\end{cases} \tag{4.110}$$

Based on a model from (Powers and Brownyard, 1947), binder hydration induced solid phase volume changes, V_{ch-s}, and capillary water phase volume changes, V_{ch-w}, can be derived as follows:

$$dV_{ch-s}=V\alpha_{ch-s}d\xi=V\frac{\left(v_{ch-w}+v_{ab-w}\right)R_{n-w/hc}}{\left(w/c\right)v_w+v_c+\left(1/C_m-1\right)v_{tailings}}d\xi \tag{4.111}$$

$$dV_{ch-w}=V\alpha_{ch-w}d\xi=V\frac{2v_wR_{n-w/hc}}{\left(w/c\right)v_w+v_c+\left(1/C_m-1\right)v_{tailings}}d\xi \tag{4.112}$$

where w/c and C_m are the CPB mixing parameters and respectively denote the water to cement ratio and binder content, v_w, v_{ch-w}, v_{ab-w}, v_c and $v_{tailings}$ represent the specific volume (i.e., the inverse of density) of the capillary water, chemically combined water, physically absorbed water, cement and tailings, respectively. Based on previous studies (Powers and Brownyard, 1947; Brouwers, 2004) the following parameter values are used in this study: v_w =10^{-3} m^3/kg, v_{ch-w} =7.2×10^{-4} m^3/kg, v_{ab-w} =9×10^{-4} m^3/kg, and v_c =3.2×10^{-4} m^3/kg. The tailings specific volume is dependent on the tailings types, and $v_{tailings}$ =3.8×10^{-4} m^3/kg is adopted in this study. $R_{n-w/hc}$ is the mass ratio of the chemically combined water, m_{n-w}, and hydrated cement, m_{hc}. Based on a previous study (Powers and Brownyard, 1947), it has been experimentally proven that $R_{n-w/hc}$ is only dependent on the cement composition (i.e., C_3S, C_2S, C_3A and C_4AF) and can be expressed as:

$$R_{n-w/hc} = m_{n-w} / m_{hc} = 0.187x_{C_3S} + 0.158x_{C_2S} + 0.665x_{C_3A} + 0.2130x_{C_4AF} \tag{4.113}$$

where x_i represents the mass fraction of the clinker composition, which is determined by cement type. In this study, x_{C_3S} =0.462, x_{C_2S} =0.232, x_{C_3A} =0.087 and x_{C_4AF} =0.096 are utilized in the simulation.

4.4.3.3. Thermal process: volume changes induced by thermal deformation

Temperature gradients induced by exothermal binder hydration and external thermal load (e.g., heat transfer between the CPB mass and surrounding rock) result in volume changes via thermal deformation (i.e., thermal expansion or contraction). It should be noted that the assumption of local thermal equilibrium, viz. $T_s = T_w = T_a = T$ is adopted in this study. Therefore, the volume changes of the solid skeleton and liquid phase can be expressed as follows:

$$dV_{Ts} = V\alpha_{Ts}dT \tag{4.114}$$

$$dV_{Tw} = \frac{e}{1+e}SV\alpha_{Tw}dT \tag{4.115}$$

where α_{Ts} and α_{Tw} are the coefficients of the thermal expansion (CTE) of the CPB solid phase and capillary water. The CTE can be in general defined as:

$$\alpha_T = \frac{1}{V}\frac{\partial V}{\partial T} = \frac{1}{\frac{1}{\rho}}\frac{\partial\left(\frac{1}{\rho}\right)}{\partial T} = -\frac{1}{\rho}\frac{\partial(\rho)}{\partial T} \tag{4.116}$$

Based on a previous study (Cui and Fall, 2015) on CPB, the CET of the solid phase of CPB can be derived from the models in (Powers and Brownyard, 1947) and (Neville and Brooks, 1987).

$$\alpha_{Ts} = \alpha_p - \frac{2v_{tailings}\left(1/C_m - 1\right)\left(\alpha_p - \alpha_{tailings}\right)}{\left[(w/c)v_w + v_c\right]\left\{1 + \left[L_1 \cdot \left(1-\phi_{hydr}\right)^{L_2}\right] / E_{tailings}\right\} + 2v_{tailings}\left(1/C_m - 1\right)} \tag{4.117}$$

$$\text{with} \begin{cases} \alpha_p = \dfrac{B_1\alpha_{uc}v_c(1-\xi) + B_2\alpha_{hp}\left[v_c + R_{n-w/hc}\left(v_{ch-w} + v_{ab-w}\right)\right]\xi}{(w/c)v_w + v_c + \left(1/C_m - 1\right)v_{tailings}} \\ \phi_{hydr} = \dfrac{(w/c)v_w - \left(v_{ch-w} + v_{ab-w}\right)R_{n-w/hc}\xi}{(w/c)v_w + v_c + \left(1/C_m - 1\right)v_{tailings}} \end{cases}$$

where L_1 and L_2 are the fitting parameters for the prediction of elastic modulus of cement paste, B_1 and B_2 are fitting parameters used to predict the CTE of cement paste.

The values of the four parameters depend on the Portland cement type. For Portland cement Type I, L_1 and L_2 respectively equal 46.03 GPa and 3.16 (Kamali et al., 2004; Cui and Fall, 2015a), B_1 and B_2 amounts to 0.284 and 1.23, respectively (Choktaweekarn and Tangtermsirikul, 2009).

According to the definition of CTE, viz. Eq. (4.116), the CTE of capillary water can be written as:

$$\alpha_{Tw} = -\frac{1}{\rho_w}\frac{\partial\left(\rho_w\right)}{\partial T} \tag{4.118}$$

The capillary water density is dependent on both temperature and pressure, and the following formula can be used to predict the evolution of the water density with temperature and pressure (Gawin et al., 1999).

$$\rho_w = \rho_r\left[1-\alpha_{Tw}\left(T-T_r\right)+\beta_{Pw}\left(P_w-P_{wr}\right)\right] \tag{4.119}$$

where ρ_r is the reference water density at the reference temperature T_r and pressure P_{wr}, and β_{Pw} is isothermal compression modulus of water and equals $4.3\times10^{-9}Pa^{-1}$.

4.4.3.4. Mechanical process: volume changes induced by mechanical deformation

As mentioned in the section on the modeling approach, the total strain $\boldsymbol{\varepsilon}$ in the CPB mass can be broken down into the following types of strains: elastic $\boldsymbol{\varepsilon}_e$, plastic $\boldsymbol{\varepsilon}_p$, binder hydration induced $\boldsymbol{\varepsilon}_c$ and thermal $\boldsymbol{\varepsilon}_T$ caused by the temperature gradient through thermal deformation, namely:

$$\boldsymbol{\varepsilon} = \boldsymbol{\varepsilon}_e + \boldsymbol{\varepsilon}_p + \boldsymbol{\varepsilon}_c + \boldsymbol{\varepsilon}_T \tag{4.120}$$

Based on Hooke's law, the elastic stress-strain relation can be expressed in the classical form as:

$$d\boldsymbol{\sigma}' = \boldsymbol{D}^e\, d\boldsymbol{\varepsilon}_e = \boldsymbol{D}^e\left(d\boldsymbol{\varepsilon} - d\boldsymbol{\varepsilon}_p - d\boldsymbol{\varepsilon}_c - d\boldsymbol{\varepsilon}_T\right) \tag{4.121}$$

where $\boldsymbol{D}^e$ is the tangent elastic modulus which is related to the mechanical properties (e.g., elasticity E and Poisson's ratio υ). Detailed prediction models of elasticity and Poisson's ratio are presented in (Cui and Fall, 2016). $\boldsymbol{\sigma}'$ is the effective stress which can be defined as:

$$\boldsymbol{\sigma}' = \boldsymbol{\sigma} + \alpha_{Biot}\bar{P}\boldsymbol{\delta}_{ij} \tag{4.122}$$

$$\text{with } \begin{cases} \alpha_{Biot} = 1 - K_b/K_s \\ \bar{P} = SP_w + \left(1-S\right)P_a \end{cases}$$

where α_{Biot} denotes the Biot's effective stress coefficient and δ_{ij} represents the Kronecker's delta, K_b and K_s represent the bulk modulus of the porous media and solid phase (grain), respectively, which will evolve with binder hydration, P_w and P_a

respectively denote the pore liquid water pressure and pore air pressure, and S accounts for the degree of saturation.

It has been experimentally observed that, under static loading, the mechanical response of CPB in the plastic regime is dominated by hardening/softening behaviors (Fall et al., 2007; Simms and Grabinsky, 2009; Ghirian and Fall, 2014), and the volumetric deformation shows a remarkable dilation trend after peak stress in triaxial tests on CPB (Cui and Fall, 2016). Therefore, an evolutive elastoplastic mechanical model has been proposed (Cui and Fall, 2016) to depict the mechanical response of CPB under static loading conditions. Moreover, for early age CPB, the stiffness of the CPB structure is relatively small due to low cohesion values in the CPB. Correspondingly, the early-age consolidation process will cause plastic volumetric strain with a dynamic backfilling process. Therefore, it is necessary to define a cap yield surface to ensure that the contractive plastic volumetric strain will occur at the early ages. Hence, double yield surfaces that consist of an evolutive shear-failure surface and an elliptic cap surface are utilized to characterize the behaviors of both chemical-strain induced hardening/softening and plastic volumetric strain development in the CPB structure.

$$F_1 = \sqrt{J_2} + \alpha_Y\left(\xi,\kappa_1\right)\left[I_1 - C_Y\left(\xi\right)\right] = 0 \tag{4.123}$$

$$F_2 = \frac{4\left(I_1 - I_a\right)^2}{\left[I_b\left(\xi,\kappa_2\right) - C_Y\left(\xi\right)\right]^2} + \frac{4\left(\sqrt{J_2}\right)^2}{\left\{\alpha_Y\left(\xi,\kappa_1\right)\left[I_b\left(\xi,\kappa_2\right) - C_Y\left(\xi\right)\right]\right\}^2} - 1 = 0 \tag{4.124}$$

where I_1 and J_2 are the first stress and the second deviatoric stress invariants, respectively, I_a and $I_b\left(\xi,\kappa\right)$ respectively denote the center point of the elliptic cap on the I_1 axis and the value of I_1 at the intersecting point of the elliptical cap and I_1 axis, $\alpha_Y\left(\xi,\kappa_1\right)$ and $C_Y\left(\xi\right)$ are the material parameters, and κ_1, and κ_2 together with the degree of binder hydration ξ are the hardening/softening parameters which control the evolution of the double yield surfaces. For the material parameters, $\alpha_Y\left(\xi,\kappa_1\right)$ and $C_Y\left(\xi\right)$ can be expressed by the internal friction angle, $\phi_B = \phi_B\left(\xi\right)$, and cohesion, $c_B = c_B\left(\xi\right)$:

$$C_Y\left(\xi\right) = 3c_B\left(\xi\right)\cdot\cot\phi_B\left(\xi\right)$$

$$\alpha_Y\left(\xi,\kappa_1\right) = \frac{2\sin\phi_B\left(\xi\right)}{\sqrt{3}\left[3+\sin\phi_B\left(\xi\right)\right]} + D_{\alpha 1}\left\{\left[1-\exp(-D_{\alpha 2}\kappa_1)\right] + \left[D_{\alpha 3}\kappa_1\exp(-D_{\alpha 4}\kappa_1)\right]\right\} \tag{4.125}$$

where $D_{\alpha 1}$, $D_{\alpha 2}$, $D_{\alpha 3}$ and $D_{\alpha 4}$ are the material parameters, which can be determined by uniaxial or triaxial compressive test data. κ_1 is the effective plastic strain and can be defined as follows:

$$\kappa_1 = \int\sqrt{\frac{2}{3}d\varepsilon_p d\varepsilon_p} \tag{4.126}$$

The cohesion and internal friction angle can be determined by the following equations (Cui and Fall, 2016).

$$c_B\left(\xi\right)=M_{c1}\xi^{M_{c2}} \tag{4.127}$$

$$\phi_B\left(\xi\right)=N_1\xi^{N_2}+N_3\xi \tag{4.128}$$

where M_{c1}, M_{c2}, N_1, N_2 and N_3 are the fitting parameters which can be determined from the experimental data. Based on the results of a regression analysis of the experimental data reported in (Cui and Fall, 2016), M_{c1}=478 kPa, M_{c2}=3.3, N_1=-176.9°, N_2=2 and N_3=174.2° are adopted in this study.

The evolution of the elliptic cap surface (i.e., the hardening/softening behavior of the cap yield surface) is controlled by the value of I_b. Due to the gradual formation of cementation bonding between the solid particles with binder hydration, the isotropic yield stress I_b will increase, viz. I_b should be a function of the degree of hydration, ξ. Moreover, as uncemented geomaterials, such as soil, commonly have hardening/softening behaviors, the evolution of I_b should be related to the plastic volumetric strain, $\kappa_2=\varepsilon_v^p$, as well. Based on the previous findings on CPB from Helinski et al. (2007), the effects of plastic volumetric strain and binder hydration on the isotropic yield stress are superimposed, namely:

$$I_b\left(\kappa_2,\xi\right)=I_{b1}\left(\kappa_2\right)+I_{b1}\left(\xi\right) \tag{4.129}$$

For the influence of the plastic volumetric strain, the following expression is employed (Chen and Baladi, 1985):

$$I_{b1}\left(\kappa_2\right)=-D\ln\left(1-\frac{\kappa_2}{\varepsilon_{\max}}\right) \tag{4.130}$$

where D is a material parameter at a specified degree of hydration, which can be determined from the experimental data obtained from the oedometer or triaxial compression tests. $\varepsilon_{\max}$ refers to the maximum plastic volumetric strain when the material reaches the maximum hydrostatic pressure I_b. The maximum plastic volumetric compaction that a material can experience under hydrostatic loading is directly determined by the available porous space in the CPB. Therefore, under drained conditions, the maximum volumetric plastic strain at a given degree of hydration can be expressed by:

$$\varepsilon_{\max}=n_0=\frac{e_0}{1+e_0} \tag{4.131}$$

where n_0 and e_0 are the initial porosity and void ratio at the specified degree of hydration, respectively. Then, the plastic volumetric strain ε_v^p can be written as:

$$\varepsilon_v^p=\kappa_2=\frac{e_0}{1+e_0}\left[1-\exp\left(-I_{b1}/D\right)\right] \tag{4.132}$$

Hence, parameter D can be back-calculated based on the experimental data from the oedometer or triaxial compression tests for different curing times. Then, the relation between D and the degree of binder hydration ξ can be derived from a regression analysis. In this study, the following polynomial equation is proposed to predict the evolution of parameter $D(\xi)$:

$$D(\xi) = d_1\xi^3 + d_2\xi^2 + d_3\xi + d_4 \tag{4.133}$$

where d_1, d_2, d_3 and d_4 are the fitting parameters. In this study, the measured data from the oedometer tests published by Helinski et al. (2007) are adopted to perform the regression analysis and d_1 =7.395e-5 kPa, d_2 =-1.587e-4 kPa, d_3 =1.117e-4 kPa and d_4 = -4.28e-5 kPa are obtained and used in this study.

Obviously, for additional hardening induced by binder hydration, I_{b2}, the degree of binder hydration, ξ, and cement content, C_m, dominate the evolution of the isotropic yield stress. Helinski et al. (2007) proposed an empirical equation to characterize the incremental yield stress of CPB based on research by Rotta et al. (2003) on cemented soil.

$$I_{b2}(\xi) = A \cdot \exp\left(\frac{X \cdot C_m + C_m^{0.1} - e_0}{Z \cdot C_m + W}\right)\xi \tag{4.134}$$

where A is a material constant with the same units as I_{b2}, and X, Z and W are dimensionless constants, which can be derived from the experimental data from either an isotropic or one-dimensional compression test. Based on the experimental data reported by Helinski et al. (2007), A =-532.1 kPa, X =1260, Z =-21.02 and W =62.89 are obtained through the regression analysis and adopted in this study. It is important to point out that, after the very early ages, the cap portion of the yield locus will become very large with binder hydration, which corresponds to the extremely high hydrostatic pressure condition.

In order to describe the evolution of the direction of the plastic strain, a non-associative flow rule is adopted in this study:

$$d\boldsymbol{\varepsilon}_P = d\lambda_P \frac{\partial Q_{CPB}}{\partial \boldsymbol{\sigma}'} \tag{4.135}$$

where λ_p is a non-negative plastic multiplier and Q_{CPB} is a plastic potential function. For the double yield functions, the corresponding plastic potential functions can be written in terms of dilation angle ψ_B as follows:

$$Q_{CPB1} = \frac{2\sin\psi_B(\xi)}{\sqrt{3}\left[3 + \sin\psi_B(\xi)\right]} I_1 + \sqrt{J_2} \tag{4.136}$$

$$Q_{CPB2} = \frac{4\left(I_1 - I_a\right)^2}{\left[I_b\left(\xi,\kappa_2\right)\right]^2} + \frac{\left(\sqrt{J_2}\right)^2}{\left\{\frac{\sin\psi_B\left(\xi\right)}{\sqrt{3}\left[3+\sin\psi_B\left(\xi\right)\right]}I_b\right\}^2} - 1 = 0 \tag{4.137}$$

During plastic loading, the stress state must lie on the yield surface in the stress space (i.e., consistency condition).

$$dF(I_1, \sqrt{J_2}, \xi, \kappa) = \frac{\partial F}{\partial \sigma'} d\sigma' + \frac{\partial F}{\partial \xi} d\xi + \frac{\partial F}{\partial \kappa} d\kappa = 0 \tag{4.138}$$

Then, the plastic multiplier λ_p can be obtained by substituting Eq. (4.121) into Eq. (4.138):

$$d\lambda_p = \frac{1}{\frac{\partial Q_{CPB}}{\partial \boldsymbol{\sigma}'}} d\varepsilon + \frac{\frac{\partial F}{\partial \xi}}{\frac{\partial Q_{CPB}}{\partial \boldsymbol{\sigma}'}\frac{\partial F}{\partial \boldsymbol{\sigma}'} D^e} d\xi - \frac{1}{\frac{\partial Q_{CPB}}{\partial \boldsymbol{\sigma}'}} d\varepsilon_c + \frac{\frac{\partial F}{\partial \kappa}}{\frac{\partial Q_{CPB}}{\partial \boldsymbol{\sigma}'}\frac{\partial F}{\partial \boldsymbol{\sigma}'} D^e} d\kappa - \frac{1}{\frac{\partial Q_{CPB}}{\partial \boldsymbol{\sigma}'}} d\varepsilon_T \tag{4.139}$$

Hence, the stress-strain relation can be derived as:

$$\begin{aligned} d\boldsymbol{\sigma}' = &\left(\boldsymbol{D}^e - \frac{\boldsymbol{D}^e \frac{\partial Q_{CPB}}{\partial \boldsymbol{\sigma}'} \frac{\partial F}{\partial \boldsymbol{\sigma}'} \boldsymbol{D}^e}{\frac{\partial F}{\partial \boldsymbol{\sigma}'} \boldsymbol{D}^e \frac{\partial Q_{CPB}}{\partial \boldsymbol{\sigma}'} - \frac{\partial F}{\partial \kappa}\frac{\partial \kappa}{\partial \boldsymbol{\varepsilon}_p}\frac{\partial Q_{CPB}}{\partial \boldsymbol{\sigma}'}} \right)\left(d\boldsymbol{\varepsilon} - d\boldsymbol{\varepsilon}_T\right) \\ &- \left(\boldsymbol{D}^e - \frac{\boldsymbol{D}^e \frac{\partial Q_{CPB}}{\partial \boldsymbol{\sigma}'} \frac{\partial F}{\partial \boldsymbol{\sigma}'} \boldsymbol{D}^e}{\frac{\partial F}{\partial \boldsymbol{\sigma}'} \boldsymbol{D}^e \frac{\partial Q_{CPB}}{\partial \boldsymbol{\sigma}'} - \frac{\partial F}{\partial \kappa}\frac{\partial \kappa}{\partial \boldsymbol{\varepsilon}_p}\frac{\partial Q_{CPB}}{\partial \boldsymbol{\sigma}'}} + \frac{\boldsymbol{D}^e \frac{\partial Q_{CPB}}{\partial \boldsymbol{\sigma}'} \frac{\partial F}{\partial \xi} \frac{1}{\beta_{ch}}}{\frac{\partial F}{\partial \boldsymbol{\sigma}'} \boldsymbol{D}^e \frac{\partial Q_{CPB}}{\partial \boldsymbol{\sigma}'} - \frac{\partial F}{\partial \kappa}\frac{\partial \kappa}{\partial \boldsymbol{\varepsilon}_p}\frac{\partial Q_{CPB}}{\partial \boldsymbol{\sigma}'}} \right) d\boldsymbol{\varepsilon}_c \end{aligned} \tag{4.140}$$

4.4.3.5. Hydraulic process: volume changes induced by seepage

According to Darcy's law, the volume changes induced by seepage into and out of CPB REV can be expressed as follows:

$$dV_{spi} = -V\left[k\frac{k_{ri}}{\mu_i}\nabla^2 P_i\right]dt \tag{4.141}$$

where k is the intrinsic permeability, k_{ri} , μ_i and P_i respectively denote the relative permeability, fluid dynamic viscosity and pore fluid pressure with respect to each fluid (i.e. pore water and pore air).

Based on the relation between intrinsic permeability and saturated hydraulic conductivity K_{sat} (i.e., coefficient of permeability), the intrinsic permeability can be written as:

$$k = K_{sat}\mu_i / \rho_i g \tag{4.142}$$

The saturated hydraulic conductivity is directly related to the skeleton structure of the CPB, namely, the K_{sat} is controlled by the available pore space in the CPB mass. As mentioned in the introduction, the microstructure will be gradually refined as the hydration products precipitate, namely, the influence of binder hydration on the saturated hydraulic conductivity is realized through a chemical reaction induced microstructural refinement. Therefore, the evolution of the saturated hydraulic conductivity should be expressed as a function of the void ratio. For the saturated hydraulic conductivity, Carrier et al. (1983) proposed a power function to characterize the influence of changes in the void ratio:

$$K_{sat} = \frac{C_K \left[e(\sigma', T, \xi) \right]^{D_K}}{1 + e(\sigma', T, \xi)} \tag{4.143}$$

where C_k and D_k are the material constants. As mentioned in the introduction, the evolution of the void ratio is controlled by the coupling processes in the CPB mass, namely, $e = e(\sigma', T, \xi)$. The governing equation of the void ratio will be derived later. The two material constants are determined based on the measured data of K_{sat} and e as reported by Ghirian and Fall (2013a, 2014): C_k =1.963e-7 m/s and D_k =12.96 and a comparison of the predicted values and measured data of the saturated hydraulic conductivity is presented in Figure 4.36.

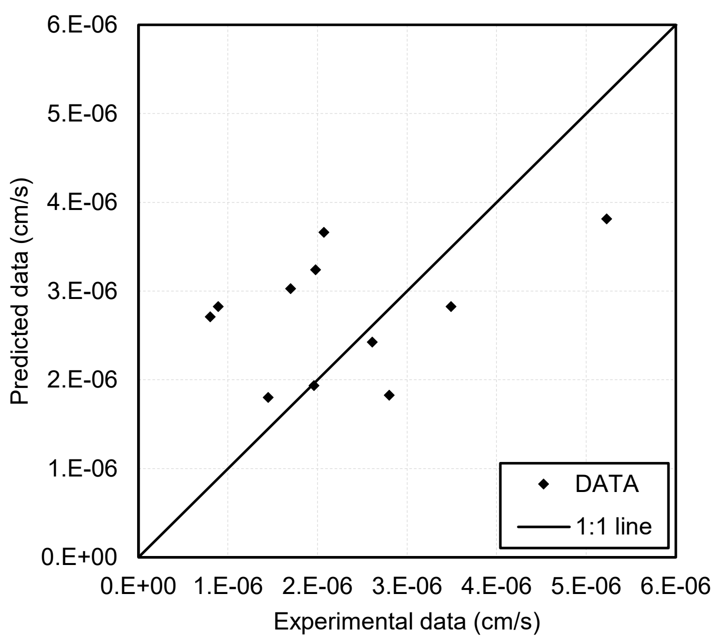

Figure 4.36. Predicted values versus experimental data of saturated hydraulic conductivity

Due to the fact that the relative permeability refers to the ratio of the effective (true) and saturated hydraulic conductivities, the saturation condition in the porous media is a dominating factor in the evolution of the relative permeability. Based on a model in

(Mualem, 1976), Van Genuchten (1980) and Luckner et al. (1989) derived prediction models of relative permeability which are adopted in this study.

$$k_{rw}\left(S_e\right)=\sqrt{S_e}\left[1-\left(1-S_e^{1/m_{WRC}}\right)^{m_{WRC}}\right]^2 \tag{4.144}$$

$$k_{ra}\left(S_e\right)=\sqrt{1-S_e}\left(1-S_e^{1/m_{WRC}}\right)^{2m_{WRC}} \tag{4.145}$$

where S_e refers to the effective saturation and can be defined as $S_e=\left(\theta-\theta_r\right)/\left(\theta_s-\theta_r\right)$, and m_{WRC} is the material defined by the WRC. For the characterization of the WRC of the CPB, it has been experimentally proven that the model by van Genuchten (1980) is able to accurately predict the WRC of CPB (Abdul-Hussain and Fall, 2011; Ghirian and Fall, 2013a).

$$\theta=\theta_r+\frac{\left(\theta_s-\theta_r\right)}{\left[1+\left(\alpha_{WRC}P_c\right)^{\frac{1}{1-m_{WRC}}}\right]^{m_{WRC}}} \tag{4.146}$$

where θ , θ_s and θ_r are the volumetric, saturated and residual water contents, respectively, α_{WRC} and m_{WRC} are the material parameters that are related to the degree of binder hydration. Based on the van Genuchten model, the effective degree of saturation can be expressed as:

$$S_e=\frac{1}{\left[1+\left(\alpha_{WRC}P_c\right)^{\frac{1}{1-m_{WRC}}}\right]^{m_{WRC}}} \tag{4.147}$$

The prediction model of the residual water content, θ_r , is developed by Abdul-Hussain and Fall (2011) based on the measured WRC data:

$$\theta_r=R_{r1}\cdot\exp(-R_{r2}\cdot\xi) \tag{4.148}$$

where R_{r1} and R_{r2} are two dimensional fitting constants and respectively equal 0.01314 and 7.538 based on the experimental data of the WRC as reported in (Abdul-Hussain and Fall, 2011).

For the two parameters α_{WRC} and m_{WRC} in Eqs. (4.146) and (4.147), the corresponding prediction models are defined by Cui and Fall (2015a):

$$m_{WRC}=f_{m1}\xi^{f_{m2}}+f_{m3} \tag{4.149}$$

$$\alpha_{WRC}=f_{\alpha1}\exp\left(f_{\alpha2}\xi\right) \tag{4.150}$$

where f_{m1} , f_{m2} , f_{m3} , $f_{\alpha1}$ and $f_{\alpha2}$ are fitting constants and can be determined by the WRC of CPB. The following values of the fitting constant are suggested by Cui and Fall (2015a) and used in this study: f_{m1}=0.0415, f_{m2}=4.231, f_{m3}=0.4073, $f_{\alpha1}$=0.2103 kPa^{-1} and $f_{\alpha2}$=-6.921.

To describe the influence of temperature on the fluid (pore water and air) dynamic viscosity (i.e., μ_w and μ_a), the pore water model developed by Thomas and Sansom

(1995) and the pore air model based on the Sutherland law (William Sutherland, 1893) are adopted in this study to predict the evolution of the fluid dynamic viscosity (Pa·s) with temperature (K):

$$\mu_w = 0.6612(T - 229)^{-1.562} \tag{4.151}$$

$$\mu_a = 1.716\times10^{-5}(T/273)^{1.5}\cdot\left[384/(T+111)\right] \tag{4.152}$$

4.4.3.6. Volume changes induced by evolution of pore-water pressure

The changes in pore-water pressure caused by the evolution of the water content in the CPB mass can generate volume changes of the capillary water:

$$dV_{Pw} = \left(\frac{e}{1+e}\right)\frac{SV}{K_w}dP_w \tag{4.153}$$

with K_w as the bulk modulus of the capillary water.

$$K_w = \rho_w \frac{dP_w}{d\rho_w} \tag{4.154}$$

Substituting Eq. (4.154) into Eq. (4.153) yields:

$$dV_{Pw} = -\frac{e}{1+e}SV\beta_{Pw}dP_w \tag{4.155}$$

where β_{Pw} represents the isothermal compression modulus of water and can be expressed as:

$$\beta_{Pw} = -\frac{1}{\rho_w}\frac{\partial\rho_w}{\partial P_w} \tag{4.156}$$

4.4.3.7. Volume changes in pore air

It is assumed that the pore air is an ideal gas and no phase changes occur in the capillary water. Therefore, the state equation of the gaseous phase can be expressed as:

$$dV_a = \frac{R\rho_a V_a}{M_a P_a - \rho_a RT}dT + \frac{RTV_a}{M_a P_a - \rho_a RT}d\rho_a - \frac{M_a V_a}{M_a P_a - \rho_a RT}dP_a \tag{4.157}$$

where M_a is the molecular mass of air (0.00029 kg/mol^{-1}) and R is a universal gas constant (8.314J mol^{-1}K^{-1}).

4.4.3.8. Consolidation equation

Due to the high coefficient of compressibility of water (e.g. water compressibility can reach 5.1×10^{-10} Pa^{-1} at 273.15 K and the limit of zero pressure (Fine and Millero, 1973)), the volume change of pore water caused by change in PWP is negligible and the influence of Eq. (4.155) on the consolidation process is omitted in this study. Substituting Eqs. (4.111), (4.112), (4.114), (4.115), (4.117), (4.118), (4.122), (4.141), (4.146), (4.147) and (4.156) into Eq.(4.108), the consolidation equation can be derived in a time rate form as follows:

$$
\begin{aligned}
&\left\{\frac{\left(2v_w - v_{ch-w} - v_{ab-w}\right)R_{n-w/hc}}{\left(w/c\right)v_w + v_c + \left(1/C_m - 1\right)v_{tailings}} - \left\{\frac{\sigma + \alpha_{Biot}\left[SP_w + \left(1-S\right)P_a\right]}{E}\right\}\left\{\frac{9\left[1-2\upsilon\right]}{E}\frac{\partial E}{\partial \xi} + 18\frac{\partial \upsilon}{\partial \xi}\right\}\right.\\
&\left.+\left[SP_w + \left(1-S\right)P_a\right]\frac{1-2\upsilon}{E}\frac{\partial \alpha_{Biot}}{\partial \xi} - \alpha_{Biot}\left(P_a - P_w\right)\frac{1-2\upsilon}{E}\left\{\left[1 - S_e\left(P_w, P_a, \xi\right)\right]\frac{\partial \theta_r}{\partial \xi} + \left(\frac{e}{1+e} - \theta_r\right)\frac{\partial S_e}{\partial \xi}\right\}\right\}\frac{\partial \xi}{\partial t}\\
&+\left\{\alpha_{Biot}S\frac{1-2\upsilon}{E} - \alpha_{Biot}\left(P_a - P_w\right)\frac{1-2\upsilon}{E}\left(\frac{e}{1+e} - \theta_r\right)\frac{\partial S_e\left(P_w, P_a, \xi\right)}{\partial P_w}\right\}\frac{\partial P_w}{\partial t}\\
&+\frac{\partial \lambda_p}{\partial t}\frac{\partial Q_{CPB}}{\partial I_1} - \frac{eSRT}{\left(1+e\right)\left(M_a P_a - \rho_a RT\right)}\frac{\partial \rho_a}{\partial t} + \frac{1-2\upsilon}{E}\frac{\partial \sigma}{\partial t} + k\frac{k_{rw}}{\mu_w}\nabla^2 P_w\\
&+\left\{\alpha_{Biot}\left(1-S\right)\frac{1-2\upsilon}{E} + \frac{eSM_a}{9\left(1+e\right)\left(M_a P_a - \rho_a RT\right)} - \alpha_{Biot}\left(P_a - P_w\right)\frac{1-2\upsilon}{E}\left(\frac{e}{1+e} - \theta_r\right)\frac{\partial S_e}{\partial P_a}\right\}\frac{\partial P_a}{\partial t}\\
&+\left[\alpha_{Ts} - \frac{e}{1+e}S\alpha_{Tw} - \frac{eSR\rho_a}{\left(1+e\right)\left(M_a P_a - \rho_a RT\right)}\right]\frac{\partial T}{\partial t}\\
&= -\alpha_{Biot}\left(P_a - P_w\right)\frac{1-2\upsilon}{e^2\left(1+e\right)^2 E}\left[S_e e + \left(1+e\right)^2\left(1 - S_e\right)\theta_r\right]\frac{\partial e}{\partial t}
\end{aligned}
\tag{4.158}
$$

It should be noted that, due to the refinement of the pore structure with the gradual increase of hydration products, viz. a chemical reaction induced mass source term is in the solid phase mass conservation, the time rate of the changes of the void ratio, $\partial e/\partial t$, is not just caused by the volumetric strain changes, $\partial \varepsilon_v/\partial t$, in the CPB mass. The evolution of the CPB void ratio is controlled by variations in the skeleton of the CPB and volume changes of the solid phase. Thus, the governing equation of the void ratio can be derived from pore space continuity:

$$
-dV_{ch-s} + dV_m + dV_{Ts} = dV_v = d\left(\frac{e}{1+e}V\right) \tag{4.159}
$$

By substituting Eqs. (4.111), (4.114), and (4.159), the governing equation of the void ratio can be derived as the following rate form:

$$
\begin{aligned}
&\left\{\left[SP_w + \left(1-S\right)P_a\right]\frac{1-2\upsilon}{E}\frac{\partial \alpha_{Biot}}{\partial \xi} - \frac{\left[\sigma + \alpha_{Biot}\left[SP_w + \left(1-S\right)P_a\right]\right]}{E}\left\{\frac{9\left[1-2\upsilon\right]}{E}\frac{\partial E}{\partial \xi} + 18\frac{\partial \upsilon}{\partial \xi}\right\}\right.\\
&\left.-\alpha_{Biot}\left(P_a - P_w\right)\frac{1-2\upsilon}{E}\left\{\left[1 - S_e\left(P_w, P_a, \xi\right)\right]\frac{\partial \theta_r}{\partial \xi} + \left(\frac{e}{1+e} - \theta_r\right)\frac{\partial S_e}{\partial \xi}\right\} - \frac{\left(1+e\right)\left(v_{ch-w} + v_{ab-w}\right)R_{n-w/hc}}{\left(w/c\right)v_w + v_c + \left(1/C_m - 1\right)v_{tailings}}\right\}\frac{\partial \xi}{\partial t}\\
&+\frac{1-2\upsilon}{E}\frac{\partial \sigma}{\partial t} + \alpha_{Biot}\frac{1-2\upsilon}{E}\left\{S - \left(P_a - P_w\right)\left(\frac{e}{1+e} - \theta_r\right)\frac{\partial S_e}{\partial P_w}\right\}\frac{\partial P_w}{\partial t} + \frac{\partial \lambda_p}{\partial t}\frac{\partial qQ_{CPB}}{\partial I_1} + \alpha_{Ts}\frac{\partial T}{\partial t}\\
&+\alpha_{Biot}\frac{1-2\upsilon}{E}\left\{\left(1-S\right) - \left(P_a - P_w\right)\left(\frac{e}{1+e} - \theta_r\right)\frac{\partial S_e}{\partial P_a}\right\}\frac{\partial P_a}{\partial t}\\
&= -\left\{\frac{1}{1+e} + \alpha_{Biot}\left(P_a - P_w\right)\frac{1-2\upsilon}{e^2\left(1+e\right)^2 E}\left[S_e e + \left(1+e\right)^2\left(1 - S_e\right)\theta_r\right]\right\}\frac{\partial e}{\partial t}
\end{aligned}
\tag{4.160}
$$

Apart from the consolidation equation, the consolidation evaluation parameters including the compressibility, C_c, and coefficient of consolidation, C_V should be defined as well. Due to the consideration of the plastic volumetric strain in this study, the compressibility C_c is defined as:

$$C_c = \frac{\partial \varepsilon_v}{\partial \sigma'_m} \tag{4.161}$$

where σ'_m represents the mean effective stress. Based on Hooke's law and the plastic flow rule, Eq. (4.161) can be rewritten as:

$$C_c = \frac{3\left[1-2\upsilon(\xi)\right]}{E(\xi)} + \frac{\partial \lambda_p}{\partial \sigma'_m}\frac{\partial Q_{CPB}}{\partial I_1} \tag{4.162}$$

Eq.(4.162) indicates that the compressibility of the CPB material is related to two mechanical properties (Poisson's ratio and elasticity), which are affected by the binder hydration and plastic volumetric strain; namely, the compressibility, C_c, will show a substantial nonlinearity with binder hydration advancement and plastic strain development.

In considering the coexistence of the pore water and pore-air in the CPB medium, the coefficient of consolidation can be expressed as:

$$C_V = \frac{K_{sat}}{C_c\left[S\rho_w + (1-S)\rho_a\right]g} \tag{4.163}$$

By substituting Eqs. (4.143) and (4.162) into Eq. (4.163), the coefficient of consolidation can be defined as:

$$C_V = \frac{C_k\left[e(\sigma', T, \xi)\right]^{D_k}}{\left[1+e(\sigma', T, \xi)\right]\left[S\rho_w + (1-S)\rho_a\right]g\left\{\frac{3\left[1-2\upsilon(\xi)\right]}{E(\xi)} + \frac{\partial \lambda_p}{\partial \sigma'_m}\frac{\partial Q_{CPB}}{\partial I_1}\right\}} \tag{4.164}$$

In order to solve the governing equations, Eqs. (4.158) and (4.160), conservation equations (mass, energy and momentum balance equations) need to be applied.

4.4.3.9. Mass conservation equations

With binder hydration advancement, the chemical reaction induced consumption of the capillary water will be converted into a solid phase in the form of hydration products. Correspondingly, the water sink term will appear in the water mass balance. By involving the solid phase mass balance equation, the capillary water and pore air mass balance equations can be written as follows:

$$\begin{aligned}&\frac{e}{1+e}S\frac{\partial\rho_w}{\partial t}+\frac{e}{1+e}\rho_w\frac{\partial S}{\partial t}+S\rho_w\left[\frac{\partial\varepsilon_v}{\partial t}+\frac{1}{(1+e)\rho_s}\frac{\partial\rho_s}{\partial t}\right]\\&-\frac{e}{1+e}S\dot{m}_{hydr}\left(\frac{\rho_w}{\rho_s}S-1\right)=-\nabla\cdot\left(\frac{eS\rho_w}{1+e}\mathbf{v}^{rw}\right)\end{aligned} \tag{4.165}$$

$$\begin{aligned}&(1-S)\rho_a\left[\frac{1}{(1+e)\rho_s}\frac{\partial\rho_s}{\partial t}+\frac{\partial\varepsilon_v}{\partial t}-\frac{eS}{(1+e)\rho_s}\dot{m}_{hydr}\right]\\&+\frac{e}{1+e}(1-S)\frac{\partial\rho_a}{\partial t}-\frac{e}{1+e}\rho_a\frac{\partial S}{\partial t}=-\nabla\cdot\left[\frac{e(1-S)\rho_a}{1+e}\mathbf{v}^{ra}\right]\end{aligned} \tag{4.166}$$

where $\dot{m}_{hydr}$ is the water sink term in the water balance equation. Based on the model in (Powers and Brownyard, 1947), the binder hydration induced water sink term can be derived as:

$$\begin{aligned}\dot{m}_{hydr}=\;&m_{hc-initial}\left(0.187x_{C_3S}+0.158x_{C_2S}+0.665x_{C_3A}+0.2130x_{C_4AF}\right)\\&\times\left\{\left(\frac{\tau}{t_e}\right)^{\beta}\left(\frac{\beta}{t_e}\right)\xi(t_e)\exp\left[\frac{E_a}{R}\left(\frac{1}{273+T_r}-\frac{1}{273+T}\right)\right]\right\}\end{aligned} \tag{4.167}$$

where $m_{hc-initial}$ is the initial cement mass.

4.4.3.10. Energy conservation equation

The heat evolution in a CPB structure is induced by heat conduction, Q_{cd}, and heat advection with the capillary fluid flow, Q_{ad}. Moreover, due to the exothermic characteristic of binder hydration, there exists a heat source term, Q_{hydr}, in the governing equation of the evolution of energy. Based on the assumption of local thermal equilibrium viz. $T_s = T_w = T_a = T$, a total energy balance equation is adopted in this study:

$$\left[(1-n)\rho_s C_s + nS\rho_w C_w + n(1-S)\rho_a C_a\right]\frac{\partial T}{\partial t} + Q_{cd} + Q_{ad} = Q_{hydr} \tag{4.168}$$

where C refers to the specific heat capacity.

4.4.3.10.1. Heat conduction

For the heat conduction in a CPB structure and which also involves the surrounding rock, Fourier's law is able to characterize the heat transfer processes:

$$Q_{cd} = \nabla\cdot\left(-k_{eff}\nabla T\right) \tag{4.169}$$

where ∇ is the differential operator del and k_{eff} is the effective thermal conductivity which can be written in the following form as proposed by Somerton et al. (1973).

$$k_{eff} = k_{dry} + \sqrt{S_e}\left(k_{sat} - k_{dry}\right) \tag{4.170}$$

where k_{sat} and k_{dry} refer to the thermal conductivity of the porous media under a saturated state and completely dry conditions, which can be expressed by the power law formulae proposed by Côté and Konrad (2005):

$$k_{sat} = k_{tailings}^{1-\phi} k_w^{\phi} \tag{4.171}$$

$$k_{dry} = k_{tailings}^{1-\phi} k_a^{\phi} \tag{4.172}$$

where $k_{tailings}$, k_w and k_a refer to the thermal conductivity of the tailings, water and air, respectively. Based on the previous study on CPB (Cui and Fall, 2015a), $k_{tailings}$=1.38 W/(m·K), k_w=0.58 W/(m·K), and k_a=0.027 W/(m·K) are adopted in this study.

4.4.3.10.2. Heat advection

As the capillary fluids (i.e., pore water and air) flow in the CPB media, the heat advection process will occur in the CPB mass and the heat transfer process, which can be expressed as:

$$Q_{ad} = \left(\rho_w C_w \boldsymbol{v}^{rw} + \rho_a C_a \boldsymbol{v}^{ra}\right) \cdot \nabla T \tag{4.173}$$

where $\boldsymbol{v}^r$ is the Darcy's velocity of fluid, and C is the fluid specific heat capacity.

4.4.3.10.3. Heat generation

The amount of heat released by binder hydration is directly related to the extent of the chemical reaction (i.e., degree of binder hydration). Moreover, it has been confirmed through experimental studies performed on cement paste (Schindler and Folliard, 2003; Poole et al., 2007) that binder hydration is influenced by the curing temperature. Therefore, the heat source term, Q_{hydr}, (W/m^3), of cementitious media can be expressed as follows (Schindler and Folliard, 2003):

$$Q_{hydr} = H_T \left(\frac{\tau}{t_e}\right)^{\beta} \cdot \left(\frac{\beta}{t_e}\right) \cdot \xi(t_e) \cdot f(T) \tag{4.174}$$

$$\text{with} \begin{cases} H_T = \left(H_{cem} \cdot X_{cem} + 461 \cdot X_{slag} + 1800 \cdot x_{CaO/FA} \cdot X_{FA}\right) C_b \\ H_{cem} = 500 x_{C_3S} + 260 x_{C_2S} + 866 x_{C_3A} + 420 x_{C_4AF} + 624 x_{SO_3} + 1186 x_{FreeCaO} + 850 x_{MgO} \\ f(T) = \exp\left[\frac{E_a}{R}\left(\frac{1}{273K + T_r} - \frac{1}{273K + T}\right)\right] \end{cases}$$

where H_T and H_{cem} refer to the total heat available for binder hydration and the cement, respectively, T_r is the reference temperature, C_b is the apparent binder density with respect to the total volume of the CPB mixture, X_i is the weight ratio of the corresponding minerals in terms of the total binder content and x_i is the mass ratio of the corresponding compound in terms of the total cement content.

4.4.3.11. Momentum conservation equation

The linear momentum balance equation for a multiphase system can be expressed in a rate form (Gawin et al., 2006) with negligence of the inertial forces due the relatively slow phenomena in the CPB structure.

$$\nabla \cdot \left(\frac{\partial \boldsymbol{\sigma}}{\partial t} \right) + \frac{\partial \left[(1-n)\rho_s + nS\rho_w + n(1-S)\rho_a \right]}{\partial t} \boldsymbol{g} = 0 \tag{4.175}$$

where σ is the total stress tensor, and $\boldsymbol{g}$ is the gravitational acceleration.

Based on the pore space continuity and conservation principles, a coupling multiphysics model that consists of Eqs.(4.158), (4.160), (4.165), (4.166), (4.168) and (4.175) is developed. Moreover, the evaluation parameters, including compressibility (i.e., Eq. (4.162)) and the coefficient of consolidation (i.e., Eq.(4.164)), are defined.

4.4.4. Model verification and simulation

The multiphysics model for consolidation behavior presented above is implemented in the FEM code-COMSOL Multiphysics. COMSOL is a multiphysics modeling tool that solves various coupled physical problems based on the Partial Differential Equations. COMSOL can perform various types of analysis including stationary and time-dependent, linear and nonlinear, eigenfrequency, modal and frequency response analyses by using FEM together with error control which employs a variety of numerical solvers (COMSOL, 2015). Based on the previous studies on CPB (Wu et al., 2012; Cui and Fall, 2015a, b, 2016), it has been proven that COMSOL Multiphysics is capable of solving the coupled THMC CPB problems. Therefore, in order to verify the developed THMC-consolidation model, a series of case studies were performed with COMSOL Multiphysics. During the simulation, the established consolidation model is implemented into 4 modules including geomechanics, porous media flow, heat transfer and user defined module. In order to analytically describe the unique characteristics of CPB, the mechanical model (e.g., yield and potential function, effective stress, chemical shrinkage, thermal expansion), hydraulic model (e.g., the 2 phases Darcy flow, WRC and water sink term), thermal model (e.g., heat conduction, advection and heat source term) and chemical model (e.g., binder hydration model, evolution equations of material properties) are implemented into the aforementioned 4 modules. The modeling results were compared with the experimental results of tests performed in this study and reported measured data. Furthermore, the key characteristics of the proposed model were demonstrated through a comparison with an analytical solution (Gibson's solution).

For the input parameters, the adopted values for each fitting parameters and constant material properties are detailed listed after the corresponding equations in the Section of Formulation of the multiphysics model. The mixture recipe dependent input parameters, initial values and boundary conditions adopted for the numerical simulation of each case study are tabulated in Table 4.5.

Table 4.5. Mixing recipe dependent input parameters, initial values and boundary conditions

	CUS test	High column test	Oedometer test	Analytical solution	Sensitivity analysis
Cement content	4.5%	4.5%	5%	4.5%	4.5%
w/c ratio	7.6	7.4	11.7	7.6	7.6
Mechanical module					
Top surface	Boundary load	Free	Boundary load	Free	Curing time ×100 (kPa/day)
Lateral sides	Roller	Roller	Roller	Roller	Roller
Bottom side	Fixed	Fixed	Fixed	Fixed	Fixed
Volume force	Gravity	Gravity	Gravity	Gravity	Gravity
Hydraulic module					
Top surface	No flow	No flow	Zero pressure	Zero pressure	No flow
Lateral sides	No flow	No flow	No flow	No flow	No flow
Bottom side	No flow (undrained test) Mass flux (drained test)	No flow	No flow	Zero pressure	No flow
Volume force	Gravity	Gravity	Gravity	Gravity	Gravity
Initial value	Hydraulic head=0	Hydraulic head=0	Hydraulic head=0	Hydraulic head=0	Hydraulic head=0
Thermal module					
Top side(°C)	22.1	23	22	22	22.1/Insulated
Lateral sides (°C)	22.1	23	22	22	22.1/Insulated
Bottom side (°C)	22.1	23	22	22	22.1/Insulated
Initial temperature (°C)	5, 25 and 35	23	22	22	25/Insulated

4.4.4.1. Consolidation behavior of CPB curing under stress and dynamic thermal loads

To quantitatively investigate the influence of coupled THMC processes on CPB consolidation, a laboratory pressure cell apparatus (CUS cell) developed by Ghirian and Fall (2013b) is adopted in this study. The main components of the CUS cell consist of (1) a Perspex cylinder with a diameter of 10 cm and height of 30 cm, (2) an axial piston mounted on the upper portion of the cylinder and (3) top and bottom plates with 3 tie rods to hold the CUS cell. A schematic view of the pressure cell apparatus is presented in Figure 4.37.

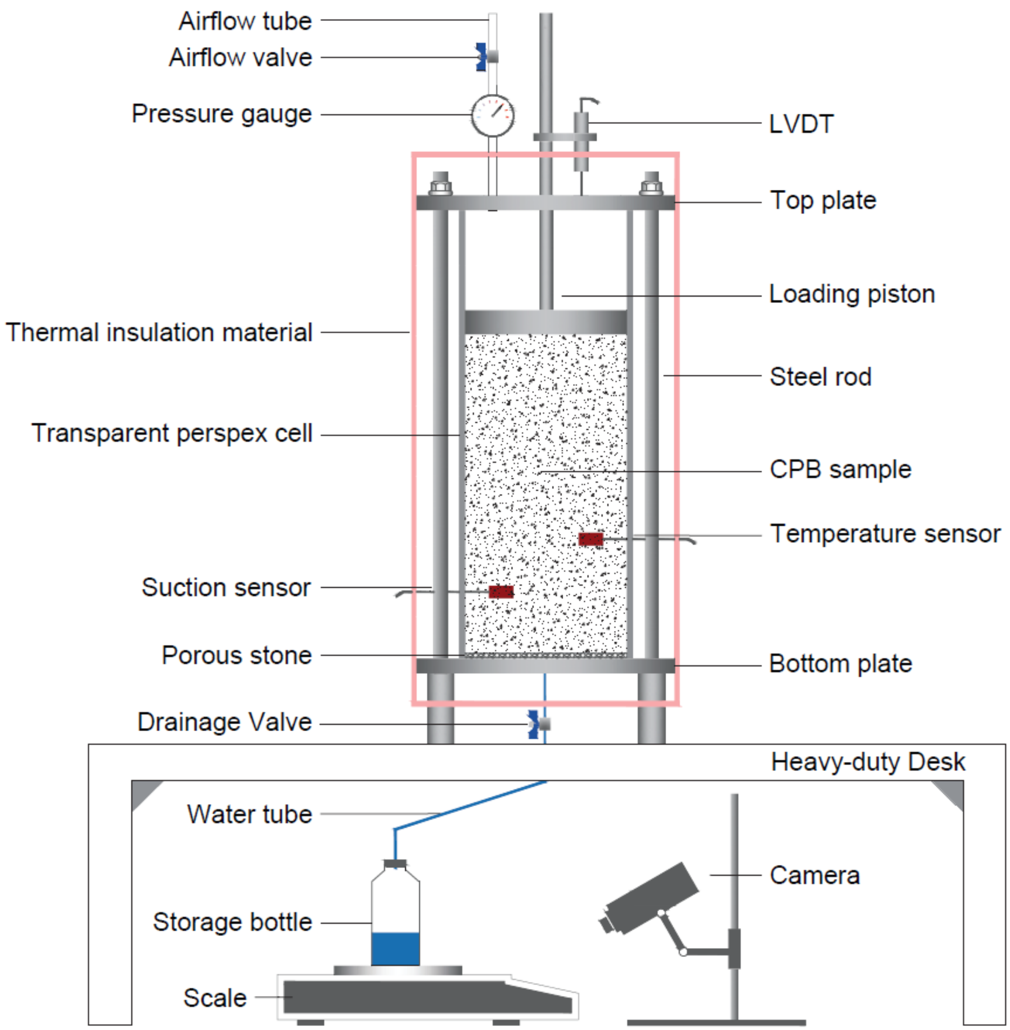

Figure 4.37. Schematic diagram of pressure cell set-up

The CUS cell was installed with a suction meter (MPS-2) and a temperature sensor (5TE) located at the lower portion of the cell. In addition, a linear variable differential transformer (LVDT) was installed on the top of the cell to measure the vertical displacement. Compressed air pressure (up to 600 kPa) was gradually applied onto the piston to simulate the in-situ backfilling process. Specifically, immediately after placement into the CUS cell, an initial air pressure of 20 kPa was applied to put the piston and top surface of CPB sample in contact. During the testing, pressures of 35, 55, 75 and 150 kPa were applied to the sample every 3 hours for the first 12 hours. Afterward, pressures of 300, 450 and 600 kPa were applied every 24 hours. The detailed procedures of pressure application are presented in Figure 4.38.

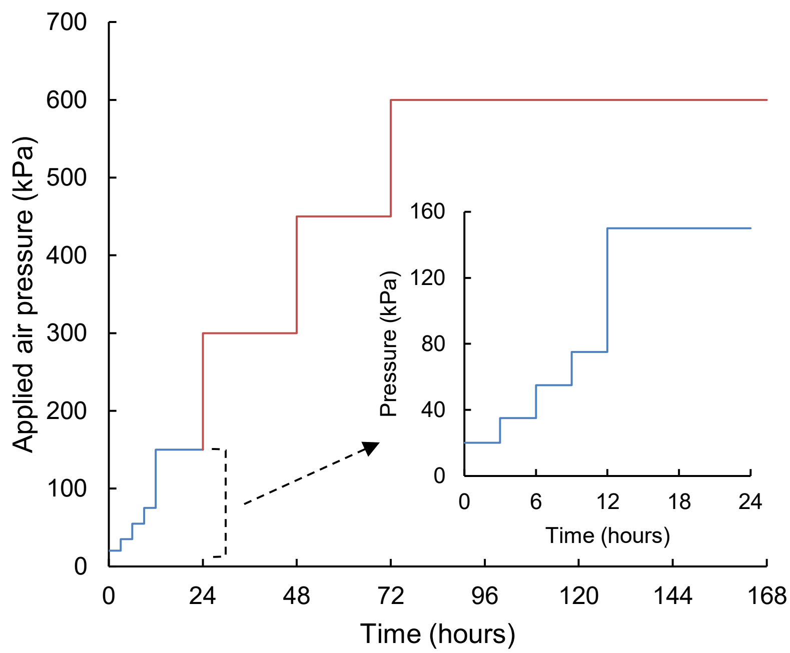

Figure 4.38. The application scheme of air pressure with curing time

For the preparation of CPB sample, the artificial ground silica tailings were used to eliminate the uncertainties related to natural tailings (Nasir and Fall, 2008; Ghirian and Fall, 2015). The silica tailings are essentially made of quartz, which is one of the primary mineral found in Canadian hard rock mine tailings. The relative density of silica tailings is 2.7. As shown in Figure 4.39, the grain size distribution of silica tailings is close to the average of 9 Canadian hard-rock mine tailings. With about 43 wt.% of fine particles (diameter <20μm), the silica tailings can be classified as medium tailings.

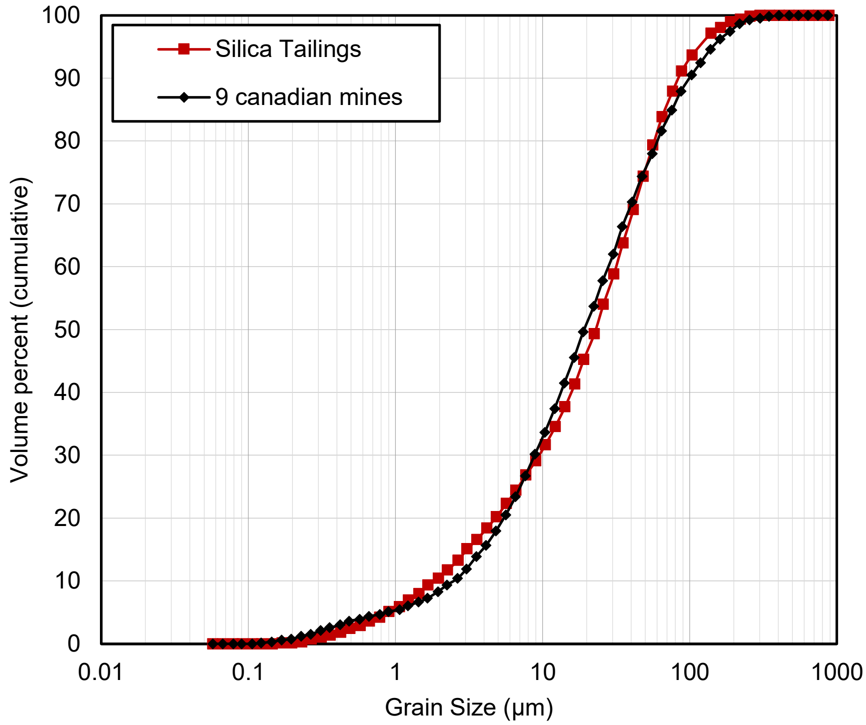

Figure 4.39. Comparison of grain size distribution for silica tailings and the average 9 Canadian mines

The mixture recipe of the CPB consisted of tailings (silica powder), tap water (w/c=7.6) and Portland cement Type 1 (4.5 wt%). In this study, three different initial temperatures of the mixing materials are used: 5°C, 20°C and 35°C. Moreover, for the tests carried out under an initial temperature of 35°C, both drained and undrained conditions are adopted. For the drainage tests, water that was leaving from the bottom hole of the CUS cell was collected into a storage bottle. The variation of the drained water was weighed by using an analytical balance (a Mars scale with a graduation of 0.01 g) and the measured data were continuously recorded by an HD camera. The corresponding mass flux of drainage water was also calculated and is presented in Figure 4.40. The CUS cell was covered with a thermal insulation glass wool blanket. The objective of the insulation was not to create adiabatic curing conditions, but to slow down the heat transfer between the backfill material and the surrounding environment, and mimic the heat transfer between a narrow CPB structure and the surrounding rock mass in the field. In the field and most cases, the CPB is surrounded by the rock mass, which cannot transfer heat very quickly (Wang and Fall, 2014). The thermal properties of the insulation material are listed in Table 4.6.

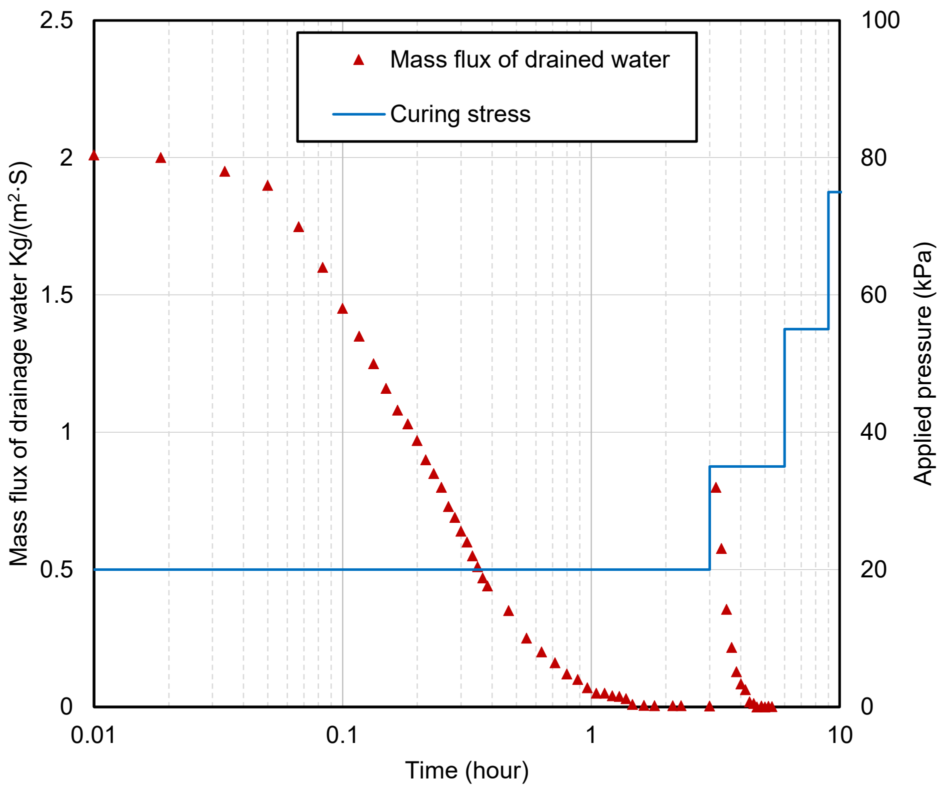

Figure 4.40. Evolution of mass flux of drainage water with time under an initial temperature of 35°C

Table 4.6. Summary of the properties of the thermal insulation material used

Property	Value
Thermal conductivity (W/(m K))	0.035
Heat capacity (J/(kg K))	840
Density (kg/m^3)	30

A 2D axisymmetric model is adopted for the simulation in this case study. The geometry model and mesh are presented in Figure 4.41.

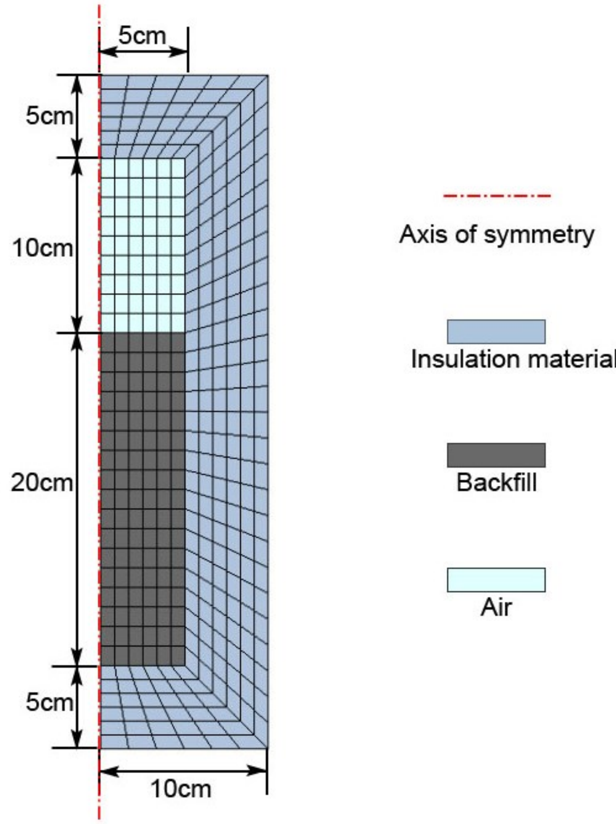

Figure 4.41. Geometry and mesh of simulated model of CUS test

As shown in Figure 4.42, the magnitude of the vertical displacement under increasing pressure is governed by the initial temperature of the CPB. Both the simulation results and experimental data reveal that the settlement of CPB increases with a higher initial temperature. As mentioned in the introduction, a higher initial temperature will significantly increase the binder hydration in CPB. Due to self-desiccation (i.e., pore water transformation to solid phase associated with volume decrease), more settlement occurs under a higher initial temperature. Moreover, for the simulation of drainage, the recorded data of the water mass flux are set as the hydraulic boundary on the bottom drainage hole. From Figure 4.42, it can be observed that a large amount of settlement occurs at a very early age (in the 1st day) under drainage conditions. Good agreement between the modeled results and measured data are obtained for CPB under both undrained and drained conditions.

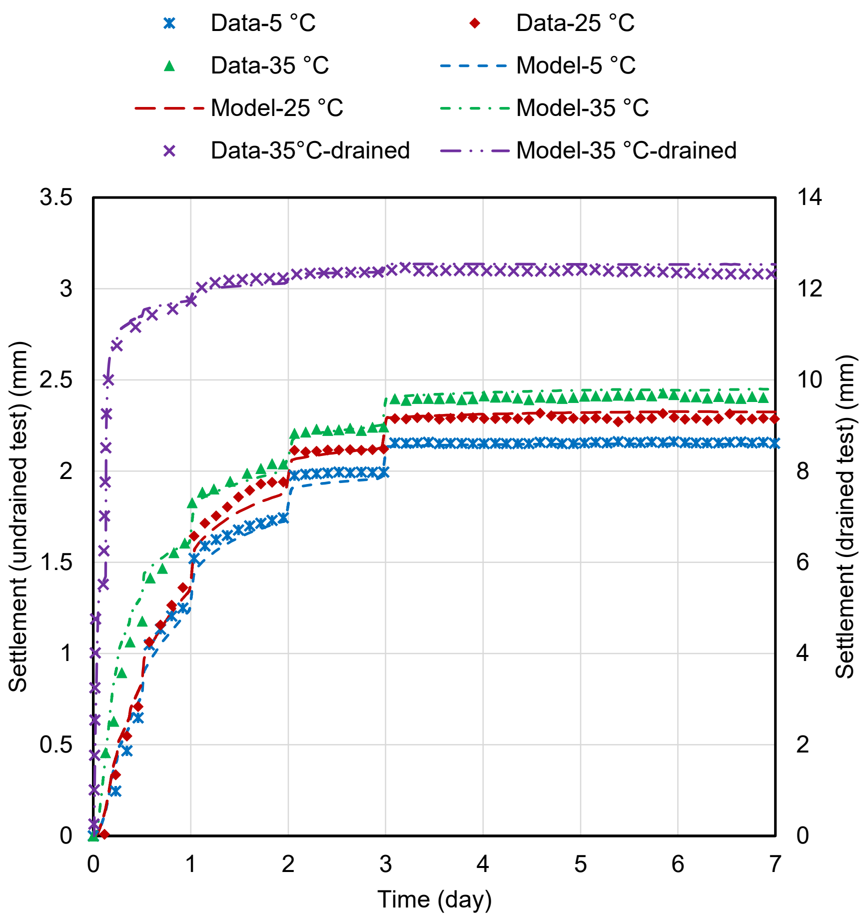

Figure 4.42. Influence of initial temperature on the consolidation behaviors of CPB

The evolution of the PWP under different initial temperatures is presented in Figure 4.43. It should be pointed out that the measurement of the water potential sensor (MPS-2) ranges from -10 to -100,000 kPa. Therefore, the initially detectable monitoring data by the suction meter does not correspond to the onset of suction in CPB, namely, the negative pore water pressure initiated at an earlier time. From Figure 4.43, it can be observed that a lower negative PWP value is observed for CPB curing under a higher initial temperature. This is because a higher initial temperature is associated with faster binder hydration and thus higher self-desiccation of the CPB. For the drainage test, the detectable measured data appear earlier than those monitored in the CPB with the same initial temperature under undrained conditions. The modeling results of the PWP for CPB under different initial temperatures and drainage conditions exhibit good agreement with the experimental results.

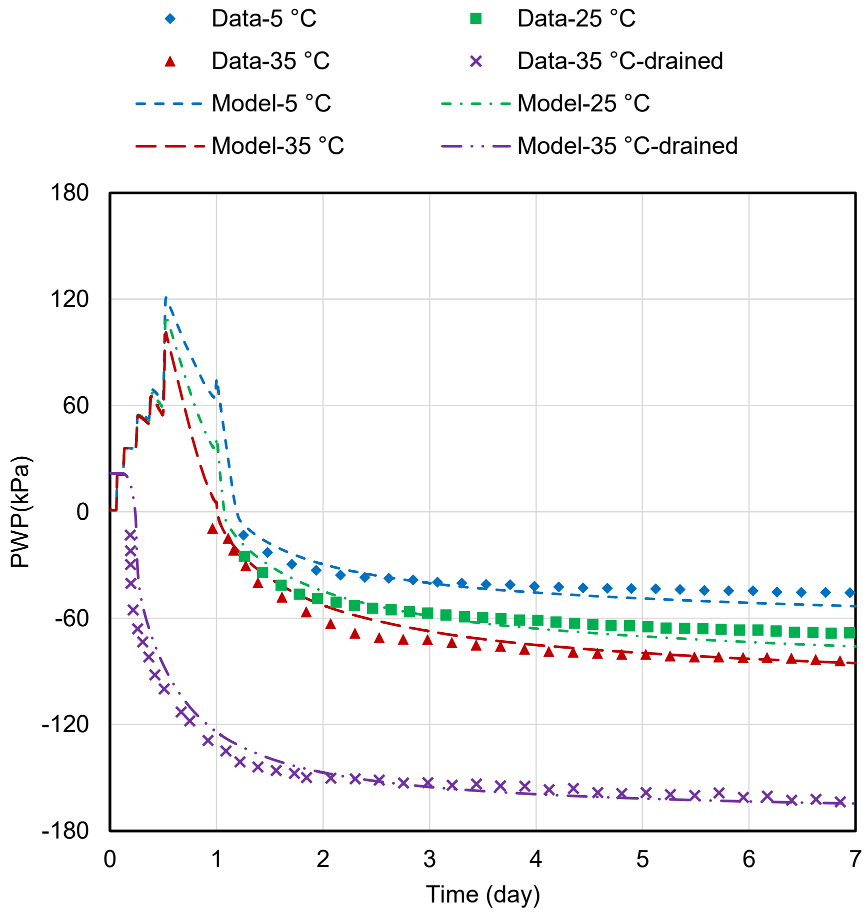

Figure 4.43. Comparison of modeling results and experimental data of PWP

For the evolution of the temperature presented in Figure 4.44, it should be noted that the initial temperature of the CPB mix components plays a dominant role. The experimental data of the tests at 5°C and 35°C show a monotonic evolution trend, and gradually approach room temperature (22.1°C) while for the test at 25°C, there exists a peak point on the evolution curve. For the drainage test, the CPB sample has a rapid drop in temperature after casting, which is due to the thermal loss with pore water drainage. The simulation results show a strong agreement with the experimental results for all of the tests.

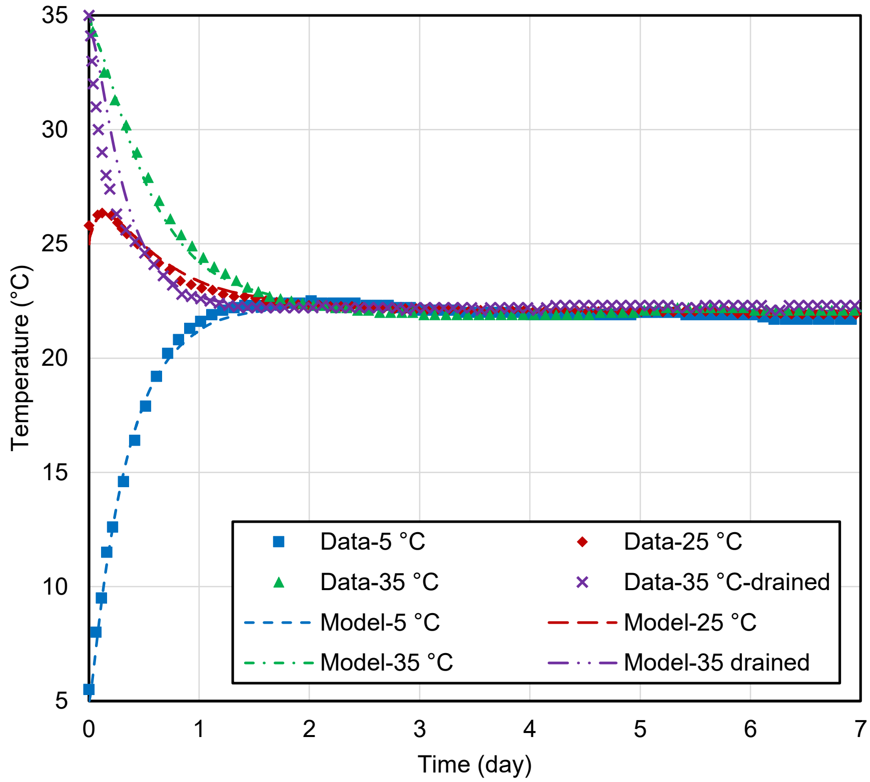

Figure 4.44. Comparison between simulation results and measured data of temperature

The objective of CUS cell tests is to verify the predictive ability of the multiphysics model of the consolidation behavior. Based on the measured data, it can be observed that the CUS cell tests are able to reproduce the consolidation behaviors under different curing conditions (e.g., curing stress, initial temperature and drainage conditions). With the aid of various types of sensors installed in the CUS cell, the evolution of multiphysics in CPB can be recorded as well. The good agreement between modeling results and experimental data indicates that the developed THMC-consolidation model is able to accurately capture the evolution of settlement, PWP and temperature of CPB samples curing under stress and dynamic thermal loads. Although the experimental setup of CUS cell test is well designed, there are still rooms for improvement for future laboratory work. For instance, the perspex cylinder (acrylic plastic) cylinder is used as the cell. Correspondingly, the fill-cell interface is smooth and the interface interaction is ignored with respect to the fill-rock mass interface in the stope (i.e., the mined-out underground space). Therefore, in order to describe the in-situ interface interaction, it is necessary to increase the roughness of the inside surface of CUS cell. Moreover, the applied air pressure is increased every certain curing time, while the in-situ backfilling process is a continuous operation. Therefore, the automatic adjustment system of applied air pressure is needed to mimic the dynamic backfilling operation. Additionally, the CUS cell allows one-dimensional consolidation testing, while, the lateral rock mass pressure is important for the consolidation behavior. Therefore, the confining pressure system can be added to experimental apparatus to improve the performance of CUS cell test.

4.4.4.2. High column test

In order to assess the consolidation behavior of CPB under self-weight, an experimental program on CPB with the use of high columns was carried out by Belem et al. (2006). The columns were manufactured with PVC materials on 3 sides and closed with a transparent polycarbonate sheet. The high columns had a column section of 31.5×30.5cm^2 and height of 300 cm. The base of the high column was impervious. The mix parameters of the CPB including the cement content and water-to-cement ratio are listed in Table 4.5. A two-stage filling strategy was adopted over a period of 24 hours. Detailed information about the experimental program can be found in (Belem et al., 2006). The vertical displacement was manually measured at a time interval of 1 hour for a period of 5 days, on which the void ratio was calculated. In order to simulate two-stage backfilling sequences, the deformed geometry interface (i.e., a built-in physics module of COMSOL Multiphysics) was utilized to model the placement of fresh CPB into the high columns. Moreover, the automatic remeshing function in COMSOL Multiphysics was activated, which can maintain high-quality tetrahedral meshes during the deformation of the geometry of CPB. The geometry and mesh are presented in Figure 4.45.

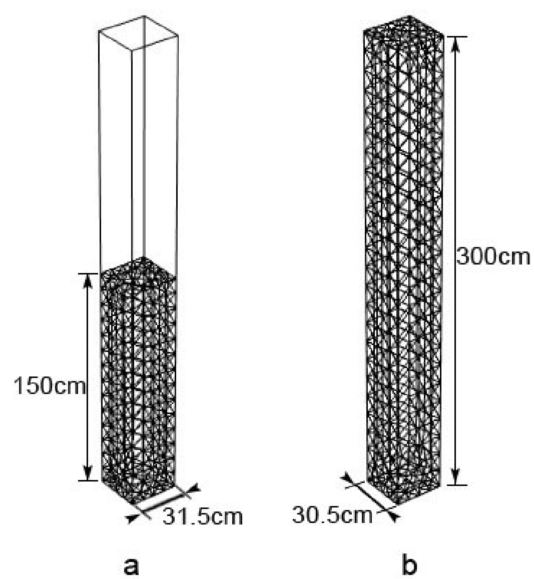

Figure 4.45. Geometry and mesh of three-dimensional model of high column: a. 1st stage backfilling; b. 2nd stage backfilling.

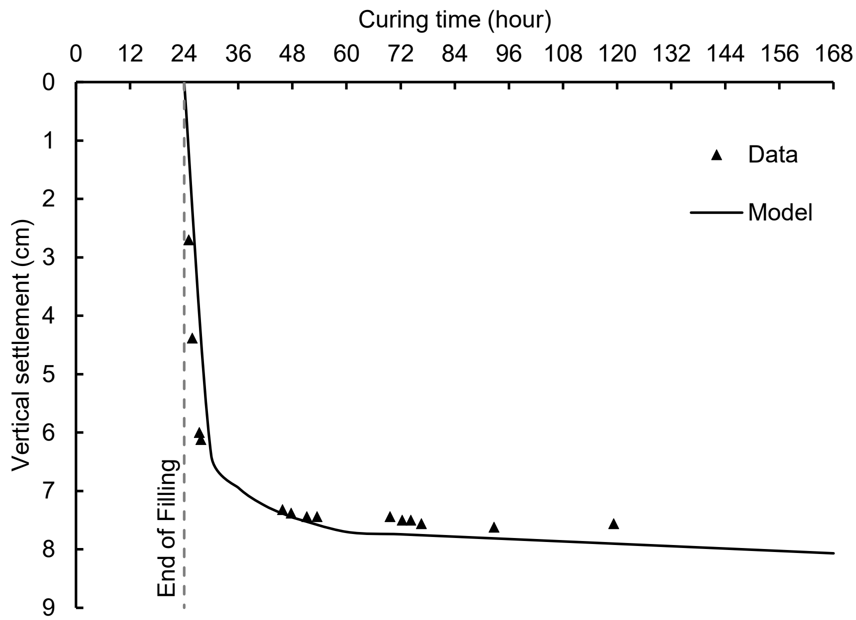

Figure 4.46. Comparison between modeling results and experimental data of vertical settlement

A comparison between the measured data and predicted values of the vertical displacement is shown in Figure 4.46. Both the experimental data and simulation results demonstrate that the major vertical displacement occurs at a very early age (in the 1st day after the end of the filling). This is mainly due to the fact that the water consumption induced by binder hydration results in the reduction of the pore space and correspondingly the volume change (i.e., chemical shrinkage). In addition, the pore water loss will contribute to the increase of effective stress. Moreover, the rate of the binder hydration is relatively fast at an early age. Correspondingly, large vertical settlement can be observed. Furthermore, as shown in Figure 4.47, the proposed model is able to capture the measured data of the void ratio. Therefore, through this case study, it can be observed that chemical shrinkage plays a critical role in the volume change of CPB under undrained conditions. The good agreement between the experimental data and simulation results of the vertical settlement further validate the predictability of the developed model.

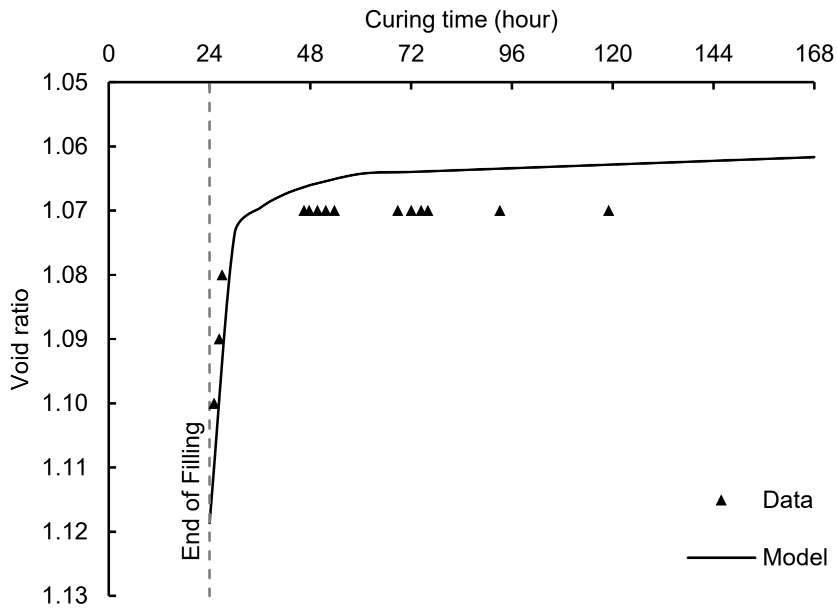

Figure 4.47. Comparison between simulation results and experimental data for void ratio

4.4.4.3. Standard consolidation test

It is well known that the conventional oedometer test is recognized as the standard method to investigate the consolidation behavior of geotechnical materials (e.g., soil) in the laboratory. A series of oedometer tests have been carried out by Le Roux (2004) to assess the consolidation characteristics of CPB. In this study, three modified loading rates (i.e., the time interval of stress increments: every 24 min, 48 min and 2 h and 24 min) are used to simulate different backfilling rates. The reported data in (Le Roux, 2004) are used to further validate the developed model. The mixture recipe of CPB used in this study is listed in Table 4.5. Due to the geometric characteristics of the oedometer ring, an axisymmetric geometry model is adopted. The geometry and mesh are presented in Figure 4.48

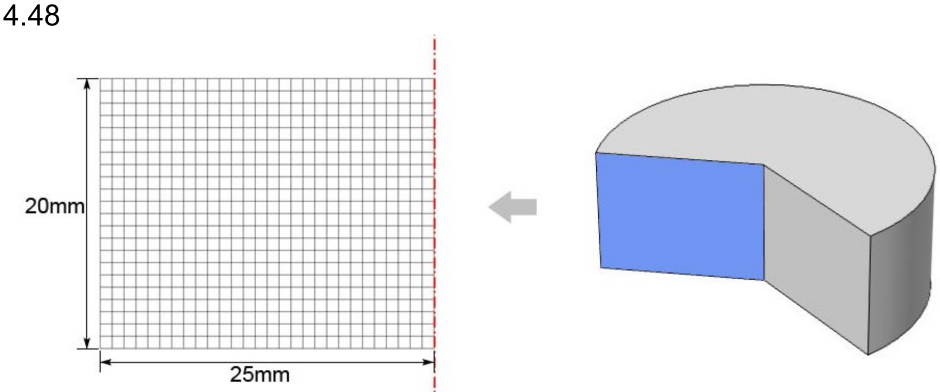

Figure 4.48. Geometry and mesh of oedometer model

The normalized void ratio is plotted against stress on a logarithmic scale as shown in Figure 4.49. It can be observed that the agreement between the simulated value and measured data is fairly good. Moreover, it is interesting to find that the loading rate strongly influences the magnitude of deformation. Specifically, both the simulation results and experimental data indicate that a rapid loading rate results in more reduction in the void ratio. Correspondingly, the slope of the normal compression line (i.e., the compression index) becomes steeper for CPB under a rapid loading rate. This is due to the fact that a rapid loading condition corresponds to a short-term curing condition when the same normal stress is applied on the CPB sample. As mentioned in the introduction, binder hydration is time dependent. Therefore, short-term curing will result in lower cementation bonding between the solid particles, which in turn, makes CPB material resist less consolidation stress. Based on the comparison between the simulated results with the experimental data from the oedometer tests, it can be confirmed that the developed model is able to predict the consolidation behavior of CPB under different loading rate conditions (i.e., different curing times).

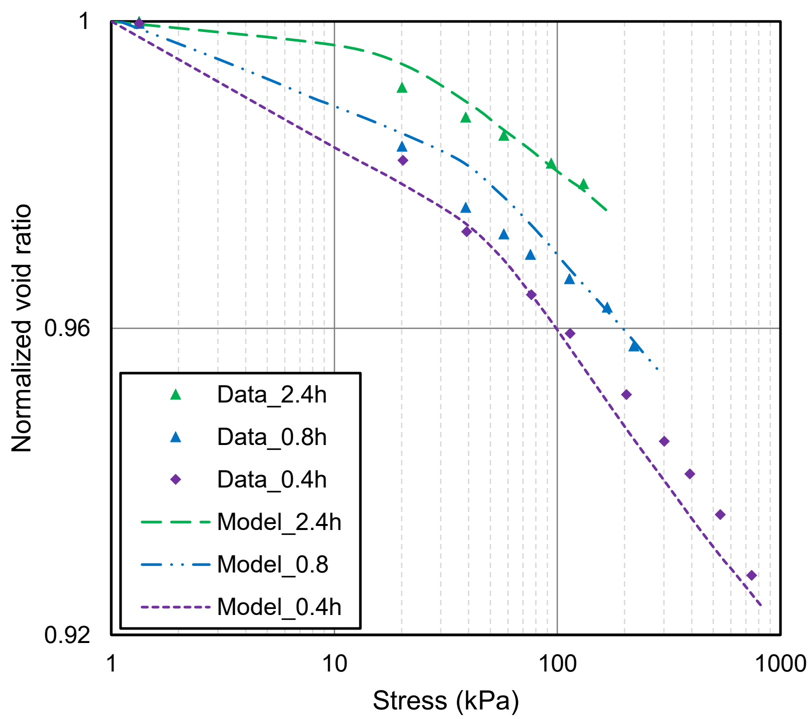

Figure 4.49. Comparison of simulation results with measured data from oedometer tests

4.4.4.4. Comparison with analytical results (Gibson's solution)

In order to quantitatively determine the pore pressure development in a layer of accreting sediment, Gibson (1958) presented a solution to the problem of pore pressure development in a layer of accreting sediment, which has a drained base and a constant filling rate. Gibson's solution is expressed in terms of the excess pore pressure, and the assumption that there is constant permeability, k, constant constrained modulus, M', and resulting constant coefficient of consolidation, c_v, is adopted.

$$u(z,t) = -\gamma_B z\left(1+\frac{v_{filling}z}{2c_v}\right)+\frac{\gamma_B v_{filling}}{2c_v}(\pi c_v t)^{-\frac{1}{2}}\exp\left(\frac{-z^2}{4c_v t}\right)\int_0^\infty \chi^2 \coth\frac{v_{filling}\chi}{2c_v}\sinh\frac{z\chi}{2c_v t}\exp\left(\frac{-\chi^2}{4c_v t}\right)d\chi \quad (4.176)$$

where γ_B is the unit weight of the CPB, z is the vertical coordinate, $v_{filling}$ is the backfilling rate, χ is an integration variable and c_v is the coefficient of consolidation (c_v = $M'k/\gamma_w$ with γ_w as the unit weight of water). Gibson's solution can be expressed in terms of the dimensionless time factor T_{factor} (i.e., $T_{factor} = v_{filling}t/c_v$).

Due to the similarity between the accretion of sediment and the backfilling process, Gibson's solution seems to provide a useful tool for assessing the consolidation of CPB. However, Gibson's solution has many limitations with respect to its application to CPB. The relevant limitations of the analytical solution in the application to mine backfill including the assumption of a constant coefficient of consolidation and no consideration of binder hydration have been identified by Fahey et al. (2010). In order to more explicitly demonstrate the characteristics of the developed model, Gibson's solution and the developed model are implemented over the same 2D geometric model. The width of the 2D geometric model is 10 m and the final filling height is set to be 30 m. Moreover, it is assumed that the coefficient of consolidation c_v is initially equal to each other for both Gibson's solution and the consolidation model. The unit weight, filling rate and initial coefficient of consolidation adopted from Gibson's solution is tabulated in Table 4.5. In this modeling, a 2D geometric model is used, the deformed geometry interface of COMSOL Multiphysics is adopted to simulate the backfilling process, and the automatic remeshing option is activated to avoid poor mesh quality.

Table 4.7. Input parameters to obtain analytical solution

Parameter	Value
Unit weight of CPB γ_B (kN/m3)	18
Coefficient of consolidation c_v (m2/d)	0.5
Backfilling rate $v_{filling}$ (m/h)	0.3

In order to clearly demonstrate the difference between the modeled results and analytical solution, 7 different values of the time factor (i.e., T_{factor} = 1, 10, 30, 60, 80, 90 and 100) are selected. As shown in Figure 4.50, it can be clearly observed that the predicted results of the multiphysics model diverge rapidly from the analytical solution with increases in the time factor. Moreover, the isochrones of the simulation results show a hysteresis compared with the corresponding isochrones of the analytical solution. The controlling mechanisms of the above mentioned phenomena are that, in reality, the constrained modulus and permeability show a strongly nonlinear evolution with the progression of the binder hydration and increase in backfill height (i.e., self-weight effect), which result in the variation of the coefficient of consolidation (as shown in Figure 4.51). In addition, pore water consumption due to binder hydration can lead to the reduction of PWP (i.e., self-desiccation), which can further increase the consolidation process in the CPB mass. Therefore, the Isochrone line of the developed model is lower than the corresponding line of the Gibson's solution. Through a comparison of the simulated results derived from the developed model against those from the Gibson's model, it can be observed that the developed model is able to reproduce the evolution of the consolidation properties such as coefficient of consolidation. Moreover, the Gibson's solution can only be used to assess the consolidation process of geomaterials under the self-weight effect, while the developed model can fully demonstrate the effects of coupled multiphysics on the consolidation behavior of CPB.

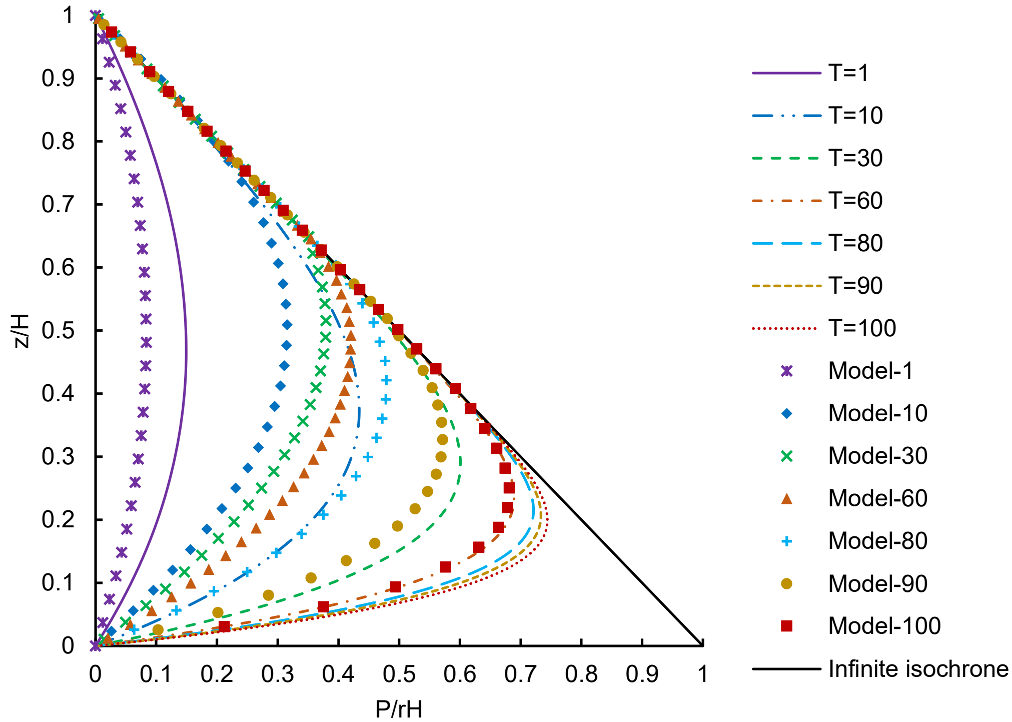

Figure 4.50. Comparison between simulation results and analytical solution

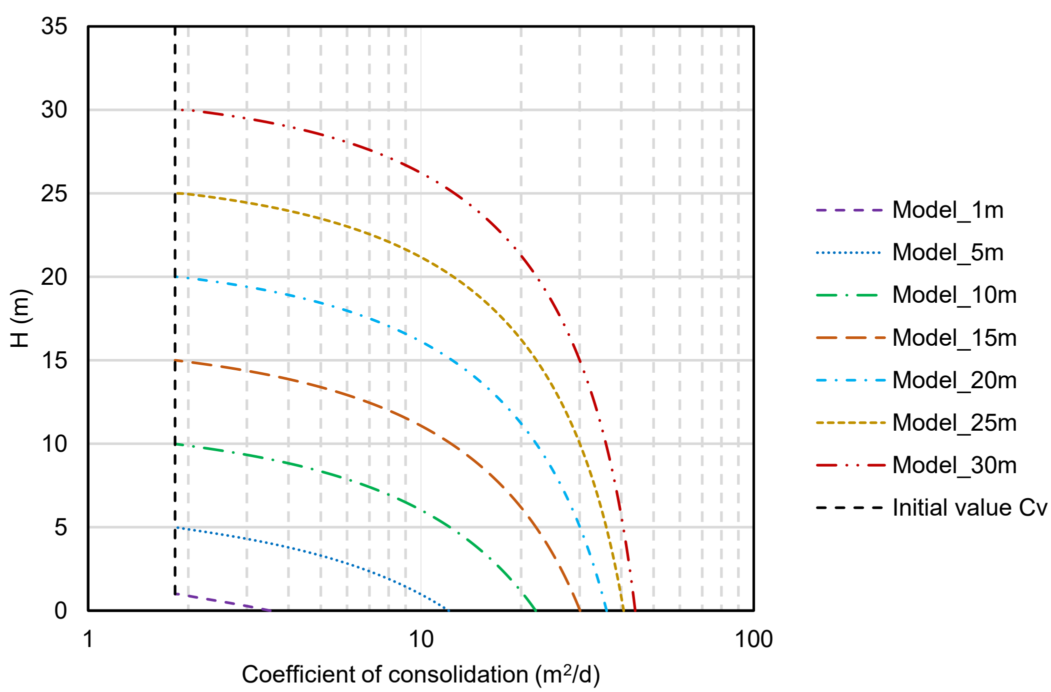

Figure 4.51. Evolution of coefficient of consolidation

4.4.5. Sensitivity analysis

The evolution of the parameters of the multiphysics model of the consolidation behavior will cause the variation of state variables (i.e., effective stress, pore water pressure, temperature, degree of hydration, etc.). Correspondingly, the consolidation behavior will be influenced. The idea of the sensitivity analysis is (1) to assess the importance of the parameters of the THMC- consolidation model; (2) to separate the coupled process to some extent and then the influence of each physical process on consolidation behavior of CPB can be detailed investigated. Therefore, the parameters from the 4 different physical (i.e., THMC) process are used to conduct the sensitivity analysis. Due to the restriction of paper length, the following parameters are selected (1) for the mechanical process, Biot's effective stress coefficient, α_{Biot}, (2) for the hydraulic process: the water retention model parameter, α_{WRC}, (3) for the chemical process, the time parameter, τ, of degree of binder hydration model in chemical shrinkage (i.e., Eqs. (4.111) and (4.112)), (4) for the thermal process (**T**), the heat source term, Q_{hydr},. All of the parameters mentioned above are time dependent, namely, these parameters will evolve with binder hydration. Therefore, in order to respectively investigate the influence of these parameters on CPB consolidation behavior, 3 different binder hydration rates (as shown in Figure 4.52) are employed to govern the evolution of the parameters. Specifically, the high (i.e., τ=0.7 [d]), medium (i.e., τ=1.4[d]) and low (i.e., τ=2.1[d]) binder hydration rates will be used to control the variation of target parameter with curing time, while the rest of parameters will share the medium hydration rate.

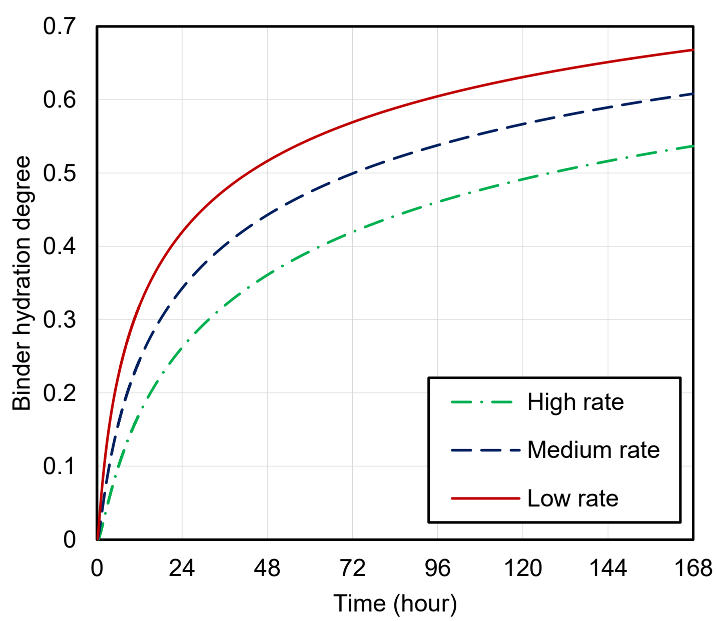

Figure 4.52. Comparison of 3 different hydration rates

The simulation of CUS cell test is used to investigate the sensitivity of the consolidation model. The detailed information about the CUS cell test and the simulation configuration are presented in the Section of "Consolidation Behavior of CPB Curing under Stress and Dynamic Thermal Loads". The geometry and mesh are presented in Figure 4.51. The initial values and boundary condition are listed in Table 4.5. In order to produce a smooth vertical displacement curve, the rate of change in applied air pressure is set to 100 kPa/day, namely, the applied pressure will reach 700 kPa when curing time approaches 7 days.

4.4.5.1. Mechanical process

The Biot's coefficient, α_{Biot}, is related directly to the effective stress which controls the mechanical behavior of CPB. As shown in Figure 4.53, the displacement curves firstly vary consistently with each other during the 1st day. Subsequently, the curves gradually deviate and the displacement curve associate with high α_{Biot} demonstrate the highest values. Therefore, the obtained results reveal that the variation of α_{Biot} with different binder hydration rates can generate significant influence on the consolidation behavior after first 24 hours, namely, the variation of effective stress becomes the dominant driving forces for consolidation after the very early age.

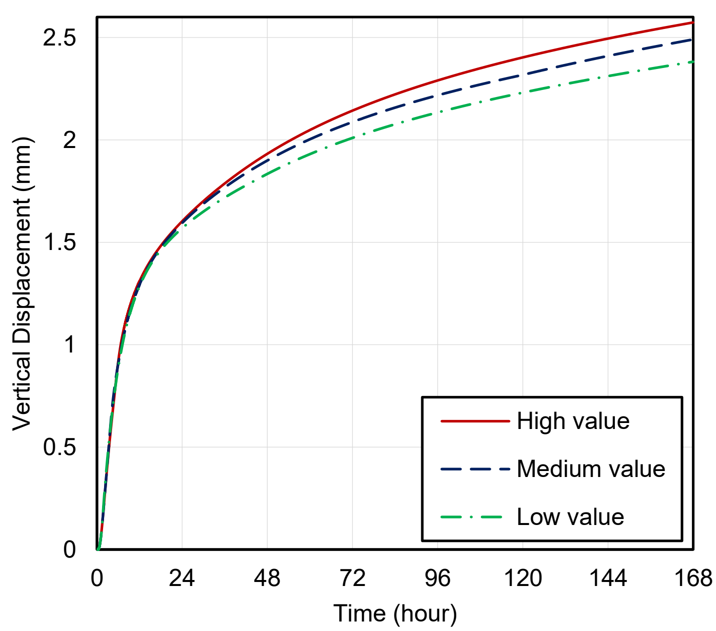

Figure 4.53. Mechanical process-influence of Biot's coefficient on the consolidation behavior of CPB

4.4.5.2. Chemical process

In comparison to the mechanical process, it is interesting to notice that the parameter τ in chemical shrinkage mainly contributes to the change of consolidation during the very early age (Figure 4.54). This is due to the fact that, as mentioned in the Section of Introduction, the relatively high hydration rate is able to consume more pore water at the very early age. Correspondingly, the chemical shrinkage plays a critical role in the consolidation behavior during this time period. As a result, the vertical displacement curves dramatically deviate from each other during the 1st day (as shown in Figure 4.54). However, after the very early age, it can be seen that the distinction between three curves gradually reduces with curing time. This is mainly attributed the facts that the aforementioned effective stress becomes the major contributor to the consolidation behavior. With the similar evolution of effective stress in CPB, the consolidation processes converge to each other to some extent.

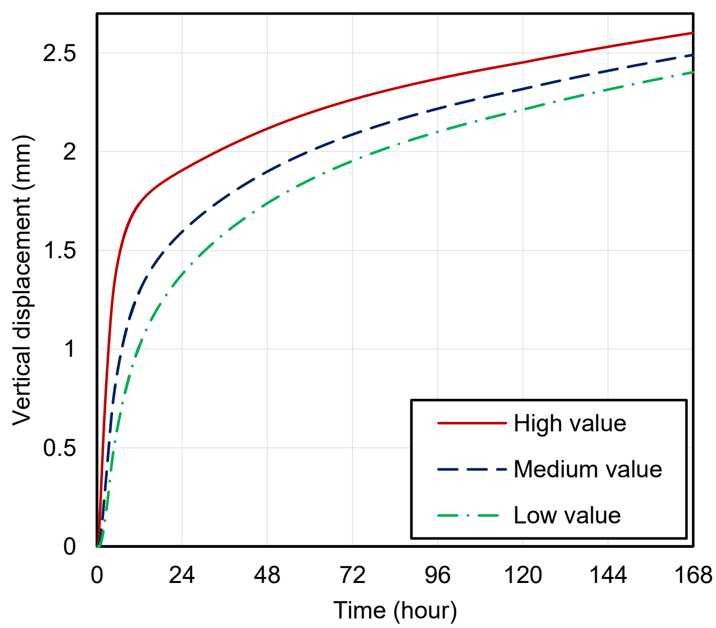

Figure 4.54. Chemical process-influence of chemical shrinkage on consolidation behavior of CPB

4.4.5.3. Thermal processes

The influence of thermal process on consolidation results from the evolution of temperature. Due to the fact that the geometry of CPB sample in CUS cell is relatively small (i.e., 20cm in height and 10cm in diameter), the temperature in CPB will be mainly controlled by the environmental temperature. As shown in Figure 4.44, the temperature of CPB with an initial temperature of 35 degrees reaches the room temperature after about 1st day. Therefore, in order to eliminate the influence of room temperature, the temperature boundary conditions are set to insulated ones for the thermal process. The simulation results are plotted in Figure 4.55. As expected, the CPB sample with high Q_{hydr} obtains higher vertical displacement with curing time. Moreover, the influence of Q_{hydr} is relatively uniform compared with the Biot's coefficient and degree of binder hydration. The reason for this can be explained by the temperature dependence of degree of binder hydration. Specifically, high value of Q_{hydr} can release more heat and result in higher temperature in CPB. Correspondingly, the higher temperature will accelerate the binder hydration (as shown in Eq. (4.109)). As a result, all of hydration-dependent material properties will evolve, which result in a relatively uniform variation of vertical displacement with curing time.

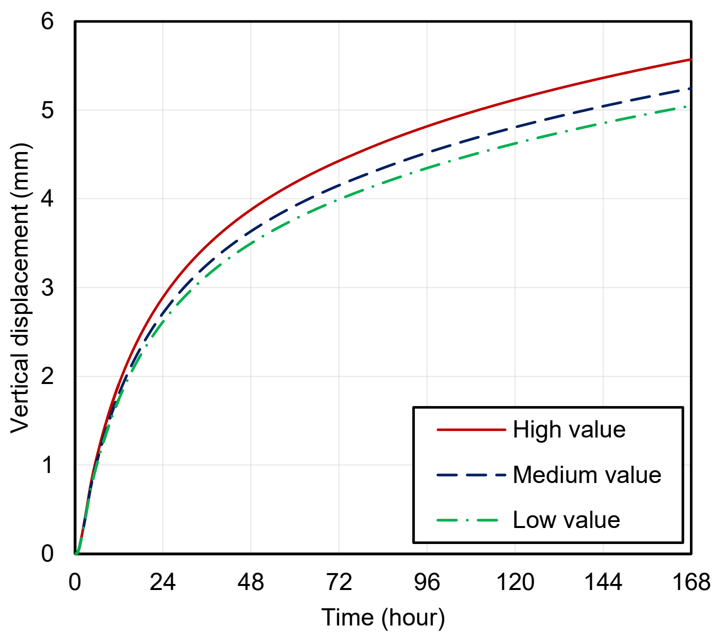

Figure 4.55. Thermal process-influence of heat source term on consolidation behavior of CPB

4.4.5.4. Hydraulic process

As a constitutive relation, the water retention model is used to describe the evolution of PWP with the change of water content (or degree of saturation). Therefore, the parameter α_{WRC} in Eq. (4.147) is selected to perform the sensitivity analysis. As can be seen in Figure 4.56, the displacement curves close to each other during the 1st day. Afterward, the deviation between these three curves appears gradually. Similar evolution trends of vertical displacements have been observed in the mechanical process (as shown in Figure 4.53). The obtained modeling results reveal that the variation of parameter α_{WRC} can impose significant impacts on the consolidation behavior after the very early age. This is due to the fact that the change of α_{WRC} will cause totally different evolutionary trends of PWP and effective stress in CPB. As aforementioned in the Section of Mechanical Process, the effective stress dominates the consolidation process after the very early age. Therefore, the influence of α_{WRC} on consolidation gradually becomes noticeable after this time period.

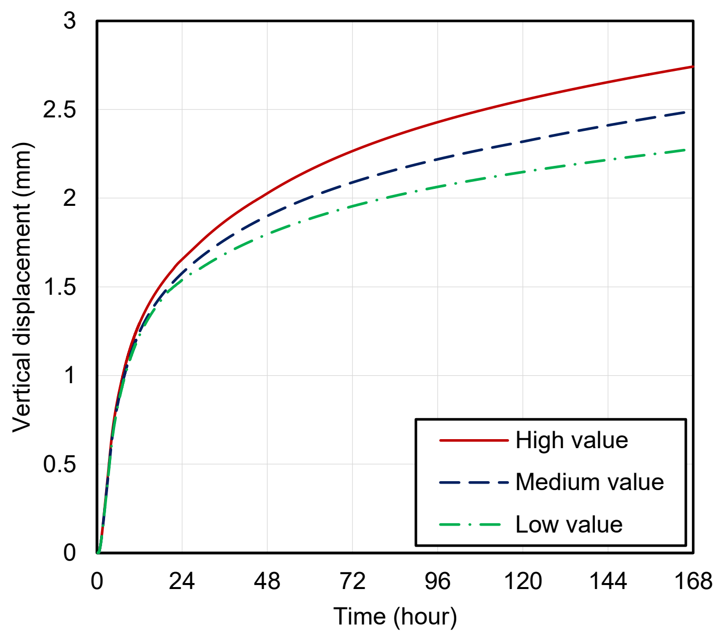

Figure 4.56. Hydraulic process-influence of parameter α of water retention model on the consolidation behavior of CPB

Based on the sensitivity analysis, it can be concluded that (1) the response of THMC-consolidation model is sensitive to the Biot's effective stress coefficient α_{WRC}, time parameter τ of degree of binder hydration in chemical shrinkage, heat source term Q_{hydr} and parameter α_{WRC} in water retention model. All of the tested parameters are able to impose significant impacts on CPB consolidation behavior, which indicates that the volume change of CPB induced by each physical process cannot be ignored. (2) Moreover, through the comparison between simulation results of different physical processes, the influence of the tested parameters on consolidation demonstrate different characteristics. Specifically, τ in chemical shrinkage mainly influences the consolidation behavior during the very early age, while the influences of α_{Biot} and α_{WRC} appear after the early ages. The Q_{hydr} in the thermal process shows a relatively uniform influence on CPB. The corresponding mechanisms controlling these phenomena are identified.

4.4.6. Summary and conclusion

The understanding and quantitative evaluation of the consolidation behavior of CPB are very important to the design of CPB in terms of safety and cost. In this paper, a multiphysics model for the consolidation behavior of CPB is developed. The following conclusions are derived from the results obtained in this study.

1. The consolidation behavior of CPB is dominated by strongly coupled multiphysics processes, including thermal (T), hydraulic (H), mechanical (M) and chemical (C) processes. Compared with the consolidation process of conventional gematerials (e.g., soil), the close interaction processes in the CPB mass not only govern the evolution of the material properties of CPB (e.g., the coefficient of permeability, elastic modulus, Poisson's ratio, etc.) but also demonstrate complex nonlinear consolidation characteristics.
2. Based on the principles of the continuity of pore space (i.e., the pore space changes related to the solid skeleton of the CPB and solid phase must equal the total volume change of the capillary water and pore air) and conservation of mass, energy and momentum, a 3D multiphysics model is developed to analyze and predict the consolidation behavior of CPB. For the constitutive relation, the manner of the heat transfer consists of conduction, convection and heat release by binder hydration in this study. For the hydraulic process, Darcy's law and water consumption by binder hydration are taken into account. For the mechanical process, the elastoplastic strain, thermal expansion and chemical shrinkage are considered. The chemical and strain hardening/softening parameters are incorporated into a double yield surface model (i.e., one that comprised a shear failure surface and a cap surface). For the chemical process, a binder hydration model is utilized to derive the water sink term and thermal source term in the modeling. Therefore, the proposed model is able to evaluate the coupled multiphysics dominated consolidation behavior of CPB.
3. The predictive ability of the developed model is verified through a comparison with the experimental results from tests performed in this study and reported laboratory data in the literature. Good agreement between the simulated results and experimental results is obtained. The comparison between the predicted data and measured values indicates that the multiphysics model has the ability to accurately

reproduce the consolidation process of CPB and predict the evolution of the multiphysics processes in CPB (i.e., temperature variation, PWP distribution, and deformation development). Furthermore, based on a comparison between the simulated and analytical results (Gibson's solution), the nonlinear evolution of the consolidation properties (e.g., coefficient of consolidation) and behavior of the CPB are clearly demonstrated. Hence, the developed 3D multiphysics model for the consolidation of CPB is a useful tool in the design of CPB.

4.4.7. References

Abdul-Hussain, N., Fall, M., 2011. Unsaturated hydraulic properties of cemented tailings backfill that contains sodium silicate. Eng Geol 123, 288-301.

Belem, T., Bussière, B., Benzaazoua, M., 2002. The effect of microstructural evolution on the physical properties of paste backfill. Proceedings of Tailings and Mine Waste'01 Fort Collins, Colorado, USA; p. 365-374.

Belem, T., El Aatar, O., Bussière, B., Benzaazoua, M., Fall, M., Yilmaz, E., 2006. Characterization of self-weight consolidated paste backfill. Proceedings of the 9th Int. Seminar on Paste and Thickened Tailings; p. 333-345.

Benzaazoua, M., Belem, T., Yilmaz, E., 2006. Novel lab tool for paste backfill. Can Min J 127, 31-31.

Brouwers, H., 2004. The work of Powers and Brownyard revisited: Part 1. Cem Concr Res 34, 1697-1716.

Carrier, W.D., Bromwell, L.G., and Somogyi, F., 1983. Design capacity of slurried mineral waste ponds. J Geotech Eng Div 109, 699-716.

Chen, W.F., Baladi, G.Y., 1985. Soil plasticity: theory and implementation. Elsevier, New York.

Choktaweekarn, P., Tangtermsirikul, S., 2009. A model for predicting coefficient of thermal expansion of cementitious Paste. Science Asia 35, 57-63.

COMSOL, 2015. COMSOL Multiphysics 5.1, http://www.comsol.com.

Côté, J., Konrad, J.-M., 2005. A generalized thermal conductivity model for soils and construction materials. Can Geotech J 42, 443-458.

Cui, L., Fall, M., 2015a. A coupled thermo-hydro-mechano-chemical model for cemented paste backfill. Tunn Undergr Sp Tech 50, 396-414.

Cui, L., Fall, M., 2015b. Multiphysics Modeling of the Behavior of Cemented Tailings Backfill Materials. Proceedings of International Conference on Civil, Structural and Transportation Engineering Ottawa, ON, Canada; p. (330) 331-337.

Cui, L., Fall, M., 2016. An evolutive elasto-plastic model for cemented paste backfill. Comput Geotech 71, 19-29.

Fahey, M., Helinski, M., Fourie, A., 2010. Consolidation in accreting sediments: Gibson's solution applied to backfilling of mine stopes. Geotechnique 60, 877-882.

Fall, M., Adrien, D., Celestin, J., Pokharel, M., Toure, M., 2009. Saturated hydraulic conductivity of cemented paste backfill. Miner Eng 22, 1307-1317.

Fall, M., Belem, T., Samb, S., Benzaazoua, M., 2007. Experimental characterization of the stress–strain behavior of cemented paste backfill in compression. J Mater Sci 42, 3914-3922.

Fall, M., Ghirian, A., 2014. Coupled thermo-hydro-mechanical-chemical evolution of cemented paste backfill and implications for backfill design-experimental results.

Proceedings of 11th International symposium on mining with backfill, MineFill 2014 Perth, Australia; p. 183-196.
Fall, M., Nasir, O., 2010. Mechanical behavior of the interface between cemented tailings backfill and retaining structures under shear loads. Geotech Geol Eng 28, 779-790.
Fall, M., Samb, S., 2009. Effect of high temperature on strength and microstructural properties of cemented paste backfill. Fire Safety J 44, 642-651.
Fine, R.A., Millero, F.J., 1973. Compressibility of water as a function of temperature and pressure. The Journal of Chemical Physics 59, 5529-5536.
Gawin, D., Majorana, C., Schrefler, B., 1999. Numerical analysis of hygro-thermal behavior and damage of concrete at high temperature. Mech Cohes-frict Mat 4, 37-74.
Gawin, D., Pesavento, F., Schrefler, B.A., 2006. Hygro-thermo-chemo-mechanical modeling of concrete at early ages and beyond. Part I: hydration and hygro-thermal phenomena. Int J Numer Meth Eng 67, 299-331.
Ghirian, A., Fall, M., 2013a. Coupled thermo-hydro-mechanical-chemical behavior of cemented paste backfill in column experiments. Part I: physical, hydraulic and thermal processes and characteristics. Eng Geol 164, 195-207.
Ghirian, A., Fall, M., 2013b. Experimental Investigations of the Thermo-Hydro-Mechanical-Chemical Behavior of Cemented Paste Backfill. Proceedings of 23rd World Mining Congr. Montreal, Canada; p. Paper #:378.
Ghirian, A., Fall, M., 2014. Coupled thermo-hydro-mechanical-chemical behavior of cemented paste backfill in column experiments: Part II: Mechanical, chemical and microstructural processes and characteristics. Eng Geol 170, 11-23.
Ghirian, A., Fall, M., 2015. Coupled Behavior of Cemented Paste Backfill at Early Ages. Geotech Geol Eng 33, 1141-1166.
Gibson, R., 1958. The progression of consolidation in a clay layer increasing in thickness with time. Geotechnique 8, 171-182.
Hansen, P.F., Pedersen, E.J., 1977. Maturity computer for controlled curing and hardening of concrete.
Helinski, M., 2008. Mechanics of mine backfill. University of Western Australia, Australia.
Helinski, M., Fahey, M., and Fourie, A., 2007. Numerical Modeling of Cemented Mine Backfill Deposition. J Geotech Geoenviron.
Helinski, M., Fahey, M., Fourie, A., 2010a. Behavior of cemented paste backfill in two mine stopes: measurements and modeling. J Geotech Geoenviron 137, 171-182.
Helinski, M., Fahey, M., Fourie, A., 2010b. Coupled two-dimensional finite element modeling of mine backfilling with cemented tailings. Can Geotech J, 1187-1200.
Hustrulid, W.A., Hustrulid, W.A., 2001. Underground mining methods: Engineering fundamentals and international case studies. Society for Mining, Metallurgy, and Exploration, Cororado, USA.
Jamali, M., 2013. Effect of binder content and load history on the one-dimensional compression of Williams mine cemented paste backfill, Department of Civil Engineering. University of Toronto, Toronto, ON, Canada.
Kamali, S., Moranville, M., Garboczi, E., Prené, S., Gérard, B., 2004. Hydrate dissolution influence on the young's modulus of cement paste. Proceedings of 5th International Conference of Fracture Mechanics of Concrete Structures, ; p. 631-638.
Le Roux, K.-A., 2004. In situ properties and liquefaction potential of cemented paste backfill. University of Toronto, Toronto, ON, Canada.
Li, L., 2013. Generalized solution for mining backfill design. Int J Geomech, 1-11.

Luckner, L., Van Genuchten, M.T., Nielsen, D., 1989. A consistent set of parametric models for the two‐phase flow of immiscible fluids in the subsurface. Water Resources Research 25, 2187-2193.
Mualem, Y., 1976. A new model for predicting the hydraulic conductivity of unsaturated porous media. Water Resour Res 12, 513-522.
Nasir, O., Fall, M., 2008. Shear behavior of cemented pastefill-rock interfaces. Eng Geol 101, 146-153.
Neville, A.M., Brooks, J.J., 1987. Concrete technology. Longman Scientific & Technical Harlow, New York.
Orejarena, L., Fall, M., 2010. The use of artificial neural networks to predict the effect of sulphate attack on the strength of cemented paste backfill. Bulletin of Engineering Geology and the Environment 69, 659-670.
Pokharel, M., Fall, M., 2010. Coupled thermochemical effects on the strength development of slag-paste backfill materials. J Mater Civil Eng 23, 511-525.
Pokharel, M., Fall, M., 2013. Combined influence of sulphate and temperature on the saturated hydraulic conductivity of hardened cemented paste backfill. Cem Concr Compos 38, 21-28.
Poole, J.L., Riding, K.A., Folliard, K.J., Juenger, M.C., Schindler, A.K., 2007. Methods for calculating activation energy for Portland cement. Aci Mater J 104, 303-311.
Powers, T.C., Brownyard, T.L., 1947. Studies of the physical properties of hardened Portland cement paste. J. ACI 43, 249-336.
Reddy, J.N., 2006. An introduction to the finite element method, 3rd ed. The McGraw-Hill, New York, USA.
Rotta, G.V., Consoli, N.C., Prietto, P.D.M., Coop, M.R., Graham, J., 2003. Isotropic yielding in an artificially cemented soil cured under stress. Geotechnique 53, 493-501.
Saebimoghaddam, A., 2010. Liquefaction of early age cemented paste backfill. University of Toronto, Canada.
Schindler, A.K., 2004. Effect of temperature on hydration of cementitious materials. Aci Mater J 101, 72-81.
Schindler, A.K., Folliard, K.J., 2003. Influence of supplementary cementing materials on the heat of hydration of concrete, Adv. in Cem. and Concr. IX Conf. American Society of Civil Engineers, pp. 17-26.
Seneviratne, N.H., Fahey, M., Newson, T.A., Fujiyasu, Y., 1996. Numerical modeling of consolidation and evaporation of slurried mine tailings. Int J Numer Anal Met 20, 647-671.
Simms, P., Grabinsky, M., 2009. Direct measurement of matric suction in triaxial tests on early-age cemented paste backfill. Can Geotech J 46, 93-101.
Somerton, W.H., Chu, S.L., Keese, J.A., 1973. Thermal behavior of unconsolidated oil sands. Soc Pet Eng J 14, 513-521.
Thomas, H.R., Sansom, M.R., 1995. Fully coupled analysis of heat, moisture, and air transfer in unsaturated soil. Journal of Engineering Mechanics 121, 392-405.
Van Genuchten, M.T., 1980. A closed-form equation for predicting the hydraulic conductivity of unsaturated soils. Soil Sci Soc Am J 44, 892-898.
Wang, Y., Fall, M., 2014. Initial temperature-dependence of strength development and self-desiccation in cemented paste backfill that contains sodium silicate. Cem Concr Compos 67, 101-110.
William Sutherland, 1893. The viscosity of gases and molecular force. Philosos. Mag. 5, 36:223, 507-531.
Wood, D.M., Doherty, J.P., 2014. Coupled Chemical Shrinkage and Consolidation: Some Benchmark Solutions. Transport Porous Med 105, 349-370.

Wu, D., Fall, M., Cai, S.J., 2012. Coupled modeling of temperature distribution and evolution in cemented tailings backfill structures that contain mineral admixtures. Geotech Geol Eng 30, 935-961.
Yilmaz, E., 2010. Investigating the hydrogeotechnical and microstructural properties of cemented paste backfills using the versatile CUAPS apparatus. Université du Québec, Canada.
Yilmaz, E., Belem, T., Benzaazoua, M., 2014. Effects of curing and stress conditions on hydromechanical, geotechnical and geochemical properties of cemented paste backfill. Eng Geol 168, 23-37.
Yilmaz, E., Belem, T., Bussière, B., Mbonimpa, M., Benzaazoua, M., 2015. Curing time effect on consolidation behavior of cemented paste backfill containing different cement types and contents. Constr Build Mater 75, 99-111.
Yilmaz, E., Benzaazoua, M., Belem, T., Bussière, B., 2009. Effect of curing under pressure on compressive strength development of cemented paste backfill. Miner Eng 22, 772-785.

4.5. Paper V: Multiphysics Modeling of Arching Effects in Fill Mass

Published in Computers and Geotechnics 83 (2017) 114-131

Liang Cui, Mamadou Fall

Abstract

A numerical modeling study is conducted to assess and gain a better understanding of the arching effects of field cemented tailings backfill (CTB). An integrated multiphysics model is developed that can illustrate and capture the changes in the material properties of CTB, consolidation behavior of CTB mass, and the shear behavior at the CTB/Rockwall interface. The predictive ability of the model has been successfully verified with comparisons of the predicted results with monitoring data taken from a series of field studies.The model is then used to simulate a series of applications that are relevant to CTB in practice.

Keywords: Mine; Cemented paste backfill; Tailings; Interface; Multiphysics; Arching.

4.5.1. Introduction

Soil arching, a phenomenon commonly encountered in geotechnical engineering, was described by Terzaghi (1943) as "one of the most universal phenomena encountered in soils both in the field and in the laboratory". He defined the arching effect as the transfer of pressure from a yielding mass of soil onto the adjoining stationary parts(Terzaghi 1943). Soil arching, which involves load transfer and stress redistribution, should be and has been taken into account in the analysis of many geotechnical issues (Iglesia et al. 1999), such as earth pressure on retaining walls (e.g., Take and Valsangkar 2001; Goel and Patra 2008), vertical stress and support requirements above tunnels and other underground situations (e.g.,Ono and Yamada 1993; Iglesia et al. 1999), and mine tailings backfilling (e.g., Fahey et al. 2009; Li 2014).

Assessing the arching effects of mine cemented tailings fill or backfill (CTB) is a complex task due mainly to the changing properties of the CTB medium and the complex coupled thermal (T; e.g., temperature, heat transfer), hydraulic (H; e.g., pore water pressure (PWP), suction, fluid flow), mechanical (M; e.g., stress, deformation, strength) and chemical (C; e.g.; binder chemical reaction) processes that occur in CTB and their effect on its geotechnical behavior (Ghirian and Fall 2013; Fall et al. 2015). CTB is essentially made of tailings (human-made soils; that is, materials that remain after minerals of value are removed), binder (e.g., Portland cement, blast furnace slag, fly ash), and water. After preparation and placement, the hardening CTB must satisfy certain requirements of mechanical stability to ensure a safe working environment for underground mining personnel. To assess the in-situ mechanical performance of CTB under static loading condition, the uniaxial compressive strength (UCS) of hardened CTB is often adopted in practice (Fall et al. 2015). Based on previous studies on CTB (Belem et al. 2002; Cui and Fall 2016b), it has been found that the curing stress (mechanical factor), temperature (thermal factor), suction associated with moisture content (hydraulic factor) and binder type and chemistry (chemical factor) (i.e., the coupled THMC processes) govern the UCS development. Moreover, to prevent the CTB from flowing into the active mining zone, retaining structures (called barricades or bulkheads) are commonly constructed in the drawpoints (access points at the base of the stopes). It is critical that the horizontal pressure or stress developed by the CTB is not greater than the resistance of the retaining structure because its failure can have drastic work safety consequences and significant financial ramifications (Doherty 2015; Fall et al. 2015). Therefore, an understanding of the stress development and distribution in CTB structures is critically important for the optimal geotechnical design of CTB structures and barricades.

Field investigations (e.g., Thompson et al. 2009; Li et al. 2014) have previously confirmed that the vertical stress in the CTB is significantly less than the overburden stress due to the arching effect, which primarily results from the consolidation process of the CTB, and the improvement of CTB/rock mass interface properties with binder hydration. The consolidation of the CTB results in the development of settlement and effective (horizontal) stresses, thus enabling shear stresses to develop at the CTB-rock interface (Fahey et al. 2009). As a result, the stress in the CTB will be redistributed and the vertical stress gradually becomes less than the self-weight stress (i.e., the arching effect takes place). Therefore, it is evident that to investigate and evaluate arching and the stress distribution in CTB, it is necessary to understand and assess the changes in the interface shear stress and the consolidation of CTB during and after filling. This development of the interface shear stress and consolidation behavior is strongly influenced by the THMC processes (Figure 4.57) in CTB (Fall and Nasir 2010). It is well known that the consolidation and interface shear behavior of CTB are not only affected by mechanical loads, but also by thermal, hydraulic and chemical (binder hydration) processes or their various combinations. Reproducing these THMC processes and assessing the arching effect in a laboratory on a CTB structure that measures several dozens of meters or in the field are technically difficult and extremely costly. Consequently, it is clear that a proper assessment and understanding of the arching effect of CTB and the resulting stress redistribution require integrated multiphysics models that can illustrate and capture the changes in the material properties of CTB (thus, a THMC model), consolidation behavior of the evolutive CTB mass, and the shear behavior at the interface between the CTB with changes in its properties and the rock wall. However, to date, no studies have addressed these issues and there is no model that can describe the aforementioned mechanisms and thus enable a proper assessment of the arching effects of CTB.

Indeed, most of the previous modeling studies devoted to arching in CTB are based on analytical approaches (e.g., Aubertin et al. 2003; Li and Aubertin 2009) which provide an estimate of the total and effective stresses under specific assumptions including: (1) uniformly distributed vertical stress along any of the horizontal planes (Aubertin et al. 2003), and (2) constant material properties, such as adhesion, interface friction angle, Poisson's ratio and elastic modulus (Aubertin et al. 2003; Fahey et al. 2009). Therefore, the disadvantages of using analytical methods are obvious. First, the assumptions, such as uniformly distributed vertical stress along any of the horizontal planes, do not represent the real stress distribution in CTB. Secondly, the analytical solutions do not capture the effect of the coupled THMC processes on the material properties and consolidation behavior of the CTB as well as on the CTB interface. Consequently, because of these limitations, the analytical approaches are unsuitable for a proper assessment and understanding of the arching effects and stress distribution in CTB. Apart from these analytical based studies, very few other studies (e.g., Helinski et al. 2007; Doherty and Wood 2016) have been carried out that numerically investigate the arching in CTB. For instance, Helinski et al. (2010) numerically investigated arching in CTB based on a 2D consolidation model that considers THM couplings. However, none of these numerical studies incorporate and take into account the influence of the coupled THMC processes on the material properties and consolidation behavior of the CTB as well as on the CTB interface. In consideration of the research gaps, the main objectives of this paper are therefore as follows:

(i) to develop and validate integrated multiphysics models that can capture and illustrate the changes in the material properties of CTB, consolidation behavior of CTB with changing properties, and shear behavior at the interface between the CTB with changes in its properties and the rock wall;
(ii) to assess the arching and stress redistributions in the CTB mass in various practical field conditions by using the developed model.

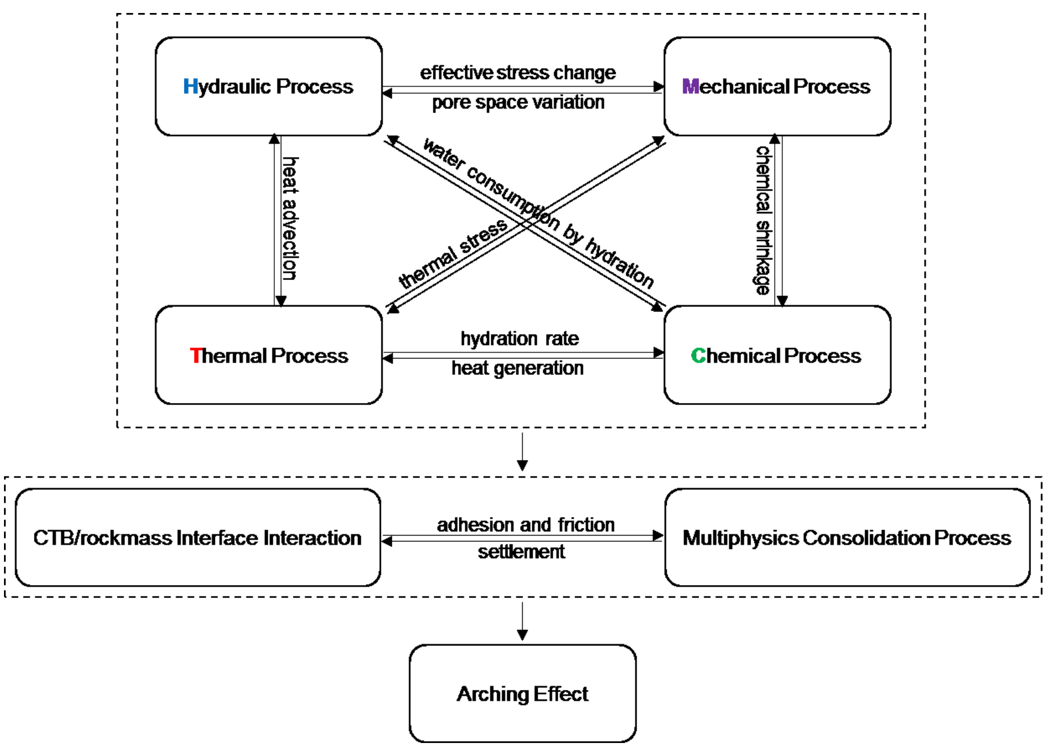

Figure 4.57. Schematic diagram of key controlling mechanisms of arching effect in fill mass

4.5.2. Model development

4.5.2.1. Modeling Assumptions

CTB is assumed to be a porous medium with changing properties, which consists of solid (i.e., binder, tailings and hydrates), liquid (i.e., capillary water) and gaseous (i.e., pore air) phases. In this study, the following main assumptions are adopted:

(i) the solid particles are incompressible, but the pore structure of the CTB can deform;
(ii) there is thermodynamic equilibrium in the representative elementary volume (REV), i.e. locally, the multiphases are at the same temperature. For heat conduction, Fourier's law is valid;
(iii) there is seepage discharge in the CTB which obeys Darcy's law; and
(iv) strain due to tensile stress is positive.

4.5.2.2. Formulation of multiphysics model

The developed model consists of three integrated components, including a fully coupled THMC model to illustrate and capture the changes in the CTB material properties, a multiphysics model of the consolidation behavior and a model of the changes in the rock/backfill interface. The formulation of these models is described in the following subsections.

4.5.2.2.1. Coupled THMC Model

Four balance equations, including fluid (pore water and air), mass (Eqs. (4.177) and (4.178)), momentum (Eq. (4.179)) and energy (Eq. (4.180)) conservation equations are adopted in the fully coupled THMC model. The formulation of the THMC model is summarized below, but a detailed description of the formulation is provided in (Cui and Fall 2015a).

$$\phi S\frac{\partial \rho_w}{\partial t}+\phi\rho_w\frac{\partial S}{\partial t}+S\rho_w\left[\frac{\partial \varepsilon_v}{\partial t}+\frac{(1-\phi)}{\rho_s}\frac{\partial \rho_s}{\partial t}\right]-\nabla\cdot\left(\phi S\rho_w k\frac{k_{rw}}{\mu_w}\nabla\left(P_w-\rho_w g\right)\right)=\phi S\left(\frac{\rho_w}{\rho_s}S-1\right)$$
$$\times\left\{2m_{hc0}\left(0.187x_{C_3S}+0.158x_{C_2S}+0.665x_{C_3A}+0.2130x_{C_4AF}\right)\left\{\left(\frac{\tau}{t_e}\right)^{\beta}\left(\frac{\beta}{t_e}\right)\xi\exp\left[\frac{E_a}{R}\left(\frac{1}{273+T_r}-\frac{1}{273+T}\right)\right]\right\}\right\} \quad (4.177)$$

$$\phi(1-S)\frac{\partial \rho_a}{\partial t}-\phi\rho_a\frac{\partial S}{\partial t}+(1-S)\rho_a\left[\frac{(1-\phi)}{\rho_s}\frac{\partial \rho_s}{\partial t}+\frac{\partial \varepsilon_v}{\partial t}\right]-\nabla\cdot\phi(1-S)\rho_a k\frac{k_{ra}}{\mu_a}\nabla\left(P_a-\rho_a g\right)=\left[(1-S)\phi S\rho_a/\rho_s\right]$$
$$\times\left\{2m_{hc0}\left(0.187x_{C_3S}+0.158x_{C_2S}+0.665x_{C_3A}+0.2130x_{C_4AF}\right)\left\{\left(\frac{\tau}{t_e}\right)^{\beta}\left(\frac{\beta}{t_e}\right)\xi\exp\left[\frac{E_a}{R}\left(\frac{1}{273+T_r}-\frac{1}{273+T}\right)\right]\right\}\right\} \quad (4.178)$$

$$\nabla \cdot \left(\frac{\partial \boldsymbol{\sigma}}{\partial t}\right) + \frac{\partial\left[\left(1-\phi\right)\rho_s + \phi S \rho_w + \phi\left(1-S\right)\rho_a\right]}{\partial t}\boldsymbol{g} = 0 \tag{4.179}$$

$$\left[\left(\frac{1}{1+e}\right)\rho_s C_s + \frac{e}{1+e} S \rho_w C_w + \frac{e}{1+e}\left(1-S\right)\rho_a C_a\right]\frac{\partial T}{\partial t} + \nabla \cdot \left(-k_{eff} \nabla T\right) + \left(\rho_w C_w \mathbf{v}^{rw} + \rho_a C_a \mathbf{v}^{ra}\right)\cdot \nabla T$$
$$= \left(H_c \cdot X_c + 461 \cdot X_{slag} + 1800 \cdot x_{CaO/FA} \cdot X_{FA}\right) C_b \left(\frac{\tau}{t_e}\right)^{\beta} \cdot \left(\frac{\beta}{t_e}\right) \cdot \xi \cdot \exp\left[\frac{E_a}{R}\left(\frac{1}{273+T_r} - \frac{1}{273+T}\right)\right] \tag{4.180}$$

where ϕ is the porosity; S denotes the degree of saturation; ρ_i is the density (i refers to air, water and solid); t is the elapsed time; ε_v is the volumetric strain; k is the intrinsic permeability of CTB; k_{rw} and k_{ra} respectively denote the relative permeability of pore water and pore air; μ_w and μ_a is the dynamic viscosity of pore water and pore air; P_w and P_a represent the pore-water pressure and pore-air presure; $\boldsymbol{g}$ is the gravitational acceleration; m_{hc0} is the initial cement mass; x_i is the weight ratio of the compounds in cement in terms of the total cement content(i refers to cement compounds); ξ is the binder hydration degree; τ , t_e and β are the parameters of the binder hydration model and respectively represent time parameter, equivalent age, and hydration shape parameter; E_a is the apparent activation energy; R is the ideal gas constant; T and T_r refers to the current temperature of CTB and the reference temperature; σ is the (macroscopic) total stress tensor; e is the void ratio; C_i is the specific heat capacity (i refers to air, water and solid); k_{eff} is the effective thermal conductivity; $\mathbf{v}^{rw}$ and $\mathbf{v}^{ra}$ stand for Darcy's velocity of pore water and pore air, respectively; H_c refers to the total heat released by cement hydration; X_i is the weight proportion of the binder components to the total binder weight (i refers to cement, fly ash and blast furnace slag); C_b is the apparent binder density with respect to the total volume of the CTB mixture. To solve the balance equations (i.e., Eqs. (4.177), (4.178), (4.179) and (4.180)), the constitutive relations and material properties are needed. The detailed information on the development of constitutive relations and determination of prediction functions of material properties are provided in (Cui and Fall 2015a; 2016a)

4.5.2.2.2. Multiphysics Model of Consolidation Behavior

To quantitatively assess the volume changes in CTB, pore space continuity (i.e., volume change of solid phase and skeleton must equal the volume change of pore water and pore air) is used to develop the multiphysics consolidation model. The consolidation equation can be derived as follows and is given in detail in (Cui and Fall 2015b; 2016c):

$$\begin{aligned}
&\left\{\left[SP_w+(1-S)P_a\right]\frac{1-2\upsilon}{E}\frac{\partial\alpha_{Biot}}{\partial\xi}-\frac{\left[\sigma+\alpha_{Biot}\left[SP_w+(1-S)P_a\right]\right]}{E}\left\{\frac{9[1-2\upsilon]}{E}\frac{\partial E}{\partial\xi}+18\frac{\partial\upsilon}{\partial\xi}\right\}\right.\\
&\left.-\alpha_{Biot}\left(P_a-P_w\right)\frac{1-2\upsilon}{E}\left\{\left[1-S_e\left(P_w,P_a,\xi\right)\right]\frac{\partial\theta_r}{\partial\xi}+\left(\frac{e}{1+e}-\theta_r\right)\frac{\partial S_e}{\partial\xi}\right\}-\frac{(1+e)\left(v_{ch-w}+v_{ab-w}\right)R_{n-w/hc}}{(w/c)v_w+v_c+\left(1/C_m-1\right)v_{tailings}}\right\}\frac{\partial\xi}{\partial t}\\
&+\frac{1-2\upsilon}{E}\frac{\partial\sigma}{\partial t}+\alpha_{Biot}\frac{1-2\upsilon}{E}\left\{S-\left(P_a-P_w\right)\left(\frac{e}{1+e}-\theta_r\right)\frac{\partial S_e}{\partial P_w}\right\}\frac{\partial P_w}{\partial t}+\frac{\partial\lambda_p}{\partial t}\frac{\partial Q_{CTB}}{\partial I_1}+\alpha_{Ts}\frac{\partial T}{\partial t}\\
&+\alpha_{Biot}\frac{1-2\upsilon}{E}\left\{(1-S)-\left(P_a-P_w\right)\left(\frac{e}{1+e}-\theta_r\right)\frac{\partial S_e}{\partial P_a}\right\}\frac{\partial P_a}{\partial t}\\
&=-\left\{\frac{1}{1+e}+\alpha_{Biot}\left(P_a-P_w\right)\frac{1-2\upsilon}{e^2(1+e)^2E}\left[S_e e+(1+e)^2\left(1-S_e\right)\theta_r\right]\right\}\frac{\partial e}{\partial t}
\end{aligned} \tag{4.181}$$

where υ and E denote the Poisson's ratio and elastic modulus, respectively; α_{Biot} is the Biot's effective stress coefficient; S_e refers to the effective degree of saturation (i.e., S_e = $\left(\theta-\theta_r\right)/\left(\theta_s-\theta_r\right)$, θ , θ_s and θ_r are the volumetric, saturated and residual water contents, respectively); v_w , v_{ch-w} , v_{ab-w} , v_c and $v_{tailings}$ denote the specific volume of the capillary water, chemically combined water, physically absorbed water, cement and tailings, respectively; $R_{n-w/hc}$ is the mass ratio of the chemically combined water and hydrated cement; w/c is the water to cement ratio; C_m denotes the binder content; λ_p is a non-negative plastic multiplier; Q_{CTB} is a plastic potential function; I_1 is the first stress invariant; α_{Ts} is the coefficient of the thermal expansion (CTE) of the CTB solid phase.

4.5.2.2.3. Evolutive Interface Model

To describe the interface shear behavior between CTB and the surrounding rock wall in stopes, an evolutive elastoplastic interface model is developed in this study. The relative displacement can be decomposed into elastic and plastic parts (i.e., $d\Delta$ = $d\Delta_e$ + $d\Delta_p$). The incremental form of the constitutive relation can be expressed in terms of the effective stress $\boldsymbol{\sigma}'$, and the elastic part of the relative displacement Δ_e :

$$d\boldsymbol{\sigma}'=\boldsymbol{K}^e d\boldsymbol{\Delta}_e=\boldsymbol{K}^e\left(d\boldsymbol{\Delta}-d\boldsymbol{\Delta}_p\right) \tag{4.182}$$

where K^e is the interface stiffness matrix which contains the shear K_s^e, normal K_n^e, and tensile K_t^e stiffnesses. The tensile stiffness is assumed identical to the normal stiffness (i.e., $K_t^e = K_n^e$) in this study. The interface stiffness is determined as shown in the Section 4.5.2.3.5. Biot's theory is applied to define the effective stress in terms of the total stress, $\boldsymbol{\sigma}$, and the average pore pressure, $\bar{P}$, through Biot's effective stress coefficient α_{Biot}:

$$\boldsymbol{\sigma}' = \boldsymbol{\sigma} - \alpha_{Biot}\bar{P}\boldsymbol{\delta}_{ij} \tag{4.183}$$

$$\text{with } \begin{cases} \alpha_{Biot} = 1 - K_b / K_s \\ \bar{P} = S_e P_w + (1 - S_e) P_a \end{cases}$$

where $\boldsymbol{\delta}_{ij}$ is Kronecker's delta; K_s is the bulk modulus of the tailings, and depends on the composition of the tailings; K_b is the bulk modulus of the CTB matrix, and will change as the binder hydration and consolidation process progress. K_b can be determined with the elastic modulus E and Poisson's ratio υ (i.e., $K_b = E/3(1-2\upsilon)$). Detailed information on determining the elastic modulus and Poisson's ratio is provided in the Section 4.5.2.3.2. In this study, the van Genuchten model (Van Genuchten 1980) (with time-dependent model parameters) is adopted to determine the relation between the effective degree of saturation, S_e, and matric suction, $(P_a - P_w)$:

$$S_e = \frac{1}{\left\{1 + \left[\alpha_{WRC}(P_a - P_w)\right]^{\frac{1}{1-m_{WRC}}}\right\}^{m_{WRC}}} \tag{4.184}$$

where α_{WRC} and m_{WRC} are the material parameters of the water retention curve, which change with binder hydration. These two material parameters are described in the Section 4.5.2.3.3.

To characterize the yield behavior of the interface, the Drucker-Prager (D-P) yield criterion is adopted to describe the initial yield surface in this study.

$$F_{intf}(I_1, \sqrt{J_2}, \xi, \Delta_\kappa) = \sqrt{J_2} + \alpha_{intf}(\xi, \Delta_\kappa)\left[I_1 - C_{intf}(\xi)\right] = 0 \tag{4.185}$$

where I_1 and J_2 respectively denote the first stress invariant and the second deviatoric stress invariant; and α_{intf} and C_{intf} are the material parameters of D-P criterion, which can be expressed by interface friction angle δ_{intf}, interface adhesion c_{intf}, cumulative plastic displacement Δ_κ, and hydration degree ξ.

$$\alpha_{intf} = R_{intf1}\left\{\left[1 - \exp(-R_{intf2}\Delta_\kappa)\right] + \left[R_{intf3}\Delta_\kappa \exp(-R_{intf4}\Delta_\kappa)\right]\right\} + \frac{2\sin\delta_{intf}(\xi)}{\sqrt{3}\left[3 + \sin\delta_{intf}(\xi)\right]} \tag{4.186}$$

$$C_{intf} = 3c_{intf}(\xi)\cdot\cot\delta_{intf}(\xi) \tag{4.187}$$

where Δ_κ represents the cumulative plastic displacement (i.e., $\Delta_\kappa = \int\sqrt{(2/3)d\boldsymbol{\Delta}_p d\boldsymbol{\Delta}_p}$), and R_{intf1}, R_{intf2}, R_{intf3} and R_{intf4} are the material constants. Detailed information on how these four parameters are determined will be provided in the Section 4.5.2.3.5. For the assessment of CTB/rock mass interface properties, the following equations are proposed to characterize the changes in the interface friction angle δ_{intf} and adhesion c_{intf} :

$$\delta_{intf} = \phi_B(\xi) - F_\delta(\xi)\left|\phi_r - \phi_B(\xi)\right| / R_L \tag{4.188}$$

$$c_{intf} = c_B(\xi)\left[1 - F_c(\xi)/R_L\right] \tag{4.189}$$

where ϕ_r is the internal friction angle of the surrounding rock; c_B and ϕ_B denote the cohesion and internal friction angle of the CTB, respectively, which will change with the degree of binder hydration ξ ; R_L is the roughness index of the rock wall (i.e., the ratio of the true length of the fracture profile and its apparent projected length on the mean topographic direction of the profile (Gokhale and Underwood 1990)); and F_δ and F_c are the fitting parameters and will be discussed in the Section 4.5.2.3.5. From the proposed interface friction angle model (Eq. (4.188)) and adhesion model (Eq.(4.189)), it can be seen that the effect of binder hydration (i.e., the degree of binder hydration ξ), material properties of CTB (i.e., cohesion c_B and internal friction angle ϕ_B) and rock mass (i.e., rock-wall roughness R_L and rock internal friction angle ϕ_r) are considered. Therefore, the proposed interface friction angle model and adhesion model can capture the evolution of material properties of CTB/rock mass interface. Moreover, based on previous studies on interface analysis (e.g., Raous 2011; Hu et al. 2012), it has been found that interface adhesion is dependent on the interface friction angle (i.e., the coupling between interface adhesion and friction angle). As indicated in the Eq. (4.188) and (4.189), both interface adhesion and interface friction angle are expressed as functions of rock-wall surface roughness R_L . Hence, the effect of interface friction angle on the interface adhesion can be captured by substituting Eq. (4.188) into Eq. (4.189) with the aid of rock-wall surface roughness R_L . Therefore, the proposed interface adhesion and friction angle model can capture the interaction between interface adhesion and friction angle as well.

To assess the incremental plastic displacement, the non-associated flow rule is adopted to derive the evolutive interface model. The plastic potential function Q_{intf} is defined in terms of interface dilation angle ψ_{intf} :

$$Q_{intf} = \sqrt{J_2} + \frac{2\sqrt{3}\sin\left(\psi_{intf}\right)}{3\left[3 + \sin\left(\psi_{intf}\right)\right]} I_1 \tag{4.190}$$

Previous experimental studies on the rock/CTB interface (Nasir and Fall 2008; Fall and Nasir 2010; Koupouli et al. 2016) have demonstrated that the binder hydration, normal pressure and rock surface roughness have a significant influence on the dilation behavior of the interface. Therefore, the following equation is proposed to depict the variation of the dilation angle of the rock/CTB interface.

$$\psi_{intf} = \begin{cases} K_{\Psi} R_L / \exp\left(w_{\Psi} \boldsymbol{\sigma}'_n\right) & \boldsymbol{\sigma}'_n \leq 0 \\ \varphi_{intf} & \boldsymbol{\sigma}'_n > 0 \end{cases} \tag{4.191}$$

where $\boldsymbol{\sigma}'_n$ is the effective normal stress that acts on the interface; w_{ψ} equals to the inverse of one GPa; and K_{ψ} is a material parameter that is dependent on the binder hydration and will be determined in the Section 4.5.2.3.5.

4.5.2.3. Determining the model parameters

In this section, several prediction functions or equations are proposed to determine the parameters of the developed multiphysics model. The prediction functions contain a number of model coefficients or fitting parameters, which also enable to take into account the different types of CTB (different binder content, w/c ration, tailings type, water chemistry, etc.). The values of these coefficients or fitting parameters have been determined for the CTBs studied in this work. For any type of CTB to be simulated or studied, the values of these coefficient or fitting parameters need to be determined, because the fitting parameters or coefficients can vary with the type of CTB.

4.5.2.3.1. Chemical processes (C)

To quantitatively characterize the progress of the binder hydration, the following exponential equation proposed by Schindler and Folliard (2003) is applied because it has been proven to accurately predict the development of binder hydration in CTB materials (Wu et al. 2012; Cui and Fall 2015a; 2016a; c)

$$\xi(t_e) = \xi_u \cdot \exp\left[-\left(\frac{\tau}{t_e}\right)^{\beta}\right] \tag{4.192}$$

$$\text{with} \begin{cases} \xi_u = \dfrac{1.031 \cdot w/c}{0.194 + w/c} + 0.5 \cdot X_{FA} + 0.30 \cdot X_{slag} \\ t_e = \int_0^t \exp\left[\dfrac{E_a}{R}\left(\dfrac{1}{T_r} - \dfrac{1}{T}\right)\right] dt \\ E_a(T) = \begin{cases} 33{,}500 + 1{,}470 \times (293.15 - T) & T < 293.15K \\ 33{,}500 & T \geq 293.15K \end{cases} \end{cases}$$

where ξ_u denotes the ultimate degree of hydration, and E_a is the apparent activation energy.

4.5.2.3.2. Mechanical processes (M)

Previous studies on the changes in the elastic modulus of CTB have observed that the elastic modulus is a function of the binder content C_m, water to cement ratio w/c, degree of cement hydration ξ and void ratio e. Hence, the following equation is proposed to predict the changes in the stiffness of the CTB.

$$E\left(\xi, C_m, w/c, e\right) = \left(v_1 E_T + v_2 E_{u\_p}\xi\right)\left[\frac{f_{E1}\left(1-e\right)^{f_{E2}\xi^{f_{E3}}}}{1+f_{E4}e_0}\right] \tag{4.193}$$

where E_T denotes the elastic modulus of the tailings; E_{u_p} is the ultimate stiffness of the dense cement paste; v_1 and v_2 respectively stand for the volume fraction of tailings and the ultimate cement paste with respect to the total volume of the solid phase; e_0 is the initial void ratio of the CTB; and f_{E1}, f_{E2}, f_{E3} and f_{E4} are the fitting parameters. To predict the volume fractions, v_1 and v_2, the following equations are derived from the previous work on CTB by Cui and Fall (2015a):

$$v_1 = \frac{\left(1/C_m - 1\right)v_{tailings}}{\left(w/c\right)v_w + v_c + \left(1/C_m - 1\right)v_{tailings} - \left(2v_w - v_{ch-w} - v_{ab-w}\right)R_{n-w/hc}\xi} \tag{4.194}$$

$$v_2 = \frac{\left[v_c + \left(v_n + v_{ab-w}\right)R_{n-w/hc}\right]\xi}{\left(w/c\right)v_w + v_c + \left(1/C_m - 1\right)v_{tailings} - \left(2v_w - v_{ch-w} - v_{ab-w}\right)R_{n-w/hc}\xi} \tag{4.195}$$

For the chemically combined water and the physically absorbed water, it has been proven that the specific volume of these two types of water (i.e., v_{ch-w} and v_{ab-w}) does not vary for all types of cement (Brouwers 2004), and equals to 0.72 cm^3/g and 0.90 cm^3/g, respectively. v_c and $v_{tailings}$ are the specific volume of cement and tailings, and the values of these two parameters depend on the selected type of cement and tailings. $R_{n-w/hc}$ is the mass ratio of the chemically combined water and hydrated cement, which can be expressed in terms of the mass fraction x_i of the clinker compositions:

$$R_{n-w/hc} = 0.187x_{C_3S} + 0.158x_{C_2S} + 0.665x_{C_3A} + 0.2130x_{C_4AF} \tag{4.196}$$

Based on the reported experimental data on the elastic modulus of cement paste (Janotka 2001; Lura et al. 2003; Ye et al. 2004), the fitting parameter E_{u_p} in Eq.(4.193) can be determined by using a regression analysis and is equal to 28.49 GPa. The void ratio and elastic modulus of the CTB reported by Ghirian and Fall (2014) were used to determine the fitting parameters f_{E1}, f_{E2}, f_{E3} and f_{E4}. Based on the results of the regression analysis, f_{E1} =177.5, f_{E2} =4.363, f_{E3} =-1.047 and f_{E4} =3000. As shown in

Figure 4.58, the predicted values of the elastic modulus show good agreement with the experimental data and the coefficient of determination, R^2, equals 0.95.

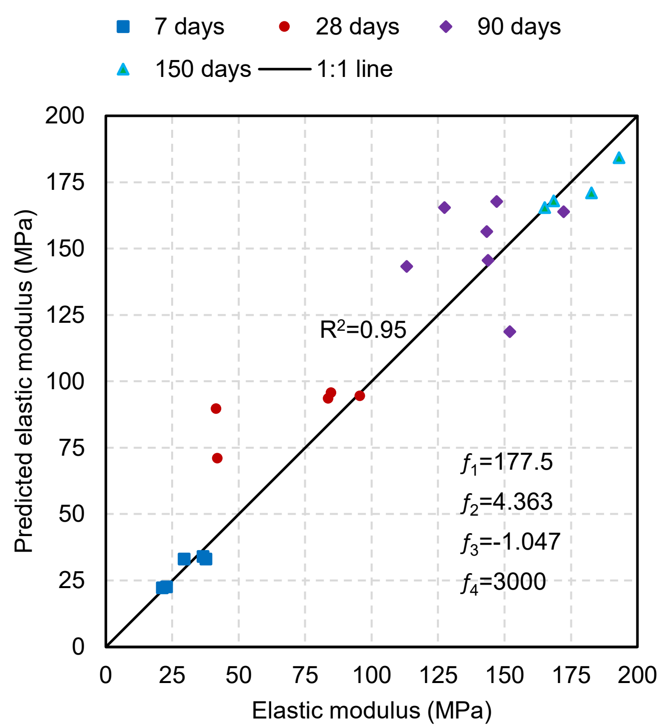

Figure 4.58. Experimental data versus predicted values of elastic modulus (experimental data from (Ghirian and Fall 2014))

In terms of the changes in the cohesion, the following equation is proposed to determine the influence of the cement content and degree of hydration (i.e., curing time) on cohesion (kPa):

$$c_B = c_{B1} C_m \xi^{c_{B2}} \quad (4.197)$$

where c_{B1} and c_{B2} are the fitting parameters of CTB cohesion. Based on the experimental data on cohesion reported in (Donovan 1999; Ghirian and Fall 2014; Cui and Fall 2015a), c_{B1}=9507 kPa and c_{B2}=3.2 in this study. As shown in Figure 4.59, a good agreement between the experimental data and predicted values of cohesion is obtained and the corresponding coefficient of determination equals 0.96. It should be underlined that this cohesion c_B is an effective stress strength parameter. For the measurement of effective cohesion at laboratory scale, triaxial compression tests (Marinho et al. 2016; Xing et al. 2016) or direct shear test (e.g., Borana et al. 2016; Bravo et al. 2016) can be conducted on CTB samples cured at different times. for which the ongoing binder hydration reactions have been stopped and the free pore water has been removed (dry sample) before testing. Two main techniques, namely the solvent replacement drying technique or method of oven-drying at 50°C (quick drying at 50°C does not cause cracking (Ghirian and Fall 2015) or changes in the crystal structure of hydration product (e.g., C-S-H) (Hunnicutt 2013)), can be applied to stop the binder hydration and remove the free pore water of CTB to reach full desaturation of the sample. Therefore, when mechanical tests (e.g. conventional direct shear, DST) are performed on these dry CTB samples with different curing time, the total stress and effective stress are identical and thus the obtained strength parameter can be considered as effective stress strength parameter (e.g. effective stress cohesion). Moreover, the corresponding curing time and adopted mixture recipe can be used to calculate hydration degrees ξ based on the hydration degree model (i.e., Eq.(4.197)). Then, the relation between cohesion c_B and degree of binder hydration ξ can be developed through regression analysis on the experimental data. Similarly, the internal friction angle ϕ_B and the following model parameters can be determined through the same approach. The prediction function of internal CTB friction angle ϕ_B can be found in (Cui and Fall 2016a).

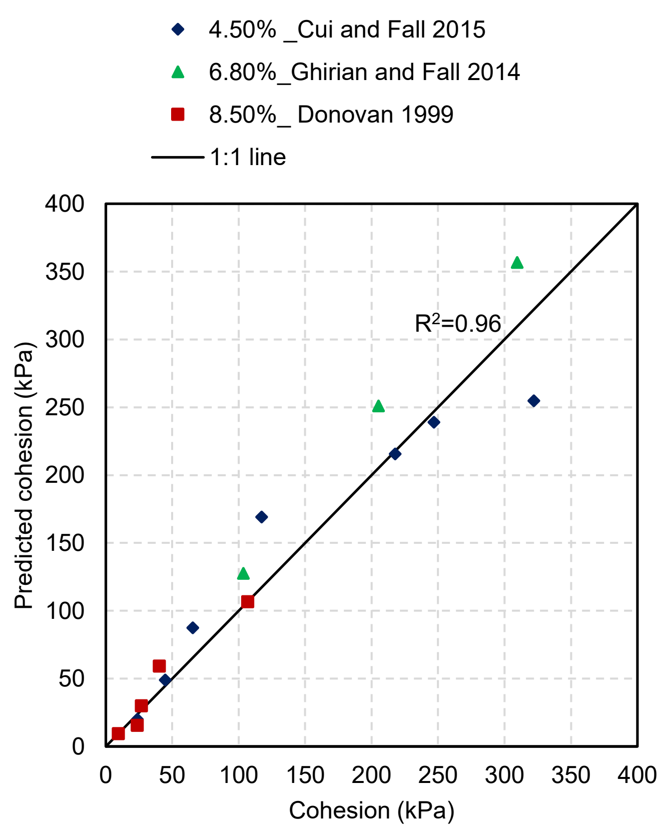

Figure 4.59. Experimental data versus predicted values of cohesion

4.5.2.3.3. Hydraulic processes (H)

In hydraulic processes, the hydraulic conductivity directly governs the pore fluid migration in CTB. The changes in the saturated hydraulic conductivity K_{sat} are closely related to the variations in the void ratio e of CTB. The equation for predicting K_{sat} which was proposed by Carrier et al. (1983) is adopted:

$$K_{sat} = C_k \frac{e^{D_k}}{1+e} \tag{4.198}$$

where C_K and D_K denote the material constants. Cui and Fall (2016c) recommended C_K =1.963e-5 cm/s and D_K =12.96 as the two material constants. As for the changes in the void ratio, it can be predicted by using the developed multiphysics model of the consolidation behavior (i.e., Eq.(4.181)).

To determine the time-dependent (induced by the progress of the binder hydration) changes of the residual water content, θ_r, the function proposed by Abdul-Hussain and Fall (2011) is adopted to describe the effect of binder hydration on θ_r.

$$\theta_r = R_{r1} \cdot \exp\left(-R_{r2} \cdot \xi\right) \tag{4.199}$$

where R_{r1} and R_{r2} are the fitting constants. The fitting constants in (Abdul-Hussain and Fall 2011), R_{r1} =0.01314 and R_{r2} =7.538, are adopted.

To determine the time-dependent changes in the α_{WRC} and m_{WRC} in the water retention model (i.e., Eq. (4.184)), the measured water retention curves in (Abdul-Hussain and Fall 2011; Ghirian and Fall 2013) of CTB samples with different curing times are used to determine the two parameters. The following functions are proposed:

$$m_{WRC} = f_{m1}\xi^{f_{m2}} + f_{m3} \tag{4.200}$$

$$\alpha_{WRC} = f_{\alpha 1} \exp\left(f_{\alpha 2}\xi\right) \tag{4.201}$$

where f_{m1}, f_{m2}, f_{m3}, $f_{\alpha 1}$ and $f_{\alpha 2}$ are the fitting parameters. Based on the experimental data reported in (Abdul-Hussain and Fall 2011; Ghirian and Fall 2013), f_{m1} =0.0415, f_{m2} =4.231, f_{m3} =0.4073, $f_{\alpha 1}$ =0.2103 kPa^{-1} and $f_{\alpha 2}$ =-6.921 are obtained through regression analysis.

4.5.2.3.4. Thermal processes (T)

The thermal conductivity is needed to characterize the heat transfer between the CTB mass and surrounding rock. Previous studies on CTB materials (Abbasy 2009; Ghirian and Fall 2013) have found that the tailings type and degree of saturation predominantly influence the thermal conductivity. Therefore, binder hydration induced water consumption can affect the thermal conductivity of CTB. To describe the changes in the thermal conductivity k_{eff}, the following equation proposed by Somerton et al. (1974) is adopted:

$$k_{eff} = k_{dry} + \sqrt{S_e}\left(k_{sat} - k_{dry}\right) \tag{4.202}$$

$$with \quad \begin{cases} k_{sat} = k_{tailings}^{1-\phi} k_w^{\phi} \\ \\ k_{dry} = k_{tailings}^{1-\phi} k_a^{\phi} \end{cases}$$

where k_{sat} and k_{dry} respectively denote the thermal conductivity of the porous media in the saturated state and a completely dry condition; $k_{tailings}$, k_w and k_a denote the thermal conductivity of the tailings, water and air, respectively; ϕ is the porosity of CTB.

4.5.2.3.5. Interface parameters

To determine the changes in the interface stiffness (i.e., K_s^e and K_n^e) induced by binder hydration, the experimental data in (Nasir and Fall 2008; Fall and Nasir 2010) are used to develop the following functions that predict the changes in the interface stiffness:

$$K_s^e = c_{s1}\xi^{c_{s2}} - c_{s3}\xi \tag{4.203}$$

$$K_n^e = c_{n1}\exp\left(c_{n2}\xi\right) \tag{4.204}$$

where c_{s1}, c_{s2}, c_{s3}, c_{n1} and c_{n2} are the fitting parameters. Based on a regression analysis of the experimental data collected in (Nasir and Fall 2008; Fall and Nasir 2010), the following fitting parameter values are used: c_{s1} =0.252 GPa/m, c_{s2} =2, c_{s3} =0.012 GPa/m, c_{n1}=0.831 GPa/m and c_{n2} =3.535. A comparison between the experimental data and predicted results of the interface shear and normal stiffnesses are presented in Figure 4.60 and Figure 4.61. The corresponding coefficient of determination is 0.91 and 0.96, respectively.

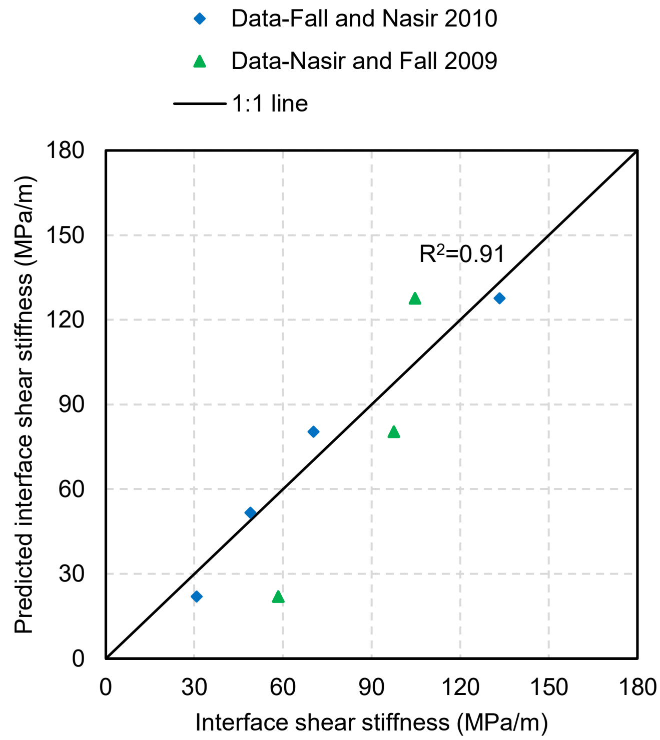

Figure 4.60. Experimental data versus predicted values of interface shear stiffness

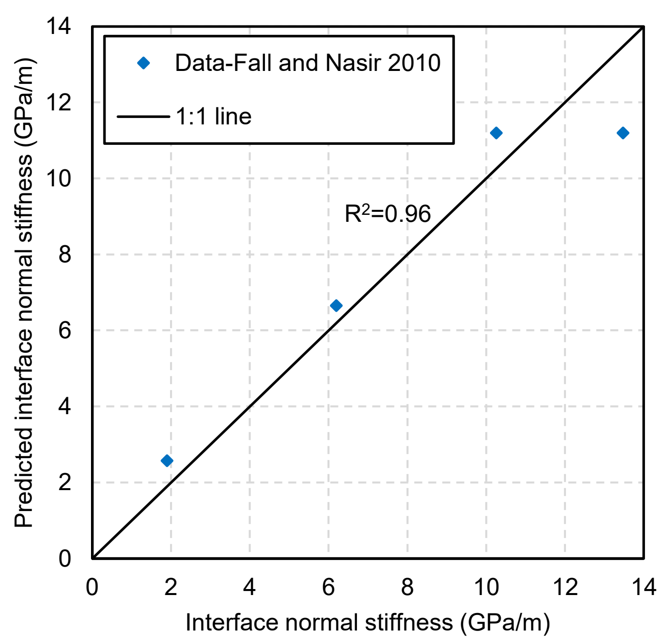

Figure 4.61. Experimental data versus predicted values of interface normal stiffness

Based on the reported experimental data from DSTs on CTB/rock samples with different curing time (Fall and Nasir 2010), the fitting parameter F_δ of interface friction angle in Eq. (4.188) can be determined and described by using the following equation:

$$F_\delta(\xi) = n_1\xi^2 + n_2\xi \quad (4.205)$$

where n_1 and n_2 are the fitting parameters; n_1 =-3.954 and n_2 =2.935, based on the experimental data published in (Fall and Nasir 2010). As shown in Figure 4.62, there is a good agreement (R^2=0.91) between the experimental data and predicted results.

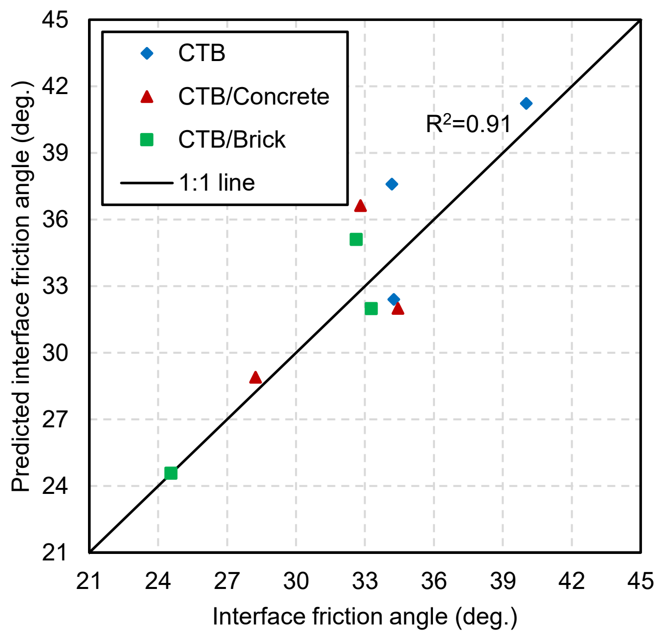

Figure 4.62. Experimental results versus predicted values of interface friction angle (based on (Fall and Nasir 2010))

The dimensionless parameter F_c in Eq. (4.189) is determined by developing a quadratic polynomial equation as follows:

$$F_c = n_3\xi^2 + n_4\xi \quad (4.206)$$

where n_3 and n_4 are the fitting parameters; n_3 =0.919 and n_4 =0.732, based on the experimental data reported in (Fall and Nasir 2010).

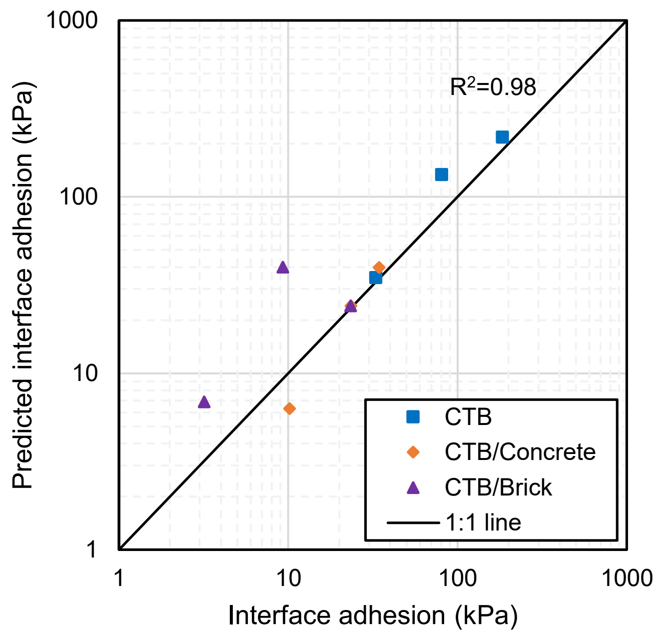

Figure 4.63. Experimental results versus predicted values of interface adhesion (experimental data from (Fall and Nasir 2010))

To determine the hardening and softening parameters R_{intf1}, R_{intf2}, R_{intf3} and R_{intf4} in Eq.(4.186), The experimental data from direct shear test (DST), specifically from (Nasir and Fall 2008; Fall and Nasir 2010), are adopted in this study. For determination of the four parameters, the yield function (i.e., Eq. (4.185)) is used. The stress invariants (I_1 and J_2) adopted in yield function can be determined by the principle stresses which can be back calculated by the measured shear stress of DST and applied normal stress. In addition, the yield function parameter C_{intf} can be determined by Eq. (4.187). As a result, the unknown yield function parameter α_{intf} can be calculated for CTB with different curing time. After that, the prediction function of α_{intf} (i.e., Eq.(4.186)) can be used to perform data fitting through regression analysis. Consequently, the four parameters R_{intf1}, R_{intf2}, R_{intf3} and R_{intf4} in Eq.(4.186) can be determined for CTB with different curing, and the corresponding prediction function for each parameter is derived as follows:

$$R_{intf1} = b_1\xi^2 + b_2\xi + b_3 \tag{4.207}$$

$$R_{intf2} = b_4\xi^{b_5} \tag{4.208}$$

$$R_{intf3} = b_6\xi^{b_7} \tag{4.209}$$

$$R_{intf4} = b_8\xi^2 + b_9\xi + b_{10} \tag{4.210}$$

where b_i is the fitting constant (i =1 to 10). After carrying out a regression analysis on the experimental data taken from (Nasir and Fall 2008; Fall and Nasir 2010), b_1 =-0.1068,

b_2 =-0.0027, b_3 =0.18, b_4 =80.984, b_5 =0.4226, b_6 =497.03, b_7 =3.3332, b_8 =-54.091, b_9 =109.9 and b_{10} =20.564. It can be seen in Figure 4.64 that there is fairly good consistency between the predicted results and experimental results of the hardening and softening parameters.

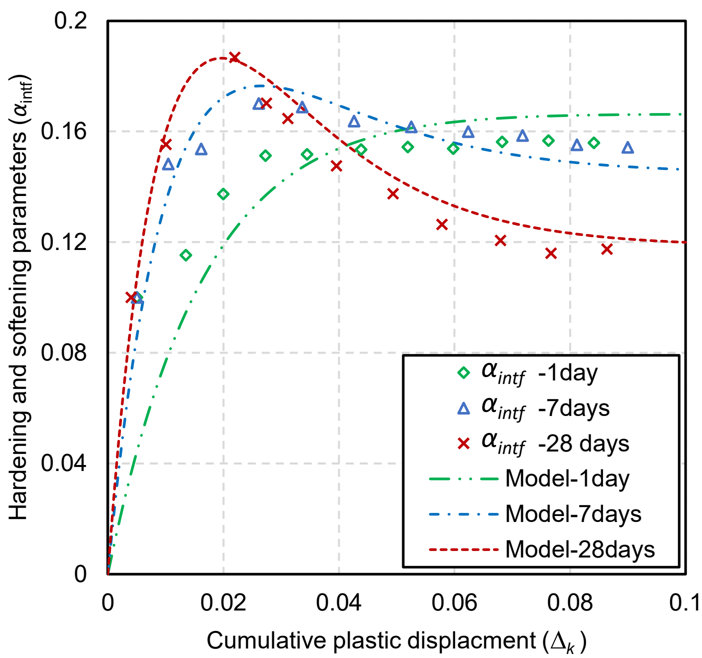

Figure 4.64. Comparison between predicted results and experimental data of hardening/softening parameters for different curing times (experimental data from (Nasir and Fall 2008))

To determine the fitting parameter, K_ψ , for the dilation angle (i.e., Eq.(4.191)), the vertical deformation versus horizontal strain curves published in (Nasir and Fall 2008; Fall and Nasir 2010) are used to develop the relevant prediction models. Based on a regression analysis, the following prediction function is proposed:

$$K_\psi\left(\xi\right) = w_1 \xi^{w_2} \tag{4.211}$$

where w_1 and w_2 are the fitting constants. In this study, w_1 =196.29° and w_2 =6.44 based on the regression analysis on the reported data (Nasir and Fall 2008; Fall and Nasir 2010).

4.5.3. Model validation

To validate the integrated multiphysics model that was developed to assess arching in CTB, the predicted results obtained were compared with those of the in-situ experimental results obtained from a series of monitoring programs on CTB in the field.

The selected field studies or field CTB structures differ from each other in terms of the stope geometry, drainage condition, mixture recipe, and backfilling rate and strategy. Hence, a comparison between the modeling results and in-stope experimental results can demonstrate the quality of the predictive ability of the developed model under different backfilling conditions in the field. The implementation of the proposed model was made possible by utilizing COMSOL Multiphysics (a FEM commercial code (Comsol 2015)). To implement the interface interaction model, a user-defined PDE interface and a modified spring foundation boundary (called the contact pair) are integrated in this study. For analysis of total stress and effective stress in stope, the corresponding vertical stress is adopted in the following model validation (Section 4.5.3) and model application (Section 4.5.4). Detailed information on the input parameters, initial values and boundary conditions considered in the field studies are listed in Table 4.8, and adopted mix recipe for each field study is tabulated in Table 4.9.

Table 4.8. Input parameters, initial values and boundary conditions

Property	Values or B.C.
Rock mass property	
Unit weight (kN/m3)	25
Elastic modulus (GPa)	30
Poisson’s ratio	0.3
Backfilling sequences	2
Initial value	
Initial temperature of CTB (°C)	35
Initial temperature of rock (°C)	35
CTB module	
Mechanical	Interface model
Hydraulic	No flow
Thermal	Continuity
Rock mass module	
Mechanical	Fixed at bottom Roller at side wall
Hydraulic	N/A
Thermal	Dirichlet B.C. (temperature)

*B.C.: boundary condition

Table 4.9. Mix recipe adopted in field studies

Mix recipe	Field study 1	Field study 2	Field study 3
Water to cement ratio	6.1 (plug) 14.2 (residual fill)	10.8	6.8
Cement content (%)	7 (plug) 3 (residual fill)	3.1	5

4.5.3.1. Field Study 1: Undrained Backfill with Plug Layer

To study the changes in the internal stresses that develop in the CTB mass, Belem et al. (2004) conducted in-situ measurements at the Doyon Gold Mine (Canada). The stope chosen for measurement had a width of 11 m and a height of 29 m. Their backfilling method first consisted of the construction of a plug with a cement content of 7% and solid content of 70%, and after 3-day of curing, the rest of the stope was backfilled with cemented paste backfill with a cement content of 3% and solid content of 70%. The bulk unit weight of the backfill was 18 kN/m^3, and the plug and residual fill had the same initial porosity of 0.54. The backfilling strategy is shown in Figure 4.65.

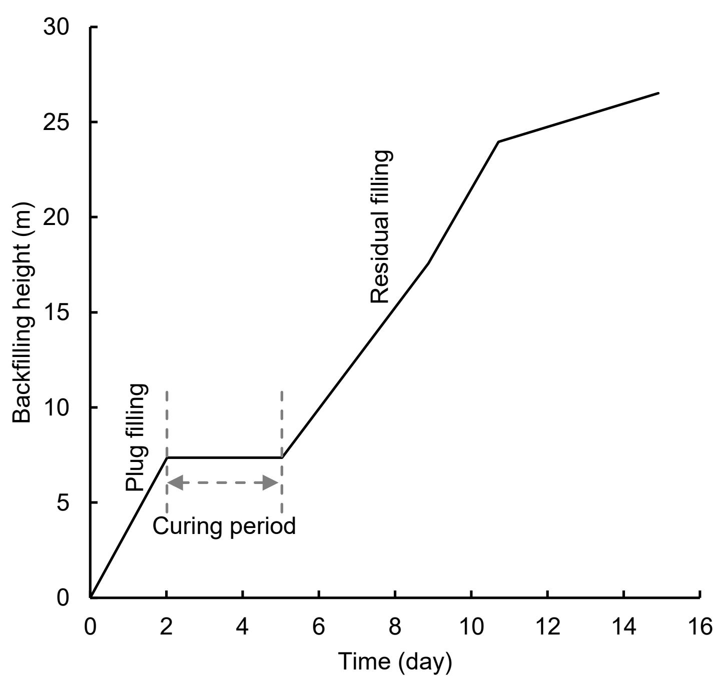

Figure 4.65. Backfilling strategy at Doyon Gold Mine by Belem et al. (2004)

Earth pressure cells (TPC series) were used to monitor the changes in the total stress, and respectively installed at the bottom (elevated 0.6 m) and the plug/residual fill interface (elevated 7.3 m) (Figure 4.66). The Doyon Gold Mine tailings contained a clay fraction of more than 40%. There was very limited drainage through the CTB due to the clayey nature of its tailings. Hence, the pore water pressure (PWP) was not measured during the monitoring and the influence of drainage on the PWP is neglected. Consequently, for the model implementation, the barricade structure and water drainage boundary condition are not applied in this case study.

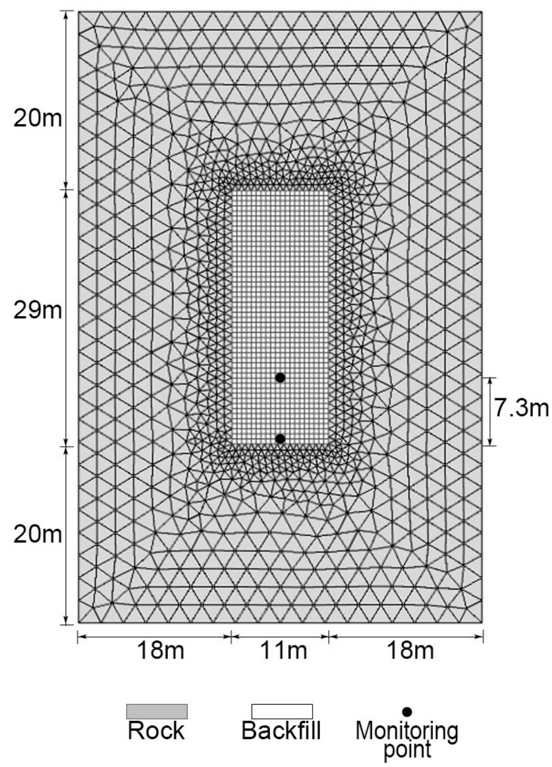

Figure 4.66. Mesh and geometry of simulated stope at Doyon Gold Mine

As can be seen in Figure 4.67, both the predicted results and monitoring data demonstrated that: (1) initially, the total stress in CTB increases with backfilling height, while the discrepancy between total stress and self-weight stress (i.e., the overburden stress= $\rho_{CTB} \cdot g \cdot h_{filling}$ with backfilling density ρ_{CTB} and filling height $h_{filling}$) (mainly induced by arching) gradually appears; (2) during the curing period (after 2 days), the total stress shows a slight decrease, which is attributed to the stress transfer from CTB mass to surrounding rock mass via interface interaction with the development of consolidation in CTB; (3) when the second sequence of the filling commenced (after 5 days), the total stress at the bottom monitoring point increases immediately. However, the increase in total stress is relatively limited, especially after 10 days. When the backfilling operation was completed, the self-weight stress is almost 3 times that of the measured and predicted total stresses; and (4) for the monitoring point at the plug/residual interface (see dashed line in Figure 4.67), the changes in the total stress are similar to those on the floor of the stope, namely, there are no apparent changes in the total stress after about 10 days. As shown in Figure 4.67, the agreement between the modeling results and monitoring data is fairly good. Thus, the model can capture well the changes in the in-situ total stress in the CTB under undrained condition.

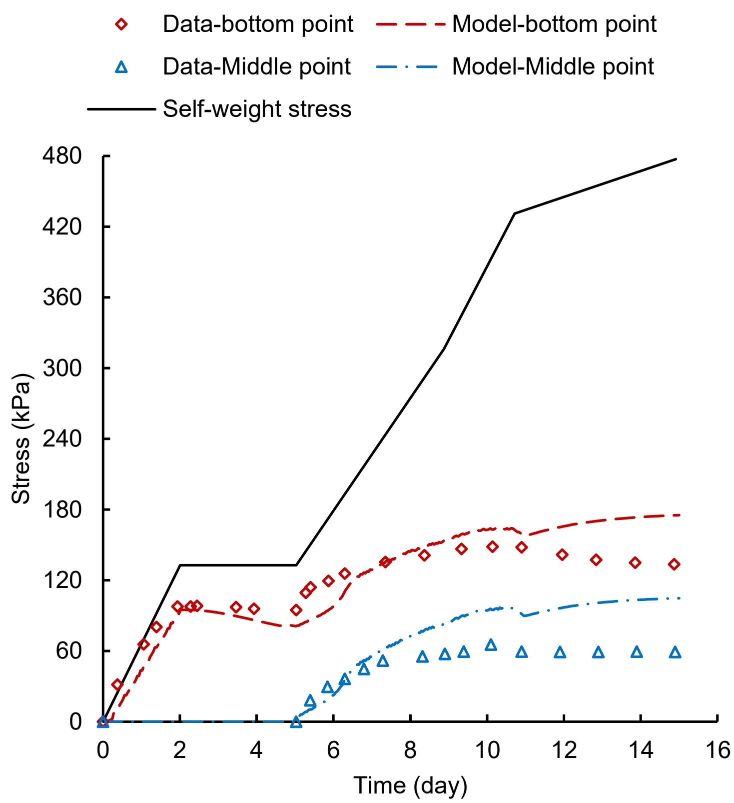

Figure 4.67. Changes in total stress vs. changes self-weight stress: comparison between modeling results and measured total stress values at Doyon Gold Mine

To further reveal and better understand the stress transfer to rock wall and its effect on the evolution of total stress in CTB, the development of interface shear stress on the rock wall is simulated. The simulation results of the evolution of the interface shear stress at a rock wall point (located 7.3 m from stope floor) are presented in Figure 4.68. It can be observed that (1) the interface shear stress gradually develops with filling operation; (2) The nonlinear development of interface shear stress under constant filling rate becomes progressively apparent with curing time; (3) As the filling rate reduces after 10.7 days, the rate of change of interface shear stress slows down as well. These results are consistent with the evolution of the total stress in CTB presented in Figure 4.67 and previously discussed. This suggests that the proposed model can capture well the stress transfer to rock wall, and thus can describe well changes in the in-situ total stress in the CTB under undrained condition.

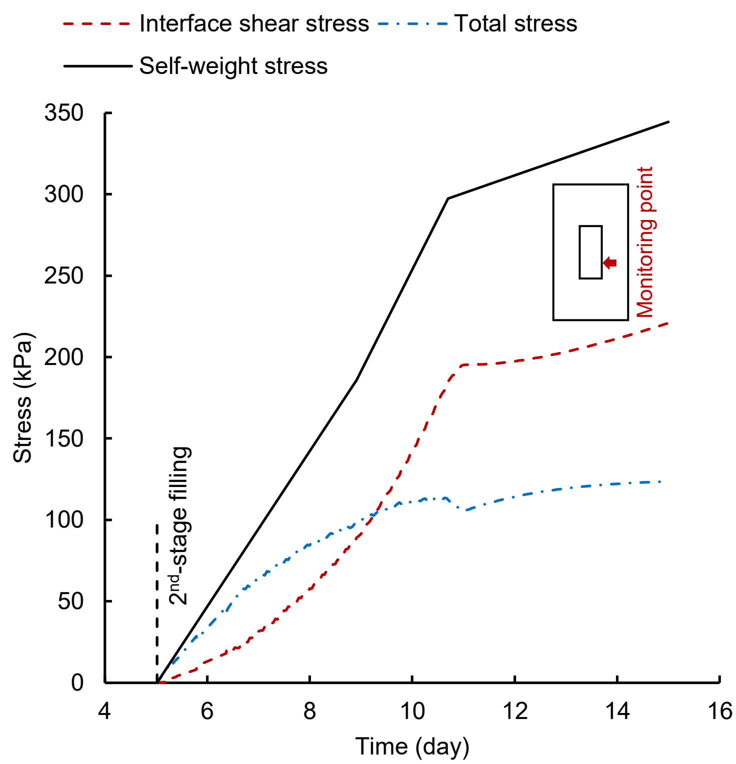

Figure 4.68. Development of interface shear stress at the elevation of 7.3m from stope floor

In undrained condition, the water consumption by binder hydration governs the dissipation of PWP in CTB. Therefore, the spatial distribution of PWP in this field (undrained) CTB structure can be used to assess the effect of binder hydration on the evolution of CTB (Figure 4.69). From Figure 4.69, it can be observed that: (1) as expected, the positive PWP increases with filling depth at curing age of 2 day (i.e., the after the complement of 1st-stage filling) (see Figure 4.69a). (2) Afterwards, during the 2nd-stage placement (see Figure 4.69b), the newly poured CTB has very limited impacts on the increase of PWP in CTB, and the magnitude of PWP at the stope base after 2

(Figure 4.69a) and 8.9 (Figure 4.69b) days of curing remains relatively similar. This is attributed to the pore-water consumption by binder hydration (i.e., the self-desiccation process). (3) As curing time further increases, negative PWP appears within the CTB mass due to the self-desiccation. Similar evolution and spatial distribution of PWP were observed in a previous study on CTB (Cui and Fall 2015a). The obtained results indicate binder hydration can play a significant role in the evolution of PWP in CTB.

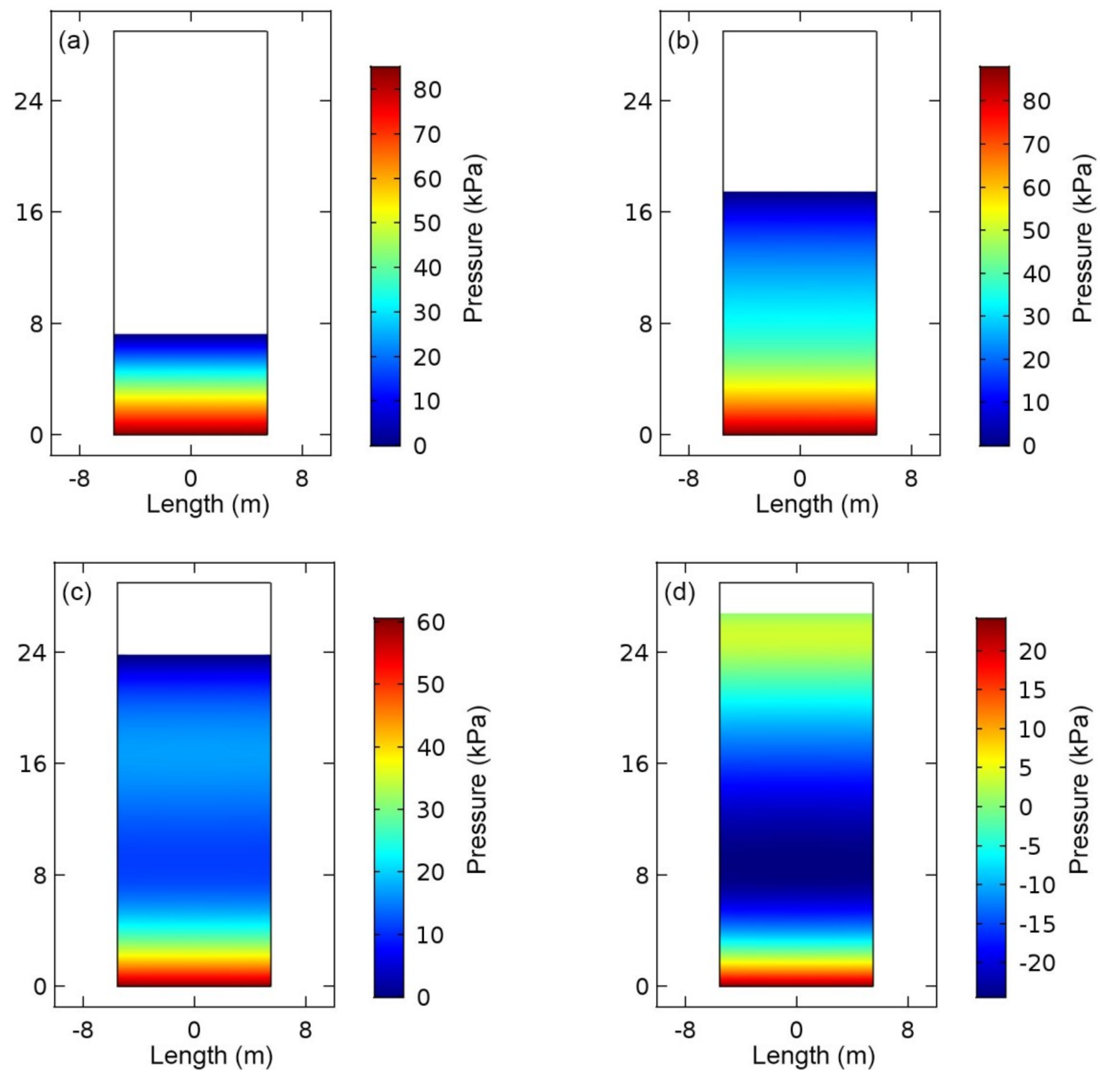

Figure 4.69. Spatial distribution of PWP in stope with different curing times: (a) 2 days; (b) 8.9 days; (c) 10.7 days; and (d) 15 days

4.5.3.2. Field Study 2: Drained Backfilled Stope without Inclination

To investigate the changes in the stress and PWP in CTB, Helinski et al. (2010) conducted in-situ monitoring at the Kanowna Belle (KB) Gold Mine (Australia). The tested stope was 15 m wide × 40 m high. The drawpoints had a dimension of 6 m wide × 6 m high. Fresh CTB with a solid content of 75% and cement content of 3.1% was used as the mixture recipe. Backfilling was carried out in two stages (Figure 4.70). During the field testing, a vibrating wire piezometer and a Geokon 4850-01 total pressure cell were placed at the center of the stope floor to record the pore pressure and total stress, respectively. In comparison to Field Study 1, water drainage through the retaining wall (barricade) was observed during the backfilling period. Therefore, to validate the developed model in this study under drained condition, the experimental results from the KB Gold Mine are used. The corresponding mesh and geometry for the numerical simulation are shown in Figure 4.71. To predict the drainage through the barricade, a mass flux boundary condition is applied to the right vertical side of the drawpoint. The drainage mass flux is equal to the water density times the velocity through the retaining wall structure. The pore water velocity is determined by using Darcy's law.

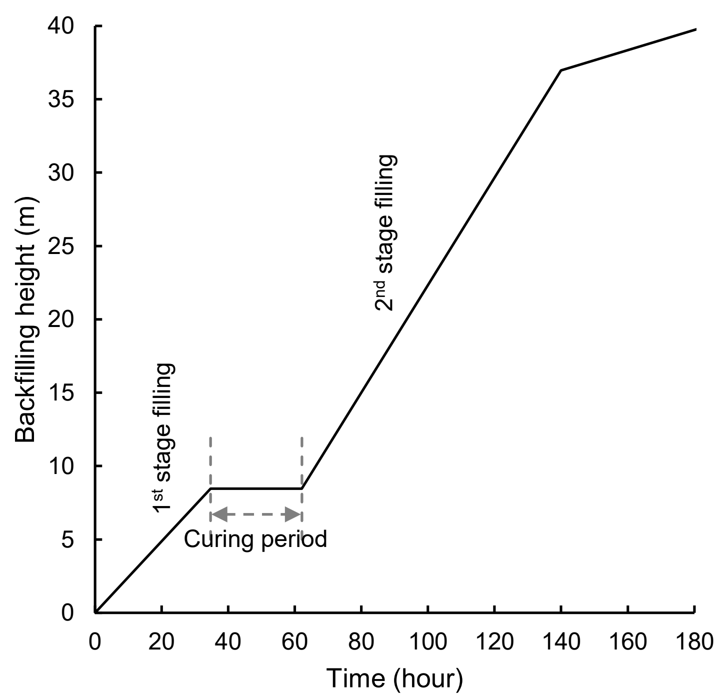

Figure 4.70. Backfilling of trial stope at KB Gold Mine

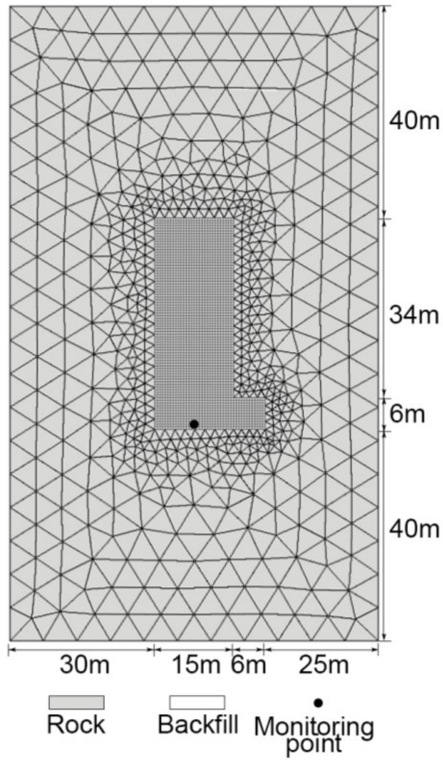

Figure 4.71. Mesh and geometry of simulated stope at KB Gold Mine

As shown in Figure 4.72, the total stress is significantly less than the estimated self-weight stress at the end of the backfilling. Therefore, it is clear that arching has a major effect on the total stress in the stope. It should be pointed out that, during the suspension period of filling (from 33-62 h), the total stress showed a slight reduction. This is due to the combined effects of water drainage through the barricade, and the improvement of arching effect with curing time. In terms of the changes in the PWP, the PWP initially increased at a similar rate as the changes in the total stress. After about 20 hours, the rate of increase of the PWP gradually diverged from the changes in the total stress. Moreover, during the curing period (from 33-62 h) the reduction of PWP proceed to a larger extent compared with the variation of total stress. This is because of their different controlling mechanisms. The evolution of PWP is mainly controlled by the water drainage through barricade and the pore-water consumption by binder hydration. However, as mentioned above, the change in total stress is controlled by the development of arching effect and water loss via drainage. In addition, similar to the evolution of total stress, the effect of residual filling (the 2nd stage filling) on variation of PWP is relatively limited. As can be seen in Figure 4.72, the PWP shows a decreasing trend after around 80 hours regardless of the following CPB placement. Based on the obtained results, it can be seen that the predicted results are in a good agreement with the in-stope monitored data (including both total stress and PWP), which confirms that the developed multiphysics model can adequately predict the arching effect in CTB and the resulting stress distribution under drained conditions of backfilling.

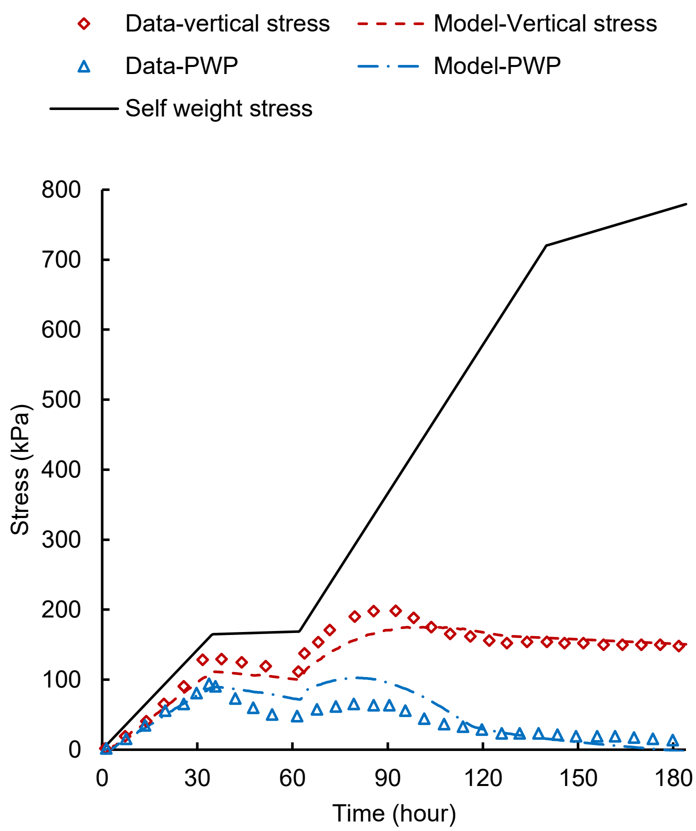

Figure 4.72. Comparison of modeling and experimental results of total stress and pore water pressure at KB Gold Mine

The spatial distribution of the total stress in the different stages of backfilling is presented in Figure 4.73. After completion of the first stage of backfilling (Figure 4.73a), the toal stress increase with depth of the CTB. At the end of the curing period (Figure 4.73b), there is a slight reduction in the total stress in comparison to the total stress after 34 hours (Figure 4.73a). With further filling of the stope, the non-uniform distribution of the total stress becomes more apparent, namely, the stress in the vicinity of the surrounding rock wall is less than that in the center of the backfill mass for any given elevation. Moreover, compared with the total stress distribution under undrained condition (Figure 4.69), the stress in the CTB with drained condition shows an asymmetrical distribution with respect to the centre line of the CTB body, in particular for the region near the drawpoint. This is because (1) the asymmetric geometry of stope around the drawpoint region can affect the transfer of self-weight stress to the rock wall compared with the counterpart on the opposite side of fill mass, and (2) the water drainage through barricade can contribute to the change of total stress and thus further strengthen the asymmetric distribution of stress in CPB. Therefore, the developed model is able to reproduce the evolution and complex spatial distribution of stress in CTB under drained condition.

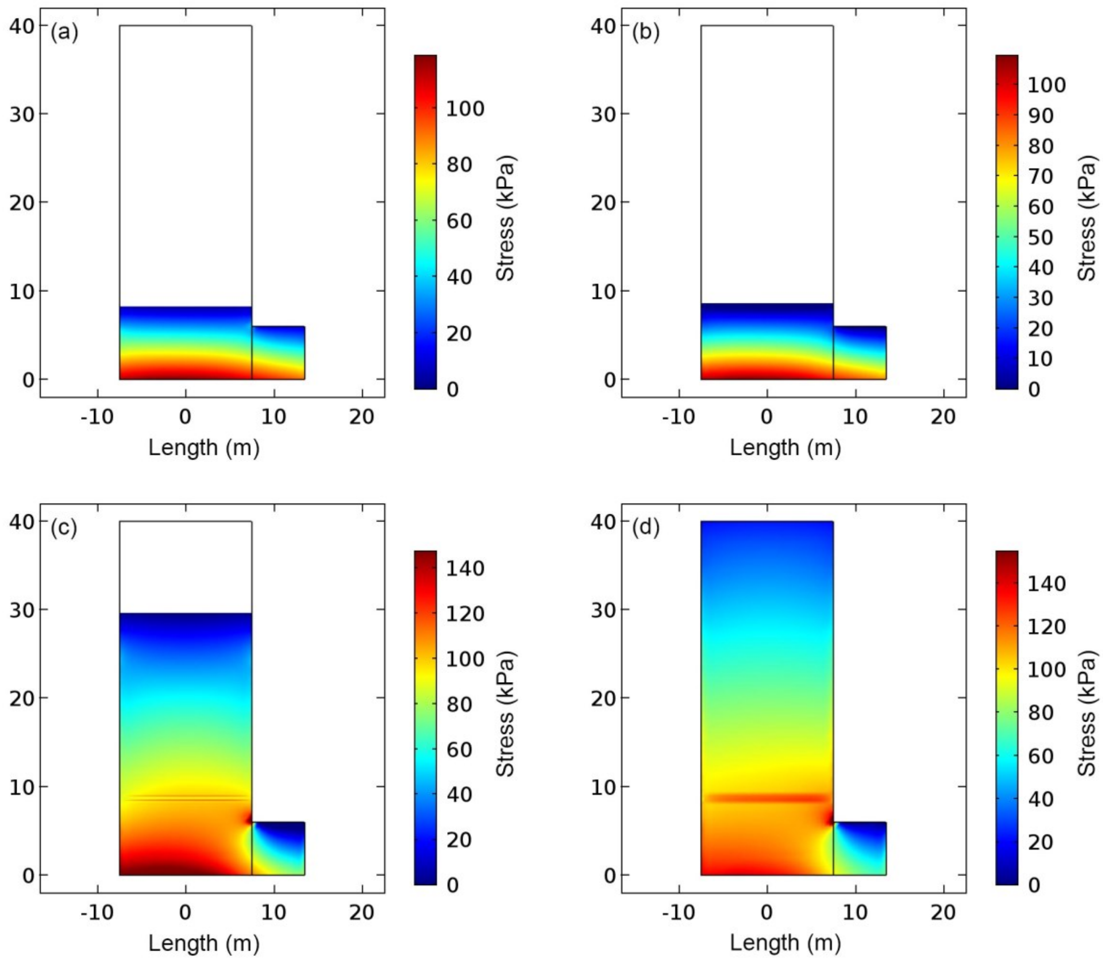

Figure 4.73. Spatial distribution of total stress for different backfilling times: (a) 34 hours; (b) 62 hours; (c) 120 hours; and (d) 184 hours.

4.5.3.3. Field Study 3: Inclined Backfilled Stope with Drainage

Inclined stoping is a very commonly used mining operation due to the irregularities of the ore bodies. In-stope monitoring was conducted by Doherty et al. (2015) at the Raleigh mine (USA) to analyze the stress state in an inclined stope. The monitored stope had a dip angle of 65° with respect to the horizontal plane. A barricade wall had a height of 3.5 m and width of 3.5 m. A cement content of 5% and solid content of 74.5% were used to prepare the CTB. Two sequences of backfilling were carried out on this trial stope (Figure 4.74). The monitoring point was located on the stope floor at a distance of 9.5 m away from the barricade. A vibrating wire NATM stress cell and a piezometer were installed to record the changes in the total stress and PWP, respectively. The corresponding 3D geometry model and dimensions are presented in Figure 4.75.

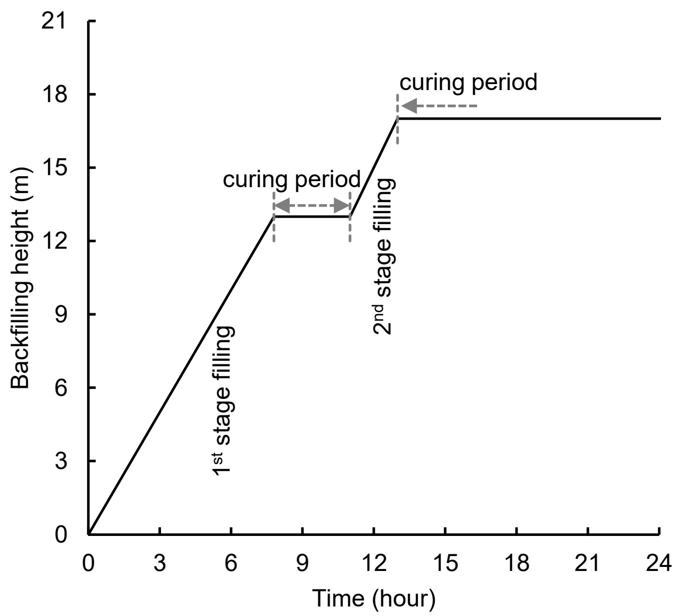

Figure 4.74. Backfilling of trial stope at Raleigh Mine

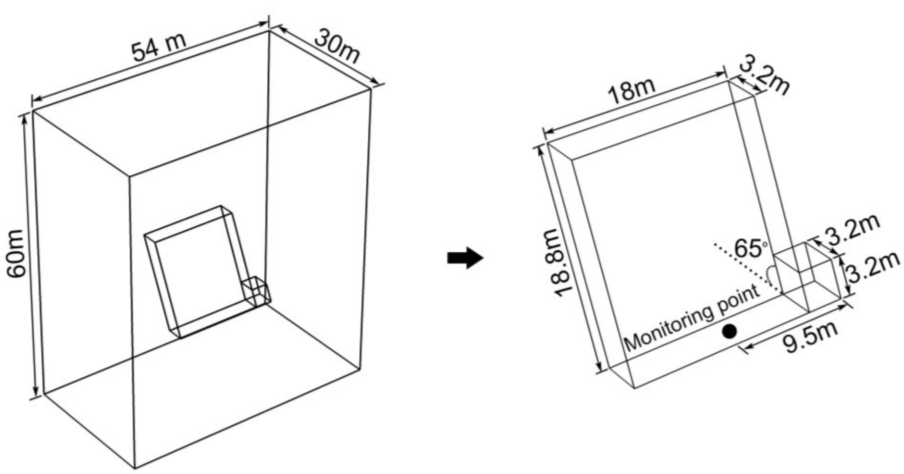

Figure 4.75. Geometry and dimensions of simulated stope at Raleigh mine

From Figure 4.76, it can be seen that the modeling results are in excellent agreement with the experimental results for both total stress and PWP. The total stress and PWP show a monotonic increase with backfilling height during the first sequence of filling. Then, there is a monotonic decrease in the total stress and PWP during curing (7.8 to 11 h). After the second sequence of filling commenced, the total stress and PWP only slightly increased. Then, both the PWP and total stress continuously decreased. After 16 hours, the changes in both the PWP and total stress gradually slowed down with time. The predictive ability of the developed model is further confirmed as shown by the good agreement between the simulation results and in-situ monitored data.

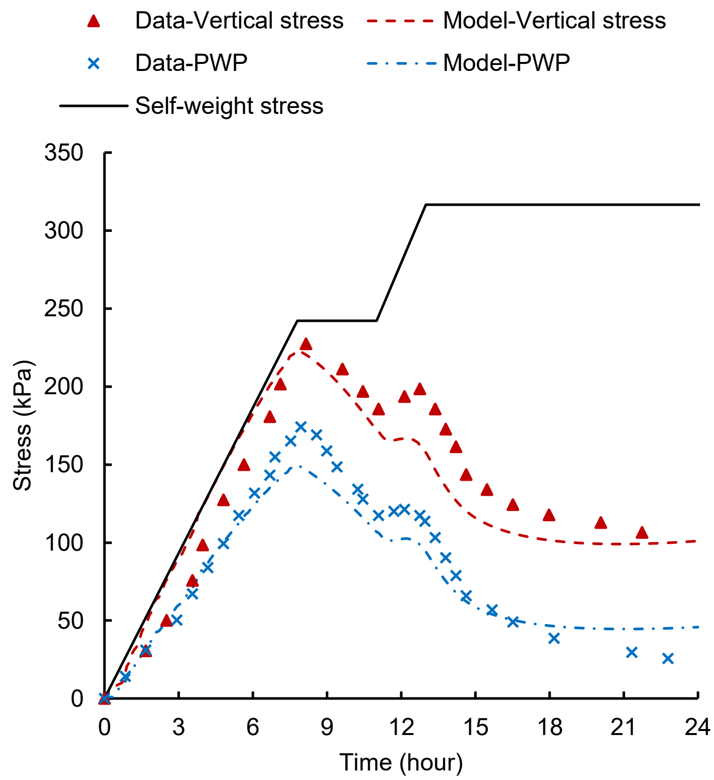

Figure 4.76. Comparison of modeling and experimental results (location: stope floor)

To clearly show the stress distribution in the CTB, both the sliced view and surface view of total stress from this field study are plotted in Figure 4.77. It can be clearly seen that the longitudinal stress (along the longitudinal rock walls) is asymmetrically distributed, especially at the drawpoint. As mentioned in Field Study 2, this asymmetrical distribution of the stress near the drawpoint is mainly due to the effects of water drainage and the asymmetric geometry of the fill mass. For the effect of water drainage, it should be pointed out that due to the fracture of rock walls is not considered in this study, the water drainage through barricade dominates the water loss from fill mass, which further contributes to the asymmetric distribution of total stress near the drawpoint. Moreover, the transverse stress on the lower longitudinal wall is always greater than that on the opposite longitudinal wall at any given elevation (due to stress transfer to the lower longitudinal rock wall under gravitational effect). In addition, around the interface of the first and second backfill layers, the total stress concentration gradually becomes apparent with curing time (see Figure 4.77). The reasons for this phenomenon are due to (i) the distinct interface properties, and (ii) inconsistent consolidation near the backfill interface and its associated effect on pore-water flow between the staged filling interface.

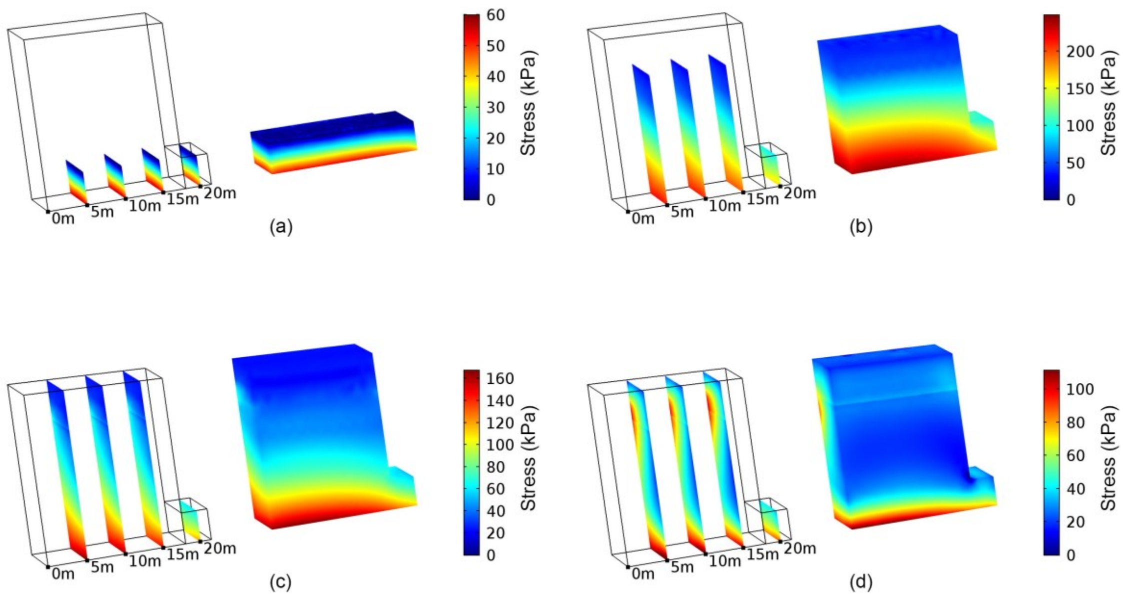

Figure 4.77. Spatial distribution of total stress for different backfilling times: (a) 2 hours; (b) 7.8 hours; (c) 13 hours; and (d) 24 hours.

4.5.4. Model application

After the validation of the model with different field data, the model was then applied to other relevant engineering applications. Practical problems were addressed to investigate the effects of the stope geometry, rock wall roughness, binder content, backfilling rate, filling strategy and initial backfill temperature on arching and the stress distribution in the CTB structure. The relevant input parameters, initial values and boundary conditions (see Table 4.8 and Table 4.9), and the stope geometry (see Figure 4.75) from Field Study 3 were adopted with the exception of some specific adjustments. Meanwhile, a water to cement ratio of 7.6 was adopted.

4.5.4.1. Effect of Stope Geometry (Size and Inclination)

The irregularities of ore bodies and strategies used in mine planning may lead to variations in the stope in terms of both size and inclination. Therefore, it is necessary to investigate the effect of the stope geometry on the stress distribution in CTB. The investigated stope sizes are 2 m (W)×5 m (L)× 17 m (H), 4 m (W)×10 m (L)×17m (H) and 8 m (W)×20 m (L)× 17m (H). All of the selected stopes have the same height as this will eliminate the influence of the self-weight stress on the CTB. Figure 4.78 shows the vertical stress distribution in the CTB after the completion of stope filling for the different stope sizes. The obtained results illustrate that, with the same backfill height, increases in the stope length and width will cause higher levels of stress in a CTB mass at a given elevation. This means that the arching effect is less as the stope length and width increase. This is due to the fact that, with respect to the centre line of the stope, the effect of the interface shear stress reduces with greater distance from the rock wall at a given height. Thus, with increases in the longitudinal and transverse size, more stress is induced in the CTB.

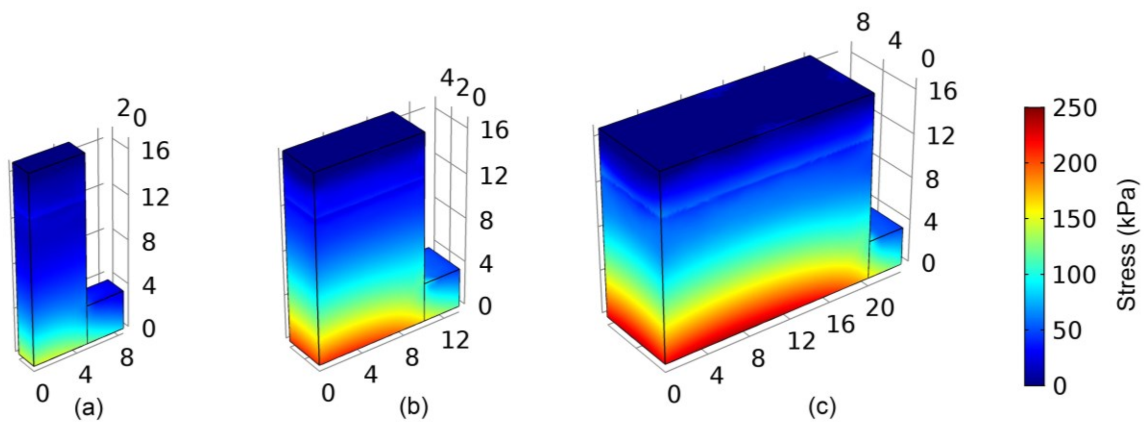

Figure 4.78. Effect of stope size on stress distribution: (a) Stope of 2 m×5 m×17 m; (b) Stope of 4 m×10 m×17 m; and (c) Stope of 8 m×20 m×17 m.

Three dip angles (i.e., 90°, 75° and 60°) are used to study the effect of the stope inclination. The three stopes have the same longitudinal and transverse size (i.e., 4 m (W)×10 m (L)), and backfill height (17 m). As shown in Figure 4.79, less stress is induced in the stope with a reduced dip angle (i.e., larger inclination), which is consistent with the findings obtained in previous studies (e.g., Ting et al. 2010). Moreover, the level of the stress in the vicinity of the low longitudinal wall (i.e., the foot wall) is higher than that on the low rock wall (i.e., the hanging wall) at a given height. This is mainly due to the fact that, with a smaller dip angle, the gravitational effect facilitates more vertical stress to act on the low longitudinal wall. Therefore, it is clear that stope inclination has a significant effect on the level and distribution of stress in stopes.

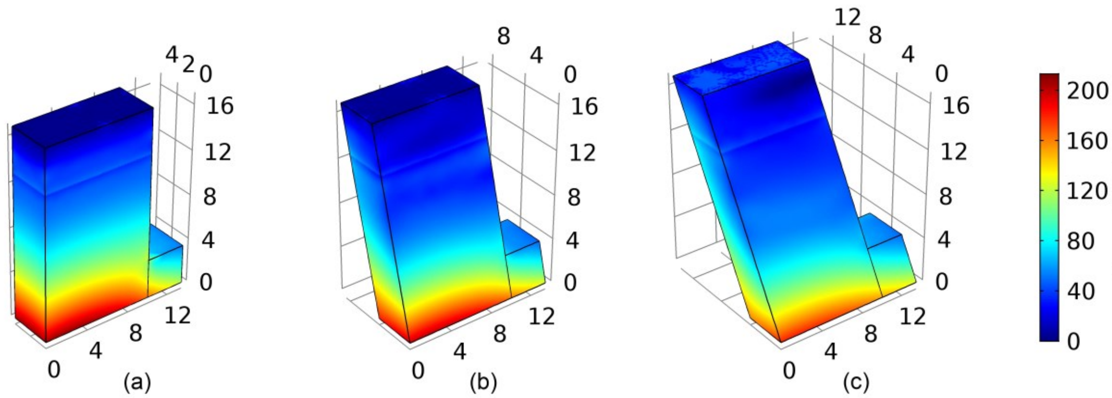

Figure 4.79. Effect of stope inclination on stress distribution: (a) 90°; (b) 75°; and (c) 65°.

4.5.4.2. Effect of Rock Wall Roughness

As indicated in the Eqs. (4.188) and (4.189), the rock mass properties including rock wall roughness index R_L and rock internal friction angle ϕ_r are incorporated into the prediction models of interface properties (interface friction angle δ_{intf} and interface adhesion c_{intf}). Therefore, from a mathematical point of view, R_L and ϕ_r play similar roles in the development of interface shear stress and thus internal stress distribution in CTB. Moreover, as explosives are used during mining operations, the rock walls roughness may vary to a large extent from one stope to another. Therefore, the rock wall roughness index R_L is selected to analyze the effect of rock mass properties on the stress distribution in CTB. In the present study, three different roughness indexes, R_L , including 1 (smooth surface), 1.5 and 2 are adopted. The simulated results are presented in Figure 4.80. It can be observed that the rock wall roughness has a significant influence on the stress distribution in the stope. Specifically, with an increase in the rock wall roughness, the vertical stress that acts on the stope floor can be significantly reduced. This is attributed to the effect of rock surface roughness on the interface adhesion and friction angle, namely, a higher R_L (i.e., rougher rock wall) can improve the interface properties (adhesion and friction angle) thus resulting in higher interface shear strength. Therefore, the obtained results reveal that the internal stress distribution of CTB is sensitive to the change of interface properties resulted from the variation of rock mass properties.

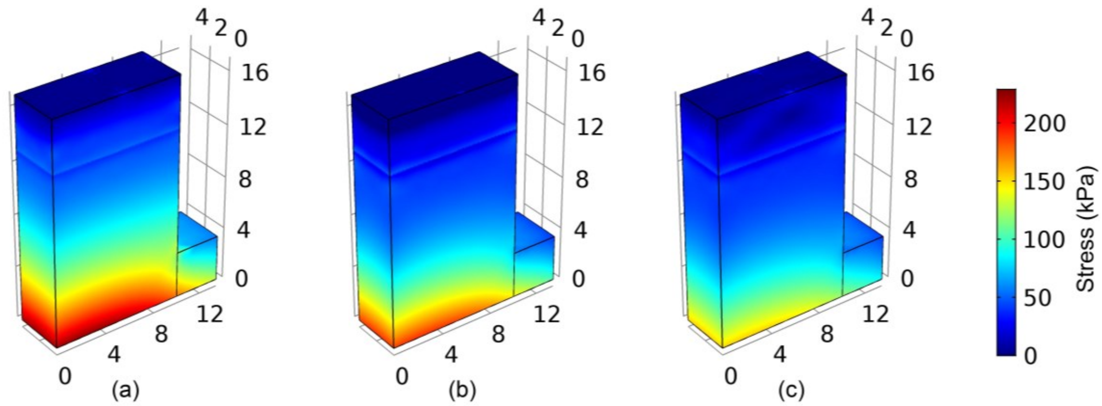

Figure 4.80. Effect of rock wall roughness on stress distribution: R_L= (a) 1; (b) 1.5; and (c) 2.

4.5.4.3. Effect of Binder Content

The binder consumption can represent up to 75% of the cost of the CTB (Grice 1998; Fall et al. 2008). Therefore, binder content is one of the most important factors for an optimal CTB design. It is crucial to obtain an appropriate binder content to fulfill both the mechanical stability of the CPB and reduce its cost. In this study, three different binder contents, including 1% (16.7kg/m^3), 4.5% (60.4 kg/m^3) and 7% (82.2 kg/m^3) are used to investigate the corresponding effect on the stress distribution in the CTB. From Figure 4.81, it can be seen that as the binder content increases, the stress level decreases in the CTB. This is partially because a higher binder content leads to the formation of more hydration products along the rock mass/CTB interface, which can result in higher interface shear strength. Moreover, a higher binder content is associated with a greater consumption of the capillary water due to binder hydration (i.e., self-desiccation) (Abdul-Hussain and Fall 2012), which results in higher effective stress and thus more pronounced consolidation of the CTB.

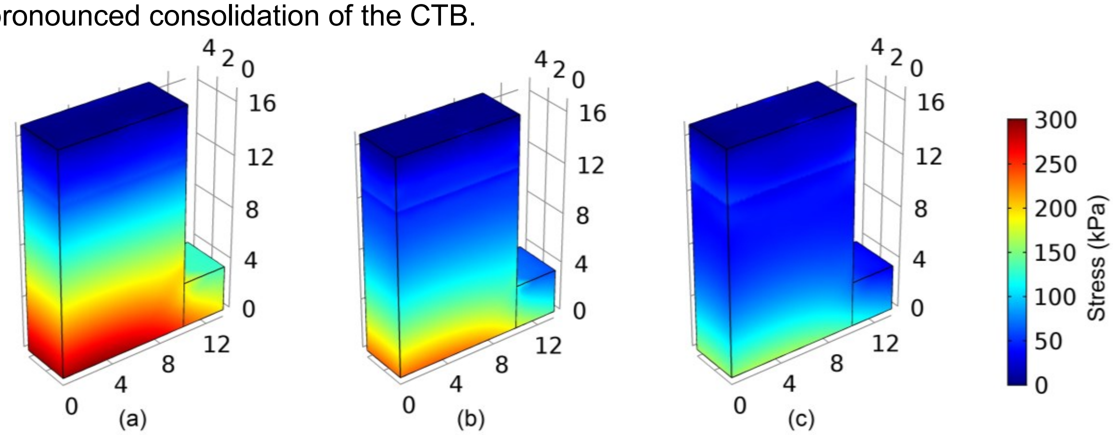

Figure 4.81. Effect of binder content on stress distribution: binder content: (a) 1%; (b) 4.5%; and (c) 7%.

4.5.4.4. Effect of Stope Filling Strategy

In backfilling practices in the field, the backfilling strategy (with or without an initial plug) is very important. For instance, to prevent excess pressure on the barricade, some stopes are filled in two stages, with the initial plug cured for a day or more (Ghirian and Fall 2013; Li 2014). The backfilling strategy (i.e., continuous or multiple sequences of filling) can directly influence the mining operation schedule, and thus the mine productivity. Therefore, it is necessary to assess the effects of different types of filling strategies on the stress distribution in CTB. In this study, various filling sequences, including one stage (no plug), two stages (7.8-hour plug) and three stages (7.8-hour plug plus 2.5 hours of curing in the second stage) are examined. The modeling results are presented in Figure 4.82. It can be seen that the filling strategy has a significant impact on the development of arching in CTB. In particular, with an increase in the number of filling sequences (i.e. continuous filling to multiple stages of filling), there is a clear downward trend in the level of the stress in the stope. Consequently, the arching effect is more pronounced in the stope that is filled in multiple stages, which is consistent with the in-situ measurements reported in (Yumlu 2008). This is because at the same filling rate, the strategy that involves multiple stages of filling allows more curing time for CTB mass, which is obviously related to greater consolidation and interface shear strength as previously discussed. Hence, backfilling operations that are carried out in stages add to the stability of CTB structures, but will result in longer mining cycle, thereby negatively affecting mine productivity.

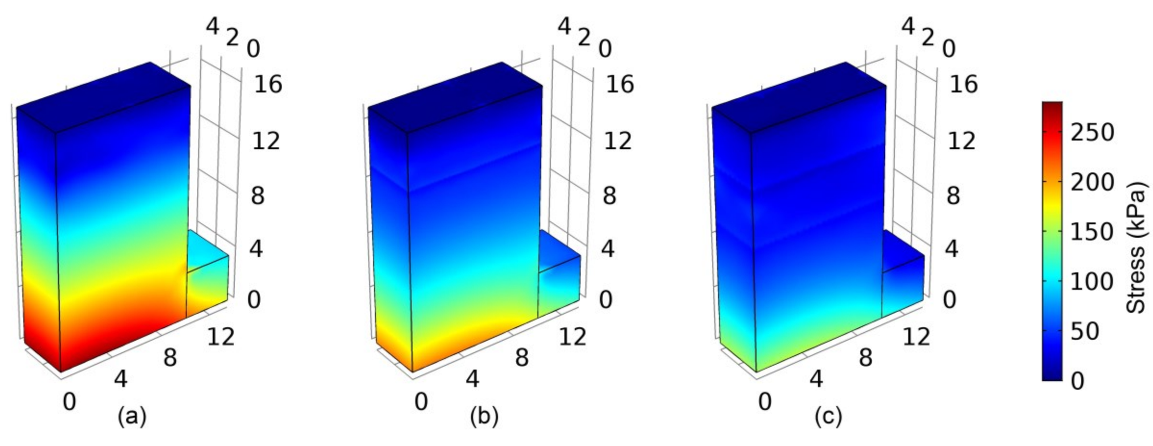

Figure 4.82. Effect of backfilling strategy on stress distribution: (a) one stage (continuous filling); (b) two stages (7.8-hour plug); and (c) three stages (7.8-hour plug and 2.5 hours of curing in second stage).

4.5.4.5. Effect of Initial Backfill Temperature

The initial backfill temperature varies due to several factors, such as the initial temperature of the mix components, geographical location of the mine, increase of the temperature of the backfill during its transport in pipes, and moderate heat added to the CTB (Wu et al. 2012; Walske 2014; Fall et al. 2015). To study the effect of the initial CTB temperature on the stress distribution in stopes, three different initial temperatures of 5°C, 35°C and 55°C are used in the numerical simulation. The obtained results (Figure 4.83) indicate that a higher initial backfill temperature will increase arching and thus effectively reduces the level of stress in the CTB. This can be explained by the fact that a more rapid binder hydration under a warmer initial temperature results in more pronounced consolidation of the CTB (Cui and Fall 2016c) and enhances the interface adhesion (Nasir and Fall 2010). This higher consolidation is obviously associated with higher relative displacement along the rock mass/CTB interface, and thereby results in higher interface shear stress. Moreover, the temperature induced enhancement of the interface adhesion leads to higher interface shear strength (Nasir and Fall 2010), which means that the interface has the potential to bear higher shear stresses.

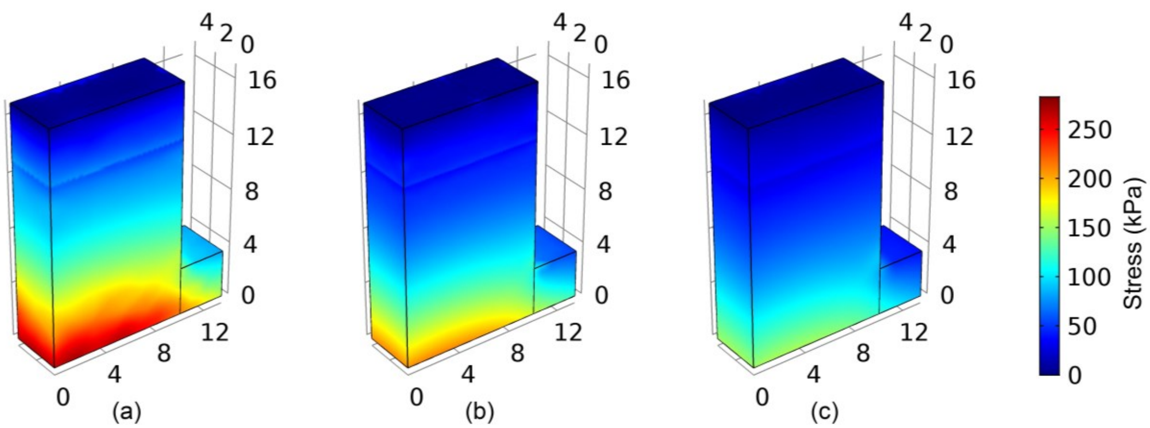

Figure 4.83. Effect of initial backfill temperature on stress distribution: (a) 5°C; (b) 35°C; and (c) 55°C.

4.5.5. Summary and conclusion

The following conclusions are made based on the obtained results in this study.

1. An integrated multiphysics model has been developed to assess and predict the arching effect and the resulting stress development and distribution in the CTB mass with changes in its properties. The time-dependent elastoplastic mechanical behavior of the CTB/rock mass interface is fully considered in the developed model. Double

hardening/softening parameters are incorporated into the modeling of the rock/backfill interface to characterize the effect of binder hydration and plastic displacement along the interface. In terms of the two types of interface resistance, including the interface adhesion and friction angle, the effect of the host rock (i.e., internal rock friction, rock surface roughness) and binder hydration are taken into consideration.

2. The developed model in this study fully considers the effects of multiphysics processes, consolidation behavior and interaction between the rock mass/backfill interface. The relevant model coefficients are identified in terms of measurable parameters.
3. The good agreement between the in-situ measurements and predicted results indicates that the developed model can predict the arching effect and stress distribution in CTB mass with good accuracy.
4. The effects on backfilling from factors related to the surrounding rock (i.e., stope geometry, inclination and rock surface roughness), CTB itself (i.e., mixture recipe and initial CTB temperature) and backfilling strategy are numerically investigated with the developed model. The obtained results show that all of the factors mentioned above have a significant influence on arching and the stress distribution in CTB.
5. The developed model and the obtained modeling results will contribute to a better understanding and assessment of arching in CTB, thus optimizing the design of CTB structures.

4.5.6. References

Abbasy, F. (2009). "Thermal conductivity of mine backfill." Master thesis, Concordia University, Montreal, Quebec, Canada.

Abdul-Hussain, N., and Fall, M. (2011). "Unsaturated hydraulic properties of cemented tailings backfill that contains sodium silicate." *Eng. Geol.*, 123(4), 288-301.

Abdul-Hussain, N., and Fall, M. (2012). "Thermo-hydro-mechanical behaviour of sodium silicate-cemented paste tailings in column experiments." *Tunn. Undergr. Sp. Tech.*, 29, 85-93.

Aubertin, M., Li, L., Arnoldi, S., Belem, T., Bussière, B., Benzaazoua, M., and Simon, R. (2003). "Interaction between backfill and rock mass in narrow stopes." *Proc., Soil and Rock America*, Verlag Glückauf, Cambridge, Massachusetts, USA, 1157-1164.

Belem, T., Benzaazoua, M., Bussière, B., and Dagenais, A. (2002). "Effects of settlement and drainage on strength development within mine paste backfill." *Proc., 9th International Conference, Tailings and Mine Waste*, 139-148.

Belem, T., Harvey, A., Simon, R., and Aubertin, M. (2004). "Measurement and prediction of internal stresses in an underground opening during its filling with cemented fill."

Proc., 5th International Symposium on Ground Support in Mining and Underground Construction, Australian Centre for Geomechanics, Perth, Australia, 28-30.
Borana, L., Yin, J.-H., Singh, D., and Shukla, S. (2016). "Interface Behavior from Suction-Controlled Direct Shear Test on Completely Decomposed Granitic Soil and Steel Surfaces." *Int. J. Geomech.*, D4016008.
Bravo, O., Neupane, D. K., Levorson, S. M., and Smith, E. M. (2016). "Correlation between Laboratory Tested Soil Samples to Obtain Effective Strength Envelopes Based on Field Data." *Proc., Geotechnical and Structural Engineering Congress 2016*, 1655-1663.
Brouwers, H. (2004). "The work of Powers and Brownyard revisited: Part 1." *Cem. Concr. Res.*, 34(9), 1697-1716.
Carrier, W. D., Bromwell, L. G., and Somogyi, F. (1983). "Design capacity of slurried mineral waste ponds." *J. Geotech. Eng.*, 109(5), 699-716.
Comsol (2015). "Comsol Multiphysics 5.1." <http://www.comsol.com>. (Sept. 20, 2016).
Cui, L., and Fall, M. (2015a). "A coupled thermo-hydro-mechano-chemical model for underground cemented tailings backfill." *Tunn. Undergr. Sp. Tech.*, 10.1016/j.tust.2015.08.014, 50, 396-414.
Cui, L., and Fall, M. (2015b). "Modeling and Simulation of the Consolidation Behaviour of Cemented Paste Backfill." *Proc., 2015 Comsol Conference*, Boston, MA, USA, 1-5.
Cui, L., and Fall, M. (2016a). "An evolutive elasto-plastic model for cemented paste backfill." *Comput. Geotech.*, 10.1016/j.compgeo.2015.08.013, 71, 19-29.
Cui, L., and Fall, M. (2016b). "Mechanical and thermal properties of cemented tailings materials at early ages: Influence of initial temperature, curing stress and drainage conditions." *Constr. Build. Mater.*, 10.1016/j.conbuildmat.2016.08.080, 125, 553-563.
Cui, L., and Fall, M. (2016c). "Multiphysics model for consolidation behaviour of cemented paste backfill." *Int. J. Geomech.*, 10.1061/(ASCE)GM.1943-5622.0000743, 040160771-0401607723.
Doherty, J. P. (2015). "A numerical study into factors affecting stress and pore pressure in free draining mine stopes." *Comput. Geotech.*, 10.1016/j.compgeo.2014.10.001, 63, 331-341.
Doherty, J. P., Hasan, A., Suazo, G. H., and Fourie, A. (2015). "Investigation of some controllable factors that impact the stress state in cemented paste backfill." *Can. Geotech. J.*, 10.1139/cgj-2014-0321, 52(12), 1901-1912.
Doherty, J. P., and Wood, D. M. (2016). "Back analysis of the Kanowna Belle stope filling case history." *Comput. Geotech.*, 76, 201-211.
Donovan, J. G. (1999). "The effects of backfilling on ground control and recovery in thin-seam coal mining." Master thesis, Virginia Polytechnic Institute and State University, USA.
Fahey, M., Helinski, M., and Fourie, A. (2009). "Some aspects of the mechanics of arching in backfilled stopes." *Can. Geotech. J.*, 10.1139/T09-063, 46(11), 1322-1336.
Fall, M., Benzaazoua, M., and Saa, E. (2008). "Mix proportioning of underground cemented tailings backfill." *Tunn. Undergr. Sp. Tech.*, 10.1016/j.tust.2006.08.005, 23(1), 80-90.
Fall, M., and Nasir, O. (2010). "Mechanical behaviour of the interface between cemented tailings backfill and retaining structures under shear loads." *Geotech. Geol. Eng.*, 28(6), 779-790.
Fall, M., Nasir, O., Cui, L., and Han, F. (2015). "Coupled modeling of the strength development and distribution within cemented paste backfill structure." *Proc., 49th US Rock Mechanics/Geomechanics Symposium*, American Rock Mechanics Association, San Francisco, California, USA, 587-595.

Ghirian, A., and Fall, M. (2013). "Coupled thermo-hydro-mechanical-chemical behaviour of cemented paste backfill in column experiments. Part I: physical, hydraulic and thermal processes and characteristics." *Eng. Geol.*, 164, 195-207.
Ghirian, A., and Fall, M. (2014). "Coupled thermo-hydro-mechanical-chemical behaviour of cemented paste backfill in column experiments: Part II: Mechanical, chemical and microstructural processes and characteristics." *Eng. Geol.*, 10.1016/j.enggeo.2013.12.004, 170, 11-23.
Ghirian, A., and Fall, M. (2015). "Coupled Behavior of Cemented Paste Backfill at Early Ages." *Geotech. Geol. Eng.*, 10.1007/s10706-015-9892-6, 33(5), 1141-1166.
Goel, S., and Patra, N. (2008). "Effect of arching on active earth pressure for rigid retaining walls considering translation mode." *Int. J. Geomech.*, 8(2), 123-133.
Gokhale, A., and Underwood, E. (1990). "A general method for estimation of fracture surface roughness: Part I. Theoretical aspects." *Metallurgical Transactions A*, 21(5), 1193-1199.
Grice, T. (1998). "Underground mining with backfill." *Proc., the 2nd Annual Summit-Mine Tailings Disposal Systems*, 234-239.
Helinski, M., Fahey, M., and Fourie, A. (2010). "Behavior of cemented paste backfill in two mine stopes: measurements and modeling." *J. Geotech. Geoenviron.*, 10.1061/(ASCE)GT.1943-5606.0000418, 137(2), 171-182.
Helinski, M., Fourie, A., Fahey, M., and Ismail, M. (2007). "Assessment of the self-desiccation process in cemented mine backfills." *Can. Geotech. J.*, 44(10), 1148-1156.
Hu, S., Xia, Z., and Gao, X. (2012). "Strong adhesion and friction coupling in hierarchical carbon nanotube arrays for dry adhesive applications." *ACS applied materials & interfaces*, 4(4), 1972-1980.
Hunnicutt, W. A. (2013). "Characterization of Calcium-silicate-hydrate and Calcium-alumino-silicate-hydrate." Master Thesis, University of Illinois at Urbana-Champaign, Illinois, USA.
Iglesia, G. R., Einstein, H. H., and Whitman, R. V. (1999). "Determination of vertical loading on underground structures based on an arching evolution concept." *Proc., Geo-Engineering for Underground Facilities*, 495-506.
Janotka, I. (2001). "Hydration of the cement paste with Na2CO3 addition." *Ceram-silikaty.*, 45(1).
Koupouli, N. J., Belem, T., Rivard, P., and Effenguet, H. (2016). "Direct shear tests on cemented paste backfill-rock wall and cemented paste backfill-backfill interfaces." *J. Rock Mech. Geotech. Eng.*, 10.1016/j.jrmge.2016.02.001, 8, 472-479.
Li, L. (2014). "Analytical solution for determining the required strength of a side-exposed mine backfill containing a plug." *Can. Geotech. J.*, 51(5), 508-519.
Li, L., Aubertin, J. D., and Dubé, J.-S. (2014). "Stress distribution in a cohesionless backfill poured in a silo." *Open Civ. Eng. J.*, 10.2174/1874149501408010001, 8, 1-8.
Li, L., and Aubertin, M. (2009). "A three-dimensional analysis of the total and effective stresses in submerged backfilled stopes." *Geotech. Geol. Eng.*, 27(4), 559-569.
Lura, P., Jensen, O. M., and van Breugel, K. (2003). "Autogenous shrinkage in high-performance cement paste: an evaluation of basic mechanisms." *Cem. Concr. Res.*, 33(2), 223-232.
Marinho, F. A. M., Guzmán, G. C. G., and Orlando, P. D. G. (2016). "Constant Water Content Compression Tests on Unsaturated Compacted Soil with Suction Measurement Using a HCT." *Int. J. Geomech.*, 10.1061/(ASCE)GM.1943-5622.0000609, D4015008.
Nasir, O., and Fall, M. (2008). "Shear behaviour of cemented pastefill-rock interfaces." *Eng. Geol.*, 101(3), 146-153.

Nasir, O., and Fall, M. (2010). "Coupling binder hydration, temperature and compressive strength development of underground cemented paste backfill at early ages." *Tunn. Undergr. Sp. Tech.*, 25(1), 9-20.
Ono, K., and Yamada, M. (1993). "Analysis of the arching action in granular mass." *Geotechnique*, 43(1), 105-120.
Raous, M. (2011). "Interface models coupling adhesion and friction." *Comptes Rendus Mécanique*, 339(7), 491-501.
Schindler, A. K., and Folliard, K. J. (2003). "Influence of supplementary cementing materials on the heat of hydration of concrete." *Proc., Advances in Cement and Concrete IX Conference*, Engineering Conferences International, Inc., Colorado, USA, 17-26.
Somerton, W., Keese, J., and Chu, S. (1974). "Thermal behavior of unconsolidated oil sands." *Soc. Pet. Eng. J.*, 14(05), 513-521.
Take, W., and Valsangkar, A. (2001). "Earth pressures on unyielding retaining walls of narrow backfill width." *Can. Geotech. J.*, 38(6), 1220-1230.
Terzaghi, K. (1943). *Theory of Consolidation*, John Wiley & Sons Inc., Hoboken, NJ, USA.
Thompson, B., Grabinsky, M., Bawden, W., and Counter, D. (2009). "In-situ measurements of cemented paste backfill in long-hole stopes." *Proc., the 3rd CANUS Rock Mechanics Symposium*, Toronto, Canada, 197-198.
Ting, C. H., Shukla, S. K., and Sivakugan, N. (2010). "Arching in soils applied to inclined mine stopes." *Int. J. Geomech.*, 10.1061/(ASCE)GM.1943-5622.0000067, 11(1), 29-35.
Van Genuchten, M. T. (1980). "A closed-form equation for predicting the hydraulic conductivity of unsaturated soils." *Soil Sci. Soc. Am. J.*, 44(5), 892-898.
Walske, M. L. (2014). "An experimental study of cementing paste backfill." Ph.D. thesis, University of Western Australia, Perth, Australia.
Wu, D., Fall, M., and Cai, S. J. (2012). "Coupled modeling of temperature distribution and evolution in cemented tailings backfill structures that contain mineral admixtures." *Geotech. Geol. Eng.*, 30(4), 935-961.
Xing, X., Li, T., and Fu, Y. (2016). "Determination of the related strength parameters of unsaturated loess with conventional triaxial test." *Environmental Earth Sciences*, 75(1), 1-11.
Ye, G., Sun, Z., Voigt, T., Van Breugel, K., and Shah, S. (2004). "A micromechanic model for characterization of cement paste at early age validated with experiments." *Proc., Proceedings of the RILEM International Symposium on Advances in Concrete through Science and Engineering*.
Yumlu, M. (2008). "Barricade pressure monitoring in paste backfill." *Gospodarka Surowcami Mineralnymi*, 24(4/3), 233-244.

4.6. Chapter Conclusions

In this chapter, a series of theoretical frameworks for multiphysics modeling have been developed that capture and characterize the behaviors of CTB. The following conclusions are drawn based on the obtained results.

1. A new chemo-mechanical model (evolutive elastoplastic model) is developed that describes the mechanical behaviors of CTB. The model validation results demonstrate that the evolutive elastoplastic model can accurately characterize

chemical hardening, strain hardening/softening, volumetric response and enhanced material properties due to the binder hydration in CTB materials.

2. A fully coupled thermo-hydro-mechano-chemical model has been successfully developed and validated to evaluate the interaction of the multiphysics processes and the resulting influence on the CTB properties and behaviors from the early to the advanced ages.
3. A multiphysics model on the consolidation processes is derived based on the principles of the continuity of pore space and conservation of mass, energy and momentum. The model validation results indicate that the developed model accurately evaluates the volume changes in CTB under the effect of the coupled THMC processes.
4. A multiphysics model that analyzes changes in the interface behavior is established to simulate the arching effect in CTB. This model captures the elastoplastic behaviors (chemical hardening and strain hardening/softening) along the interface of the rock mass and CTB, and the related changes in the interface properties (interface friction angle and adhesion).

The developed fundamental multiphysics models have been validated against a series of case studies at both the laboratory and field scales. Therefore, they will be applied in Chapter 5 to simulate the key field behaviors of CTB structures that are relevant for their optimal design.

CHAPTER 5

Multiphysics Simulation of the Behavior of Cemented Tailings Backfill Structures

5.1. Introduction

A reliable evaluation of the behavior and performance of cemented tailings backfill (CTB) is important for designing CTB structures due to the complex multiphysics processes in CTB. With the use of the validated multiphysics models in Chapter 4, multiphysics simulation of the field behavior and performance of a CTB structure is conducted in this chapter for engineering applications. Field behaviors that are relevant for the optimal design of CTB structures are numerically investigated. Specifically, this chapter comprises four technical papers, which include multiphysics simulation of the self-desiccation of CTB (Section 5.2), consolidation behavior of CTB (Section 5.3), changes in barricade pressure (Section 5.4), and strength development in CTB structures (Section 5.5). The pertinent numerical simulation is carried out to investigate the CTB behavior under different field conditions in terms of the mixture recipe (cement content, water-to-cement ratio and initial CTB temperature), backfilling conditions (filling rates and strategies), host rock conditions (stope geometry, inclination, rock wall roughness and initial rock temperature) and drainage conditions. The obtained results provide valuable technical information and knowledge for the optimal design of CTB structures.

5.2. Paper VI: Simulation of Self-desiccation in a Cemented Tailings Backfill Structure

Liang Cui, Mamadou Fall

Abstract

After placement of cemented tailings backfill (CTB), which is a mixture of tailings (man-made soil), water and binder, into underground mined-out voids (known as stopes), the hydration reaction of the binder converts the capillary water into chemically bound water, which results in the reduction of the water content in the pores of the CTB, thereby causing a reduction in the pore water pressure (PWP) in the CTB (self-desiccation). Self-desiccation has a significant impact on the PWP and effective stress development in CTB, and paramount and practical importance for the stability assessment and design of CTB structures and barricades. However, self-desiccation in CTB structures is complex, since it is a function of the multiphysics or coupled (i.e., thermal (T), hydraulic (H), mechanical (M), and chemical (C); THMC) processes that occur in CTB. To understand the self-desiccation behavior of CTB, an integrated multiphysics model of self-desiccation is developed in this study, which fully considers the coupled THMC processes and the consolidation process in CTB. All model coefficients are determined in terms of measurable parameters. Moreover, the predictive ability of the model is verified with extensive case studies. A series of engineering issues are examined with the validated model to investigate the self-desiccation process in CTB structures with respect to the changes in the mixture recipe, backfilling and the surrounding rock and curing conditions. The obtained results provide in-depth insight into the self-desiccation behavior of CTB structures. The developed multiphysics model is therefore a potential tool for assessing and predicting self-desiccation in CTB structures.

Keywords: Cemented paste backfill; Tailings; Self-desiccation; Multiphysics; Pore water pressure.

5.2.1. Introduction

Cemented tailings backfill (CTB) is an engineered mixture of dewatered tailings (man-made soil), hydraulic binder (e.g., ordinary Portland cement, fly ash and blast-furnace slag) and water (Belem et al. 2002; Suazo et al. 2016). As a novel and effective means of mine waste disposal and ground control management, CTB technology has been increasingly and widely adopted in underground mining operations around the world for the last few decades (Li and Yang 2015; Cui and Fall 2016a; Koupouli et al. 2016). After preparation, fresh CTB paste is transported from underground cavities (stopes) through gravity and/or pipeline systems by using high-pressure pumps (Cui and Fall 2015). Retaining walls (barricades) are commonly built across an access drift at the stope base to confine the fresh CTB in order to prevent the CTB from flowing into the active mining zone.

During and after pouring of CTB into the stope, complex multiphysics or coupled (thermal (T), hydraulic (H), mechanical (M), and chemical (C); i.e., THMC) processes take place in the CTB structure and thus control its behavior and performance (Ghirian and Fall 2013). Among the different processes, binder hydration (a chemical reaction) has a significant role. Specifically, with progression of the hydration reaction, the capillary water (free water) is gradually converted into chemically bound water (solid phase; the volume of the resultant hydrates is less than the total volume of the original cement and water), which results in the reduction of the water content in the CTB matrix (phenomenon of self-desiccation), thereby leading to a reduction in the pore water pressure (PWP) and/or generation of suction in CTB. Consequently, self-desiccation has a significant effect on the PWP and effective stress development in CTB structures. Hence, self-desiccation has paramount and practical importance for stability analysis as well as the cost-effective design of CTB structures and barricades.

The self-desiccation process in CTB is affected by the THMC processes. For example, experimental studies on CTB have concluded that the rate of binder hydration is sensitive to the curing temperature (Walske 2014) and curing stress (Cui and Fall 2016b; Walske et al. 2016). This means the self-desiccation behavior is also affected by thermal (temperature) and mechanical processes. Therefore, coupled multiphysics processes must be taken into account in the assessment of the self-desiccation behavior of CTB.

To understand the self-desiccation process in CTB, extensive laboratory (e.g., Walske 2014; Li and Fall 2016) and field studies (e.g., Thompson et al. 2009; Helinski et al. 2010; Thompson et al. 2012) have been conducted to investigate the changes in the PWP and/or suction in CTB, the factors that affect them, and their effect on the CTB properties (e.g., strength development). These laboratory and field studies have contributed to providing a good understanding of the fundamental mechanisms of the self-desiccation process in CTB from an experimental point of view. However, there is a paucity of related modelling studies, and thus very little progress has been made in modelling the self-desiccation process in CPB. Helinski et al. (2007b) derived an analytical model to quantify the changes in the PWP in CTB under fully saturated and undrained conditions. Wu et al. (2014) proposed a partially coupled thermo-hydro-chemical (THC) model to predict the suction build-up in CTB. However, none have taken into account the coupled multiphysics (THMC) processes in CTB in the development of a self-desiccation model. This means, at the time of writing, there is no model or modelling study that considers these multiphysics processes in the assessment of the self-desiccation behavior of CTB. This research gap has resulted in the current modelling study, in which an integrated multiphysics model of the self-desiccation process in CTB is developed. Then, the model is validated against both experimental data and in-situ measurements. Moreover, the model is used to assess the self-desiccation behavior of CTB structures under different backfill design strategies (i.e., with different mixture recipes, backfilling sequences and rates of backfilling) and backfilling conditions (stope geometry, inclination, rock surface roughness and initial temperature of the CTB and rock mass).

5.2.2. Mathematical Model

The following assumptions are made in the development of the proposed model:

(i) CTB is a multiphase porous medium which consists of a solid skeleton filled with capillary water and/or dry air,
(ii) the water vapor induced by evaporation is negligible,
(iii) pore water is considered to be an incompressible liquid,
(iv) the velocity of the solid skeleton is negligible compared to that of the pore water,
(v) the solid skeleton is deformable while the solid particles are incompressible,
(vi) there is thermal equilibrium between all of the phases (i.e., pore water, pore air and solid phase), and
(vii) compared with solid skeleton deformation, the thermal expansion of water is negligible. Hence, the changes in water content caused by the thermal expansion of water are not considered in this study.

To quantitatively determine the changes in the capillary water in a CTB matrix, the mass conservation principle for pore water is used, which indicates that the rate of the changes that take in the pore water (i.e., time and spatial derivatives) equals the water sink (or source) term. To solve the state variable (PWP) in mass balance, constitutive equations are incorporated into a continuity equation (i.e., mass balance equation). Hence, the water retention relationship, pore water flow, degree of binder hydration and related model parameters are identified. Moreover, a description of the heat transfer process in CTB is necessary as the rate of the binder hydration is temperature dependent. Thus, an energy balance equation and the relevant constitutive relations (i.e., heat conduction, advection and generation caused by hydration) are considered. In addition, due to the porosity dependence of the hydraulic properties (e.g., hydraulic conductivity), the volume changes of the CTB mass should be determined as well. Therefore, the multiphysics model that analyzes the consolidation process in CTB proposed by Cui and Fall (2016c) will be used in this study to characterize the volumetric deformation of CTB during its consolidation process.

5.2.2.1. Conservation Equations

The pore-water mass balance equation is expressed as:

$$n\rho_w \frac{\partial S}{\partial t} + nS\frac{\partial \rho_w}{\partial t} + S\rho_w \frac{\partial n}{\partial t} + \nabla \cdot \left(nS\rho_w \mathbf{v}^{rw} \right) = -nS\dot{r}_{hydr} \tag{5.1}$$

where ρ_w is the water density, n denotes the porosity, S refers to the degree of saturation, $\mathbf{v}^{rw}$ indicates the relative apparent velocity of the pore water with respect to the solid phase velocity $\mathbf{v}_s$, and $\dot{r}_{hydr}$ is the rate of water consumption per unit volume in the liquid phase due to binder hydration.

As mentioned earlier, the heat transfer and resultant temperature changes in CTB due to the effects of temperature on the rate of hydration should be examined to determine the degree of binder hydration. In terms of the heat transfer in CTB, the heat conduction due to the temperature gradient, heat advection induced by the fluid flow, and heat generation due to binder hydration are considered in this study. The energy balance equation is written as follows:

$$\begin{aligned} &\left[\left(1-n\right)\rho_s C_s + nS\rho_w C_w + n\left(1-S\right)\rho_a C_a \right] \frac{\partial T}{\partial t} + \left(\rho_w C_w \mathbf{v}^{rw} + \rho_a C_a \mathbf{v}^{ra} \right) \cdot \nabla T \\ &-\nabla \cdot \left(k_{eff} \nabla T \right) = Q_{hydr} \end{aligned} \tag{5.2}$$

where C_i refers to the specific heat capacity (i : air, water and solid phase), $\mathbf{v}^{rw}$ and $\mathbf{v}^{ra}$ denotes the fluid Darcy velocity, k_{eff} is the effective thermal conductivity of the CTB, and Q_{hydr} denotes the heat produced by the binder hydration.

Moreover, with the development of the volumetric deformation in CTB, the porosity will change with time, which can result in changes to the porosity-dependent properties (e.g., hydraulic conductivity). Therefore, consolidation induced volume changes should be incorporated into the proposed model in this study. A previous study on the consolidation behavior of CTB (Cui and Fall 2016c) found that the coupled multiphysics processes govern the consolidation behavior through chemical shrinkage, the effects of self-weight, water drainage through the barricade and thermal expansion. Hence, the fully coupled multiphysics model developed in Cui and Fall (2016c) will be used in this study. For detailed information on how the model is derived and related coefficients are determined, see (Cui and Fall 2016c).

$$\begin{aligned}
&\left\{\left[SP_w+(1-S)P_a\right]\frac{1-2\upsilon}{E}\frac{\partial\alpha_{Biot}}{\partial\xi}-\left\{\frac{\sigma+\alpha_{Biot}\left[SP_w+(1-S)P_a\right]}{E}\right\}\left\{\frac{9[1-2\upsilon]}{E}\frac{\partial E}{\partial\xi}+18\frac{\partial\upsilon}{\partial\xi}\right\}\right.\\
&\left.-\alpha_{Biot}\left(P_a-P_w\right)\frac{1-2\upsilon}{E}\left\{\left[1-S_e\left(P_w,P_a,\xi\right)\right]\frac{\partial\theta_r}{\partial\xi}+\left(n-\theta_r\right)\frac{\partial S_e}{\partial\xi}\right\}-\frac{\left(v_{ch-w}+v_{ab-w}\right)R_{n-w/hc}/(1-n)}{(w/c)v_w+v_c+\left(1/C_m-1\right)v_{tailings}}\right\}\frac{\partial\xi}{\partial t}\\
&+\frac{1-2\upsilon}{E}\frac{\partial\sigma}{\partial t}+\alpha_{Biot}\frac{1-2\upsilon}{E}\left\{S-\left(P_a-P_w\right)\left(n-\theta_r\right)\frac{\partial S_e}{\partial P_w}\right\}\frac{\partial P_w}{\partial t}+\frac{\partial\lambda_p}{\partial t}\frac{\partial Q_{CTB}}{\partial I_1}+\alpha_{Ts}\frac{\partial T}{\partial t}\\
&+\alpha_{Biot}\frac{1-2\upsilon}{E}\left\{(1-S)-\left(P_a-P_w\right)\left(n-\theta_r\right)\frac{\partial S_e}{\partial P_a}\right\}\frac{\partial P_a}{\partial t}\\
&=-\left\{(1-n)+\alpha_{Biot}\left(P_a-P_w\right)\frac{1-2\upsilon}{n^2E}\left[n(1-n)S_e+\left(1-S_e\right)\theta_r\right]\right\}\frac{\partial n}{\partial t}
\end{aligned}\qquad(5.3)$$

where P_w and P_a respectively denote the pore-water and pore-air pressures, S_e is the effective degree of saturation, α_{Biot} is the Biot's effective stress coefficient, E and υ denote the elastic modulus and Poisson's ratio, respectively, ξ is the degree of binder hydration, θ_r is the residual water content, v_w, v_{ch-w}, v_{ab-w}, v_c and $v_{tailings}$ respectively stand for the specific volume of the capillary water, chemically combined water, physically absorbed water, cement and tailings, C_m is the binder content, w/c represents the water to cement ratio, $R_{n-w/hc}$ is the mass ratio of the chemically combined water and hydrated cement, λ_p is a non-negative plastic multiplier and Q_{CTB} is a plastic potential function, and α_{Ts} is the coefficient of the thermal expansion (CTE) of the solid phase of the CTB. For detailed information on the multiphysics model of consolidation, see (Cui and Fall 2016c).

The variation of the pore air in CTB is considered in Eq. (5.3). Consequently, the pore-air mass balance equation is expressed as follows:

$$n(1-S)\frac{\partial\rho_a}{\partial t}-n\rho_a\frac{\partial S}{\partial t}+(1-S)\rho_a\frac{\partial n}{\partial t}+\nabla\cdot\phi(1-S)\rho_a\mathbf{v}^{ra}=0\qquad(5.4)$$

5.2.2.2. Constitutive Relations

5.2.2.2.1. Water Retention Model

The water retention curve (WRC) shows how the volumetric water content, θ, may be related to the capillary pressure, P_c, (i.e., matric suction) (Williams 1982). Many empirical models (e.g., Brooks and Corey 1964; Van Genuchten 1980; Hogarth et al. 1988; Fredlund and Xing 1994) have been developed to predict the WRC. In previous studies on CTB (Abdul-Hussain and Fall 2011; Ghirian and Fall 2013), the van Genuchten model (Van Genuchten 1980) has been modified and successfully applied to simulate the WRC for CTB. This model can be expressed as a three-parameter formula as follows:

$$\theta = \theta_r + \frac{\left(\theta_s - \theta_r\right)}{\left[1+\left(\alpha_{WRC} P_c\right)^{n_{WRC}}\right]^{m_{WRC}}} \tag{5.5}$$

where α_{WRC}, n_{WRC} and m_{WRC} are three different model parameters and change with the binder hydration, θ_s refers to the saturated water content and equals the CTB porosity n, and θ_r is the residual water content. n_{WRC} is assumed to be related to m_{WRC} through $n_{WRC} = 1/\left(1-m_{WRC}\right)$. Based on the definition of the effective degree of saturation (i.e., S_e = $\left(\theta-\theta_r\right)/\left(\theta_s-\theta_r\right)$), the water retention model is rewritten as follows:

$$S_e = \frac{1}{\left[1+\left(\alpha_{WRC} P_c\right)^{\frac{1}{1-m_{WRC}}}\right]^{m_{WRC}}} \tag{5.6}$$

The corresponding water retention model parameters (α_{WRC}, n_{WRC} and m_{WRC}) are provided in the subsection on model coefficient determination.

5.2.2.2.2. Pore Fluid Flow Model

As discussed earlier, both the pore-air and pore-water flow are taken into account in this study. Due to the relatively low pore fluid flow in CTB, Darcy's law is assumed to be valid and used to describe the fluid flow for liquid water $\mathbf{v}^{rw}$ and dry air $\mathbf{v}^{ra}$:

$$\mathbf{v}^{ri} = -K_{sat} \frac{k_{ri}}{\rho_i g}\left(\nabla P_i - \rho_i g \nabla D_i\right) \tag{5.7}$$

where K_{sat} refers to the saturated hydraulic conductivity, k_{ri} denotes the relative permeability with respect to each fluid, and P_i denotes the pore fluid pressure, and D_i refers to the changes. The hydraulic conductivity K_{sat} is related to the viscosity pore fluid and the CTB porosity (Pokharel and Fall 2013). Due to the development of the consolidation of the CTB, variation of the porosity will result in changes in K_{sat}. Detailed information on determining the hydraulic conductivity is provided in the subsection on model coefficient determination.

Based on previous studies on the pore-fluid flow in porous media (Li et al. 2006; Rotisciani et al. 2015), the relative permeability of the pore water k_{rw} and pore air k_{ra} is controlled by the degree of saturation. In this study, the prediction models proposed by Van Genuchten (1980) and Luckner et al. (1989) based on the Mualem model (Mualem 1976) are adopted.

$$k_{rw}\left(S_e\right)=\sqrt{S_e}\left[1-\left(1-S_e^{1/m_{WRC}}\right)^{m_{WRC}}\right]^2 \tag{5.8}$$

$$k_{ra}\left(S_e\right)=\sqrt{1-S_e}\left(1-S_e^{1/m_{WRC}}\right)^{2m_{WRC}} \tag{5.9}$$

where m_{WRC} is a water retention model parameter and will be determined in the subsection on model coefficient determination.

5.2.2.3. Degree of Binder Hydration Model

As previously mentioned, the progression of binder hydration can cause pore-water consumption, heat generation and pore space refinement (Helinski et al. 2007b; Cui and Fall 2015). The degree of binder hydration ξ should therefore be identified to quantitatively evaluate the effect of hydration reaction on CTB. In this study, an exponential function proposed by Schindler and Folliard (2003) is applied to predict the progression of binder hydration, which has been successfully applied to CTB materials in previous studies (e.g., Cui and Fall 2015; Lu and Fall 2016).

$$\xi=\left(\frac{1.031\cdot w/c}{0.194+w/c}+0.5\cdot X_{FA}+0.30\cdot X_{slag}\right)\cdot\exp\left\{-\left\{\tau\Big/\int_0^t\exp\left[\frac{E_a}{R}\left(\frac{1}{T_r}-\frac{1}{T}\right)\right]dt\right\}^{\beta}\right\} \tag{5.10}$$

with

$$\tau=66.78{x_{C_3A}}^{-0.154}\cdot{x_{C_3S}}^{-0.401}\cdot x_{SO_3}\cdot{S_{Blaine}}^{-0.804}\cdot\exp\left(2.178X_{slag}+9.5X_{FA}X_{FA-CaO}\right)$$

$$\beta=181.4{x_{C_3A}}^{0.146}\cdot{x_{C_3S}}^{0.227}\cdot{x_{SO_3}}^{0.558}\cdot{S_{Blaine}}^{-0.535}\cdot\exp\left(-0.647X_{slag}\right)$$

$$E_a\left(T\right)=\begin{cases}33{,}500+1{,}470\times\left(293.15-T\right) & T<293.15K\\ 33{,}500 & T\geq 293.15K\end{cases}$$

where w/c denotes the water to cement ratio, X_{FA} and X_{slag} respectively stand for the weight fraction of the fly ash and blast furnace slag relative to the total binder weight, τ and β respectively refer to the hydration time (hours) and shape parameters, t_e is the equivalent age at the reference temperature T_r, E_a is the activation energy (J/mol), R is a universal gas constant, x_i represents the mass ratio of the i component to the total binder weight (i =*C₃A*, *C₃S* and *SO₃*), and X_{FA-CaO} is the weight ratio of *CaO* to fly ash.

The degree of binder hydration model (Eq.(5.10)) can be used to determine the sink terms for pore water $\dot{m}_{hydr}$ in Eq. (5.1) and heat source term Q_{hydr} in Eq. (5.2). Based on previous research on cement hydration (Powers and Brownyard 1947; Schindler and Folliard 2003), $\dot{m}_{hydr}$ and Q_{hydr} are derived as follows:

$$\dot{m}_{hydr} = m_{hc-initial}\left(0.187x_{C_3S} + 0.158x_{C_2S} + 0.665x_{C_3A} + 0.2130x_{C_4AF}\right) \times\left\{\left(\frac{\tau}{t_e}\right)^{\beta}\left(\frac{\beta}{t_e}\right)\xi\left(t_e\right)\exp\left[\frac{E_a}{R}\left(\frac{1}{273+T_r}-\frac{1}{273+T}\right)\right]\right\} \tag{5.11}$$

$$Q_{hydr} = \left(H_{cem}X_{cem} + 461X_{slag} + 1800x_{CaO/FA}X_{FA}\right)C_b \times\xi\left(\frac{\tau}{t_e}\right)^{\beta}\left(\frac{\beta}{t_e}\right)\exp\left[\frac{E}{R}\left(\frac{1}{273+T_r}-\frac{1}{273+T}\right)\right] \tag{5.12}$$

where $m_{hc-initial}$ is the initial cement mass, H_{cem} is the total heat of hydration of the cement, C_b is the apparent binder density relative to the total volume of the CTB, X_i is the weight fraction of the minerals with respect to the total binder content, and x_i is the weight ratio of the clinker composition relative to the total cement content.

5.2.2.4. Model Coefficient Determination

It has been observed that with the progression of binder hydration, the residual water content will be reduced with curing time, especially for early-age CTB (Abdul-Hussain and Fall 2011). To characterize the changes in the residual water content, θ_r, Abdul-Hussain and Fall (2011) proposed a prediction function based the measured WRCs for different curing times:

$$\theta_r = R_{r1}\cdot\exp\left(-R_{r2}\cdot\xi\right) \tag{5.13}$$

where R_{r1} and R_{r2} are the fitting constants. The measured WRCs reported in (Abdul-Hussain and Fall 2011), R_{r1}=0.01314 and R_{r2}=7.538, are adopted in this study.

Moreover, to characterize the relationship between the water content and matric suction, the water retention model parameters m_{WRC} and α_{WRC} in Eq. (5.5) should be determined; therefore, the following prediction functions are proposed based on the measured WRCs of the CTB reported in (Abdul-Hussain and Fall 2011):

$$m_{WRC} = f_{m1}\xi^{f_{m2}} + f_{m3} \tag{5.14}$$

$$\alpha_{WRC} = f_{\alpha1}e^{f_{\alpha2}} \tag{5.15}$$

where f_{m1}, f_{m2}, f_{m3}, $f_{\alpha1}$ and $f_{\alpha2}$ are the fitting constants. Based on the experimental results reported in (Abdul-Hussain and Fall 2011), f_{m1}=0.0415, f_{m2}=4.231, f_{m3}=0.4073,

$f_{\alpha 1}$=0.2103 kPa^{-1} and $f_{\alpha 2}$=-6.921 which are obtained through regression analysis. As shown in Figure 5.1, the proposed water retention model can accurately capture the effect of binder hydration on the WRC.

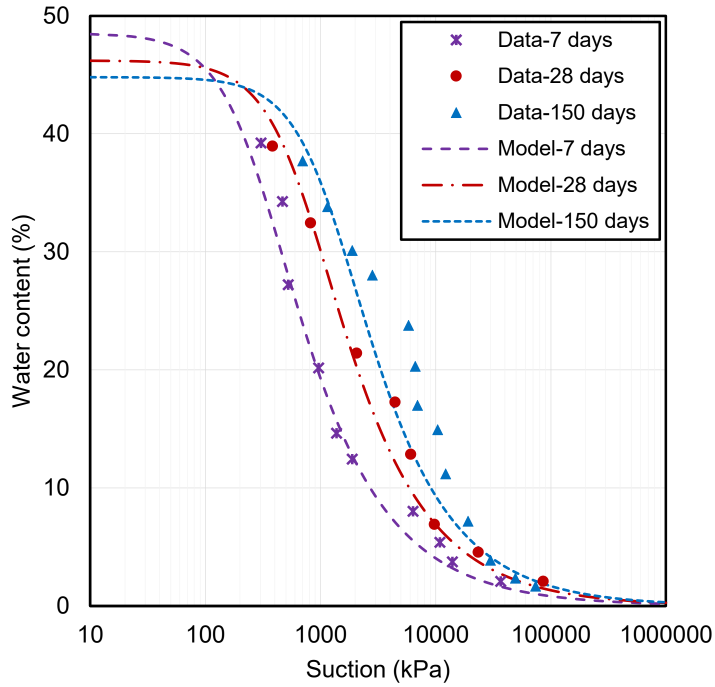

Figure 5.1. Comparison between predicted and experimental results for WRCs (experimental data from (Ghirian and Fall 2013))

The hydraulic conductivity K_{sat} needs to be determined to characterize the pore-fluid flow in CTB. Due to the dependence of K_{sat} on the porosity n (Mehrabian and Abousleiman 2015; Shin et al. 2015), the consolidation processes can induce changes in the hydraulic conductivity of CTB. Therefore, the following prediction equation of K_{sat} developed by Carrier et al. (1983) is used in this study:

$$K_{sat} = C_{K1}\left(\frac{n}{1-n}\right)^{C_{K2}} \Big/ \left(\frac{1}{1-n}\right) \tag{5.16}$$

where C_{K1} and C_{K2} are the fitting constants. Cui and Fall (2016c) suggested two material constants, C_{K1} =1.963e-5 cm/s and C_{K2} =12.96. The changes in the porosity can then be predicted by using multiphysics model of consolidation (i.e., Eq. (5.3)). As shown in Figure 5.2, the predicted data are in good agreement with the experimental data of K_{sat} reported in (Yilmaz 2012; Cui and Fall 2016c), and the coefficient of determination equals 0.96.

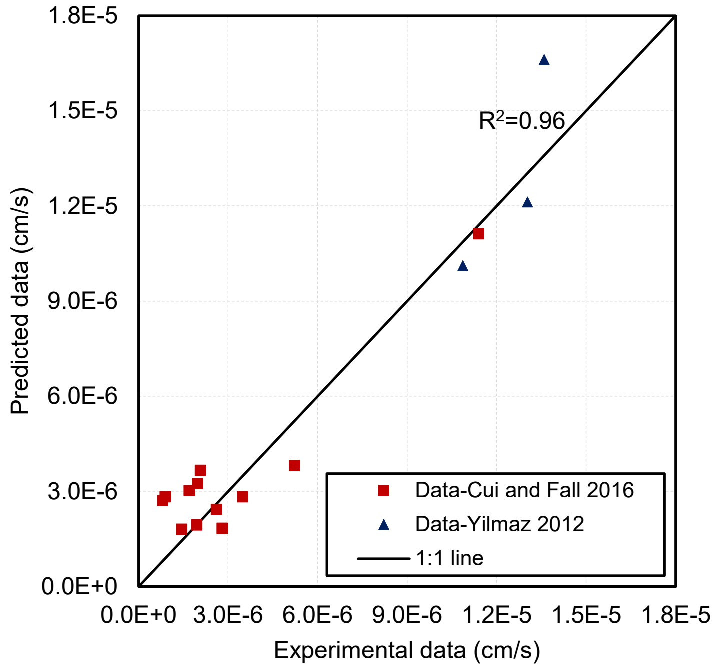

Figure 5.2. Comparison of predicted and experimental data on hydraulic conductivity

The thermal conductivity k_{eff} in Eq. (5.2) has to be determined to predict the heat transfer and temperature changes in CTB. Previous studies on CTB materials (Abbasy 2009; Ghirian and Fall 2013) have observed that the thermal conductivity value depends on the type of tailings and degree of saturation. Hence, the changes in the degree of saturation as a result of self-desiccation can affect the thermal conductivity. To predict the changes in thermal conductivity k_{eff}, the following equation proposed by (Somerton et al. 1974) is adopted in this study:

$$k_{eff} = k_{dry} + \sqrt{S_e}\left(k_{sat} - k_{dry}\right) \quad (5.17)$$

$$with \begin{cases} k_{sat} = k_{tailings}^{1-n} k_w^n \\ k_{dry} = k_{tailings}^{1-n} k_a^n \end{cases}$$

where k_{sat} and k_{dry} are the thermal conductivity of the porous media in the saturated state and a completely dry condition respectively, and $k_{tailings}$, k_w and k_a denote the thermal conductivity of the tailings, water and air, respectively. As shown in Figure 5.3, there is a good agreement between the predicted results and experimental values (coefficient of determination equals 0.97).

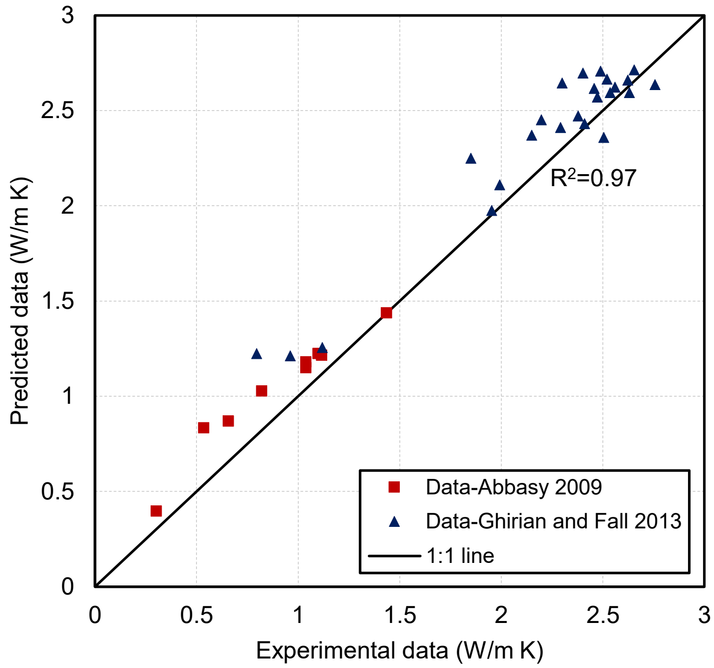

Figure 5.3. Comparison between predicted and experimental data for thermal conductivity

5.2.3. Model Validation

To validate the multiphysics model of self-desiccation, a series of case studies are applied in this study, which include those with both experimental and field measurements. The developed model is implemented into a finite element method (FEM) code, COMSOL Multiphysics. COMSOL can perform various types of analyses, including stationary, time-dependent, linear and nonlinear. Moreover, COMSOL Multiphysics provides a powerful simulation platform for modelling coupled multiphysics systems (Comsol 2015). Details on the input parameters, and initial values and boundary conditions for each case study and of each model application are provided in Table 5.1.

Table 5.1. Input parameters, and initial and boundary conditions

	Cell Tests - THMC	Column Tests - THMC	Field Study 1	Field Study 2
Cement content (wt %)	4.5	4.5	7.4	3.1
w/c ratio	7.6	7.6	7.6	10.8
Backfilling rate (m/h)	0.31	N/A	0.35	0.26
Backfilling strategy	N/A	Placed in 3 stages	Placed in 3 stages	Placed in 2 stages
Mechanical module				
Top surface	Boundary load	Free	Free	Free
Lateral sides	Roller	Roller	Roller	Roller
Bottom side	Fixed	Fixed	Fixed	Fixed
Volume force	Gravity	Gravity	Gravity	Gravity
Hydraulic module				
Top surface	No flow	No flow	No flow	No flow
Lateral sides	No flow	No flow	No flow	No flow
Barricade side	N/A	N/A	N/A	Mass flux
Bottom side	No flow	No flow	No flow	No flow
Volume force	Gravity	Gravity	Gravity	Gravity
Initial value	Hydraulic head=0	Hydraulic head=0	Hydraulic head=0	Hydraulic head=0
Thermal module				
Top side (°C)	22	23	35	35
Lateral sides (°C)	22	23	35	35
Bottom side (°C)	22	23	35	35
Initial temp. (°C)	5 and 35	23	35	35

N/A: not applicable

5.2.3.1. Validation against Results of THMC Cell Experiments

To investigate the effects of the hydration reaction of the binder and consolidation on self-desiccation, a series of cell tests were conducted under different curing stresses and thermal loads in this study with the THMC cell apparatus developed in Ghirian and Fall (2015). The experimental apparatus and setup are shown in Figure 5.4. The THMC cell comprises a Perspex cylinder (10 cm (diameter) × 30 cm (height)), an air-pressure driven piston and two plates (top and bottom) with three tie rods to hold the THMC cell.

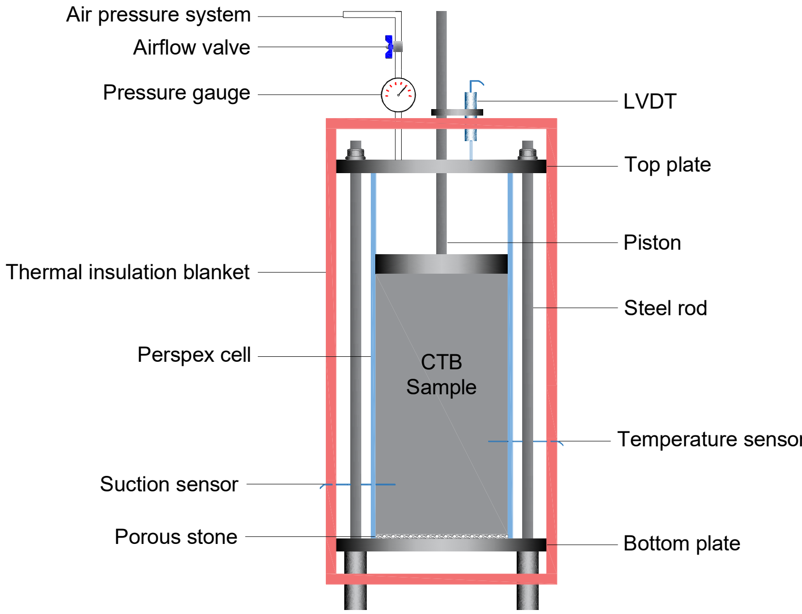

Figure 5.4. Schematic diagram of THMC cell set-up

The experimental set up included an MPS-2 suction meter and a 5TE soil moisture sensor to monitor the temperature which were installed in the THMC cell. Moreover, a linear variable differential transformer (LVDT) was installed on the top of the cell to monitor the vertical settlement. To apply pressure onto the piston, a compressed air system was incorporated into the THMC cell apparatus, which can apply up to 600 kPa of pressure onto the piston to simulate the in-stope backfilling process. A piston seal (o-ring seal) was installed to prevent the infiltration of air into the CTB sample. The details on the application of pressure onto the piston are shown in Figure 5.5.

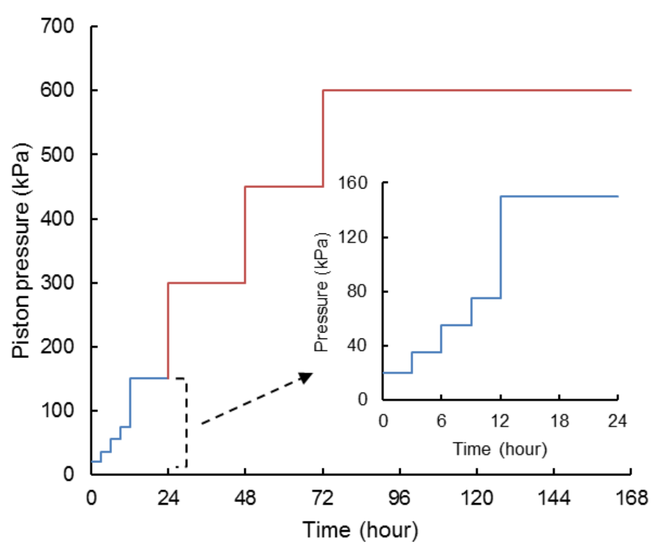

Figure 5.5. Application of pressure onto piston in THMC cell test

Artificial silica tailings (made of mineral quartz, which is the most common type of mineral found in Canadian hard rock mines), tap water (w/c=7.6) and Portland cement Type 1 (4.5 wt%) were used in the preparation of the CTB samples. Two different initial temperatures of 5°C and 35°C were used to investigate the effect of the initial temperature of the CTB on self-desiccation behavior. The THMC cell was covered with a glass wool blanket for thermal insulation (the properties of thermal insulation material is presented in Table 5.2), and curing of the samples took place in a temperature controlled laboratory room (~22°C).

Table 5.2. Properties of glass wool blanket (thermal insulation material)

Density kg/m3	Thermal conductivity W/(m K)	Heat capacity J/(kg K)
30	0.035	840

A 2D axisymmetric model is adopted in this case study for simulation purposes. The geometry and mesh of the model are shown in Figure 5.6.

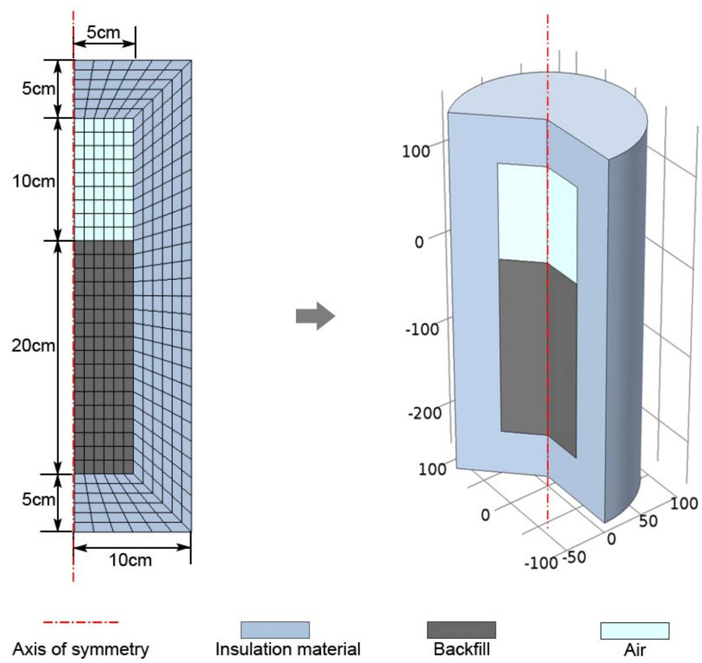

Figure 5.6. Geometry and mesh of simulated model of THMC cell test

As shown in Figure 5.7, both the predicted results and experimental data demonstrate that: (1) the PWP changes with curing time, which can be attributed to the water consumption caused by the hydration reaction. The chemical reaction induced water loss can cause a reduction in the water content of the CTB and thus result in the build-up of negative PWP (self-desiccation); (2) a higher initial temperature can give rise to higher negative PWP with curing time. This is due to the temperature dependence of the rate of hydration (see Eq.(5.10)). A higher initial temperature can increase the hydration reaction and result in more pore-water depletion at a given curing time; in other words, it leads to more intense self-desiccation (Fall et al. 2010). Consequently, increased dissipation of the PWP can be observed in the CTB with a higher initial temperature for a given curing time; (3) the water-potential sensor used (MPS-2, Decagon Devices, Pullman, Washington) has a range of -10 kPa to -100,000 kPa. Hence, the positive PWP changes at a very early-age (during the 1st day of curing) were not monitored, and only the simulation results are presented for the early-age CTB in Figure 5.7. It can be observed that the applied pressure can significantly affect the variation of the PWP for the early-age CTB. Specifically, an immediate increase in PWP can be observed each time after pressure is applied, which is followed by a decrease in the PWP caused by the self-desiccation process. Although no measured data can validate the PWP at the early ages, the simulation results still can be used to demonstrate the trends of changes in the PWP when pressure is applied in multiple stages; namely, the developed model has the potential capability to characterize the effect of numerous backfilling operations on the PWP changes in a stope.

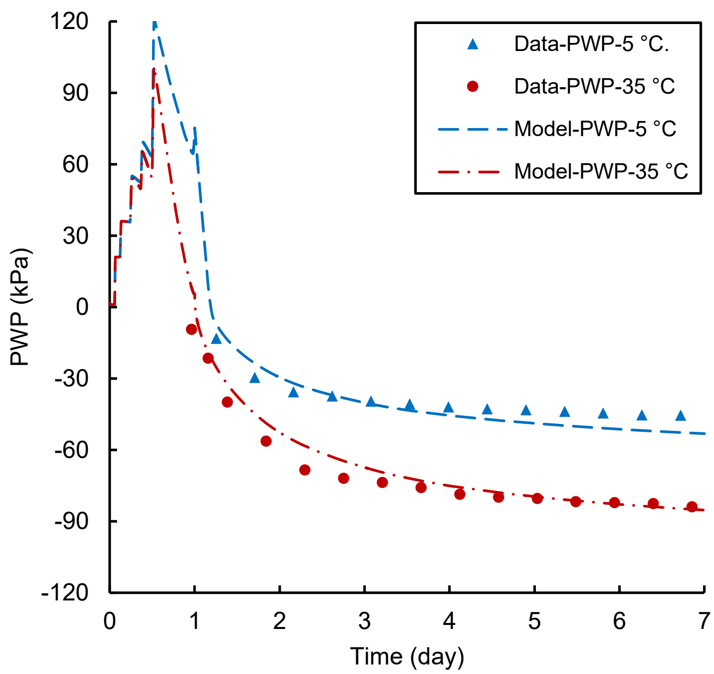

Figure 5.7. Comparison between modelling results and experimental data for PWP from THMC cell test

As shown in Figure 5.7, the initial temperature can have significant impacts on the self-desiccation of CTB. Therefore, it is important to examine the temperature changes in CTB. Figure 5.8 presents a comparison of the predicted results with the experimental data on the temperature in the CTB. It can be observed that a higher initial temperature (i.e., 35°C) results in higher temperatures in the CTB at the early ages (the first 1.5 days). After that, the temperature gradually approaches room temperature (around 22°C). This is because a higher initial temperature can accelerate the binder hydration that occurs in CTB (Walske et al. 2016; A. Wu et al. 2016), and thus a relatively large amount of heat can be released by the exothermic reaction in the CTB. Therefore, a higher initial temperature means a higher temperature in the CTB. However, with the progression of binder hydration, the chemical reaction rate gradually decreases with curing time (D. Wu et al. 2016), and thus the rate of heat generation due to binder hydration is reduced with time. As a result, the heat transfer between the CTB and the surrounding environment becomes a more significant contributor to the variation in temperature in the CTB. Therefore, the temperature in the CTB increasingly approaches room temperature with curing time. As evident in Figure 5.8, the developed model captures the temperature changes in the CTB well in terms of both trends in changes and magnitude.

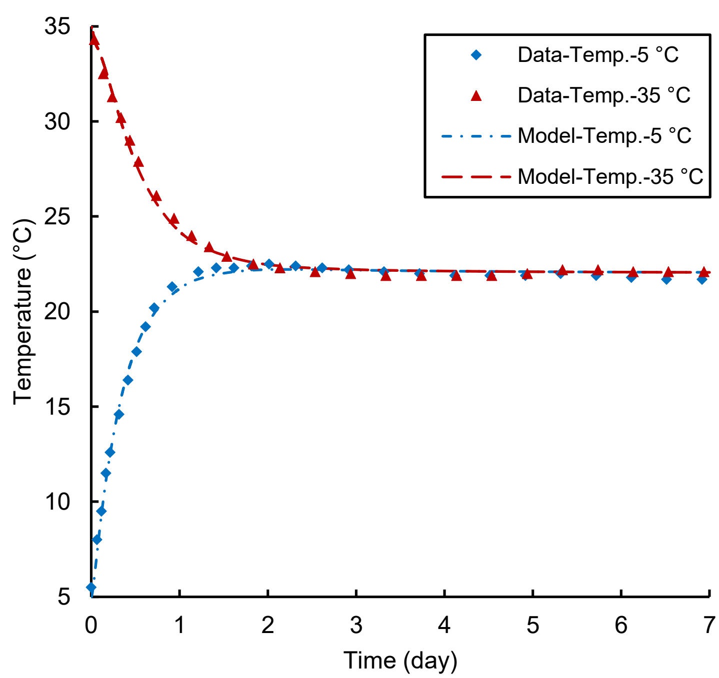

Figure 5.8. Comparison between predicted results and experimental data for temperature from THMC cell test (Temp.: temperature)

The coefficient of permeability controls the pore fluid flow, and thus can influence the self-desiccation behavior. Due to the porosity dependence of permeability, it is important to evaluate the development of the deformation and hydraulic conductivity of CTB with curing time. Figure 5.9 shows that (1) the vertical settlement of the sample increases with applied pressure onto the piston, and (2) the CTB sample adds to the vertical deformation under a higher initial temperature. This is due to the chemical shrinkage that occurred in the CTB (Cui and Fall 2016b). With the progression of binder hydration, the capillary water is converted into chemically combined water (solid phase). However, the resultant volume of hydrate products is less than the original volume of binder and water. As a result, chemical reaction induced deformation (i.e., chemical shrinkage) takes place. As mentioned above, a higher initial temperature can lead to higher temperatures in the CTB and thus accelerate binder hydration, which can result in greater settlement of the CTB. As illustrated in Figure 5.9, there is a good agreement between the predicted results and monitored data.

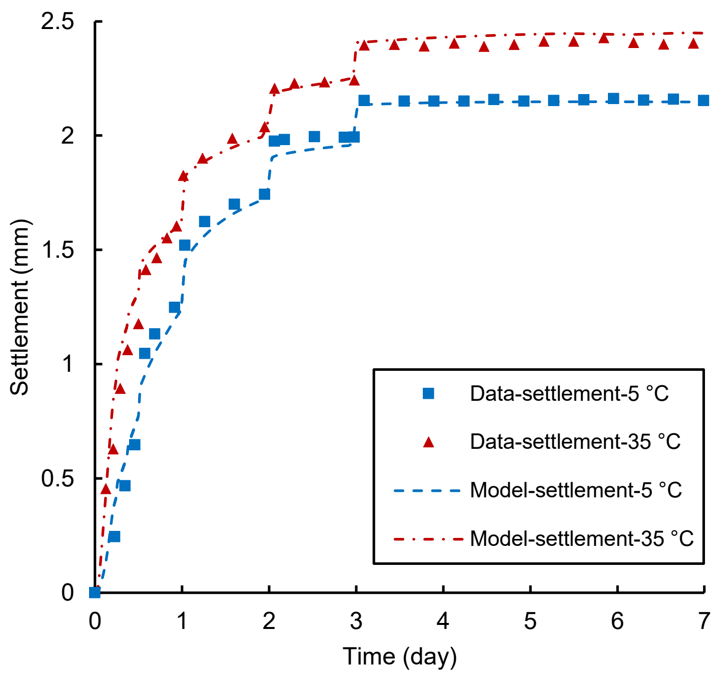

Figure 5.9. Comparison between predicted results and experimental data for settlement of CTB from THMC cell test

The predicted and measured hydraulic conductivities are plotted in Figure 5.10. A comparison of the hydraulic conductivities shows a decreasing trend with curing time. Moreover, the CTB with a higher initial temperature produces a smaller coefficient of permeability. The changes in the hydraulic conductivity are consistent with the volume changes in the CTB (re: Figure 5.9). The good agreement between the modelling and experimental results indicates that the developed model is able to accurately capture the dependency of the hydraulic conductivity on porosity.

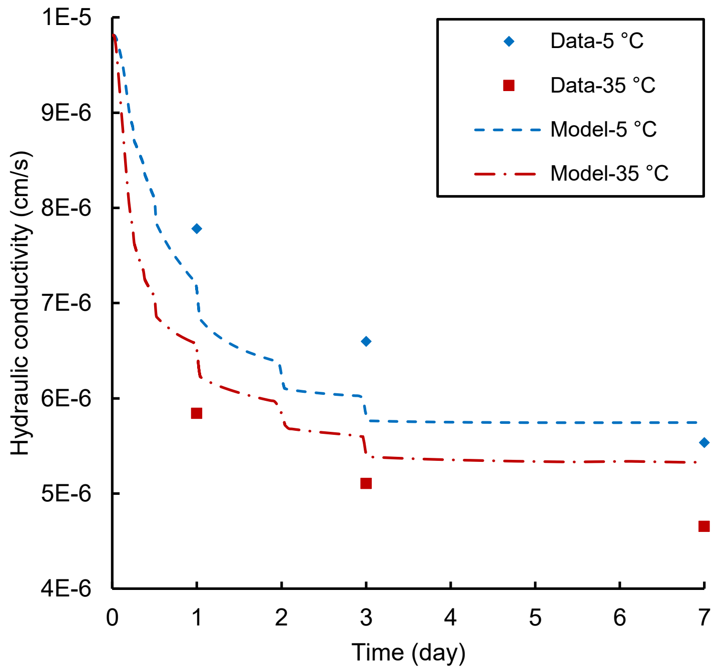

Figure 5.10. Comparison between predicted results and experimental data for hydraulic conductivity from THMC cell test

5.2.3.2. Validation against Results of THMC Column Experiments

To study the coupled multiphysics behavior of CTB, a series of column experiments on the THMC interactions were conducted by Ghirian and Fall (2013). During the column tests, a backfilling strategy that involved three stages of backfilling (backfill height of 50 cm for three consecutive days) was adopted. For each stage of filling, the placement was completed after approximately 5 minutes. Moreover, similar to the THMC cell used in the pressure cell tests, the THMC column was covered with thermal insulation foam to mimic the real conditions of CTB cured in a stope environment. During the column tests, water drainage was not allowed. To obtain the experimental data, suction sensors were installed in the columns at three different locations (i.e., 25 cm, 75 cm and 125 cm from the bottom of the columns). Detailed information on the experimental program can be found in (Ghirian and Fall 2013). An axisymmetric geometry model was used to simulate the column experiment on the THMC interactions. The geometry, mesh and monitored points of the model are presented in Figure 5.11.

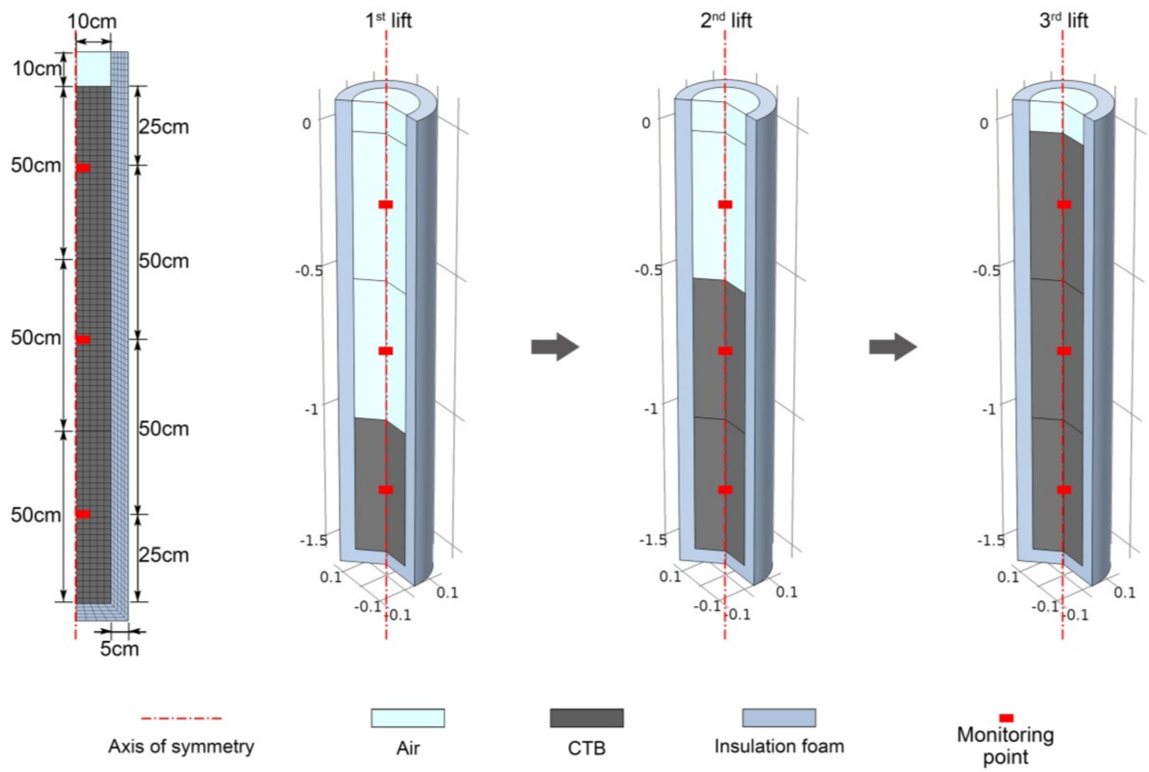

Figure 5.11. Modelled geometry and mesh of column and and backfilling processes in experiment on THMC interactions

The changes in the PWP in the CTB column is presented in Figure 5.12, from which it can be observed that: (1) the filling operation which took place in stages has significant impacts on the PWP changes. Specifically, after placement of each lift, the PWP immediately increases. This is due to the combined effect of the downward flow of the pore water under the effects of the self-weight of CTB, and the increase in the total pressure from the newly placed lift of CTB. In this regard, it should be noted that the increase in PWP due to the filling operation will also affect the barricade pressure and thus its stability (Thompson et al. 2009). Therefore, compared to continuous backfilling, a filling operation that takes place in stages requires a relatively long placement time and curing time between each filling sequence (Yumlu 2008). Consequently, the dissipation of PWP can be greater in CTB, which is more favourable for the stability of the CTB structure; (2) a negative PWP appears after approximately one-day of curing for each lift. Afterwards, the reduction in the PWP is less apparent. This is because the rate of hydration is relatively faster at the very early ages (Haj-zamani 2010), and thus there is greater dissipation of the PWP. However, as the hydration reaction progresses, the solid hydrates that are precipitated in the pore space can inhibit the diffusion of the capillary water and thus contact with the unhydrated cement (Poole et al. 2007). As a result, the hydration reaction slows down and slow dissipation of the PWP is observed; (3) the differences in the PWP at the monitored points become more obvious with curing time. As shown in Figure 5.12, a higher negative PWP can be found in the top lift compared with the negative PWP in the monitored points that are lower on the column. Under undrained conditions, the dissipation of PWP is mainly attributed to the pore-water consumption caused by binder hydration (i.e., self-desiccation effect) (Helinski et al. 2007b). Hence, with PWP dissipation and the associated downward pore-water flow due to the effect of the self-weight of CTB, the negative PWP gradually increases on the top part of the CTB mass. The good agreement between the simulated results and experimental data further proves the predictive capability of the developed model.

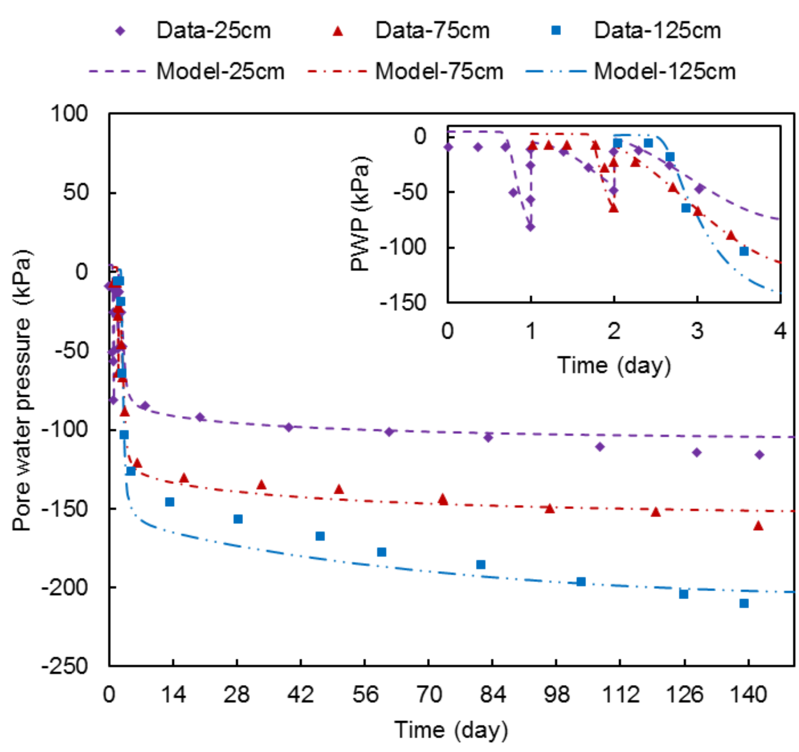

Figure 5.12. Comparison between prediction results and experimental data for PWP from THMC column test (experimental data from (Ghirian and Fall 2013))

5.2.3.3. Validation against Field Results - Case Study 1

To further validate the developed model, a field monitoring program conducted by Yumlu (2008) in the Çayeli mine was selected for simulation. In this monitoring program, a piezometer (model: Geokon 4500S) was installed onto a rigid instrument frame to record the PWP changes in the stope environment. The backfilling operation and the curing were conducted under undrained conditions. The monitored point was located 0.5 m from the stope floor along the centerline of the stope. Details of the monitoring program (i.e., the binder recipe, backfilling strategy, and initial and boundary conditions) are provided in Table 5.1. In terms of the simulation, the modelled geometry, sensor location, mesh grid and monitored point are presented in Figure 5.13.

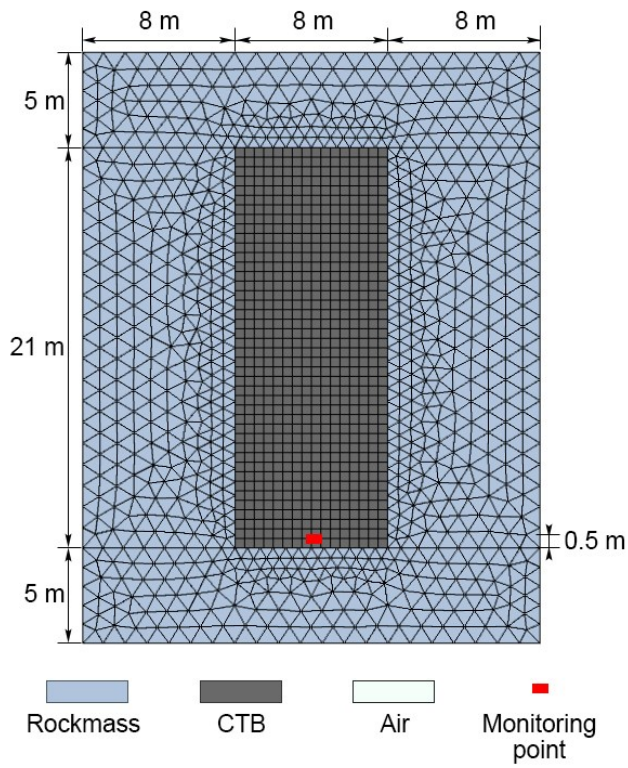

Figure 5.13. Modelled geometry, mesh and monitored point at Çayeli mine

Figure 5.14 shows the three stages of changes in the PWP with the filling process. It can be seen that: (1) similar to the obtained results in Sections 5.2.3.1 and 5.2.3.2, the PWP increases immediately after fresh CTB is placed into the stope, which further confirms the significant influence of backfilling operations on the PWP changes in CTB. However, it should be noted that the rate of change of the PWP during the first stage of filling shows a slight reduction with time. As water drainage is not allowed on this stope, water consumption caused by binder hydration dominates the dissipation of the PWP in the CTB (Helinski et al. 2007b), which results in the nonlinear increase of the PWP with filling. Moreover, with continuous water loss due to binder hydration, reductions in the PWP are found before the end of the first stage of filling, which further demonstrates the influence of the self-desiccation process on the PWP changes in CTB; (2) after completion of the first stage of filling, the PWP shows a trend of reduction at the early ages of curing (from 0.8 to 2.8 days). Specifically, the PWP gradually dissipates from 45 kPa to approximately 0 kPa during this stage. The PWP reduction can significantly contribute to the increase of the effective stress in CTB and thus to its stability (Shahsavari and Grabinsky 2015). Therefore, the obtained results further prove the significance of a filling strategy that is carried out in stages on the stability of a CTB structure; (3) afterwards, a slight increase in the PWP is observed during the filling sequences that followed. Hence, the backfilling operation that followed has very limited effects on the PWP changes in CTB compared to the measured PWP during the first stage of filling. This is primarily because the pore water in the newly poured CTB cannot completely offset the influence of the water loss through the self-desiccation process during the previous curing stage. Consequently, the increase in the PWP is not very evident, as observed. As shown in Figure 5.14, the trend and changes in the PWP are adequately captured by the model.

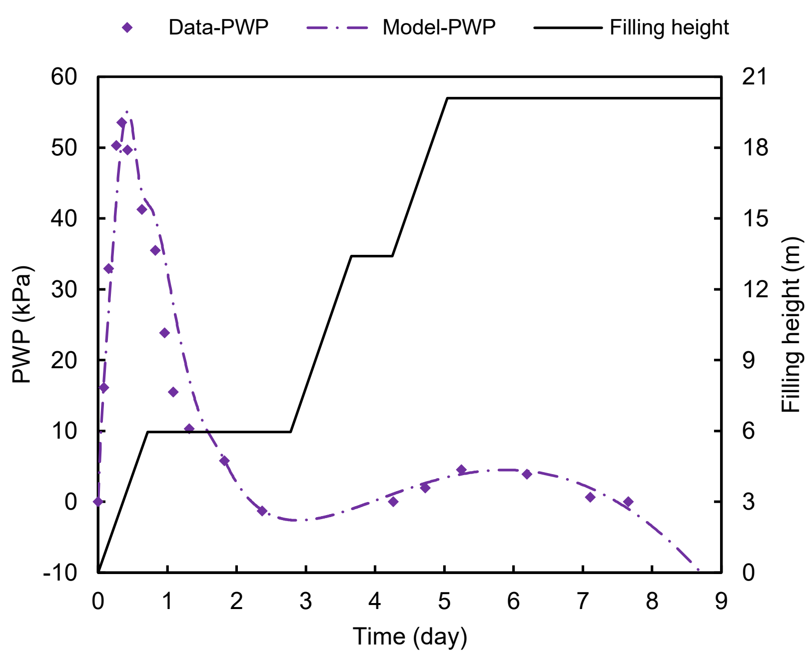

Figure 5.14. Comparison between numerical prediction results and experimental data for PWP from field measurements in Çayeli mine (experimental data from (Yumlu 2008))

5.2.3.4. Validation against Field Results – Case Study 2

To further validate the proposed model against field data, the in-situ measurements of PWP in CTB obtained by Helinski et al. (2010) in the Kanowna Belle Gold Mine are examined in this study. To monitor the PWP changes in the CTB at the early ages, a piezometer was installed in the center of the stope base. The monitoring time in the field measurements was set to 8 days. The stope was backfilled in two stages, and drainage through the barricade was allowed in this monitoring program. During and after the filling operation, water drainage through the barricade was allowed. For the numerical simulation of the drained condition in CTB, a water mass flux boundary condition was applied on the barricade side. The water mass flux can be calculated by multiplying the pore water density and its velocity through the retaining wall. The latter can be computed by using Darcy's law. Details on the mixture recipe, filling rate, and initial and boundary conditions are summarized in Table 5.1. The geometry and mesh of the model are presented in Figure 5.15.

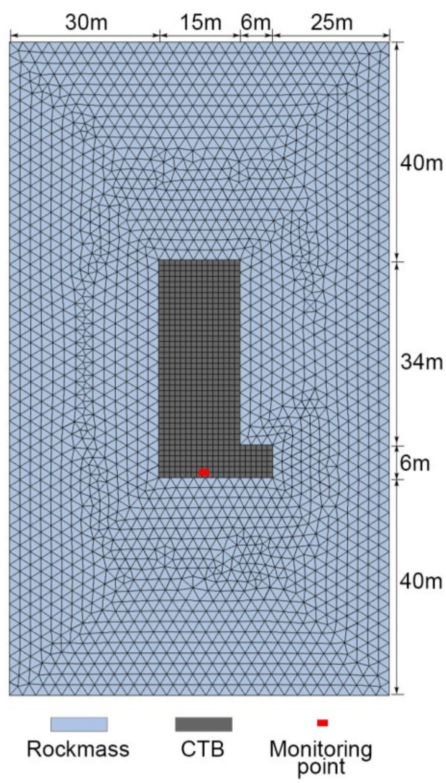

Figure 5.15. Mesh and geometry of simulated stope at Kanowna Belle Gold Mine

A comparison between the recorded data from Helinski et al. (2010) and the predicted results of the PWP is presented in Figure 5.16. It can be observed that there is an increase in the PWP during the first stage of filling, which is similar to the change in overburden stress. Then, at the early ages of curing (36 to 62 hours), there is a reduction in the PWP in the CTB. This can be attributed to the combined effects of water drainage through the barricade and water consumption caused by binder hydration. During the curing period, no fresh CTB is poured into the stope. Therefore, the continuous dissipation of PWP is observed with water loss in the CTB during this stage. Afterwards, the PWP shows a slight increase for the following stage of filling, which results in a large discrepancy between the PWP and stress due to the self-weight of the CTB. The good agreement between the predicted results and in-situ measurements further confirms the good predictive ability of the developed model.

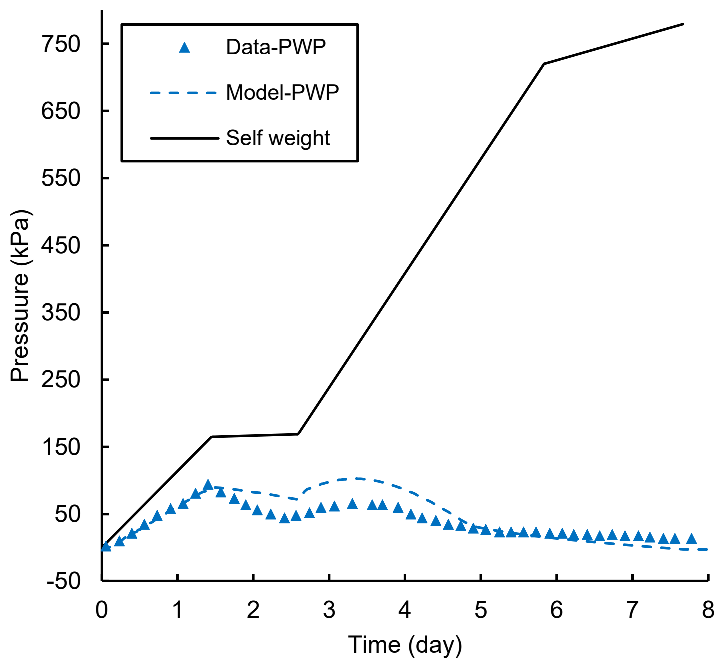

Figure 5.16. Comparison between modelling results and measurements of total stress and PWP at Kanowna Belle Gold Mine (experimental data from (Helinski et al. 2010))

Apart from the analysis on the PWP at the monitored point, it is of great interest to examine the spatial distribution of the PWP in the CTB for the different stages of filling. As shown in Figure 5.17: (1) the PWP is uniformly reduced from the bottom to the top of the CTB mass after the completion of the first stage of filling (Figure 5.17a), (2) during the curing period, no fresh CTB paste is poured into the stope, and a negative PWP appears at the top part of the CTB mass (see Figure 5.17b), and (3) in the following filling sequences, a negative PWP appears near the interface of the first fill layer and upper part of the CTB mass (see Figure 5.17c andFigure 5.17d). The development of negative PWP is attributed to the self-desiccation process and water drainage through the barricade (retaining wall). Moreover, as can be seen in Figure 5.17c and Figure 5.17d, the lowest PWP is mainly found in the vicinity of the interface of the two stages of filling, which indicates that the water loss by self-desiccation and water drainage through the barricade is faster than the replenishment from the pore-water in the upper part of the CTB mass. With the build-up of negative PWP, effective stress further develops in the first fill layer, and the PWP acting on the barricade structure can be dissipated to a greater extent. Therefore, filling in stages is a good strategy to ensure the stability of CTB structures and barricades.

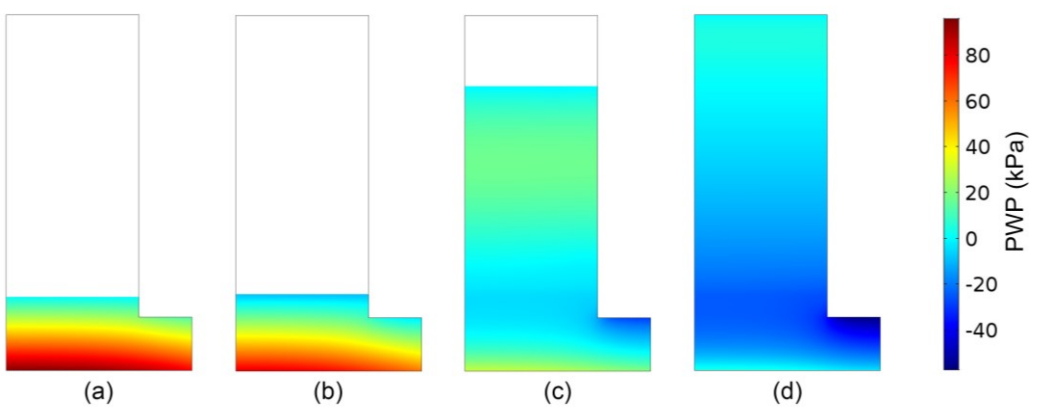

Figure 5.17. Spatial distribution of PWP of the investigated stope at Kanowna Belle Gold Mine for different fill times: (a) 32 hours; (b) 62 hours; (c) 120 hours; and (d) 184 hours.

5.2.4. Model Applications

After the successful validation of the multiphysics model of self-desiccation, the model was applied to examine a series of engineering issues. These include the investigation of the effects of curing time, stope geometry, mixture recipe, backfilling rate and strategy, and initial temperature of the CTB and rock mass on the self-desiccation behavior of the CTB structure. To demonstrate the impacts of these factors, a control CTB mass was used as the reference for the model application. The mixture recipe, backfilling conditions, and initial and boundary conditions of the control CTB are listed in Table 5.3. All of the numerical investigations on these influential factors are conducted by changing the conditions of the control stope, and except for the listed factors, the field conditions and CTB design are the same as the CTB in the control stope. The geometry and mesh of the control CTB mass and stope are presented in Figure 5.18. To evaluate the PWP changes in the CTB, a monitoring point located at 0.1 m from the floor of the stope is examined.

Table 5.3. Input parameters, and initial and boundary conditions adopted for control stope for model application

Parameter	Value/condition
Cement content (wt %)	4.5 Plug: 7
w/c ratio	7.6
Backfilling rate (m/h)	0.5
Backfilling strategy	Placed in 2 stages
Mechanical module	
Top surface	Free
Lateral sides	Roller
Bottom side	Fixed
Volume force	Gravity
Hydraulic module	
Top surface	No flow
Lateral sides	No flow
Bottom side	No flow
Volume force	Gravity
Initial value	Hydraulic head=0
Thermal module	
Top side (°C)	25
Lateral sides (°C)	25
Bottom side (°C)	25
Initial temp. (°C)	25

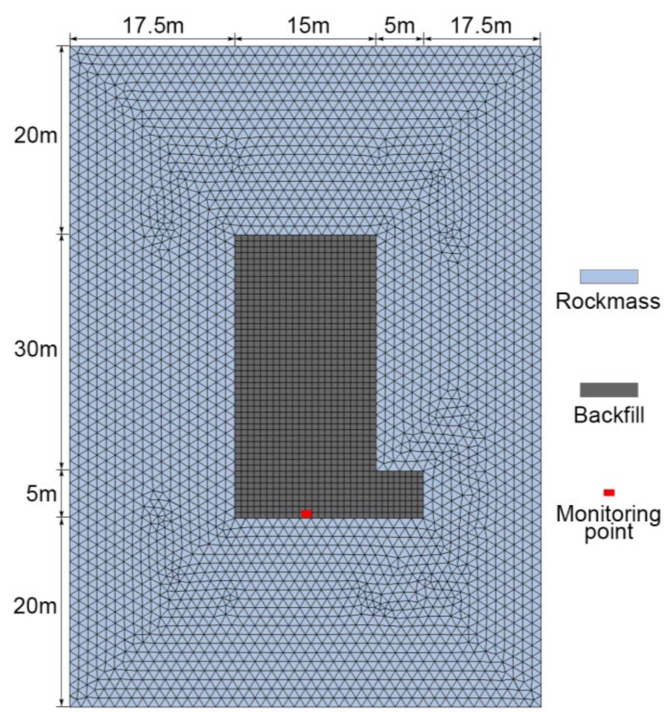

Figure 5.18. Mesh and geometry of control CTB and stope for model application

After CTB is placed into a stope, the water consumption due to binder hydration and water drainage through the barricade can both contribute to changes in the PWP, namely, both self-desiccation and water drainage can cause PWP changes. Therefore, to determine more clearly the effect of self-desiccation on the PWP, water drainage is not considered in the model application (including Sections 5.2.4.1 to 5.2.4.4).

5.2.4.1. Effect of Curing Time

The PWP changes in CTB with curing time are plotted in Figure 5.19. It can be observed that (1) the PWP increases as the filling progresses, especially during the first backfilling sequence, (2) there is discrepancy between the PWP and stress due to self-weight which gradually develops during the backfilling process, and becomes very apparent during the second stage of filling, (3) over the first day of curing after the first stage of filling, there is a slight reduction in the PWP, and (4) similar to the situation after 1-day of curing, there is a reduction in the PWP in the post-filling stage (i.e., after 3.5 days) which gradually approaches a value of 160 kPa. Therefore, the obtained results indicate that curing time can significantly affect the PWP in CTB. With curing time, the PWP is progressively dissipated in the CTB resultant of the water consumption due to binder hydration; however, there is a limit. As shown in Figure 5.19, the PWP is gradually reduced and becomes constant at approximately 160 kPa after the completion of the backfilling. Previous studies (Helinski et al. 2007a; Witteman 2013) have confirmed that the cement content is the dominant factor for the PWP reduction in CTB under undrained conditions. Moreover, as discussed in the section on the THMC column experiments, the rate of hydration progressively decreases with curing time, which can reduce the dissipation rate of the PWP. Therefore, a slight decline in the PWP appears first in the post-filling stage, and then the PWP remains constant at around 160 kPa.

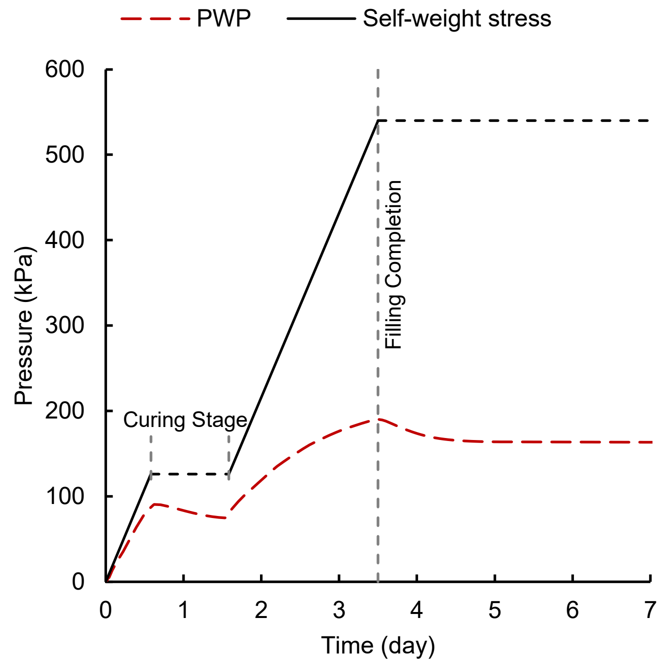

Figure 5.19. Changes in PWP with curing time in control stope

5.2.4.2. Effect of stope geometry

Ore bodies are naturally irregular masses and the applied stoping methods may differ for each mine. Hence, the resultant stope geometry may differ in terms of the stope size (height/length ratio, H/L) and inclination angle. To investigate the effect of the H/L ratio, the length of the CTB structure is set to be the same (15 m), and the increment of the fill height for each case is 15 m. Three different H/L ratios, including 1:1 (15 m×15 m), 2:1 (30 m×15 m) and 4:1 (45 m×15 m), are examined in this study. Three different inclination angles of 90°, 70° and 50° are used to analyze the impact of stope inclination.

Figure 5.20 depicts the PWP changes in CTB with different H/L ratios. From this figure, it can be observed that, as expected, the PWP increases with backfill height. However, the increments of increase of the PWP are not proportional to the changes in the backfill height. More specifically, the PWP peaks at 133 kPa, 190 kPa and 210 kPa in the CTB for the three H/L ratios of 1:1, 2:1 and 3:1 respectively at the end of the filling. Therefore, the PWP of the 2:1 stope increases by 43% in comparison to the PWP of the 1:1 stope, while there is only an 11% increment of increase in the PWP for the 3:1 stope in comparison to the 2:1 stope. This non-proportional increase in PWP is due to the self-desiccation process. Under the same filling rate and strategy, a higher fill height requires a longer time. Thus, the self-desiccation process consumes more capillary water and further reduces the PWP in CTB.

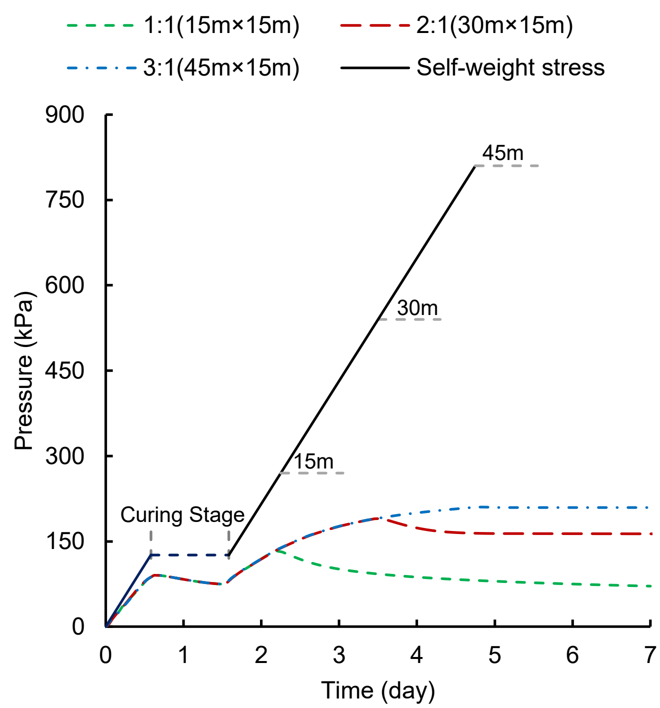

Figure 5.20. PWP changes in stopes with different H/W ratios

Figure 5.21 presents the PWP changes in the CTB with different inclination angles (i.e., 90°, 70°, and 50°). The obtained results show that (1) over the first day of curing after the first stage of filling, the PWP in all of the different stopes follow a similar trend of change, (2) after the commencement of the second stage of filling, the differences in the PWP between the stopes become progressively more pronounced as filling progressed. In particular, a lower PWP is found in the more inclined stope, which is attributed to the variation of the pore-water flow patterns. More capillary water flows towards the footwall under the gravity effect. Thus, the PWP near the footwall is higher than that in the vicinity of the hanging wall at a given elevation (see Figure 5.22). Moreover, previous studies on the stress distribution in inclined stopes (Ting et al. 2010; Cui and Fall 2016c) have found that the arching effect is more apparent in inclined stopes, namely, more stress is transferred to the footwalls. Consequently, relatively greater volumetric deformation which develops near the footwall can further reduce the permeability of CTB, which can reduce the capillary water flow in the CTB, and thus reduce the dissipation of

PWP near the footwalls. As a result, a non-uniform distribution of PWP is more obvious in inclined stopes.

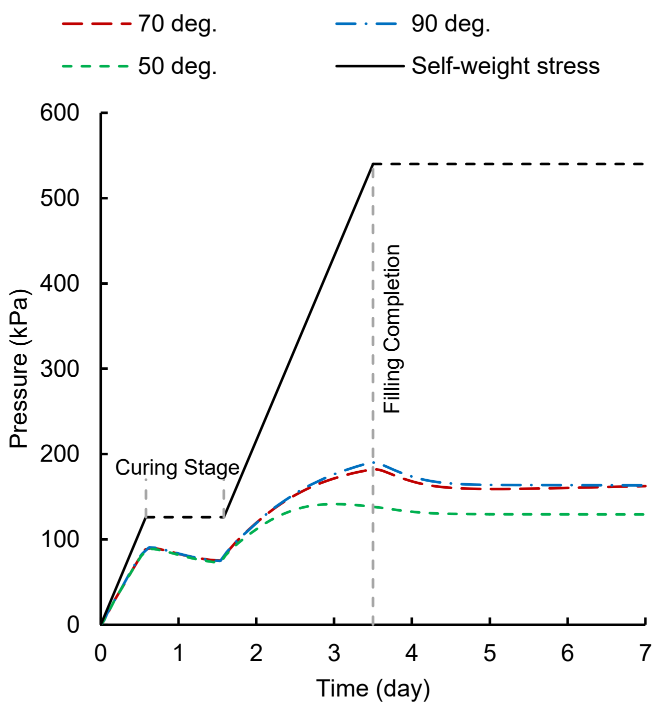

Figure 5.21. PWP changes in stopes with different inclination angles

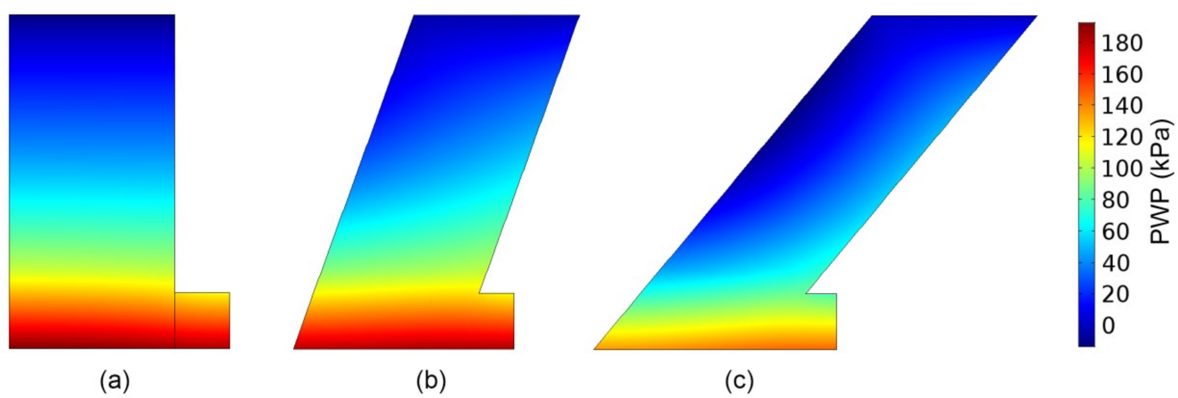

Figure 5.22. Spatial distribution of PWP in stopes with different inclination angles at completion of backfilling

5.2.4.3. Effect of backfill mix components

The mixture recipe not only affects CTB stability, but also the cost of the CTB, and thus the cost of underground mining operations (Cui and Fall 2016c). Therefore, it is important to investigate the effect of the mix components on self-desiccation. The binder content has the most significant effect on the cost of CTB. In this study, three different cement contents, including 1 wt% (17 kg/m^3), 4.5 wt% (75 kg/m^3), and 7 wt% (117 kg/m^3) (wt%: weight percentage of cement with respect to the total weight of the solid phase in the CTB) are examined to investigate their impacts on self-desiccation. The changes in the PWP in CTB with the different cement contents are plotted in Figure 5.23. It is evident that obvious changes in the PWP start from the first day of curing. As the backfilling proceeds, it can be seen that the PWP is significantly reduced in the CTB with a higher cement content. For instance, the PWP peak with a cement content of 7 wt% is reduced by 46% (i.e., from 272 kPa to 147 kPa) in comparison to a cement content of 1 wt%. Moreover, the PWP peak appears before the completion of backfilling with a cement content of 7 wt%; namely, water consumption due to hydration with greater cement content can counteract the effect of fresh CTB placement. This is because a greater cement content will mean the consumption of more capillary water at the same filling rate and/or at the same curing time. Consequently, a lower PWP is obtained in CTB with a greater cement content.

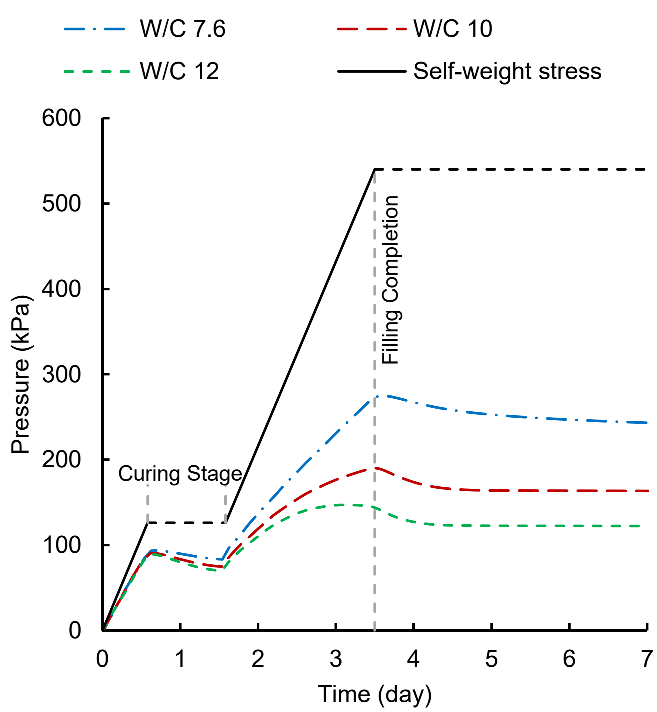

Figure 5.23. PWP changes in CTB with different cement contents

In terms of the cement type, Portland cement can be classified into five different types in accordance with C150 (C150 1999), which differs with respect to the mass percentage of Portland clinker, including tricalcium silicate (C_3S), dicalcium silicate (C_2S), tricalcium aluminate (C_3A) and tetracalcium aluminoferrite (C_4AF). As indicated in the binder hydration model (Eq.(5.10)), water sink term (Eq. (5.11)) and heat source term (Eq. (5.12)), the cement type and related amount of Portland clinker are needed to determine the degree of binder hydration, and the water consumption and heat generation caused by binder hydration. Therefore, to investigate the effect of cement type on self-desiccation, all five types of Portland cement are examined in this study. The weight percentage of the cement composition for each type of Portland cement is provided in Table 5.4.

Table 5.4. Composition of different types of Portland cement (ASTM (C150 1999))

	Type I	Type II	Type III	Type IV	Type V
C3S wt%	55	51	57	28	38
C2S wt%	19	24	19	49	43
C3A wt%	10	6	10	4	4
C4AF wt%	7	11	7	12	9

Figure 5.24 presents the PWP changes in CTB with different types of cement. The results indicate that the type of Portland cement has a negligible effect on self-desiccation. Therefore, from the perspective of self-desiccation, availability and cost are the key factors for the type of cement considered in CTB design. However, it should be noted that cement type has a significant effect on the development of compressive strength (Benzaazoua et al. 2002), total cost (Ercikdi et al. 2009), and material properties (Belem et al. 2000). Therefore, these factors should be considered when selecting the type of Portland cement for the preparation of CTB.

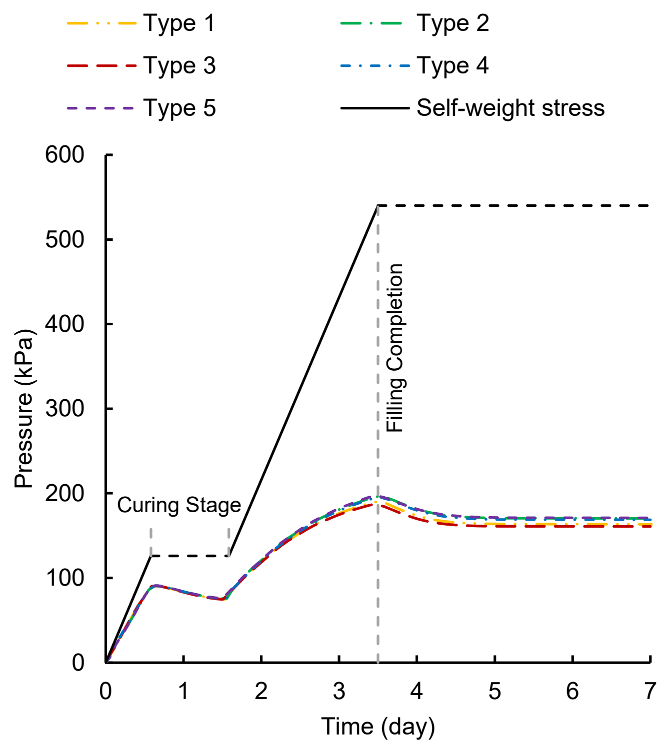

Figure 5.24. Effect of cement type on PWP changes in CTB

5.2.4.4. Effect of backfilling rate and strategy

The different mining methods and mining schedules mean that the backfilling rate and strategy may vary from one mining site to another. To determine the impact of the backfilling rate, three different rates of 0.5 m/h, 1 m/h and 2 m/h are applied in the control stope. Figure 5.25 shows the changes in the PWP of the CTB with different backfilling rates. It can be observed that rapid backfilling will result in a higher PWP at the end of the CTB placement. In particular, the PWP peak increases from 190 kPa (fill rate of 0.5 m/h) to 250 kPa (fill rate of 2 m/h). This is because a rapid rate of filling results in a short curing time for a given fill height, namely, relatively less water will be consumed by the hydration reaction (weaker self-desiccation). Consequently, a rapid rate of filling will produce greater PWP at the completion of the backfilling, which not only can lower the effective stress within the CTB, but also increase the barricade pressure and the risk of barricade failure.

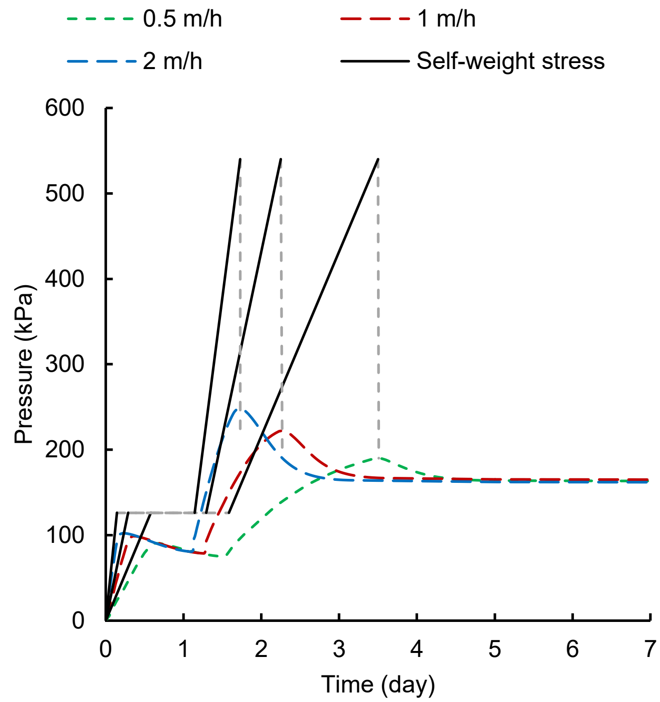

Figure 5.25. Effect of backfilling rate on PWP changes in CTB

In terms of the backfilling strategy, the sequential placement of CTB into a stope is a practical method commonly used in many underground backfilling operations. In particular, CTB placement is routinely carried out in two stages, with a plug layer and a main layer. The former has a relatively higher cement content and cured for 1 to 7 days (Ghirian 2016). To investigate the effect of the backfilling strategy on self-desiccation, three different filling sequences, including continuous placement and backfilling in two stages with a curing time of one and two days of the plug layer, are examined. The PWP changes in the stope with the different filling strategies are plotted in Figure 5.26. It can be observed that, compared to continuous filling, more dissipation of the PWP (stronger self-desiccation) is found in CTB with backfilling carried out in stages. Moreover, as expected, a longer curing time of the plug layer can further reduce the PWP in CTB. The variation of the PWP in CTB with different backfilling strategies depends on the backfilling time. As discussed earlier in the section on the effects of the backfilling rate, a longer hydration time will lead to increased consumption of capillary water and further reduce the PWP in CTB. Obviously, under the same backfilling rate, filling carried out in stages will mean a longer filling time, and thus result in a lower PWP.

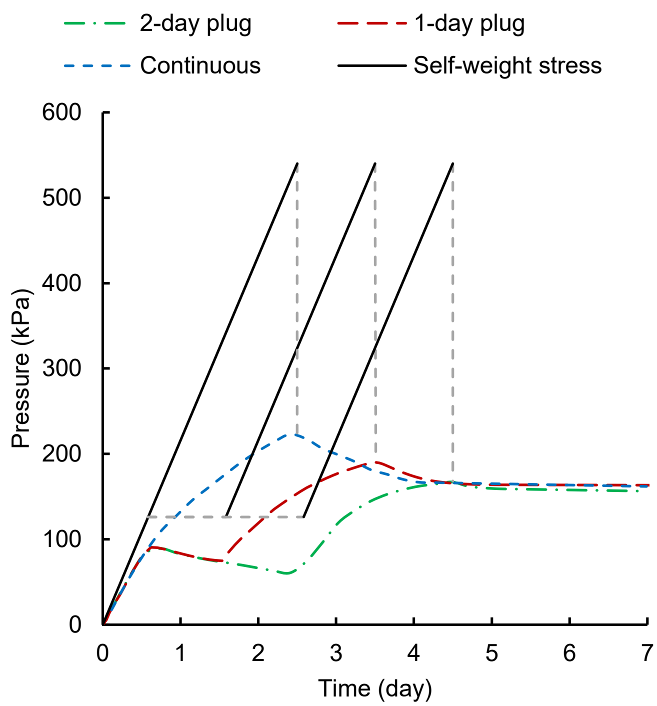

Figure 5.26. Effect of filling strategy on PWP changes in CTB

5.2.5. Summary and Conclusions

The following conclusions are made based on the obtained results.

(i) An integrated multiphysics model of self-desiccation is adopted to predict the PWP changes induced by the self-desiccation process in CTB. The predictive functions of time-dependent material properties, and corresponding model coefficients are determined with measured parameters.

(ii) Many case studies are used to validate the predictive ability of the developed model with good agreement between the modelling results and laboratory and in-situ measurements.

(iii) The developed model is used to examine a series of engineering issues, including the effect of the curing time, stope geometry, mixture recipe, backfilling rate and strategy, and the initial temperature of the CTB and rock mass. The obtained results show that these issues affect the self- desiccation process in CTB to different extents, and thus the PWP in the CTB.

(iv) The developed multiphysics model of self-desiccation and the simulation results have the potential for evaluating and obtaining a good understanding of the self-desiccation of hydrating CTB structures in field loading conditions, and thus contribute to the design of cost-effective CPB structures.

5.2.6. Acknowledgments

The authors would like to thank the University of Ottawa and the National Natural Sciences and Engineering Research Council of Canada (NSERC) for supporting this research.

5.2.7. References

Abbasy, F. (2009). "Thermal conductivity of mine backfill." Master thesis, Concordia University, Montreal, Quebec, Canada.

Abdul-Hussain, N., and Fall, M. (2011). "Unsaturated hydraulic properties of cemented tailings backfill that contains sodium silicate." *Eng. Geol.*, 123(4), 288-301.

Belem, T., Benzaazoua, M., and Bussière, B. (2000). "Mechanical behaviour of cemented paste backfill." *Proc., 53rd Canadian Geotechnical Conference*, Canadian Geotechnical Society, Montreal, QC, Canada, 373-380.

Belem, T., Benzaazoua, M., Bussière, B., and Dagenais, A. (2002). "Effects of settlement and drainage on strength development within mine paste backfill." *Proc., 9th International Conference, Tailings and Mine Waste*, 139-148.

Benzaazoua, M., Belem, T., and Bussiere, B. (2002). "Chemical factors that influence the performance of mine sulphidic paste backfill." *Cem. Concr. Res.*, 32(7), 1133-1144.

Brooks, and Corey (1964). "Hydraulic properties of porous media." *Colorado State University, Hydro Papers*, 3, 1-27.

C150, A. (1999). "Standard Specification for Portland Cement." ASTM International, West Conshohocken <www.astm.org>.

Carrier, W. D., Bromwell, L. G., and Somogyi, F. (1983). "Design capacity of slurried mineral waste ponds." *J. Geotech. Eng.*, 109(5), 699-716.

Comsol (2015). "Comsol Multiphysics 5.1." <http://www.comsol.com>. (Sept. 20, 2016).

Cui, L., and Fall, M. (2015). "A coupled thermo-hydro-mechano-chemical model for underground cemented tailings backfill." *Tunn. Undergr. Sp. Tech.*, 10.1016/j.tust.2015.08.014, 50, 396-414.

Cui, L., and Fall, M. (2016a). "An evolutive elasto-plastic model for cemented paste backfill." *Comput. Geotech.*, 10.1016/j.compgeo.2015.08.013, 71, 19-29.

Cui, L., and Fall, M. (2016b). "Mechanical and thermal properties of cemented tailings materials at early ages: Influence of initial temperature, curing stress and drainage conditions." *Constr. Build. Mater.*, 10.1016/j.conbuildmat.2016.08.080, 125, 553-563.

Cui, L., and Fall, M. (2016c). "Multiphysics model for consolidation behaviour of cemented paste backfill." *Int. J. Geomech.*, 10.1061/(ASCE)GM.1943-5622.0000743, 040160771-0401607723.

Ercikdi, B., Kesimal, A., Cihangir, F., Deveci, H., and Alp, İ. (2009). "Cemented paste backfill of sulphide-rich tailings: Importance of binder type and dosage." *Cem. Concr. Compos.*, 31(4), 268-274.

Fall, M., Célestin, J., Pokharel, M., and Touré, M. (2010). "A contribution to understanding the effects of curing temperature on the mechanical properties of mine cemented tailings backfill." *Eng. Geol.*, 114(3), 397-413.

Fredlund, D. G., and Xing, A. (1994). "Equations for the soil-water characteristic curve." *Can. Geotech. J.*, 31(4), 521-532.

Ghirian, A. (2016). "Coupled thermo-hydro-mechanical-chemical (THMC) processes in cemented tailings backfill structures and implications for their engineering design." Ph.D. Thesis, University of Ottawa, Canada.

Ghirian, A., and Fall, M. (2013). "Coupled thermo-hydro-mechanical-chemical behaviour of cemented paste backfill in column experiments. Part I: physical, hydraulic and thermal processes and characteristics." *Eng. Geol.*, 164, 195-207.

Ghirian, A., and Fall, M. (2015). "Coupled Behavior of Cemented Paste Backfill at Early Ages." *Geotech. Geol. Eng.*, 10.1007/s10706-015-9892-6, 33(5), 1141-1166.

Haj-zamani, S. (2010). "Effect of curing temperature on hydraulic backfill performance with consideration of a new type of binder." M.Sc. Thesis, Concordia University, Montreal, Canada.

Helinski, M., Fahey, M., and Australia, W. (2007a). "An effective stress approach to modelling mine backfilling." *Proc., Bulletin of the Canadian Institute of Mining, Metallurgy and Petroleum*, 1-8.

Helinski, M., Fahey, M., and Fourie, A. (2010). "Behavior of cemented paste backfill in two mine stopes: measurements and modeling." *J. Geotech. Geoenviron.*, 10.1061/(ASCE)GT.1943-5606.0000418, 137(2), 171-182.

Helinski, M., Fourie, A., Fahey, M., and Ismail, M. (2007b). "Assessment of the self-desiccation process in cemented mine backfills." *Can. Geotech. J.*, 44(10), 1148-1156.

Hogarth, W., Hopmans, J., Parlange, J.-Y., and Haverkamp, R. (1988). "Application of a simple soil-water hysteresis model." *J. Hydrol.*, 98(1), 21-29.

Koupouli, N. J., Belem, T., Rivard, P., and Effenguet, H. (2016). "Direct shear tests on cemented paste backfill-rock wall and cemented paste backfill-backfill interfaces." *J. Rock Mech. Geotech. Eng.*, 10.1016/j.jrmge.2016.02.001, 8, 472-479.

Li, L., and Yang, P. (2015). "A numerical evaluation of continuous backfilling in cemented paste backfilled stope through an application of wick drains." *Int. J. Min. Sci. Technol.*, 10.1016/j.ijmst.2015.09.004, 25(6), 897-904.

Li, W., and Fall, M. (2016). "Sulphate effect on the early age strength and self-desiccation of cemented paste backfill." *Constr. Build. Mater.*, 106, 296-304.

Li, X., Li, R., and Schrefler, B. A. (2006). "A coupled chemo-thermo-hygro-mechanical model of concrete at high temperature and failure analysis." *Int. J. Numer. Anal. Met.*, 10.1002/nag.495, 30(7), 635-681.

Lu, G., and Fall, M. (2016). "A coupled chemo-viscoplastic cap model for simulating the behavior of hydrating cemented tailings backfill under blast loading." *Int. J. Numer. Anal. Met.*, 10.1002/nag.2475, 40(8), 1123-1149.

Luckner, L., Van Genuchten, M. T., and Nielsen, D. (1989). "A consistent set of parametric models for the two-phase flow of immiscible fluids in the subsurface." *Water Resour. Res.*, 25(10), 2187-2193.

Mehrabian, A., and Abousleiman, Y. N. (2015). "Gassmann equations and the constitutive relations for multiple-porosity and multiple-permeability poroelasticity with applications to oil and gas shale." *Int. J. Numer. Anal. Met.*, 10.1002/nag.2399, 39(14), 1547-1569.

Mualem, Y. (1976). "A new model for predicting the hydraulic conductivity of unsaturated porous media." *Water Resour. Res.*, 12(3), 513-522.

Pokharel, M., and Fall, M. (2013). "Combined influence of sulphate and temperature on the saturated hydraulic conductivity of hardened cemented paste backfill." *Cem. Concr. Compos.*, 38, 21-28.

Poole, J. L., Riding, K. A., Folliard, K. J., Juenger, M. C., and Schindler, A. K. (2007). "Methods for calculating activation energy for Portland cement." *Aci Mater. J.*, 104(1), 303-311.
Powers, T., and Brownyard, T. (1947). "Studies of the physical properties of hardened Portland cement paste." *ACI J. Proc.*, 249-336.
Rotisciani, G. M., Sciarra, G., Casini, F., and Desideri, A. (2015). "Hydro-mechanical response of collapsible soils under different infiltration events." *Int. J. Numer. Anal. Met.*, 10.1002/nag.2359, 39(11), 1212-1234.
Schindler, A. K., and Folliard, K. J. (2003). "Influence of supplementary cementing materials on the heat of hydration of concrete." *Proc., Advances in Cement and Concrete IX Conference*, Engineering Conferences International, Inc., Colorado, USA, 17-26.
Shahsavari, M., and Grabinsky, M. (2015). "Mine backfill pore water pressure dissipation: numerical predictions and field measurements." *Proc., GeoQuébec*, 1-8.
Shin, H. S., Kim, K. Y., and Pande, G. N. (2015). "On computation of strain-dependent permeability of rocks and rock-like porous media." *Int. J. Numer. Anal. Met.*, 10.1002/nag.2334, 39(8), 821-832.
Somerton, W., Keese, J., and Chu, S. (1974). "Thermal behavior of unconsolidated oil sands." *Soc. Pet. Eng. J.*, 14(05), 513-521.
Suazo, G., Fourie, A., and Doherty, J. (2016). "Experimental Investigation of Propagation and Transmission of Compressional Stress Waves in Cemented Paste Backfill." *J. Geotech. Geoenviron.*, 10.1061/(ASCE)GT.1943-5606.0001468, 04016104.
Thompson, B., Bawden, W., and Grabinsky, M. (2012). "In situ measurements of cemented paste backfill at the Cayeli Mine." *Can. Geotech. J.*, 10.1139/t2012-040, 49(7), 755-772.
Thompson, B., Grabinsky, M., Bawden, W., and Counter, D. (2009). "In-situ measurements of cemented paste backfill in long-hole stopes." *Proc., the 3rd CANUS Rock Mechanics Symposium*, Toronto, Canada, 197-198.
Ting, C. H., Shukla, S. K., and Sivakugan, N. (2010). "Arching in soils applied to inclined mine stopes." *Int. J. Geomech.*, 10.1061/(ASCE)GM.1943-5622.0000067, 11(1), 29-35.
Van Genuchten, M. T. (1980). "A closed-form equation for predicting the hydraulic conductivity of unsaturated soils." *Soil Sci. Soc. Am. J.*, 44(5), 892-898.
Walske, M. L. (2014). "An experimental study of cementing paste backfill." Ph.D. thesis, University of Western Australia, Perth, Australia.
Walske, M. L., McWilliam, H., Doherty, J., and Fourie, A. (2016). "Influence of curing temperature and stress conditions on mechanical properties of cementing paste backfill." *Can. Geotech. J.*, 10.1139/cgj-2014-0502, 53(1), 148-161.
Williams, P. J. (1982). *The surface of the earth: an introduction to geotechnical science*, Longman Inc., New York.
Witteman, M. L. (2013). "Unsaturated flow in hydrating porous media: application to cemented paste backfill." *Proc., Pan-Am CGS Geotechnical conference*, Toronto, Canada, 1-8.
Wu, A., Wang, Y., Zhou, B., and Shen, J. (2016). "Effect of initial backfill temperature on the deformation behavior of early age cemented paste backfill that contains sodium silicate." *Advances in Materials Science and Engineering*, 2016.
Wu, D., Fall, M., and Cai, S.-j. (2014). "Numerical modelling of thermally and hydraulically coupled processes in hydrating cemented tailings backfill columns." *Int. J. Min. Reclam. Environ.*, 10.1080/17480930.2013.809194, 28(3), 173-199.

Wu, D., Zhang, Y., and Liu, Y. (2016). "Mechanical performance and ultrasonic properties of cemented gangue backfill with admixture of fly ash." *Ultrasonics*, 64, 89-96.

Yilmaz, E. (2012). "One-Dimensional Consolidation Parameters Of Cemented Paste Backfills/Parametry Jednowymiarowej Konsolidacji Podsadzki W Postaci Cementowej Pasty." *Gospodarka Surowcami Mineralnymi-Mineral Res. Manage.*, 28(4), 29-45.

Yumlu, M. (2008). "Barricade pressure monitoring in paste backfill." *Gospodarka Surowcami Mineralnymi*, 24(4/3), 233-244.

5.3. Paper VII: Numerical Simulation of Consolidation Behavior of Fill Mass

Liang Cui, Mamadou Fall

Department of Civil Engineering, University of Ottawa, Ottawa, Ontario, Canada

Abstract

Underground mined-out voids (called “stopes”) need to be backfilled for the stability of the surrounding rock and also to increase ore extraction from adjacent pillars. One of the relatively newer means is cemented paste backfilling, which has been extensively adopted in underground mining operations around the world. During and after the placement of cemented paste backfill (CPB) into stopes, complex multiphysics (thermal, hydraulic, mechanical and chemical) processes take place and control the consolidation behavior of CPB. As consolidation progresses, the stress distribution and magnitude of the stress may vary in the CPB mass, which in turn affect the stability of the CPB structure. Hence, an analysis of the consolidation process in CPB mass is essential for the assessment of CPB behavior and cost-effective designs in practice. In this paper, multiphysics simulation of the consolidation behavior of CPB mass is performed under different conditions, including the mixture recipe, and backfilling, drainage, surrounding rock and curing conditions. The obtained results can facilitate a better understanding on the development of CPB consolidation for backfill designers and engineers.

Keywords: Mine; Cemented paste backfill; Tailings; Consolidation; Multiphysics; Interface.

5.3.1. Introduction

Cemented paste backfill (CPB) is an engineered mixture of dewatered full-stream tailings (man-made soils), hydraulic binder and water (Fall et al. 2007). After preparation in a backfill plant usually located on the mine surface, the fresh CPB is transported into underground stopes (mined-out voids) via reticulated pipelines and/or gravity system (Haiqiang et al. 2016). As the hardening process of the fill mass progresses, CPB provides ground support to the adjacent stopes (Zhang et al. 2015; Cui and Fall 2016a), which can maximize ore recovery (Fall et al. 2010; Yilmaz et al. 2011), and reduce surface subsidence (Fried et al. 2007). Moreover, the relatively high amount of binder and solid content ensure that the CPB mass gains strength more quickly compared to rockfill and hydraulic fill (Ghirian and Fall 2014; Cui and Fall 2015a). In addition, the application of CPB enables a reduction of approximately 50%-60% of the sulphidic tailings deposited on the surface (Potvin and Thomas 2005; Khaldoun et al. 2016). Hence, from an environmental point of view, cemented paste backfilling is an alternative means of reducing environmental issues (e.g., acid mine drainage) associated with surface tailings disposal. Consequently, cemented paste backfilling has been widely employed in the underground mines throughout the world (Haiqiang et al. 2016).

In engineering practices, mechanical stability is considered as one of the most important design criteria of CPB structures (Fall et al. 2015). The mechanical performance of CPB structures is closely related to the consolidation process in the CPB. The backfilling process is flexible (i.e., the process is continuous or carried out in different filling stages), which means that the dissipation of pore water pressure (PWP) will take place in CPB due to water drainage through the barricade (a retaining wall built to contain backfill material) and/or from the surrounding fractured rock mass, and/or water consumption caused by binder hydration, which can result in an increase in the effective stress and strength (Cui and Fall 2015c). Moreover, binder hydration induced chemical shrinkage will further contribute to volume changes (Cui and Fall 2016d) and thus to the densification of CPB, which is desirable for increased strength. In addition, the temperature dependence of binder hydration (Schindler and Folliard 2003; Cui and Fall 2015b) means that the heat transfer and resultant temperature changes must be taken into account in the analysis of CPB performance. Therefore, the consolidation process is controlled by complex multiphysics (i.e., thermo-hydro-mechano-chemical, THMC) processes that occur in the CPB. Apart from the coupled THMC processes, the rock mass/backfill interaction (interface) can affect the stress distribution and thus the volume changes in the fill mass (Fahey et al. 2009). Specifically, with the development of consolidation, relative displacement along the rock mass/CPB interface will occur, and the resultant interface stress will reduce the influence of the self-weight stress of CPB (i.e., the arching effect will occur) (Koupouli et al. 2016; Cui and Fall 2017), which will result in non-uniform volume changes in the CPB. Therefore, analysis of backfill-rock interface behavior in stopes is essential for the assessment of the consolidation behavior of CPB mass.

However, conventional analysis techniques on consolidation, such as Terzaghi (1943) consolidation theory and Biot (1955) consolidation theory, only focus on the volume contraction behavior triggered by the dissipation of excess pore water in saturated soils or porous media, namely, the analysis of coupled hydro-mechanical (HM) processes. Therefore, these classical theories are not suitable for the assessment of the coupled THMC consolidation behavior of CPB materials. To address this problem, Cui and Fall (2016c) developed a fully coupled multiphysics model that analyzes the consolidation process in CPB and incorporates the THMC processes that occur in CPB and thus affect its consolidation behavior. This new approach fully considers the effect of self-weight, pore water flow and drainage, chemical shrinkage, thermal expansion, and temperature on the binder hydration. Moreover, Cui and Fall (2017) developed an elastoplastic model to analyze changes in the interface behavior during the interaction of rock mass/backfill. In the elastoplastic model, the hardening/softening behavior, chemical hardening process and the effect of the rock wall roughness on the interface properties (interface adhesion and friction angle) are taken into account. Therefore, the fully coupled multiphysics model for analyzing consolidation problems and the evolutive elastoplastic interface model will allow prediction of the consolidation behavior of CBP at the field scale. In the present study, these two models are integrated to numerically model the consolidation behavior of CPB mass under various field conditions, including the filling rate, stope geometry and inclination angle, rock wall roughness, mix components (cement content) and drainage conditions.

5.3.2. Mathematical Models

In this study, two models are integrated to examine the volume changes of the fill mass in a stope: a fully coupled multiphysics model that analyzes the consolidation process in CPB as proposed in Cui and Fall (2016c), and an elastoplastic model that analyzes changes in the interface behavior during the interaction of rock mass/backfill, as provided in Cui and Fall (2017). Details on these two models including the assumptions made, model derivation and determination of model coefficients are provided in Cui and Fall (2016c; 2017). A brief description of the two models is provided in Sections 5.3.2.1 and 5.3.2.2, respectively.

5.3.2.1. Fully coupled multiphysics model for consolidation process

Due to the strongly coupled THMC processes that occur in fill mass, the consolidation behavior of CPB in a slurry state is a very complex process compared to that of conventional geomaterials, such as natural soils. A multiphysics model for the consolidation behavior of CPB must satisfy the principle of pore space continuity (Cui and Fall 2016c), which requires that the pore space changes associated with the CPB skeleton and solid phase must be consistent with the volume changes in the pore water and pore air. Hence, based on the principle of pore space continuity, a consolidation equation based on multiphysics can be derived as follows and is elaborated in detail in (Cui and Fall 2015b; 2016c):

$$\begin{aligned}
&\left\{\left[SP_w+(1-S)P_a\right]\frac{1-2\upsilon}{E}\frac{\partial\alpha_{Biot}}{\partial\xi}-\left\{\frac{\sigma+\alpha_{Biot}\left[SP_w+(1-S)P_a\right]}{E}\right\}\left\{\frac{9[1-2\upsilon]}{E}\frac{\partial E}{\partial\xi}+18\frac{\partial\upsilon}{\partial\xi}\right\}\right.\\
&\left.-\alpha_{Biot}(P_a-P_w)\frac{1-2\upsilon}{E}\left\{\left[1-S_e(P_w,P_a,\xi)\right]\frac{\partial\theta_r}{\partial\xi}+(n-\theta_r)\frac{\partial S_e}{\partial\xi}\right\}-\frac{(v_{ch-w}+v_{ab-w})R_{n-w/hc}/(1-n)}{(w/c)v_w+v_c+(1/C_m-1)v_{tailings}}\right\}\frac{\partial\xi}{\partial t}\\
&+\frac{1-2\upsilon}{E}\frac{\partial\sigma}{\partial t}+\alpha_{Biot}\frac{1-2\upsilon}{E}\left\{S-(P_a-P_w)(n-\theta_r)\frac{\partial S_e}{\partial P_w}\right\}\frac{\partial P_w}{\partial t}+\frac{\partial\lambda_p}{\partial t}\frac{\partial Q_{CTB}}{\partial I_1}+\alpha_{Ts}\frac{\partial T}{\partial t}\\
&+\alpha_{Biot}\frac{1-2\upsilon}{E}\left\{(1-S)-(P_a-P_w)(n-\theta_r)\frac{\partial S_e}{\partial P_a}\right\}\frac{\partial P_a}{\partial t}\\
&=-\left\{(1-n)+\alpha_{Biot}(P_a-P_w)\frac{1-2\upsilon}{n^2E}\left[n(1-n)S_e+(1-S_e)\theta_r\right]\right\}\frac{\partial n}{\partial t}
\end{aligned} \tag{5.18}$$

where S is the degree of saturation; P_w and P_a denote the PWP and pore-air pressure, respectively; υ and E denote the Poisson's ratio and elastic modulus, respectively; α_{Biot} is the Biot's coefficient; ξ is the degree of binder hydration; σ is a total stress tensor; S_e is the effective degree of saturation; θ_r is the residual water content; n refers to the CPB porosity; v_w, v_{ch-w}, v_{ab-w}, $v_{tailings}$ and v_c denote the specific volume of the capillary water, chemically consumed water, physically adsorbed water, tailings and cement respectively; $R_{n-w/hc}$ means the mass ratio of the chemically consumed water and hydrated cement; w/c is the water to cement ratio; C_m is the binder content; t refers to the elapsed time; λ_p denotes a non-negative plastic multiplier; Q_{CTB} is a plastic potential function; I_1 represents the first stress invariant; and α_{Ts} refers to a coefficient of the thermal expansion of the solid phase in the CPB.

As demonstrated in the consolidation model (i.e., Eq.(5.18)), the chemical process is incorporated into the volume changes in CPB through the variable ξ , namely, the degree of binder hydration. To characterize the progress of the hydration reaction in CPB, the following exponential equation proposed by Schindler and Folliard (2003) is adopted:

$$\xi(t)=\left(\frac{1.031\cdot w/c}{0.194+w/c}+0.5\cdot X_{FA}+0.30\cdot X_{slag}\right)\cdot\exp\left\{-\left\{\tau\Big/\int_0^t\exp\left[\frac{E_a}{R}\left(\frac{1}{T_r}-\frac{1}{T}\right)\right]dt\right\}^{\beta}\right\} \tag{5.19}$$

with

$$E_a(T)=\begin{cases}33{,}500+1{,}470\times(293.15-T) & T<293.15K\\ 33{,}500 & T\geq 293.15K\end{cases}$$

where τ and β respectively represent the time parameter (hours), and hydration shape parameter, T_r refers to the reference temperature (K), R is the ideal gas constant (8.314 J/mol/K), E_a refers to the apparent activation energy (J/mol), and X_{slag} and X_{FA} denote the weight proportion of the blast furnace slag and fly ash relative to the total binder mass, respectively. In accordance with the definition of the degree of binder hydration (i.e., Eq.(5.19)), the influence of temperature, mixture recipe and elapsed time are incorporated to determine the progression of the hydration reaction.

5.3.2.2. Evolutive elastoplastic interface model

To incorporate the effect of the interface behavior between the CPB/rock mass into the analysis of the consolidation process, an evolutive elastoplastic interface model developed by Cui and Fall (2017) is adopted to assess the interface shear stress in the present study. In this model, the changes of the yield surface in the stress space is characterized by a modified Drucker-Prager (D-P) yield function F_{intf} , and the changes in the direction of the plastic displacement is determined with a non-associative plastic flow rule (i.e., the plastic potential function Q_{intf} differs from the yield function F_{intf}).

$$F_{intf}(I_1,\sqrt{J_2},\xi,\Delta_\kappa)=\sqrt{J_2}+\alpha_{intf}\left(\xi,\Delta_\kappa\right)\left[I_1-C_{intf}\left(\xi\right)\right]=0 \tag{5.20}$$

$$Q_{intf}=\sqrt{J_2}+2\sqrt{3}\sin\left(\psi_{intf}\right)I_1\Big/\left[9+3\sin\left(\psi_{intf}\right)\right] \tag{5.21}$$

where J_2 is a second deviatoric stress invariant, Δ_κ is the effective plastic displacement, α_{intf} and C_{intf} are the yield function parameters, and ψ_{intf} denotes the interface dilation angle which will change with binder hydration and normal stress level acting on the interface. Details on how the interface model coefficients are determined can be found in Cui and Fall (2017).

5.3.3. Model Validation Examples

The two models presented above are first implemented into COMSOL Multiphysics (a commercial finite element method (FEM) code software; (Comsol 2015)). Then, the integrated model is validated against results obtained from laboratory investigations on the consolidation behavior of CPB and field measurements. Typical examples and results that validate the model are then presented. Additional examples and results that validate the model are also presented elsewhere (Cui and Fall 2015b; 2016c; 2017).

5.3.3.1. THMC Consolidation Test - Lab

To study the consolidation behavior of CPB, a series of pressure cell tests were conducted by using a THMC pressure cell apparatus (see Figure 5.27). This pressure cell apparatus was originally developed by Ghirian and Fall (2013), which is mainly composed of an air pressure system, a Perspex cylinder (10 cm (diameter) × 30 cm (height)), an air-pressure driven piston and two plates with three tie rods to hold the THMC cell. The adopted air pressure system can apply up to 600 kPa of air pressure onto the CPB sample to simulate the increase of self-weight stress in a stope during backfilling operations. To collect the data, a linear variable displacement transformer (LVDT) was mounted onto the top of the cell to record the vertical settlement, and a suction meter (model: MPS-2) and a temperature sensor (model: 5TE) were installed inside the THMC cell. Artificial silica tailings, Portland cement Type 1 (4.5 wt%) and tap water (w/c=7.6) were used to prepare the CPB samples. After placement, the pressure cell was covered with a thermal insulation blanket to slow down the heat transfer between the CPB sample and the surrounding environment. In terms of the application of air pressure, the applied pressure was gradually increased to 150 kPa in the first 12 hours. Then, the pressure was increased every 24 hours until 600 kPa. Moreover, two different initial temperatures of the CPB (5°C and 25°C) were used to investigate their effects on the consolidation process.

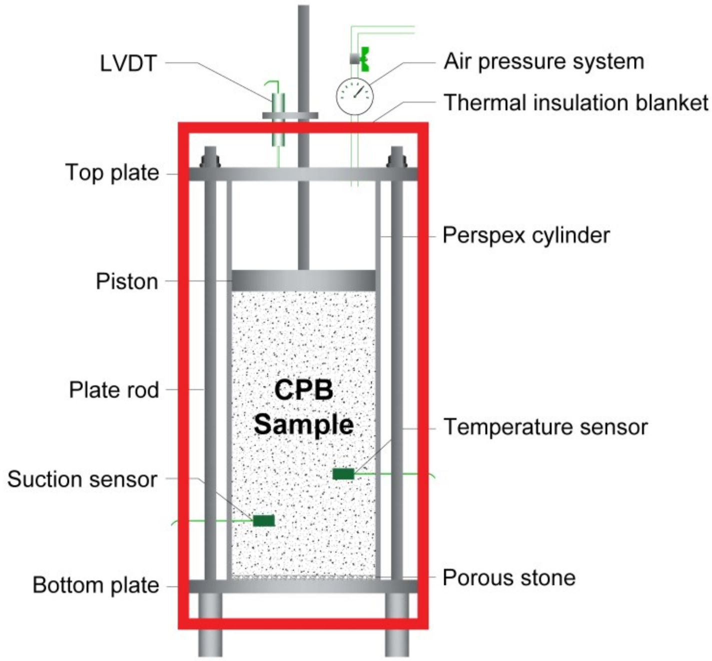

Figure 5.27. Schematic diagram of THMC pressure cell

A 2D axisymmetric model was used to simulate the pressure cell test. The geometry model and mesh are presented in Figure 5.28.

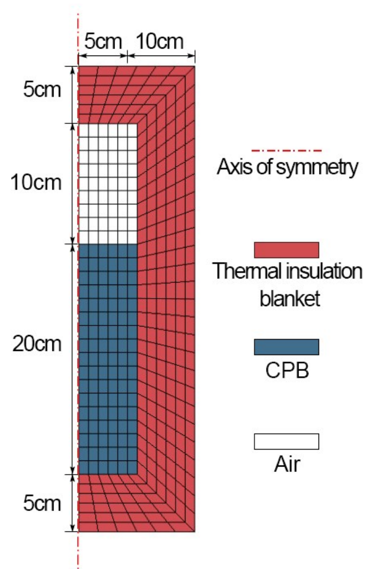

Figure 5.28. Geometry and mesh of simulated model of cell test

A comparison of the simulation results and monitored data from the vertical settlement is plotted in Figure 5.29. It can be clearly seen that the simulated results are in good agreement with the recorded data in terms of both changes in trend and magnitude. Moreover, the results show that (1) the vertical displacement increases with applied air pressure, which confirms that the developed model is able to capture the effect of backfilling operations on the self-weight stress, and thus its effects on the consolidation behavior of CPB; (2) the initial temperature of the CPB has a significant effect on its vertical settlement. As shown in Figure 5.29, the vertical settlement of the CPB with an initial temperature of 25°C increases by approximately 8% compared to that of the CPB with an initial temperature of 5°C at 7 days; (3) during each curing age, the air pressure applied is constant but the vertical settlement continues to increase, which indicates that chemical shrinkage contributes to the volume changes in the CPB.

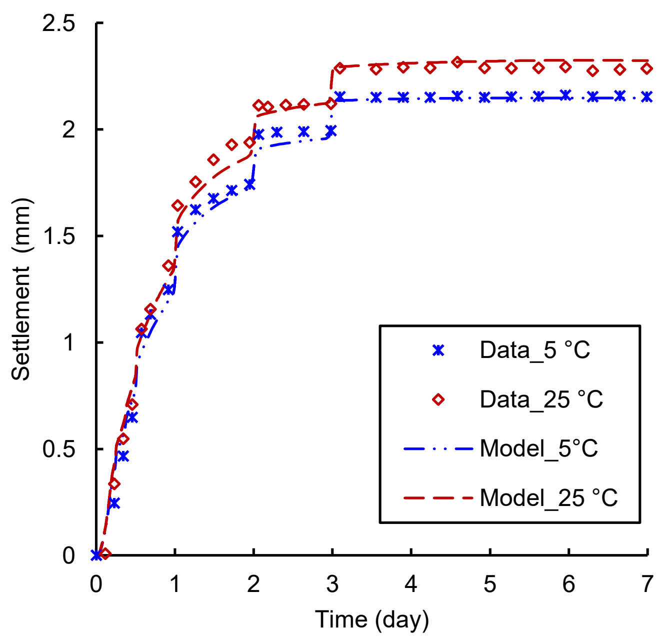

Figure 5.29. Comparison of predicted results and experimental data for settlement

Apart from the settlement, the changes in the PWP (Figure 5.30a), and temperature (Figure 5.30b) can also be accurately captured by using the developed model. From these two figures, it is evident that (1) the major changes in the PWP and temperature occur at the very early ages, which coincides with changes in the vertical settlement (see Figure 5.29). This is because the binder hydration takes place rapidly at the very early ages. As a result, a relatively large volume of pore water is consumed, which in turn results in a significant change in the PWP. Meanwhile, the rapid binder hydration releases a large amount of heat and thus affects the temperature in the CPB at the early ages; (2) similar to the obtained results from the vertical settlement, the initial temperature of the CPB can also impose a significant impact on the changes in the PWP and temperature. The good agreement between the numerical simulations and results from the laboratory tests further confirms that the developed model can reliably simulate the consolidation behavior of CPB.

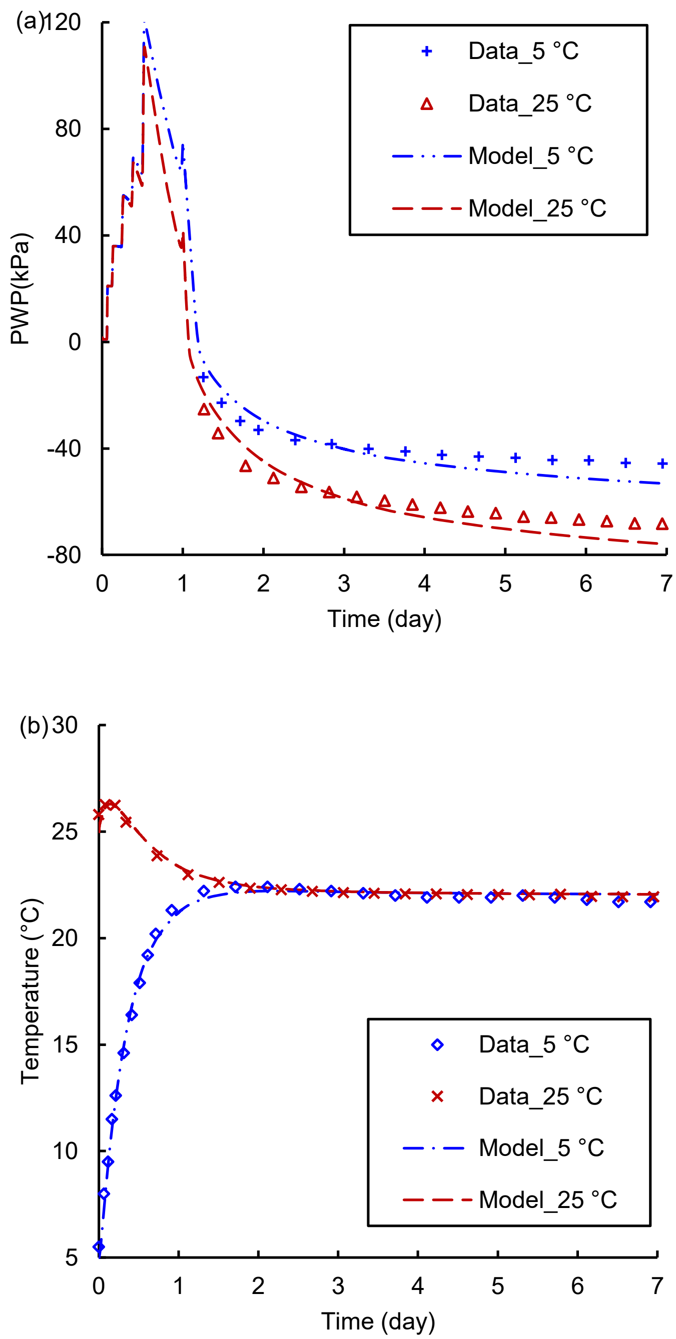

Figure 5.30. Comparison of predicted results and measured data: (a) PWP; (b) temperature

5.3.3.2. Field Study 1-Undrained CPB mass

To study the field behaviors of CPB, a series of field monitoring programs have been carried out (e.g., Thompson et al. 2009; Helinski et al. 2010; Li et al. 2014). Although the reported field data are limited to total stress (e.g., Hassani et al. 2001), PWP (e.g., Shahsavari and Grabinsky 2015) and temperature (e.g., Williams et al. 2001) in the CPB, the obtained results can still provide useful information on the field behaviors of CPB, including the consolidation process.

In the present study, the predicted results are compared with the measured data from a field monitoring program conducted by Belem et al. (2004) at the Doyon Gold (DG) Mine (Canada). The investigated stope has a height of 29 m and a width of 11 m with a dip of 90° and an azimuth of 90°. A backfilling operation that consists of two stages was adopted, which includes a plug layer (cement content: 7% and solid content: 70%). After 3-days of curing, the residual stope was filled with CPB with a cement content of 3% and a solid content of 70%. An earth pressure cell (TPC series) was used to record the changes in the total pressure at the stope base (elevated 0.6 m). Water drainage was not allowed on this stope. The corresponding mesh and stope geometry are shown in Figure 5.31.

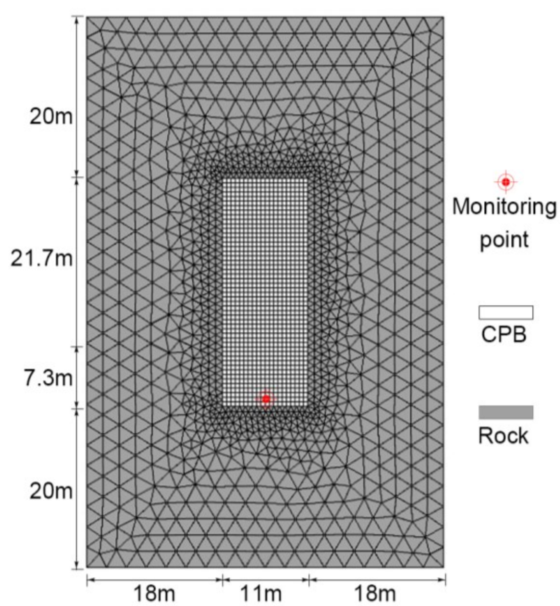

Figure 5.31. Mesh and geometry of simulated stope at DG Mine

A comparison of the predicted results and monitored total stress values is presented in Figure 5.32. Based on the obtained results, it can be found that (1) as expected, the filling processes have significant impacts on the changes in total stress, especially during the plug placement stage; (2) during the curing of the plug layer (from the 2nd to the 5th day), there is a slight reduction in total stress which gradually took place and can be attributed to the transfer of stress from the fill mass to the rock walls (arching effect) with the development of consolidation of the CPB mass; and (3) after the residual filling commenced (from the 5th day), the total stress shows a relatively limited increase compared with that observed during the plug-fill, which further contributes to the discrepancy between the total stress and self-weight stress. From Figure 5.32, it can be seen that the predicted results are in good agreement with the monitored data. Hence, the developed model is able to reliably assess the changes in total stress in CPB under undrained conditions.

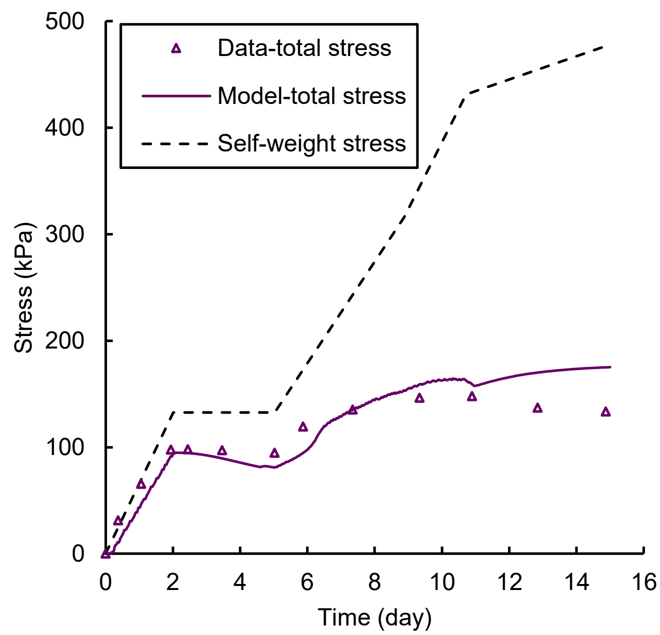

Figure 5.32. Comparison of predicted results and measured total stress values at DG Mine

5.3.3.3. Field Study 2-Drained CPB mass

To investigate the field behavior of CPB under drained conditions, in-situ measurements were conducted by Helinski et al. (2010) in the Kanowna Belle mine. In this monitoring program, a piezometer was installed at the center of the stope base to monitor the changes in the PWP in the CPB. The backfilling strategy was to carry out filling in two stages. Pore-water drainage through the retaining structure (i.e., the barricade) was allowed. More details on the CPB design are provided in (Helinski et al. 2010). The geometry model and mesh are presented in Figure 5.33.

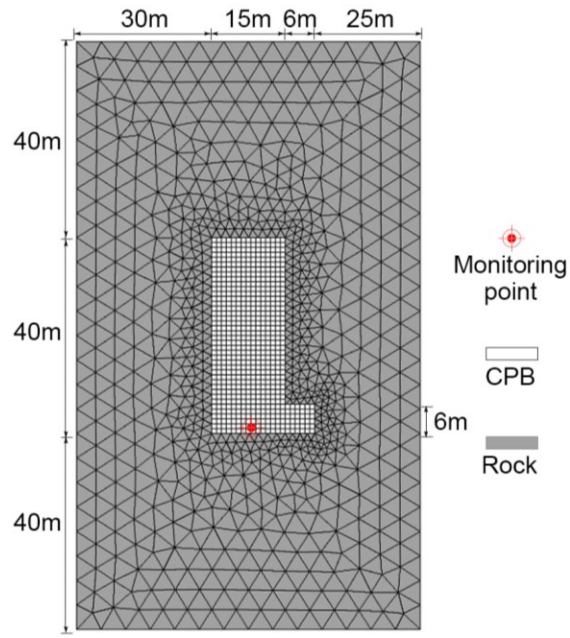

Figure 5.33. Mesh and geometry of simulated stope at Kanowna Belle mine

As can be seen in Figure 5.34, the changes in the PWP are captured well by the developed model. Specifically, during the first stage of filling， the PWP gradually increases with filling. After 1.4 days (the commencement of the curing of the plug layer), dissipation of the PWP is observed in the CPB, which is attributed to the water drainage through the barricade and binder hydration induced water consumption (i.e., the self-desiccation process). The dissipation of the PWP can directly contribute to reductions in pore space and thus to the consolidation process of CPB. In addition, from Figure 5.34, it can be observed that the effect of the residual filling on PWP is minimal, and a slight increase in the PWP appears during the middle of the second and third days. Then, the PWP decreases regardless of the backfilling that followed, which can further contribute to the volume changes in the fill mass. Therefore, the good agreement between the predicted results and field data further validates the predictive ability of the developed model for CPB behavior under drained conditions.

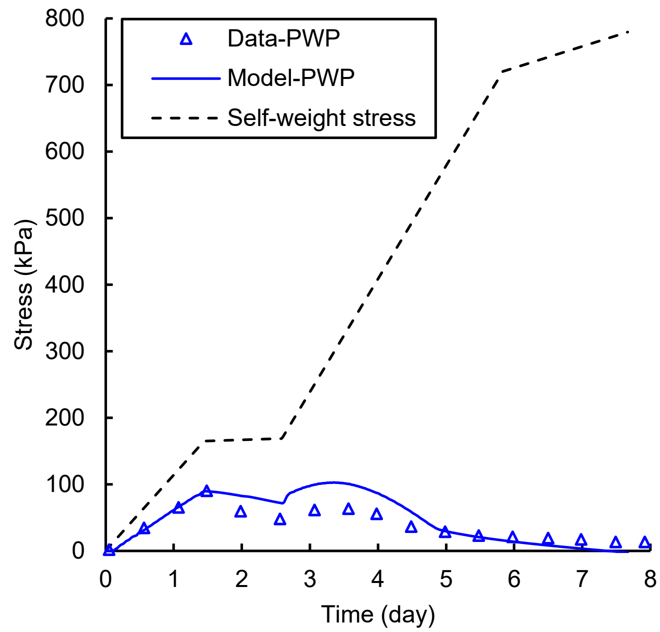

Figure 5.34. Comparison of predicted results and measured values of PWP at Kanowna Belle mine

5.3.4. Model Applications

After the successful validation of the models, a series of numerical simulations were carried out to investigate the field consolidation behavior of CPB mass under various conditions or with various factors. They included different curing ages, stope geometries, inclination angles, rock wall roughness, cement contents, backfilling rates and strategies, and drainage conditions. To assess the consolidation behavior of CPB under different conditions, a control stope with a predefined geometry, backfilling strategy and rate, mix recipe and curing condition was utilized as a reference. All numerical investigations were performed by modifying the conditions of the control stope. Details on the input parameters, and initial and boundary conditions of the control stope are listed in Table 5.5.

Table 5.5. Input parameters, and initial and boundary conditions

Input item	Parameter	Value
CPB	Stope geometry (m)	15 m (W)×30 m (H)
	Inclination angle (°)	90
	Cement content (wt%)	Residual fill: 4.5 (60.4 kg/m^3), and plug fill: 7 (80.2 kg/m^3)
	w/c ratio	7.6
	Initial void ratio	1
	Backfilling rate (m/h)	0.5
	Backfilling strategy	2-stages of filling with 1-day plug
Rock mass	Density (kg/m^3)	2500
	Young's modulus (GPa)	30
	Poisson's ratio	0.3
	Thermal conductivity (W/m K)	3.9
	Heat capacity (J/kg K)	790
Mechanical module	Top surface	Free
	Lateral sides	Roller
	Bottom side	Fixed
	Volume force	Gravity
Hydraulic module	Top surface	No flow
	Lateral sides	No flow
	Bottom side	No flow
	Volume force	Gravity
	Initial value	Hydraulic head=0
Thermal module	Top side (°C)	25
	Lateral sides (°C)	25
	Bottom side (°C)	25
	Initial temp. (°C)	25

wt%: weight percentage with respect to the total weight of the solid phase in CPB

The geometry and mesh for the control CPB mass and stope are presented in Figure 5.35. Three monitored points are examined: 29.5 m, 7 m and 0.5 m from the stope floor. These three monitored points are used to investigate the development of consolidation with curing time. Moreover, the monitored point of 7 m is located on the interface where the filling takes place, and thus can provide useful information about the backfilling operation including both the curing time of the plug layer and the effects of subsequent filling. Therefore, this monitored point is used to study the effects of the stope geometry, rock wall roughness, mix components, and backfilling and drainage conditions.

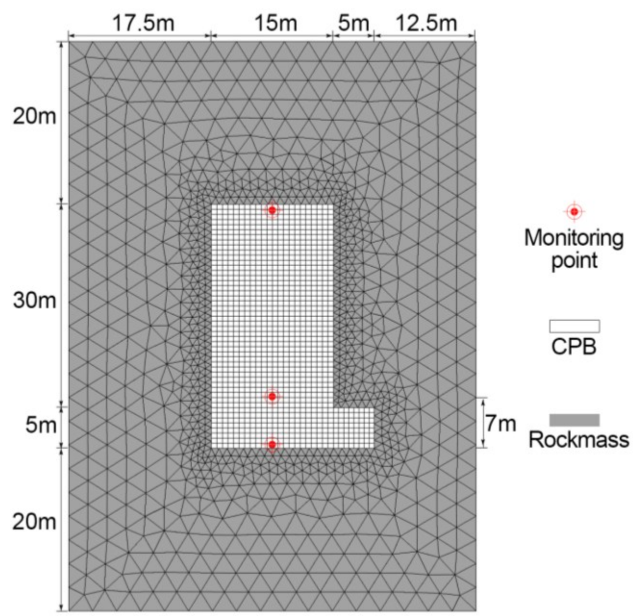

Figure 5.35. Mesh and geometry of control CPB and stope

The backfilling strategy (filling operation carried out in two-stages) and rate (0.5 m/hour) adopted in the control stope is presented in Figure 5.36. After the first layer of CPB was placed into the stope, the fresh plug layer was allowed to cure for 1 day. Then, residual backfilling was carried out.

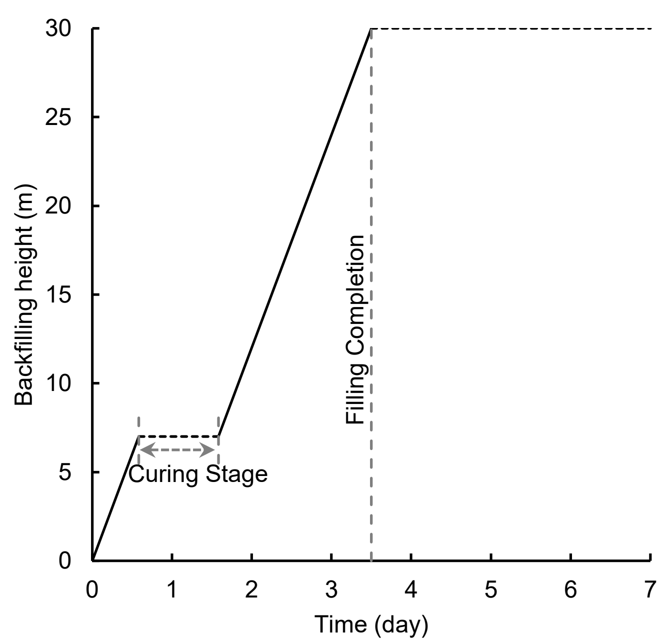

Figure 5.36. Backfilling operation for the control stope

During and after filling, water drainage through the barricade was allowed. For the numerical implementation of the drained condition in the CPB, a water mass flux boundary condition was incorporated into the hydraulic module and applied on the right vertical side of the drawpoint. The water mass flux can be computed by multiplying the pore water density and its velocity through the retaining wall. The latter can be determined by using Darcy's law.

5.3.4.1. Effect of curing time

With curing time, binder hydration induced chemical shrinkage, water drainage through the barricade and/or fractured rock mass, and self-weight induced volume changes will contribute to the consolidation process in CPB. Moreover, due to the temperature dependence of binder hydration (Schindler and Folliard 2003; Cui and Fall 2015b), the heat generated by hydration reactions, and heat transfer between the CPB and surrounding rock can affect the chemical reaction rate and thus the consolidation process. Therefore, the effect of curing time on the consolidation behavior of CPB needs to be examined. Figure 5.37 presents the changes in the average degree of consolidation (i.e., the ratio of the vertical settlement at any time and the final settlement) for three different heights of the CPB. From this figure, the following characteristics that depict the changes in the consolidation process in the CPB are found:

i. CPB strongly demonstrates time-dependent consolidation behavior. The changes in the rate of consolidation with time (i.e., the slope of the consolidation curve) can be attributed to the hardening process of the CPB skeleton, reduction in the rate of hydration with time, and reduction in the permeability of the CPB. Specifically, in terms of the effect of the hardening process, the CPB stiffness will be progressively increased by enhancing the bonding between tailings particles with the precipitation of binder hydration products in the capillary pore space (Benzaazoua et al. 2004; Cui and Fall 2016b), and the densification process through the consolidation of the CPB (Fall et al. 2007; Tariq 2012). The resultant stiffer CPB can resist larger loadings and thus reduce the rate of consolidation under a constant filling rate with time. Secondly, in terms of the effect of the rate of binder hydration, previous experimental studies (e.g., Ghirian and Fall 2015; Han et al. 2016) on cementitious materials have found that precipitated hydration products on the surface of an unhydrated binder can delay water diffusion into the unhydrated binder particles. As a result, there will be gradual reductions in the rate of binder hydration, and thus the contribution of chemical shrinkage to the development of consolidation is gradually reduced. In addition, another contributor to the delay in consolidation is the reduction of CPB permeability as consolidation of the CPB proceeds (Helinski et al. 2010) and thus gradually reduces the amount of water drainage through the barricade, which can in turn delay seepage-induced consolidation. Consequently, the time rate of the change in consolidation shows a decreasing trend with time.

ii. Moreover, CPB also shows a distinct consolidation behavior between the filling stages and curing of the plug layer (i.e., 1-day of curing from 14 hours to 38 hours). Specifically, greater volume changes take place during the filling stages due to the increase in the overburden stress by the placement of fresh CPB. With increased self-weight stress, the CPB becomes more consolidated.

iii. In addition, by comparing the consolidation behavior at three different heights of the CPB mass, it can be observed that the CPB becomes more consolidated at greater heights for any given filling and curing time. This is because the relatively fresh CPB is poured at higher elevation in backfilling operations that take place in different stages. The fresh CPB has relatively low stiffness, higher permeability and faster rate of hydration. Hence, CPB becomes more consolidated with greater height. Consequently, the development of spatially non-uniform consolidation appears in the CPB.

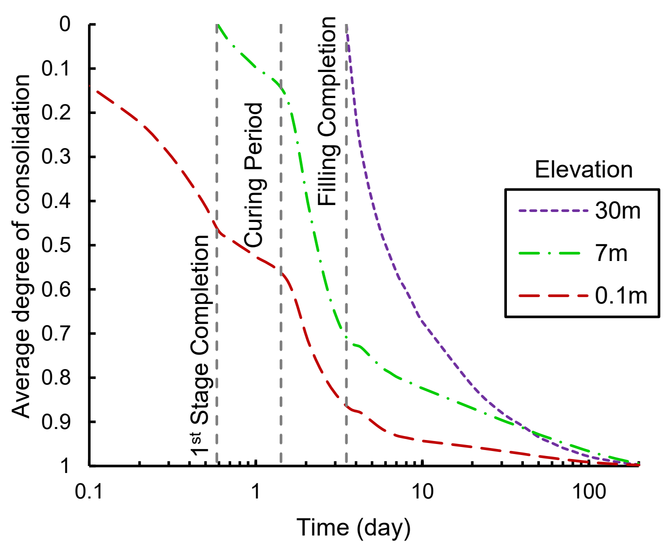

Figure 5.37. Variation of average degree of consolidation with curing time

To further illustrate the spatial distribution and development of the consolidation process in CPB, void ratio changes in the control stope are investigated and presented in Figure 5.38. It can be observed that the development of consolidation of CPB is relatively uniform at a given height at the early ages (see Figure 5.38a and 5.38b). With time, the non-uniform distribution of the void ratio becomes apparent, especially in the vicinity of the rock walls (see Figure 5.38c). The non-uniform change in the void ratio is mainly attributed to the arching effect (Yilmaz et al. 2013). In addition, Figure 5.38 shows that a major change in the void ratio takes place around the layer interface when the filling takes place in stages (i.e., 7 m from the stope base). This is due to (1) the distinct interface properties and inconsistent rate of consolidation near the layer interface (Cui and Fall 2016c), and (2) the difference in the refinement of the capillary pore space around the layer interface when filling takes place in stages. More specifically, the interface adhesion and friction angle will be gradually increased during the 1-day of curing. Therefore, the first layer (i.e., the plug layer) is able to form higher shearing resistance along the backfill/rock-wall interface compared to the second CPB layer. Moreover, the precipitation of hydration products also plays an important role in the reduction of the void ratio. Compared with the fresh residual CPB layer, more hydration products can form in the pore space of the plug layer, which can contribute to the changes in the void ratio near the layer interface. In addition, compared to the plug layer, binder hydration occurs more quickly in relatively fresh CPB (i.e., second layer), which causes significant chemical shrinkage and thus contributes more to the development of consolidation of the CPB along the layer interface. Consequently, the variations in the void ratio near the interface of the different backfill layers gradually become more pronounced with time. Similar results have been found in previous studies on CPB (e.g., Li and Aubertin 2009; El Mkadmi et al. 2013)

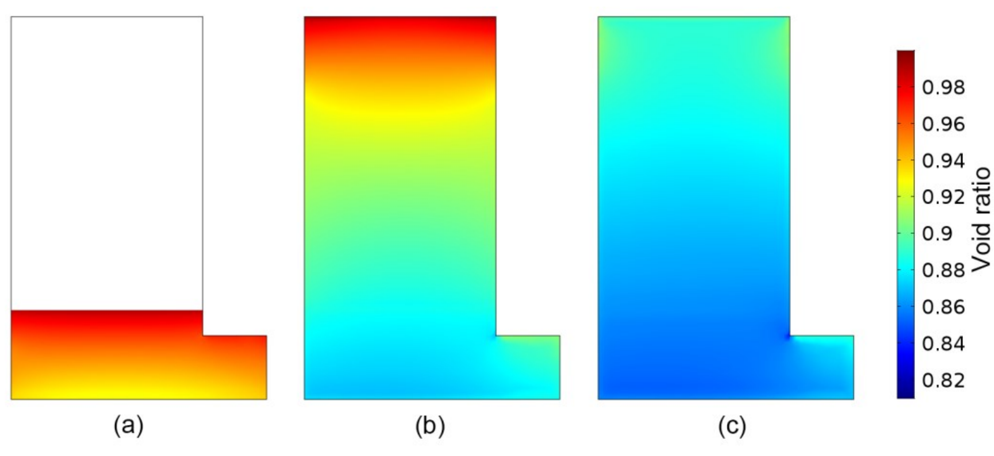

Figure 5.38. Changes in void ratio with curing time: (a) 14 hours (completion of plug filling); (b) 84 hours (completion of filling operation; and (c) 168 hours.

5.3.4.2. Effect of stope geometry

Due to the different ore bodies and adopted stoping methods, the resultant stopes may differ in terms of size and inclination angle (Dirige et al. 2009; Cui and Fall 2016d). To investigate the effect of the stope geometry, three stopes with different height-to-width (H/W) ratios, including 1:1 (15 m×15 m), 2:1 (30 m×15 m) and 4:1 (45 m×15 m) are chosen for further investigation in this study. The changes in the average degree of consolidation at a monitored point of 7 m from the stope floor with different H/W ratios are plotted in Figure 5.39. It can be seen that the changes in the H/L ratio have significant impacts on the consolidation behavior of CPB, especially in the post-filling stage. Specifically, during the filling stage, the consolidation curves for the different H/L ratios follow a similar trend of change, namely, an increase in the self-weight stress with filling can significantly affect the consolidation behavior of CPB. However, after the filling takes place, there is an apparent discrepancy in the consolidation behavior of the CPB stopes with different H/L ratios, and a lower rate of consolidation is obtained in the stope with a high H/L ratio. This is because the CPB placed at a greater height exerts more overburden stress onto the monitored point. As a result, there are more volume changes in the CPB with a higher H/L ratio (re: Figure 5.40) during the filling process, which can further increase CPB stiffness (Cui and Fall 2016c). Consequently, after placement, the stiffer CPB placed at a greater height can significantly reduce the rate of consolidation. Hence, CPB demonstrates distinct post-filling consolidation behavior in stopes with different H/L ratios.

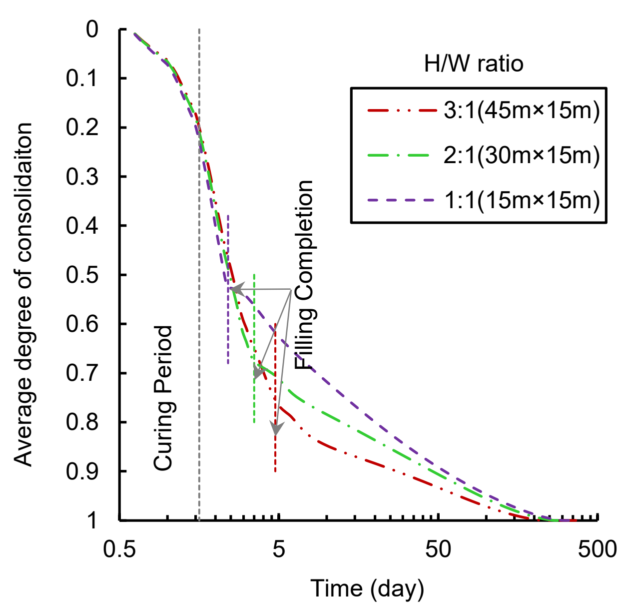

Figure 5.39. Effect of H/W ratios on the consolidation process of CPB

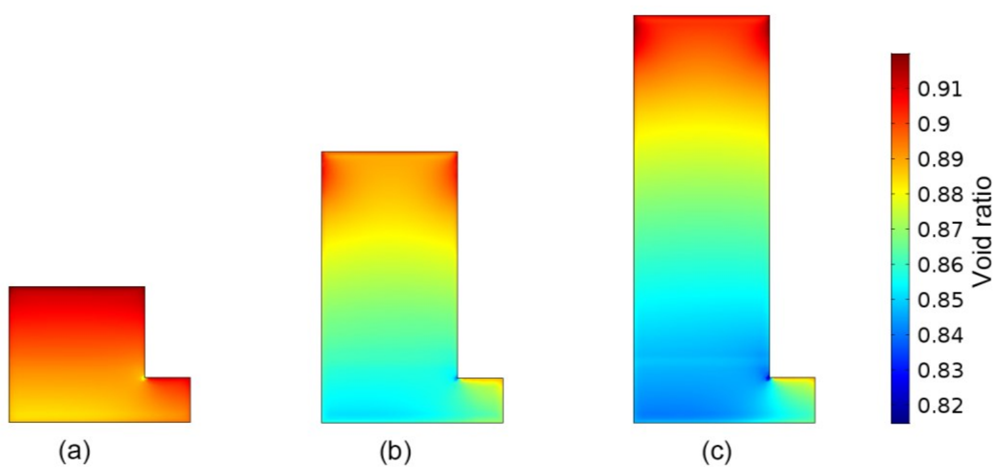

Figure 5.40. Spatial distribution of void ratio of CPB with different H/W ratios after 7 days of curing: (a) 1:1 (15 m×15 m); (b)2:1 (30 m×15 m); and (c) 3:1 (45 m×15 m)

Apart from the H/W ratio, the stope inclination angle is another key factor that affects the resultant backfill geometry. To investigate the effect of the stope inclination on the consolidation behavior, two dip angles of 90° and 50° are selected for further examination in this study. To isolate the effect of self-weight, the backfill height (i.e., 30 m) and backfilling strategy (i.e., filling that takes place in two stages with 1-day plug) are set to be same for these two cases. The modeling results are presented in Figure 5.41, and indicate that during the curing of the plug layer and in the early onset of the second stage of filling, the development of consolidation for these two cases follows a similar trend of change. However, the differences in the degree of consolidation between these two stopes become progressively more evident after approximately 2.75 days. In particular, a lower degree of consolidation is observed in the inclined stope due to the effect of the inclination angle on the stress distribution in CPB. Previous studies on CPB (Cui and Fall 2016c; 2017) found that under the gravity effect, more overburden stress is transferred to the footwall (i.e., lower rock wall). As a result, non-symmetrical distribution of stress and volume changes emerge in the inclined stope, and become more pronounced with reductions in the inclination angle (see Figure 5.42). Moreover, the inclined stope can further contribute to the arching effect (Ting et al. 2010; Cui and Fall 2016c; d; 2017). As a result, vertical stress acting on the monitored point is reduced with the enhanced arching effect in the inclined stope. Therefore, there are smaller volume changes in the inclined CPB, which is clearly shown in Figure 5.42 as well.

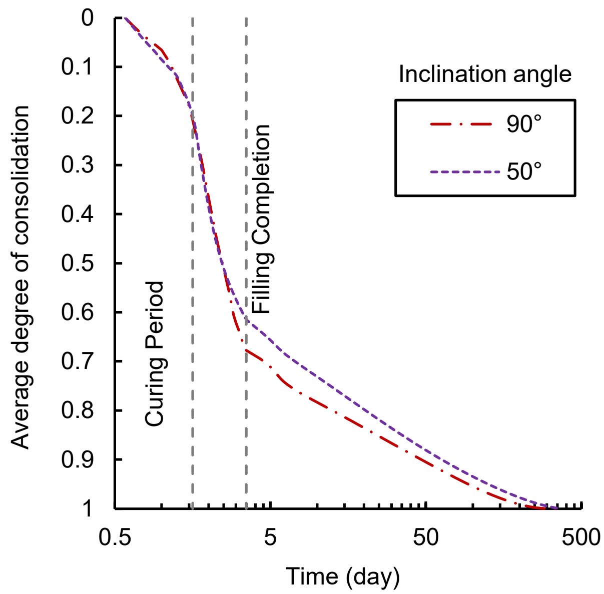

Figure 5.41. Effect of inclination angles on the consolidation process of CPB

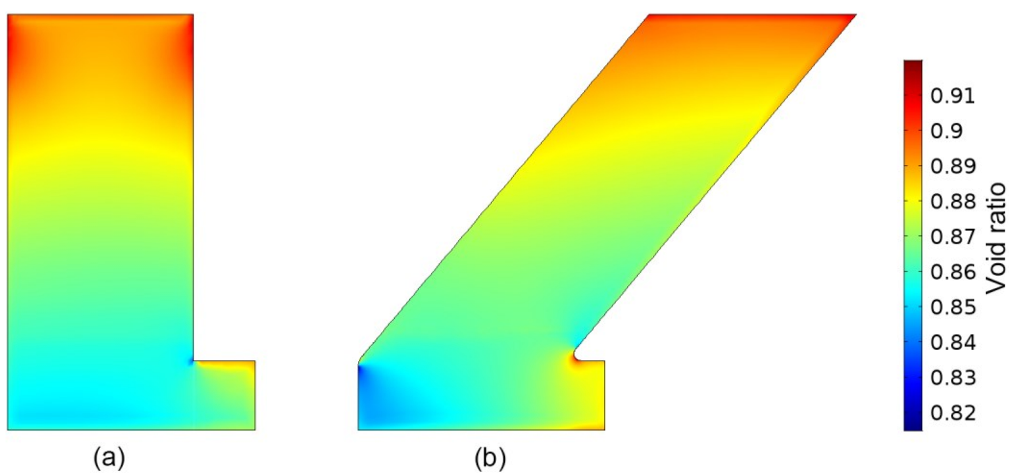

Figure 5.42. Spatial distribution of void ratio of CPB with different inclination angles after 7 days of curing: (a) 90°; (b) 50°.

5.3.4.3. Effect of rock wall roughness

Ore extraction operations (e.g., the use of explosives) cause the roughness of rock walls. However, the roughness of rock walls can affect the rock mass/CPB interface behavior or properties (i.e., friction angle and adhesion) and thus influence the consolidation process of CPB. To quantitatively characterize the roughness of a rock wall, the roughness index R_L (i.e., the ratio of the actual and projected lengths along the rock wall in the shearing direction) is used in this study. Three different R_L including 1 (smooth rock wall), 1.5 and 2 are selected to investigate the effect of rock wall roughness on the consolidation behavior of CPB. The modeling results are presented in Figure 5.43. It is evident that the rock wall roughness has significant impacts on the consolidation behavior of the CPB. The changes in the consolidation curves which start from the second stage of filling becomes more apparent with each layer. As demonstrated in Figure 5.43, with increases in the rock wall roughness, there is a greater degree of consolidation of the CPB during filling, namely, the volume changes in a stope with more rough rock walls are reduced after the completion of the stope filling process (post filling stage). This can be attributed to the increased arching effect with a CPB/rock mass interface that has more surface roughness (Cui and Fall 2017). As a result, the resultant vertical stress acting on the monitored point decreases with an increased arching effect, and thus the associated volume changes are reduced in the stope with a more rough rock wall during the post filling stage.

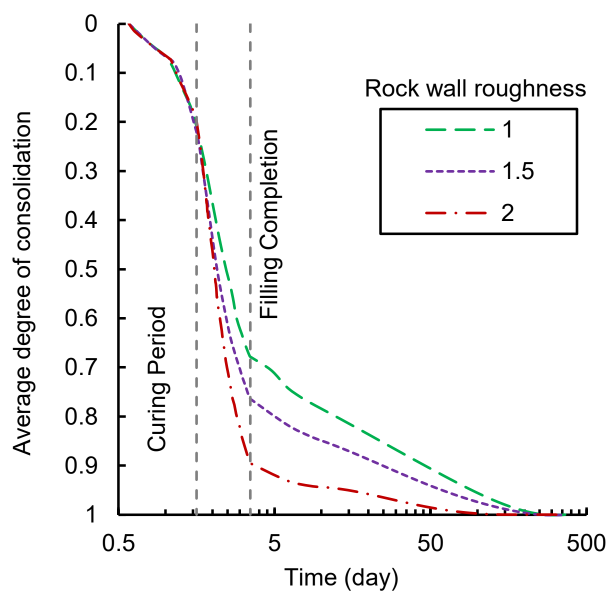

Figure 5.43. Effect of rock wall roughness on the consolidation process of CPB

5.3.4.4. Effect of CPB mix components

The mix recipe plays a key role in the stability of CPB structures (Cui and Fall 2016d). In fact, cement consumption can account for up to 75% of the production costs of CPB (Grice 1998; Fall et al. 2008). In other words, a cost-effective design of CPB structures largely depends on the cement content. Due to the significance of the cement content in CPB design, three different binder contents, including 3 wt% (43.9 kg/m^3), 4.5 wt% (60.4 kg/m^3) and 7 wt% (82.2 kg/m^3) are examined to study their impacts on the consolidation behavior of CPB. The effect of cement content on the changes in the void ratio of the CPB is plotted in Figure 5.44. It can be seen that the discrepancy in the consolidation behavior in CPB with different cement contents appears since the very early ages, and becomes progressively more obvious with filling and the curing that follows. Specifically, CPB with less cement content shows a higher rate of consolidation up to the completion of the filling. After completion of the filling, CPB with more cement content becomes more consolidated. This is because during the filling process, more cement content generates more cement hydration products which can further increase the stiffness of the CPB. As a result, the increase in the overburden stress by the newly placed CTB will cause a lower degree of consolidation when the cement content is higher. However, after the completion of the filling, consolidation induced by chemical shrinkage may be prevalent. As a result, CPB with a higher binder content becomes more consolidated during the post-filling stage. Therefore, this study clearly demonstrates the combined effect of hardening induced by binder hydration, overburden stress and chemical shrinkage on the consolidation behavior of CPB.

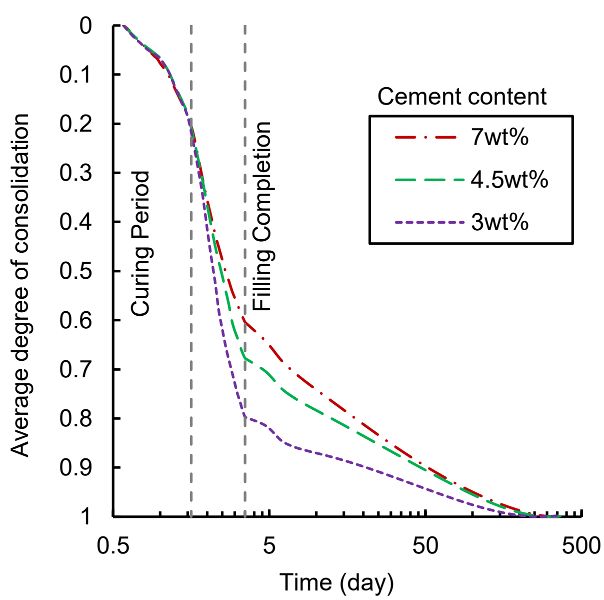

Figure 5.44. Effect of cement content on the consolidation process of CPB

5.3.4.5. Effect of backfilling rate

Due to the differences in planning and scheduling underground mining, the backfilling rate may vary from one stope to another. The differences in filling rate affect the CPB operation time and thus the mining cycle and mine productivity (Veenstra et al. 2011; Khaldoun et al. 2016). Therefore, it is necessary to study the effect of the filling rate on the consolidation behavior of the CPB. In this study, a range of backfilling rates including 0.5 m/h (i.e., 12 m/d), 1 m/h (i.e., 24 m/d) and 2 m/h (i.e., 48 m/d) are simulated. The simulation results are presented in Figure 5.45. It can be observed that the filling rate has a significant effect on the development of CPB consolidation. As the filling rate is reduced, there is an increase in the consolidation at the end of the filling sequence. For example, after the filling operation is carried out; i.e., 1.625 days for 2 m/h, 2.25 days for 1 m/h, and 3.5 days for 0.5 m/h, the average degree of consolidation is 0.57, 0.62 and 0.67 respectively. This is because a reduced rate of filling results in a longer filling time (and thus curing time) for a given CPB height. Consequently, the consolidation process can continue longer, and the precipitation of more hydration products can further refine the pore space. Thus, the CPB becomes more consolidated with a slower rate of filling.

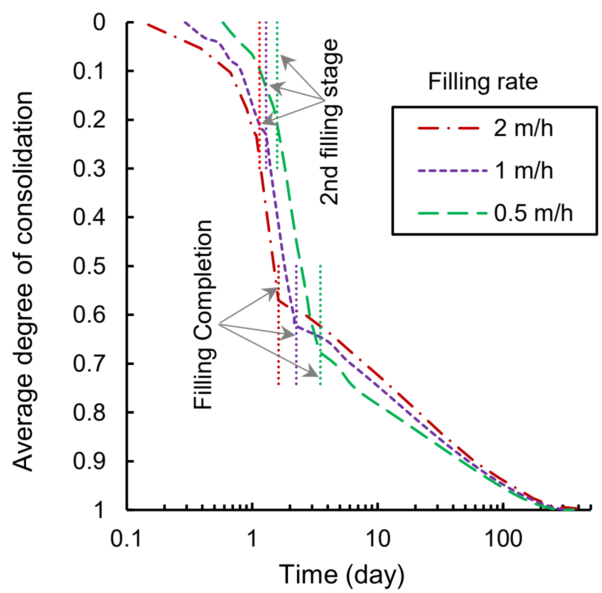

Figure 5.45. Effect of filling rate on consolidation process of CPB

5.3.4.6. Effect of drainage conditions

During and after pouring into underground stopes, CPB may be subjected to drained (e.g., Thompson et al. 2009; Thompson et al. 2012) or undrained (e.g., Helinski et al. 2010; Doherty et al. 2015; Suazo and Fourie 2015) conditions. Water seepage through the barricade not only causes the dissipation of PWP, but also contributes to the consolidation of CPB. Hence, CPB placed into a stope in both drained and undrained conditions is investigated in this study. The variations in the void ratio at a monitored point is plotted in Figure 5.46. The obtained results demonstrate that the differences in the consolidation behavior starts from the second stage of filling. As the filling operation progresses, and stops (post filling stage), the difference between the drained and undrained conditions becomes even more evident. As shown in Figure 5.46, the major change in the consolidation of the CPB for the undrained condition mainly occurs during the filling stage, namely an increase in the overburden stress due to the filling operation significantly contributes to the volume changes in CPB in the undrained condition. However, the degree of consolidation in the drained condition is only 0.72 after filling is carried out, namely, greater volume changes take place in the CPB in the drained condition after filling is carried out. This is due to water drainage which can further contribute to the densification of the CPB skeleton, and is thus more favorable for the stability of the CPB structure.

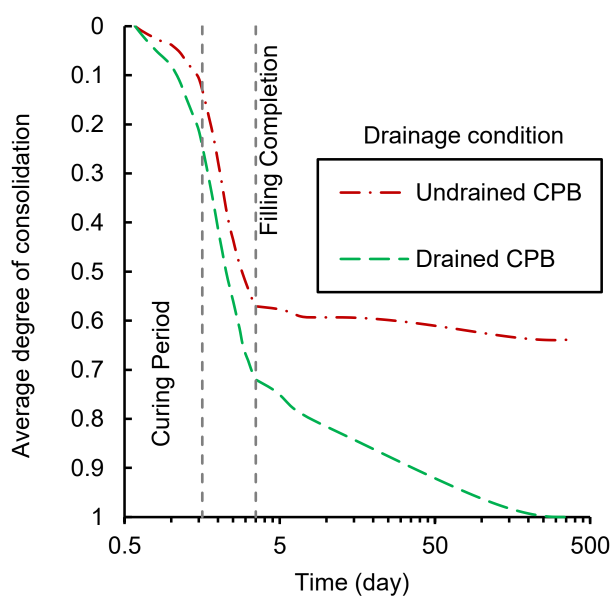

Figure 5.46. Effect of drainage conditions on consolidation process of CPB

The spatial distribution of the void ratio of CPB is presented in Figure 5.47. It can be seen that the arching effect in the stope in the drained condition (i.e., Figure 5.47b) is more obvious in comparison with that in the undrained condition (i.e., Figure 5.47a). This is because more settlement occurs in the former. Correspondingly, there is also relatively more interface displacement. Therefore, a large degree of shear stress will take place on the interface resistance which can further contribute to the arching effect in CPB. Moreover, it is evident in Figure 5.47 that there is a pronounced change in the void ratio which occurs around the interface during the filling stages (i.e., 7 m from the stope floor) for the drained condition. This is due to the fact that there is more reduction in the pore space in the drained condition during and after plug placement. As a result, after 1-day of curing, the plug layer becomes stiffer in comparison to that in the undrained condition. Therefore, after subsequent filling, there is a greater difference in the stiffness of the CPB at the interface, which can result in strain concentration in the corresponding regime for the drained condition.

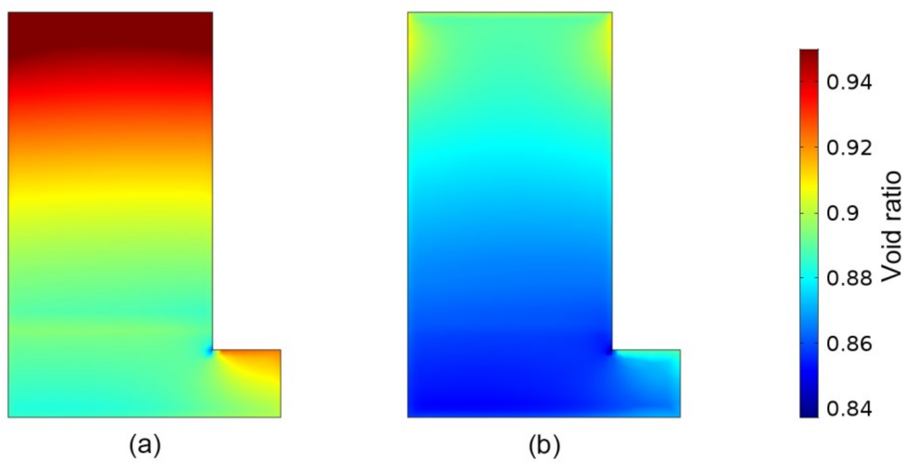

Figure 5.47. Spatial distribution of void ratio of CPB under different drainage conditions after 7-days of curing: (a) undrained CPB; (b) drained CPB.

5.3.5. Conclusions

The following conclusions are made based on the obtained results in this study.

(i) The in-situ consolidation behavior of CPB structures is controlled by the coupled THMC processes through the effect of the self-weight of CPB, water drainage through the barricade, temperature changes induced by the heat transfer between the CPB and the surrounding environment, and chemical shrinkage caused by the development of binder hydration.

(ii) The consolidation behavior of CPB structures is time-dependent, that is, the void ratio significantly varies with curing time. Moreover, changes in the void ratio mainly take place at the early ages.

(iii) The rock mass conditions, including the geometry and rock wall roughness, can affect the consolidation process of CPB structures. Increased rock mass/CPB interface roughness and low inclination angles can further contribute to the development of the arching effect in CPB, which is more favorable for its stability.

(iv) Cement content plays a crucial role in the consolidation process of CPB. The variations in the degree of consolidation of CPB with different cement contents are more evident from the second stage of filling, which clearly demonstrates that chemical shrinkage affects consolidation behavior.

(v) A slower rate of filling can further increase the volume changes in the CPB, and thus will be beneficial for its stability. However, the differences in filling rate affect the CPB operation time and thus the mining cycles and mine productivity

(vi) Water drainage through barricades can drastically reduce the pore space of CPB, and thus contributes to the stability of retaining structures and CPB mass in stopes.

5.3.6. References

Belem, T., Harvey, A., Simon, R., and Aubertin, M. (2004). "Measurement and prediction of internal stresses in an underground opening during its filling with cemented fill." *Proc., 5th International Symposium on Ground Support in Mining and Underground Construction*, Australian Centre for Geomechanics, Perth, Australia, 28-30.

Benzaazoua, M., Fall, M., and Belem, T. (2004). "A contribution to understanding the hardening process of cemented pastefill." *Miner. Eng.*, 10.1016/j.mineng.2003.10.022, 17(2), 141-152.

Biot, M. A. (1955). "Theory of elasticity and consolidation for a porous anisotropic solid." *J. Appl. Phys.*, 10.1063/1.1721956, 26(2), 182-185.

Comsol (2015). "Comsol Multiphysics 5.1." <http://www.comsol.com>. (Sept. 20, 2016).

Cui, L., and Fall, M. (2015a). "A coupled thermo-hydro-mechano-chemical model for underground cemented tailings backfill." *Tunn. Undergr. Sp. Tech.*, 10.1016/j.tust.2015.08.014, 50, 396-414.

Cui, L., and Fall, M. (2015b). "Modeling and Simulation of the Consolidation Behaviour of Cemented Paste Backfill." *Proc., 2015 Comsol Conference*, Boston, MA, USA, 1-5.

Cui, L., and Fall, M. (2015c). "Multiphysics Modelling of the Behaviour of Cemented Tailings Backfill Materials." *Proc., International Conference on Civil, Structural and Transportation Engineering*, Internatioanl ASET Inc., Ottawa, ON, Canada, 1-7.

Cui, L., and Fall, M. (2016a). "An evolutive elasto-plastic model for cemented paste backfill." *Comput. Geotech.*, 10.1016/j.compgeo.2015.08.013, 71, 19-29.

Cui, L., and Fall, M. (2016b). "Mechanical and thermal properties of cemented tailings materials at early ages: Influence of initial temperature, curing stress and drainage conditions." *Constr. Build. Mater.*, 10.1016/j.conbuildmat.2016.08.080, 125, 553-563.

Cui, L., and Fall, M. (2016c). "Multiphysics model for consolidation behaviour of cemented paste backfill." *Int. J. Geomech.*, 10.1061/(ASCE)GM.1943-5622.0000743, 040160771-0401607723.

Cui, L., and Fall, M. (2016d). "Simulation of self-desiccation process in cemented tailings backfill structure." *Int. J. Numer. Anal. Methods Geomech. (submitted)*.

Cui, L., and Fall, M. (2017). "Multiphysics modeling of arching effects in fill mass." *Comput. Geotech.*, 10.1016/j.compgeo.2016.10.021, 83, 114-131.

Dirige, A., McNearny, R., and Thompson, D. (2009). "The effect of stope inclination and wall rock roughness on back-fill free face stability." *Proc., the 3rd Canada–US Rock Mechanics Symposium*, CIM, 1-12.

Doherty, J. P., Hasan, A., Suazo, G. H., and Fourie, A. (2015). "Investigation of some controllable factors that impact the stress state in cemented paste backfill." *Can. Geotech. J.*, 10.1139/cgj-2014-0321, 52(12), 1901-1912.

El Mkadmi, N., Aubertin, M., and Li, L. (2013). "Effect of drainage and sequential filling on the behavior of backfill in mine stopes." *Can. Geotech. J.*, 10.1139/cgj-2012-0462, 51(1), 1-15.

Fahey, M., Helinski, M., and Fourie, A. (2009). "Some aspects of the mechanics of arching in backfilled stopes." *Can. Geotech. J.*, 10.1139/T09-063, 46(11), 1322-1336.

Fall, M., Belem, T., Samb, S., and Benzaazoua, M. (2007). "Experimental characterization of the stress–strain behaviour of cemented paste backfill in compression." *J. Mater. Sci.*, 10.1007/s10853-006-0403-2, 42(11), 3914-3922.

Fall, M., Benzaazoua, M., and Saa, E. (2008). "Mix proportioning of underground cemented tailings backfill." *Tunn. Undergr. Sp. Tech.*, 10.1016/j.tust.2006.08.005, 23(1), 80-90.

Fall, M., Célestin, J., and Sen, H. (2010). "Potential use of densified polymer-pastefill mixture as waste containment barrier materials." *Waste Manage.*, 10.1016/j.wasman.2010.07.016, 30(12), 2570-2578.

Fall, M., Nasir, O., Cui, L., and Han, F. (2015). "Coupled modeling of the strength development and distribution within cemented paste backfill structure." *Proc., 49th US Rock Mechanics/Geomechanics Symposium*, American Rock Mechanics Association, San Francisco, California, USA, 587-595.

Fried, E., Benzaazoua, M., Bussière, B., and Belem, T. (2007). "Study of the leaching behaviour and metal fixation within cemented paste backfill materials." *Proc., the 9th International Symposium in Mining with Backfill*, 1-11.

Ghirian, A., and Fall, M. (2013). "Experimental Investigations of the Thermo-Hydro-Mechanical-Chemical Behavior of Cemented Paste Backfill." *Proc., 23rd World Mining Congr.*, Canadian Institute of Mining, Metallurgy and Petroleum (CIM), (378) 371-311.

Ghirian, A., and Fall, M. (2014). "Coupled thermo-hydro-mechanical-chemical behaviour of cemented paste backfill in column experiments: Part II: Mechanical, chemical and microstructural processes and characteristics." *Eng. Geol.*, 10.1016/j.enggeo.2013.12.004, 170, 11-23.

Ghirian, A., and Fall, M. (2015). "Coupled Behavior of Cemented Paste Backfill at Early Ages." *Geotech. Geol. Eng.*, 10.1007/s10706-015-9892-6, 33(5), 1141-1166.

Grice, T. (1998). "Underground mining with backfill." *Proc., the 2nd Annual Summit-Mine Tailings Disposal Systems*, 234-239.

Haiqiang, J., Fall, M., and Cui, L. (2016). "Yield stress of cemented paste backfill in sub-zero environments: Experimental results." *Miner. Eng.*, 10.1016/j.mineng.2016.03.014, 92, 141-150.

Han, F., Zhang, Z., Liu, J., and Yan, P. (2016). "Hydration kinetics of composite binder containing fly ash at different temperatures." *J. Therm. Anal. Calorim*, 10.1007/s10973-016-5295-z, 124(3), 1691-1703.

Hassani, F., Ouellet, J., and Servant, S. (2001). "In situ measurements in a paste backfill: backfill and rock mass response in the context of rockburst." *Proc., 17th International Mining Congress and Exhibition of Turkey*, Chamber of Mining Engineers of Turkey, 165-175.

Helinski, M., Fahey, M., and Fourie, A. (2010). "Behavior of cemented paste backfill in two mine stopes: measurements and modeling." *J. Geotech. Geoenviron.*, 10.1061/(ASCE)GT.1943-5606.0000418, 137(2), 171-182.

Khaldoun, A., Ouadif, L., Baba, K., and Bahi, L. (2016). "Valorization of mining waste and tailings through paste backfilling solution, Imiter operation, Morocco." *Int. J. Min. Sci. Technol.*, 10.1016/j.ijmst.2016.02.021, 26(3), 511-516.

Koupouli, N. J., Belem, T., Rivard, P., and Effenguet, H. (2016). "Direct shear tests on cemented paste backfill-rock wall and cemented paste backfill-backfill interfaces." *J. Rock Mech. Geotech. Eng.*, 10.1016/j.jrmge.2016.02.001, 8, 472-479.

Li, L., Aubertin, J. D., and Dubé, J.-S. (2014). "Stress distribution in a cohesionless backfill poured in a silo." *Open Civ. Eng. J.*, 10.2174/1874149501408010001, 8, 1-8.

Li, L., and Aubertin, M. (2009). "Numerical investigation of the stress state in inclined backfilled stopes." *Int. J. Geomech.*, 10.1061/(ASCE)1532-3641(2009)9:2(52), 9(2), 52-62.

Potvin, Y., and Thomas, E. (2005). *Handbook on mine fill*, Australian Centre for Geomechanics, Crawley, WA, Australia.

Schindler, A. K., and Folliard, K. J. (2003). "Influence of supplementary cementing materials on the heat of hydration of concrete." *Proc., Advances in Cement and Concrete IX Conference*, Engineering Conferences International, Inc., Colorado, USA, 17-26.

Shahsavari, M., and Grabinsky, M. (2015). "Mine backfill pore water pressure dissipation: numerical predictions and field measurements." *Proc., GeoQuébec*, 1-8.

Suazo, G., and Fourie, A. (2015). "Numerical simulation of blast response of cemented paste backfills." *Proc., the 15th Pan-American Conference on Soil Mechanics and Geotechnical Engineering*, IOS Press, 2394-2401.

Tariq, A. (2012). "Synergistic and Environmental Benefits of Using Cement Kiln Dust With Slag and Fly Ash in Cemented Paste Tailings." Ph.D. Thesis, University of Western Ontario, Canada.

Terzaghi, K. (1943). *Theory of Consolidation*, John Wiley & Sons Inc., Hoboken, NJ, USA.

Thompson, B., Bawden, W., and Grabinsky, M. (2012). "In situ measurements of cemented paste backfill at the Cayeli Mine." *Can. Geotech. J.*, 10.1139/t2012-040, 49(7), 755-772.

Thompson, B., Grabinsky, M., Bawden, W., and Counter, D. (2009). "In-situ measurements of cemented paste backfill in long-hole stopes." *Proc., the 3rd CANUS Rock Mechanics Symposium*, Toronto, Canada, 197-198.

Ting, C. H., Shukla, S. K., and Sivakugan, N. (2010). "Arching in soils applied to inclined mine stopes." *Int. J. Geomech.*, 10.1061/(ASCE)GM.1943-5622.0000067, 11(1), 29-35.

Veenstra, R., Bawden, W., Grabinsky, M., and Thompson, B. (2011). "An approach to stope scale numerical modelling of early age cemented paste backfill." *Proc., 45th*

US Rock Mechanics/Geomechanics Symposium, American Rock Mechanics Association, 1-7.
Williams, T. J., Denton, D. K., Larson, M. K., Rains, R. L., Seymour, J. B., and Tesarik, D. R. (2001). "Geomechanics of reinforced cemented backfill in an underground stope at the Lucky Friday Mine." *Report of Investigations*, National Institute for Occupational Safety and Health, 1-24.
Yilmaz, E., Belem, T., Benzaazoua, M., Kesimal, A., Ercikdi, B., and Cihangir, F. (2011). "Use of high-density paste backfill for safe disposal of copper/zinc mine tailings." *Gospodarka Surowcami Mineralnymi*, 27, 81-94.
Yilmaz, E., Tikou, B., Aatar, O. E., and Benzaazoua, M. (2013). "Laboratory and in situ analysis of consolidation behaviour of cemented paste backfill." *Proc., 23rd International Mining Congress and Exhibition of Turkey* 1841-1850.
Zhang, Q., Zhang, J., Guo, S., Gao, R., and Li, W. (2015). "Design and application of solid, dense backfill advanced mining technology with two pre-driving entries." *Int. J. Min. Sci. Technol.*, 10.1016/j.ijmst.2014.12.008, 25(1), 127-132.

5.4. Paper VIII: Multiphysics simulation of pressure on retaining structures for fill mass

Liang Cui, Mamadou Fall

Abstract

To retain fresh cemented tailings backfill (CTB) in a stope (underground mining excavations), a retaining structure (called a barricade) must be constructed at the base of the stope. Due to the coupled thermo-hydro-mechano-chemical (THMC) processes that occur in CTB, changes in the total horizontal stress and pore water pressure (PWP) take place with backfilling operations that are flexible, which directly affects the stability of the barricade. Hence, an investigation of the changes and distribution of barricade pressure is crucial for the assessment of the stability of CTB and the barricade. In this paper, an integrated multiphysics model composed of a fully coupled THMC model, a fully coupled multiphysics model that analyzes the consolidation process in CTB and an elastoplastic model that analyzes changes in the interface behavior during the interaction of rock mass/backfill is adopted. The predictive ability of the model is validated by the good agreement between the simulation results and in-situ measurements from a series of field monitoring programs. Then, the validated multiphysics model is used to numerically investigate the changes and spatial distribution of barricade pressure under various conditions (including curing time, barricade location and shape, backfilling strategy, initial temperature, and drainage conditions). The obtained results can provide practical insight into the factors that affect the stability of barricade structures.

Keywords: Mining; Cemented paste backfill; Multiphysics; THMC; Barricade pressure.

5.4.1. Introduction

Cemented tailings backfill (CTB) is an engineered mixture of dewatered full stream tailings, hydraulic binder and water (Ghirian and Fall 2016). The application of CTB can improve ground stability, enhance ore recovery and reduce ground surface subsidence (Belem and Benzaazoua 2004; Cui and Fall 2015a; Li and Yang 2015; Ghirian 2016; Haiqiang et al. 2016). Moreover, due to the rapid increase in strength compared to the use of rock fill and hydraulic fill (Yilmaz et al. 2004; Veenstra 2013), the integration of CTB into mining operations can significantly reduce the mining cycles and thus increase productivity. In addition, tailings are utilized as a key component for CTB preparation, and then transported into underground mined-out voids (called stopes). Thus, CTB technology can be considered as an effective alternative to surface tailings storage, and reduce the risk of the environmental pollution (e.g., acid mine drainage) associated with surface tailings disposal. Therefore, CTB technology has been increasingly and widely utilized in underground mining operations around the world (Benzaazoua et al. 2006; Fall et al. 2015).

After preparation, the fresh CTB paste is transported through pipelines or gravity and poured into a stope. To keep the fresh CTB in a stope, a retaining structure called a barricade (also called bulkhead or fill fence) must be constructed in the crosscut (Helinski et al. 2010a). The failure of the barricade may result in catastrophic consequences (e.g., personnel injury and/or fatalities, drift flooding, equipment damage and related financial ramifications) (Li et al. 2009; Nasir and Fall 2009). Thus, barricade stability is considered to be a crucial design criterion of a CTB structure.

To analyze the stability of barricade structures will require determining the barricade pressure. After placement of fresh CTB into a stope, the barricade pressure is controlled by the complex multiphysics processes that occur in the CTB, including thermal, hydraulic, mechanical and chemical (THMC) processes (Cui and Fall 2015b; Doherty 2015). Specifically, the backfilling operation is flexible, and can take place in stages or different sequences, and thus the pressure exerted onto the stope base and barricade structure increases with increases in the fill height. Therefore, mechanical processes can directly contribute to barricade pressure. Moreover, water consumption caused by binder hydration (i.e., the chemical process) and the water drainage through the barricade (i.e., the hydraulic process) can also contribute to the changes of barricade pressure. In addition, the thermal process has significant impacts on the rate of binder hydration (Haiqiang et al. 2016; Walske et al. 2016) and thus the dissipation of the pore-water pressure (PWP) induced by binder hydration, which means that the thermal process must be considered during the assessment of barricade pressure. Therefore, an understanding of the multiphysics processes in CTB and modeling of these processes are crucial for reliably assessing and predicting the barricade pressure. Furthermore, the consolidation process in CTB can result in relative displacement between the rock walls and backfill (El Mkadmi et al. 2013; Cui and Fall 2016c). As a result, interface resistance (including interface adhesion and shear stress) will develop, which results in the transfer of stress from the CTB mass to the rock walls (i.e. the arching effect) (Li and Aubertin 2009; Cui and Fall 2017), and thus reduces the barricade pressure. Therefore, the coupled THMC processes, consolidation behavior and the backfill/rock mass interface interaction must be taken into consideration in the evaluation and prediction of stress on bulkheads in practice.

To provide more in-depth insight into the changes in barricades pressure, several field monitoring programs of backfilled stopes have been discussed in the literature (e.g., Belem et al. 2004; Yumlu 2008; Thompson et al. 2012; Doherty et al. 2015). Some of the factors that affect pressure are identified based on the field measurements. For example, Yumlu (2008) found that filling sequences that are carried out in stages can significantly enhance the dissipation of excess PWP compared to the use of a strategy that involves continuous filling. Aside from the backfilling strategy, CTB recipe, stope geometry, filling rate and drainage conditions are also identified as significant factors that affect the barricade pressure (Thompson et al. 2009; Doherty et al. 2015). Moreover, the field measurements conducted by Belem et al. (2004) demonstrated that the barricade pressure initially increases with fill height. However, with increased fill height, the barricade pressure gradually approaches its maximum value. A similar trend of change in the barricade pressure was observed in the field monitoring program conducted by Helinski et al. (2010a). These in-situ investigations have made a tremendous contribution to the understanding of the characteristics of change in barricade pressure during and after filling operations, which provide in-depth insight into the mechanisms that control barricade pressure and the related influential factors.

With an improved understanding of the changes in barricade pressure in stopes, several analytical models have been subsequently developed to quantitatively assess the pressure that acts on barricades. For example, Belem et al. (2004) and Li et al. (2009) respectively derived an analytical model from Marston's cohesionless model (Marston 1930) based on limit equilibrium analysis of CTB stopes. The closed-form analytical solution provides a simple method to assess the pressure exerted onto barricades. However, the applicability of the analytical models is limited because of their assumptions (e.g., constant material properties, and uniform distribution of horizontal stress at a given height). Therefore, several partially and fully coupled multiphysics models have been developed to reliably predict the changes in the pressure in stopes. For instance, Helinski et al. (2007) developed a hydro-mechanical-chemical (HMC) model to predict the volume changes and PWP in CTB. Wu et al. (2014) developed a thermo-hydro-chemical (THC) model to predict the PWP and temperature changes with the progression of binder hydration. A fully coupled THMC model for CTB material was developed by Cui and Fall (2015a) to simulate for the first time, time-dependent changes of the material properties of CTB under various multiphysics loading conditions. Then, this fully coupled THMC model was used to derive a multiphysics model that analyzes the consolidation process in CTB (Cui and Fall 2016c) and then further incorporated into an evolutive elastoplastic model that analyzes changes in the behavior of the rock mass/backfill interface (Cui and Fall 2017) and simulates the arching effect in CTB. However, a more accurate assessment of barricade pressure in stopes at the field scale can be carried out with the integration of these models into one model. Therefore, in this paper, a fully coupled THMC model (Cui and Fall 2015a), coupled multiphysics model (Cui and Fall 2016c) and elastoplastic model (Cui and Fall 2017) are combined to numerically investigate the changes in barricade pressure under different backfilling conditions.

5.4.2. Mathematical Models

To characterize the interaction of the multiphysics processes and their influence on the pressure acting on the barricade, a fully coupled THMC model proposed by Cui and Fall (2015a), multiphysics model that analyzes the consolidation process in CTB derived by Cui and Fall (2016c) and elastoplastic model that analyzes changes in the interface behavior during the interaction of rock mass/backfill developed by Cui and Fall (2017) are adopted in the present study. Details on all of these models including the model assumptions, and derivation and determination of the model coefficients are presented in (Cui and Fall 2015a; 2016c; 2017). A brief description of the three models is provided in Sections 5.4.2.1, 5.4.2.2 and 5.4.2.3, respectively. Moreover, it should be noted that in practice, the barricade pressure refers to the total horizontal stress rather than the PWP acting on the barricade structure (Yumlu 2008; Li et al. 2009). Hence, this convention is also adopted in this paper.

5.4.2.1. Coupled THMC model

To assess the coupled multiphysics process, the fully coupled THMC model proposed by Cui and Fall (2015a) is adopted in this study. In this THMC model, the transport of conserved quantities, such as mass, energy and momentum in a CTB structure is described by four equilibrium equations: (i) water mass, (ii) air mass, (iii) momentum (mechanical equilibrium), and (iv) energy conservation equations:

$$\phi S\frac{\partial \rho_w}{\partial t}+\phi\rho_w\frac{\partial S}{\partial t}+S\rho_w\left[\frac{\partial \varepsilon_v}{\partial t}+\frac{(1-\phi)}{\rho_s}\frac{\partial \rho_s}{\partial t}\right]-\phi S\dot{m}_{hydr}\left(\frac{\rho}{\rho_s}S-1\right)=-\nabla\cdot\left(\phi S\rho_w\mathbf{v}^{rw}\right) \quad (5.22)$$

$$\phi(1-S)\frac{\partial \rho_a}{\partial t}-\phi\rho_a\frac{\partial S}{\partial t}+(1-S)\rho_a\left[\frac{(1-\phi)}{\rho_s}\frac{\partial \rho_s}{\partial t}+\frac{\partial \varepsilon_v}{\partial t}-\frac{\phi S}{\rho_s}\dot{m}_{hydr}\right]=-\nabla\cdot\phi(1-S)\rho_a\mathbf{v}^{ra} \quad (5.23)$$

$$\nabla\cdot\left(\frac{\partial \boldsymbol{\sigma}}{\partial t}\right)+\frac{\partial\left[(1-\phi)\rho_s+\phi S\rho_w+\phi(1-S)\rho_a\right]}{\partial t}\mathbf{g}=0 \quad (5.24)$$

$$\left[(1-\phi)\rho_s C_s+\phi S\rho_w C_w+\phi(1-S)\rho_a C_a\right]\frac{\partial T}{\partial t}+Q_{ad}+Q_{cd}=Q_{hydr} \quad (5.25)$$

where ϕ denotes the porosity; S refers to the degree of saturation; ρ_i is the density (i = air, water and solid); t represents the elapsed time; ε_v stands for the volumetric strain; $\dot{m}_{hydr}$ refers to the time rate of changes in the pore-water mass per unit volume due to binder hydration; $\mathbf{v}_s$ and $\mathbf{v}^{ri}$ respectively represent the phase velocity with respect to the current configuration (Eulerian quantity), and the corresponding relative apparent velocity of the fluids in the porous medium; $\boldsymbol{\sigma}$ is a total stress tensor; $\mathbf{g}$ refers to the acceleration of gravity; C_i denotes the specific heat capacity (i =solid, water and air); Q_{ad} and Q_{cd} stand for the heat transfer via advection and conduction, respectively; and Q_{hydr} is the heat generated through exothermic binder hydration.

The developed THMC model was implemented into COMSOL Multiphysics (a finite element code, (Comsol 2015)). Specifically, conservation equations contain three terms including time rate of conserved quantities (i.e., temperature, displacement and pore water pressure), convective terms (i.e., transfer of matters, energy and momentum), and source or sink terms. For fluid mass equilibrium equations (Eqs.5.22 and 5.23), the time derivative terms can be converted into storage term to interpret contributions of compressibility of fluid and matrix, and the moisture capacity to changes of fluid mass. The fluid compressibility can be specified directly in COMSOL, and the moisture capacity can be obtained by the water retention curve of CTB. Moreover, the matrix compressibility (the third term on the left-hand side of Eqs.5.22 and 5.23) has been expressed by the rate of change of volumetric strain which can be derived from mass equilibrium equation of solid phase. Then, the matrix compressibility terms can be respectively combined with the sink term of pore water, and source term of pore air, and implemented into the source node in COMSOL. In addition, the convective terms can be further expressed by Darcy's law and thus converted into a term contained pore fluid pressure. Thus, the Darcy's law interface in COMSOL was incorporated in this study as well. For the momentum equilibrium equation, the stress-strain relation is needed to convert the Cauchy stress term (i.e., $\boldsymbol{\sigma}$) into a displacement term. In this study, the total strain consists of elastoplastic strain, chemical shrinkage and thermal strain. Detailed information about the stress-strain constitutive relation was provided by Cui and Fall (2015a). Then, yield function and plastic potential function can be implemented into COMSOL via the aid of soil plasticity node in COMSOL to estimate the plastic strain. The chemical shrinkage can be implemented into the initial value node in COMSOL. With the help of thermal expansion node in COMSOL, the thermal strain can be implemented as well. The energy equilibrium equation (Eq.5.25) was implemented via the interface of heat transfer in porous media in COMSOL. The heat advection due to fluid flow can be obtained from the Darcy's law which has been implemented in the hydraulic interface of COMSOL. The heat conduction term Q_{cd} can be calculated through Fourier's law. For the heat generation term, the total heat available from binder hydration can be determined through the composition of binder. Then the energy source term can be obtained by performing time differentiation on the product of total heat and binder hydration degree. More details on the three terms of heat transfer can be found in Cui and Fall (2015a). Similarly, the obtained source term can be implemented via source node in COMSOL.

To evaluate the impacts of binder hydration on CTB behaviors and material properties, the development of binder hydration needs to be quantitatively characterized (i.e., the degree of binder hydration ξ). Previous studies on CTB have indicated that the mixture recipe (e.g., Belem et al. 2000), curing time (e.g., Koohestani et al. 2016) and temperature (Da Luz and Hooton 2015; Aldhafeeri et al. 2016; e.g., Cui and Fall 2016b) have significant influence on the development of binder hydration. Moreover, to reduce the cost of CTB and improve its properties (e.g., microstructure, resistance to sulfate attack and strength), mineral admixture such as blast furnace slag and flys ash is now increasingly blended with portland cement (Benzaazoua et al. 1999; Pokharel and Fall 2010). To fully consider the factors that affect binder hydration, an exponential equation proposed by Schindler and Folliard (2003) is adopted here:

$$\xi\left(t,T,w/c,X_{FA},X_{slag}\right)=\left(\frac{1.031\cdot w/c}{0.194+w/c}+0.5\cdot X_{FA}+0.30\cdot X_{slag}\right)\times\exp\left\{-\left\{\tau\Big/\int_0^t\exp\left[\frac{E_a}{R}\left(\frac{1}{T_r}-\frac{1}{T}\right)\right]dt\right\}^{\beta}\right\} \tag{5.26}$$

with

$$E_a\left(T\right)=\begin{cases}33{,}500+1{,}470\times\left(293.15-T\right) & T<293.15K\\ 33{,}500 & T\geq 293.15K\end{cases}$$

$$\tau=66.78{x_{C_3A}}^{-0.154}\cdot {x_{C_3S}}^{-0.401}\cdot x_{SO_3}\cdot {S_{Blaine}}^{-0.804}\cdot\exp\left(2.178X_{slag}+9.5X_{FA}X_{FA-CaO}\right)$$

$$\beta=181.4{x_{C_3A}}^{0.146}\cdot {x_{C_3S}}^{0.227}\cdot {x_{SO_3}}^{0.558}\cdot {S_{Blaine}}^{-0.535}\cdot\exp\left(-0.647X_{slag}\right)$$

where T and T_r respectively denote the CTB temperature and the reference temperature; w/c , X_{FA} and X_{slag} respectively represent the water-to-cement ratio, and the weight fraction of the fly ash and blast furnace slag with respect to the total binder weight; τ and β are the parameters of the binder hydration model and respectively represents the time and hydration shape parameters; R is the ideal gas constant; and E_a is the apparent activation energy. To demonstrate the effect of binder hydration parameters and temperature on the binder hydration, a control state of CTB is adopted as a reference (see Table 5.6). Relevant investigations are carried out through specific modification of parameter values. Figure 5.48 shows the variation of the degree of binder hydration with different curing temperature and binder hydration parameters. It can be found that warm temperature can contribute to progress of binder hydration (see Figure 5.48a). Moreover, as shown in Figure 5.48b and Figure 5.48c, the binder hydration degree is sensitive to the change of binder hydration parameters, which implies the effect of binder composition on the progress of binder hydration in CTB. Therefore, the binder hydration model can fully demonstrate the effects of curing temperature and binder recipe on the progress of chemical reaction. In addition, as indicated in Eq.5.26, the binder hydration parameters τ and β can be determined directly by the composition of binder.

Table 5.6. Binder hydration parameters adopted in this study.

Parameter	T_r (°C)	w/c (-)	X_{FA} (-)	X_{slag} (-)	τ (h)	β (-)	R (J/mol K)	E_a (J/mol)
value	20	7.6	0	50%	3	0.35	8.13	33500

-: dimensionless

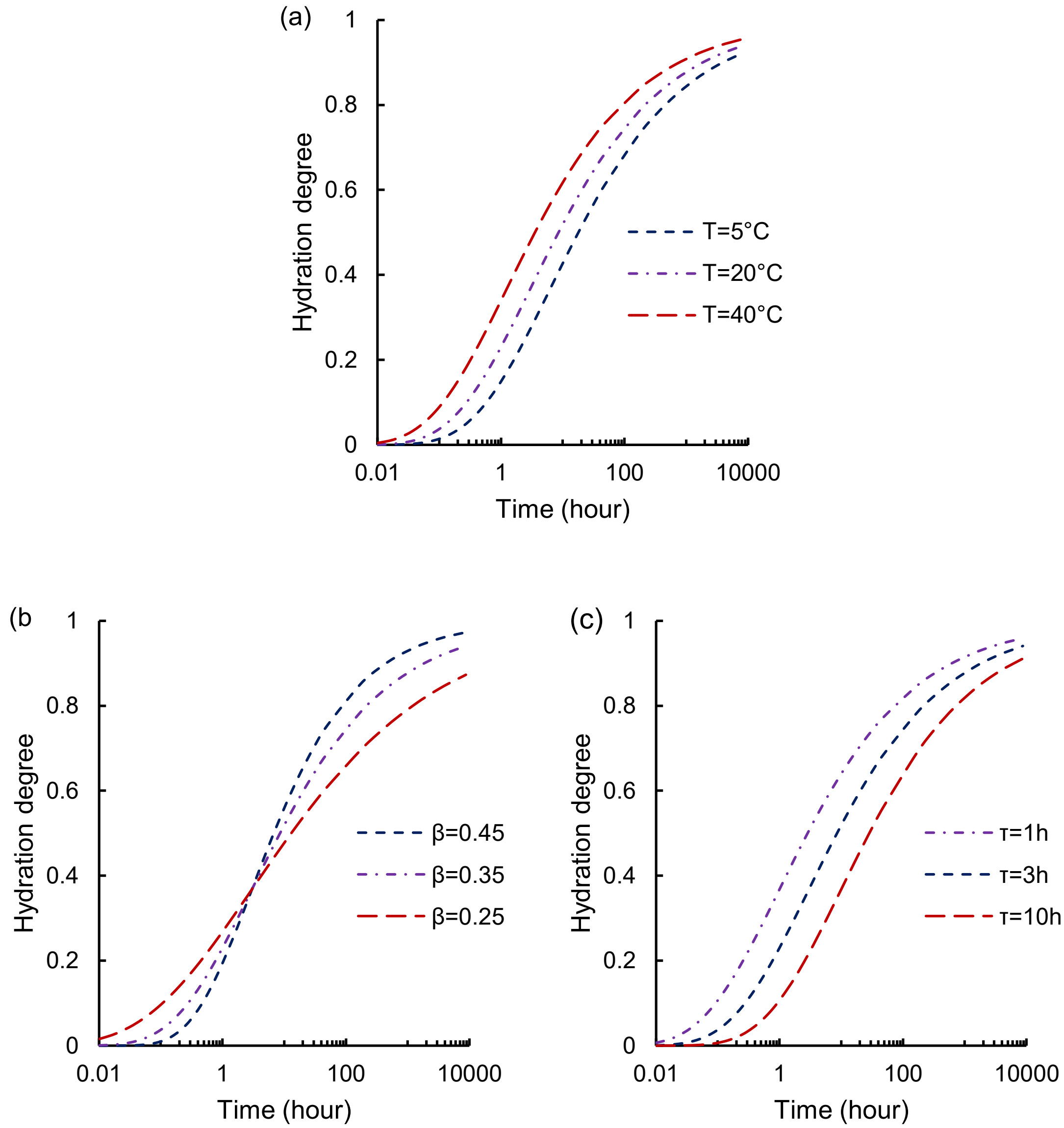

Figure 5.48. Degree of binder hydration over time with different values of (a) temperature, (b) hydration shape parameter, and (c) time parameter.

5.4.2.2. Multiphysics Model of Consolidation Process

Coupled THMC processes control the field behavior of CTB including the consolidation process. With the development of consolidation, porosity dependent material properties such as the coefficient of permeability will change as well, and thus affect the hydraulic process and the changes in the PWP. Consequently, the pressure acting on the barricade structure will change along with the consolidation process in the CTB. To assess and predict the volume changes in CTB, Cui and Fall (2016c) derived a multiphysics model of the consolidation process based on the principle of pore space continuity (i.e., volume changes in the solid phase and skeleton must be equal to the volume changes in the pore water and pore air).

$$
\begin{aligned}
&\left\{\left[SP_w+(1-S)P_a\right]\frac{1-2\upsilon}{E}\frac{\partial\alpha_{Biot}}{\partial\xi}-\left\{\frac{\sigma+\alpha_{Biot}\left[SP_w+(1-S)P_a\right]}{E}\right\}\left\{\frac{9\left[1-2\upsilon\right]}{E}\frac{\partial E}{\partial\xi}+18\frac{\partial\upsilon}{\partial\xi}\right\}\right.\\
&\left.-\alpha_{Biot}\left(P_a-P_w\right)\frac{1-2\upsilon}{E}\left\{\left[1-S_e\left(P_w,P_a,\xi\right)\right]\frac{\partial\theta_r}{\partial\xi}+\left(\phi-\theta_r\right)\frac{\partial S_e}{\partial\xi}\right\}-\frac{\left(v_{ch-w}+v_{ab-w}\right)R_{n-w/hc}/(1-\phi)}{\left(w/c\right)v_w+v_c+\left(1/C_m-1\right)v_{tailings}}\right\}\frac{\partial\xi}{\partial t}\\
&+\frac{1-2\upsilon}{E}\frac{\partial\sigma}{\partial t}+\alpha_{Biot}\frac{1-2\upsilon}{E}\left\{S-\left(P_a-P_w\right)\left(\phi-\theta_r\right)\frac{\partial S_e}{\partial P_w}\right\}\frac{\partial P_w}{\partial t}+\frac{\partial\lambda_p}{\partial t}\frac{\partial Q_{CTB}}{\partial I_1}+\alpha_{Ts}\frac{\partial T}{\partial t}\\
&+\alpha_{Biot}\frac{1-2\upsilon}{E}\left\{(1-S)-\left(P_a-P_w\right)\left(\phi-\theta_r\right)\frac{\partial S_e}{\partial P_a}\right\}\frac{\partial P_a}{\partial t}\\
&=-\left\{(1-\phi)+\alpha_{Biot}\left(P_a-P_w\right)\frac{1-2\upsilon}{\phi^2E}\left[\phi(1-\phi)S_e+\left(1-S_e\right)\theta_r\right]\right\}\frac{\partial\phi}{\partial t}
\end{aligned}
\tag{5.27}
$$

where P_w and P_a respectively denote the pore-water and pore-air pressures; υ is the Poisson's ratio; E refers to the elastic modulus, α_{Biot} is the Biot's effective stress coefficient; S_e is the effective degree of saturation; θ_r represents the residual water content; v_i refers to the specific volume (i =the capillary water, chemically combined water, physically absorbed water, cement and tailings); $R_{n-w/hc}$ represents the mass ratio of the chemically combined water and hydrated cement; C_m is the binder content; λ_p denotes the variant; and α_{Ts} refers to the coefficient of the thermal expansion (CTE) of the CTB solid phase. It is important to point out that, due to the effect of the coupled THMC processes, the material properties (e.g., α_{Ts} , α_{Biot} , υ and E) cannot be considered constant. Based on previous studies on these parameters (Cui and Fall 2015a; 2016c; a), the following prediction functions are adopted to characterize the evolution of material properties of CTB.

$$\upsilon=0.5\exp\left(B_{\upsilon1}\xi\right)+B_{\upsilon2}\xi^{B_{\upsilon3}}\exp\left(B_{\upsilon4}\xi^{B_{\upsilon5}}\right) \tag{5.28}$$

$$E\left(\xi,C_m,w/c,e\right)=\left(v_1E_{tailings}+v_2E_{u\_p}\xi\right)\left[\frac{f_{E1}\left(1-e\right)^{f_{E2}\xi^{f_{E3}}}}{1+f_{E4}e_0}\right] \tag{5.29}$$

with

$$
\begin{cases}
v_1=\dfrac{\left(1/C_m-1\right)v_{tailings}}{\left(w/c\right)v_w+v_c+\left(1/C_m-1\right)v_{tailings}-\left(2v_w-v_{ch-w}-v_{ab-w}\right)R_{n-w/hc}\xi}\\
v_2=\dfrac{\left[v_c+\left(v_n+v_{ab-w}\right)R_{n-w/hc}\right]\xi}{\left(w/c\right)v_w+v_c+\left(1/C_m-1\right)v_{tailings}-\left(2v_w-v_{ch-w}-v_{ab-w}\right)R_{n-w/hc}\xi}
\end{cases}
$$

$$\alpha_{Biot}=1-K_b/K_s \tag{5.30}$$

$$\alpha_{Ts} = \alpha_p - \frac{2v_{tailings}\left(1/C_m - 1\right)\left(\alpha_p - \alpha_{tailings}\right)}{\left[\left(w/c\right)v_w + v_c\right]\left\{1 + \left[L_1 \cdot \left(1 - n_{hydr}\right)^{L_2}\right]/E_T\right\} + 2v_{tailings}\left(1/C_m - 1\right)} \tag{5.31}$$

with

$$\begin{cases} \alpha_p = \dfrac{B_1\alpha_{uc}v_c\left(1-\xi\right) + B_2\alpha_{hp}\left[v_c + R_{n-w/hc}\left(v_{ch-w} + v_{ab-w}\right)\right]\xi}{\left(w/c\right)v_w + v_c + \left(1/C_m - 1\right)v_{tailings}} \\ n_{hydr} = \dfrac{\left(w/c\right)v_w - \left(v_n + v_{ab-w}\right)R_{n-w/hc}\xi}{\left(w/c\right)v_w + v_c + \left(1/C_m - 1\right)v_{tailings}} \\ R_{n-w/hc} = 0.187x_{C_3S} + 0.158x_{C_2S} + 0.665x_{C_3A} + 0.2130x_{C_4AF} \end{cases}$$

where $B_{\upsilon 1}$, $B_{\upsilon 2}$, $B_{\upsilon 3}$, $B_{\upsilon 4}$ and $B_{\upsilon 5}$ are dimensionless fitting parameters for Poisson's ratio; v_1 and v_2 respectively represent the volume fraction of tailings and the ultimate cement paste relative to the total volume of the solid phase; $E_{tailings}$ and E_{u_p} are the elastic modulus of the tailings, and the ultimate stiffness of the dense cement paste; e_0 refers to the initial void ratio of the CTB; f_{E1}, f_{E2}, f_{E3} and f_{E4} are dimensionless fitting parameters for elasticity of CTB; K_s is the bulk modulus of the tailings, and depends on the composition of tailings; K_b is the bulk modulus of the CTB matrix, and can be determined with the elastic modulus E and Poisson's ratio ν (i.e., $K_b = E/3\left(1-2\nu\right)$); α_p, $\alpha_{tailings}$, α_{uc}, and α_{hp} respectively represent the CTE of binder paste, tailings, unhydrated cement and hydration products; L_1 and L_2 are the fitting parameters for the prediction of elastic modulus of cement paste; n_{hydr} refers to the change of porosity induced by binder hydration; B_1 and B_2 are fitting parameters for the CTE of cement paste. Based on previous studies on these parameters (Cui and Fall 2015a; 2016c; a), the values listed in Table 5.7 and Table 5.8 are adopted in this study. It should be noted that the adopted mixture recipe in this study is a commonly adopted one in backfilling practice. For a specific filling case, the associated mixture recipe parameters should be adjusted. Therefore, the adopted values in Table 5.7 and Table 5.8 can be used as reference values for practical application.

Table 5.7. Model parameters of multiphysics consolidation model

Material parameters	v_n (cm^3/g)	v_{ab-w} (cm^3/g)	v_c (cm^3/g)	$v_{tailings}$ (cm^3/g)	v_w (cm^3/g)	$\alpha_{tailings}$ (1/K)	α_{uc} (1/K)	α_{hp} (1/K)
values	0.72	0.90	0.32	0.38	1	0.6e-6	14.4e-6	20e-6
Material parameters	C_m (wt%)	e_0 (-)	E_T (GPa)	E_{u_p} (GPa)	x_{C_3S} (wt%)	x_{C_2S} (wt%)	x_{C_3A} (wt%)	x_{C_4AF} (wt%)
value	4.5	1	73.1	28.49	0.462	0.232	0.087	0.096

wt%: weight percentage; -: dimensionless

Table 5.8. Fitting parameters of prediction function of material properties

Fitting parameters	B_1 (-)	B_2 (-)	B_3 (-)	B_4 (-)	B_5 (-)	L_1 (GPa)	L_2 (-)
value	-0.2	-1.5e4	7	-10.9	0.7	46.03	3.16
Fitting parameters	f_1 (-)	f_2 (-)	f_3 (-)	f_4 (-)	d_1 (-)	d_2 (-)	
value	177.5	4.36	-1.05	3e3	0.28	1.23	

-: dimensionless

5.4.2.3. CTB/rockmass interface model

As settlement progresses in CTB, relative displacement between the CTB and rock mass takes place. As a result, there is interface resistance (including interface adhesion and frictional shear stress), which in turn, affects the stress distribution in CTB. As settlement progresses in CTB, relative displacement between the CTB and rock mass takes place. As a result, there is interface resistance (including interface adhesion and friction shear stress), which in turn, affects the stress distribution in CTB. Therefore, the interface interaction must be incorporated into assessments of barricade pressure. To understand the interface interaction between the CTB/rock mass, an evolutive elastoplastic interface model developed by Cui and Fall (2017) is used:

$$F_{intf}(I_1,\sqrt{J_2},\xi,\Delta_\kappa)=\sqrt{J_2}+\alpha_{intf}\left(\xi,\Delta_\kappa\right)\left[I_1-C_{intf}\left(\xi\right)\right]=0 \quad (5.32)$$

where I_1 denotes the first stress invariant; J_2 stands for the second deviatoric stress invariant; Δ_κ refers to the cumulative plastic displacement (i.e., $\Delta_\kappa=\int\sqrt{(2/3)\,d\boldsymbol{\Delta}_p d\boldsymbol{\Delta}_p}$ with Δ_p the plastic displacement). The yield function parameters α_{intf} and C_{intf} can be defined in terms of the interface friction angle, δ_{intf}, and adhesion, c_{intf}.

$$\alpha_{intf}=R_{intf1}\left\{\left[1-\exp(-R_{intf2}\Delta_\kappa)\right]+\left[R_{intf3}\Delta_\kappa\exp(-R_{intf4}\Delta_\kappa)\right]\right\}+\frac{2\sin\delta_{intf}\left(\xi\right)}{\sqrt{3}\left[3+\sin\delta_{intf}\left(\xi\right)\right]} \quad (5.33)$$

With

$$\begin{cases} R_{intf1}=b_1\xi^2+b_2\xi+b_3 \\ R_{intf2}=b_4\xi^{b_5} \\ R_{intf3}=b_6\xi^{b_7} \\ R_{intf4}=b_8\xi^2+b_9\xi+b_{10} \end{cases}$$

$$C_{intf}=3c_{intf}\left(\xi\right)\cdot\cot\delta_{intf}\left(\xi\right) \quad (5.34)$$

where R_{intfi} (i =1 to 4) is a material constant which can be determined by direct shear testing (Cui and Fall 2017); b_i is the fitting constant (i =1 to 10). Based on previous study on these parameters (Cui and Fall, 2017), b_1=-0.1068, b_2=-0.0027, b_3 =0.18, b_4 =80.984, b_5=0.4226, b_6=497.03, b_7=3.3332, b_8=-54.091, b_9=109.9 and b_{10}=20.564 are recommended.

To determine the interface friction angle and interface adhesion, the effects of binder hydration and rock wall roughness are incorporated as follows:

$$\delta_{intf} = \phi_B(\xi) - F_\delta(\xi)\left|\phi_r - \phi_B(\xi)\right| / R_L \tag{5.35}$$

$$c_{intf} = c_B(\xi)\left[1 - F_c(\xi)/R_L\right] \tag{5.36}$$

with

$$\begin{cases} c_B = c_{B1} C_m \xi^{c_{B2}} \\ \phi_B = N_1 \xi^{N_2} + N_3 \xi \\ F_\delta(\xi) = n_1 \xi^2 + n_2 \xi \\ F_c = n_3 \xi^2 + n_4 \xi \end{cases}$$

where ϕ_r and ϕ_B respectively denote the rock and internal friction angles of the CTB, c_B is the cohesion of the CTB which changes with the binder hydration ($\phi_B = \phi_B(\xi)$), and F_δ and F_c are the fitting parameters. To determine the effects of the rock wall roughness, the roughness index R_L is adopted in this model, which is defined as the ratio of the true length of the fracture profile to its projected length in the mean topographic direction of the profile (Gokhale and Underwood 1990); c_{B1}, c_{B2}, N_1, N_2, N_3, n_1, n_2, n_3, and n_4 are fitting parameters. Based on the regression analysis on the experimental data published in (Donovan, 1999; Fall and Nasir, 2010; Ghirian and Fall, 2014; Cui and Fall, 2015a), c_{B1}=9507 kPa, c_{B2}=3.2, N_1=-176.9°, N_2=2, N_3=174.2°, n_1=-3.954, n_2=2.935, n_3=0.919, and n_4=0.732 are recommended by Cui and Fall (2017).

Moreover, to accurately assess the changes in the direction of plastic displacement, a plastic potential function Q_{intf} is defined in terms of the interface dilation angle ψ_{intf} (i.e., non-associated plastic flow rule):

$$Q_{intf} = \sqrt{J_2} + 2\sqrt{3}\sin(\psi_{intf}) I_1 / \left[9 + 3\sin(\psi_{intf})\right] \tag{5.37}$$

with

$$\psi_{intf} = \begin{cases} w_1 \xi^{w_2} R_L / \exp(w_\psi \boldsymbol{\sigma}'_n) & \boldsymbol{\sigma}'_n \le 0 \\ \delta_{intf} & \boldsymbol{\sigma}'_n > 0 \end{cases}$$

where $\boldsymbol{\sigma}'_n$ is the effective normal stress that acts on the interface; w_ψ equals to the inverse of one GPa; w_1 and w_2 are the fitting constants. Based on regression analysis on the reported data (Nasir and Fall, 2008; Fall and Nasir, 2010), w_1 =196.29° and w_2 =6.44 are suggested byCui and Fall (2017).

5.4.3. Model Validation

To validate the predictive ability of the integrated 3D multiphysics model, in-situ measurements from a series of field studies were collected and compared with the simulation results. FEM code-COMSOL Multiphysics is adopted in this study for model implementation.

The recommended values of model parameters listed in Table 5.6, 5.7, 5.8 and subsection 5.4.2.3 are adopted for model validation. Moreover, the mixture recipe, filling strategy and stope conditions adopted in field studies are different from each other (see Table 5.9). The adopted boundary conditions and initial values in field studies are tabulated in Table 5.10. Furthermore, the filling height will increase with backfilling operation. Therefore, predefined stope domain can be divided into filled and unfilled regions, which can be determined by filling strategy (i.e., filling rate, elapsed time and rest period between filling stages). To strict the adopted models within the filled regions, the Pointwise Constraint (PC) node in COMSOL was adopted in this study. With the help of PC node, the multiphysics models and interface model can strictly activate within the filled regions. More detailed information about the features of PC node was provided in (Comsol, 2015). In addition, due to the relatively small permeability of rock, the water flow between CTB and surround rock is omitted in this study. Therefore, no flow boundary condition is adopted. However, it should be pointed out that during filling process, the volume change occurs within CTB, which directly contributes to the rate of change of porosity (i.e., the third term in Eq.5.22). Consequently, the pore-water pressure will vary with volume change in CTB, and an outward flow of pore water through top surface of fill mass may occur. To accommodate this phenomenon, a Dirichlet boundary condition (zero pressure) was incorporated into PC node and applied on the top boundary of activated region (i.e., filled region). Therefore, when non-zero PWP occurred near the top regime of CTB. The zero-PWP pressure boundary condition can be considered as the dissipation of excess PWP via out-flow of pore water during filling stage. Moreover, because the zero-PWP boundary condition was incorporated into PC node, this specified boundary condition can change position with filling process. Therefore, the downward flow of pore water within filled domain are allowed as well. During the rest period and post-filling stage, the zero-pressure boundary condition incorporated into the PC node will be automatically removed through predefined logical expression based on filling strategy. Correspondingly, no flow boundary condition will be activated. Therefore, with the integration of no flow boundary condition, zero-pressure boundary condition, and PC node in COMOSL, the outward flow of pore water through CTB surface, and downward flow within filled domain can be captured.

Table 5.9. Summary of mixture recipe and stope conditions in field studies

Parameter	Field study 1	Field study 2	Field study 3
Cement content (%)	8.5 (0-8 m) 6.5 (8 m-15 m)	4.5	5 (plug fill) 4 (residual fill)
Filling rate (m/h)	0.2	0.35	1.7
Filling sequence	continuous	continuous	filling operation carried out in 3 stages
Stope geometry (m)	20(L)×17(H)	19.5(L)×6.2(W)×19.5(H)	18(L)×3.5(W)×17(H)
Dip angle (°)	90	90	70
Barricade size (m)	5.5(H) (2D model)	6.2(W)×5.5(H) (3D model)	3.5(W)×3.5(H) (3D model)

Table 5.10**.** Specified boundary conditions and initial values in field studies

Type of B.C.[a]	Specified B.C. or values
Mechanical module	
Top surface	Free
Lateral sides	Roller
Bottom side	Fixed
Volume force	Gravity
Hydraulic module	
Surrounding surfaces	No flow
Barricade surface	Mass flux
Volume force	Gravity
Initial value	Hydraulic head=0
Thermal module	
Surrounding surfaces(°C)	29 (Field study 1) 20 (field study 2) 22 (Field study 3)
Initial temperature of CTB (°C)	29 (Field study 1) 20 (field study 2) 22 (Field study 3)

[a]B.C.: boundary condition.

5.4.3.1. Field Study 1-Continous filling with varying binder contents

To study the changes in the in-situ pressure acting on a barricade structure, Thompson et al. (2012) conducted a monitoring program at the Çayeli Mine. The selected stope has a height of 17 m and length of 20 m. The monitored stope was filled continuously. The changes in the binder content from 8.5% to 6.5% occurred at 1.8 days and the fill height was 15 m. Information on the stope geometry, CTB mixture recipe, filling strategy and rate of filling are provided in Table 5.9. More details on the monitoring program are found in (Thompson et al. 2012). For the model implementation, the input parameters, initial values and boundary conditions are listed in Table 5.9, and the adopted geometry model and mesh division are presented in Figure 5.49.

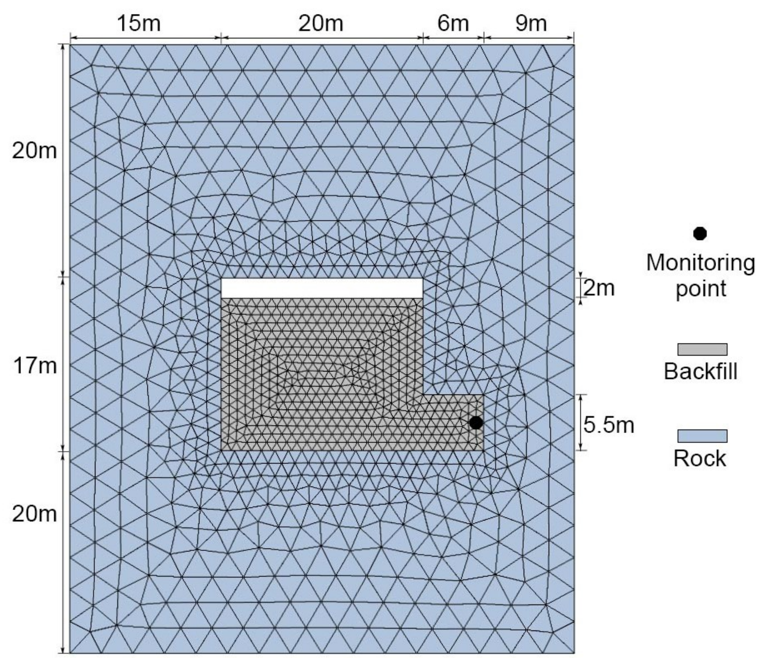

Figure 5.49. Geometry and mesh of the simulated stope at Çayeli Mine

A comparison between the simulation results and recorded values is presented in Figure 5.50. It can be seen that the changes in the total horizontal pressure and PWP acting on the barricade can be accurately captured by the developed multiphysics model. Changes in the total stress and PWP primarily take place at the early ages, especially at the drawpoint during filling. After the completion of filling at the drawpoint (approximately 25 hours), the total stress and PWP are gradually reduced and remain constant during the following backfilling operation. This is because as the placement of CTB proceeds, the consolidation induces an arching effect in the CTB mass and thus reduces the influence of the self-weight stress on the total stress. Moreover, due to water drainage through the barricade, the total stress can be further decreased with time. In addition, the water drainage together with the pore-water consumption caused by binder hydration govern the dissipation of the PWP in CTB. Consequently, after the completion of backfilling at the drawpoint, the PWP demonstrates a trend of decrease with time regardless of subsequent placement of fresh CTB.

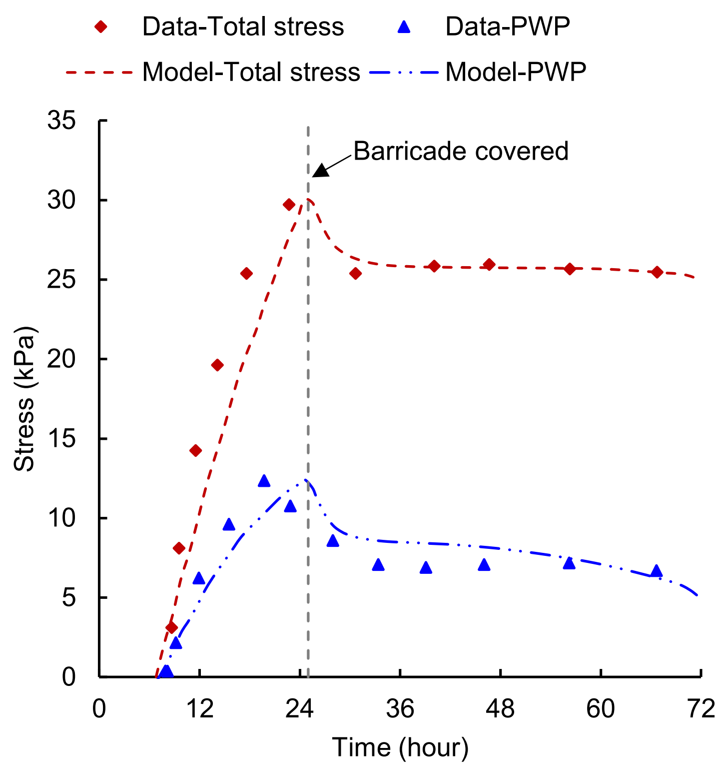

Figure 5.50. Comparison of modeling results and monitored values of total stress and PWP at Çayeli Mine

To further demonstrate the predictability of the integrated multiphysics model, the comparison of modeling results and monitored data is carried out at the stope point. As shown in Figure 5.51, the evolutionary trends and magnitudes of total stress and PWP within stope is well captured by the model. Moreover, it is interesting to note that both monitored data and predicted results show that the peak values of total stress and PWP within CTB are obtained when the backfilling is completed, while the peak values of barricade pressure occur after the barricade is covered. Similar results have be found in previous field measurements (e.g., Yumlu, 2008; Doherty et al., 2015). This is because the variation of total stress within CTB is mainly attributed to backfilling operation, while the change of barricade pressure results from the transfer of total vertical stress within stope to horizontal stress. However, due to the combined effect of CTB/rockmass interface resistance and brow reaction, the resultant horizontal stress acting on barricade will be dramatically reduced compared with the stress level within stope. Hence, the obtained results prove the integrated multiphysics model is able to accurately assess the variation of both barricade pressure and stress within stope.

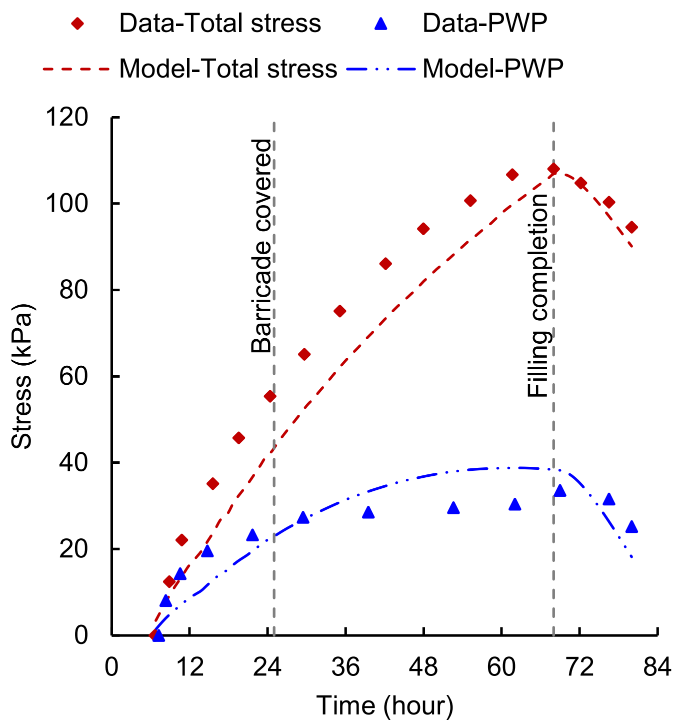

Figure 5.51. Comparison of modeling results and monitored values of total stress and PWP at the stope point

5.4.3.2. Field Study 2-Barricade aligned with stope brow

Yumlu (2008) conducted an in-situ instrumentation and monitoring program to study the changes in the stress acting on the CTB barricade during and after filling operations. The trial stope had a length of 19.5 m, width of 6.2 m and height of 19.5 m. The stope was continuously filled at a rate of 0.35 m/h (8 m/day). During and after the filling operation, the horizontal stress acting on the CTB retaining structure was recorded by using a total pressure cell (model: Geokon 4800). The adopted barricade offset (i.e., distance from the stope brow) was zero for the selected stope. Detailed information on the CTB recipe is presented in Table 5.9, and the adopted geometry and dimensions are plotted in Figure 5.52.

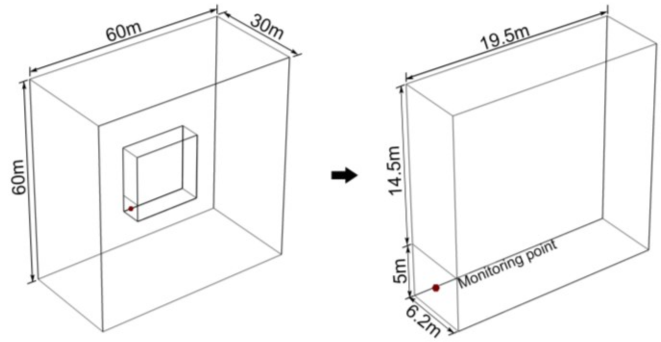

Figure 5.52. Geometry and dimensions of simulated stope in Field Study 2

Figure 5.53 shows a comparison between the recorded values and modeling results for the total stress acting on the barricade. It can be observed that both demonstrate (1) an initial increase in total stress with filling, (2) a trend of reduction in the total stress acting on the barricade after around 24 hours. These can be attributed to the combined effects of water drainage through the barricade, and stress transfer from the CTB to the rock mass resultant of the arching effect (i.e., consolidation process induced interface interaction between the CTB and rock wall). However, the time rate of change in total stress decreases with time, and (3) no apparent changes in the total stress after 58 hours (i.e., the completion of the filling operation). Based on the obtained results, it can be found that the recorded amount of total stress is well captured by the modeling results in terms of both magnitude and trend of change.

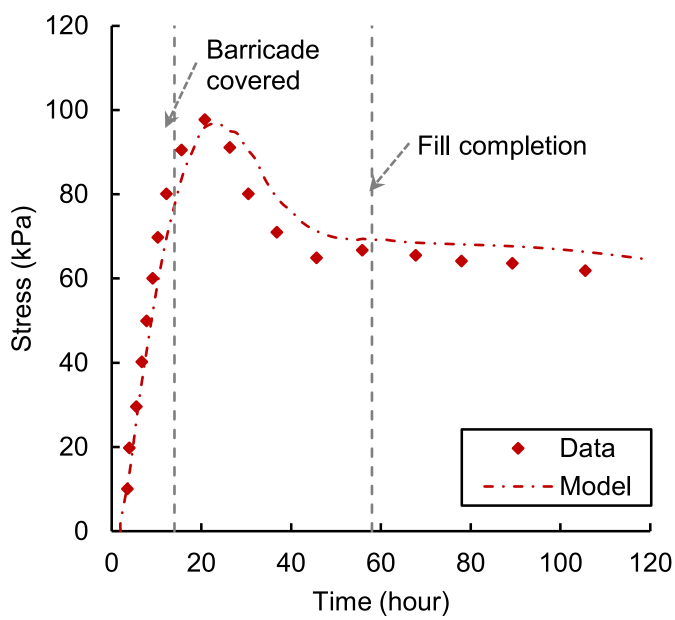

Figure 5.53. Comparison of predicted results and measured values of total horizontal stress acting on barricade

To clearly show the spatial distribution of the barricade pressure and the corresponding total horizontal stress in the test stope, the barricade surface and the cut slice along the central line of the stope in the longitudinal direction are used in this field study (see Figure 5.54). It can be found that compared with barricade-coverage stage (see Figure 5.54a), the nonuniform distribution of total stress along the longitudinal direction becomes more apparent after filling completion (see Figure 5.54b). As discussed previously, this is induced by the combined effects of barricade drainage, and arching effect occurred in CTB. Consequently, a decrease in barricade pressure transferred from total stress can be obtained. Hence, the multiphysics model can be used as a useful tool to assess the development of barricade pressure for CTB design.

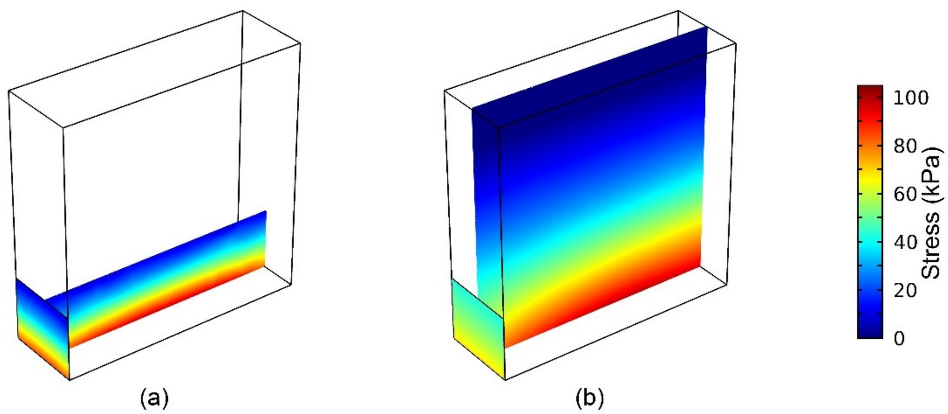

Figure 5.54. Spatial distribution of total horizontal stress in CTB for different filling stages: (a) barricade covered-14 hours; (b) filling completion-58 hours.

5.4.3.3. Field Study 3-Multiple stages of filling in inclined stope

Doherty et al. (2015) carried out a field investigation to monitor the barricade pressure in an inclined stope during a filling operation that took place in stages to assess the in-situ performance of the CTB and barricade structure at the Raleigh Mine in Australia. The test stope has an inclination angle of 70°, and a strategy with three stages of filling was adopted. Detailed information on the stope geometry and dimensions are presented in Figure 5.55, and the CTB recipe is provided in Table 5.9. For the stope instrumentation, a total stress cell (model: Geokon 4850NPST) was mounted at the center point of the barricade to record the changes in the barricade pressure with time.

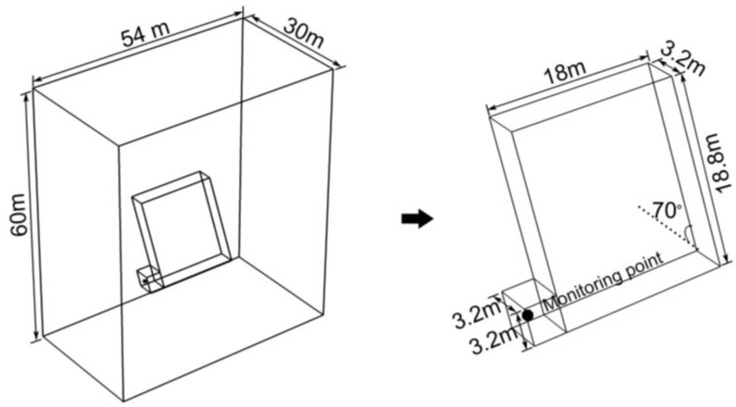

Figure 5.55. Geometry and dimension of simulated stope in Field Study 3

As shown in Figure 5.56, filling that takes place in multiple stages has significant impacts on the total horizontal stress changes in the barricade. Specifically, the total stress has minimal increases during filling, followed by a reduction in the total stress during the rest period. The change in total stress is due to the arching effect which results in the stress transfer from the CTB to the surrounding rock mass, and water drainage through the barricade. It can be observed in Figure 5.56 that the in-situ measurements of the total stress are accurately captured by the simulation results, which can further validate the predictive ability of the developed multiphysics model to simulate changes in the barricade pressure in an inclined stope with multiple filling sequences.

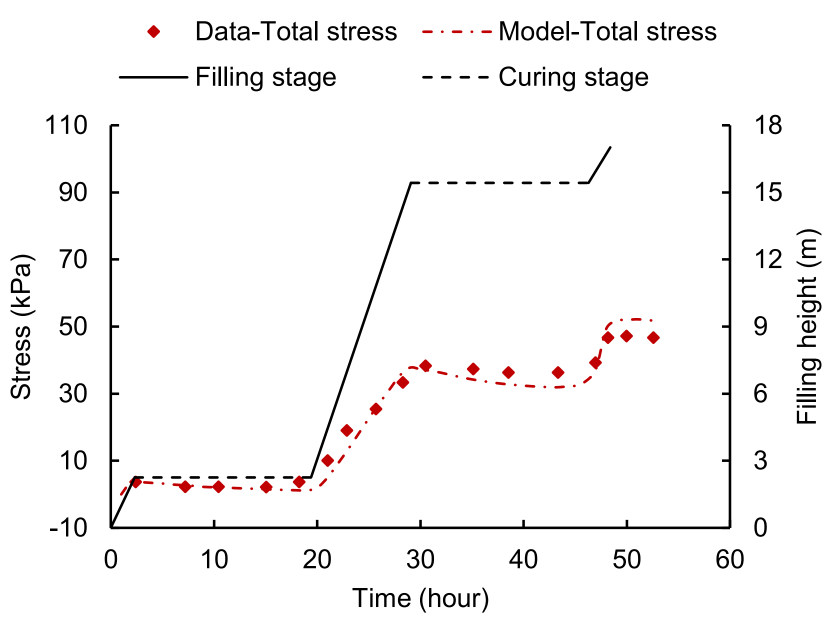

Figure 5.56. Comparison of predicted results and measured values of total horizontal stress acting on barricade at Raleigh Mine

To clearly show the spatial distribution of the barricade pressure and the corresponding total horizontal stress in the test stope, the barricade surface and the cut slice along the central line of the stope in the longitudinal direction are used in this field study (see Figure 5.57). In Figure 5.55, it can be seen that there is (1) a non-uniform distribution of the total stress in CTB which becomes more apparent with the progression of the filling operation. This can be attributed to the combined effect of water drainage through the barricade and the asymmetric geometry in the vicinity of barricade, and (2) stress concentration near the interface of the layers that are placed in sequence. This is due to the distinct CTB properties and inconsistent behavior of the consolidation that developed in the vicinity of the interface of the layers placed in sequence. The results indicate that the developed multiphysics model can be used to describe and understand the changes in the barricade pressure under multiple filling sequences in a stope with a complex geometry.

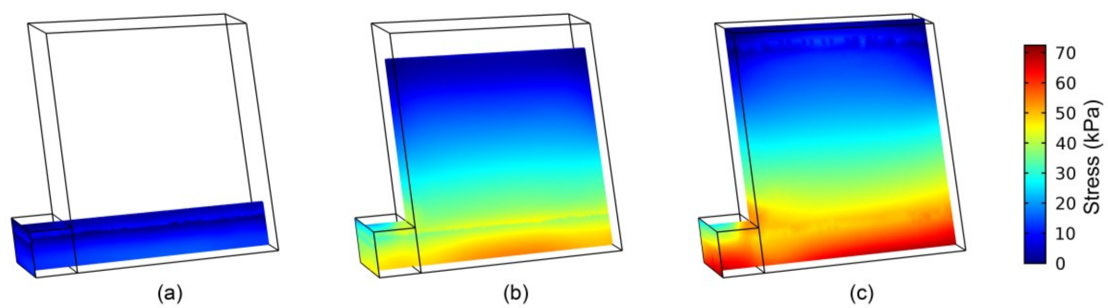

Figure 5.57. Spatial distribution of total horizontal stress in CTB for different filling times: (a) 21.9 hours (barricade covered); (b) 29.2 hours (completion of 2nd-stage of filling); (c) 47.4 hours (completion of 3rd-stage of filling)

5.4.4. Model Applications

To investigate the impacts of the changes in the load on the barricade and related influential factors, the coupled THMC model, multiphysics model that analyzes the consolidation process in CTB and evolutive elastoplastic interface model were implemented into a commercial FEM code software (COMSOL Multiphysics (Comsol 2015)). Due to the different ore bodies, the adopted stoping methods, CTB preparation, and curing conditions, the stability requirements for barricade structures will differ from site to site. Therefore, in the present study, various filling strategies, mix recipes, barricade geometries, stope-wall roughnesses, drainage conditions and initial temperatures of the CTB are considered to investigate the load acting on the barricade. These factors should be taken into consideration when designing CTB structures.

Therefore, the simulation results obtained from this study can provide useful information for the optimum design of barricade structures. A control barricade with dimensions of 5 m (W) ×5 m (H) and a control stope of 15 m (L) ×8 m (W) ×15 m (H) were used for reference. The barricade was located at the base of the stope and on the side of the longitudinal wall (see Figure 5.58). All numerical investigations were conducted by specifically making modifications to the control stope and barricade. The input parameters (i.e., mixture recipe, filling strategy and rate of filling, rock mass properties), initial values (including the initial temperature of the CTB and rock mass) and boundary conditions of the control stope and barricade are provided in Table 5.11.

Table 5.11. Input parameters, initial values and boundary conditions of control CTB and rock mass

Parameter	Value
Backfill	
Stope size (m)	15(L) ×8(W)×15(H)
Barricade size(m)	5(W) ×5(H)
Stope inclined angle (°)	90
Cement content (wt%)	Residual fill: 4.5, and Plug fill: 7
w/c ratio	7.6
Initial void ratio	1
Filling rate (m/h)	0.5
Rock mass	
Density (Kg/m^3)	2500
Young's modulus (GPa)	30
Poisson's ratio	0.3
Thermal conductivity (W/m K)	3.9
Heat capacity (J/Kg K)	790
Mechanical component	
Top surface	Free
Lateral sides	Roller
Bottom side	Fixed
Volume force	Gravity
Hydraulic component	
Surrounding surfaces	No flow
Volume force	Gravity
Initial value	Hydraulic head=0
Thermal component	
Surrounding surfaces (°C)	25
Initial temp. (°C)	25

* wt%: weight percentage with respect to total weight of solid phase in CTB

The geometry and dimensions of the control rock mass, stope and barricade are presented in Figure 5.58. The center point of the barricade (i.e., 2.5 m from the floor, and 2.5 m away from the wall of the undercut drift) is selected as the monitored point in this study.

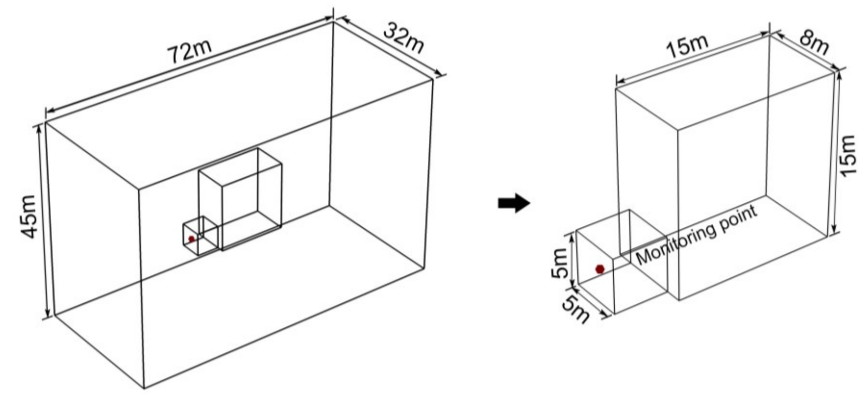

Figure 5.58. Geometry and dimensions of control CTB and stope

A filling strategy that involves two-stages with a filling rate of 0.5 m/h is adopted for the backfilling operation in the control stope. After the completion of the first stage of filling, curing was carried out for 12-hours followed by residual filling. For the implementation of the drainage condition, a mass flux (i.e., a product of water density and Darcy's velocity) boundary condition is applied on the barricade surface.

5.4.4.1. Effect of curing time

Based on previous laboratory studies (e.g., Cui and Fall 2016b; Haiqiang et al. 2016; Walske et al. 2016) and field measurements (e.g., Helinski et al. 2010a; Thompson et al. 2012), it has been found that the CTB behavior is time-dependent due to the development of binder hydration in the backfill mass. Therefore, it is necessary to investigate the changes in the total horizontal stress acting on the barricade with time. The filling operation in the control stope required 42 hours (including a curing time of the 12-hours after the completion of the first filling). As shown in Figure 5.59, the total horizontal stress and PWP acting on the barricade change with time. Specifically, during the different stages of filling, both the total stress and PWP increase with time. This is attributed to the placement of fresh CTB into the stope and the related increase in self-weight stress. However, it should be pointed out that the rate of change in the total stress during the second filling sequence is less than that obtained during plug filling. This is due to the fact that consolidation can increase during the second stage of filling, and thus more vertical stress can be transferred to the rock mass through the interface interaction of the CTB/rock mass (i.e., the arching effect). Moreover, a decrease in total stress and PWP is observed during the rest period (i.e., 14 h to 26 h). The variation in total stress is due to the combined effect of water loss through the barricade and stress transfer from the CTB to the surrounding rock walls due to the arching effect, while the changes in PWP are governed by the pore-water consumption caused by binder hydration and water drainage through the CTB mass. Similar time-dependent characteristics of barricade pressure have been observed in field studies (e.g., Thompson et al. 2011; Doherty et al. 2015)

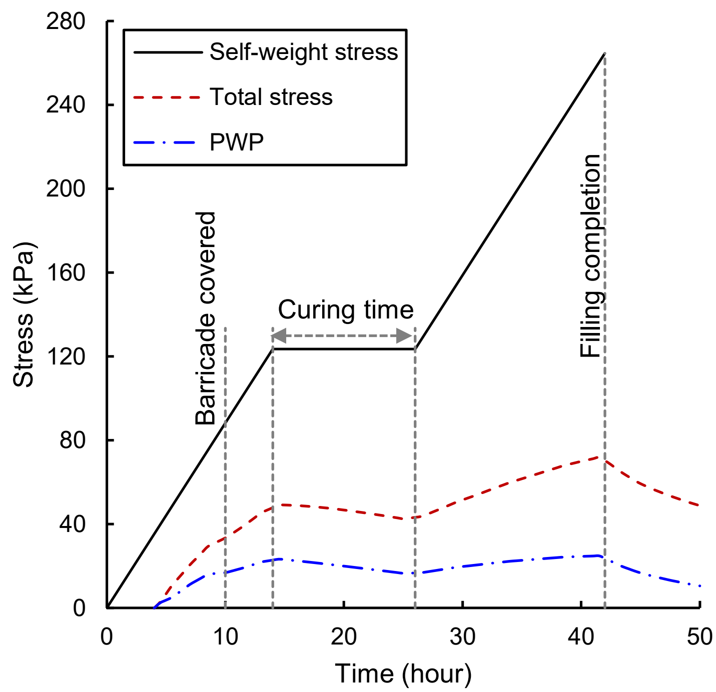

Figure 5.59. Effect of curing time on changes in the total horizontal stress and PWP acting on the barricade

To show the spatial distribution of the total horizontal stress and PWP in the CTB with time, two cut slices of CTB mass were used, including the barricade and the longitudinal slices along the central line of the stope. As can be seen in Figure 5.60, the non-uniform distribution of the total stress becomes more obvious with time, especially in the vicinity of the access drift. This is due to the water drainage through the barricade, which not only results in the dissipation of PWP in the CTB (see Figure 5.61), but also causes the change in total stress near the barricade structure. Meanwhile, the asymmetric geometry of a stope near the barricade area can further contribute to the non-uniform distribution of the total stress and PWP in CTB. The obtained results are consistent with the findings obtained in previous studies on CTB (e.g., Helinski et al. 2010b; Cui and Fall 2016d; 2017).

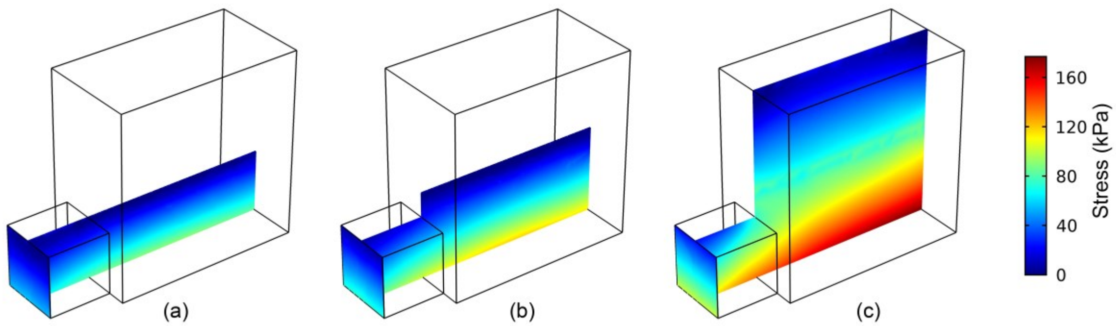

Figure 5.60. Spatial distribution of total horizontal stress in control CTB: (a) 10 hours (barricade covered); (b) 14 hours (completion of 1st stage of filling); and (c) 42 hours (filling completion)

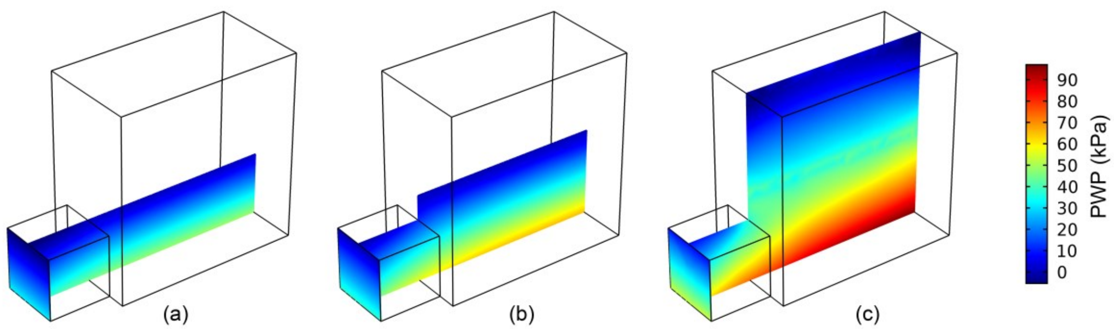

Figure 5.61. Spatial distribution of PWP in control CTB: (a) 10 hours (barricade covered); (b) 14 hours (completion of first stage of filling); and (c) 42 hours (filling completion)

5.4.4.2. Effect of Barricade Location and Geometry

Due to the differences in planning and scheduling as well as the geomechanical conditions, the barricade location and shape may vary from one stope to another. Therefore, it is necessary to study the corresponding effects on the stress acting on barricade structures. In the present study, the stope bulkhead is constructed at three different locations along the undercut drift (5 m, 4 m and 3 m back from the open stope brow, respectively). The obtained total horizontal stresses on the barricade are plotted in Figure 5.62. It is apparent that the total stress acting on the barricade increases with reduced distance between the barricade and stope brow. For example, when the filling operation is completed (i.e., after 42-hours), the total stress on the barricade with a distance of 4 m (78.3 kPa) and 3 m (85.6 kPa) between the barricade and stope brow increases by 9% and 19% respectively, compared to that with a distance of 5 m (71.9

kPa). This finding is consistent with the in-stope measurements obtained by Helinski et al. (2010a). Moreover, the reduced distance between the barricade and stope brow only increases the barricade pressure, but also subjects mining workers to potential risks, such as falling rocks and/or debris from the brow. Therefore, the barricade location should be taken into consideration as a significant factor during the design of barricade structures.

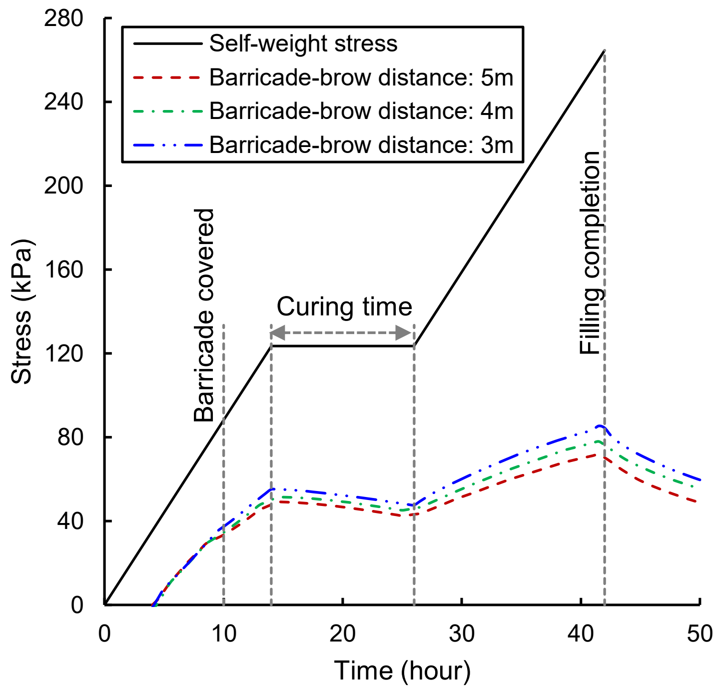

Figure 5.62. Effect of barricade location on changes in total horizontal stress acting on barricade

Aside from the barricade location, the barricade shape is also important and different shapes have been adopted in CTB design. The common shapes used in practice include those that are flat (e.g., Hughes 2008; Helinski et al. 2010a), and arched (e.g., Thompson et al. 2009). To investigate the influence of barricade shapes, both flat and arched are examined in this study. As previously discussed, the location of the barricade can affect the total horizontal stress acting on the barricade. To eliminate this problem, the distance between the peak point of both the arched and flat barricades and stope brow is set to 5 m. The geometry and dimensions of three types of barricades are presented in Figure 5.63.

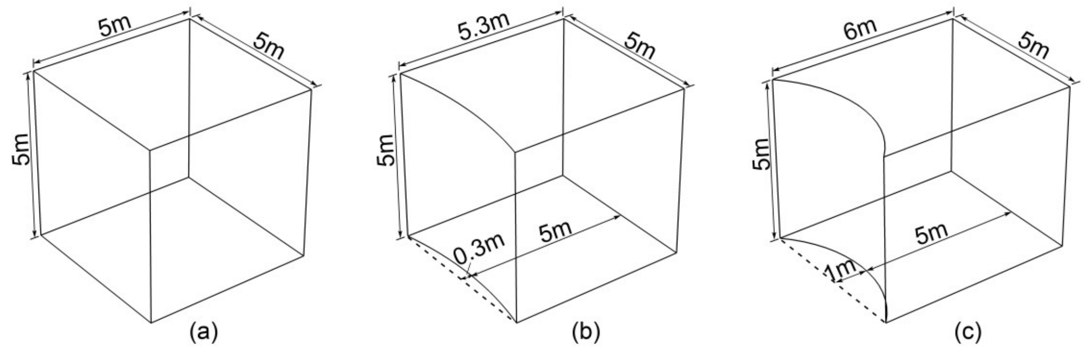

Figure 5.63. Geometry and dimensions of adopted barricades: (a) flat barricade; (b) arched barricade with arch depth of 0.3 m; and (c) arched barricade with arch depth of 1 m

The simulation results are plotted in Figure 5.64. The results indicate that the barricade shape has a negligible effect on the changes in the total horizontal stress. However, it should be noted that the bulkhead is usually constructed by using concrete or porous brick which has a higher compressive strength than its tensile strength. It is well known that when the total horizontal stress is continuously acting on the barricade, compressive stress will dominate in the arched structure (Hughes 2008), which is more favorable for the stability of the barricade structure compared to the use of a flat structure.

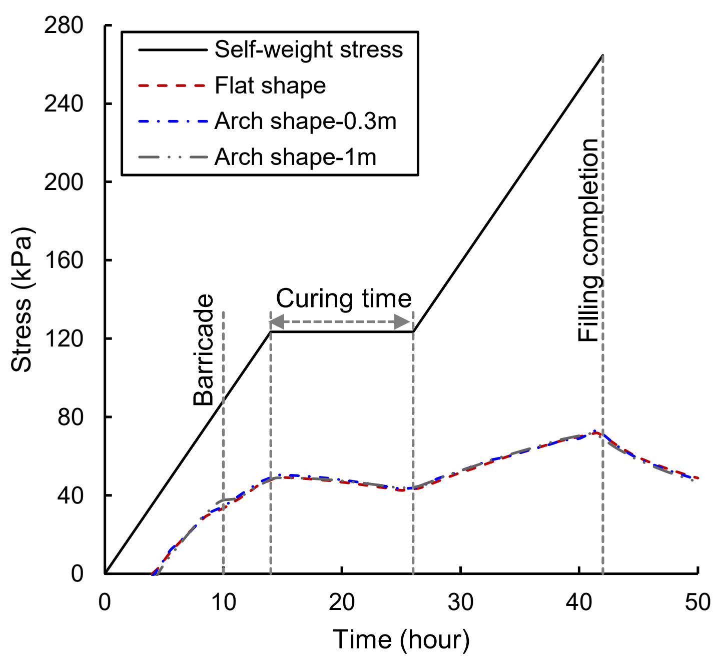

Figure 5.64. Effect of barricade shape on changes in total horizontal stress acting on barricade

Although barricade shape has very limited influence on the changes in the total horizontal stress acting on the barricade at the monitored point (i.e., the centre line of the barricade), it is still interesting to examine the spatial distribution of the horizontal stress on the barricade. It can be observed in Figure 5.65 that the barricade shape can affect the spatial distribution of the barricade pressure. The total stress in the flat barricade shows a uniform distribution at a given height of the barricade, while with increases in the depth of the arch (from 0.3 m to 1 m), a non-uniform distribution of the horizontal stress gradually becomes more apparent. Specifically, at a given height, the stress level along the centre line of the barricade is greater than that near the drift wall. As previously discussed for the effect of the barricade location, the distance between the barricade and stope brow can have significant impacts on the resulting barricade pressure. The distance between the barricade and stope brow is the same for all points on the bulkhead for a flat barricade, and thus the stress shows a uniform distribution. However, for the arched fence, the distance between the barricade and stope brow increases as the point of the barricade approaches the drift wall with reference to the centre line of the barricade structure. Therefore, at a given height, a lower total stress is obtained for the point of the barricade with greater the distance between the barricade and slope brow.

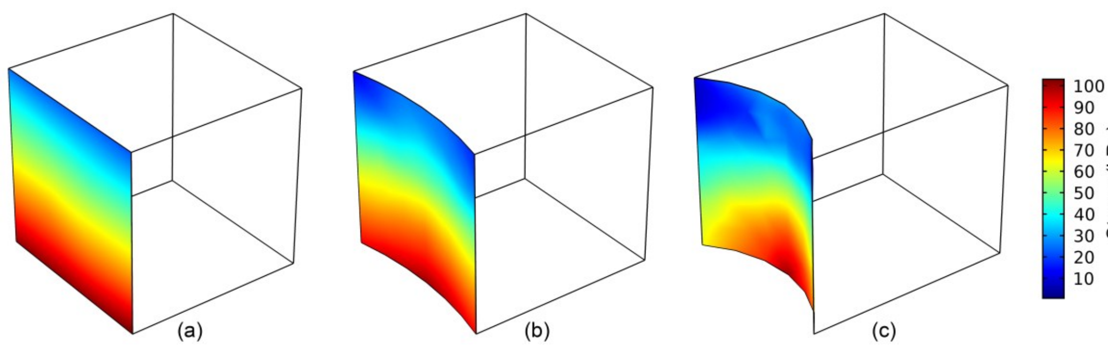

Figure 5.65. Effect of barricade shape on spatial distribution of total horizontal stress after completion of filling operation (after 42 hours)

5.4.4.3. Effect of Cement Content

As a significant parameter of the CTB mixture recipe, cement content not only directly determines the CTB strength, but also governs the cost of filling operations and thus the cost of mining production (Cui and Fall 2016c). Therefore, it is important to investigate the effect of cement content on the barricade pressure. As can be seen in Figure 5.66, the total horizontal stress acting on the barricade is very sensitive to the changes in cement content. Specifically, the peak value of the barricade pressure is 119 kPa for a cement content of 1%, 72 kPa for 4.5% and 52 kPa for 7%. The reduction in barricade pressure with increases in cement content can be attributed to the strong dependence of the development of consolidation and the arching effect on the binder hydration. A higher cement content can contribute to a more consolidated CTB and thus to the development of the arching effect for a given curing time. Meanwhile, a higher cement content can further improve the CTB/rock mass interface properties and their rate of acquisition. Consequently, the stress transfer between the CTB and rock mass can be increased in CTB with a higher cement content. Therefore, lower barricade pressure is observed in CTB with a higher cement content.

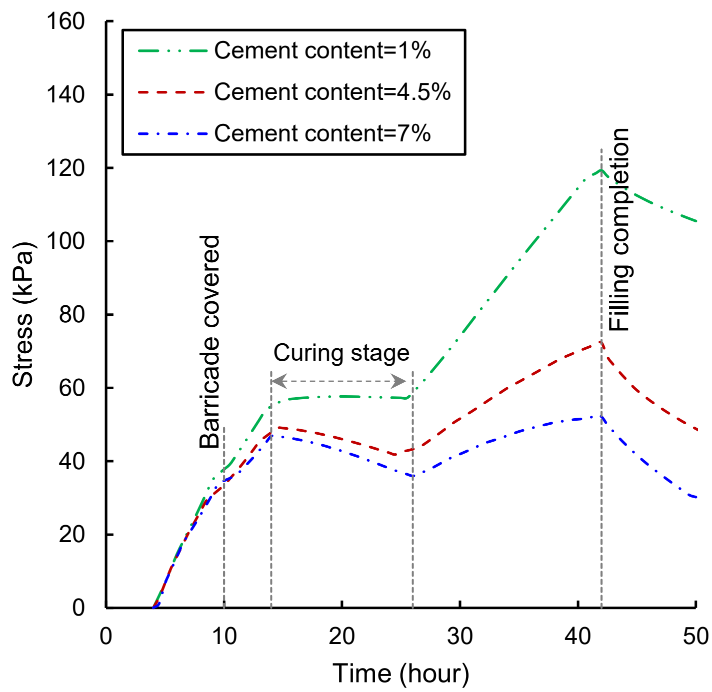

Figure 5.66. Effect of cement content on changes in total horizontal stress acting on barricade

The spatial distribution of total horizontal stress in CTB with different cement contents are plotted in Figure 5.67. It can be observed that (1) the stress level in CTB shows a decreasing trend with increased cement content, which results in the reduction of stress acting on barricade, and (2) the stress concentration occurs along the interface (7 m from the stope floor) when filling in stages. The reason for the occurrence of stress concentration in the vicinity of the interface when filling in stages has been discussed in Section 5.4.4.3.

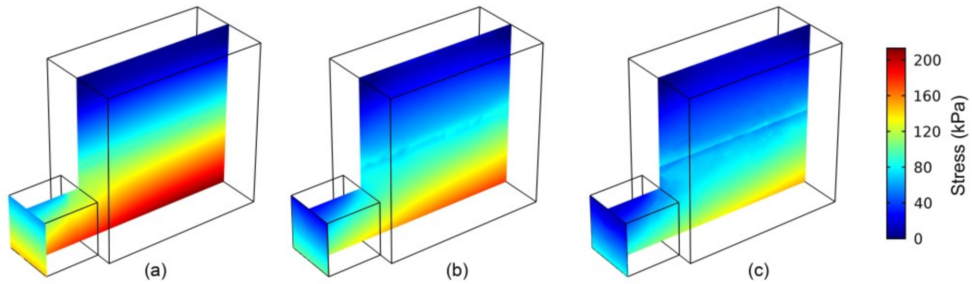

Figure 5.67. Spatial distribution of total horizontal stress in CTB after completion of filling operation: (a) cement content=1%; (b) cement content=4.5%; (c) cement content=7%

5.4.4.4. Effect of Stope Wall and Wall Roughness

Due to the different ore bodies and blasting in the stoping process, the rock wall roughness of the resultant stope may change from one stope to another. Therefore, three different roughness indexes R_L (including 1 (smooth wall surface), 2 and 3) of the rockwall are adopted for the control CTB to investigate their influence on the stress acting on the barricade. Figure 5.68 shows the changes in the total horizontal stress acting on the barricade with different degrees of surface roughness. From this figure, it can be seen that a more rough wall can reduce the total stress acting on the barricade. This is because a wall with a more rough surface further contributes to the enhancement of the CTB/rock mass interface properties (i.e., interface friction angle and adhesion, see Eqs.(4.188) and (4.189)). Consequently, the arching effect increases in the stope with a rougher wall, and thus more stress can transfer to the rock mass. Therefore, there is lower total horizontal stress on the barricade with increased wall roughness.

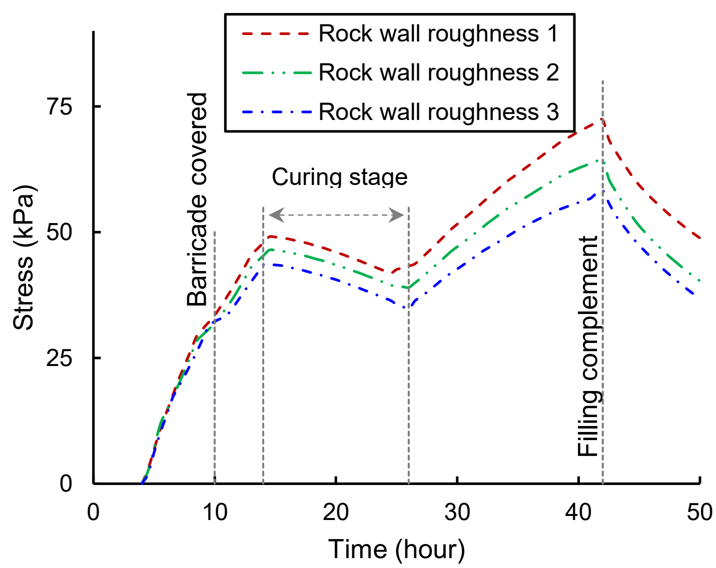

Figure 5.68. Effect of rock wall roughness on the changes in total horizontal stress acting on barricade

5.4.4.5. Effect of initial temperature of CTB

Due to the temperature dependence of binder hydration (Aldhafeeri et al. 2016), the variations in the initial temperature may affect changes in the material properties, coupled THMC behaviors and the resultant consolidation process. Therefore, for the analysis of barricade pressure, it is necessary to study the effect of the initial temperature of the CTB. In this study, three different initial temperatures (including 5°C, 25°C and 45°C) are examined. It can be seen in Figure 5.69 that the total horizontal stress shows a decreasing trend in CTB with a higher initial temperature. Specifically, compared with the peak stress (i.e.,102 kPa) obtained in CTB with an initial temperature of 5°C, the stress acting on the barricade is reduced by 29.3% (71 kPa) for an initial temperature of 25°C, and 59.2% (42 kPa) for 45°C. This is mainly because higher temperatures can accelerate the binder hydration and thus further contribute to the development of consolidation of the CTB. Moreover, the CTB/backfill interface properties (i.e., interface friction angle and adhesion) can be further improved with rapid hydration reactions. Consequently, the arching effect can facilitate stress transfer from the CTB to the rock mass to a larger extent. Therefore, a lower barricade pressure is observed in CTB with a higher initial temperature.

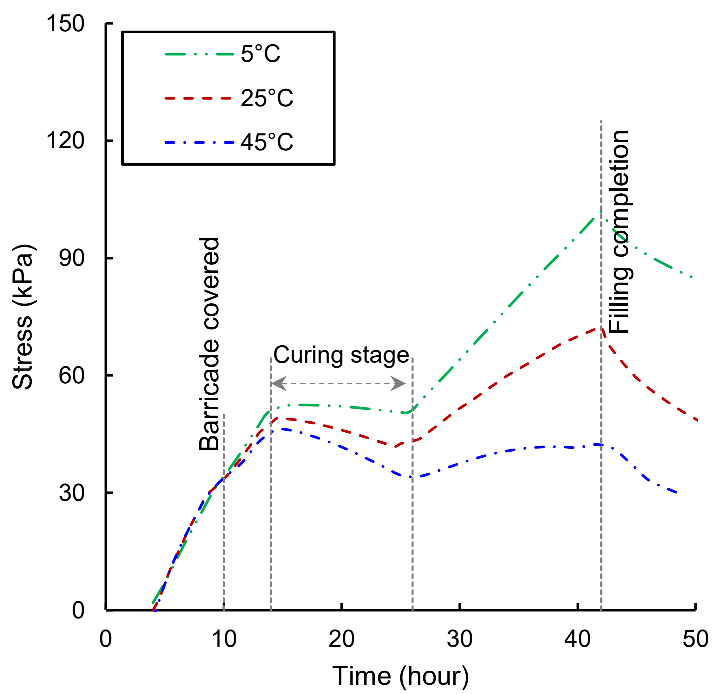

Figure 5.69. Effect of initial temperature of CTB on the changes in total horizontal stress acting on barricade

5.4.4.6. Effect of Water Drainage

After placement into a stope, the fresh CTB may be subjected to drained (Thompson et al. 2012) or undrained (Doherty et al. 2015) conditions. Consequently, the CTB behavior and related barricade pressure may change with different drainage conditions. In this study, both drained and undrained CTB are investigated. From Figure 5.70, it can be found that, as expected, the barricade pressure significantly increases under undrained conditions. Moreover, based on the spatial distribution of the horizontal stress in CTB after completion of the filling operation (see Figure 5.71), the undrained CTB (Figure 5.71a) shows a uniform distribution of horizontal stress at any given height compared with that of CTB under drained conditions (Figure 5.71b). Therefore, the developed multiphysics model can be used to study the stress acting on the barricade under different drainage conditions.

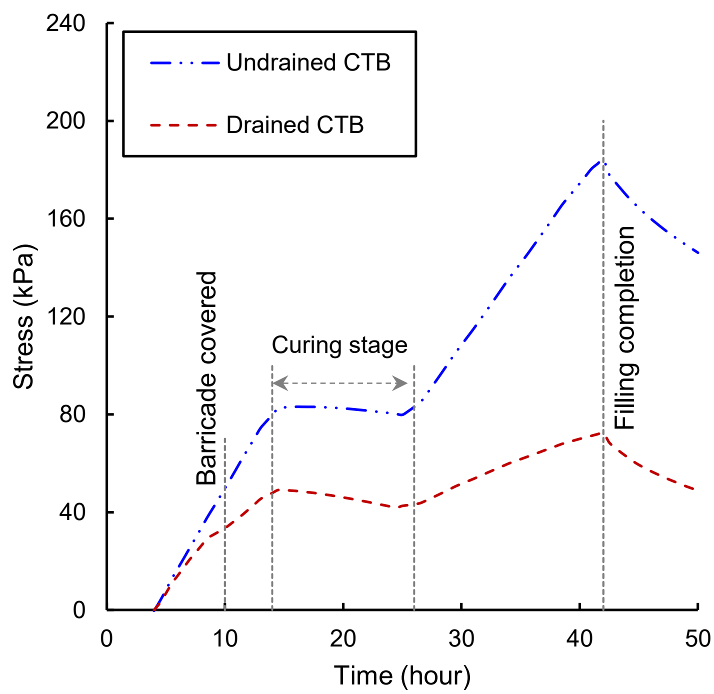

Figure 5.70. Effect of drainage conditions on the changes in total horizontal stress acting on barricade

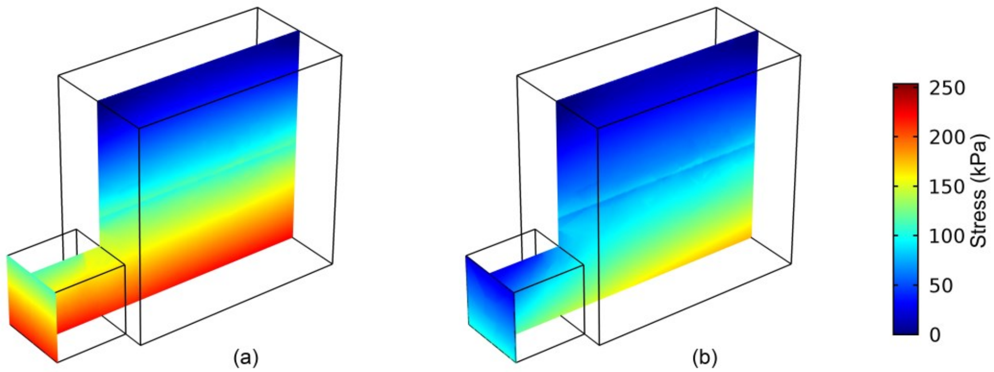

Figure 5.71. Spatial distribution of total horizontal stress in CTB after completion of filling operation: (a) undrained CTB; (b) drained CTB

5.4.5. Conclusions

The following conclusions are made based on the obtained results in the present study.

(i) The changes in barricade pressure are significantly influenced by coupled THMC processes, consolidation process and the stress transfer from the CTB to the rock mass due to the arching effect. The validation results prove that the multiphysics model can be used to accurately simulate the changes in the stress acting on a barricade.

(ii) Due to the complex multiphysics processes in CTB and filling operations that are flexible, the changes in the barricade pressure are time-dependent.

(iii) The barricade location in undercut drift has a significant influence on the changes in barricade pressure, while the barricade shape mainly affects the stress distribution on the barricade.

(iv) Barricade pressure is very sensitive to cement content. With increases in cement content, the multiphysics simulation shows a lower barricade pressure, which further validates the contribution of the chemical process to multiphysics behaviors and thus to the changes in barricade pressure.

(v) The initial temperature of CTB has significant impacts on the changes in the barricade pressure. Higher initial temperatures can accelerate the binder hydration, which further improves the CTB/rock mass interface properties, consolidation process and stress transfer from the CTB to the rock mass due to the arching effect. Consequently, a lower barricade pressure is observed in CTB with a higher initial temperature.

(vi) Increased rock wall roughness can reduce the total horizontal stress acting on the barricade, and thus contribute to barricade stability.

(vii) Water drainage directly contributes to reductions in the barricade pressure and thus increases the stability of the retaining structure.

5.4.6. References

Aldhafeeri, Z., Fall, M., Pokharel, M., and Pouramini, Z. (2016). "Temperature dependence of the reactivity of cemented paste backfill." *Appl. Geochem.*, 10.1016/j.apgeochem.2016.06.005, 72, 10-19.

Belem, T., and Benzaazoua, M. (2004). "An overview on the use of paste backfill technology as a ground support method in cut-and-fill mines." *Proc., the 5th International Symposia on Ground support in Mining and Underground Construction*, Australian Centre for Geomechanics, Perth, Australia, 28-30.

Belem, T., Benzaazoua, M., and Bussière, B. (2000). "Mechanical behaviour of cemented paste backfill." *Proc., 53rd Canadian Geotechnical Conference*, Canadian Geotechnical Society, Montreal, QC, Canada, 373-380.

Belem, T., Harvey, A., Simon, R., and Aubertin, M. (2004). "Measurement of internal pressures of a gold mine pastefill during and after the stope backfilling." *Proc., 5th International Symposium on Ground Support in Mining and Underground Construction*, Australian Centre for Geomechanics, Perth, Australia, 619-630.

Benzaazoua, M., Fiset, J.-F., Bussière, B., Villeneuve, M., and Plante, B. (2006). "Sludge recycling within cemented paste backfill: study of the mechanical and leachability properties." *Miner. Eng.*, 10.1016/j.mineng.2005.09.055, 19(5), 420-432.

Benzaazoua, M., Ouellet, J., Servant, S., Newman, P., and Verburg, R. (1999). "Cementitious backfill with high sulfur content physical, chemical, and mineralogical characterization." *Cem. Concr. Res.*, 29(5), 719-725.

Comsol (2015). "Comsol Multiphysics 5.1." <http://www.comsol.com>. (Sept. 20, 2016).

Cui, L., and Fall, M. (2015a). "A coupled thermo-hydro-mechano-chemical model for underground cemented tailings backfill." *Tunn. Undergr. Sp. Tech.*, 10.1016/j.tust.2015.08.014, 50, 396-414.

Cui, L., and Fall, M. (2015b). "Modeling and Simulation of the Consolidation Behaviour of Cemented Paste Backfill." *Proc., 2015 Comsol Conference*, Boston, MA, USA, 1-5.

Cui, L., and Fall, M. (2016a). "An evolutive elasto-plastic model for cemented paste backfill." *Comput. Geotech.*, 10.1016/j.compgeo.2015.08.013, 71, 19-29.

Cui, L., and Fall, M. (2016b). "Mechanical and thermal properties of cemented tailings materials at early ages: Influence of initial temperature, curing stress and drainage conditions." *Constr. Build. Mater.*, 10.1016/j.conbuildmat.2016.08.080, 125, 553-563.

Cui, L., and Fall, M. (2016c). "Multiphysics model for consolidation behaviour of cemented paste backfill." *Int. J. Geomech.*, 10.1061/(ASCE)GM.1943-5622.0000743, 040160771-0401607723.

Cui, L., and Fall, M. (2016d). "Simulation of self-desiccation process in cemented tailings backfill structure." *Int. J. Numer. Anal. Methods Geomech. (submitted)*.

Cui, L., and Fall, M. (2017). "Multiphysics modeling of arching effects in fill mass." *Comput. Geotech.*, 10.1016/j.compgeo.2016.10.021, 83, 114-131.

Da Luz, C. A., and Hooton, R. (2015). "Influence of curing temperature on the process of hydration of supersulfated cements at early age." *Cem. Concr. Res.*, 10.1016/j.cemconres.2015.07.002, 77, 69-75.

Doherty, J. P. (2015). "A numerical study into factors affecting stress and pore pressure in free draining mine stopes." *Comput. Geotech.*, 10.1016/j.compgeo.2014.10.001, 63, 331-341.
Doherty, J. P., Hasan, A., Suazo, G. H., and Fourie, A. (2015). "Investigation of some controllable factors that impact the stress state in cemented paste backfill." *Can. Geotech. J.*, 10.1139/cgj-2014-0321, 52(12), 1901-1912.
El Mkadmi, N., Aubertin, M., and Li, L. (2013). "Effect of drainage and sequential filling on the behavior of backfill in mine stopes." *Can. Geotech. J.*, 10.1139/cgj-2012-0462, 51(1), 1-15.
Fall, M., Nasir, O., Cui, L., and Han, F. (2015). "Coupled modeling of the strength development and distribution within cemented paste backfill structure." *Proc., 49th US Rock Mechanics/Geomechanics Symposium*, American Rock Mechanics Association, San Francisco, California, USA, 587-595.
Ghirian, A. (2016). "Coupled thermo-hydro-mechanical-chemical (THMC) processes in cemented tailings backfill structures and implications for their engineering design." Ph.D. Thesis, University of Ottawa, Canada.
Ghirian, A., and Fall, M. (2016). "Strength evolution and deformation behaviour of cemented paste backfill at early ages: Effect of curing stress, filling strategy and drainage." *Int. J. Min. Sci. Technol.*, 10.1016/j.ijmst.2016.05.039, 26(15), 809-817.
Gokhale, A., and Underwood, E. (1990). "A general method for estimation of fracture surface roughness: Part I. Theoretical aspects." *Metallurgical Transactions A*, 21(5), 1193-1199.
Haiqiang, J., Fall, M., and Cui, L. (2016). "Yield stress of cemented paste backfill in sub-zero environments: Experimental results." *Miner. Eng.*, 10.1016/j.mineng.2016.03.014, 92, 141-150.
Helinski, M., Fahey, M., and Fourie, A. (2007). "Numerical modeling of cemented mine backfill deposition." *J. Geotech. Geoenviron.*, 10.1061/(ASCE)1090-0241(2007)133:10(1308), 133(10), 1308-1319.
Helinski, M., Fahey, M., and Fourie, A. (2010a). "Behavior of cemented paste backfill in two mine stopes: measurements and modeling." *J. Geotech. Geoenviron.*, 10.1061/(ASCE)GT.1943-5606.0000418, 137(2), 171-182.
Helinski, M., Fahey, M., and Fourie, A. (2010b). "Coupled two-dimensional finite element modelling of mine backfilling with cemented tailings." *Can. Geotech. J.*, 10.1139/T10-020, 1187-1200.
Hughes, P. B. (2008). "Performance of paste fill fences at Red Lake Mine." Master Thesis, University of British Columbia, Vancouver, Canada.
Koohestani, B., Belem, T., Koubaa, A., and Bussière, B. (2016). "Experimental investigation into the compressive strength development of cemented paste backfill containing Nano-silica." *Cem. Concr. Compos.*, 10.1016/j.cemconcomp.2016.06.016, 72, 180-189.
Li, L., and Aubertin, M. (2009). "Horizontal pressure on barricades for backfilled stopes. Part II: Submerged conditions." *Can. Geotech. J.*, 10.1139/T08-105, 46(1), 47-56.
Li, L., Ouellet, S., and Aubertin, M. (2009). "A method to evaluate the size of backfilled stope barricades made of waste rock." *Proc., GeoHalifax*, Canadian Geotechnical Society, Halifax, Canada, 497-503.
Li, L., and Yang, P. (2015). "A numerical evaluation of continuous backfilling in cemented paste backfilled stope through an application of wick drains." *Int. J. Min. Sci. Technol.*, 10.1016/j.ijmst.2015.09.004, 25(6), 897-904.
Marston, A. (1930). "The theory of external loads on closed conduits in the light of the latest experiments." *Proc., the 9th Annual Meeting of the Highway Research Board*, Highway Research Board, Washington, D.C., USA, 138-170.

Nasir, O., and Fall, M. (2009). "Modeling the heat development in hydrating CPB structures." *Comput. Geotech.*, 10.1016/j.compgeo.2009.05.008, 36(7), 1207-1218.
Pokharel, M., and Fall, M. (2010). "Coupled thermochemical effects on the strength development of slag-paste backfill materials." *J. Mater. Civil. Eng.*, 23(5), 511-525.
Schindler, A. K., and Folliard, K. J. (2003). "Influence of supplementary cementing materials on the heat of hydration of concrete." *Proc., Advances in Cement and Concrete IX Conference*, Engineering Conferences International, Inc., Colorado, USA, 17-26.
Thompson, B., Bawden, W., and Grabinsky, M. (2012). "In situ measurements of cemented paste backfill at the Cayeli Mine." *Can. Geotech. J.*, 10.1139/t2012-040, 49(7), 755-772.
Thompson, B., Grabinsky, M., and Bawden, W. (2011). "In situ monitoring of cemented paste backfill pressure to increase backfilling efficiency." *CIM Journal*, 2(4), 199-209.
Thompson, B., Grabinsky, M., Bawden, W., and Counter, D. (2009). "In-situ measurements of cemented paste backfill in long-hole stopes." *Proc., the 3rd CANUS Rock Mechanics Symposium*, Toronto, Canada, 197-198.
Veenstra, R. L. (2013). "A design procedure for determining the in situ stresses of early age cemented paste backfill." Ph.D. Thesis, University of Toronto, Canada.
Walske, M. L., McWilliam, H., Doherty, J., and Fourie, A. (2016). "Influence of curing temperature and stress conditions on mechanical properties of cementing paste backfill." *Can. Geotech. J.*, 10.1139/cgj-2014-0502, 53(1), 148-161.
Wu, D., Fall, M., and Cai, S.-j. (2014). "Numerical modelling of thermally and hydraulically coupled processes in hydrating cemented tailings backfill columns." *Int. J. Min. Reclam. Environ.*, 10.1080/17480930.2013.809194, 28(3), 173-199.
Yilmaz, E., Kesimal, A., and Ercikdi, B. (2004). "Strength development of paste backfill simples at Long term using different binders." *Proc., the 8th Symposium MineFill*, Beijing, China, 281-285.
Yumlu, M. (2008). "Barricade pressure monitoring in paste backfill." *Gospodarka Surowcami Mineralnymi*, 24(4/3), 233-244.

5.5. Paper IX: Multiphysics modeling and simulation of strength development and distribution in cemented tailings backfill structures

Liang Cui, Mamadou Fall

Abstract

Cemented tailings backfill structures are complex underground geomechanical systems. After fresh cemented tailings backfill (CTB; a mix of tailings, binder and water) is poured into underground stopes (mined-out voids), its strength which is a geomechanical key design criterion of CTB structures, gradually develops with time. The development of CTB strength is governed by the coupled thermo-hydro-mechanical-chemical (THMC) processes in the CTB mass. Therefore, to assess and predict the changes to CTB strength and its distribution within the CTB mass, a multiphysics model on CTB strength is proposed in this study, and has been successfully validated against a series of experimental data. Then, the validated model is used to investigate the changes in the strength of CTB structure under various influential factors in the field (e.g., backfilling strategy, inclination angle of stope, and filling rate). The obtained results provide better insight into the process of the strength increase and spatial distribution in CTB structures as well as contribute to more cost-effective engineering designs of CTB structures.

Keywords: Mine; Cemented paste backfill; THMC; Multiphysics; Strength; Tailings.

5.5.1. Introduction

Due to its significant environmental (Aldhafeeri and Fall 2016), technical (Suazo et al. 2016a) and economic (Cui and Fall 2015a) benefits, cemented tailings backfill (CTB; a cementitious material made of unclassified tailings (human-made soils), hydraulic binders, and mine processed water) has been widely applied in underground mines (Suazo et al. 2016b). Since the failure of CTB structures can have substantial financial ramifications and cause severe injuries and/or fatalities (Nasir and Fall 2009), mechanical stability has been considered as a significant design criterion of CTB structures. To satisfy the design criterion of mechanical stability of CTB structures in underground mines, CTB strength is typically in the range of 0.5 to 2.5 MPa (Jefferis and Wilson 2012). However, increases in CTB strength is substantially affected by the coupled thermo-hydro-mechanical-chemical (THMC) processes that occur in the CTB mass as shown in Figure 5.72 and briefly discussed below. Specifically, as binder hydration progresses, the resultant bonds between the tailings particles directly contribute to the development of CTB strength (Belem et al. 2002; Fall et al. 2010; Yılmaz et al. 2014). Moreover, due to the temperature dependence of binder hydration (Barnett et al. 2006; Cui and Fall 2016b), the thermal process can affect the development of CTB strength as well. For the hydraulic process, the pore-water consumption caused by binder hydration (D. Wu et al. 2016) and water drainage through the barricade (a retaining structure built at the floor base) (Doherty 2015) can cause the build-up of suction and thus increase the effective stress which can further improve the CTB strength. In addition, stope (underground mine excavation or cavity) backfilling can be carried out in many ways and thus affects the consolidation behavior of CTB (Cui and Fall 2016c). As a result, the void ratio related properties, such as hydraulic conductivity, will change as well. Correspondingly, the pore-water pressure (PWP) and thus effective stress will be affected with the development of consolidation. Therefore, to accurately assess the development of CTB strength, the coupled THMC processes must be fully considered.

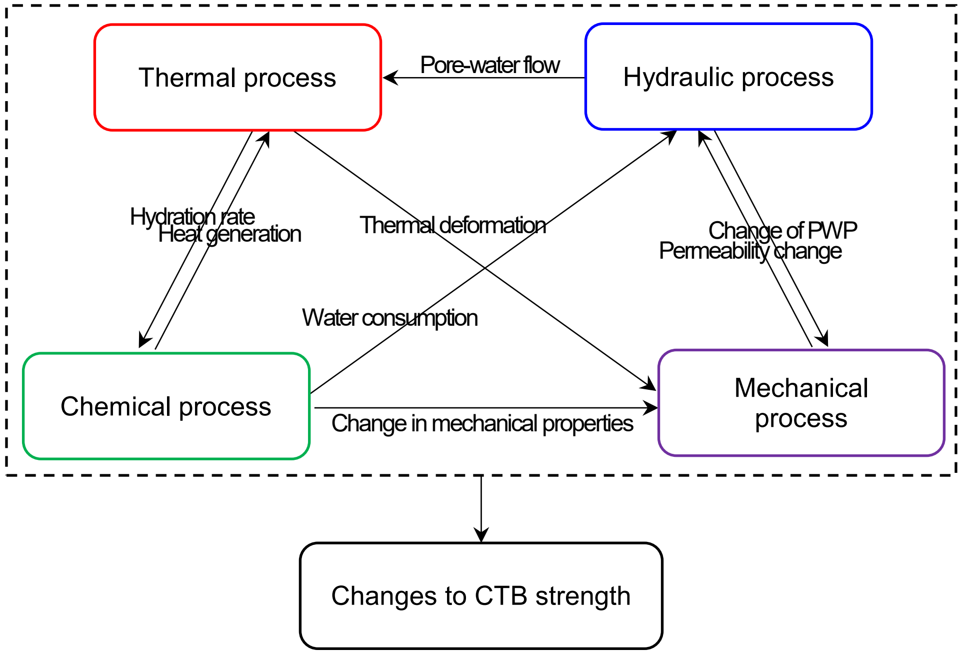

Figure 5.72. Schematic diagram of primary controlling mechanisms of changes to CTB strength

As the mechanical stability of CTB structures is important, there have been extensive studies that examine CTB strength at both the laboratory and in-situ scales. These studies have identified several factors that significantly affect the development of CTB strength, such as the curing temperature (e.g., Fall et al. 2010; Wang and Fall 2014), mixture recipe (e.g., Ercikdi et al. 2009; Hamberg et al. 2015), sulphate content in the tailings (e.g., Benzaazoua et al. 2002; Fall and Benzaazoua 2005; Fall et al. 2008; Li and Fall 2016), curing pressure (e.g., Yilmaz et al. 2011; Ghirian and Fall 2015), drainage conditions (e.g., Belem et al. 2006; Cui and Fall 2016b), and filling strategy (e.g., Ghirian and Fall 2016b). These experimental findings have provided in-depth insight into the changes to CTB strength. Moreover, several empirical and partially coupled mathematical models have been developed to predict the changes in CTB strength based on the controlling mechanisms. For instance, Nasir and Fall (2010) developed a hybrid numerical/analytical model to predict the changes in CTB strength with variations in the temperature and progression of binder hydration. This model can evaluate the changes in temperature in CTB and binder hydration with curing time. However, the proposed model on the strength of CTB did not take into consideration all of the main coupled THMC processes that occur in CTB structures which affect their strength development. Mozaffaridana (2011) proposed a maturity method to incorporate the combined effects of curing time and temperature into the prediction of CTB strength.

However, this model requires measurements of CTB temperature during the prediction periods and does not consider the effects of the mixture recipe and mechanical load (e.g., stress) and deformation (e.g., consolidation); that is, the model is empirical. Similarly, based on a regression analysis on the unconfined compressive strength (UCS) values for different curing ages, an empirical correlation between CTB strength, curing time and sample size was proposed by Yilmaz et al. (2015). To date, however, no study has been performed to develop a fully coupled THMC model on the strength of CTB materials. This THMC model on the strength of CTB will contribute to an optimal design of CTB structures and reliable analysis of their mechanical stability. Therefore, the aims of this paper include:

(1) To develop a multiphysics model on the strength of CTB, which fully considers the effects of coupled THMC processes, and
(2) To investigate the changes in CTB strength in the field under different curing and loading conditions.

5.5.2. Modelling Approach

To develop the multiphysics model on CTB strength, the prerequisite is to quantitatively simulate: (1) the mechanical behavior (especially the stress-strain relationship obtained from UCS testing) and (2) changes in the mechanical properties. For the CTB materials, it has been found that chemical hardening and strain hardening/softening become more apparent with curing time (Belem et al. 2000; Fall et al. 2007). Therefore, an evolutive elastoplastic model is needed to understand the stress-strain relationship of CTB with curing time. Correspondingly, if the hardening/softening behavior can be accurately evaluated (i.e., the mathematical description of the expansion (hardening) and contraction (softening) of the yield surface in stress space with the development of plastic strain), the CTB strength (i.e., the peak point of stress-strain curve) can be determined by using the first derivative test on the hardening/softening parameter with respect to the cumulative plastic strain. Moreover, to describe the effects of coupled THMC processes on the changes to the CTB strength, the related mechanical properties (e.g., cohesion and internal friction angle) cannot be considered constant with time (i.e., a predictive function for each mechanical property is required). In addition, it should be noted that CTB strength should be defined in terms of effective stress. Therefore, in the present study, Biot’s effective stress is integrated into the derivation of the multiphysics model on CTB strength. Consequently, the pore fluid pressure (hydraulic process), volume change (mechanical process) induced by the consolidation process in CTB, binder hydration (chemical process) process and its temperature dependence (thermal process) are fully considered.

5.5.3. Mathematical Formulation

A yield function is required to derive CTB strength. Due to the influence of the binder hydration, the mechanical properties (e.g., cohesion and internal frictional angle) will change with time. Therefore, an evolutive elastoplastic mechanical model based on a modified Drucker-Prager (D-P) yield criterion was proposed by Cui and Fall (2016a). This proposed model is adopted here to derive the model on CTB strength.

$$F = \sqrt{J_2} + \alpha(\xi,\kappa)\left[I_1 - C(\xi)\right] = 0 \tag{5.38}$$

With

$$\alpha_{D-P}(\xi,\kappa) = \frac{2\sin\phi_B(\xi)}{\sqrt{3}\left[3+\sin\phi_B(\xi)\right]} + D_{\alpha 1}\left\{\left[1-\exp(-D_{\alpha 2}\kappa)\right] + \left[D_{\alpha 3}\kappa\exp(-D_{\alpha 4}\kappa)\right]\right\}$$
$$C_{D-P}(\xi) = 3c_B(\xi)\cdot\cot\phi_B(\xi) \tag{5.39}$$

where I_1 and J_2 respectively represent the first stress invariant and the second deviatoric stress invariant; α_{D-P} and C_{D-P} denote the material properties of the yield function, and change with degree of binder hydration ξ and cumulative plastic strain κ ($\kappa = \int\sqrt{2/3 d\varepsilon_P d\varepsilon_P}$ with plastic strain ε_P), namely $\alpha_{D-P} = \alpha_{D-P}(\xi,\kappa)$ and $C_{D-P} = C_{D-P}(\xi)$; $D_{\alpha i}$ is a material parameter and changes with the degree of binder hydration (i =1-4); c_B and ϕ_B are the cohesion and internal friction angle of the CTB, which are functions of the degree of binder hydration ($c_B = c_B(\xi)$ and $\phi_B = \phi_B(\xi)$).

It should be noted that CTB strength must be defined in terms of the effective stress $\boldsymbol{\sigma}'$. Therefore, Biot's effective stress is incorporated into the derivation of the model on CTB strength in the present study,:

$$\boldsymbol{\sigma}' = \boldsymbol{\sigma} + \left(1 - K_b/K_s\right)\cdot\left(SP_w + (1-S)P_a\right)\boldsymbol{\delta}_{ij} \tag{5.40}$$

where $\boldsymbol{\sigma}'$ and $\boldsymbol{\sigma}$ denote the Biot's effective stress and total stress tensor, respectively; K_b and K_s respectively represent the bulk modulus of the CTB skeleton and solid phase; S is the degree of saturation; P_w and P_a refer to the pore-water and pore-air pressures; and $\boldsymbol{\delta}_{ij}$ is the Kronecker's delta. It should be noted that the compressive stress is taken to be negative in this study.

For the stress state of CTB under UCS testing, the true strength of the CTB $\boldsymbol{\sigma}_s$ should be defined in terms of the peak value of the axial total stress $\boldsymbol{\sigma}_{p\_axial}$, pore-water pressure P_w, and pore-air pressure P_a:

$$\boldsymbol{\sigma}_s = \boldsymbol{\sigma}_{p\_axial} + \left(1 - K_b / K_s\right) \cdot \left(SP_w + \left(1 - S\right) P_a\right) \boldsymbol{\delta}_{ij} \tag{5.41}$$

It should be noted that for the measurement method of the UCS (i.e., uniaxial compressive strength test), the measured peak stress refers to the axial stress applied by using a UCS device, namely, the measured peak stress value equals $\boldsymbol{\sigma}_{p\_axial}$. Correspondingly, the stress invariants can be rewritten in terms of $\boldsymbol{\sigma}_{p\_axial}$:

$$I_1 = \boldsymbol{\sigma}_{p\_axial} \tag{5.42}$$

$$J_2 = \boldsymbol{\sigma}^2_{p\_axial} / 3 \tag{5.43}$$

Therefore, the peak value of the axial total stress $\boldsymbol{\sigma}_{p\_axial}$ can be solved by substituting Eqs.(5.42) and (5.43) into the yield function (i.e., Eq.(5.38)):

$$\boldsymbol{\sigma}_{p\_axial} = \sqrt{3} C_{D-P}\left(\xi\right) \Big/ \left[\sqrt{3} - \frac{1}{\alpha_{D-P}\left(\xi, \kappa_s\right)}\right] \tag{5.44}$$

where κ_s refers to the value of the cumulative plastic strain when $\alpha_{D-P}\left(\xi,\kappa\right)$ reaches its peak point. From Eq.(5.44), it can be observed that for a given degree of hydration, the axial total stress reaches its maximum value when the peak value of $\alpha_{D-P}\left(\xi,\kappa\right)$ is obtained. Based on the definition of strain hardening and softening, there is only one inflection point of $\alpha_{D-P}\left(\xi,\kappa\right)$ (i.e., the inflection point corresponds to $\alpha_{D-P}\left(\xi,\kappa_s\right)$). Then, κ_s can be derived through the first derivative test of $\alpha_{D-P}\left(\xi,\kappa\right)$ with respect to the cumulative plastic strain κ, namely:

$$\frac{\partial \alpha_{D-P}\left(\xi,\kappa\right)}{\partial \kappa} = 0 \Rightarrow D_{\alpha 2} \exp(-D_{\alpha 2}\kappa_s) + B_3\left(1 - D_{\alpha 4}\kappa_s\right)\exp(-D_{\alpha 4}\kappa_s) = 0 \tag{5.45}$$

Then, the value of the cumulative plastic strain when $\alpha_{D-P}\left(\xi,\kappa\right)$ reaches its peak point can be derived (details on the derivation of κ_s are provided in Appendix C):

$$\kappa_s = \frac{{D_{\alpha 2}}^2 + D_{\alpha 4} + \sqrt{{D_{\alpha 4}}^2 + {D_{\alpha 2}}^2 D_{\alpha 4} - {D_{\alpha 2}}^4}}{{D_{\alpha 2}}^3} \tag{5.46}$$

Substituting Eq.(5.39) into Eq.(5.44), the peak value of the axial total stress can be written as:

$$\boldsymbol{\sigma}_{p\_axial} = \frac{3\sqrt{3} c_B\left(\xi\right) \cdot \cot \phi_B\left(\xi\right)}{\sqrt{3} + 1 \Big/ \left\{\frac{2 \sin \phi_B\left(\xi\right)}{\sqrt{3}\left[3 + \sin \phi_B\left(\xi\right)\right]} + D_{\alpha 1}\left\{\left[1 - \exp(-D_{\alpha 2}\kappa_s)\right] + D_{\alpha 3}\kappa_s \exp(-D_{\alpha 4}\kappa_s)\right\}\right\}} \tag{5.47}$$

Then, the true model on CTB strength can be derived by substituting Eq.(5.47) into Eq.(5.41):

$$\boldsymbol{\sigma}_s = \frac{3\sqrt{3}c_B(\xi)\cdot\cot\phi_B(\xi)}{\sqrt{3}+1 \Big/ \left\{\frac{2\sin\phi_B(\xi)}{\sqrt{3}\left[3+\sin\phi_B(\xi)\right]} + D_{\alpha1}\left\{\left[1-\exp(-D_{\alpha2}\kappa_s)\right] + D_{\alpha3}\kappa_s\exp(-D_{\alpha4}\kappa_s)\right\}\right\}} + \tag{5.48}$$

$$\left(1-K_b/K_s\right)\left[SP_w + (1-S)P_a\right]\boldsymbol{\delta}_{\mathbf{ij}}$$

With

$$\kappa_s = \frac{{D_{\alpha2}}^2 + D_{\alpha4} + \sqrt{{D_{\alpha4}}^2 + {D_{\alpha2}}^2 D_{\alpha4} - {D_{\alpha2}}^4}}{{D_{\alpha2}}^3}$$

It should be noted that (1) Eq.(5.48) represents the true CTB strength which incorporates the effect of pore pressure into the characterization of CTB strength. However, the common testing method of CTB strength (i.e., the UCS tests) records the axial total stress applied by the UCS device and then directly uses the peak value (i.e., $\boldsymbol{\sigma}_{p\_axial}$) of the axial total stress to represent CTB strength (i.e., the nominal CTB strength). Therefore, both the nominal (Eq. (5.47)) and true (Eq. (5.48)) models on CTB strength are derived in this study, (2) because the tensile stress is considered to be positive in this study, the derived nominal and true CTB strength values from Eqs. (5.47) and (5.48) are negative. To follow the convention of strength analysis, a positive value of CPB strength is adopted in the following sections, (3) as demonstrated in Eq.(5.48), the prediction of CTB strength requires pore pressure values and the corresponding degree of saturation values. Therefore, modelling and simulation of hydraulic processes in CTB are necessary. As previously discussed in the Introduction, CTB behavior is controlled by coupled THMC processes, namely, each physical process interacts with other processes. Hence, defining the hydraulic processes in CTB requires a fully coupled THMC model specific for CTB materials. In this regard, Cui and Fall (2015a) developed a fully coupled THMC model which can be used to predict the pore pressure and degree of saturation. More details on the coupled THMC model can be found in (Cui and Fall 2015a).

5.5.4. Determination of model parameters

As demonstrated in the model on CTB strength (i.e., Eq. (5.48)), there are a series of model parameters that need to be determined. As discussed earlier in the Introduction, binder hydration plays a crucial role in the changes of the material properties of CTB. Therefore, a quantitative assessment of the progression of binder hydration should be first carried out. In this study, the exponential model proposed by Schindler and Folliard

(2003) is adopted to characterize the development of binder hydration in CTB materials, which fully considers the effect of the mixture recipe (including water-to-cement ratio, addition of fly ash and blast furnace slag, cement type), curing temperature and curing time.

$$\xi\left(w/c, X_{FA}, X_{slag}, T, t\right) = \left(\frac{1.031 \cdot w/c}{0.194 + w/c} + 0.5 \cdot X_{FA} + 0.30 \cdot X_{slag}\right) \times \exp\left\{-\left\{\tau \Big/ \int_0^t \exp\left[\frac{E_a}{R}\left(\frac{1}{T_r} - \frac{1}{T}\right)\right] dt\right\}^{\beta}\right\} \tag{5.49}$$

With

$$\tau = 66.78 x_{C_3A}{}^{-0.154} \cdot x_{C_3S}{}^{-0.401} \cdot x_{SO_3} \cdot S_{Blaine}{}^{-0.804} \cdot \exp\left(2.178 X_{slag} + 9.5 X_{FA} X_{FA-CaO}\right)$$

$$\beta = 181.4 x_{C_3A}{}^{0.146} \cdot x_{C_3S}{}^{0.227} \cdot x_{SO_3}{}^{0.558} \cdot S_{Blaine}{}^{-0.535} \cdot \exp\left(-0.647 X_{slag}\right)$$

$$E_a(T) = \begin{cases} 33{,}500 + 1{,}470 \times \left(293.15 - T\right) & T < 293.15K \\ 33{,}500 & T \geq 293.15K \end{cases}$$

where w/c refers to the water-to-cement ratio; X_{FA} and X_{slag} denote the weight fraction of the fly ash and blast furnace slag to the total binder weight, respectively; T and T_r represent the CTB temperature and its reference temperature; τ and β respectively are the time and hydration shape parameters; E_a is the apparent activation energy; R denotes an ideal gas constant; t is the curing time; x_i represents the mass ratio of the i component to the total binder weight ($i = C_3A$, C_3S and SO_3); and X_{FA-CaO} is the weight ratio of CaO to fly ash.

As demonstrated in Eq. (5.48), the CTB cohesion changes with the degree of binder hydration (i.e., $c_B = c_B\left(\xi\right)$). To assess the changes in the cohesion of CTB materials, the following predictive function is proposed:

$$c_B\left(\xi\right) = \exp\left(M_{s1} S_T\right) \cdot \left(1 - S_W\right)^{M_{s2} \exp\left(M_{s3}\xi\right)} \cdot M_{c1} \cdot C_m \cdot \xi^{M_{c2}} \tag{5.50}$$

where M_{s1}, M_{s2}, M_{s3}, M_{c1} and M_{c2} are fitting parameters; S_T represents the sulphide mass content with respect to the total mass of dry tailings; S_w refers to the sulphate content in the mixing water; and C_m is the cement content with respect to the total solid mass. Based on a regression analysis of the experimental values taken from direct shear tests (DSTs) reported in (Donovan 1999; Ghirian and Fall 2014; Koupouli et al. 2016), M_{s1} =-9.6, M_{s2} =724.3, M_{s3} =-4.553, M_{c1} =9507 kPa and M_{c2} =3.2 in this study. As shown in Figure 5.73, the predicted cohesion is in good agreement with the experimental value (R^2=0.92) reported by Cui and Fall (2016a) and Sargeant (2008). Moreover, as demonstrated in Eq.(5.50), the effect of the mixture recipe (cement content), sulphate content in the tailings and mixing water, and binder hydration are incorporated to determine CTB cohesion. In addition, due to the temperature dependence of binder hydration (see Eq. (5.49)), the effect of the thermal process is taken into account for determining CTB cohesion.

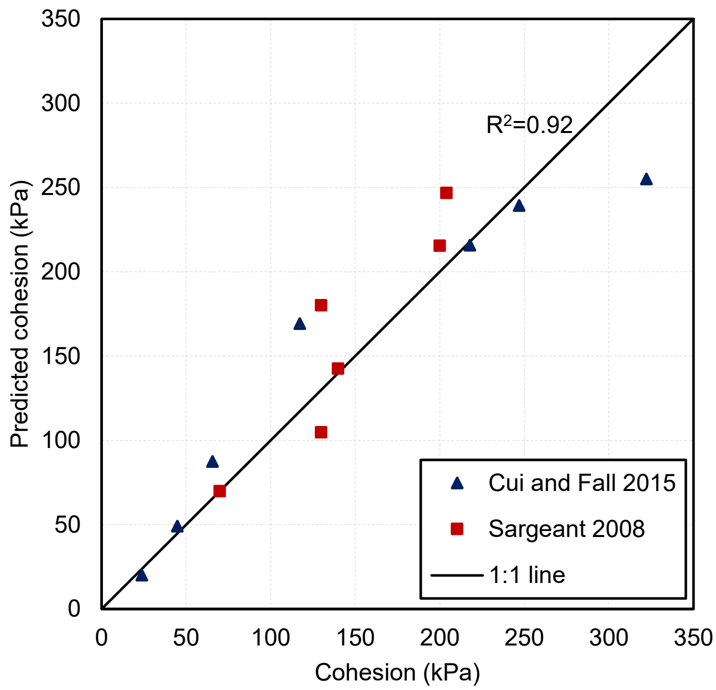

Figure 5.73. Experimental versus predicted values of cohesion

Similar to the changes in cohesion, it has been found that the internal friction angle can change with curing time (i.e., progression of binder hydration) (Nasir and Fall 2008; Veenstra 2013). To evaluate the variations of the internal friction angle, the following predictive function is proposed:

$$\phi_B(\xi) = \left[\exp(N_0 S_T)\right] \cdot \left(N_1 \xi^{N_2} + N_3 \xi\right) \tag{5.51}$$

where N_i is a fitting constant (i =0 to 3) which can be determined through regression analysis on the experimental values of DSTs on CTB samples with different curing times. Based on the reported data of the DSTs (Veenstra 2013; Koupouli et al. 2016), N_0 =-0.33, N_1 =-176.9°, N_2 =2 and N_3 =174.2° are adopted in this study. A comparison between the experimental and predicted values of the internal friction angle is presented in Figure 5.74. It can be seen that there is a fairly good agreement between the predicted results and measured data reported by Cui and Fall (2016a), Rankine and Sivakugan (2007), and Fall and Nasir (2010) (R^2=0.85).

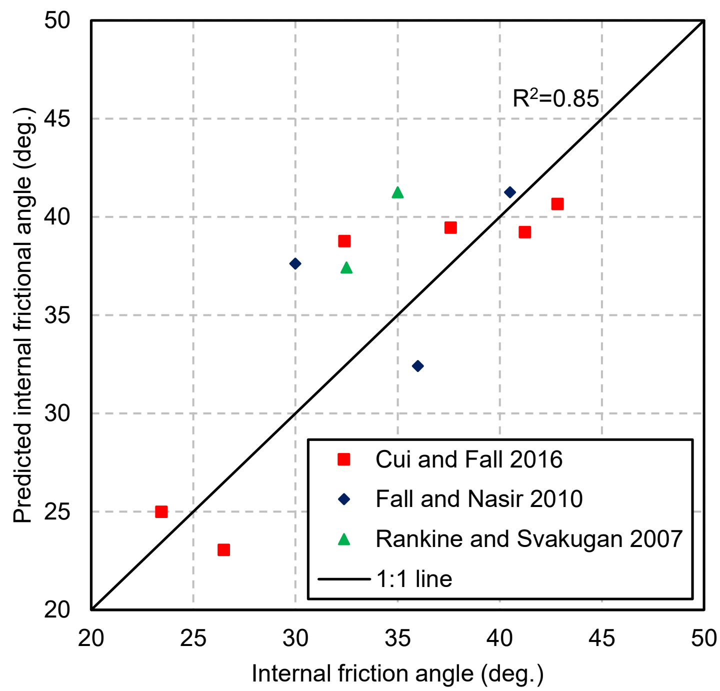

Figure 5.74. Experimental versus predicted values of internal friction angle

To evaluate the contribution of the PWP to the changes in CTB strength, the bulk moduli K_b and K_s in Eq.(5.48) are required. The bulk modulus of the solid phase K_s depends on the type of tailings. The bulk modulus of the porous media K_b can be directly measured through isotropic compression testing (Luo et al. 2015) or determined by using the elastic modulus E and Poisson's ratio υ of CTB (i.e., $K_b = E/\left[3(1-\upsilon)\right]$). In this study, the latter is adopted to describe the changes in K_b. Previous studies on the stress-strain relation in CTB (Fall et al. 2007; Rankine and Sivakugan 2007; Ghirian and Fall 2014) found that the sulphide and cement contents, void ratio and degree of binder hydration have significant impacts on elastic modulus changes. Hence, the following equation is proposed to characterize the variations of E :

$$E = \left[\exp\left(f_{E0} S_T\right)\right]\left(v_1 E_T + v_2 E_{u\_p}\xi\right)\left\{\left[f_{E1}\left(\frac{1}{1+e}\right)^{f_{E2}\xi^{f_{E3}}}\right] \Big/ \left[1+f_{E4}\left(\frac{e_0}{1+e_0}\right)\right]\right\} \quad (5.52)$$

where f_{Ei} is a fitting constant of the elastic modulus (i =0 to 4); v_1 and v_2 respectively refer to the volume ratio of tailings and ultimate volume of cement paste relative to the total volume of the solid phase; E_T and E_{u_p} respectively represent the elastic modulus of the tailings, and the ultimate value of the elastic modulus of the cement paste at complete hydration; e and e_0 denote the void ratio and initial void ratio of the CTB, respectively. The variations in the void ratio e of CTB are controlled by the consolidation process. To predict the volume change and the resultant void ratio, Cui and Fall (2016c) developed a multiphysics model on the consolidation process which is incorporated into the present study. More details on this model can be found in (Cui and Fall 2015b; 2016c). The five fitting constants f_{Ei} can be obtained through a regression analysis on the experimental data of E from the UCS tests of the CTB considered. In this study, the experimental data reported by Fall et al. (2007) and Ghirian and Fall (2014) are used to determine the fitting constants. Correspondingly, f_{E0} =-5.2, f_{E1} =177.5, f_{E2} =4.363, f_{E3} =-1.047 and f_{E4} =3000 are adopted in this study. Moreover, E_{u_p} can be determined by using a regression analysis on the experimental values of the elastic modulus of cement paste reported by Janotka (2001), Lura et al. (2003) and Ye et al. (2004). Correspondingly, E_{u_p} =28.49 GPa is obtained in this study. In addition, the volume ratio v_1 and v_2 can be derived from a previous study on CTB conducted by Cui and Fall (2015a):

$$v_1 = \frac{\left(1/C_m - 1\right) v_{tailings}}{\left(w/c\right) v_w + v_c + \left(1/C_m - 1\right) v_{tailings} - \left(2v_w - v_{ch-w} - v_{ab-w}\right) R_{n-w/hc} \xi}$$

$$v_2 = \frac{\left[v_c + \left(v_{ch-w} + v_{ab-w}\right) R_{n-w/hc}\right] \xi}{\left(w/c\right) v_w + v_c + \left(1/C_m - 1\right) v_{tailings} - \left(2v_w - v_{ch-w} - v_{ab-w}\right) R_{n-w/hc} \xi} \quad (5.53)$$

With

$$R_{n-w/hc} = 0.187 x_{C_3S} + 0.158 x_{C_2S} + 0.665 x_{C_3A} + 0.2130 x_{C_4AF}$$

where v_w , v_c , $v_{tailings}$, v_{ch-w} and v_{ab-w} represent the specific volume (i.e., the inverse of density) of water, cement, tailings, chemically combined water and physically absorbed water, respectively. For the values of the specific volume, v_w , v_c , and $v_{tailings}$ are constant when the mixture recipe is determined. Moreover, a previous study on cement paste (Brouwers 2004) proved that v_{ch-w} =0.72 cm^3/g and v_{ab-w} =0.90 cm^3/g, and the specific volume of these two types of water does not change for all types of cement. $R_{n-w/hc}$ refers to the mass fraction of the chemically combined water and hydrated cement, and x_i stands for the mass fraction of the clinker compositions of cement (i =C_3S, C_2S, C_3A and C_4AF). The good agreement (R^2=0.85) between the experimental values of the elastic modulus reported by Ghirian and Fall (2016a) and A. Wu et al. (2016), and prediction results validates the predictive ability of the elastic modulus (i.e., Eq.(5.52)) proposed in this study.

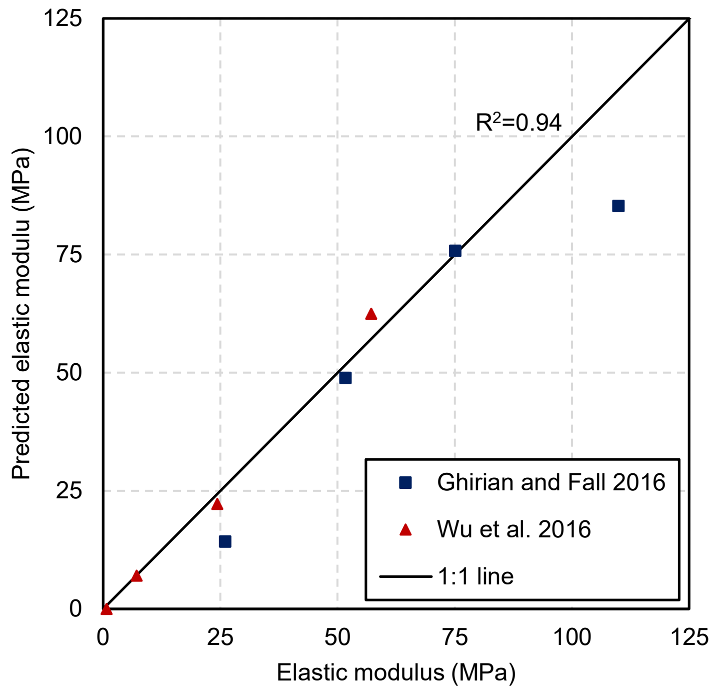

Figure 5.75. Experimental versus predicted values of elastic modulus

Apart from the elastic modulus E (see Eq.(5.52)), the Poisson's ratio υ is also important for determining the bulk modulus K_b. Previous experimental studies on the Poisson's ratio of CTB (Abdelaal 2011) and cement paste (Boumiz et al. 1996; Bittnar 2006) observed that both binder hydration and cement content can affect the changes in υ. Hence, the following predictive function is developed to describe the effect of the degree of binder hydration and cement content on υ:

$$\upsilon = 0.5\exp\left(N_{\upsilon 1} C_m^{N_{\upsilon 2}} \xi\right) + N_{\upsilon 3} \xi^{N_{\upsilon 4}} \exp\left(N_{\upsilon 5} C_m^{N_{\upsilon 2}} \xi^{N_{\upsilon 6}}\right) \quad (5.54)$$

where $N_{\upsilon i}$ denotes the fitting parameters (i =1 to 6), which are influenced by the type of CTB. Based on a regression analysis on the measured υ reported in (Galaa et al. 2011), $N_{\upsilon 1}$ =-0.21, $N_{\upsilon 2}$ =0.02, $N_{\upsilon 3}$ =-15000, $N_{\upsilon 4}$ =7, $N_{\upsilon 5}$ =-11.66 and $N_{\upsilon 6}$ =0.7 in the present study. Figure 5.76 shows that the measured values reported by Abdelaal (2011), Smilauer and Bittnar (2006) and Veenstra (2013) are well captured by the developed predictive function (Eq. (5.54)) and the coefficient of determination is 0.85.

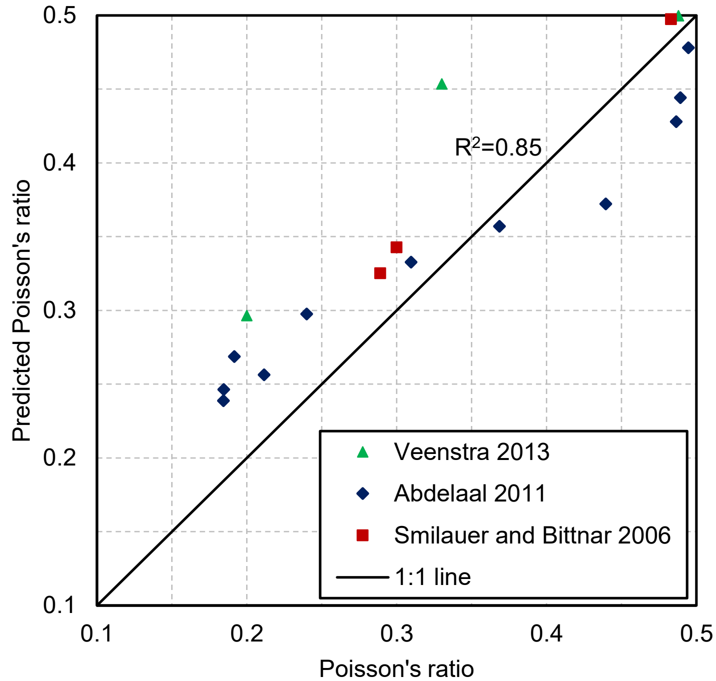

Figure 5.76. Experimental versus predicted values of Poisson's ratio

To predict the CTB strength, four material parameters $D_{\alpha 1}$, $D_{\alpha 2}$, $D_{\alpha 3}$ and $D_{\alpha 4}$ in the hardening and softening parameters $\alpha_{D-P}(\xi,\kappa)$ should be determined as well. As already discussed in Section 5.5.3 Mathematical Formulation, the hardening/softening behavior of CTB becomes more obvious with curing time, which indicates that the four material parameters will change with the progression of binder hydration. To describe the effect of the binder hydration on the hardening/softening behavior, the following predictive functions developed by Cui and Fall (2016a) are adopted in this study.

$$\begin{aligned} D_{\alpha 1} &= R_{\alpha 1}\xi^{R_{\alpha 2}} + R_{\alpha 3} \\ D_{\alpha 2} &= R_{\alpha 4}\xi^{R_{\alpha 5}} + R_{\alpha 6} \\ D_{\alpha 3} &= R_{\alpha 7}\xi^{R_{\alpha 8}} + R_{\alpha 9} \\ D_{\alpha 4} &= R_{\alpha 10}\xi^{R_{\alpha 11}} + R_{\alpha 12} \end{aligned} \tag{5.55}$$

where $R_{\alpha i}$ is a fitting constant (i =1 to 12) and depends on the type of CTB. $R_{\alpha 1}$=-0.05, $R_{\alpha 2}$ =4.178, $R_{\alpha 3}$ =0.071, $R_{\alpha 4}$ =-200, $R_{\alpha 5}$ =10, $R_{\alpha 6}$ =360.5, $R_{\alpha 7}$ =832.3, $R_{\alpha 8}$ =3, $R_{\alpha 9}$ =110, $R_{\alpha 10}$ =260.1, $R_{\alpha 11}$ =3.5 and $R_{\alpha 12}$ =80, as suggested by Cui and Fall (2016a) are adopted in this study.

It is important to point out that the model on CTB strength (i.e., Eq.(5.48)) and predictive function for each model parameter provide a general means to simulate the changes in backfill strength because each model parameter can change with the mixture recipe, tailings type (especially the sulphide content), and binder hydration. Moreover, as demonstrated in Eq.(5.49), the binder hydration model fully considers the effect of the mixture recipe, curing temperature and curing time. Therefore, the resultant model on CTB strength and the related predictive functions of the model parameters can be used for any type of tailings if the mixture recipe and curing conditions can be specified. The validation of the developed model on strength will be further discussed in the following section.

5.5.5. Model validation

To validate the predictive ability of the developed multiphysics model on CTB strength, a series of case studies were examined at both the laboratory and field scales. The developed model was implemented into a finite element method (FEM) code (Comsol 2015). Moreover, to assess the sensitivity of the developed model to curing conditions including curing time and initial CTB temperature, the authors also performed a series of laboratory experiments including monitoring the temperature and suction changes in CTB and related measurements of UCS values of CTB with different curing times and initial temperatures.

It should be noted that there are two ways to apply the developed model on CTB strength. First, the multiphysics model on strength (i.e., Eq.(5.48)) can be directly used to predict CTB strength if the mixture recipe, PWP, pore-air pressure and temperature are given for the CTB samples. Otherwise, as already mentioned in Section 5.5.4 (i.e., Determination of Model Parameters), the fully coupled THMC model (Cui and Fall 2015a) and multiphysics model on consolidation (Cui and Fall 2016c) can be used to predict the pore pressure and temperature changes in CTB. In this study, the latter is adopted for the following case study and model application.

5.5.5.1. Case Study 1-Changes to CTB strength with different initial temperatures

Due to changes in geographical locations (e.g., warm to permafrost regions), underground mine depth, rock mass conditions and seasonal changes, the prepared fresh CTB may have different initial temperatures (Célestin and Fall 2009; Nasir and Fall 2010). Moreover, previous studies have shown that CTB strength can considerably change at the early ages (Belem et al. 2000; Fall et al. 2015; Cui and Fall 2016b). Therefore, to study the short-term changes in CTB strength under different initial temperatures, a laboratory monitoring and testing program is conducted in this study.

For the laboratory experiment, CTB samples were prepared with three different initial temperatures of 5°C, 25°C, and 35°C. The mixture recipe for preparing the CTB samples is provided in Table 5.12.

Table 5.12. Mixture recipe for preparation of CTB samples

Cement type	Cement content (wt.%)	Mixing water	W/C ratio	Tailings type	Mixing time (mins)
Portland Cement Type I	4.5	Tap water	7.6	Ground silica tailings	7

wt.%: weight percentage of cement to total solid weight; W/C ratio: water-to-cement ratio

After mixing, the fresh CTB with different initial temperatures was poured into a cylindrical molds (10 cm in diameter × 20 cm in height) in the laboratory. To imitate the slow rate of heat exchange between the CTB and rock mass in a stope (Wang and Fall 2014), a glass wool blanket with a thickness of 50 mm was used to cover the cylinder mold. The corresponding properties of the adopted thermal insulation material of the glass wool blanket are listed in Table 5.13.

Table 5.13. Properties of thermal insulation material

Thermal conductivity W/(m K)	Heat capacity J/(kg K)	Density kg/m3
0.035	840	30

Then, the CTB samples with different curing times (including 1, 3 and 7 days) were used to investigate the development of strength. When the target curing time was reached, the CTB samples were removed from the cylinder mold and trimmed into standard cylindrical specimens that were 50 mm in diameter and 100 mm in height. Then, UCS testing was performed on them in accordance with ASTM C39. To ensure the repeatability of the testing results, three samples were tested for each curing time and each initial temperature. Meanwhile, to further study the changes in strength and related influential factors, the suction and temperature changes were monitored (see Figure 5.77). Specifically, suction meters (Model: MPS-2; Decagon) and temperature sensors (Model: 5TE; Decagon) were adopted to record the suction and temperature changes in the CTB samples.

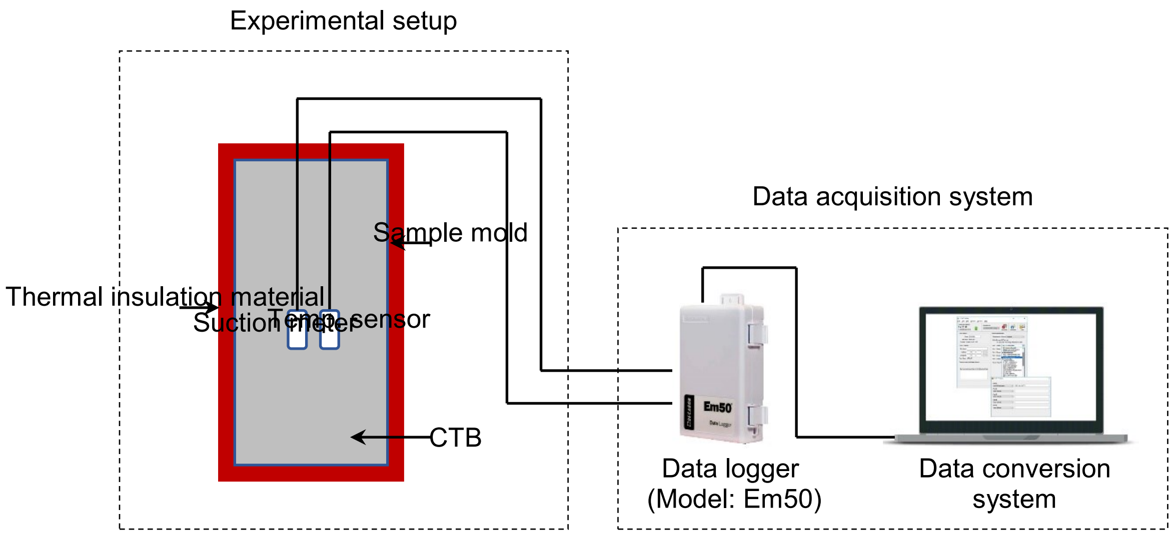

Figure 5.77. Schematic diagram of experimental setup to test CTB strength under different initial temperatures

The developed model was then implemented with COMSOL to predict the CTB strength, and an axisymmetric geometry model was adopted to represent the cylindrical mold and thermal insulation material (see Figure 5.78). The adopted initial values and boundary conditions are provided in Table 5.14**.**

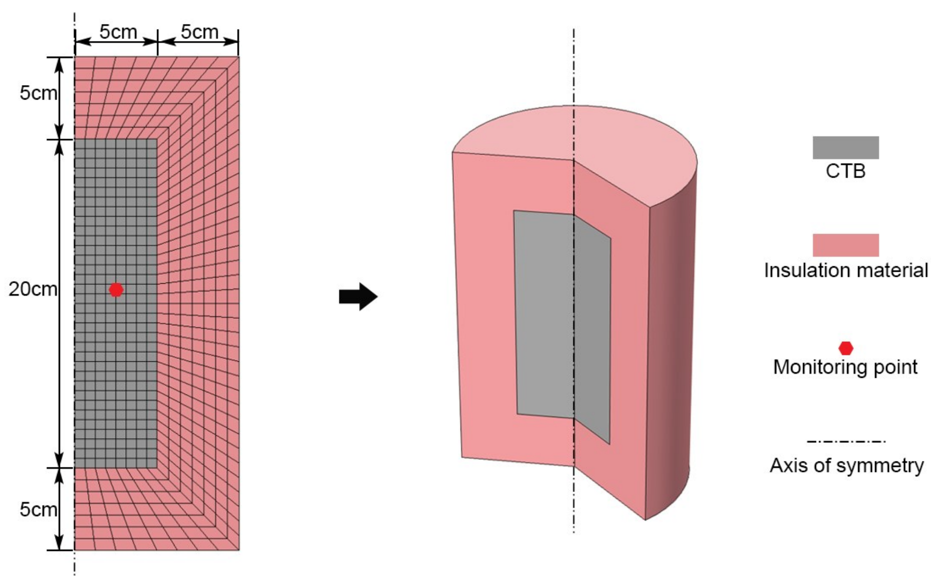

Figure 5.78. Mesh and geometry of simulated cell test

Table 5.14. Initial values and boundary conditions in Case Study 1

Parameter	Value
Mechanical component	
Top surface	Free
Lateral sides	Roller
Bottom side	Fixed
Volume force	Gravity
Hydraulic component	
Surrounding surfaces	No flow
Volume force	Gravity
Initial value	Hydraulic head=0
Thermal component	
Surrounding surfaces (°C)	22
Initial temperature (°C)	5, 25 and 35

A comparison of the predicted CTB strength and measured values is presented in Figure 5.79. It can be observed that (1) as expected, the curing time plays a significant role in changes to the CTB strength. As the curing time increases, a higher value of the strength is obtained, mainly because, as mentioned earlier, the bonding strength will progressively improve with the precipitation of the hydration products between the tailings particles. Consequently, CTB strength demonstrates an increasing trend with curing time. However, it should be noted that the time rate of change of CTB strength decreases with curing time, which is attributed to the decrease in the rate of hydration with curing time. In this regard, the PWP changes (Figure 5.80a) in the CTB can further prove the reduction of the rate of binder hydration with time. As can be seen in Figure 5.80b, both the simulated and monitored PWP demonstrate a reduction with curing time. However, the rate of change of the PWP (i.e., the curved slope) becomes smaller with time. Since water drainage and evaporation on the top surface of the CTB sample are not allowed in this cell test, the resultant variation of the PWP in the CTB sample is controlled by the pore-water consumption caused by binder hydration (i.e., self-desiccation process). Therefore, the changes in the PWP are directly associated with the variations in the rate of hydration in the CTB, namely a decrease in rate of hydration occurs with curing time, (2) both the simulated results and measured values indicate that the initial CTB temperature can affect the CTB strength, especially at the very early ages. This is due to the temperature dependence of the rate of binder hydration (Cui and Fall 2017). Specifically, the different initial temperatures can significantly affect temperature changes in CTB samples at the very early ages (especially the first two days, see Figure 5.80b). Correspondingly, the resulting degree of hydration of the CTB samples with different initial temperatures differ. As a result, a higher temperature can accelerate the development of binder hydration, and thus generate more hydration products (Nasir and Fall 2010; Wu et al. 2013). Therefore, higher CTB strength is observed in CTB with a higher initial temperature. In addition, as shown in Figure 5.80b, the temperature in all of the CTB samples gradually approaches room temperature (i.e., 22°C) after approximately two-days of curing. Correspondingly, as indicated in Figure 5.79a, the difference in CTB strength becomes smaller with reduced temperature differences. However, due to the contribution of the PWP to the CTB strength (see Figure 5.80a), there is still a small difference in the CTB strength among the CTB samples at the same room temperature even after two-days of curing, (3) it can be found that in Figure 5.79b, the changes to the CTB strength can be well captured by the developed model on strength (the coefficient of determination is 0.97). Therefore, the developed model can be used to predict the development of CTB strength with different curing times and initial temperatures.

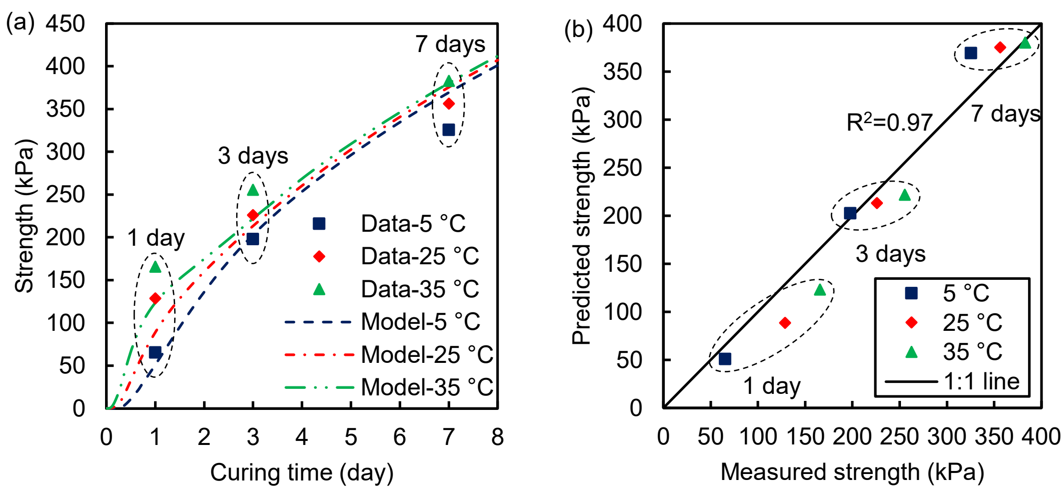

Figure 5.79. Comparison of predicted results and experimental values of true CTB strength: (a) changes to CTB strength with curing time, and (b) correlation between simulated results and measured values

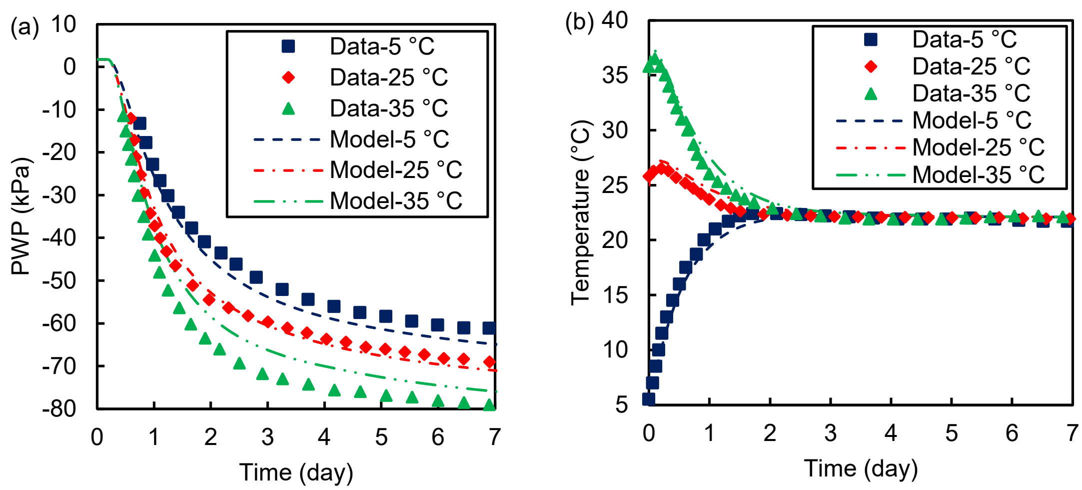

Figure 5.80. Comparison of predicted results and experimental values: (a) temperature, and (b) PWP.

5.5.5.2. Case Study 2- Changes to CTB strength with different sulphate contents

Due to the inhibition of cement hydration by sulphate ions (Li and Fall 2016), previous experimental studies (e.g., Fall and Benzaazoua 2005; Ercikdi et al. 2009; Fall and Pokharel 2010) on CTB have observed that the sulphate content in the mixing water has a significant effect on the development of CTB strength. To further validate the developed model for CTB materials with different sulphate contents, the experimental data reported in (Li and Fall 2016) were collected and then compared with the predicted results. The adopted mixture recipe and the design of the testing program for this experimental study are provided in Table 5.15 and Table 5.16, respectively.

Table 5.15. Mixture recipe in Case Study 2

Sulphate type	Sulphate concentration (ppm)	Cement content (wt%)	Cement type	W/C ratio
Ferrous sulphate ($FeSO_4 \cdot 7H_2O$)	0, 5000, 15,000 and 25,000	4.5	Portland Cement Type I	7.6

wt.%: weight percentage of cement to total solid weight; W/C ratio: water-to-cement ratio

Table 5.16. Testing program in Case Study 2

Curing time (days)	Testing time (days)	Curing temperature (°C)	Sample size (cm)
28	1, 3, 7 and 28	22	5(D)×10(H)

D: diameter; H: height.

Simulation with the developed model was carried out based on the design of the testing program. An axisymmetric geometry model was adopted to simulate the CTB sample (see Figure 5.81), and the adopted initial values and boundary conditions were the same as those in Case Study 1.

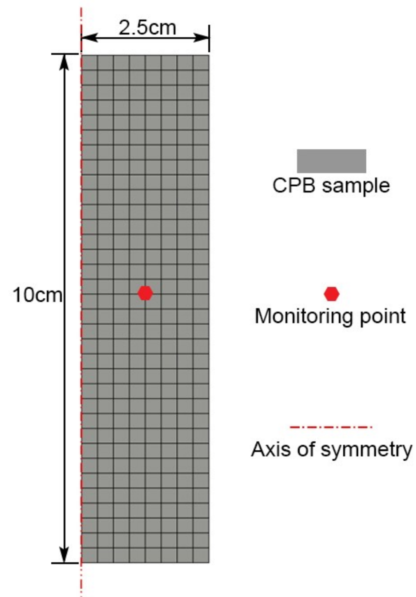

Figure 5.81. Mesh and geometry of simulated CTB sample for Case Study 2

Figure 5.82 is a comparison between the predicted results and measured values of CTB strength with different sulphate contents. As shown in Figure 5.82a, both the simulated results and measured values indicate that the sulphate content can significantly affect CTB strength. Specifically, with an increase in the sulphate content in the mixing water, the negative effects on CTB strength become more obvious. For example, compared with the values of CTB strength (677 kPa) obtained from the CTB control sample (i.e., sulphate content = 0 ppm) with a curing time of 28-days, the predicted CTB strength respectively reduces to 619 kPa for 5000 ppm of sulphate, 517 kPa for 15,000 ppm, and 431 kPa for 25,000 ppm. As mentioned, the reduction in CTB strength with increased sulphate content is due to the inhibition of the binder hydration by the sulphate ions. In addition, as can be seen in Figure 5.82b, an excellent agreement (R^2=0.98) is obtained between the experimental values and predicted results. Therefore, the developed model is able to accurately determine the effects of sulphate content on the development of CTB strength for the curing times considered in this study.

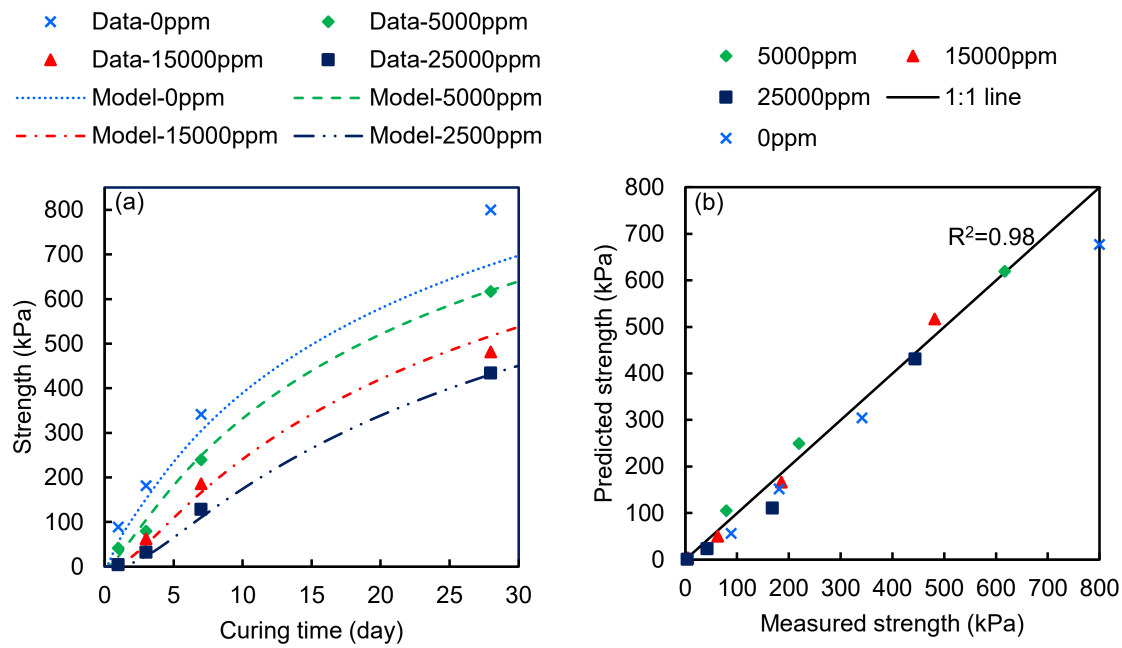

Figure 5.82. Effect of sulphate content on CTB strength: (a) changes to CTB strength with curing time; (b) correlation between predicted results and measured CTB strength values

5.5.5.3. Case Study 3-Long-term strength of CTB with various cement contents

As per the requirements of CTB design for mechanical stability and cost management, the binder content adopted in a backfilled stope may differ from one to another. To study the effects of cement content on the changes to CTB strength, extensive laboratory experiments have been carried out (e.g., Benzaazoua et al. 2004; Kesimal et al. 2005; Fall et al. 2008; Ercikdi et al. 2014). Therefore, to validate the predictive ability of the developed model for CTB with different cement contents, the laboratory experiment conducted by Belem et al. (2000) and the reported data are adopted in this study. Three different weight percentages of cement (including 3, 4.5 and 6 wt%) were considered in Belem et al. (2000). Details on the mixture recipe and the testing program are provided in Table 5.17 and Table 5.18, respectively.

Table 5.17. Mixture recipe adopted in Case Study 3

Cement type	Cement content (wt.%)	W/C ratio	Tailings type	Sulphur content of tailings (wt%)
Portland Cement Type I	3, 4.5 and 6	12, 8 and 6	Tailings from metal mine	16

wt.%: weight percentage of cement to total solid weight; W/C ratio: water-to-cement ratio

Table 5.18. Testing program in Case Study 2

Curing time (days)	Testing time (days)	Curing temperature (°C)	Sample size (cm)
112	14, 28, 56, 91 and 112	22	10(D)×20(H)

D: diameter; H: height.

It should be noted that, in this experiment, the fresh CTB was first poured into a sample mold with a diameter of 10 cm and height of 20 cm. Then, the CTB sample was taken out and trimmed into standard specimen size (5 cm (D)×10 cm (H)) for UCS testing. Therefore, an axisymmetric geometry is used to simulate the CTB sample (see Figure 5.83). The same boundary conditions as those of Case Study 1 are adopted.

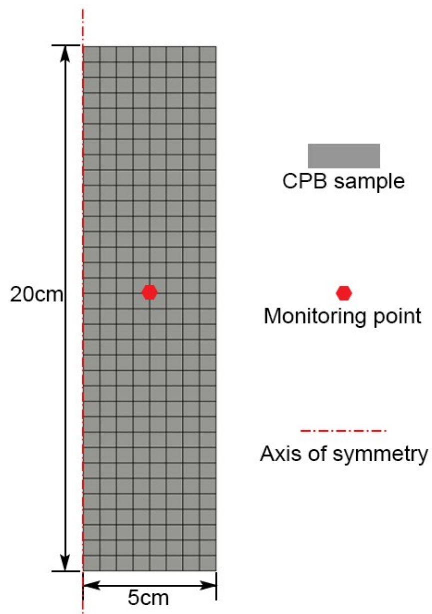

Figure 5.83. Mesh and geometry of simulated CTB sample in Case Study 3

A comparison between the predicted results and experimental values of CTB strength is presented in Figure 5.84. As can be seen in Figure 5.84a, the developed model on CTB strength is sensitive to the changes in cement content. For instance, compared with the predicted strength (410 kPa) of CTB with a cement content of 3% and curing time of 91-days, the simulated CTB strength is increased by approximately 50% for a cement content of 4.5% (strength=616 kPa), and by around 100% for a cement content of 6%

(strength=821 kPa). Therefore, the developed model can simulate the improvements in CTB strength with increased cement content. Moreover, it is apparent by looking at Figure 5.84a that the time rate of change of CTB strength decreases with curing time regardless of the cement content, which is consistent with the findings obtained in Case Study 1. The corresponding reason has been discussed in Section 5.5.5.1. In addition, the good agreement between the simulated results and measured values (see Figure 5.84b) proves the predictive ability of the developed model for long-term CTB strength with different cement contents.

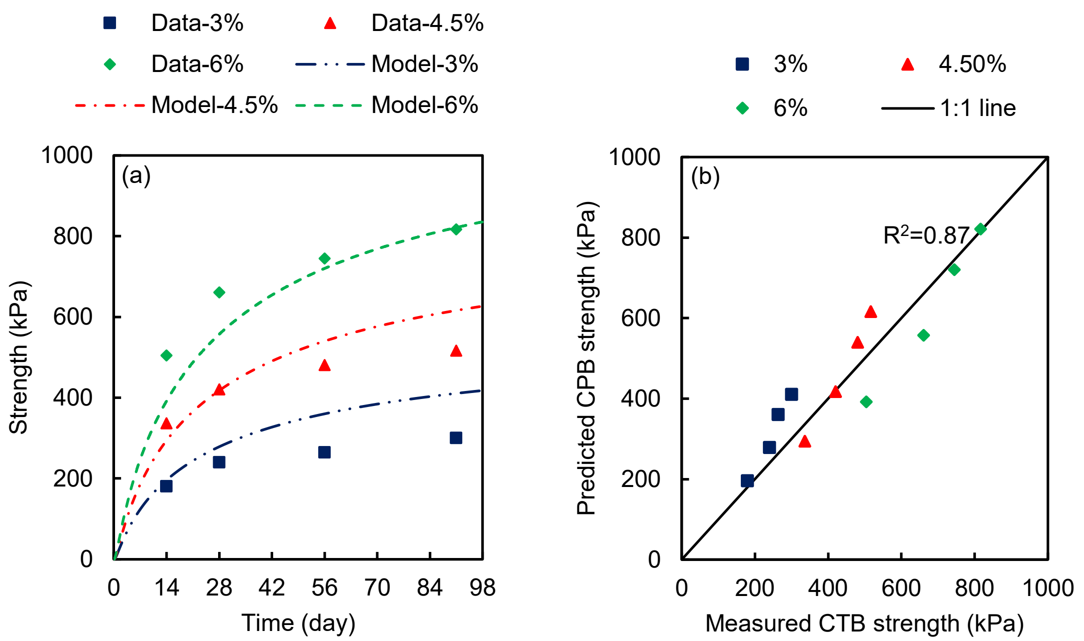

Figure 5.84. Effect of cement content on long-term CTB strength: (a) changes to CTB strength with curing time, and (b) correlation between predicted results and measured CTB strength values

5.5.6. Model application

As demonstrated in Section 5.5.5, the developed model is able to accurately evaluate the changes to CTB strength with different curing ages and mixture recipes. Therefore, a series of applications with the developed model are carried out in this study to investigate the changes in CTB strength in the field under various conditions, including different stope geometries, inclination angles, backfilling strategies and filling rates. The adopted initial values and boundary conditions are listed in Table 5.19.

Table 5.19. Input parameters, initial values and boundary conditions of control CTB and rock mass

Parameter	Value
Backfill	
Stope size (m)	8(W)×16(H)
Barricade size(m)	4(W)×4(H)
Stope inclination angle (°)	90
Cement content (wt%)	Residual fill: 4.5, and plug fill: 7
w/c ratio	7.6
Initial void ratio	1
Filling rate (m/h)	0.5
Filling strategy	2-stages with 1-day plug
Rock mass	
Density (kg/m3)	2500
Young’s modulus (GPa)	30
Poisson’s ratio	0.3
Thermal conductivity (W/m K)	3.9
Heat capacity (J/Kg K)	790
Mechanical component	
Top surface	Free
Lateral sides	Roller
Bottom side	Fixed
Volume force	Gravity
Hydraulic component	
Surrounding surfaces	No flow
Volume force	Gravity
Initial value	Hydraulic head=0
Thermal component	
Surrounding surfaces (°C)	25
Initial temp. (°C)	25

Moreover, a control stope with dimensions of 8 m (W)×16 m (H) was used as a reference. The barricade structure (4 m (W)×4 m (H)) is located at the base of the stope (see Figure 5.85). All of the numerical investigations were carried out by specifically modifying the control stope. The monitored point is located at the bottom of the stope. Moreover, to demonstrate the influence of the fill height on changes to the CTB strength, the middle of the CTB mass (i.e., 8 m away from the stope base) was examined, and a relevant discussion is presented in Section 5.5.6.1.

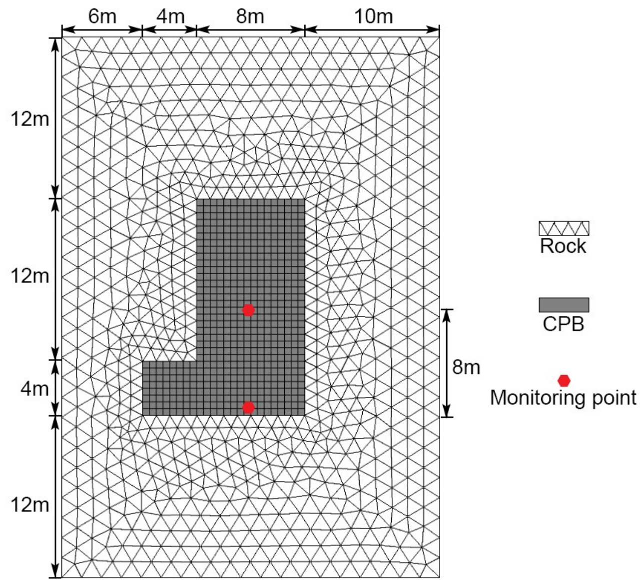

Figure 5.85. Mesh and geometry of control stope

In addition, it should be noted that the investigated CTB strength in the following subsection refers to the true CTB strength, namely the effects of coupled THMC processes that occur in CTB are fully considered.

5.5.6.1. Effect of stope geometry

Due to the different stoping methods and mining plans, the stope geometry may vary from one stope to another. To investigate the effect of stope geometry on the development of CTB strength, a range of stope sizes: 5 m (W)×10 m (H), 8 m (W)×16 m (H), and 10 m (W)×20 m (H), are considered in this study. Moreover, the same filling strategy (i.e., filling in 2 stages with 1-day plug), filling rate (0.5 m/h), barricade size, boundary and initial boundary conditions (see Table 5.19) are adopted for these three investigated stope sizes.

Figure 5.86 shows the effect of the stope geometry on the strength development in CTB. The CTB strength is represented with normalized strength (i.e., CTB strength at any time/CTB strength obtained for 160-day CTB). Here, it is assumed that after 160 days, there is no significant increase in CTB strength with curing time, namely, the 160-day strength is the ultimate CTB strength. From Figure 5.86, it can be seen that (1) CTB strength along the center line of the stope is higher relative to that near the surrounding rock walls, which is consistent with the findings in a previous study on CTB strength (Nasir and Fall 2010) Moreover, the non-uniform distribution of CTB strength becomes more obvious with time. This is partly because of the PWP changes in the CTB due to the self-desiccation process. With progression of pore-water consumption caused by binder hydration, and water drainage through the barricade, the PWP will change with time and thus affect the development of the CTB strength. Moreover, as discussed earlier in Case Study 1, the CTB strength is sensitive to variations in temperature. The temperature changes are determined by the heat transfer between the CTB and rock mass, and heat generated by binder hydration. As a result, the changes in temperature can further contribute to non-uniform distribution of CTB strength in fill mass. (2) The stope geometry has a significant effect on the development of CTB strength. Specifically, higher strength is obtained in a larger stope at a given curing age, which is consistent with the results of previous study on CTB strength (Nasir and Fall 2010). This is mainly attributed to more heat generated within larger CTB mass, which can further leads to the increase in temperature, and thus the development of CTB strength.

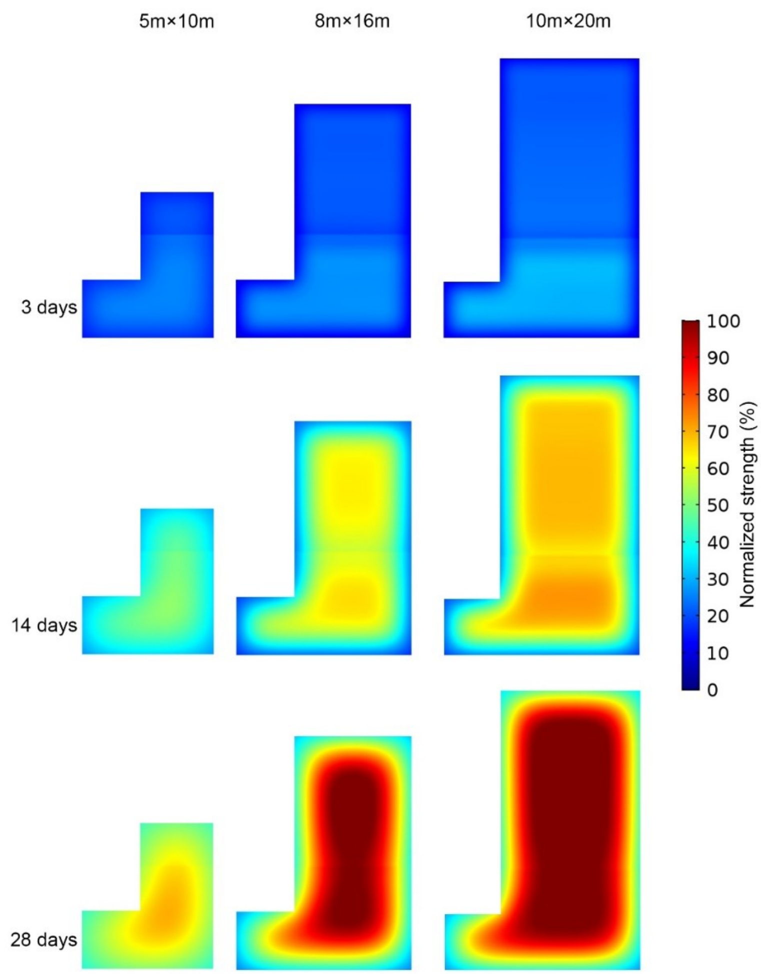

Figure 5.86. Effect of stope size on spatial distribution of CTB strength (Cement content 100 kg/m^3 i.e., 9.6wt%)

However, it should be noted that the effect of stope size on the strength is also a function of the binder content of the CTB considered. For low binder content, Figure 5.87 reveals that the CPB strength for smaller stope is higher than the strength of larger stope (higher height). This is because with the decrease in binder content, the amount of heat released by binder hydration will be reduced, which, in turn, weakens the effect of thermal process on the development of CTB strength. Moreover, the pore-water loss induced by binder hydration (i.e., self-desiccation process) and barricade drainage is similar for these three case. Consequently, smaller stope with lower total stress can result in higher effective stress with respect to similar changes in PWP. Therefore, higher strength is observed in small stope with the decrease of cement content. Therefore, the obtained results further verify that a reliable evaluation of in-situ CTB strength requires an evaluation of the multiphysics processes in the field (i.e., the modelling and simulation of field behavior of CTB).

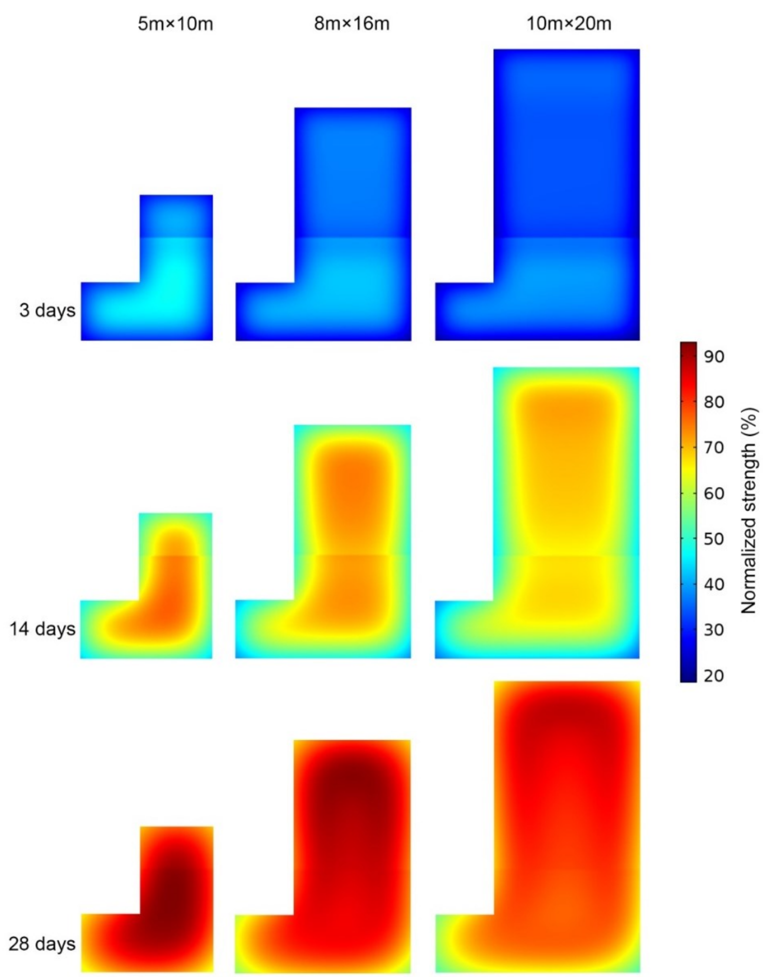

Figure 5.87. Effect of stope geometry on spatial distribution of CTB strength (Cement content 60.358 kg/m^3 i.e., 4.5wt%)

Moreover, to demonstrate the effect of the fill height on the variations in CTB strength, a comparison of the prediction results at the bottom and middle of the control CTB mass is plotted in Figure 5.88. The obtained results indicate that (1) at the very early ages, higher strength is formed at the bottom of the CTB mass compared to the middle of the CTB mass. This is because relatively fresh CTB is found higher on the filled stope due to the backfilling operation which is continuous or done by sequences. As a result, CTB found lower on the filled stope requires a longer curing time compared to that found higher on the stope. Hence, binder hydration can advance more at the bottom of the CTB, which contributes to the further enhancement of CTB strength; (2) after around 4-days of curing, the CTB strength at the middle of the CTB mass progressively increases as opposed to that at the bottom of the CTB mass. This can be attributed to the dissipation of the PWP caused by water drainage through the barricade and water consumption caused by binder hydration. With pore-water loss, a lower PWP appears at the middle of the CTB mass and thus contributes to the improvement of the CTB strength to a larger extent. Therefore, greater CTB strength gradually develops in the middle of the CTB mass with curing time.

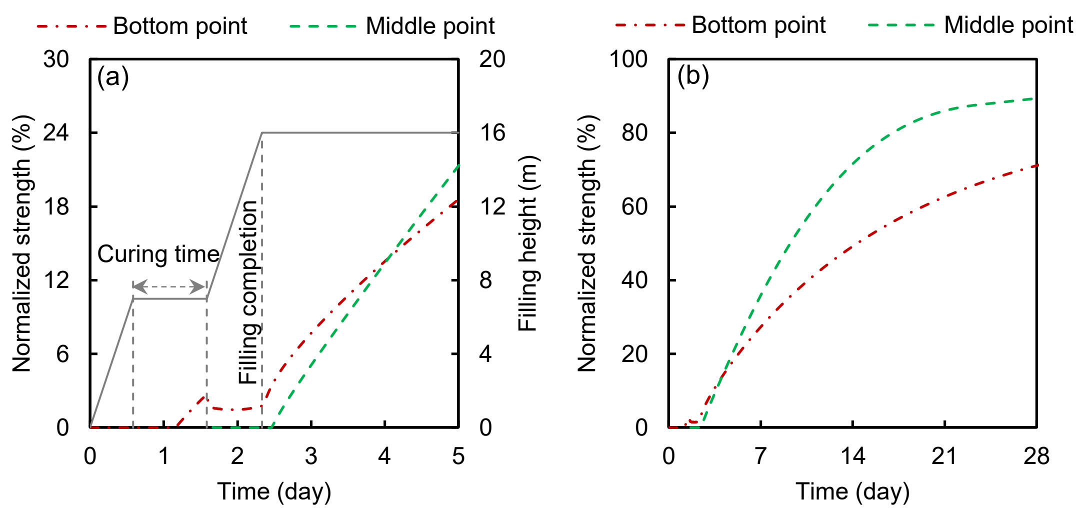

Figure 5.88. Effect of fill height on PWP changes at bottom of CTB mass: (a) filling stage, and (b) post-filling stage

5.5.6.2. Effect of inclination angles of stope

Due to influence of ore bodies, the resultant stopes may have various inclination angles (Li and Aubertin 2009; Cui and Fall 2017). Hence, the effect of inclined stopes on strength development is investigated in the present study. The inclination angles of the control stope were respectively set to 90°, 70° and 50°. Figure 5.89 shows the prediction results of CTB strength for these three inclination angles. It can be seen that the inclination angle has a very limited effect on the changes to the CTB strength and its magnitude. However, for the spatial distribution of CTB strength (see Figure 5.90), inclined stopes (i.e., Figure 5.90a and Figure 5.90b) can form a larger area with higher CTB strength compared to a vertical stope (Figure 5.90c). This is because the selected stopes have the same fill height and stope width. Consequently, the inclined stope has a relatively long hanging wall and foot wall, which can further contribute to the heat transfer between the CTB and surrounding rock. Due to the effect of geothermal gradient, the temperature of surrounding rock can be higher than the initial temperature of CPB prepared on the ground surface. As a result, relatively large amount of heat can be transferred to the CTB and thus a larger area with higher CTB strength is obtained in the inclined stope. Therefore, an inclined stope is more favorable for CTB stability, which is agreement with the conclusions in Cui and Fall (2016d).

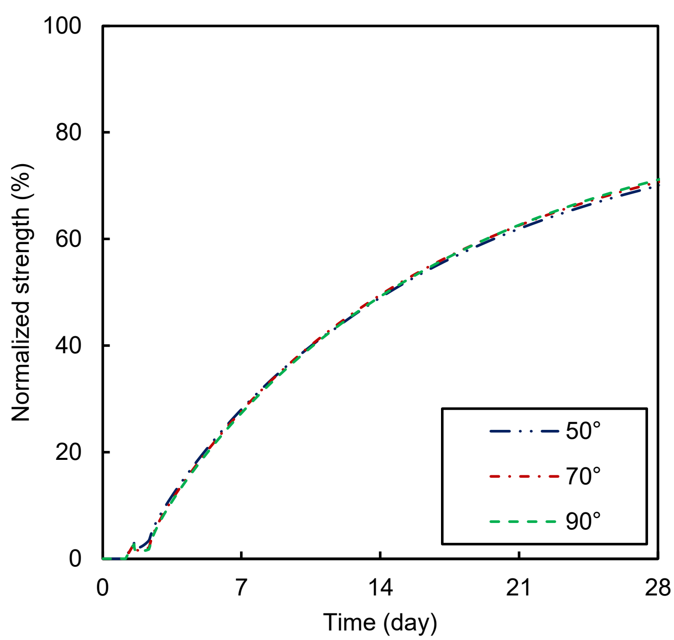

Figure 5.89. Effect of inclination angle on changes to CTB strength at bottom of CTB mass

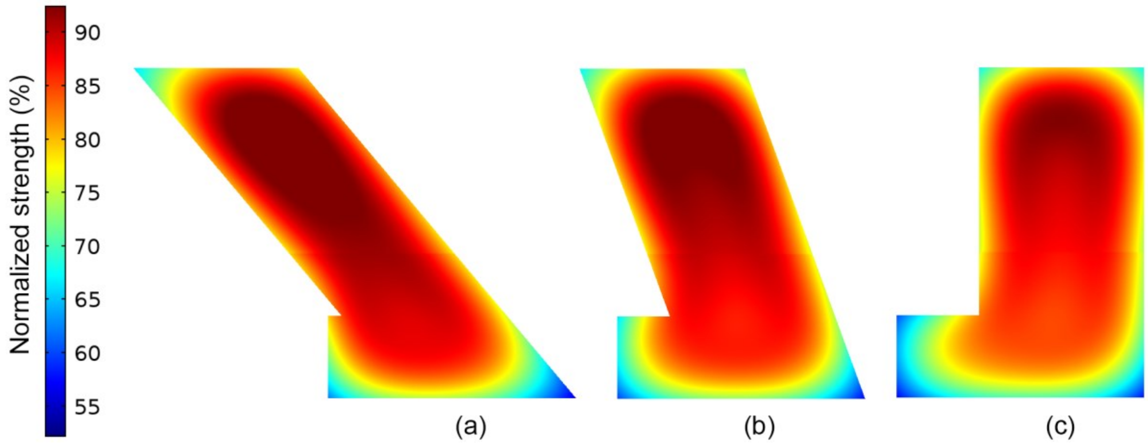

Figure 5.90. Effect of inclination angle on spatial distribution of strength of CTB with curing time of 28-days: (a) 50°; (b) 70°; and (c) 90°

5.5.6.3. Effect of backfilling strategy

Due to the differences in mining operations, CTB recipe and stope geometry, the adopted filling strategy (i.e., continuous filling or filling carried out in stages) may vary from one site to another in backfilling practices (Veenstra et al. 2011). For instance, filling operations carried out in two stages with a plug layer cured for one day or more are commonly adopted (Ghirian and Fall 2013). The adopted backfilling strategy can directly affect filling time and thus mine cycle and productivity. Therefore, it is important to investigate the effect of the filling strategy on the development of CTB strength. In this study, both continuous filling and filling carried out in stages with 1-day and 2-day plug layers are respectively investigated in the control stope. For these three cases, the adopted filling rate is 0.5 m/h. A comparison of the development of early-age strength in the control stope with the different filling strategies is presented in Figure 5.91. It can be observed that a higher CTB strength is obtained in the plug layer with longer curing time. Specifically, the plug normalized strength respectively reaches approximately 8% and 3% for the 1-day and 2-day plug layers, while there is no evident development of CTB strength for the continuous filling case. This is because filling operations carried out in stages allow a longer curing time of the CTB in the stope. Therefore, the binder hydration, heat transfer between the CTB and rock mass, water loss caused by the self-desiccation process and water drainage through the barricade are increased. Consequently, a higher CTB strength can be realized with filling operations carried out in stages with a longer curing time of the plug layer. The lower CTB strength at the early-ages associated with continuous filling could increase the cost of the barricade structure and the risk of CTB liquefaction (Abdelaal 2011), so improving CTB strength with a longer curing time of the plug layer is important for CTB stability. However, it should be noted that the filling operations carried out in stages with longer curing time of the plug layer will increase the total filling time and thus affects the mining cycle.

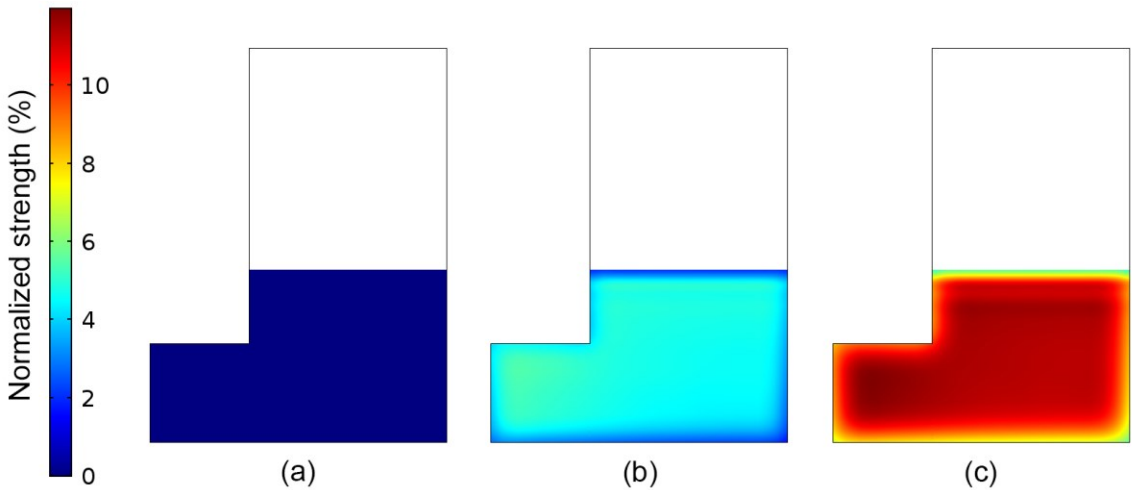

Figure 5.91. Effect of filling strategy on spatial distribution of early-age strength of CTB after curing of plug layer: (a) continuous filling (14 hours); (b) 1-day plug (38 hours); and (c) 2-day plug (62 hours).

5.5.6.4. Effect of filling rate

Apart from the filling sequences, the backfilling rate is another important factor which should be considered during CTB design. Changes in filling rates may result in different curing times for CTB material and thus affect CTB strength. In addition, similar to filling strategies, the filling rate also affects the mining cycle and productivity (Veenstra et al. 2011; Khaldoun et al. 2016). Therefore, an investigation of filling rates (including 1 m/h, 0.5 m/h, and 0.25 m/h) on the development of CTB strength is carried out in this study. A comparison of the CTB strength in a stope subjected to different filling rates is shown in Figure 5.92. It can be seen that, as expected, higher early-age strength is obtained in CTB with a slower filling rate. For example, after the rest period of the plug layer (i.e., 31 hours for 1 m/h, 38 hours for 0.5 m/h and 52 hours for 0.25m/h), the normalized CTB strength reaches approximately 1%, 3%, and 7%. Moreover, similar to the filling strategy, the effect of the filling rate also has significant impacts on the spatial distribution of early-age strength in the control stope (see Figure 5.93). As shown in Figure 5.93, higher CTB strength is formed with reduced rate of filling. This is because as discussed previously, slow backfilling process can result in longer curing time for a given filling height, and thus contribute to the development of CTB strength. As a result, the ability of a CTB structure to resist potential failures (e.g., barricade failure or CTB liquefaction) can be much improved.

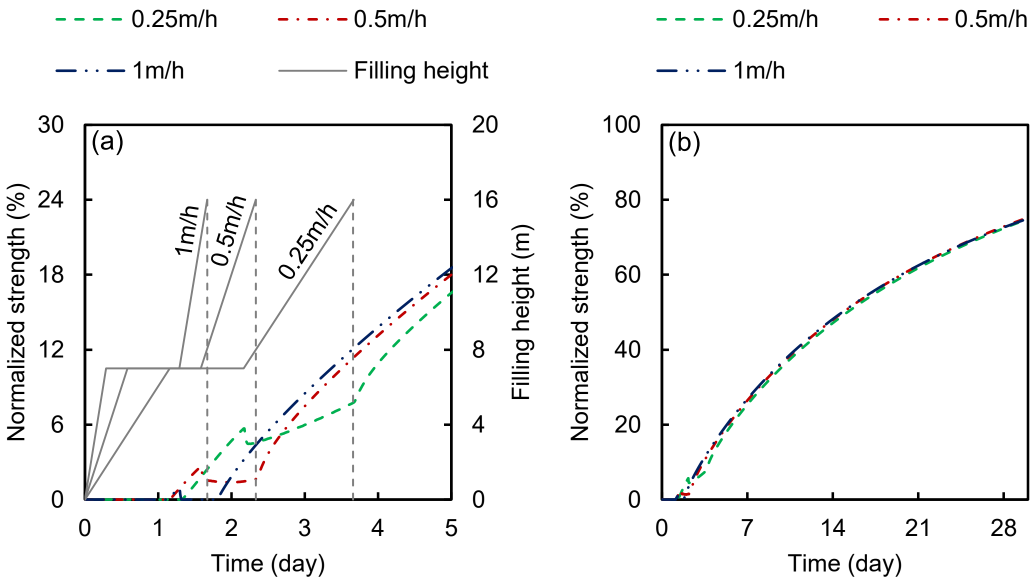

Figure 5.92. Effect of filling rate on changes to CTB strength: (a) filling stage, and (b) post-filling stage

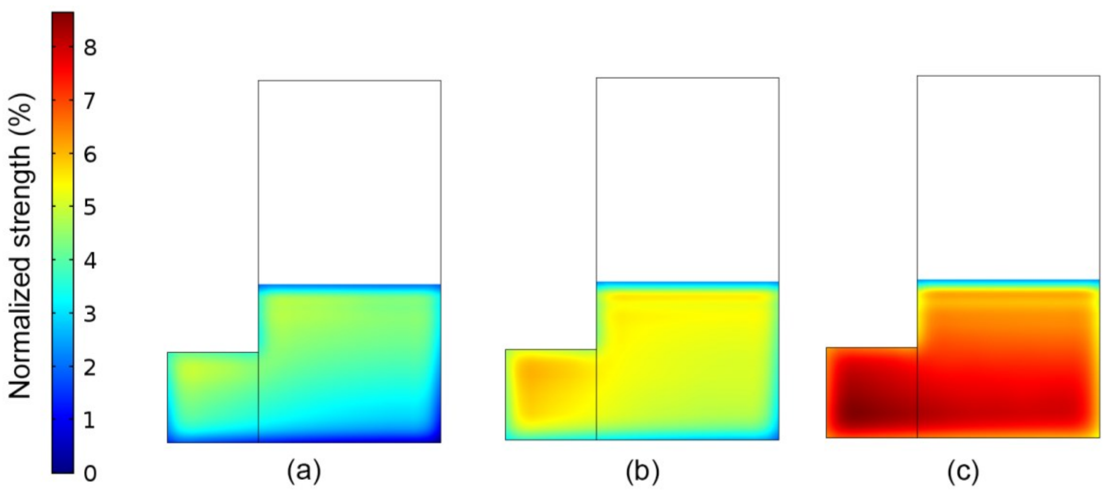

Figure 5.93. Effect of filling rate on spatial distribution of early-age strength of CTB after curing of plug layer: (a) 1 m/h (31 hours); (b) 0.5 m/h (38 hours); and (c) 0.25 m/h (52 hours).

5.5.7. Conclusions

In this study, a multiphysics model on CTB strength is developed to numerically simulate the development of CTB strength under the influence of coupled THMC processes. This developed model on CTB strength is coupled with a THMC model (Cui and Fall 2015a) and a multiphysics model on consolidation (Cui and Fall 2016c). Moreover, the effect of binder hydration, mixture recipe, tailings and mixing water (i.e., sulphate content) are fully considered for determining the material properties. The related model coefficients are determined with measurable parameters.

To validate the proposed model, the authors performed a laboratory monitoring and testing program to study the effects of the initial temperature on CTB strength. The good agreement between the prediction results and experimental values confirms the feasibility of the developed model. In addition, the model is further validated against experimental data reported in the literature. The results demonstrate not only the accuracy of the model for predictions, but also its sensitivity to the CTB temperature and mixture recipe (including the sulphate contents in the mixture water and cement content).

In terms of the model application, the obtained results demonstrate that the stope size, backfilling strategy and filling rate can significantly affect the development of in-situ CTB strength. Moreover, although the inclination angle has little influence on the amount of CTB strength, an inclined stope has a larger area with higher CTB strength which is more favorable for CTB stability. In addition, the developed model can well capture the effect of filling rate on the development of early-age strength in fill mass. Therefore, the developed multiphysics model on CTB strength can be used as a useful tool for an optimal design of CTB structures and reliable analysis of their mechanical stability.

5.5.8. References

Abdelaal, A. M. G. M. I. (2011). "Early age mechanical behavior and stiffness development of cemented paste backfill with sand." Ph.D. thesis, University of Toronto, Cananda.

Aldhafeeri, Z., and Fall, M. (2016). "Time and damage induced changes in the chemical reactivity of cemented paste backfill." *Journal of Environmental Chemical Engineering*, 4(4), 4038-4049.

Barnett, S., Soutsos, M., Millard, S., and Bungey, J. (2006). "Strength development of mortars containing ground granulated blast-furnace slag: Effect of curing temperature and determination of apparent activation energies." *Cem. Concr. Res.*, 36(3), 434-440.

Belem, T., Benzaazoua, M., and Bussière, B. (2000). "Mechanical behaviour of cemented paste backfill." *Proc., 53rd Canadian Geotechnical Conference*, Canadian Geotechnical Society, Montreal, QC, Canada, 373-380.

Belem, T., Benzaazoua, M., Bussière, B., and Dagenais, A. (2002). "Effects of settlement and drainage on strength development within mine paste backfill." *Proc., 9th International Conference, Tailings and Mine Waste*, 139-148.
Belem, T., El Aatar, O., Bussière, B., Benzaazoua, M., Fall, M., and Yilmaz, E. (2006). "Characterization of self-weight consolidated paste backfill." *Proc., the 9th Int. Seminar on Paste and Thickened Tailings*, Australian Centre for Geomechanics, Perth, Australia, 333-345.
Benzaazoua, M., Belem, T., and Bussiere, B. (2002). "Chemical factors that influence the performance of mine sulphidic paste backfill." *Cem. Concr. Res.*, 32(7), 1133-1144.
Benzaazoua, M., Fall, M., and Belem, T. (2004). "A contribution to understanding the hardening process of cemented pastefill." *Miner. Eng.*, 10.1016/j.mineng.2003.10.022, 17(2), 141-152.
Bittnar, Z. (2006). "Microstructure-based micromechanical prediction of elastic properties in hydrating cement paste." *Cem. Concr. Res.*, 36(9), 1708-1718.
Boumiz, A., Vernet, C., and Tenoudji, F. C. (1996). "Mechanical properties of cement pastes and mortars at early ages: evolution with time and degree of hydration." *Advanced Cement Based Materials*, 3(3), 94-106.
Brouwers, H. (2004). "The work of Powers and Brownyard revisited: Part 1." *Cem. Concr. Res.*, 34(9), 1697-1716.
Célestin, J. C. H., and Fall, M. (2009). "Thermal conductivity of cemented paste backfill material and factors affecting it." *Int. J. Min. Reclam. Environ.*, 23(4), 274-290.
Comsol (2015). "Comsol Multiphysics 5.1." <http://www.comsol.com>. (Sept. 20, 2016).
Cui, L., and Fall, M. (2015a). "A coupled thermo-hydro-mechano-chemical model for underground cemented tailings backfill." *Tunn. Undergr. Sp. Tech.*, 10.1016/j.tust.2015.08.014, 50, 396-414.
Cui, L., and Fall, M. (2015b). "Modeling and Simulation of the Consolidation Behaviour of Cemented Paste Backfill." *Proc., 2015 Comsol Conference*, Boston, MA, USA, 1-5.
Cui, L., and Fall, M. (2016a). "An evolutive elasto-plastic model for cemented paste backfill." *Comput. Geotech.*, 10.1016/j.compgeo.2015.08.013, 71, 19-29.
Cui, L., and Fall, M. (2016b). "Mechanical and thermal properties of cemented tailings materials at early ages: Influence of initial temperature, curing stress and drainage conditions." *Constr. Build. Mater.*, 10.1016/j.conbuildmat.2016.08.080, 125, 553-563.
Cui, L., and Fall, M. (2016c). "Multiphysics model for consolidation behaviour of cemented paste backfill." *Int. J. Geomech.*, 10.1061/(ASCE)GM.1943-5622.0000743, 040160771-0401607723.
Cui, L., and Fall, M. (2016d). "Simulation of self-desiccation process in cemented tailings backfill structure." *Int. J. Numer. Anal. Methods Geomech. (submitted)*.
Cui, L., and Fall, M. (2017). "Multiphysics modeling of arching effects in fill mass." *Comput. Geotech.*, 10.1016/j.compgeo.2016.10.021, 83, 114-131.
Doherty, J. P. (2015). "A numerical study into factors affecting stress and pore pressure in free draining mine stopes." *Comput. Geotech.*, 10.1016/j.compgeo.2014.10.001, 63, 331-341.
Donovan, J. G. (1999). "The effects of backfilling on ground control and recovery in thin-seam coal mining." Master thesis, Virginia Polytechnic Institute and State University, USA.
Ercikdi, B., Kesimal, A., Cihangir, F., Deveci, H., and Alp, İ. (2009). "Cemented paste backfill of sulphide-rich tailings: Importance of binder type and dosage." *Cem. Concr. Compos.*, 31(4), 268-274.
Ercikdi, B., Yılmaz, T., and Külekci, G. (2014). "Strength and ultrasonic properties of cemented paste backfill." *Ultrasonics*, 54(1), 195-204.

Fall, M., Belem, T., Samb, S., and Benzaazoua, M. (2007). "Experimental characterization of the stress-strain behaviour of cemented paste backfill in compression." *J. Mater. Sci.*, 10.1007/s10853-006-0403-2, 42(11), 3914-3922.

Fall, M., and Benzaazoua, M. (2005). "Modeling the effect of sulphate on strength development of paste backfill and binder mixture optimization." *Cem. Concr. Res.*, 35(2), 301-314.

Fall, M., Benzaazoua, M., and Saa, E. (2008). "Mix proportioning of underground cemented tailings backfill." *Tunn. Undergr. Sp. Tech.*, 10.1016/j.tust.2006.08.005, 23(1), 80-90.

Fall, M., Célestin, J., Pokharel, M., and Touré, M. (2010). "A contribution to understanding the effects of curing temperature on the mechanical properties of mine cemented tailings backfill." *Eng. Geol.*, 114(3), 397-413.

Fall, M., and Nasir, O. (2010). "Mechanical behaviour of the interface between cemented tailings backfill and retaining structures under shear loads." *Geotech. Geol. Eng.*, 28(6), 779-790.

Fall, M., Nasir, O., Cui, L., and Han, F. (2015). "Coupled modeling of the strength development and distribution within cemented paste backfill structure." *Proc., 49th US Rock Mechanics/Geomechanics Symposium*, American Rock Mechanics Association, San Francisco, California, USA, 587-595.

Fall, M., and Pokharel, M. (2010). "Coupled effects of sulphate and temperature on the strength development of cemented tailings backfills: Portland cement-paste backfill." *Cem. Concr. Compos.*, 32(10), 819-828.

Galaa, A. M., Thompson, B. D., Grabinsky, M. W., and Bawden, W. F. (2011). "Characterizing stiffness development in hydrating mine backfill using ultrasonic wave measurements." *Can. Geotech. J.*, 48(8), 1174-1187.

Ghirian, A., and Fall, M. (2013). "Coupled thermo-hydro-mechanical-chemical behaviour of cemented paste backfill in column experiments. Part I: physical, hydraulic and thermal processes and characteristics." *Eng. Geol.*, 164, 195-207.

Ghirian, A., and Fall, M. (2014). "Coupled thermo-hydro-mechanical-chemical behaviour of cemented paste backfill in column experiments: Part II: Mechanical, chemical and microstructural processes and characteristics." *Eng. Geol.*, 10.1016/j.enggeo.2013.12.004, 170, 11-23.

Ghirian, A., and Fall, M. (2015). "Coupled Behavior of Cemented Paste Backfill at Early Ages." *Geotech. Geol. Eng.*, 10.1007/s10706-015-9892-6, 33(5), 1141-1166.

Ghirian, A., and Fall, M. (2016a). "Long-term coupled behaviour of cemented paste backfill in load cell experiments." *Geomech. Geoeng.*, 1-15.

Ghirian, A., and Fall, M. (2016b). "Strength evolution and deformation behaviour of cemented paste backfill at early ages: Effect of curing stress, filling strategy and drainage." *Int. J. Min. Sci. Technol.*, 10.1016/j.ijmst.2016.05.039, 26(15), 809-817.

Hamberg, R., Maurice, C., and Alakangas, L. (2015). "The use of low binder proportions in cemented paste backfill–Effects on As-leaching." *Miner. Eng.*, 78, 74-82.

Janotka, I. (2001). "Hydration of the cement paste with Na2CO3 addition." *Ceram-silikaty.*, 45(1).

Jefferis, S., and Wilson, S. (2012). "Mine Paste Backfill-The Use of Grouts at Massive Scale." *Grouting and Deep Mixing 2012*, 1879-1888.

Kesimal, A., Yilmaz, E., Ercikdi, B., Alp, I., and Deveci, H. (2005). "Effect of properties of tailings and binder on the short-and long-term strength and stability of cemented paste backfill." *Mater. Lett.*, 59(28), 3703-3709.

Khaldoun, A., Ouadif, L., Baba, K., and Bahi, L. (2016). "Valorization of mining waste and tailings through paste backfilling solution, Imiter operation, Morocco." *Int. J. Min. Sci. Technol.*, 10.1016/j.ijmst.2016.02.021, 26(3), 511-516.

Koupouli, N. J., Belem, T., Rivard, P., and Effenguet, H. (2016). "Direct shear tests on cemented paste backfill-rock wall and cemented paste backfill-backfill interfaces." *J. Rock Mech. Geotech. Eng.*, 10.1016/j.jrmge.2016.02.001, 8, 472-479.
Li, L., and Aubertin, M. (2009). "Numerical investigation of the stress state in inclined backfilled stopes." *Int. J. Geomech.*, 10.1061/(ASCE)1532-3641(2009)9:2(52), 9(2), 52-62.
Li, W., and Fall, M. (2016). "Sulphate effect on the early age strength and self-desiccation of cemented paste backfill." *Constr. Build. Mater.*, 106, 296-304.
Luo, X., Were, P., Liu, J., and Hou, Z. (2015). "Estimation of Biot's effective stress coefficient from well logs." *Environmental Earth Sciences*, 73(11), 7019-7028.
Lura, P., Jensen, O. M., and van Breugel, K. (2003). "Autogenous shrinkage in high-performance cement paste: an evaluation of basic mechanisms." *Cem. Concr. Res.*, 33(2), 223-232.
Mozaffaridana, M. (2011). "Using Thermal Profiles of Cemented Paste Backfill to Predict Strength." Master Thesis, University of Toronto, ON, Canada.
Nasir, O., and Fall, M. (2008). "Shear behaviour of cemented pastefill-rock interfaces." *Eng. Geol.*, 101(3), 146-153.
Nasir, O., and Fall, M. (2009). "Modeling the heat development in hydrating CPB structures." *Comput. Geotech.*, 10.1016/j.compgeo.2009.05.008, 36(7), 1207-1218.
Nasir, O., and Fall, M. (2010). "Coupling binder hydration, temperature and compressive strength development of underground cemented paste backfill at early ages." *Tunn. Undergr. Sp. Tech.*, 25(1), 9-20.
Rankine, R. M., and Sivakugan, N. (2007). "Geotechnical properties of cemented paste backfill from Cannington Mine, Australia." *Geotech. Geol. Eng.*, 25(4), 383-393.
Sargeant, A. L. (2008). "The Application of Post Consumer Glass as a Cementing Agent in Mine Backfill."
Schindler, A. K., and Folliard, K. J. (2003). "Influence of supplementary cementing materials on the heat of hydration of concrete." *Proc., Advances in Cement and Concrete IX Conference*, Engineering Conferences International, Inc., Colorado, USA, 17-26.
Smilauer, V., and Bittnar, Z. (2006). "Microstructure-based micromechanical prediction of elastic properties in hydrating cement paste." *Cem. Concr. Res.*, 36(9), 1708-1718.
Suazo, G., Fourie, A., and Doherty, J. (2016a). "Cyclic Shear Response of Cemented Paste Backfill." *J. Geotech. Geoenviron.*, 04016082.
Suazo, G., Fourie, A., and Doherty, J. (2016b). "Experimental Study of the Evolution of the Soil Water Retention Curve for Granular Material Undergoing Cement Hydration." *J. Geotech. Geoenviron.*, 04016022.
Veenstra, R., Bawden, W., Grabinsky, M., and Thompson, B. (2011). "An approach to stope scale numerical modelling of early age cemented paste backfill." *Proc., 45th US Rock Mechanics/Geomechanics Symposium*, American Rock Mechanics Association, 1-7.
Veenstra, R. L. (2013). "A design procedure for determining the in situ stresses of early age cemented paste backfill." Ph.D. Thesis, University of Toronto, Canada.
Wang, Y., and Fall, M. (2014). "Initial temperature-dependence of strength development and self-desiccation in cemented paste backfill that contains sodium silicate." *Cem. Concr. Compos.*, 67, 101-110.
Wu, A., Wang, Y., Zhou, B., and Shen, J. (2016). "Effect of initial backfill temperature on the deformation behavior of early age cemented paste backfill that contains sodium silicate." *Advances in Materials Science and Engineering*, 2016.
Wu, D., Fall, M., and Cai, S. (2013). "Coupling temperature, cement hydration and rheological behaviour of fresh cemented paste backfill." *Miner. Eng.*, 42, 76-87.

Wu, D., Sun, G., and Liu, Y. (2016). "Modeling the thermo-hydro-chemical behavior of cemented coal gangue-fly ash backfill." *Constr. Build. Mater.*, 111, 522-528.

Ye, G., Sun, Z., Voigt, T., Van Breugel, K., and Shah, S. (2004). "A micromechanic model for characterization of cement paste at early age validated with experiments." *Proc., Proceedings of the RILEM International Symposium on Advances in Concrete through Science and Engineering*.

Yilmaz, E., Belem, T., and Benzaazoua, M. (2015). "Specimen size effect on strength behavior of cemented paste backfills subjected to different placement conditions." *Eng. Geol.*, http://dx.doi.org/10.1016/j.enggeo.2014.11.015, 185, 52-62.

Yilmaz, E., Belem, T., Bussière, B., and Benzaazoua, M. (2011). "Relationships between microstructural properties and compressive strength of consolidated and unconsolidated cemented paste backfills." *Cem. Concr. Compos.*, 33(6), 702-715.

Yılmaz, T., Ercikdi, B., Karaman, K., and Külekçi, G. (2014). "Assessment of strength properties of cemented paste backfill by ultrasonic pulse velocity test." *Ultrasonics*, 54(5), 1386-1394.

CHAPTER 6

Synthesis of the results and discussion

6.1. Introduction

To facilitate the design of cemented tailings backfill (CTB), the obtained results from this study which are discussed in detail in Chapters 4 and 5 are synthesized in this chapter. A corresponding comparative analysis on the obtained results is carried out to demonstrate the behavior of CTB under strongly coupled multiphysics processes with different backfill design strategies. Specifically, representative modelling results from Chapter 4 are presented in Section 6.2 to show the CTB behavior and changes in its material properties under coupled multiphysics processes. This can contribute to a better understanding of the interaction of the complex multiphysics processes in CTB and the related influence on CTB behaviors. Then, a summary of the features and potential application of the developed multiphysics model in this study is provided in Section 6.3. In addition, the behavior of the CTB under different backfilling conditions (i.e., stope geometry, inclination, surface roughness and initial temperature of host rock) and design strategies (mixture recipe, initial temperature of CTB materials, filling rate and strategies, and drainage conditions) are compared in Section 6.4, which can act as a useful reference source for backfill designers and engineers.

6.2. Effect of multiphysics processes

With the interaction of multiphysics processes, CTB materials demonstrate significant changes in both behavior and material properties. Correspondingly, the accurate prediction of CTB behaviors and variations in material properties has become one of the primary tasks of backfill designers and researchers. Based on a comparison of the obtained results, the influence of the multiphysics processes on CTB behaviors and material properties are summarized in Sections 6.2.1 and 6.2.2, respectively.

6.2.1. CTB behaviors under multiphysics processes

Based on the obtained results, the CTB behaviors under coupled multiphysics processes are summarized as follows.

For the thermal (**T**) response, the changes in temperature in CTB are determined by heat transfer and generation. The former is further examined as heat advection induced by the pore fluid flow, and heat conduction driven by the temperature gradient. The latter is due to the exothermic characteristics of binder hydration reactions. The modelling result of temperature changes in a stope (Figure 6.1a from Section 4.3.4.3) is selected as a representative example to analyze the thermal response of CTB. From Figure 6.1a, it can be seen that (1) the temperature difference between the monitored point and surrounding environment becomes gradually more pronounced during the first 3 days, which indicates the contribution of heat release caused by binder hydration to the increase in CTB temperature, and (2) the temperature at the monitored point and room temperature become nearly the same with curing time. This is due to the fact that, with the progression of binder hydration, the chemical reaction rate will gradually decrease and resultant heat loss will slow down as well. As a result, the heat transfer between the CTB and surrounding environment becomes a dominant contributor to the temperature variations in the CTB. Therefore, the representative example clearly demonstrates the changes in temperature with heat transfer and generation in CTB.

For the hydraulic (**H**) response, the analysis on pore water pressure (PWP) variations is very important for backfill designers due to the significance of the PWP on barricade stability and strength development in CTB. The hydraulic response is governed by pore water flow, water retention capacity of CTB materials and water loss due to binder hydration and/or drainage through the barricade. To examine the hydraulic response of CTB, the predicted result of PWP in a column test without drainage (Figure 6.1b, based on Section 4.3.4.1) is chosen for discussion. It can be observed in Figure 6.1b that the most significant change in the PWP occurs at the early ages (i.e., the first 7 days). This is due to the fact that, as discussed in the thermal response of CTB (see Figure 6.1a), the hydration reaction proceeds rapidly at the early ages. Correspondingly, the rapid rate of hydration accelerates the water consumption caused by the hydration reaction. Meanwhile, with the progression of binder hydration, the capillary water is gradually converted into solid hydrates. Correspondingly, negative PWP builds up due to the self-desiccation effect. Therefore, to understand the changes in the saturated states, water retention capacity is incorporated into the multiphysics modelling. Moreover, pore water migration may occur with the development of hydraulic gradients in CTB. Hence, as demonstrated in Figure 6.1b, the PWP and saturation states may substantially vary in CTB.

For the mechanical (**M**) response, the analysis of stress distribution and magnitude is of great importance for CTB design. After placement into stopes, multiphysics consolidation processes will take place, which result in not only the development of volumetric strain but also relative interface displacement between the CTB and rock walls. The latter can cause the formation of interface shear resistance (i.e., interface adhesion and friction stress) which can reduce the influence of the overburden pressure on the vertical stress in CTB (i.e., arching effect). Specifically, as shown in Figure 6.1c (from Section 4.5.3.3), the vertical stress first increases with backfill height and coincides with the amount of stress due to the self-weight of CTB during the first stage of filling. However, after curing, the vertical stress only shows a slight increase during the second stage of filling and substantially differs from the stress of the self-weight of CTB, namely the rock mass/CTB interface interaction causes the arching effect. Therefore, to predict the stress and strain in CTB, the multiphysics processes of consolidation and rock mass/backfill interface interaction are integrated in this study.

For the chemical (**C**) response, the progression of hydration reaction can have significant impacts on CTB behaviors. Apart from the contribution to the changes in temperature (Figure 6.1a) and PWP (Figure 6.1b), binder hydration can also generate volumetric deformation through chemical shrinkage which is an important contributor to the consolidation behavior of CTB. To demonstrate the influence of chemical shrinkage, the simulated result of the vertical settlement of CTB cured under stress (Figure 6.1d from Section 4.4.4.1) is selected as a representative example. As shown in Figure 6.1d, the vertical settlement increases immediately after an increase in the curing stress. However, it is interesting to note that at the very early ages, there is still increased vertical settlement during the curing period under a constant curing stress. This is attributed to the chemical shrinkage. Therefore, hydration reaction plays a critical role in the analysis of CTB behavior. Correspondingly, the resultant chemical shrinkage, water consumption, and heat release are fully considered and quantitatively determined through multiphysics modelling in this study.

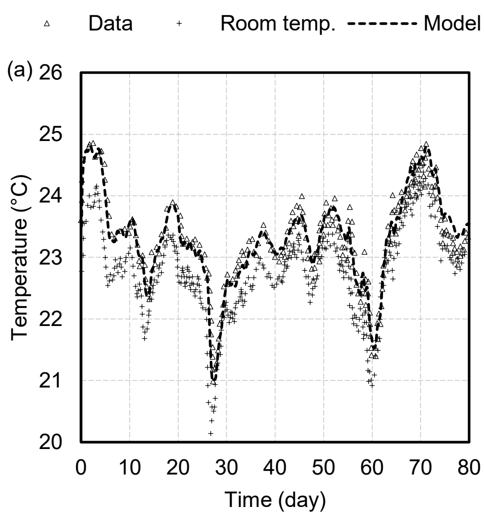

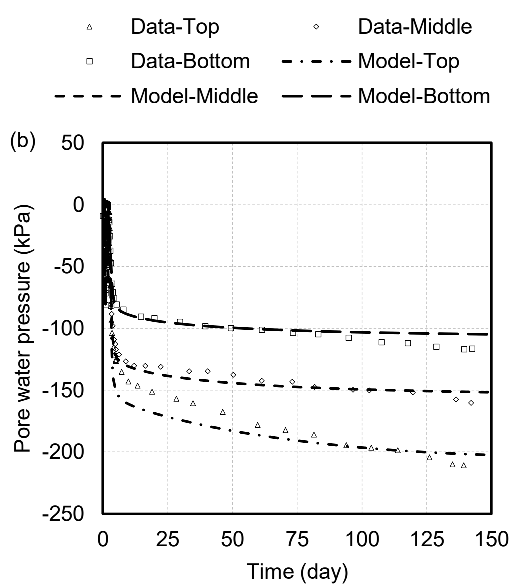

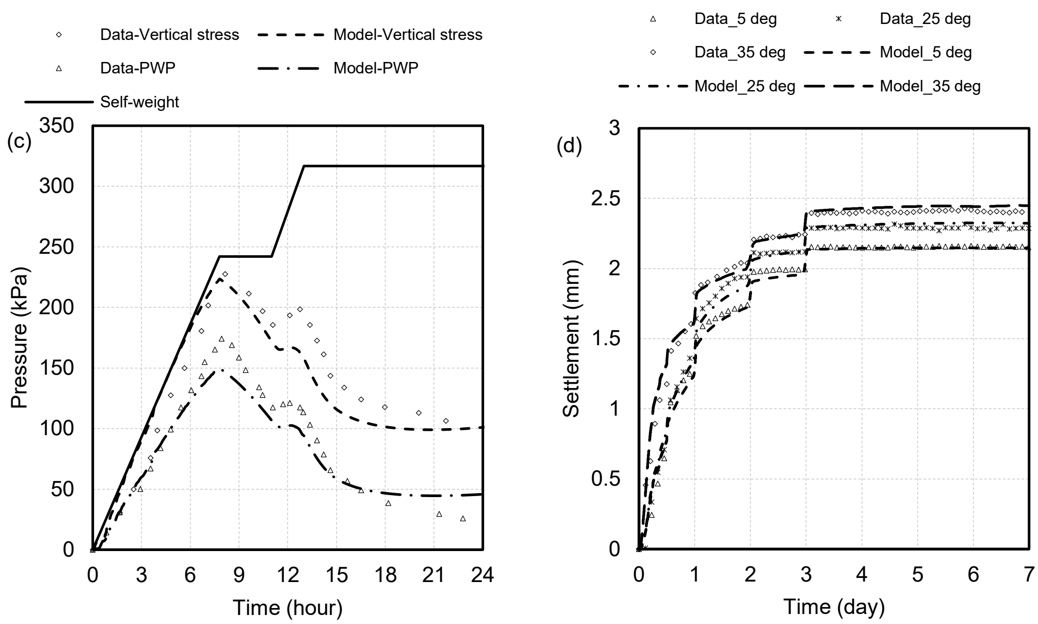

Figure 6.1 Predicted results versus experimental values of (a) temperature, (b) pore water pressure, (c) stress and (d) settlement

6.2.2. Changes in material properties under multiphysics processes

The complex coupled multiphysics processes not only cause substantial changes in CTB behavior, but also changes in the material properties. To clearly demonstrate the influence of multiphysics processes on the changes in material properties, a different material property (see Figure 6.2.) for each physical process is discussed.

In terms of the thermal (**T**) properties, thermal conductivity is one of the most critical material properties for understanding heat conduction in CTB. As discussed in Sections 4.3 and 4.4, the thermal conductivity is determined by the composition of CTB and saturation conditions. The latter, as discussed in Section 6.2.1, is affected by water consumption caused by binder hydration and drainage through the barricade. Therefore, with variations in the water content and saturation states in CTB, changes in thermal conductivity will take place. As shown in Figure 6.2a (from Section 4.3.4.1), there is good agreement between the predicted and experimental values, which indicates that the controlling mechanisms and the changes in thermal conductivity can be captured well by the developed multiphysics model. Moreover, the changes in thermal conductivity will also affect heat transfer in CTB. Therefore, thermal conductivity changes are influenced by the multiphysics processes in CTB.

In terms of the hydraulic (**H**) properties, the hydraulic conductivity (i.e., the coefficient of permeability) can be used to understand the migration capability of pore fluid in the CTB matrix, which depends on the fluid properties (density and viscosity), degree of saturation, and skeleton porosity. Hence, similar to thermal conductivity, the saturation state changes in CTB can affect the hydraulic conductivity. Moreover, as consolidation develops, the resultant volumetric deformation can reduce the porosity. Correspondingly, the hydraulic conductivity will change along with the consolidation process as well. As illustrated in Figure 6.2b (from Section 4.3.4.1), the modelling results are in good agreement with the experimental data on hydraulic conductivity. Therefore, the developed multiphysics model can simulate hydraulic conductivity changes in multiphysics processes.

In terms of the mechanical (**M**) properties, the hardening CTB materials demonstrate substantial time-dependent characteristics. With the progression of binder hydration, the strength of the bonds between the solid particles will be enhanced. Meanwhile, as mentioned in the section on the hydraulic properties, the multiphysics processes in consolidation will result in variations in porosity. As a result, porosity-dependent mechanical properties will be affected. One such mechanical property is the elastic modulus. As discussed in Sections 4.2, 4.3 and 4.4, the chemical hardening process and densification behavior with consolidation can contribute to variations in the elastic modulus. It can be seen in Figure 6.2c (from Section 4.5.2.3) that changes to the elastic modulus of the CTB are accurately predicted by the developed multiphysics model, namely, the influence of both binder hydration and consolidation on elastic modulus are accurately simulated during the multiphysics modelling.

In terms of the chemical (**C**) properties, as mentioned earlier, hydration reaction plays a crucial role in multiphysics processes. From the viewpoint of practical applications, the degree and rate of hydration are of great interest in multiphysics modelling and the related simulations for the assessment of CTB behavior and performance. Therefore, the contribution of binder hydration is quantitatively determined through a model of the degree of binder hydration in this study. Correspondingly, the differences in the degree of binder hydration with respect to time represents the chemical reaction rate which has been adopted to derive the water sink term in mass balance equations, and the heat source term in energy balance equations. However, for the development of the multiphysics models, the model on the degree of binder hydration is an empirical predictive equation rather than a constitutive relation. Correspondingly, no chemical properties are adopted by the model on binder hydration. Hence, for the analysis of the chemical process in CTB in terms of the material properties, the alternative is to evaluate hydration-dependent material properties of other physical properties, such as cohesion. In terms of the changes in CTB cohesion, binder hydration plays a key role through the formation of hydrates between the tailings particles. Therefore, the predicted cohesion can be used to evaluate the capability of the developed model to accurately capture the hydration progress. As shown in Figure 6.2d (from Section 4.5.2.3), there is very good agreement between the predicted results and experimental values, which confirms the predictive ability of the developed multiphysics model.

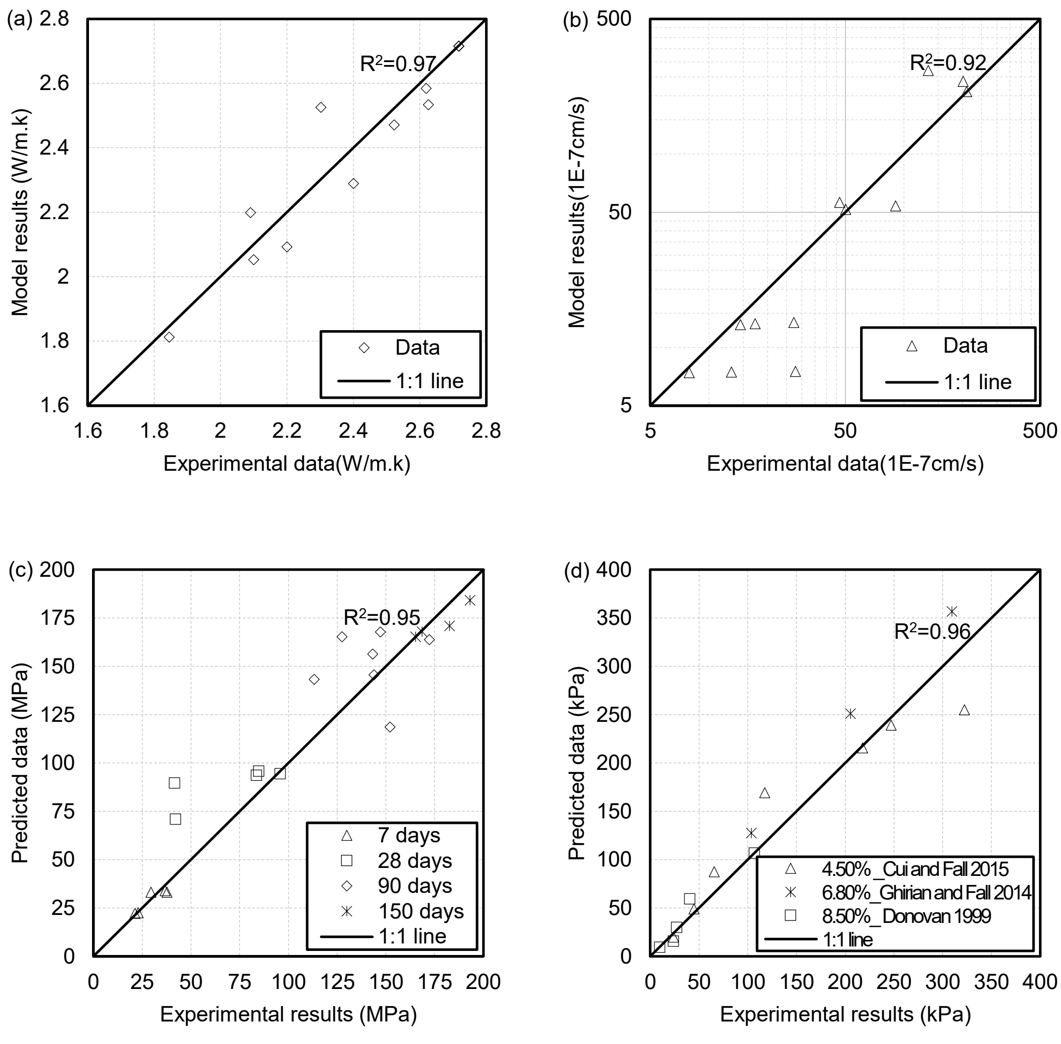

Figure 6.2 Predicted versus experimental values of (a) hydraulic conductivity, (b) thermal conductivity, (c) elastic modulus and (d) cohesion

6.3. Features and potential application of developed multiphysics models

A series of multiphysics models have been developed in this study. The features and potential applications are summarized in this section.

6.3.1. Evolutive elastoplastic model

The main features of the evolutive elastoplastic model include the following.

1. As a chemo-mechanical constitutive relation, the influence of hydration reactions is coupled into the description of elastoplastic behavior of CTB.
2. Changes to the yield surface in stress space fully take into consideration chemical and strain hardening, and post-peak strain softening behaviors.
3. Non-associative plastic flow is adopted to derive the constitutive model.
4. The relation between degree of binder hydration and the mechanical properties (i.e. cohesion, internal friction and dilation angles, stiffness, and Poisson's ratio) has been identified.

With respect to potential applications, the validated evolutive elastoplastic model can be used to predict the mechanical behaviors of CTB material under pure mechanical loads (such as UCS and triaxial compression tests). Moreover, the model can also be incorporated into multiphysics models to predict the development of strain, stress and strength in CTB structures.

6.3.2. Fully coupled thermo-hydro-mechano-chemical model

The primary features of the fully coupled THMC model are summarized as follows.

1. For the thermal process, heat conduction induced by a temperature gradient (Fourier's law), heat advection caused by pore fluid flow and heat generation caused by exothermic binder hydration are incorporated into an energy balance equation.
2. For the hydraulic process, pore fluid flow controlled by Darcy's law, water retention capability and water consumption caused by binder hydration are taken into account in a mass balance equation.

3. For the mechanical process, the developed evolutive elastoplastic model is incorporated into a strain analysis of CTB along with chemical shrinkage and thermal expansion.
4. For the chemical process, the multiphysics model fully considers the influence of binder hydration on the CTB properties and behavior.
5. All model coefficients are identified with measurable parameters.

The fully coupled THMC model can be used to accurately evaluate the strongly interacting multiphysics processes and the resultant influences on the CTB properties and behaviors. Specifically, the following can be considered with the model:

1. Used to analyze the development of volumetric strain (e.g., consolidation) in CTB in stopes.
2. Used to evaluate the self-desiccation process and the PWP changes which can facilitate analyses of barricade stability.
3. By incorporating the rock mass/CTB interface interaction, used to evaluate the arching effect in CTB structures.
4. Used to investigate temperature changes and their influence on the CTB behaviors and performance.
5. By changing the initial and boundary conditions, used to investigate the effects of different backfilling conditions and strategies on CTB behavior and performance, which provide valuable information for the optimal design of CTB structures.

6.3.3. Multiphysics model on consolidation

The developed multiphysics model on consolidation fully considers the coupled THMC processes in CTB. Therefore, the features mentioned in Section 6.3.2 are provided by considering the multiphysics processes. In addition, the unique characteristics of the developed multiphysics model on consolidation are as follows.

1. To understand the consolidation behavior of CTB, the principles of the continuity of pore space (i.e., pore space changes related to the solid skeleton of the CTB and solid phase must equal the total volume change of the capillary water and pore air) are adopted
2. Two yield surfaces that consist of a changing shear-failure surface and an elliptic cap surface are utilized to characterize the behaviors of both chemical-strain induced hardening/softening and plastic volumetric strain development in CTB structures.

The validated multiphysics model on consolidation can be utilized for the following applications.

1. By changing the initial and boundary conditions, can be used to study the effects of the development of volumetric deformation on the different backfilling conditions and strategies from the early to advanced ages.
2. Used to investigate the influence of the consolidation process on porosity-dependent material properties (e.g., hydraulic conductivity and elastic modulus).
3. Used to predict the changes in the multiphysics processes in CTB (e.g., temperature variations and PWP distribution).
4. By including rock mass/CTB interface interaction, can be used to evaluate the arching effect in CTB structures.

6.3.4. Multiphysics model of rock mass/backfill interface

The main features of the multiphysics model of the rock mass/backfill interface are summarized as follows.

1. Double hardening/softening parameters (degree of binder hydration and effective plastic displacement) are incorporated into the model of the rock mass/backfill interface to characterize the influence of binder hydration and plastic displacement along the interface.
2. For the two components of interface resistance (i.e., interface adhesion and friction shear stress), the influence of the host rock (i.e., internal rock friction, rock surface roughness) and binder hydration are taken into account.

In terms of the applications of this model, it is important to note that it can integrate the multiphysics model that analyzes the consolidation process in CPB and the elastoplastic model that analyzes changes in the interface behavior. Therefore, the following can be considered as potential applications of the multiphysics model of the rock mass/backfill interface.

1. Used to characterize the rock mass/backfill interface interaction and the resultant impacts on the stress distribution in the CTB.
2. Used to predict changes in the multiphysics processes in CTB (e.g., temperature variation, deformation development and PWP distribution).

3. By changing the initial and boundary conditions, can be used to evaluate the arching effect with different backfilling conditions and strategies, which can facilitate the optimal design of CTB structures.

6.4. Effect of backfilling conditions and design strategies

The field behavior of CTB is affected by the CTB-rock mass interaction. Therefore, based on the components of CTB-rock mass interactions, the backfilling conditions can be viewed in terms of the: (1) CTB conditions (e.g., mixture recipe, initial temperature, curing time and temperature, filling rate and sequences, and drainage conditions), (2) rock mass conditions (e.g., rock initial temperature, stope geometry and inclination angle), and (3) CTB/rock mass interface (e.g., rock surface roughness). Consequently, the combined effect of field conditions may result in complex in-situ behaviors and performance. The developed multiphysics models (the evolutive elastoplastic model, fully coupled THMC model, the multiphysics model on consolidation, and the model on CTB/rock mass interface) make the assessment of CTB field behavior possible. Therefore, extensive field simulations have been conducted here to evaluate the in-situ behaviors and performance including self-desiccation and consolidation behaviors, variations in barricade pressure, and the development of CTB strength. The obtained results from the multiphysics simulation of the behavior of CTB structures (Chapter 5) and related implications for CTB design are summarized in the following sections.

6.4.1. Effect of CTB conditions on field behavior of CTB

The results from the simulation of the multiphysics processes in the field in Chapter 5 indicate that CTB conditions can significantly affect the behaviors and performance of CTB.

1. Curing time plays a crucial role in the interaction of THMC processes in CTB. The field behaviors including self-desiccation, consolidation, barricade pressure and CTB strength are time-dependent. However, the time rate of change of the PWP, volume changes, barricade pressure and strength are gradually reduced with time.
2. The field behavior of CTB is sensitive to changes in cement content. The different trends of change in the PWP dissipation are initiated by the curing of the plug-layer and progressively increased with filling.

3. The curing temperature has significant impacts on the field behavior of CPB. Higher temperatures can accelerate hydration reactions, which further contributes to the dissipation of the PWP, development of consolidation, and improvement of CTB strength. Moreover, compared with the initial rock mass temperature, the impact of the initial CPB temperature on the field behavior of CTB and CTB performance is more evident.
4. A strategy of filling in stages (i.e., filling carried out in two-stages with a plug layer) can substantially contribute to the development of self-desiccation, volume changes, reduction of barricade pressure and improve CTB strength, especially at the early ages. Thus filling operations carried out in stages improve CTB stability. In addition, the filling rate produces similar changes in the CTB behavior. However, filling in stages and a reduced rate of filling will increase the filling time and thus affect the mining cycle.
5. Water drainage through the barricade can directly reduce the pore space of CPB (i.e., consolidation process), and PWP (i.e., the barricade pressure and self-desiccation process). With changes to the PWP, the true CTB strength will be affected as well. Thus, an effective drainage system in backfilling operations can further contribute to the stability of the retaining structure and CPB mass in a stope.

6.4.2. Effect of rock mass conditions on field behavior of CTB

It has been observed that the field behavior of CTB and CTB performance can be affected to varying degrees due to variations in the rock mass conditions,

1. The stope geometry can impose significant impacts on the field behavior of CTB. Specifically, the PWP in the stope will increase which negatively affects the CTB strength.
2. In this study, it is found that changes in the barricade pressure are significantly related to the barricade location in the undercut drift, while the barricade shape mainly affects the stress distribution in a barricade.
3. Compared to the effects of the stope height, the inclination angle has minimal influence on the field behavior of CTB, and mainly affects the spatial distribution of the PWP, consolidation, and CTB strength in the stope.

6.4.3. Effect of CTB/rock mass interface conditions on field behavior of CTB

The use of explosives in stoping operations cause different degrees of roughness in rock walls. Changes in the rock wall can directly affect the interface properties including the interface friction angle (Eq. (4.188)) and adhesion (Eq.(4.189)). As a result, the interface stress resistance will change with different degrees of roughness of a rock wall. The following conclusions are made based on simulations of the field behavior of CTB carried out in this study.

1. With an increase in the rock wall roughness, the vertical stress that acts on the stope floor is significantly reduced, namely the arching effect is more apparent in rock walls with increased surface roughness.
2. Increases in the surface roughness of the rock wall and a more pronounced arching effect mean that the volume changes in CTB are reduced in the stope as well.

CHAPTER 7

General conclusions and recommendations

7.1. General conclusions

A series of multiphysics models have been developed in this study, which can evaluate and predict the field behavior of CTB and CTB performance. Extensive field simulations have been conducted with these models. The following conclusions are drawn based on the obtained results.

1. CTB materials are part of a complex and nonlinear multiphysics system of different interactions.
2. An evolutive elastoplastic model, that is, a coupled chemo-elastoplastic model specific to CTB materials has been first developed in this study that characterizes the mechanical behaviors of hydrating CTB. The model takes into account chemical and strain hardening, post-peak strain softening and hydration induced changes in the mechanical properties (i.e. cohesion, internal friction and dilation angles, stiffness, and Poisson’s ratio). Moreover, non-associative plastic flow is used to derive a mechanical constitutive model to accurately predict the plastic behavior. Based on the good agreement between the predicted and experimental values, the model can be used to predict the mechanical behavior under the influence of binder hydration.
3. A fully coupled THMC model has been developed that evaluates the multiphysics processes of interactions with accuracy and the resulting influence on the CTB properties and behaviors. In terms of the thermal process, heat conduction through a temperature gradient, heat advection due to pore fluid flow and heat generation caused by exothermic binder hydration are incorporated into an energy balance equation. In terms of the hydraulic process, pore fluid flow controlled by Darcy’s law, water retention capability and water consumption caused by binder hydration are taken into account in a mass balance equation. In terms of the mechanical process, the developed evolutive elastoplastic model is incorporated into a strain analysis of CTB together with chemical shrinkage and thermal expansion. Finally, in terms of the chemical process, the multiphysics model fully considers the influence of binder hydration on the CTB properties and behavior. A series of predictive models on the changes in CTB material properties are established. Moreover, the good agreement between the modeling results and measured values in terms of both laboratory experiments and in-situ measurements demonstrates the capability of the developed THMC model to well capture the changes in CTB properties and behaviors.

4. A 3D multiphysics model of the consolidation behavior of CTB materials has been derived based on the principles of the continuity of pore space (i.e., the pore space changes related to the solid skeleton of the CTB and that the solid phase must equal the total volume changes in the capillary water and pore air) and conservation equations of mass, energy and momentum, The predictive ability of the developed model is verified through a comparison with the experimental results from tests performed in this study and reported laboratory data in the literature. The good agreement between the simulated and experimental results indicates that the multiphysics model is able to accurately explain the consolidation process of CTB and predict the changes in the multiphysics processes in CTB (i.e., temperature variation, PWP distribution, and development of deformation).
5. The developed multiphysics model on the interface behavior of rock mass/backfill can characterize their interaction and the resulting impacts (arching effect) on the stress distribution in CTB.
6. The developed multiphysics models in this thesis fully consider the influence of multiphysics processes, consolidation behavior and rock mass/backfill interface interaction. The related model coefficients are identified in terms of measurable parameters. Therefore, the developed models and the related predictive functions of the material properties have the potential for wide application towards optimal backfill designs.
7. The field behaviors including the arching effect, self-desiccation process, consolidation behavior, changes in barricade pressure, and the development of CTB strength are strongly influenced by coupled THMC processes. Therefore, the developed and validated multiphysics models in this study can predict and evaluate the field behaviors of CTB structures.
8. CTB conditions (i.e., the mixture recipe, initial temperature, curing time and temperature, filling rate and sequences, and drainage conditions) can significantly affect the field behavior of CTB structures. The obtained results indicate that CTB performance in the field can be improved by changing specific conditions, including using a longer curing time, higher cement content, higher initial temperature and effectively drained conditions. Moreover, the filling operations carried out in multiple stages with a plug fill layer and reduced rate of filling can further contribute to the improvement of the stability of CTB structures.
9. With respect to the rock mass conditions (i.e., initial rock temperature, stope geometry and inclination angle), the obtained results show that the stope geometry has a

significant influence on the PWP changes in the stope, while its effects on the development of CTB strength are minimal. Moreover, the barricade location in the undercut drift can affect the barricade pressure, while the barricade shape mainly affects the stress distribution on the barricade. In addition, the inclination angle mainly affects the spatial distribution of the PWP, consolidation, and CTB strength in the stope.

10. The CTB/rock mass interface properties (e.g., rock surface roughness) has a significant effect on the field behavior of CTB structures. When the rock walls have increased surface roughness, the arching effect becomes more apparent, which also reduces the volume changes in the stope.

7.2. Recommendations

The following recommendations are proposed for future works.

1. After placement into stopes, CTB materials are subjected to different types of mechanical loads (e.g., depositing of backfill layers in different stages, extracting of adjacent pillars and loading of mining equipment). The resultant deformation can reduce the strength of the bonds between solid particles. However, with the progression of binder hydration, the reduced strength of the bonds can be recovered to a certain extent (i.e., self-healing phenomenon), especially for CTB at the early ages. Therefore, the cycles of damage and self-healing can be included in the mechanical model.
2. In polar and some of the plateau regions, backfilling operations have to be carried out in frozen underground conditions. As such, more investigations are needed to model the phase changes in which fluid water transforms into ice and the resultant influence on CTB behavior and performance.
3. Creep behaviour is not included in the THMC model, and future studies should take this into consideration.
4. The focus is on mechanically static loading conditions. Therefore, dynamic loading conditions such as those induced by blast, earthquake or rock burst are not considered. These should therefore be considered in future works on modeling.

APPENDIXES

APPENDIX A: Determination of parameters of water retention curve

The water retention curve (WRC) can be used to characterize the relationship between suction and water content (or degree of saturation). However, previous experimental studies on CTB have found that the water retention properties of CTB are time-dependent due to the development of binder hydration. Correspondingly, the parameters of the WRC model cannot be considered constant. The associated predictive functions have been proposed in Chapter 4, and details on determining the parameters of the WRC are provided here.

The measured values of the WRCs published in (Abdul-Hussain and Fall 2011) were applied. Then, the van Genuchten model (Van Genuchten, 1980) was used to fit the WRCs. Based on a nonlinear multiple regression analysis, the parameters (θ_r, α_{WRC} and m_{WRC}) of the WRC model (i.e., Eq.(4.91)) can be identified for a given curing time (see Table Appendix A. 1).

Table Appendix A. 1. Parameters of WRC model

Curing time (day)	θ_r	α_{WRC} (kPa-1)	m_{WRC}
7	0.016	2.06×10-3	0.412
28	0.005	0.85×10-3	0.419
150	0.002	0.53×10-3	0.429

Then, based on the obtained data in Table Appendix A. 1, the associated predictive function for each WRC model parameter can be developed by using the binder hydration model (i.e., Eq. (4.45)):

$$\theta_r = R_{r1} \cdot \exp(-R_{r2} \cdot \xi) \quad \text{(Appendix.1)}$$

$$\alpha_{wrc} = f_{\alpha 1} \exp\left(f_{\alpha 2} \xi\right) \quad \text{(Appendix.2)}$$

$$m_{wrc} = f_{m1} \xi^{f_{m2}} + f_{m3} \quad \text{(Appendix.3)}$$

where R_{r1}, R_{r2}, $f_{\alpha 1}$, $f_{\alpha 2}$, f_{m1}, f_{m2} and f_{m3} are the fitting parameters. Based on a regression analysis on the data from Table Appendix A. 1, R_{r1}=1.314, R_{r2}=7.538, $f_{\alpha 1}$=0.0415, $f_{\alpha 2}$=4.231, f_{m1}=0.4073, f_{m2}=0.2103 kPa^{-1} and f_{m3}=-6.921 are recommended. To verify the predictive ability of the WRC model, the measured values of the WRCs reported in (Abdul-Hussain and Fall 2011) were applied and compared with the predicted results. As illustrated in Figure Appendix A. 1, the changes in the WRCs with curing time are captured well by the WRC model.

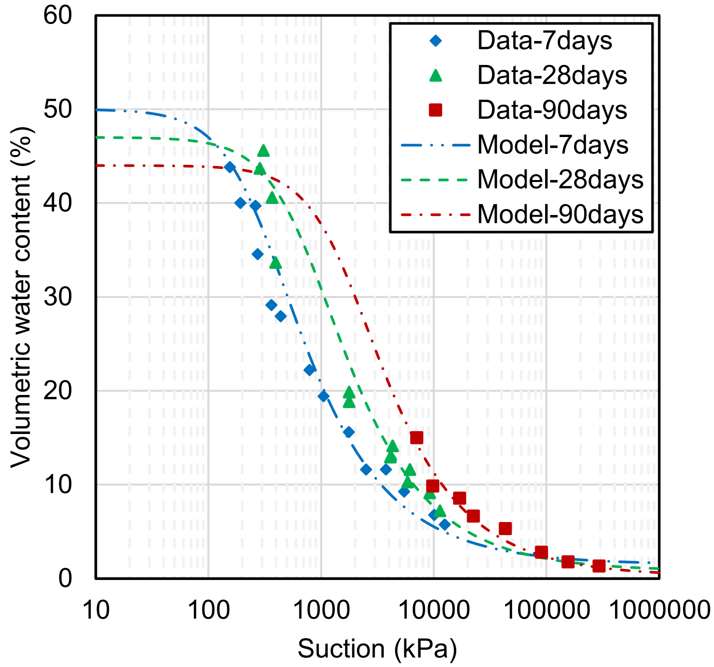

Figure Appendix A. 1. Comparison between predicted and experimental results for WRC (experimental data from (Ghirian and Fall 2013))

Additionally, it should be noted that the temperature differences can affect the changes in water retention capacity of geomaterials (Salager et al. 2011). As indicated in the binder hydration model (Eq. (4.35)), the effect of temperature is considered during the development of binder hydration and thus incorporated into the WRC model. Therefore, the effect of temperature on water retention capacity is considered in this study.

APPENDIX B: Comparison between multiphysics simulation results and analytical solution

In Section 4.4.4.4, a comparison between the simulation results carried out by multiphysics modeling and the Gibson's solution is carried out. As can be seen in Figure 4.50, the isochrones of the simulation results show a hysteresis curve compared with the corresponding isochrones of the analytical solution due to the effect of the multiphysics processes in CTB. Therefore, the developed model can fully simulate the effects of coupled multiphysics on the consolidation behavior of CTB, while Gibson's solution can only be used to evaluate the consolidation process of geomaterials under the effect of the self-weight of CTB.

To further confirm the findings, additional simulation is performed to evaluate the predictive ability of the developed model with constant binder hydration (ξ =0) and hydraulic conductivity (K_{sat} =5.5×10^{-5}cm/s). These two additional conditions can ensure that the developed model and analytical method of Gibson are performed under the same conditions. This is because zero hydration which indicates the contribution of pore-water consumption caused by hydration to PWP changes is eliminated from the developed model. Meanwhile, constant hydraulic conductivity can offset the influence of void ratio changes on permeability. Then, a comparison between the predicted results and Gibson's solution can be used to further validate the multiphysics model on consolidation when there is no cement hydration (chemical reaction).

For the simulation, the adopted geometry model, boundary conditions, initial values and input parameters here are the same as those in the case study in Section 4.4.4.4 (re: Table 4.5 and Table 4.7). A comparison between the simulation results and analytical solution is presented in Figure Appendix B.1. It can be observed that (1) when zero hydration and constant hydraulic conductivity are applied, the predicted results agree with Gibson's solution (see Figure Appendix B.1a), (2) compared to the results obtained from the CTB on the effect of binder hydration and changes in hydraulic conductivity (see Figure Appendix B.1b), it can be found that the multiphysics processes on consolidation have significant impacts on the PWP changes. Therefore, a reliable evaluation of CTB behavior can be obtained by the developed multiphysics model.

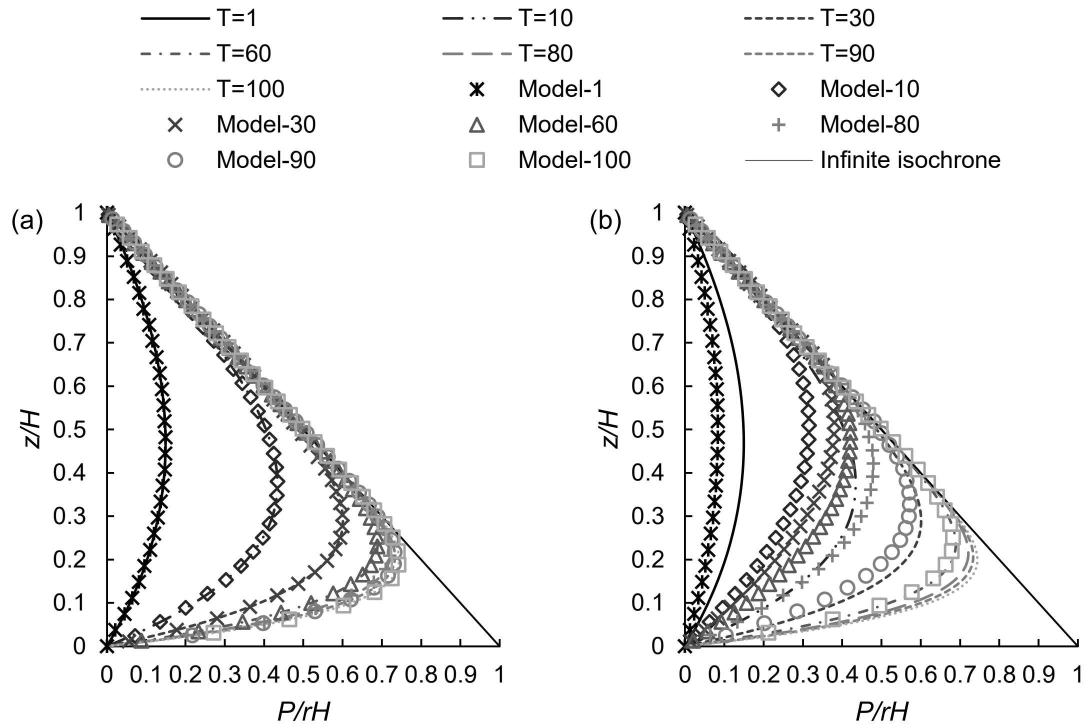

Figure Appendix B.1. Comparison between simulation results and analytical solution: (a) zero binder hydration and constant hydraulic conductivity; (b) Effect of binder hydration and changes in hydraulic conductivity taken into consideration (re: Figure 4.50).

APPENDIX C: Determination of coefficient κ_s

First, the 2-term exponential equation (5.45) can be rewritten as:

$$D_{\alpha 2}\exp(-D_{\alpha 2}\kappa_s)+D_{\alpha 3}\exp(-D_{\alpha 4}\kappa_s)=D_{\alpha 3}D_{\alpha 4}\kappa_s\exp(-D_{\alpha 4}\kappa_s) \quad \text{(Appendix.4)}$$

Taking the natural logarithm (i.e., ln) of both sides:

$$\ln D_{\alpha 2}-D_{\alpha 2}\kappa_s+\ln D_{\alpha 3}-D_{\alpha 4}\kappa_s=\ln\left(D_{\alpha 3}D_{\alpha 4}\right)+\ln\kappa_s-D_{\alpha 4}\kappa_s \quad \text{(Appendix.5)}$$

Namely

$$\ln D_{\alpha 2}+\ln D_{\alpha 3}-\ln\left(D_{\alpha 3}D_{\alpha 4}\right)=\ln\kappa_s+D_{\alpha 2}\kappa_s \quad \text{(Appendix.6)}$$

and applying a natural logarithm property:

$$\ln\left(\frac{D_{\alpha 2}}{D_{\alpha 4}}\right)=\ln\kappa_s+B_2\kappa_s \quad \text{(Appendix.7)}$$

Then, the exponential of both sides are taken:

$$\frac{D_{\alpha 2}}{D_{\alpha 4}}\exp\left(-D_{\alpha 2}\kappa_s\right)=\kappa_s \quad \text{(Appendix.8)}$$

To derive a closed-form solution to Eq. (Appendix.8), Taylor series expansion is applied to the exponential term (i.e., $\exp\left(-D_{\alpha 2}\kappa_s\right)$):

$$\exp\left(-D_{\alpha 2}\kappa_s\right)=1+\left(-D_{\alpha 2}\right)\kappa_s+{D_{\alpha 2}}^2{\kappa_s}^2/2 \quad \text{(Appendix.9)}$$

Then, Eq. (Appendix.8) can be transformed into a quadratic polynomial by substituting Eq. (Appendix.9) into Eq. (Appendix.8):

$${D_{\alpha 2}}^3{\kappa_s}^2-2\left({D_{\alpha 2}}^2+D_{\alpha 4}\right)\kappa_s+2D_{\alpha 2}=0 \quad \text{(Appendix.10)}$$

Then, the solution to the second-order polynomial Eq. (Appendix.10) can be derived by using the quadratic formula:

$$\kappa_s=\frac{\left({D_{\alpha 2}}^2+D_{\alpha 4}\right)\pm\sqrt{{D_{\alpha 4}}^2+{D_{\alpha 2}}^2D_{\alpha 4}-{D_{\alpha 2}}^4}}{{D_{\alpha 2}}^3} \quad \text{(Appendix.11)}$$

It should be noted that the discriminant term (i.e., the square-root part of Eq. (Appendix.11)) is greater than zero based on the allowed range of values of $D_{\alpha 2}$ and $D_{\alpha 4}$ (see Eq. (5.55)). Moreover, based on the definition of cumulative plastic strain κ_s, the solution with a "positive" discriminant is adopted to determine the cumulative plastic strain corresponding to the peak stress (i.e., the nominal CTB strength).

$$\kappa_s=\frac{{D_{\alpha 2}}^2+D_{\alpha 4}+\sqrt{{D_{\alpha 4}}^2+{D_{\alpha 2}}^2D_{\alpha 4}-{D_{\alpha 2}}^4}}{{D_{\alpha 2}}^3} \quad \text{(Appendix.12)}$$

APPENDIX D: Effect of the initial hydraulic conductivity of tailings on PWP pressure in CTB structure

The hydraulic conductivity of tailings can be variable, and thus will affect the hydraulic conductivity of the cemented backfill (i.e., K_{sat} in Eq. 4.85). The hydraulic conductivity of tailings depends of several factors, such as the amount of fines, mineralogy of the ore, and density of the material. Therefore, a sensivity analysis is conducted to assess the effect of the initial hydraulic conductivity of tailings on K_{sat}, and thus on PWP development and distribution in CTB structure. It should be recalled that the hydraulic conductivity of tailings, K_T, is incorporated into the predictive function of K_{sat} (as shown in Eq. 4.86). This means any change in K_T will affect K_{sat}. For the sensitivity analysis, the K_T values of three different types of tailings (coal tailings, gold tailings, and copper tailings) were selected (Table Appendix D. 1). The sensitivity analysis (simulation) is conducted based on the field study in Subsection 4.3.4.4.

Table Appendix D. 1. Tailings adopted by the study on their effects on hydraulic process (Data from (Qiu and Sego 2001))

Tailings	Coal tailings	Gold tailings	Copper tailings
Hydraulic conductivity K_T (cm/s)	1.88×10^{-6}	5.1×10^{-5}	1.23×10^{-4}
Category of K_T	Low	Medium	High

The comparison of the effects of the K_T values of the three different types of tailings on the changes in PWP is presented in Figure Appendix D. 1. From this figure, it can be clearly observed that the hydraulic conductivity K_T of tailings has a significant influence on the evolution of PWP and its spatial distribution. Higher K_T can cause higher PWP near stope base. This is because, as indicated in Eq. 4.86, higher K_T can significantly increase the coefficient of permeability of CTB (i.e., K_{sat}), and thus speed up the pore-water flow for a given hydraulic gradient. Consequently, under same filling strategy, larger amount of pore-water can flow into the region of stope base, and thus result in higher PWP near the stope base. Therefore, the developed multiphysics model and associated predictive functions for material properties can capture effect of the initial hydraulic conductivity of the tailings on the field behavior of CTB.

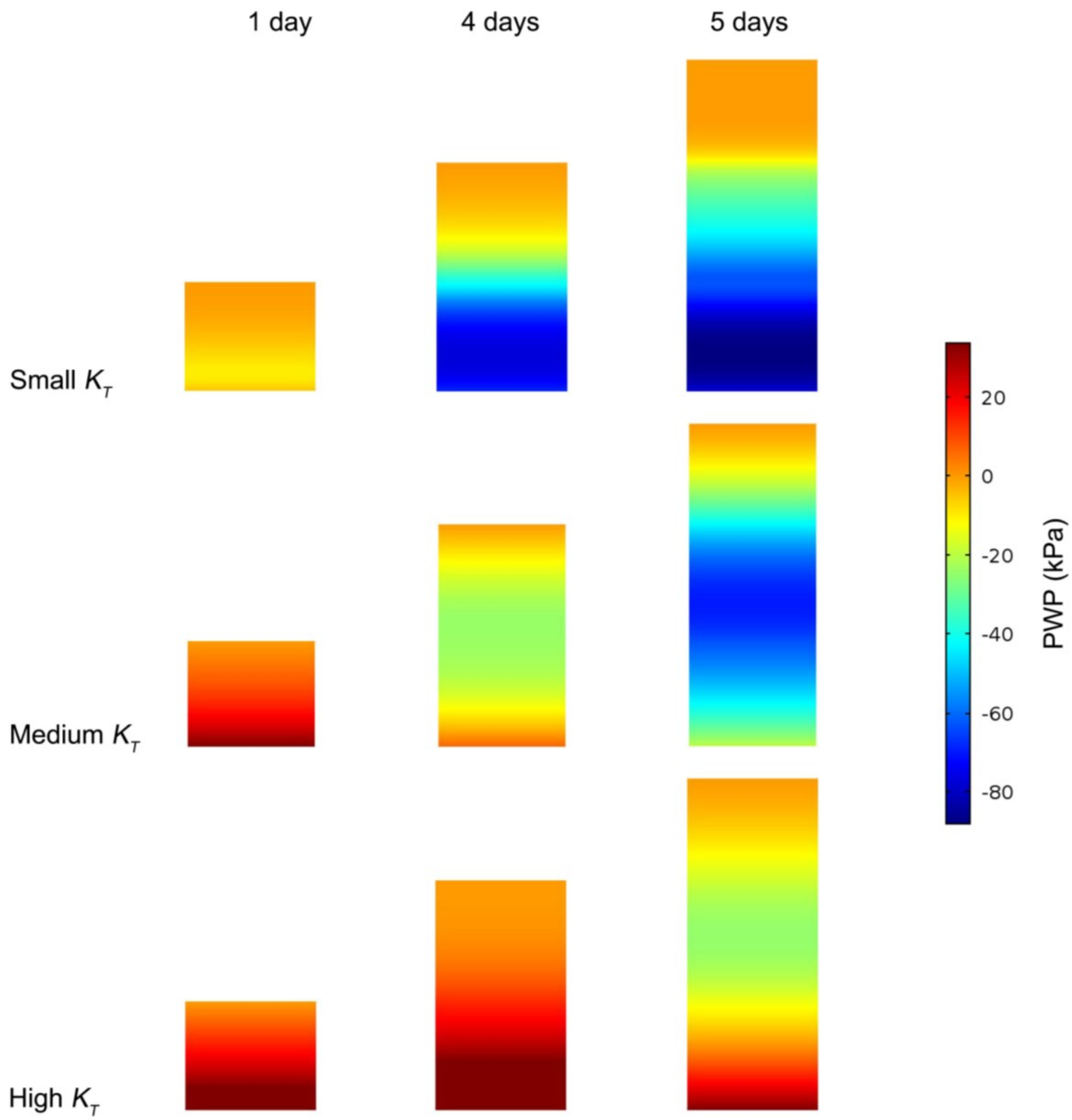

Figure Appendix D. 1. Effects of tailings on the changes in PWP

APPENDIX E: Procedures and recommendations of model implementation in COMSOL Multiphysics for CTB simulation

Details on COMSOL Multiphysics can be found in (Comsol 2015). Here, the general process of model implementation in COMSOL Multiphysics and recommendations on CTB simulation are provided.

1. Define constant parameters and variables

In multiphysics simulation, the relevant models may contain a large number of model coefficients and functions. To avoid the input of complex equations into the PDF/physics interface builder, the associated constants and predictive functions can be respectively defined in the parameter and variable nodes under the model tree. Then, the defined parameters and variables can be directly applied into the following nodes and physics interfaces. It should be noted that the dependent variables (e.g., stress, PWP and temperature) from the physics interfaces cannot be used to define parameters and variables.

2. Create geometry models

To define the geometry model, there are two options: (1) the geometrical objects (including 1D, 2D and 3D models) can be directly created in COMSOL, or (2) the geometry files from other drafting software (e.g., AutoCAD and SolidWorks) can be imported into COMSOL. The key point at this stage is to deal with the interface of different geometric entities. For example, if the stope and drawpoint domains are represented by two rectangles, the resultant interface between the two geometries should be defined as a union entity. However, when the surrounding rock domain is needed, the interface between the CTB and rock mass must be defined as an assembly entity which can allow relative displacement between CTB/rock mass interface.

3. Specify material properties (constants or predictive functions)

The definition of material properties is similar to that of constant parameters and variables. The relevant predictive function for each CTB material property can be defined in this node. Moreover, it should be noted that there is a default material library in COMSOL which provides a series of referenced property functions or constants. By making amendments to the material library, the properties of the rock mass, pore water and pore air can be specified quickly.

4. Implement mathematical models into PDF interface builder

The PDF interface is the core component of model implementation in COMSOL, which requires the input of balance equations and constitutive relations, and recalls the pre-defined parameters, variables and material properties into the PDF interface. There are two options for the development of the PDF interface including physics-based and equation-based modeling with PDF interface. The former requires users to implement the numerical model based on physics laws, while the latter requires users to input the model from a purely mathematical viewpoint. Take the implementation of energy balance equations as an example, the physics-based method is required to input all forms of heat transfer (i.e., heat advection due to the pore fluid flow, heat conduction due to the temperature gradient (Fourier's law) and heat generation (sink or source term)) into the PDF interface. Therefore, each step of the model implementation in a physics-based PDF interface has a specific physics meaning. However, equation-based modeling with the PDF interface deals with all balance equations and constitutive relations in the same way regardless of the difference in their physics meaning. Specifically, all balance equations can be expressed in the form of a second order non-linear partial differential equation (second order is due to the existence of divergence of gradient of scale qualities such as temperature and PWP, and non-linear is attributed to the time-dependent characteristics of PDF coefficients). Apart from the temporal and spatial derivative terms in a balance equation, the source (e.g., heat generation due to binder hydration) or sink (pore-water consumption caused by binder hydration) term should be recalled from the predefined variable node.

5. Define boundary conditions and initial values

For simulation of CTB, the adopted boundary conditions mainly consist of (1) Dirichlet boundary conditions such as the temperature, PWP, and fixed constraint conditions, and (2) Neumann boundary condition such as the mass flux boundary applied on the barricade structure to simulate water drainage. Compared to the boundary conditions, the initial values are used to specify the starting point of the dependent variables in a given domain such as the magnitude of the initial stress and rock mass temperature.

6. Mesh division and boundary selection

The meshing method in COMSOL is similar to that used in other numerical simulation software. The key issue at this stage is related to the selection of contact boundary elements, and the associated meshing method. First, the existence of an assembly boundary (i.e., the interface of CTB/rock mass) in the geometry model causes the contact boundary lines (for 2D cases) or surface (for 3D cases) to overlap each other, which makes the contact element selection and related specification of boundary conditions very difficult. To overcome the problem, an alternative is to show the labelling of the boundary elements with an element number. Then, the corresponding boundary can be directly selected by its element number. Additionally, to improve the stability of the simulation of contact, the contact boundaries of the rock mass should have increased thickness as opposed to those of the CTB mass.

7. Solver configurations

For the solver configuration, the major task at this stage is to improve convergence rate and solution accuracy, which is related to the analysis of the convergence criterion. To satisfy the convergence requirements, the approximate relative error (i.e., the absolute value of the difference between the current and previous solutions) must be less than the relative tolerance which can be specified in the solver node. Therefore, if the relative tolerance is increased, it becomes easier for numerical calculations to reach convergence. However, the cost is reduced accuracy. Moreover, due to the substantial changes in the CPB properties and behaviors at the very early ages, smaller time-steps should be adopted for simulation of the very early ages, and then gradually increased with curing time. Meanwhile, to strictly follow the specified time-step size, the set-up of the steps taken by the solver should be switched from “free” to “strict” in the time-dependent solver node. However, it should be noted that although smaller time-steps and lower relative tolerance may improve the simulation convergence and accuracy of the solution, the corresponding calculation time will also substantially increase.

References

Abdul-Hussain, N., and Fall, M. (2011). "Unsaturated hydraulic properties of cemented tailings backfill that contains sodium silicate." *Eng. Geol.*, 123(4), 288-301.

Comsol (2015). "Comsol Multiphysics 5.1." <http://www.comsol.com>. (Sept. 20, 2016).

Ghirian, A., and Fall, M. (2013). "Coupled thermo-hydro-mechanical-chemical behaviour of cemented paste backfill in column experiments. Part I: physical, hydraulic and thermal processes and characteristics." *Eng. Geol.*, 164, 195-207.

Qiu, Y., and Sego, D. (2001). "Laboratory properties of mine tailings." *Can. Geotech. J.*, 38(1), 183-190.

Salager, S., Rizzi, M., and Laloui, L. (2011). "An innovative device for determining the soil water retention curve under high suction at different temperatures." *Acta Geotechnica*, 6(3), 135-142.